Cardiff University

School of Chemistry

Element Specific Smart Media for Fast, Low Cost, Radionuclide Analyses

Thesis Submitted for the Degree of Doctor of Philosophy by:

Danielle Amber Merrikin

July 2021

CARDIFF UNIVERSITY

SCHOOL OF CHEMISTRY

ABSTRACT

DOCTOR OF PHILOSOPHY

Element Specific Smart Media For Fast, Low Cost Radionuclide Analyses

By Danielle Amber Merrikin

Analysis of low-level waste (LLW) within the nuclear industry is currently constrained by the use of environmentally unfriendly and toxic scintillant cocktails, time-consuming work-ups and high sample disposal costs. The work described herein hoped to address these issues *via* development of analysis utilising the Scintillation Proximity Assay (SPA).

Chapter 1 introduces the theory and techniques underpinning the work presented in the rest of the thesis.

Chapter 2 describes the synthesis of a series of novel oxazoles with a range of photophysical properties suitable for use as secondary scintillants. Incorporation into oil-in-water microemulsions, a greener alternative to industry standards, showed that they were effective scintillants for the detection of Sr-90 and Ni-63, in some cases outperforming the industrially used secondary scintillant POPOP.

Chapter 3 describes the encapsulation of the oxazoles into polystyrene/silica core/shell particles suitable for use in SPA, with aqueous dispersions also shown to scintillate in the presence of Ni-63 and Sr-90.

Chapter 4 describes the surface functionalisation of the nanoparticles with TMS-EDTA and their subsequent scintillation efficiency. Although preliminary results showed that the scintillation efficiency was not greatly increased *via* the resultant closer proximity of the radionuclide to the bead, surface analysis confirmed sequestration of a range of metal ions. Thus the work described herein paves the way for further explorations of metal-specific chelator functionalisation, potentially leading to element specific sequestration and analysis from a complex mixture of radionuclides.

Chapter 5 describes the synthesis of rhenium(I) tricarbonyl complexes bearing novel oxazole-based ligands. The varied photophysical characteristics displayed by both ligands and complexes were studied in depth, with computational analysis used to further inform experimental observations.

Chapter 6 investigated the internal core-shell particle environment and hence its role in the photophysics of encapsulated dopants, *via* encapsulation of known lanthanide complexes with environment sensitive photophysical properties.

Acknowledgements

I would like to take this opportunity to thank Professor Simon Pope and Dr Ian Fallis for giving me the opportunity to pursue my PhD studies, as well as NNL, NDA and EPSRC for funding the work herein. I would also like to thank my industrial supervisor, Dr Simon Woodbury, for your continued support, encouragement and insight throughout my PhD.

Thank you also to all those at NPL, especially Dr Hibaaq Mohamud, who not only carried out vital scintillation experiments for my PhD, but also allowed me the opportunity to visit the laboratories and gain insight into how the results were obtained. You made me feel incredibly welcome and provided a wealth of information which immensely helped in the analysis of my data. Thanks also goes to Dr Tom Davies who both trained and provided guidance in the use of the FEG-SEM equipment. Thank you to Dr Ben Ward for being a supportive mentor as well as both carrying out, and teaching me to run, DFT calculations.

A special thanks goes to everyone, both administrative and technical, who has kept The School of Chemistry running, particularly Simon James, James Griffiths, Rob Jenkins, George Summers and both the late Moira Northam and Rob Ashton, who always provided help and support when things didn’t go exactly to plan. Your jokes, stories and kind words have got me through many a stressful situation and for that I thank you.

As many people know, it is the friends and colleagues that you spend your days with that make life as a PhD student enjoyable even in the most difficult times. For that reason I would like to say thank you to everyone in the Inorganic Department, especially Dr Kaitlin Phillips, Owaen Guppy, Chris Elgar, and Nimai Mehta for your friendship and support.

Above all, I would like to take this opportunity to say thank you to my parents, Sue and Roy Merrikin, who have supported me throughout the entirety of my education and have always encouraged me to chase my dreams. Your unwavering encouragement, support, and your ability to see the best in me, even when I can’t see it myself, has made me the woman I am today and I will always consider it a gift that I have parents such as yourselves. No matter how far away we are, no matter the time of day, you have always been there with words of wisdom, advice, and support, and for that I am eternally thankful.

I would also like to thank my partner, Dr Ryan Dean, for supporting and encouraging me over the last four years. Throughout the good and the bad you have always been there, listening to my ramblings, supporting me, offering advice and always knowing when emergency thesis writing chocolate was required.

I would like to thank my cats, Nano and Dave, who have been my constant companions over the last year, providing cuddles during many late nights and early mornings of thesis writing. Music has always been a large part of my life, and so I would also like to thank Thunder, Def Leppard, Dolly Parton and Taylor Swift for providing the ultimate backing tracks for weekend and evening writing sessions, almost always leading to impromptu dancing and singing.

“We must have perseverance and above all confidence in ourselves”

Marie Curie

“We cannot direct the wind, but we can adjust the sails.”

Dolly Parton

Table of Contents

5 Photophysical Investigations into Rhenium Tricarbonyl Complexes of Functionalised 2-Pyridyl Oxazole Ligands 235

Table of Figures

Table of Tables

Table of Equations

Abbreviations

Techniques

ADF	Annular Dark Field
ASAP	Atmospheric Solids Analysis Probe
BF	Bright Field
BSE	Backscattered electrons
CCD	Charge-Coupled Device
CRT	Cathode Ray Tube
DFT	Density Functional Theory
EDAX	Energy-Dispersive X-ray Analysis
EDX/EDS	Energy Dispersive X-ray Spectroscopy
EI	Electron ionization
ES	Electrospray ionisation
FAAS	Flame atomic absorption spectroscopy
FEG	Field Emission Gun
FEG-SEM	Field Emission Gun Scanning Electron Microscope
FT	Fourier Transform
HR	High Resolution
ICP-MS	Inductively Coupled Plasma Mass Spectrometry
ICP-OES	Inductively Coupled Plasma Optical Emission Spectroscopy
ICP-QQQ	Inductively Coupled Plasma Triple Quadrupole
IMAC	Immobilised Metal Affinity Chromatography
IR	Infra-red
LR	Low Resolution
LSC	Liquid Scintillation Counting
MP-AES	Microwave Plasma Atomic Emission Spectroscopy
MRI	Magnetic resonance imaging
MS	Mass Spectrometry
NMR	Nuclear Magnetic Resonance
PCM	Polarised Continuum Model
PMT	Photomultiplier Tube
RIA	Radioimmunoassays
SATs	Suspension Array Technologies
SCRF	Self-Consistent Reaction Field
SE	Secondary electrons
SEM	Scanning Electron Microscopy
SERs	Surface-Enhanced Raman scattering
SPA	Scintillation Proximity Assay
SR-FTIR-SM	Synchrotron Radiation–based Fourier-Transform Infrared Spectro-microscopy
STEM	Scanning Transmission Electron Microscopy
TD	Time-Dependent
TDA	Tamm-Dancoff Approximation
TEM	Transmission Electron Microscopy
TGA	Thermogravimetric analysis
UV-Vis	Ultraviolet – Visible
XPS	X-ray photoelectron spectroscopy

Photophysical Terms

CIE	Commission Internationale de l'Eclairage (International Commission on Illumination)
ET	Energy Transfer
FRET	Förster or fluorescence resonance energy transfer
HOMO	Highest Occupied Molecular Orbital
IC	internal conversion
ICT	Intramolecular Charge Transfer
IL	Intraligand
ISC	Intersystem Crossing
LC	Ligand Centred
LMCT	Ligand-to-Metal Charge Transfer
LUMO	Lowest Unoccupied Molecular Orbital
MLCT	Metal-to-Ligand Charge Transfer
MLLCT	Metal-to-Ligand-to-Ligand Charge Transfer
PET	Photoinduced Electron Transfer
S	Singlet
SBLCT	sigma bond-to-metal charge transfer
T	Triplet
TICT	Twisted intramolecular charge transfer
XLCT	X→diimine charge transfer

Physical Properties and Constants

δ	Chemical Shift
Γ	Rate of Radiative Decay
ε	Extinction Coefficient
η_{sens}	Sensitisation Efficiency
λ	Wavelength
v	Frequency
σ	Energy barycentre of a transition
τ	Lifetime
ϕ	Quantum yield (also given as Q)
χ	Lorentz local field correction
Ω_J	Judd-Ofelt Intensity Parameter

$A_{0\rightarrow J}$	Coefficient of spontaneous emission
$A_{MD,0}$	Spontaneous Emission Probability
A	Interaction strength per unit area between the respective components in a microemulsion
C	Concentration
CMC	Critical Micelle Concentration
E	Energy
$\hbar$	Reduced Plancks Constant
I	Intensity
IC_{50}	Half-maximal inhibitory concentration
K	Decay rate (also given as A in Judd-Ofelt theory)
k_q	bimolecular quenching constant
K_{SV}	Stern-Volmer constant
L	Path length
$\log K_f$	stability constant
m/z	mass to charge ratio

N_A	Avogadro’s constant
n_o	Refractive index
$S_{0\rightarrow J}$	Area under emission peak
pK_{sol}	Solubility product
Q	Number of water molecules in the local coordination sphere of a lanthanide ion
R	Winsor Ratio
R_0	Förster distance

J	Total Angular Momentum
S	Spin Angular Momentum
L	Orbital Angular Momentum

$\{^1H\}$	Proton Decoupled
s	Singlet
d	Doublet
t	Triplet
m	Multiplet

app	Apparent
br	broad
fac	facial
nr	Non-radiative
Obs	Observed
rad	Radiative
sh	Shoulder
abs	Absorption
em	Emission
ex.	Excited at
ea	Excitation acquisition
vibr	vibrational

Chemicals

AA	Acetylacetone
AaRS	aminoacyl-tRNA synthetase
AcN	Acetonitrile
AIBA	2,2'-Azobis(2-methylpropionamidine) Dihydrochloride
AIBN	2,2′-Azobis(2-methylpropionitrile)
APTES	(3-aminopropyl)triethoxysilane
ATP	Adenosine Triphosphate
BBQ	7H-benzimidazo[2,1-a]benz[de]isoquinoline-7-one
BHHT	4,4’-bis(1”,1”,1”,2”,2”,3”,3”-heptafluoro-4”,6”-hexanedion-6”-yl)-*o*-terphenyl
Bis-MSB	1,4-bis(2-methylstyryl)benzene
BSA	Bovine Serum Albumin
Bpy	2,2’-bipyridine
BuOH	Butanol
Butyl PBD	2-[4-biphenylyl]-5-[4-tert-butylphenyl]-1,3,4-oxadiazole
$CHCl_3$	Chloroform
COD	1,5-Cyclooctadiene
CPTES	(3-Chloropropyl)triethoxysilane
CPTMS	(3-Chloropropyl)trimethoxysilane
DBM	Dibenzoylmethane

DCM	Dichloromethane
DDMA	1,10-Decanediol Dimethacrylate
DIN	Di-isopropylnaphthalene
DIPEA	N, N-Diisopropylethylamine, Hünig's base
DMF	Dimethylformamide
DMSO	Dimethyl sulfoxide
DNA	Deoxyribonucleic acid
DPA	Diphenylanthracene
DPO	Diphenyl Oxazole
DTPA	Diethylenetriamine Pentaacetate
EDTA	Ethylenediaminetetraacetic acid
Et	Ethyl
EtOH	Ethanol
Gyr	Gyrase
HRP	Horseradish Peroxidase
IPrOH	Isopropanol
L	Ligand
LAB	Linear Alkyl Benzene
LDL	Low Density Lipoprotein
Ln	Lanthanide
M	Metal
MCM	Mobil Composition of Matter (mesoporous material)
Me	Methyl
MeOH	Methanol
MMA	Methyl Methacrylate
MPBI	2-(2-pyridyl)-N-methyl-benzimidazole
MTC	2-(Methacryloyl)ethyltrimethylammonium Chloride
NPB	*N,N'*-di-1-naphthyl-*N,N'*-diphenylbenzidine
NTA	Naphtoyltrifluoroacetone
OAc	Acetate
OTf	Trifluoromethanesulfonate
Ox	Oxazole
PAA	Poly(Acrylic acid)
PBO	2-(2-pyridyl)benzoxazole
PBT	2-(2-pyridyl)benzothiazole
PDADMAC	Poly(Diallyldimethylammonium) Chloride
PEG	Polyethylene Glycol
Phen	1,10-phenanthroline
PLA-PEG	Polylactide-Poly(ethylene glycol)
PLGA	Poly(Lactic-co-glycolic acid)
PMMA	Poly(methyl methacrylate)
POPOP	1,4-bis(5-phenyloxazol-2-yl) benzene
PPAR	Peroxisome Proliferator-activated Receptors
PPO	Poly(p-phenylene oxide)
Ppy	2-phenylpyridine
PS	Polystyrene
PS(Ox)@SiO_2	Oxazole Encapsulated Polystyrene Core, Silica Shell Particles
PVP	Polyvinylpyrrolidone
PVT	Polyvinyltoluene
PXE	Phenylxylylethane
Py	Pyridine
Py-benzoxazole	2-(Pyridin-2-yl)benzo[*d*]oxazole
Py-oxazole	2-(Pyridin-2-yl)oxazole
Py-oxazoline	2-(Pyridin-2-yl)-4,5-dihydrooxazole
Pyta	4-(2-Pyridyl)-1,2,3-triazole

Quinox	oxazoline-quinoxazoline ligand
RNA	Ribonucleic acid
SA	Streptavidin
SBA	Santa Barbara Amorphous (mesoporous material)
SiMPs	Silica Microparticles
SPOINs	Superparamagnetic Iron Oxide Nanoparticles
Tapy	1-(2-Pyridine)-1,2,3-triazole
tBu	tert-Butyl
TEA	Triethylamine
TEOS	Tetraethyl Orthosilicate
TETA	Triethylenetetramine
TFE	Trifluoroethanol
THF	Tetrahydrofuran
TMOS	Tetramethyl orthosilicate
TMS-EDTA	Tetramethylsilane-Ethylenediaminetetraacetic acid
TOPO	Trioctylphosphine oxide
TosMIC	Toluenesulfonylmethyl Isocyanide
TPB	1,1,4,4-tetraphenyl-1,3-butadiene
TPIP	(3-ethyl-2-(4'-triphenylamino)imidazo[4,5-f]1,10-phenanthroline)
TPM	3-(Trimethyoxysilyl) Propyl Methacrylate
tRNA	transfer Ribonucleic Acid
TTA	Thenoyltrifluoroacetone
X	Axial ligand, commonly halide

Units

°C	Celsius
Ci	Curie
cm^{-1}	Wavenumber
$CPSBq^{-1}$	Counts per Second per Becquerel
Da	Dalton
eV	Electronvolt
Gy	Grey
Hz	Hertz
JKg^{-1}	Joules per Kilogram
K	Kelvin
nm	Nanometre
ppm	Parts per million
s	Second
ms	Millisecond
µs	Microsecond
ns	Nanosecond

Miscellaneous

LbL	Layer-by-Layer
NPL	National Physical Laboratory
OLED	Organic Light Emitting Diode
SCoMPI	Single Core Multimodal Probe for Imaging

1 Introduction: Analytical Techniques for the Characterisation of Organic Fluorophores, Transition-Metal Complexes and Particles

1.1 Introduction

The work presented within this thesis is of two parts. The first part, presented in **Chapters 2-4**, is focused on the synthesis and in-depth photophysical characterisation of novel fluorophores, and their use as scintillators in both a novel scintillant cocktail based on an oil-in-water microemulsion, and core-shell nanoparticles, the latter of which are then functionalised.

The second part is the synthesis and characterisation of similar fluorophores as that synthesised in **Chapter 2**, and their use as ligands for the formation of novel rhenium(I) tricarbonyl complexes, as well as further investigation into the core matrix of the particles discussed in part one, using known lanthanide complexes as probes.

Therefore, the majority of the analysis discussed within this thesis is based upon both photophysical and material characterisation. For this reason, the following chapter focuses on an introduction to photophysics and materials characterisation methods, with the former including UV-vis and luminescence spectroscopy of organic and transition metal complexes, and the latter including scanning electron microscopy (SEM), scanning transmission electron microscopy (STEM), and energy-dispersive x-ray spectroscopy (EDX).

Scintillation counting and radioactive decay are also introduced, with the mechanism, scintillation counter configuration, current liquid scintillation cocktail components and the techniques role in the nuclear industry discussed.

1.2 Photophysics

1.2.1 UV-vis

UV-visible spectroscopy measures the absorption of light by a molecule that leads to excitation of an electron from a ground state to an excited state. Therefore, the energy separation between the respective states can be recorded.

For organic molecules, transitions can occur from σ, π, or n orbitals.[1] For transition metal complexes, “charge transfer” and d-d transitions are also observed (discussed in **Section 1.2.3.2**).

The Franck-Condon principle states that due to nuclei being far heavier than electrons, the excitation of the electron from the ground state to the excited state occurs much faster than that of nuclear motion.[2] **Figure 1.1** shows that due to the nuclear coordinates not changing, vibrational fine structure occurs in the absorption (and emission spectra) because the vibrational transitions have a range of different probabilities of occurring due to their associated wavefunctions. For example, in **Figure 1.1** there is a greater overlap between the ground state (v_0) and the v_2' excited state vibrational wavefunction, which leads to this transition having a larger probability of occurring than a transition to the v_0' state. However, a smooth curve is commonly observed over these transitions due to interactions between the sample and the neighbouring solvent.[3]

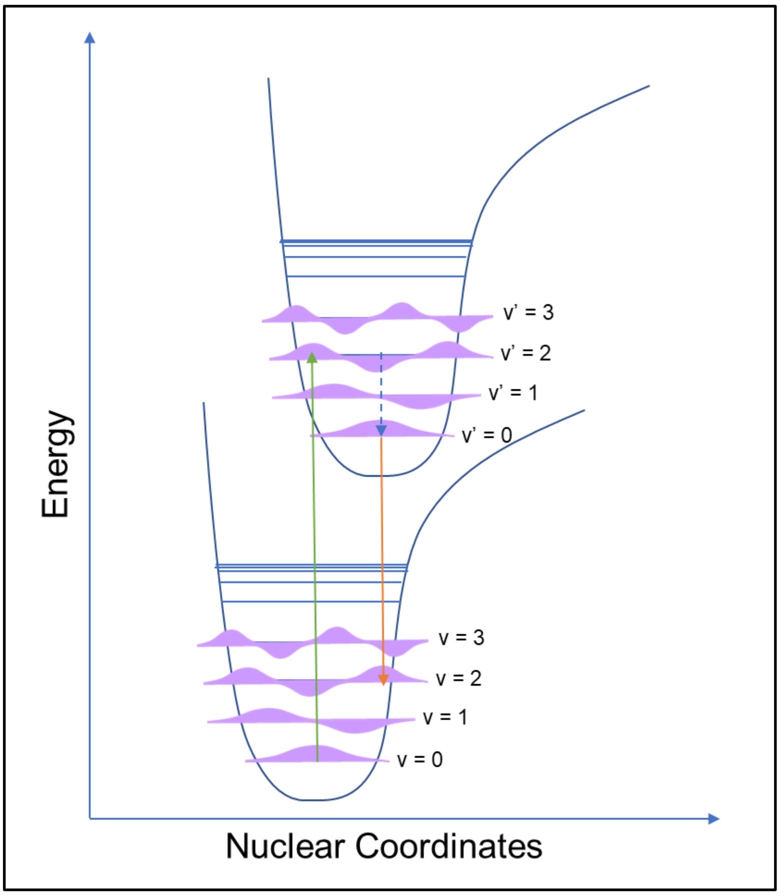

Figure 1.1 Schematic illustrating the Franck-Condon principle, with the electronic transition (green) and subsequent deactivation (dotted blue and orange).

The Beer-Lambert equation (**Equation 1.1**) relates the absorbance of the sample (A) to its concentration (c) using the molar extinction coefficient (ε), a constant for the molecule being studied regardless of concentration. The Lambert law states that the absorbance of the sample is independent of the source intensity, and Beer's law states that it is instead proportional to concentration.[3]

$$\log_{10}\frac{I_0}{I} = A = \varepsilon c l$$

Equation 1.1 Beer-Lambert Equation.

The intensity of the absorption is also related to how allowed the transition is to occur. For example, changes in multiplicity are forbidden and formally cannot occur (i.e. for a transition to occur, $\Delta S=0$ where S = spin quantum number),. However, these transitions can still be observed, albeit at low intensity (ε = 0-1000 $mol^{-1}dm^3cm^{-1}$).[1]

The solvent chosen in the measurement of a sample can have a large effect on the resultant absorption if the molecule exhibits solvatochromic properties. Molecules which have "donor" and "acceptor" regions, i.e. they undergo charge transfer upon excitation, have absorption (and emission) spectra that are extremely sensitive to the polarity of the solvent.[4] For example, polar solvents tend to cause a bathochromic shift (to longer wavelengths) in $\pi\rightarrow\pi^*$ transitions as the solvent can stabilise the dipole formed across the molecule upon excitation, and if hydrogen-bonding sites are then present as a result of excitation, they can also form hydrogen bonds.[4] These both stabilise the excited state, decreasing the transition energy. However, $n\rightarrow\pi^*$ transitions are shifted to shorter wavelengths as the ground state will have the larger dipole moment and will be more stabilised by the polar solvent. The solute-solvent complexes formed from hydrogen bonding also lead to a broader absorption, with fine-structure more commonly observed in non-polar solvents.[1]

1.2.2 Luminescence Spectroscopy

In 1845, Sir John Herschel observed a "beautiful celestial blue colour" when a solution of quinine sulphate was dissolved in water with tartaric acid (**Figure 1.2**) and held to the light.[5] Sir George Stokes would later, in 1852, define this phenomena as fluorescence[6] . The terms "fluorescence" and "phosphorescence" are used to describe the emission of light resulting in $\Delta S = 0$ and $\Delta S \neq 0$ respectively. Both of these terms are also described by the term luminescence.

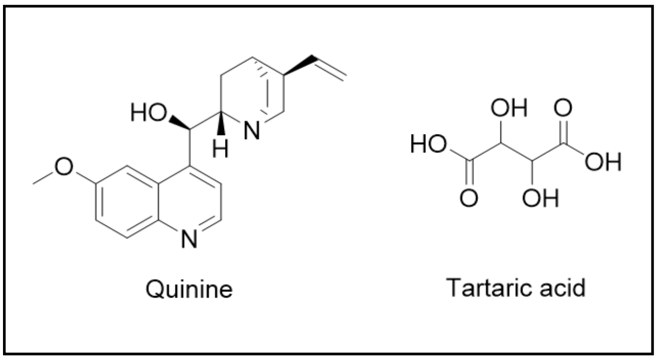

Figure 1.2 The first recorded observation of fluorescence was that of tartaric acid and quinine sulfate dissolved in water.[5]

As discussed, fluorescence is the emission of light where $\Delta S = 0$. The electrons in the excited and ground state are paired, and thus the transition back to the ground state is spin allowed, leading to short emission lifetimes (approximately 10 ns or less).[7] However, in phosphorescence, the electron in the excited state is not paired with that in the ground state, as they have the same spin, and therefore the transition to the ground state is formally forbidden. Although they are spin disallowed, the overall change in total angular momentum quantum number (J) is allowable, and thus these transitions still occur however at low probability and are characterised by longer emission lifetimes, frequently in the range of milliseconds to seconds.[7] These transitions are also more susceptible to quenching and non-radiative decay (discussed in **Section 1.2.2.5**), and thus are not always observed at room temperature or in solution.[7]

1.2.2.1 Jablonski Diagrams

In 1935, A. Jabłoński[8] published a schematic representation of the excitation and deactivation pathways of an electron, which is still widely used today.

The Jablonski diagram depicted in **Figure 1.3** helps to illustrate why some fluorescent species display evident fine structure in their emission spectrum. When excited, the electron is promoted into an excited vibrational state within the singlet level (which is the reasoning for fine structure sometimes observed in absorption spectra as discussed in **Section 1.2.1**), but then rapidly relaxes *via* internal conversion and vibrational relaxation to the lowest vibrational level. During deactivation the electron returns to the ground electronic state, however within this the electron can occupy one of the various vibrational states, thus forming vibrational fine structure in the emission spectra.[7]

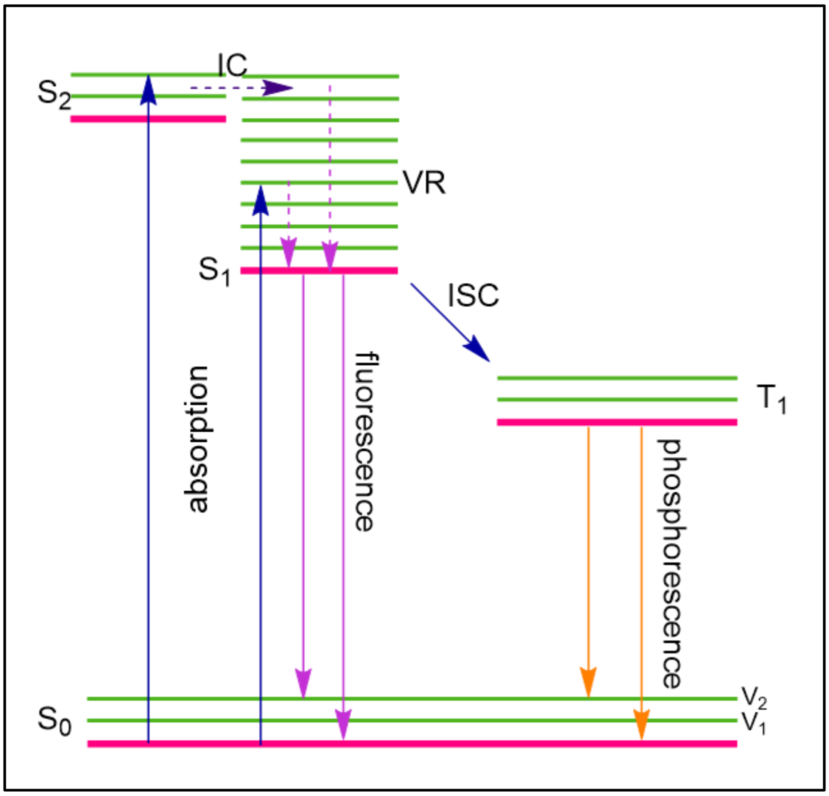

Figure 1.3 Jablonski diagram showing electronic transitions leading to fluorescence and phosphorescence, where ISC = intersystem crossing, IC = internal conversion and VR = vibrational relaxation. Adapted from *Principles of Fluorescence Spectroscopy*[7].

1.2.2.2 Stokes Shift

As briefly mentioned previously, Sir George Stokes first used the term “fluorescence” in 1852.[6] However it was also at this time that he observed, using quinine, that absorption occurs at a higher energy than emission, which is shown in the Jablonski diagram in **Figure 1.3**. The phenomena of internal conversion in the excitation process, and deactivation to higher vibrational levels in the ground state during emission, is the basis for this observation, called the Stokes Shift[6] (schematically represented in **Figure 1.4**). It should also be noted that further Stokes Shifts can be found in changes to the local solvent if the fluorophore displays Solvatochromic properties. If the, fluorophore in the excited state has a larger dipole than when in the ground state, the solvent molecules in polar solvents can reorient around the larger dipole, stabilising the excited state and thus lowering the energy of emission, leading to a larger Stokes shift.[7]

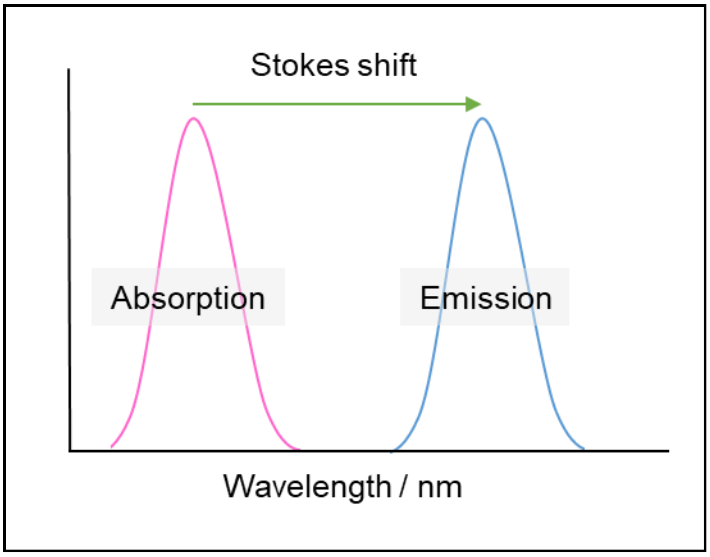

Figure 1.4 Schematic representation of the Stokes shift in an emission spectrum.

1.2.2.3 Kasha's Rule

Another phenomena that occurs as a result of internal conversion and vibrational relaxation in the excited state is that of Kasha's Rule.[9] In 1950, M. Kasha observed that the emission spectra is independent of the excitation wavelength,[9] which is easily explained by both the previous discussion and the Jablonski diagram in **Figure 1.3**. When an electron is excited to a higher electronic state, internal conversion occurs whereby excess energy is lost and the electron is situated in the lowest level of the excited state. Therefore, the electron will almost always relax to the lowest vibrational level of the electronic state, regardless of the excitation energy.

1.2.2.4 Luminescence Parameters

As well as the emission spectra, two further parameters are typically calculated to characterise a luminescent species; the quantum yield and emission lifetime.

The quantum yield is defined as the proportion of photons emitted from a luminophore, relative to those that were absorbed initially. Therefore, a luminophore with a higher quantum yield will emit more brightly than one with a low quantum yield. This parameter can be linked to the rate of deactivation, both *via* emission (radiative) and non-radiative, and is given by **Equation 1.2**.[7]

$$Q = \frac{k_r}{k_r + k_{nr}}$$

Equation 1.2 Calculation of quantum yield *via* the rate of radiative and non-radiative deactivation, where k_r and k_{nr} are the rates of emission and non-radiative decay respectively.

Quantum yields of novel luminophores can be measured *via* comparison to known standards. These standards, of which examples are presented in **Figure 1.5**, typically have high quantum yields. Phosphorescent species, due to the forbidden transition between the excited triplet and ground singlet state, typically have low quantum yields in aerated solution as the rate of non-radiative decay is far larger than that of radiative decay[7] This is because the radiative decay pathway is forbidden, and thus quenching (particularly *via* triplet oxygen in aerated solution[10]) and non-radiative decay are also likely to occur.

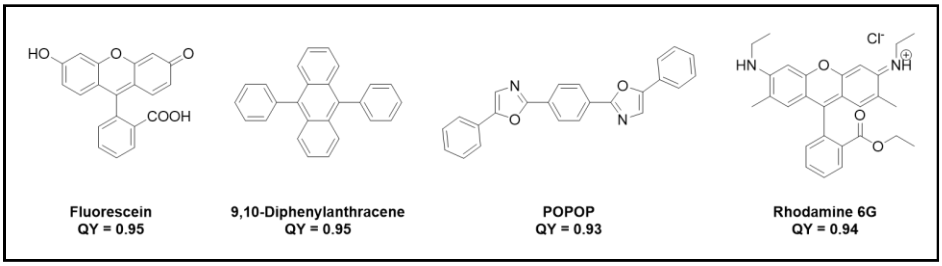

Figure 1.5 Examples of different quantum yield standards from (*left to right*) J. Brannon *et al*[11] (0.1M NaOH) , M. Mardelli *et al*[12] (cyclohexane), I. Berlman[13] (cyclohexane) and M. Fischer *et al*[14] (ethanol).

The emission lifetime is the time taken for an excited electron to return to the ground state, and can be represented by **Equation 1.3**.[7]

$$\tau = \tau_0 \times Q$$

Equation 1.3 Relationship between observed lifetime, τ, the intrinsic lifetime τ_0 and the quantum yield, Q.

τ_0 is the intrinsic emission lifetime, when only radiative deactivation processes are present, and can be given by **Equation 1.4**.[7]

$$\tau_n = \frac{1}{k_r}$$

Equation 1.4 The natural lifetime, τ_n, represents the time taken for an excited electron to return to the ground state in absence of non-radiative decay.

Scintillators, which are discussed in **Section 1.3** and **Chapter 2**, are known to possess short nanosecond lifetimes and large quantum yields.[15] 1,4-bis(5-phenyloxazol-2-yl) benzene (POPOP), a known scintillator, is also used as a quantum yield standard and is shown in **Figure 1.5**.

1.2.2.5 Quenching

As described previously, non-radiative decay from the excited state can occur due to quenching, whereby the intensity of the emission is decreased due to an external factor. This can take the form of collisional quenching, where the excited state is deactivated due to contact between the fluorophore and another molecule, or static quenching where the fluorophore being studied interacts with another molecule, and forms a non-fluorescent complex.[7] Oxygen[16,17], halogens[18,19] and electron deficient molecules such as acrylamide[20] are all common examples of collisional quenchers. In 1948, G. Weber[21] examined a variety of possible static quenchers, including the ability of hydroquinone to statically quench Rhodamine B and Eosine Yellow, with the structures presented in **Figure 1.6**. More recently, it has been shown that Rhodamine B can also be statically quenched by carbon nanotubes,[22] which can be used to characterise nanotube suspensions. As collisional quenching is related to the excited state, and static quenching to the ground state, the quenching involved in a system can be characterised by the emission lifetime, which static quenching does not affect.[23] Static quenching only occurs in the ground state, whereas dynamic quenching (such as Forster Resonance Energy Transfer (FRET) and Dexter electron transfer) is characterised by the fact that it occurs in the excited state.

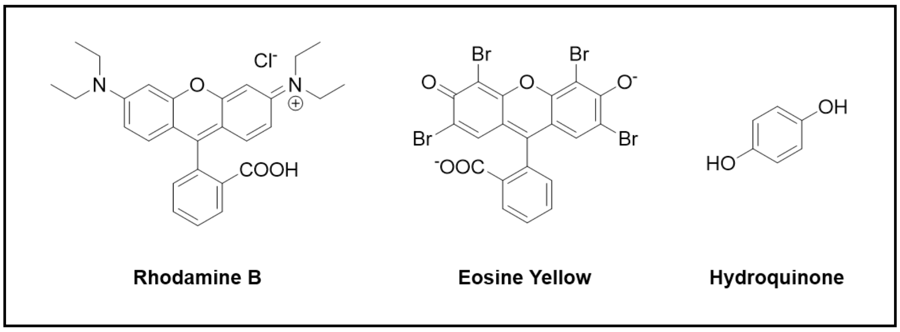

Figure 1.6 Hydroquinone was shown to be an effective static quencher to both Rhodamine B and Eosine Yellow.[21]

The Stern-Volmer equation effectively describes the effect of collisional quenching on the emission intensity of the fluorophore, and is presented in **Equation 1.5**.[24]

$$\frac{I_0}{I} = 1 + K_{SV}[Q] = 1 + k_q\tau_0[Q]$$

Equation 1.5 Stern-Volmer equation.

Where K_{SV} represents the Stern-Volmer constant, and is a measure of the fluorophore's sensitivity to Q, the quencher. k_q is the bimolecular quenching constant, and τ_0 is the lifetime of the fluorophore in the absence of the quencher.[24] A Jablonski diagram representing the quenching process is presented in **Figure 1.7**.

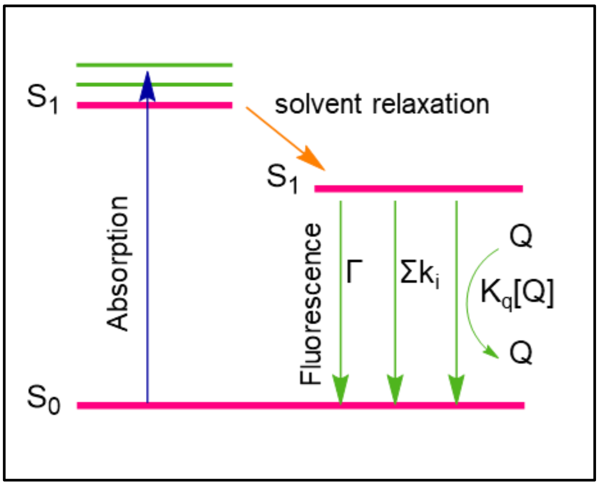

Figure 1.7 Jablonski diagram showing the radiative and non-radiative deactivation routes.Adapted from *Principles of Fluorescence Spectroscopy*[7].

1.2.2.6 Measurement of Spectra

1.2.2.6.1 Steady State *vs* Time-Resolved Measurements

Dependent on the information desired, two types of measurements can be undertaken; steady-state or time-resolved. Steady-state measurements are the most common, with the emission spectra described in the work herein all being steady-state measurements. In these measurements, the sample is observed under constant excitation, however decay in the emission intensity cannot be obtained *via* this measurement. In time-resolved studies, used in lifetime measurements, a pulse of light is used to excite the sample, and the decay in intensity is measured over time. This decay can be described by **Equation 1.6**, where I_0 is the initial intensity after excitation (at t = 0).[7]

$$I(t) = I_0 e^{-\frac{t}{\tau}}$$

Equation 1.6 Intensity decay over time, using a pulsed excitation source, where τ is the emissive lifetime of the sample.

The decay time can also be related to the intensity of steady-state emission (I_{ss}) by **Equation 1.7**.

$$I_{ss} = \int_0^\infty I_0 e^{-\frac{t}{\tau}} dt = I_0 \tau$$

Equation 1.7 Steady-state emission intensity can be related to the initial intensity by the emission lifetime.

1.2.2.6.2 Emission *vs* Excitation Spectra

Two types of luminescence spectra are used in the following work; emission spectra, where the intensity at each wavelength is measured when excited at a specific wavelength, and excitation spectra (explained below).

Excitation spectra measure the dependence of a specific wavelength in the emission spectra to each excitation wavelength.[7] In general, luminophores follow Kasha's rule,[9] and thus the excitation spectra are comparable to the absorption spectra of the molecule. In the work described herein, excitation spectra are used to investigate energy transfer between dopant and external matrix.

1.2.2.6.3 Spectrometer Set-Up

A simplified representation of a luminescence spectrometer is presented in **Figure 1.8**.

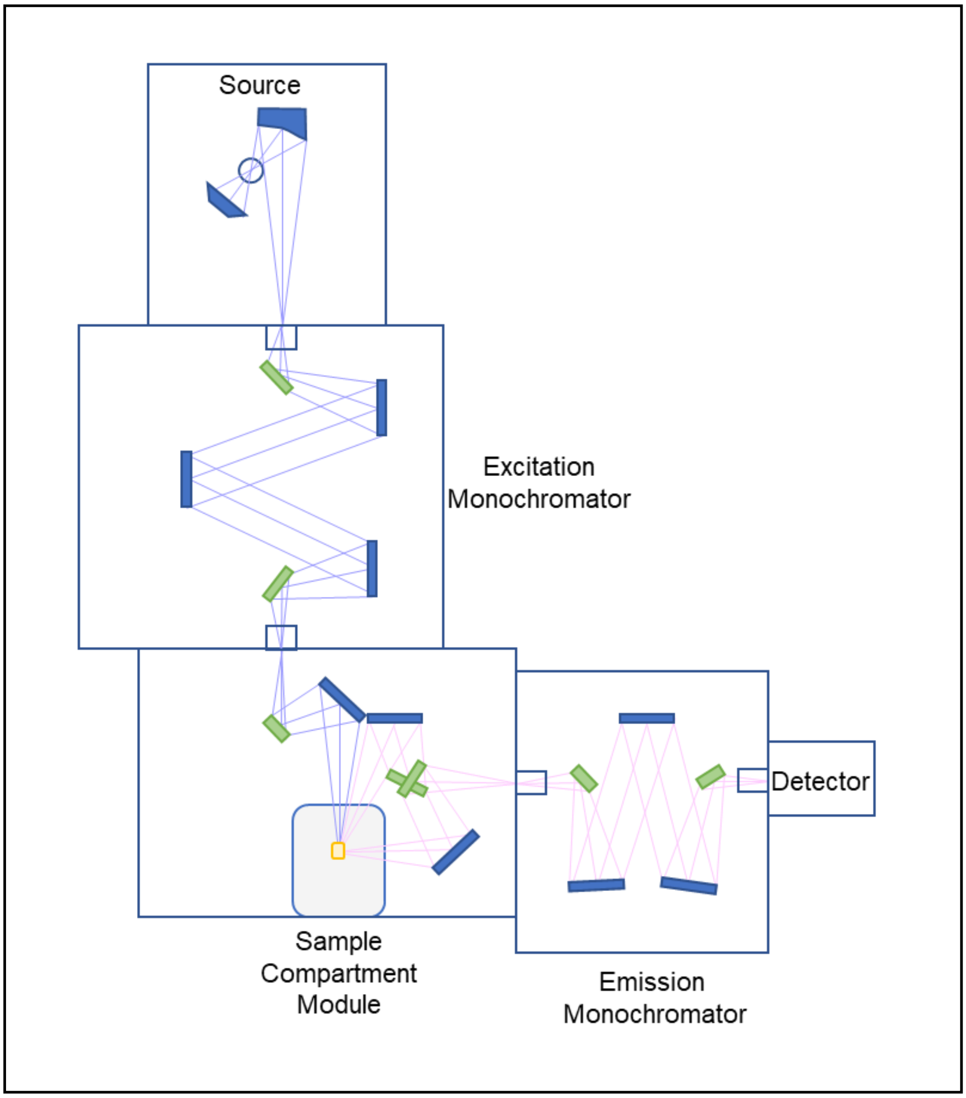

Figure 1.8 Simplified schematic representation of the luminescence spectrometer. Adapted from the Horiba Fluorolog-3 manual.[25] The spectrometer used in the work herein is based upon this set-up.

A xenon lamp is used to produce the excitation photons,[7] which are then filtered *via* monochromators in the excitation component of the spectrometer ensuring only a single wavelength of light reaches the sample compartment.[25] The sample is then excited by the incoming photons and deactivates, emitting light that is sequentially filtered across the wavelength range by the monochromator in the emission component of the spectrometer.[25] This allows the intensity at each wavelength to be detected and recorded by the photomultiplier tube.

1.2.3 Examples of Luminophores

1.2.3.1 Organic Fluorophores

Figure 1.5 shows well known examples of fluorophores used in the measurement of quantum yield, all of which are highly aromatic. The photophysical properties can be varied *via* increase in aromaticity, and introduction of electron withdrawing or donating substituents. Increasing the aromaticity across the fluorophore can bathochromically shift the emission wavelength, and thus the emission can be fine-tuned *via* intelligent design of the luminophore. An example of the effect of differing substituents can be found when comparing rhodamine dyes, shown in **Figure 1.9**.

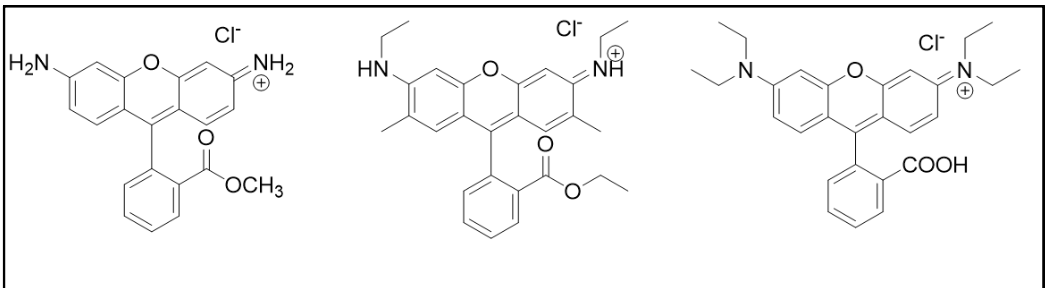

Rhodamine 123
λ_{em}= 534 nm

Rhodamine 6G
λ_{em}= 558 nm

Rhodamine B
λ_{em}= 568 nm

Figure 1.9 A range of different rhodamine dyes, showing how changes to substituents can alter the emissive wavelength.[26]

More recent examples of organic fluorophores are presented in **Figure 1.10**, displaying more complex fluorescence properties. A. Kundu *et al*[27] synthesised novel triphenylamine-benzothiazole derivatives (**Figure 1.10a**), showing twisted intramolecular charge transfer (TICT) between the triphenyl-amine and the benzothiazole groups. The fluorescence was temperature, pH and polarity sensitive due to the locally excited and TICT states, with emission ranging between

450 to 600 nm dependent on conditions. In polar solvents, acidic conditions, or high temperature, the TICT state was formed and the fluorophore showed weaker red-shifted fluorescence with longer lifetimes, however, in non-polar solvents an increase in intensity and blue shift in emission was attributed to the higher energy locally excited state. Y. Liu *et al*[28] followed on from this work, and synthesised a further novel triphenylamine-benzothiazole derivative for use as a cyanide detector (**Figure 1.10b**). Upon interaction with cyanide, emission intensity increased drastically at 484 nm, with a visible colour change from red to colourless, and a detection limit of 2.62x10^{-8} mol dm^{-3}, lower than the limit of cyanide allowed in drinking water.

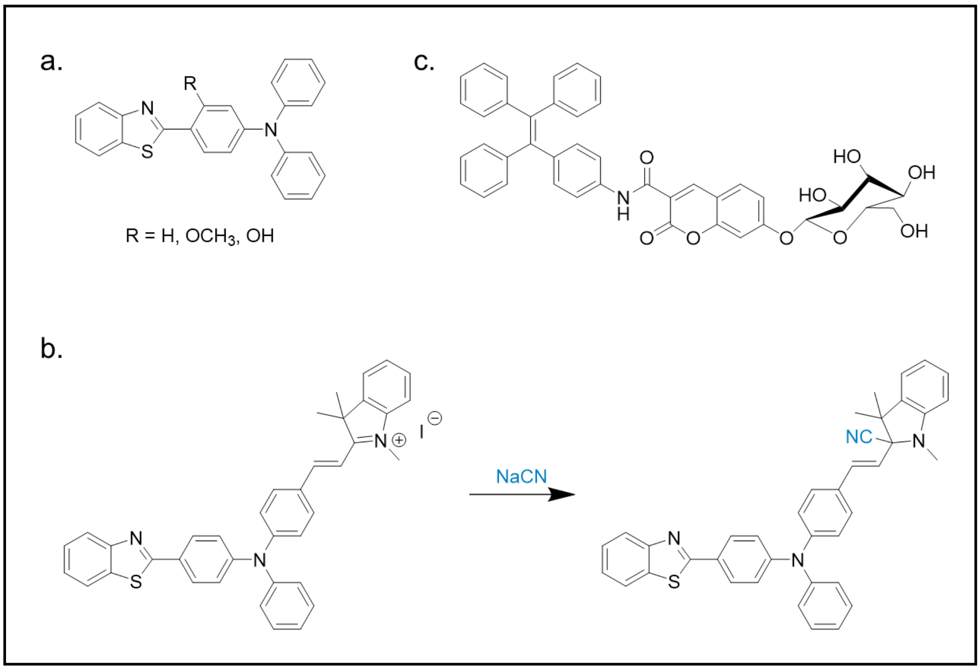

Figure 1.10 A range of novel fluorophores presented by A. Kundu *et al*[27] (a), Y. Liu *et al*[28] (b) and Y. Niu *et al*[29] (c).

Many of the fluorophores synthesised in this thesis display possible intramolecular charge transfer characteristics. A further modern example of charge transfer is provided by Y. Niu *et al*[29], in which a novel fluorescent probe suitable for β-galactosidase was synthesised (**Figure 1.10c**). The probe consists of tetraphenylethylene and coumarin fluorescent groups, coupled to a galactose group for enzyme recognition. The authors suggest that the tetraphenylethylene group quenches the emission due to TICT about the phenyl rings, however as tetraphenylethylene is known to exhibit aggregation induced emission, which has a high non radiative decay rate in solution, this is the more likely cause of the lack of fluorescence observed. When in the presence of β-galactosidase, the galactose group is cleaved leaving a hydroxyl moiety which is strongly electron donating. The electron donating hydroxyl group promotes intramolecular charge transfer across the fluorophore, leading to emission at 445 nm.

1.2.3.2 Transition Metal Complexes

In the work described herein, rhenium tricarbonyl complexes were synthesised with an interesting array of luminescent properties. Transition metal complexes are interesting luminophores due to their diverse luminescent properties, bought about by changes to ligands, geometry and the metal ion itself.[30] In the following section, the photophysical properties of those based on d^6 metal centres will be discussed.

When coordinated to ligands, the d-orbitals of the Re metal centre are split into two sets of degenerate orbitals, t_2 and e, with the six d-electrons filling the lower orbitals.[7] As shown in **Figure 1.11**, these are accompanied with the π and π* orbitals of the ligands forming a variety of electronic states. The electronic transitions in transition metal complexes are subject to selection rules which predict the probability of emission occurring from the resultant excited state. The first rule is that a transition must not cause a change in electron spin, therefore singlet→triplet absorption and triplet→singlet emission are forbidden.[1] The second rule, known as the Laporte rule, states that for a molecule possessing a centre of symmetry, transitions within the same set of orbitals (*i.e*. d→d) are forbidden.[7] Spin-orbit coupling and mixing of states can cause these formally forbidden transitions to take place,[30] as discussed below.

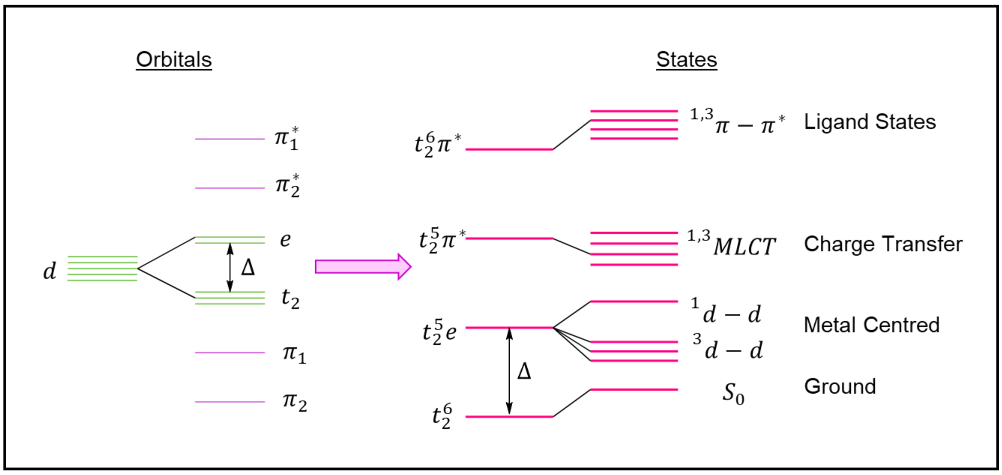

Figure 1.11 Schematic representation of orbitals, electronic energy levels and states involved in a d^6 transition metal complex emission. Adapted from J. Demas *et al*[30].

Metal-centred transitions involve the excitation of an electron from the t_2 to the e orbitals, and thus do not involve the coordinated ligands.[31] However, this transition is formally forbidden, and thus have long radiative lifetimes and can be easily quenched, leading to low quantum yields. As well as this, the e orbitals of the metal centre are antibonding with respect to the metal-ligand coordination bond, and thus the excited states formed are unstable.[30]

Metal-to-ligand charge transfer (MLCT) occurs when an electron in a t_2 orbital is excited into a ligand π* antibonding orbital. The MLCT transition can be used to analyse the redox properties of the complex, with the metal centre formally oxidised during the transition. Therefore, complexes with low lying MLCT states are more easily oxidised, with the MLCT states being greatly influenced by the metal ion.[31] **Figure 1.12** shows a simplified Jablonski diagram of the MLCT transition, whereby intersystem crossing (ISC) to the triplet MLCT state is fast, and results in deactivation from the triplet state. Although formally forbidden, phosphorescence occurs due to spin-orbit coupling with the heavy metal ion.[7]

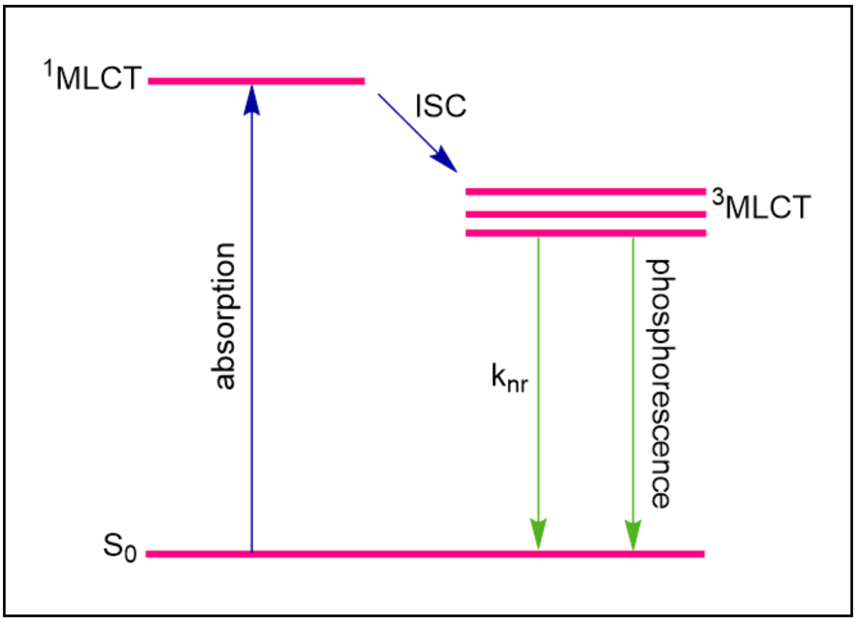

Figure 1.12 Jablonski diagram of the MLCT transition. Adapted from *Principles of Fluorescence Spectroscopy*[7].

Ligand-centred (LC) states involve the excitation of an electron in the ligand from a π to a π* orbital.[31] Spin-orbit coupling and mixing of the ligand-centred states with MLCT states can bring about ligand-centred phosphorescence.[30]

Ligand-to-metal charge transfer (LMCT) occurs when an electron in a π-orbital of the ligand is excited into the e orbital of the metal.[31] This state is not shown in **Figure 1.11** due to the fact that diimine ligands (of which are the focus in this discussion) are easily reduced and thus only charge transfer from the metal to the ligand is observed.[30]

As mentioned previously, the diverse luminescent properties shown in transition metal complexes can be attributed to changes in ligands, the metal ion and the geometry.[30] This is due to the fact that these variables can all affect the ordering of the energy levels within the complex.

In **Section 1.2.2.3** it was stated that deactivation from the excited state to the ground state occurs at the lowest excited state due to internal conversion from higher states. This, paired with the fact that spin-orbit coupling from the metal centre leads to intersystem crossing to the triplet state, means that metal complexes deactivate from their lowest triplet state and thus phosphorescent emission arises.[30]

To prevent instability of the resultant complex, this therefore also means that the metal-centred state must be far above that of the charge transfer or ligand centred states. However, this can be brought about *via* changes in either the ligands coordinated or the metal centre to increase crystal field strength, Δ.[30] MLCT and LMCT states are affected by the redox abilities of the metal and ligands respectively, as mentioned earlier; the more easily oxidised and reduced the metal and ligands are respectively, the lower in energy the MLCT state is.[31] In the case of the energies of the ligand-centred states, these are predominantly derived from the ligands, with changes to the aromaticity and substituents having a marked effect.[30]

That being said, charge transfer and ligand centred states cannot be too low in energy due to the energy gap law, which states that non-radiative decay pathways are more efficient than radiative decay at lower energies.[30] To increase the likelihood of strong emission, spin-orbit coupling is required to be large so that radiative deactivation from the triplet state can proceed more than non-radiative decay, which can be achieved with heavier metals.[30]

The effect of ligands chosen on the resultant emission of the transition metal complex is demonstrated by a series of 2,2'-bipyridine (bpy) and 2-phenylpyridine (ppy) based iridium complexes presented **Figure 1.13**. Work by C. Lentz *et al*[32], using both photophysical and DFT analysis, showed that the excited state changes dependent on the ratio of Ir-C:Ir-N bonds, with the lowest excited state of [Ir(ppy)$_3$] being assigned to an ^{3}MLLCT state, as opposed to ^{3}LC for [Ir(bpy)$_3$]$^{3+}$. This is due to the relative sigma-donor ability of N *vs* C donors, with the latter being a stronger sigma donor to the metal centre[33] and thus increasing the electron density of the iridium(III) centre leading to it being more oxidizable.[34] Whereas for [Ir(bpy)$_3$]$^{3+}$, the electron density of the metal centre is comparatively low.

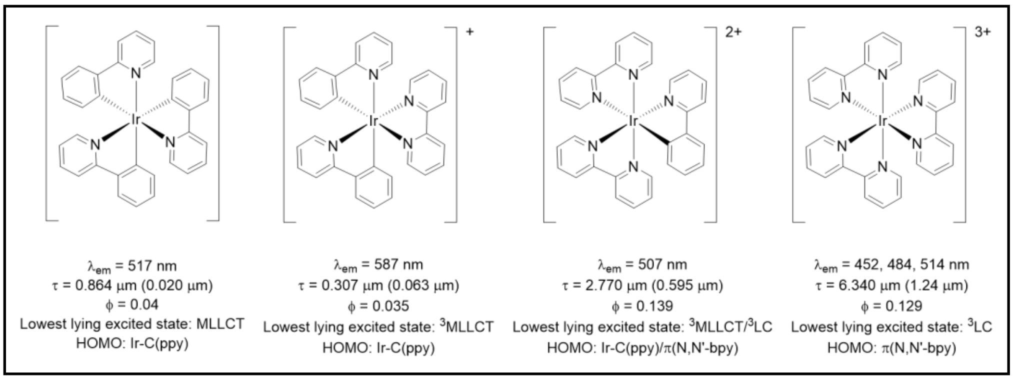

Figure 1.13 Series of iridium(III) complexes with differing ratios of ppy:bpy. Photophysical data obtained from C. Lentz *et al*[32], recorded in AcN. Lifetime measurements recorded under argon, those in brackets recorded in air.

As mentioned previously, the choice of metal centre also governs the photophysical parameters. Unlike $[Ir(bpy)_3]^{3+}$, $[Ru(bpy)_3]^{2+}$ and $[Os(bpy)_3]^{2+}$ (**Figure 1.14**) are both dominated by an ^{3}MLCT lowest excited state,[35,36] however $[Ru(bpy)_3]^{2+}$ has a much longer emissive lifetime than $[Os(bpy)_3]^{2+}$. This is due to the fact that $[Os(bpy)_3]^{2+}$ has a larger spin-orbit coupling effect owing to the fact that osmium, being in the 6th row of the periodic table, is larger than ruthenium (larger number of protons), and hence radiative deactivation from the triplet MLCT state is more allowed leading to a shorter emissive lifetime.

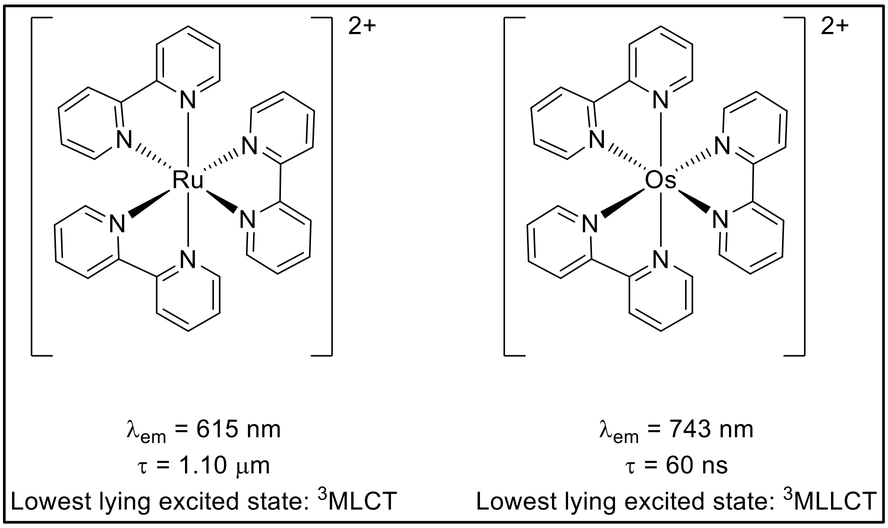

Figure 1.14 $[Ru(bpy)_3]^{2+}$ and $[Os(bpy)_3]^{2+}$, photophysical data obtained from A. Juris *et al*[35] and E. Kober *et al*[36] respectively.

1.3 Liquid Scintillation Counting and its role in the Nuclear Industry

The ability of certain organic fluorophores to emit light as a result of interaction with radioactive species was first discovered in the early 1950s.[37] This phenomena is the basis of liquid scintillation counting, a technique used for the detection of radioactive samples, having applications in biological (pharmaceuticals and medical), agrochemical and environmental research[38]. One of the main industrial uses, and the focus of the work herein, is that of monitoring low level waste produced in nuclear facilities. There are 93 nuclear reactors in Europe alone (including the UK), with 258 across the rest of the world, all of which rely on stringent local environmental sampling to ensure wider public safety.[38]

To understand the mechanism of scintillation and its use in environmental sampling, it is important to first understand the process of radioactive decay. When an unstable isotope undergoes radioactive decay, changes in the nucleus lead to the emission of particles or electromagnetic radiation. There are three types of emission products; alpha and beta particles, and gamma electromagnetic radiation. Although liquid scintillation counting can be used in the detection of alpha and gamma decay, for the purpose of the work described herein, only beta particles will be focussed upon.

Beta particles are high energy electrons, emitted with an antineutrino when a neutron is transformed to a proton, as shown in **Equation 1.8.** The combined energy of the emitted beta particle and neutrino is constant for the radioisotope, and therefore can be used in the detection of radioisotopes.

$$n \rightarrow p^{+} + \beta^{-} + \overline{\nu_{e}}$$

Equation 1.8 Radioactive decay in which a neutron is converted to a proton, releasing a beta particle and neutrino.

When an isotope decays to a point where a stable isotope is formed, it will stop decaying, and therefore the total amount of radiation released can be quantified. The half-life of radiative decay is defined by Encyclopaedia Britannica as the "time interval required for the number of disintegrations per second of a radioactive material to decrease by one-half".[39]

This is a fundamental parameter in the nuclear industry when decommissioning power plants, as it can be used to calculate the amount of radiation left after a given time. In the work described here, the main focus has been on Sr-90 and Ni-63, which both pose different issues in the decommissioning of nuclear reactors.

Sr-90 is generated *via* nuclear fission, and thus environmental Sr-90 is mainly as a result of nuclear weapons testing and discharges from nuclear plants.[40] It is a pure beta emitter, having a high beta energy of 543 keV[41] and a half-life of 28.7 years, decaying to Y-90, which is also unstable but has a much shorter half-life of 64 hours. Due to there being such a large amount of Sr-90 produced in the fission process, and its reasonably long half-life, there are large quantities that are yet to be disposed of.[41] For example, 10 PBq of Sr-90 was released into the environment during the Chernobyl accident, predominantly in the near zone of the incident, making up 4-6 % of the total inventory.[42] 0.14 PBq was predicted to have been released into the atmosphere as a result of the Fukushima incident, with between

0.1-1 PBq released into the ocean until 2013.[43] Sr-90 is also highly toxic, and can accumulate in many systems such as milk, meat, vegetation and bone, as well as water. Sr-90 is therefore an ideal hard emitter (hard emitters are defined by their beta particle energy) to study, as the need to analyse it in waste streams is fundamental to the decommissioning of nuclear reactors due to the existence of such large deposits.[41]

Structural components of nuclear reactors, particularly the primary coolant system, contain stable Ni-62, which undergoes neutron activation during the fission process to give the unstable Ni-63 isotope.[44] Ni-63 has a long half-life of 100 years, decaying *via* beta emission (beta energy maximum 67 KeV) to stable isotope Cu-63,[41] and so outlives the life of a nuclear reactor (nuclear plants have a lifetime between 20-40 years).[45] As Ni-63 is formed inside the reactor, there is no way to decrease the inventory, and in fact the amount present increases linearly with reactor use.[44] Over 40 years, if a plant is operated at 80%, there would be approximately $1x10^6$ Ci of Ni-63[46] and so therefore it is an important radioisotope to measure at the end of the power plant's lifespan. Most Ni-63 found in the environment is in fact the result of the deconstruction of reactors[44] and is found in effluents from nuclear facilities[40], and so it was an ideal soft emitter (low beta energy) to study. Although other radioactive isotopes formed as a result of neutron bombardment of the stainless steel reactors include iron (Fe-55) and cobalt (Co-60),[44] these were not analysed in this study.

When conducting liquid scintillation experiments, the sample is first pre-treated *via* a series of steps detailed in **Section 1.3.3**. After the sample has been appropriately purified and concentrated, it is introduced to a scintillation cocktail to form a homogenous solution.[37] The scintillation cocktail primarily comprises organic fluorophores, known as scintillants, dissolved in a suitable aromatic solvent. If the sample is aqueous, the cocktail may further comprise surfactants, however this is covered in more detail in **Chapter 2**, with particular examples from the leading manufacturers. The most important factors in the selection of cocktail components are toxicity, flash point and the ease of disposal.

The radionuclides in the solution decay, resulting in the emission of beta particles. These beta particles interact with the local solvent molecules, leading to activation of these solvent molecules which then leads to energy transfer to the scintillant fluorophores in the cocktail. The scintillant fluorophores are then excited, leading to fluorescence after deactivation to the ground state. The emission wavelength, and hence energy released, is dependent on the scintillator, however the intensity (i.e. number of photons detected, which is approximately 10 photons per keV of beta-particle decay energy) is dependent on the energy of the nuclear decay as this determines how many solvent molecules are excited initially.[37] The number of light flashes detected per unit time is related to the number of nuclear decays (i.e. the radioactivity of the sample).[37] Thus, it is important that the scintillant fluorophore absorbance overlaps well with the solvent emission profile, and the scintillant possesses a high quantum yield, so that the maximum number of photons are emitted.

1.3.1 Liquid scintillation Counter

A simple schematic of a liquid scintillation counter is shown in **Figure 1.15**, with the most important components highlighted. The detectors are photomultiplier tubes (PMTs), which convert the light photons emitted into an amplified electrical signal. The photons hit a photocathode in the PMT, producing photoelectrons which are then accelerated towards a positive dynode, amplifying the signal by the generation of secondary electrons. The PMT consists of a series of dynodes with increasing positive voltage, so that the secondary electrons are accelerated to each one, resulting in amplification of signal (**Figure 1.15**), with an amplification factor of $> 10^6$.[37]

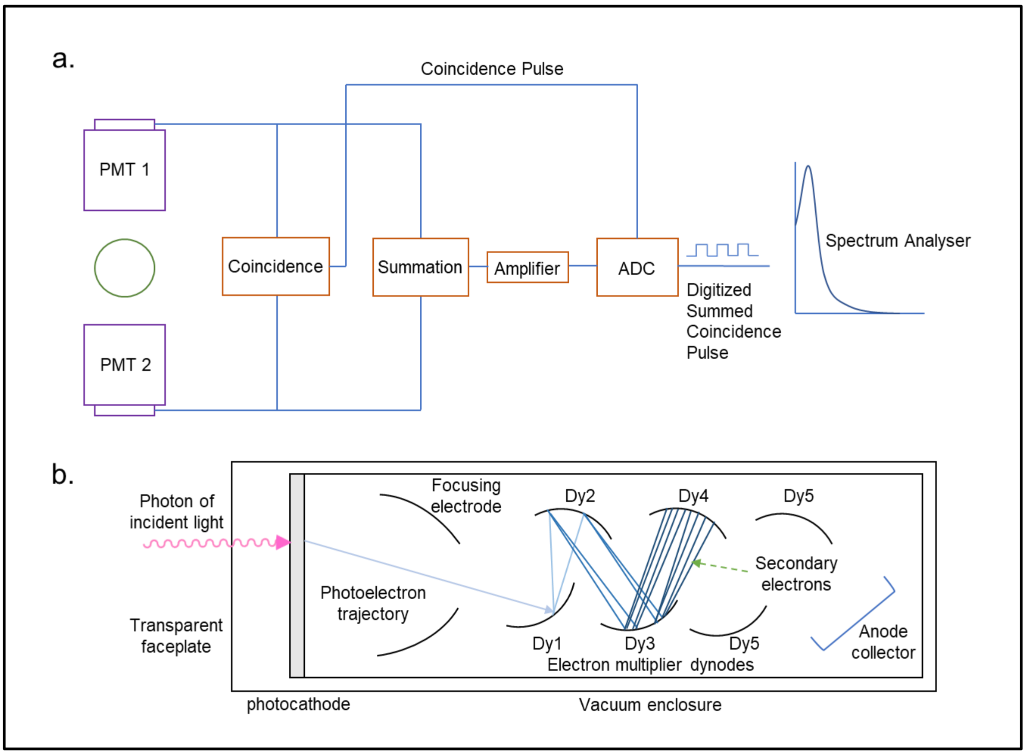

Figure 1.15 a) Schematic of Liquid Scintillation Counter; **b)** Schematic of PMT detector. Both adapted from M. L'Annunziata[37].

Two PMTs are used, which allows distinction between background signal and true events. Background occurs in the 0-10 keV region and is predominantly due to the low work function of the photocathode and the amplification of any released electrons by the dynodes. However, if two PMTs are used, true nuclear events can be distinguished *via* the coincidence circuit connecting the PMTs. When a true nuclear event occurs, light is produced in all directions as the decay process leads to multi-photon events, as discussed in previously. The decay process is quick as scintillants typically have short emission lifetimes, therefore the coincidence resolving time between the two PMTs is set to 18 ns and if a signal is detected by both PMTs within this timeframe, it is registered as a true event. The signal that is registered as a true event is analogue, possessing a pulse height that is proportional to the nuclear decay energy.[37]

The summation circuit "sums" the intensity of the two coincident signals to produce a single signal, which increases the signal-to-noise ratio. Summing the two signals also compensates for the difference in distance between the position of the decay event in the vial and the two PMT detectors. For example, if the photons are emitted near the edge of the vial, the PMT closer to that edge will register a brighter flash than that of the other PMT if the sample is coloured. However, if both the signals are summed the final signal is not affected.[37]

The signal is then amplified again, and then converted from an analogue signal to a number by the ADC (analogue-to-digital converter). The final digital pulses are then sorted based on this number, which either represents the pulse height (sorted *via* pulse height analysis) or the intensity (sorted *via* multichannel analysis). Pulse height analysis only counts pulses that fall between a set upper and lower limit to analyse an energy of interest and to reduce background interferences. The more common method however is multichannel analysis, which sorts the different pulse heights into a series of channels. This can be done linearly or logarithmically, with each channel either representing a linear increase of 0.5 keV of energy for the former, or plotted logarithmically in the latter.[37]

1.3.2 Liquid Scintillation Cocktail

Liquid scintillation cocktails are divided into two groups, those formulated from “classical” components, and those that utilise more environmentally friendly and less harmful components. They can also be divided into emulsifying cocktails and organic cocktails. Emulsifying cocktails, being more suited for aqueous samples, contain a solvent, surfactant and scintillator, whereas organic cocktails (also called nonaqueous cocktails) do not contain surfactant. These components will be discussed briefly here, with a more detailed account including safety regulations and examples of cocktails used today, in **Chapter 2.**

Regardless of classification, the solvent chosen in scintillation cocktails is aromatic, with a high density of π-electrons to allow efficient energy transfer. Examples in classical cocktails include pseudocumene, xylene and toluene, however due to their toxicity, flammability and vapour pressure they have been gradually replaced with “safer” solvents such as di-isopropylnapthalene (DIN), phenyxyylethane (PXE) and dodecybenzene (LAB) (**Figure 1.16**). These safer solvents have a low toxicity, high flash point and low vapour pressure, and in the case of PXE and DIN, both give an increased counting efficiency compared to cocktails containing classical solvents.

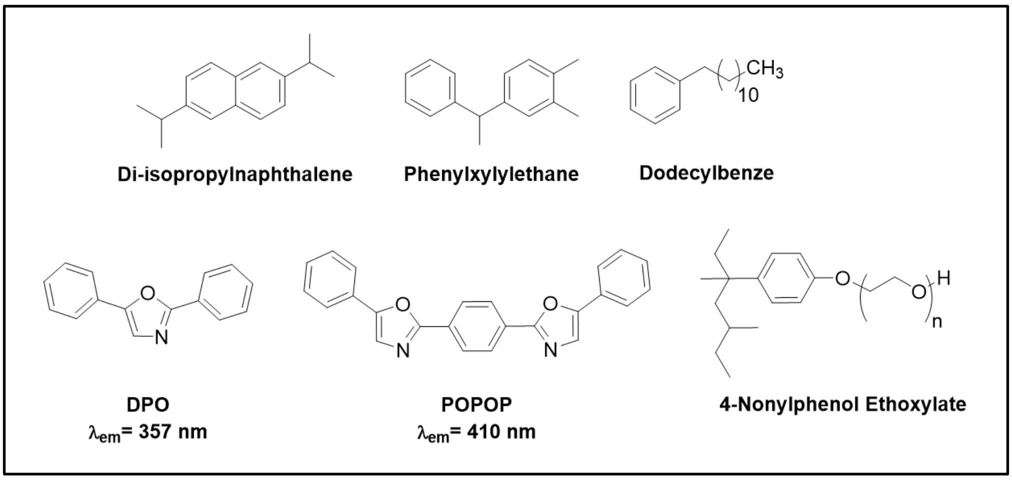

Figure 1.16 Common components of Liquid Scintillation Cocktails.

Scintillators in cocktails can be divided into two groups; primary and secondary. The primary scintillator interacts with the solvent molecules, leading to the first energy transfer. However, the emitted light from the primary scintillator is not within the sensitivity window of the scintillation counter PMT (>400 nm, particularly 420 nm). The secondary scintillator, or “wavelength shifter”, absorbs this light, and then emits at a higher wavelength which is detectable by the PMT. For efficient interaction between the primary and secondary scintillators, the secondary scintillants absorption profile must overlap with the primary scintillants emission profile, with the secondary scintillant having a large Stokes’ shift. Both scintillators require a high quantum yield (photon yield), short fluorescence lifetime, and low quenching sensitivity. Oxazole-based scintillants, particularly primary, are more commonly used, however there are other examples, discussed in more detail in **Chapter 2**. DPO and POPOP, two common oxazole-based primary and secondary scintillants respectively, are shown in **Figure 1.16**.

Despite energy transfer being more efficient in solvents with high density of π-electrons (organic aromatic solvents), most samples requiring analysis are aqueous in nature. Therefore, surfactants are required so that the aqueous phase can come into close contact with the organic phase, and thus allow energy transfer. This is called a “water-in-oil” microemulsion, wherein small droplets of water are dispersed in the organic solvent. There are four different classifications of surfactant; non-ionic, anionic, cationic and amphoteric. Both microemulsions and surfactants will be discussed in **Chapter 2**.

Although surfactants allow the introduction of an aqueous sample to an organic media, one of the disadvantages of the use of scintillation cocktails is that samples still require multiple-step purifications before introduction to the cocktail. The most popular surfactants, 4-nonyl-phenol-ethoxylates (**Figure 1.16**), which are present in over 57 different cocktails, are also incredibly toxic to the aquatic environment and are beginning to be restricted in use.[38,47] One of the more popular solvents, DIN, may also be subject to future restrictions due to it being a suspected bioaccumulator, despite being listed as a “safer” alternative.[38] Therefore, new media for scintillation that can replace these existing cocktails is paramount.

1.3.3 Sample Preparation

As discussed previously, radioactive samples require a series of purification steps for the sample to be appropriate for use in a scintillation cocktail. This is predominantly to separate other radionuclides in a complex mixture, or to remove organic components that may bring about chemiluminescence in the sample, and includes pre-treatment and preconcentration processes. Different radionuclide samples require slightly different preparation steps, and thus those for Ni-63 and Sr-90 will be discussed herein.

Waste samples of Ni-63 are predominantly liquid, including waste water and coolant water from nuclear power plants.[40] Pre-treatment of samples containing organic components first involves wet or dry ashing, and then leaching of the residue using hydrochloric or nitric acid which dissolves the individual elements, including nickel. The sample may then be concentrated to allow analysis, particularly with samples such as seawater. To remove other competing radionuclides, for example metal complexes such as iron hydroxides, ammonia is used with nickel remaining in solution. Nickel can also be precipitated using dimethylglyoxime, producing an insoluble Ni-DMG complex. DMG is also used as a chelator coated onto a solid support for resin extraction. These steps can be used individually or in combination dependent on sample, and also include liquid extraction, cation or anion exchange, and extraction chromatography. Multiple-steps are particularly needed for samples derived from nuclear wastes, as these contain mixtures of radionuclides that can mask the scintillant signal due to Ni-63.[40]

Sr-90 samples are typically water, soil, milk and bone among others. Sr-90 mimics calcium and other alkaline earth elements which are more abundant in typical environmental samples, thus separation is challenging.[40] The main techniques used for Sr-90 preparation are precipitation, liquid-liquid extraction, ion chromatography and extraction chromatography. One method, called the "classical" method, involves ten precipitations; first calcium and alkali metals are removed by two nitric acid preparations, then yttrium and other fission products are removed *via* hydroxide precipitation, barium and radium are then removed by chromate precipitation, which is followed by a carbonate and nitrate precipitation before strontium is precipitated as a carbonate. This does not remove all of the ^{90}Y, and thus further precipitations are required to calculate the ^{90}Sr content from the combined ^{89}Sr, ^{90}Sr and ^{90}Y sample. A more recent, and now more used, method of ^{90}Sr purification involves the use of a Sr-specific resin in extraction chromatography. The resin is formed by dissolving [bis-4,4'(5')-tert-butyl-cyclohexano-18-crown-6] in 1-octanol and sorbing the solution onto a polymeric resin, however this still requires some pre-concentrating and precipitation steps before the sample is introduced to the column.[40]

Despite the purification and separation techniques described successfully leading to radionuclide characterisation, they rely on harsh conditions and the process, particularly for Ni-63, is time consuming. Although a similar method may be required for the oil-in-water microemulsion in **Chapter 2**, the use of functionalised particles of the like developed in **Chapters 3** and **4** would minimise the pre-treatment required, being specific for the radionuclide of choice and being less sensitive to other contaminants within the sample.

1.3.4 Quenching Pathways

Much like in luminescence spectroscopy, the intensity of the pulse of light recorded is dependent on the number of photons detected by the PMT detector, which is subject to various quenching mechanisms that can reduce the amount of photons that ultimately reach the detector. There are three main quenching pathways in liquid scintillation; chemical, ionization and colour quenching.[37]

Chemical quenching is caused by molecules in the sample solution which absorb the nuclear decay energy before it can be transferred to the solvent. This has two affects; reducing the number of light pulses and therefore reducing the number of counts recorded, and also decreasing the number of photons emitted, leading to a reduction in pulse height.[37]

Ionization quenching is the result of the interaction between a low energy beta particle and a high density of solvent molecules. Beta particles which exhibit a high linear energy transfer (LET) create a large number of excited solvent molecules. When the concentration of these excited molecules is high, the probably of forming super-excited solvent molecules is high (where two excited solvent molecules interact, with one transferring its energy to the other). This results in the scintillant molecule not being excited, resulting in a reduction in photon intensity and thus reduced count rate or reduction in pulse height. This is particularly relevant to low energy beta emitters such as tritium, as these exhibit high linear energy transfer compared to higher energy beta emitters.[37]

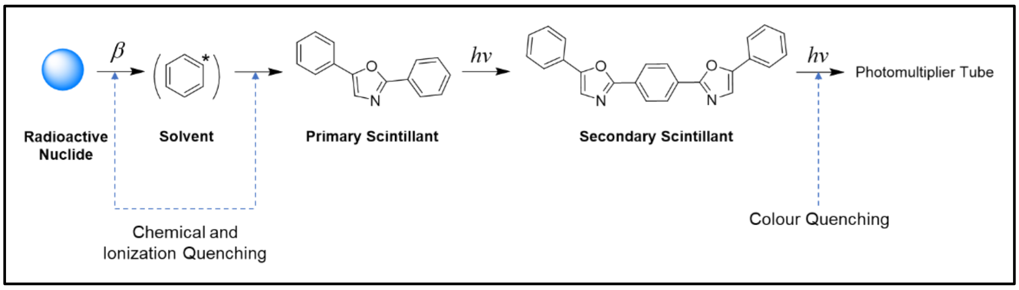

Figure 1.17 Schematic of scintillation mechanism, with occurrences of quenching identified. Adapted from M. L'Annunziata.[37]

Colour quenching occurs in coloured samples, whereby the sample absorbs the photons of light emitted before they reach the PMT detector. Colour quenching is rarely a problem encountered in liquid scintillation counting, as samples are predominantly colourless.[37]

Plastic scintillators, such as those discussed in **Chapter 3**, are prone to colour quenching due to the fact that they do not require the same level of separation steps that liquid scintillator cocktails require, and thus their advantage over liquid scintillation cocktails can lead to a coloured sample. However, as the fluorophore and solvent molecules are within the particles, plastic scintillators are not prone to chemical quenching.[37,48]

There are four main methods to correct for quenching in liquid scintillation counting; internal standard method, sample spectrum method, external standard method and direct DPM method.[37] However, as the results obtained in **Chapters 2-4** herein were not corrected for quench, it is not within the scope of this work and will not be expanded upon.

Although not a quenching pathway, both photoluminescence and chemiluminescence can lead to inaccurate counting if not controlled.[37] In scintillation counting “luminescence” refers to light emission due to energy absorption not originally from nuclear radiation (whereas “scintillation” originates from nuclear decay).

Photoluminescence occurs when the sample (including the cocktail) is in the presence of UV light. However, as the luminescence arising from the scintillants within the cocktail is typically short lived, photoluminescence within the sample can be circumvented by delaying the count start time as the scintillation counter is shielded from external light sources.[37] Thus, any photoluminescence that occurs will be before the counting starts.

Chemiluminescence is the emission of light as a result of a chemical reaction, and can occur when the cocktail is added to the radioactive sample. Examples include if the sample is basic (particularly in the presence of inorganic basis such as NaOH or KOH), or if it contains additives such as hydrogen peroxide. To prevent chemiluminescence, the samples can be kept in the dark as with the photoluminescence example, however stabilisation of count rate can take longer than photoluminescence. The sample can also be neutralised by adding acetic acid to the scintillation cocktail, or neutralising the radioactive sample, however these methods may cause precipitation of sample components. The temperature of the sample can also be modified to either push the chemical reaction to its end point, or to slow the reaction and thus reduce the counts from chemiluminescence. As well as this, there are scintillation cocktails, such as Insta-Fluor (a commercial cocktail by Perkin Elmer) which contain chemiluminescence inhibitors.[37]

For all luminescence events, the counting regions can be modified to detect and remove possible events as they occur in the low energy window. The coincidence circuit, discussed in **Section 1.3.1**, can also be modified to pick up all signals (as a result of luminescence and scintillation) and then only those as a result of luminescence by modification of the counting delay mode between the PMT detectors, and thus remove the luminescence signals from the final result.[37]

1.4 Characterisation of Particles

1.4.1 Electron Microscopy

Electron microscopy involves the use of an electron beam to analyse materials, both man-made and biological, by probing both surface structure and internal properties dependent on technique.

Electrons are classed as ionising radiation as they are able to transfer energy to electrons located both in the outer and inner shell of an atom, leading to their ejection from the material and observation by the microscope.[49] In fact, a variety of different processes can occur in a material upon electron irradiation, as depicted in **Figure 1.18**.

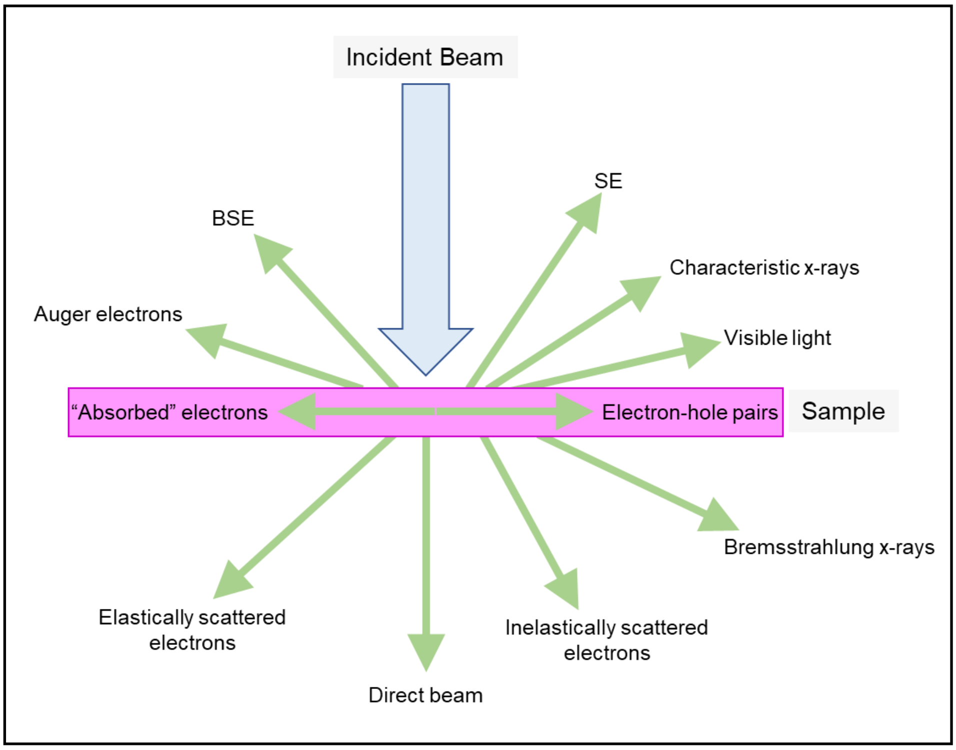

Figure 1.18 Schematic diagram showing the different processes that can occur within a sample upon irradiation with an electron beam. Adapted from *Transmission electron microscopy: a textbook for materials science*[49].

The techniques used in the work herein are described in the following sections, with SEM reliant on back-scattered and secondary electrons,[50] EDX utilising x-rays[51] and STEM involving the detection of electrons that have transferred through the sample[52].

1.4.1.1 Scanning Electron Microscopy (SEM)

In 1935, M. Knoll imaged silicon iron *via* electron microscopy, and thus the first image using an SEM spectrometer was created.[53] SEM can be used to probe and analyse the surface of a material, yielding information on the composition and crystallography as well as the topography.[50]

The technique relies on the detection of backscattered electrons (BSE) and secondary electrons (SE). Backscattered electrons are beam electrons that are scattered by the atomic electric fields in the sample, withholding the majority of their original energy (**Figure 1.19**)[50]. Secondary electrons are a lot weaker however, as these are electrons that originate from the sample as a result of interaction with the electron beam. The electron beam inelastically scatters in the sample (**Figure 1.19**), causing ejection of weakly bound electrons (in the valence or conduction band dependent on material) with low kinetic energies (<50 eV).[49,50] Due to their low energy, only those that are near the surface have enough energy to be ejected from the sample.[49]

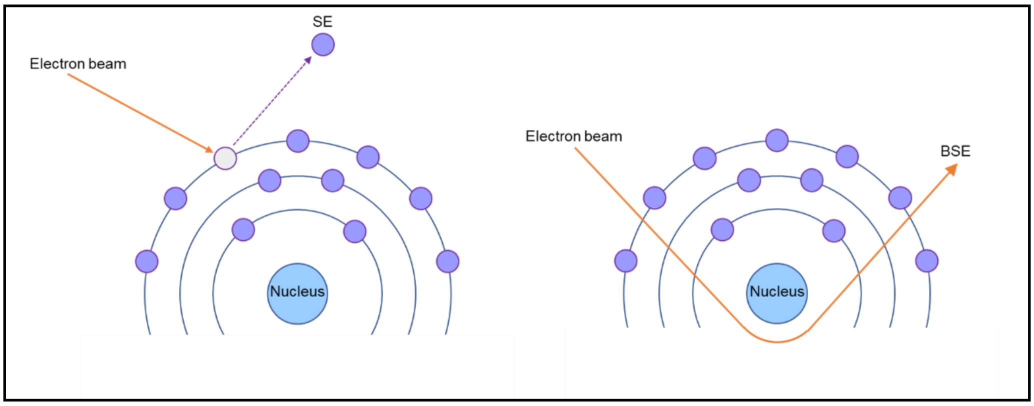

Figure 1.19 Schematic diagram of mechanism for SE (*left*) and BSE (*right*) electron formation. Based upon the mechanism of Auger electron formation found in *Engineered Nanoparticles*[54].

A simplified schematic of the electron microscope used in SEM is presented in **Figure 1.20**. The source of the electron beam is commonly either a cold cathode under a high electric field (FEG-SEM), or a hot filament.[51] The electron beam is focussed using a series of electrostatic lenses, before scanning the sample in a raster. The electrons emitted (back-scattered or secondary, dependent on application) at each point in the raster pattern are collected by a specific detector for the type of emission, the signal amplified and projected onto the computer. To prevent scattering of both the electron beam and the emitted electrons from the sample by atoms present in air, the system is kept under vacuum. Vacuum conditions also prevent contamination in the chamber, and oxidation of the filament.[51]

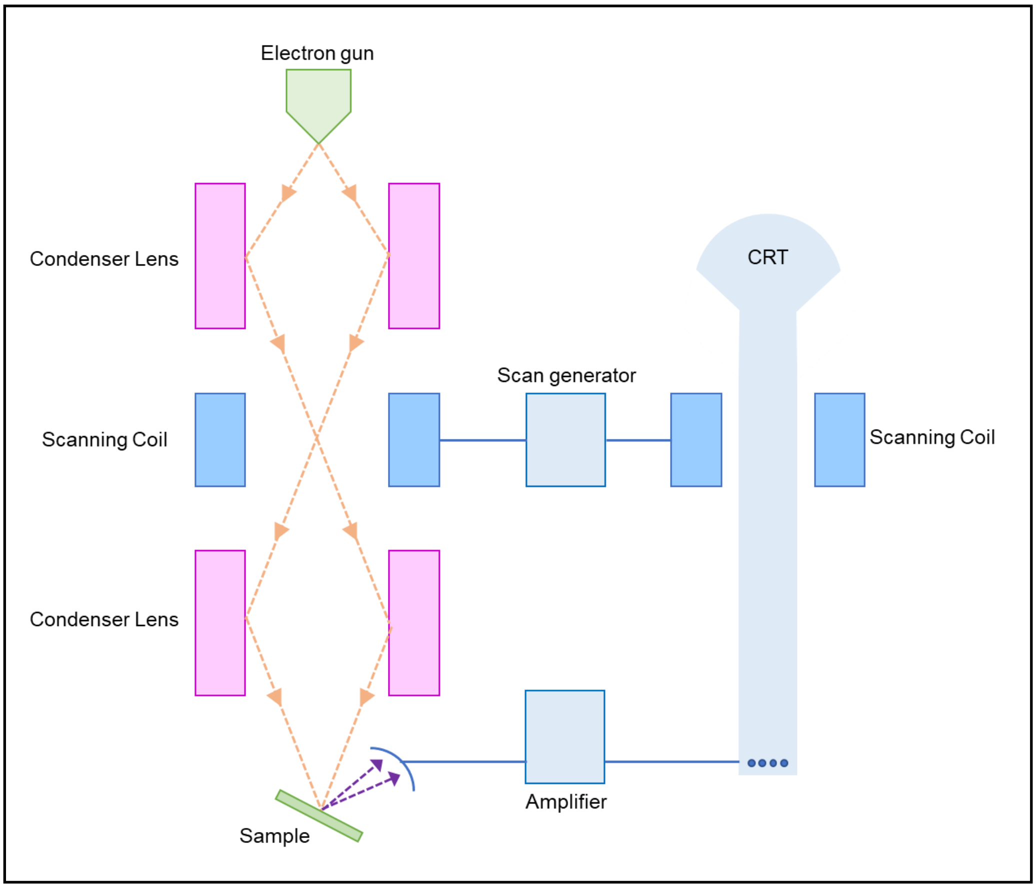

Figure 1.20 Simplified schematic of SEM microscope, adapted from *Nanotechnology: Principles and Practices*[51].

To produce an image of a sample at a higher resolution, a smaller beam diameter can be used.[50] However, reducing the beam diameter also leads to a reduction in beam current, which decreases the visibility and hence contrast of the image. To increase the depth-of-field, the divergence angle of the beam can be reduced by changes to the aperture size and working distance (the distance between sample and lenses). However, small apertures also lead to a reduction in beam current.[50]

1.4.1.2 EDX

Electron microscopy can also be used to probe the composition of the sample, *via* analysis of characteristic x-rays emitted. The electron beam inelastically scatters with inner shell electrons of the sample atoms, resulting in ionisation and ejection of a core electron (**Figure 1.21**).[49] A weaker bound electron then moves to the new vacancy, resulting in emission of an x-ray, that is then detected. The x-rays emitted are specific to each element, as atomic shell energies are well defined.[50] For successful x-ray emission, the beam electron energy must be greater than the electron binding energy for the particular shell (K, L, M or N) in the atom, which is defined as the critical ionisation energy.[50] The sensitivity of EDX is generally 0.1 wt%, however it can be entirely dependent on the sample being studied, with light and low energy X-ray elements more difficult to determine over background signals (bought about by Bremsstahlung x-rays discussed below), compared to heavier higher energy elements.

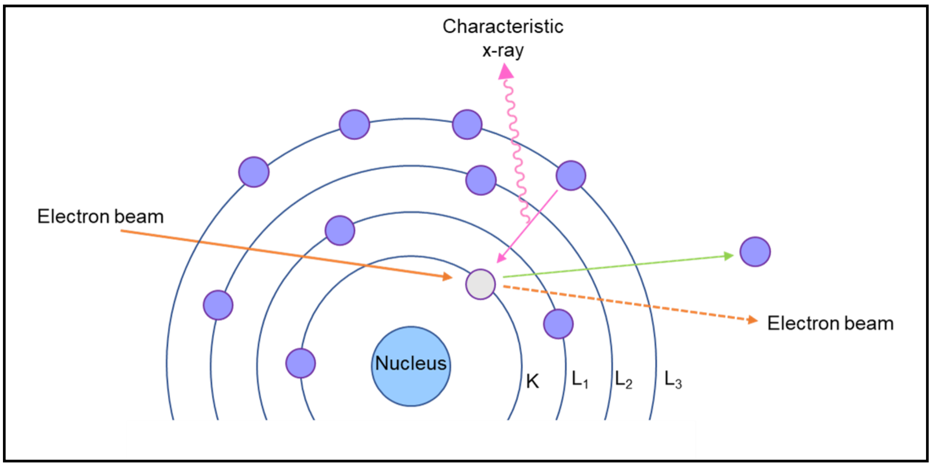

Figure 1.21 Schematic diagram of mechanism for EDX formation. Based upon the mechanism of Auger electron formation found in *Engineered Nanoparticles*[54] , and adapted from *Transmission electron microscopy: a textbook for materials science*[49].

As well as characteristic x-rays, Bremsstrahlung x-rays are also emitted from the sample. Bremsstrahlung x-rays, also known as continuum x-rays,[51] are formed when the electron beam interacts inelastically with the nucleus instead of the electrons. Interaction with the coulomb field of the nucleus results in large energy loss of the electrons in the beam, resulting in x-ray emission.[49] However, the energy loss is not well-defined, as it depends on the amount of interaction taken place, and therefore the x-rays emitted can have a range of energies[49] and cannot be used to characterise the atoms within the sample.

1.4.1.3 STEM

Whereas SEM relies on BSE and SE to analyse the particle surface, transmission electron microscopy (TEM) instead measures electrons from the initial beam that have passed through the sample.[51]

Although the general principle of operation is similar, TEM utilises a focussed electron beam on a particular point in the sample, however in scanning electron microscopy (STEM) the electron beam is scanned across the sample.[55] In the work described herein, FEG-STEM was used in particle analysis. FEG-STEMs are modified with a field emission gun (FEG), which can focus the electron beam diameter to less than 1.5 nm.[55] This modification results in an electron beam that can be stopped at particular points in the sample, and used for EDX spectroscopy as well as STEM image analysis.

There are a variety of different types of electrons that can be collected during STEM imaging, however two main types of electrons collected that are particularly important in the work described herein are those collected in bright field (BF) and annular dark field (ADF) modes.[52] BF field mode collects only electrons that are transmitted through the sample at a low angle to the electron beam (e.g. “Direct Beam” in **Figure 1.22**), whereas ADF mode collects those that are ejected at higher angles.[52]

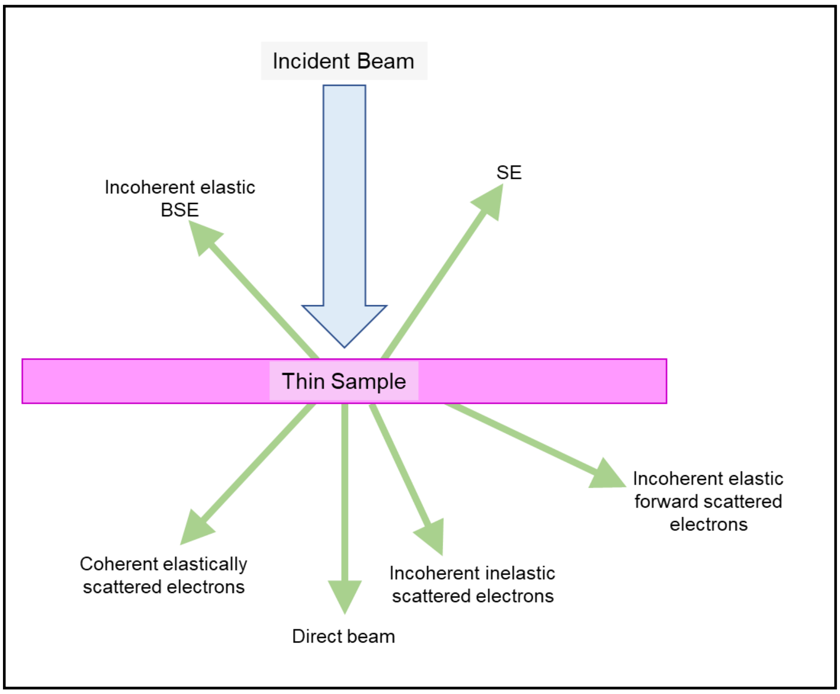

Figure 1.22 Schematic diagram showing both eleastic and inelastic electrons scattered during irradiation with an electron beam. In STEM, only those scattered through the sample are measured. Adapted from *Transmission electron microscopy: a textbook for materials science*[49].

Scattering of electrons through the sample can be described as elastic or inelastic.[49] Elastic scattering leads to no loss of energy, and normally leads to coherent electrons. However, inelastic scattering leads to a loss of energy of the electrons, and normally leads to incoherent electrons. At higher scattering angles, for example in the case of BSE in SEM imaging, elastic scattering is more incoherent. In general, electrons that are scattered < 90° to the incident beam are classed as forward scattered (instead of backscattered) and collected during STEM/TEM analysis, with elastically scattered electrons giving contrast to the images generated.[49]

The general layout of the STEM microscope is similar to that of SEM, with a series of condenser lenses and scan coils to focus the beam and allow it to act as a probe on the sample surface, shown in **Figure 1.23**. However, as the electrons detected transmit through the sample, an objective lens above and below the sample is also present, forming the primary image of the sample.[49] Beneath the lens, detectors for bright field, dark field and high-angle dark field modes can be introduced or retracted, with the final image being sent to the computer system.[49,52] It is important to note that STEM images are not magnified by the series of lenses, unlike in TEM, with the magnification instead due to the dimensions of the area being scanned and the computer screen it is projected on.[49]

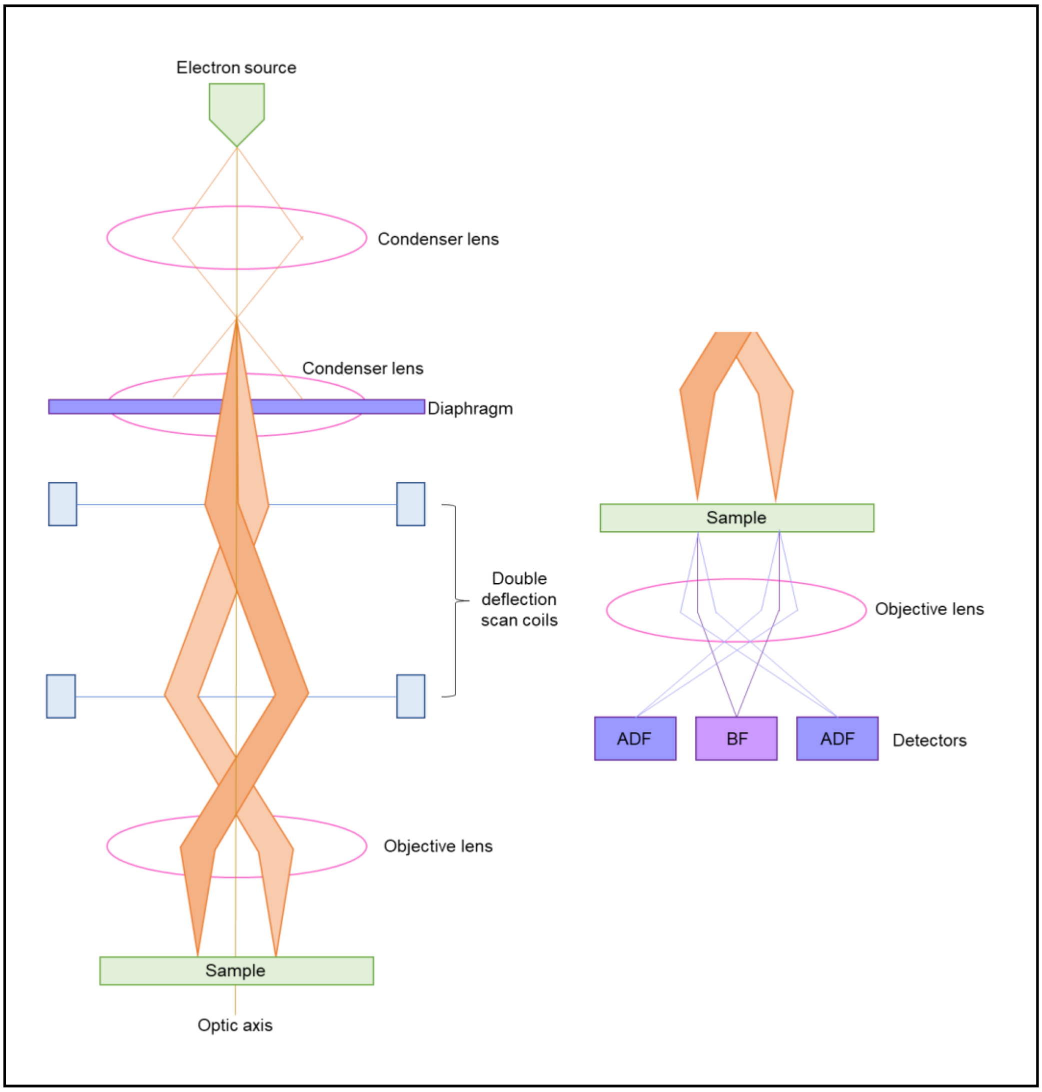

Figure 1.23 Simplified schematic of the STEM microscope. Adapted from *Transmission electron microscopy: a textbook for materials science*[49] and *The Principles of STEM Imaging*[52].

1.5 Thesis Aims

As introduced above, liquid scintillation is used extensively in the nuclear industry for the analysis of environmental radionuclide samples. However, liquid scintillation cocktails contain a high organic content, forming water-in-oil microemulsions with the aqueous sample, which coupled with the environmentally unfriendly components and radiation in the resultant scintillant mixture means that the disposal of samples is difficult and costly. With some popular cocktail components either currently being phased out or due to be restricted for industrial use, a new composition is needed for use in the nuclear industry that combines low cost with environmentally friendly components so that the large quantities that are required for analysis, both in decommissioning and in waste water around a nuclear site, can be disposed of safely and in line with current regulations.

To achieve this, the first aim was to develop a range of novel oxazole-based fluorophores to act as secondary scintillants by having high quantum yields and photophysics complementary to the scintillation mechanism. The second aim was to test these in both an oil-in-water microemulsion and encapsulated within functionalised core-shell nanoparticles.

As far as the author is aware oil-in-water microemulsions are not currently used in liquid scintillation counting, however these systems would greatly reduce the organic content of the resultant sample, and make it easier to test aqueous environmental samples due to the large water component already in the cocktail. The composition tested also contains no NPEs, and thus would not be restricted in use, and although the solvent used is a more traditional solvent, it is in a far smaller quantity owing to the final composition being an oil-in-water formulation.

Scintillant nanoparticles are already utilised in scintillation counting within the biological sector, frequently with low energy radionuclides such as tritium, as discussed in more detail in **Chapter 3**. However the same scintillation mechanism applies as that discussed for liquid scintillation in **Section 1.3,** and the same scintillation counter can be employed. The advantages of core-shell nanoparticles is that they can be dispersed in a completely aqueous environment, and thus reduce sample preparation steps. They are also reusable, as separation from the sample is straightforward (i.e. filtration), and thus reduce overall waste and cost. Functionalisation of the surface provides element specificity, which again would reduce the preparation steps needed for low energy beta emitters such as Ni-63, which are frequently masked when in a mixture of higher energy radionuclides.

Thus, these two compositions would provide a new range of environmentally friendly and low cost alternatives to the current state of the art.

The final aims of the work herein were to investigate the use of oxazole-based polyaromatic fluorophores as bidentate ligands in *fac*-[ReL$(CO)_3$Br] complexes, and to investigate the core-shell particles used in the scintillant compositions, particularly their effect on the resultant photophysics of the dopant, by encapsulating environmentally sensitive lanthanide probes.

1.6 General Experimental for all Chapters

All reagents listed in experimental were commercial grade and used without further purification.

NMR spectra (^1H and $^{13}C\{^1H\}$) were measured using an NMR-FT Bruker 400 or 500 MHz spectrometer, with samples dissolved in $CDCl_3$ or d6-DMSO. NMR spectra were analysed using MestReNova software.

Low resolution mass spectra were obtained by staff at Cardiff University. High-resolution mass spectra were carried out by either staff at Cardiff University or by the EPSRC National Mass Spectrometry Service at Swansea University.

UV-Vis studies were performed using a Shimadzu UV-1800 in a quartz cuvette (1 cm path length). Samples were recorded in a range of solvents (10^{-5} mol dm^{-3}), and stated in each case. Nanoparticle samples were recorded in water (0.04% wt/v).

Solid-state UV-Vis studies were performed using a modular Ocean Optics Flame-S-UV-VIS-ES spectrometer fitted with a DH-mini deuterium-tungsten light source connected *via* fibre optic cables. The solid sample was packed into a well, in which the fibre optic cables fitted within.

Photophysical data were recorded in aerated solutions using a JobinYvon-Horiba Fluorolog spectrometer fitted with a JY TBX picosecond photodetection module, resulting in uncorrected emission spectra and instrument corrected excitation spectra. The pulsed source was a NanoLED configured for 295 or 355 nm output dependent on sample, operating at 1 MHz. Luminescence lifetime profiles were obtained using the JobinYvon-Horiba FluoroHub single photon counting module and the data fits yielded the lifetime values using the provided DAS6 deconvolution software. In some cases, particularly those of nanoparticles, biexponential lifetimes were recorded. The percentage of each component is the relative amplitude, which is the percentage of photons originating from the different decays[56]. Examples of mono- and bi-exponential fits are given in the **Appendix**.

Quantum yield measurements were obtained in aerated solutions using the comparative method[57,58], with quinine sulfate in 0.05 M H_2SO_4 as a reference standard (Φ = 0.6[59]). The UV-vis absorbance spectrum was recorded for the samples and standard at a series of different concentrations yielding an absorbance below 0.1 at the excitation wavelength to be used. The emission spectra was then recorded at the excitation wavelength chosen, and the integrated emission intensity calculated. A graph was plotted of integrated emission intensity *vs* the absorbance at that concentration, yielding a straight line. The gradient, labelled m, was then used in the **Equation 1.9** to calculate the quantum yield.

$$Q_s = Q_r\left(\frac{A_r}{A_s}\right)\left(\frac{E_s}{E_r}\right)\left(\frac{n_s}{n_r}\right)^2 = Q_r\left(\frac{m_s}{m_r}\right)\left(\frac{n_s}{n_r}\right)^2$$

$$where\ Q = quantum\ yield, \qquad A = absorbance,$$

$$E = integrated\ emission\ intensity, \qquad n = refractive\ index\ of\ solvent,$$

$$m = gradient\ of\ inegrated\ emission\ intesity\ vs\ absorbance\ of\ sample$$

$$where\ the\ subscript\ s\ and\ r\ refer\ to\ sample\ and\ reference\ respectively$$

Equation 1.9 Calculation of quantum yield *via* the comparative method.[57,58,60]

Low temperture measurements were carried out at 77 K, with samples dissolved in a 4:1 EtOH:MeOH solvent system to form a glass at low temperature. The sample was placed within an EPR tube and introduced to liquid nitrogen within an optical quartz adapter designed to fit within the sample chamber.

Near-IR measurements presented in **Chapter 6** were measured using the JobinYvon-Horiba Fluorolog spectrometer fitted with a JY TBX picosecond photodetection module, with an additional Hamamatsu R5509-73 detector on the T channel.

For luminescence lifetime and quantum yield measurements, instrument errors were assumed to be ±10% of the recorded value.

Infra-red spectra were obtained from a Shimadzu IR-Affinity-1S FTIR, as solid samples.

Microscopy was performed on a Tescan Maia3 field emission gun scanning electron microscope (FEG-SEM) operating at 15 kV or 30 kV for SEM and STEM imaging respectively, and fitted with an Oxford Instruments XMAXN 80 energy dispersive X-ray detector (EDX). Images were acquired using the secondary electron and backscattered electron detectors for SEM imaging, and STEM bright and dark field detectors for STEM imaging. Samples were suspended in aqueous solution, and pipetted onto holey 300 mesh carbon film copper grids and analysed uncoated. Aztec software was used for EDX data-acquisition and processing. Error associated in EDX measurements was calculated based upon the wt% sigma for each elements studied, which is defined as the error associated with the particular reading.

ImageJ software was used throughout for the measurement of particle size. This was undertaken by setting the scale to the scale present in the SEM/STEM image *via* the use of the line tool and the “set scale” function. A selection of particles across the sample set in each sample were then sized by hand using the line tool set to this scale. These were automatically accumulated within the software, and the mean, minimum, maximum and standard deviation calculated. Error was calculated as the standard deviation of the sample set divided by the square root of the sample size.

Scintillation measurements were recorded by Dr Hibaaq Mohamud at NPL, using a Tricarb 2910TR (Perkin Elmer) for 6 mins with 10 cycles completed in total, with the exception of those containing disubstituted oxazoles or functionalised particles which were instead measured for 30 minutes with 10 cycles completed in total. Pre-dispersed nanoparticle samples or cocktails were spiked with a known amount of Ni-63 (2.0 kBq/g) prepared in 0.1 mol dm^{-3} HCl, or Sr-90 (96.99 Bq/g) prepared in 1 mol dm^{-3} HNO_3, with the sources containing 100 μg g^{-1} of inactive nickel and 50 μg g^{-1} inactive strontium and yttrium, respectively. All samples were measured in duplicate.

The nominal activity for each sample was calculated based on the activity of the stock solution and the amount spiked within the sample. The counts per minute (CPM) for each cycle were automatically calculated by the detector, and these were converted into counts per second (CPS). The CPS for each cycle was then divided by the nominal activity to obtain the efficiency for the cycle, which were then averaged across the entire run to yield the final efficiency for the sample.

DFT calculations were performed using the Gaussian 09 suite.[61] Geometries were optimised using the B3LYP hybrid functional[62–65] for oxazoles **1-7**, and the PBE functional[66,67] for **8-19** and ***fac*-[Re(14-19)(CO)$_3$Br]**. 6-311+G(d,p)[68] and def2SVP[69] were used as basis sets for these respectively. Absorption spectra predictions were performed using TD-DFT and TDA based TD-DFT calculations, using the same level of theory as geometry optimisations. The polarised continuum model (PCM)[70] was used in all calculations, with the solvent defined as either acetonitrile (AcN) or chloroform ($CHCl_3$). In **Chapter 5**, calculated percentage contributions of selected orbitals to the overall states of the ***fac*-[Re(L)(CO)$_3$Br]** complexes were calculated using POP=REG of the optimised geometry used for TDA based TD-DFT calculations.

1.7 References

1. G. M. Lampman, D. L. Pavia, G. S. Kriz and J. R. Vyvyan, *Spectroscopy*, Brooks/Cole Cengage learning, Belmont, 2010.
2. C. E. Housecroft and A. G. Sharpe, *Inorganic chemistry*, Pearson, Harlow, England ; New York, 4th ed., 2012.
3. D. H. Williams and I. Fleming, *Spectroscopic Methods in Organic Chemistry*, McGraw-Hill, London, 2008.
4. A. Marini, A. Muñoz-Losa, A. Biancardi and B. Mennucci, *J. Phys. Chem. B*, 2010, **114**, 17128–17135.
5. J. F. W. Herschel, *Philos. Trans. R. Soc. Lond.*, 1845, **135**, 143–145.
6. G. G. Stokes, *Philos. Trans. R. Soc. Lond.*, 1852, **142**, 463–562.
7. J. R. Lakowicz, *Principles of fluorescence spectroscopy*, Springer, New York, 3rd ed., 2006.
8. A. Jabłoński, *Z. Für Phys.*, 1935, **94**, 38–46.
9. M. Kasha, *Discuss. Faraday Soc.*, 1950, **9**, 14–19.
10. O. L. J. Gijzeman, F. Kaufman and G. Porter, *J. Chem. Soc. Faraday Trans. 2 Mol. Chem. Phys.*, 1973, **69**, 708–720.
11. J. H. Brannon and D. Magde, *J. Phys. Chem.*, 1978, **82**, 705–709.
12. M. Mardelli and J. Olmsted, *J. Photochem.*, 1977, **7**, 277–285.
13. I. B. Berlman, in *Handbook of Fluorescence Spectra of Aromatic Molecules*, Elsevier, Amsterdam, 2nd edn., 1971, pp. 107–415.
14. M. Fischer and J. Georges, *Chem. Phys. Lett.*, 1996, **260**, 115–118.
15. J. Thomson, in *Handbook of Radioactivity Analysis*, Elsevier, Amsterdam, 2012, pp. 575–623.
16. J. R. Lakowicz and G. Weber, *Biochemistry*, 1973, **12**, 4161–4170.
17. W. R. Ware, *J. Phys. Chem.*, 1962, **66**, 455–458.
18. H. A. Khwaja, G. P. Semeluk and I. Unger, *Can. J. Chem.*, 1982, **60**, 1767–1774.
19. I. B. Berlman, *J. Phys. Chem.*, 1973, **77**, 562–567.
20. S. R. Phillips, L. J. Wilson and R. F. Borkman, *Curr. Eye Res.*, 1986, **5**, 611–620.
21. G. Weber, *Trans. Faraday Soc.*, 1948, **44**, 185–189.
22. A. Ahmad, T. Kurkina, K. Kern and K. Balasubramanian, *ChemPhysChem*, 2009, **10**, 2251–2255.

23. A. Jain, C. Blum and V. Subramaniam, in *Advances in Biomedical Engineering*, ed. P. Verdonck, Elsevier, Amsterdam, 2009, pp. 147–176.
24. M. H. Gehlen, *J. Photochem. Photobiol. C Photochem. Rev.*, 2020, **42**, 100338.
25. Fluorolog-3 Manual, https://www.horiba.com/fileadmin/uploads/Scientific/Downloads/UserArea/Fluorescence/Legacy/Complete_FluoroLog3_Manual.pdf, (accessed 16 April 2021).
26. R. F. Kubin and A. N. Fletcher, *J. Lumin.*, 1982, **27**, 455–462.
27. A. Kundu, S. Karthikeyan, Y. Sagara, D. Moon and S. P. Anthony, *ACS Omega*, 2019, **4**, 5147–5154.
28. Y. Liu, J. shi Du, S. long Qi, L. bao Zhu, Q. biao Yang, H. Xu and Y. xian Li, *Luminescence*, 2021, **36**, 336–344.
29. Y. Niu, H. Wang, Y. Wang and L. Feng, *Microchem. J.*, 2021, **166**, 106205.
30. J. N. Demas and B. A. DeGraff, *Anal. Chem.*, 1991, **63**, 829A-837A.
31. G. A. Crosby, *Acc. Chem. Res.*, 1975, **8**, 231–238.
32. C. Lentz, L. Marcélis, L. Troian-Gautier, K. Robeyns, E. Cauët and B. Elias, *J. Photochem. Photobiol. Chem.*, 2021, **405**, 112957.
33. R. Bevernaegie, S. A. M. Wehlin, B. Elias and L. Troian-Gautier, *ChemPhotoChem*, 2021, **5**, 217–234.
34. S. Sprouse, K. A. King, P. J. Spellane and R. J. Watts, *J. Am. Chem. Soc.*, 1984, **106**, 6647–6653.
35. A. Juris, V. Balzani, P. Belser and A. von Zelewsky, *Helv. Chim. Acta*, 1981, **64**, 2175–2182.
36. E. M. Kober, J. V. Caspar, R. S. Lumpkin and T. J. Meyer, *J. Phys. Chem.*, 1986, **90**, 3722–3734.
37. M. F. L’Annunziata and M. J. Kessler, in *Handbook of Radioactivity Analysis (Third Edition)*, ed. M. F. L’Annunziata, Academic Press, Amsterdam, 2012, pp. 423–573.
38. V. Binns and J. Thomson, 24.
39. Half-life | Definition & Facts, https://www.britannica.com/science/half-life-radioactivity, (accessed 11 February 2020).
40. L. Salonen, L. Kaihola, B. Carter, G. T. Cook and C. J. Passo, in *Handbook of Radioactivity Analysis (Third Edition)*, ed. M. F. L’Annunziata, Academic Press, Amsterdam, 2012, pp. 625–693.

41. Internationale Atomenergie-Organisation, Ed., *Radiological characterization of shut down nuclear reactors for decommissioning purposes*, IAEA, Vienna, 1998.
42. Chernobyl, https://www.oecd-nea.org/jcms/pl_13598/chernobyl-assessment-of-radiological-and-health-impacts-2002?details=true, (accessed 28 November 2021).
43. P. P. Povinec, M. Aoyama, D. Biddulph, R. Breier, K. Buesseler, C. C. Chang, R. Golser, X. L. Hou, M. Ješkovský, A. J. T. Jull, J. Kaizer, M. Nakano, H. Nies, L. Palcsu, L. Papp, M. K. Pham, P. Steier and L. Y. Zhang, *Biogeosciences*, 2013, **10**, 5481–5496.
44. M. L. Carboneau and J. P. Adams, *National Low-Level Waste Management Program Radionuclide Report Series. Volume 10, Nickel-63*, U.S. Department of Energy Office of Scientific and Technical Information, 1995.
45. S. Novak and M. Podest, *Nuclear Power Plant Ageing and Life Extension: Safety Aspects*, IAEA, 1987.
46. T. M. Beasley, *J. Environ. Radioact.*, 1986, **4**, 1–10.
47. Endocrine Disrupting Chemicals (EDCs), https://www.who.int/ceh/risks/cehemerging2/en/, (accessed 10 February 2020).
48. M. F. L’Annunziata, in *Handbook of Radioactivity Analysis (Third Edition)*, ed. M. F. L’Annunziata, Academic Press, Amsterdam, 2012, pp. 1021–1115.
49. D. B. Williams and C. B. Carter, *Transmission electron microscopy: a textbook for materials science*, Springer, New York, 2nd ed., 2008.
50. J. I. Goldstein, D. C. Joy, J. R. Michael, D. E. Newbury, N. W. M. Ritchie and J. H. J. Scott, *Scanning Electron Microscopy and X-Ray Microanalysis*, Springer New York : Imprint: Springer, New York, NY, 4th ed., 2018.
51. S. K. Kulkarni, *Nanotechnology: principles and practices*, Springer, New York, 2014.
52. P. D. Nellist, in *Scanning Transmission Electron Microscopy*, Springer, New York, NY, 2011, p. 25.
53. D. McMullan, *Scanning*, 1995, **17**, 175–185.
54. A. K. Singh, in *Engineered Nanoparticles*, ed. A. K. Singh, Academic Press, Boston, 2016, pp. 125–170.

55. C. A. English, J. M. Hyde, G. R. Odette, G. E. Lucas and L. Tan, in *Structural Alloys for Nuclear Energy Applications*, eds. G. R. Odette and S. J. Zinkle, Elsevier, Boston, 2019, pp. 103–161.
56. DAS-6 Software Operation Manual, https://www.horiba.com/fileadmin/uploads/Scientific/Downloads/UserArea/Fluorescence/Manuals/DAS67_Manual.pdf, (accessed 9 December 2021).
57. A. T. R. Williams, S. A. Winfield and J. N. Miller, *Analyst*, 1983, **108**, 1067–1071.
58. A Guide to Recording Fluorescence Quantum Yields, https://www.chem.uci.edu/~dmitryf/manuals/Fundamentals/Quantum%20yield%20determination.pdf, (accessed 9 December 2021).
59. A. M. Brouwer, *Pure Appl. Chem.*, 2011, **83**, 2213–2228.
60. APP Determination of Relative Fluorescence Quantum Yields using FL6500 Fluorescence Spectrometer, https://resources.perkinelmer.com/lab-solutions/resources/docs/APP_Determination_of_Relative_Fluorescence Quantum_Yields_using_FL6500_Fluorescence_Spect.pdf, (accessed 9 December 2021).
61. M. J. Frisch, G. W. Trucks, J. R. Cheeseman, G. Scalmani, M. Caricato, H. P. Hratchian, X. Li, V. Barone, J. Bloino, G. Zheng, T. Vreven, J. A. Montgomery, G. A. Petersson, G. E. Scuseria, H. B. Schlegel, H. Nakatsuji, A. F. Izmaylov, R. L. Martin, J. L. Sonnenberg, J. E. Peralta, J. J. Heyd, E. Brothers, F. Ogliaro, M. Bearpark, M. A. Robb, B. Mennucci, K. N. Kudin, V. N. Staroverov, R. Kobayashi, J. Normand, A. Rendell, R. Gomperts, V. G. Zakrzewski, M. Hada, M. Ehara, K. Toyota, R. Fukuda, J. Hasegawa, M. Ishida, T. Nakajima, Y. Honda, O. Kitao and H. Nakai, *Gaussian 09*, Revision D.01, Gaussian Inc. Wallingford CT 2009.
62. A. D. Becke, *J. Chem. Phys.*, 1993, **98**, 5648–5652.
63. C. Lee, W. Yang and R. G. Parr, *Phys. Rev. B*, 1988, **37**, 785–789.
64. S. H. Vosko, L. Wilk and M. Nusair, *Can. J. Phys.*, , DOI:10.1139/p80-159.
65. P. J. Stephens, F. J. Devlin, C. F. Chabalowski and M. J. Frisch, *J. Phys. Chem.*, 1994, **98**, 11623–11627.
66. C. Adamo and V. Barone, *J. Chem. Phys.*, 1999, **110**, 6158–6170.
67. M. Ernzerhof and G. E. Scuseria, *J. Chem. Phys.*, 1999, **110**, 5029–5036.

68. R. Krishnan, J. S. Binkley, R. Seeger and J. A. Pople, *J. Chem. Phys.*, 1980, **72**, 650–654.
69. F. Weigend and R. Ahlrichs, *Phys. Chem. Chem. Phys.*, 2005, **7**, 3297–3305.
70. J. Tomasi, B. Mennucci and R. Cammi, *Chem. Rev.*, 2005, **105**, 2999–3094.

2 Synthesis of Oxazole-Based Fluorophores and their use in Scintillation Media

2.1 Overview

The aim of this chapter was to develop a series of novel oxazoles with a broad range of photophysical properties suitable for their use as secondary scintillants in Liquid Scintillation Counting (LSC). As discussed in **Chapter 1**, and in more detail in the following introduction, scintillant cocktails currently used are composed of an organic solvent and surfactant (as well as scintillants) and thus form a water-in-oil microemulsion. These generate a large amount of organic waste, typically composed of environmentally unfriendly and toxic components. Therefore, the secondary aim of this chapter was the incorporation of the novel scintillant into a novel oil-in-water microemulsion, which contains a low organic content and would therefore be easier to dispose of. These were to be tested for their scintillation viability against a hard beta emitter, Sr-90, and a soft beta emitter, Ni-63, to develop a greener and low-cost cocktail with high efficiency.

2.2 Oxazoles

Oxazoles are a type of azole, a five membered ring constituting one nitrogen and one heteroatom. In the case of the oxazole ring, the heteroatom is an oxygen. The parent oxazole was first prepared in 1947[1] (presented in **Figure 2.1**, along with other common azoles) and is a liquid at room temperature with a boiling point of 69°C.

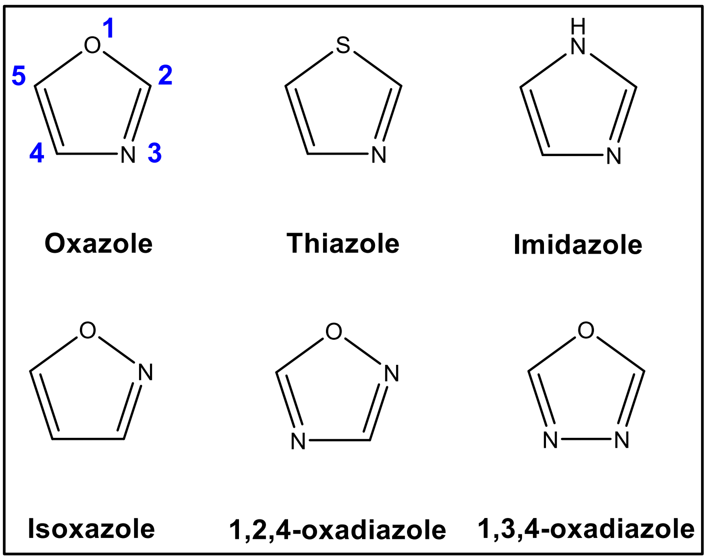

Figure 2.1 Oxazole, and a range of other common azoles

The nitrogen of the oxazole ring is weakly basic, however this can be increased by substituents at the 2-position, whereas electron withdrawing substituents at the 5-position can further decrease the basicity.[2] Both the 2- and 5- positions are weakly acidic,[3] and the reactivity of the 2, 4, and 5 positions of the ring increase in reactivity in the order 4<5<2.[2]

2.2.1 Synthesis of Oxazoles

Since the formation of the parent oxazole in 1947[1], there have been a range of different methods for the synthesis of oxazoles developed and discussed in a variety of reviews including those by I. Turchi[4,5] and R. Wiley[6]. Of particular note however are those of the Robinson-Gabriel synthesis[7–9], the Fischer oxazole synthesis[10] and the method used in the following work developed by A. van Leusen *et al*[11].

The Fischer oxazole synthesis, developed by E. Fischer in 1896[10], describes the anhydrous HCl mediated reaction between aromatic aldehydes and cyanohydrins, forming di-substituted 2,5-oxazoles (**Figure 2.2a**, with the reaction mechanism presented in **Figure 2.2c**). However, a Schiff base side-product is typically formed,[12] as shown in **Figure 2.2b**.

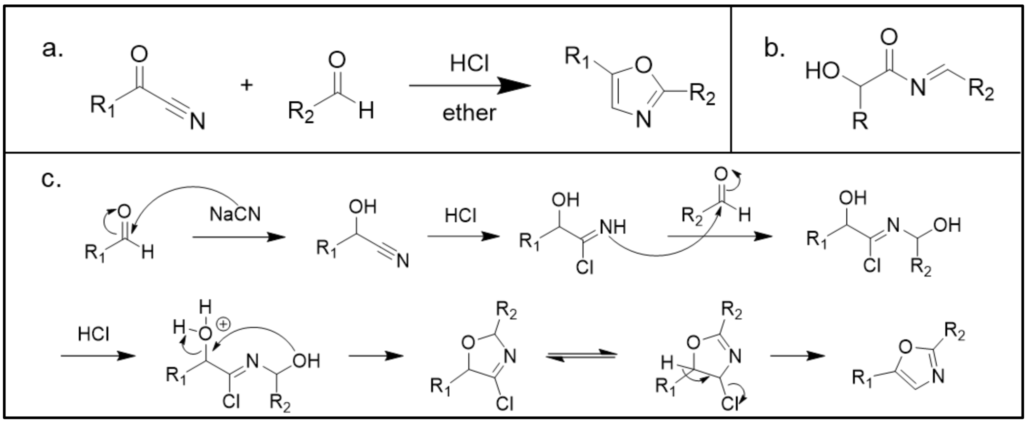

Figure 2.2 a) Fischer oxazole synthesis reaction scheme; b) common side-product of synthesis[12]; c) Reaction mechanism for Fischer oxazole synthesis, adapted from G. E. Schiltz.[13]

As well as this, one notable example of the incompatibility of this method is in the attempted synthesis of 2-(4-bromophenyl)-5-phenyloxazole, using 4-bromobenzaldehyde and the respective cyanohydrin.[5] Chlorination of the oxazole ring occurs, forming 2,5-bis(4-bromophenyl)-4-chlorooxazole (**Figure 2.3**), as well as 2,5-bis(4-bromophenyl)-4-oxazolidinone which is another common side product.[5]

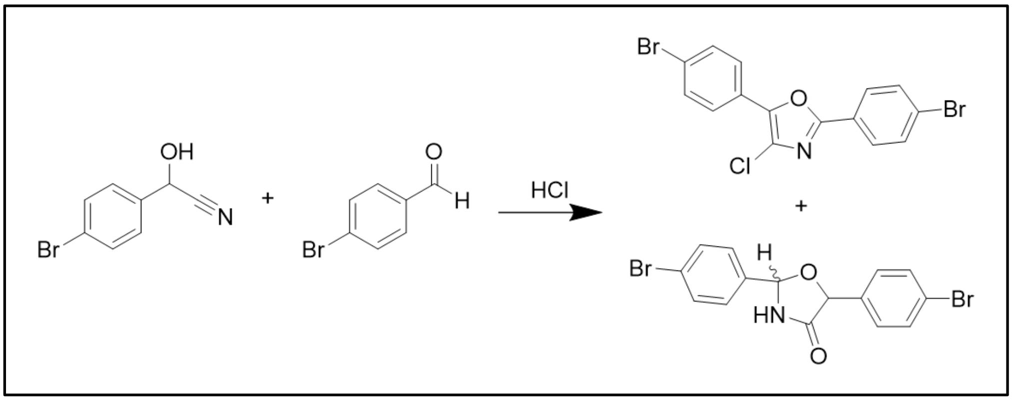

Figure 2.3 Formation of unwanted products 2,5-bis(4-bromophenyl)-4-chlorooxazole and 2,5-bis(4-bromophenyl)-4-oxazolidinone using the Fischer oxazole synthesis.[5]

The Robinson-Gabriel synthesis, developed by R. Robinson[7] and S. Gabriel[8,9] simultaneously between 1909-1910, describes the formation of tri-substituted oxazoles *via* the intramolecular dehydration reaction of 2-acylamino-ketones in the presence of a strong dehydration agent such as H_2SO_4, PCl_5, P_2O_5, $POCl_3$ or $SOCl_2$ [5] (**Figure 2.4a**). Although the synthesis was developed in the early 1900's, the mechanism (**Figure 2.4b**) was not fully realised until 1973 by H. Wasserman *et al*[14] by O-18 labelling the ketone portion of the 2-acylamino-ketone.

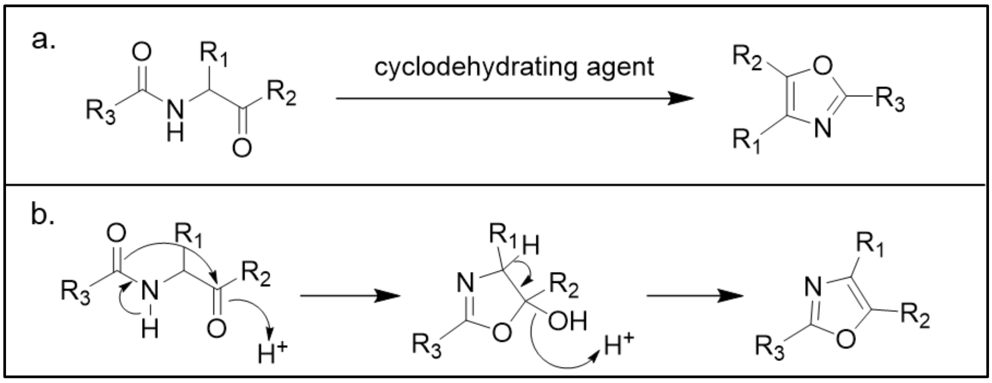

Figure 2.4 a) Robinson-Gabriel oxazole synthesis reaction scheme; b) Reaction mechanism for Robinson-Gabriel oxazole synthesis, adapted from H. Wasserman *et al.*[14]

Both reaction methodologies discussed above yield multiple substitutions on the oxazole ring, however work by A. van Leusen in 1977[11] provides a synthetic route to yield mono-substituted oxazoles. This provided an opportunity for not just mono-oxazoles, but also post modification. In the work, aromatic aldehydes are reacted with toluenesulfonylmethyl isocyanide (TosMIC) in a one-pot synthesis to yield the desired 5-substituted oxazoles, with both the reaction scheme and mechanism presented in **Figure 2.5**.

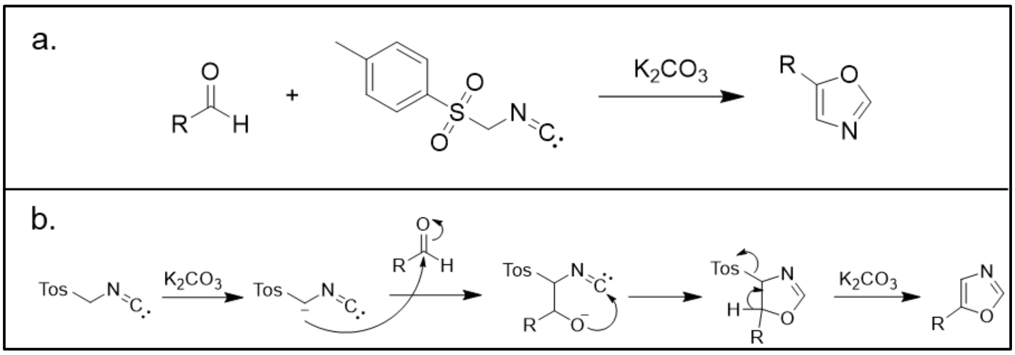

Figure 2.5 a) van Leusen oxazole synthesis reaction scheme ; b) Reaction mechanism for van Leusen oxazole synthesis adapted from A. van Leusen *et al.*[11]

The reaction is extremely versatile, being able to be used not just with aldehydes but also acid chlorides and anhydrides. If lower temperatures are used when aldehydes are the starting material, 4-tosyl-5-R-oxazolines can instead be formed due to toluenesulfinic acid no longer being eliminated.[11] Nitriles can be formed if ketones are used instead of aldehydes with TosMIC[15], and TosMIC can also be utilised in the synthesis of disubstituted imidazoles[16].

2.2.2 Applications of Oxazoles

Although for the purpose of this thesis the main attribute of oxazoles is from a scintillation viewpoint, as discussed in **Chapter 1**, oxazoles are also present in larger molecules used in antimicrobial, anticancer and anti-inflammatory applications described in detail in a range of reviews by S. Kakkar *et al*[17] and H Zhang *et al*[18]*.* However, two are of note due to the fact that they are still prescribed are anti-inflammatories; ditazole[19,20] and oxaprozin[21] (**Figure 2.6**) Both are classed as non-steroidal anti-inflammatory agents, the latter used in the treatment of inflammation and stiffness caused from osteoarthritis and rheumatoid arthritis, and Ditazole also marketed as Ageroplas as a platelet aggregator.[20,22] Both have the same tri-substituted pattern, with phenyl groups at the 4- and 5- position.

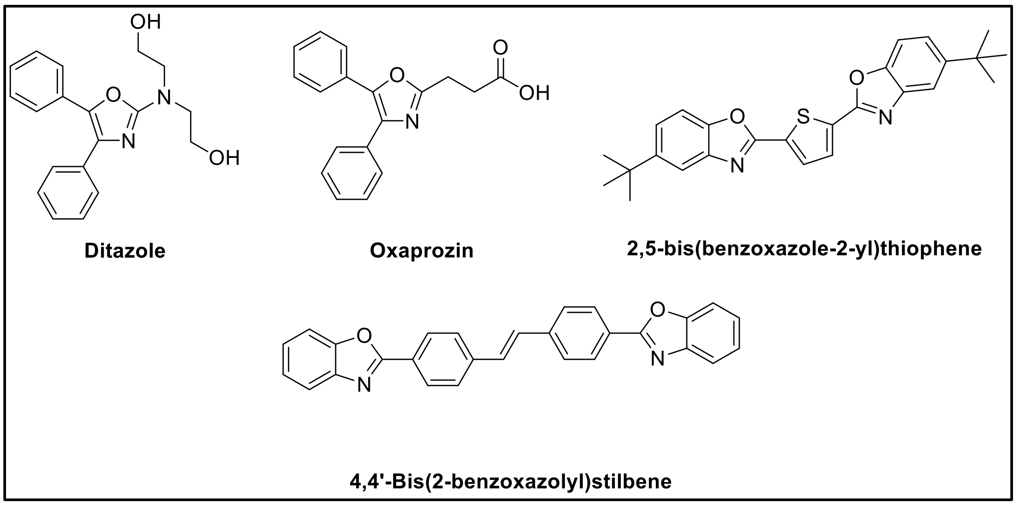

Figure 2.6 Both Ditazole and Oxaprozin are prescribed as anti-inflammatory medication. 2,5-Bis(5-tert-butyl-benzoxazol-2-yl)thiophene and 4,4′-Bis(2-benzoxazolyl)stilbene are both used as fluorescent whitening agents.

Oxazoles have also been used as fluorescent whitening agents, particularly in detergents. Fluorescent whitening agents absorb light between 340-370 nm, and then emit between 420-470 nm.[23] This makes yellowing materials, such as cotton or paper, look whiter by replacing the blue light reflected from the material with blue emission.[24] Examples of oxazole based whitening agents still used today are 2,5-Bis(5-tert-butyl-benzoxazol-2-yl)thiophene and 4,4′-Bis(2-benzoxazolyl)stilbene[25] (**Figure 2.6**), both having similar structures containing two fused oxazole rings but differing in their central unit; the former contains a central thiophene whereas the latter a central stilbene unit. Despite their slight differences in the central unit, both absorb between 350-400 nm and emit between 400-500 nm (tetrachloroethane).[25]

The main application of oxazoles, and the role they play herein, are their extensive use as primary and secondary scintillants in scintillation cocktails. In fact, the scintillant ability of oxazoles has been known from as early as 1955, first published by F. N. Hayes *et al.*[26]

The composition of liquid scintillation cocktails and their use in analysis has been introduced in **Chapter 1**, and a more in-depth discussion of their composition will be discussed in greater detail in **Section 2.4**. As discussed in **Chapter 1**, to allow sensitive detection of the beta decay, energy transfer between the scintillants must be efficient[27,28]. To achieve this, the emission of the primary scintillant must ideally overlap with the absorption of the secondary scintillant, and quantum yields must be high to ensure that the intensity of the light emitted is proportional to the energy of the beta particle (10 photons per keV of beta energy). The emissive wavelength of the secondary scintillant must be above 400, ideally above 420 nm, as this is within the sensitivity window of the PMT, and the emissive lifetimes of both primary and secondary scintillants must be short, to prevent overlap of signals.[28,29] Lastly, both scintillants must have a high solubility in organic solvents and not be sensitive to quenching agents.[28,29]

For these reasons, two commonly used primary and secondary scintillants are 2,5-diphenyloxazole (DPO) and 1,4-bis[5-phenyloxazole-2-yl]benzene (POPOP) respectively, and are shown in a simple schematic of the scintillation detection process in **Figure 2.7**. DPO exhibits a broad emission with maxima at 357 and 375 nm, a lifetime of 1.4 ns and a quantum yield of 100% (cyclohexane).[30] Both the high quantum yield and short lifetime are suitable for scintillation as discussed earlier, however the wavelength is unsuitable for effective detection of signal. POPOP has an emission wavelength of 410 nm, and a quantum yield and lifetime of 93% and 1.47 ns (cyclohexane) respectively.[30] The high quantum yield ensures that the relationship between the released beta particle and intensity of the light emitted remains proportional, and the short lifetime as before means that there is little overlap of signal. By shifting the emission to near 420 nm, the signal is picked up more sensitively by the PMT. The absorption of POPOP also overlaps perfectly with the emission of DPO,[30] leading to efficient transfer of energy.

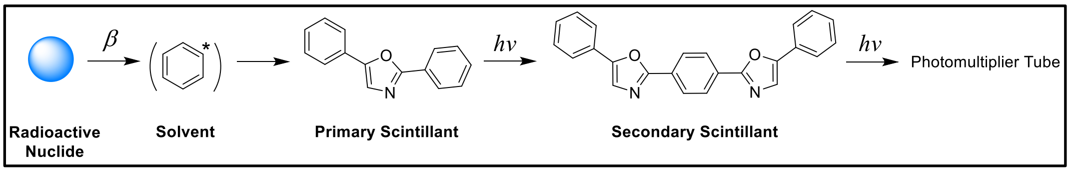

Figure 2.7 Schematic representation of liquid scintillation counting, showing the primary scintillant, DPO, and the secondary scintillant, POPOP.

2.3 Microemulsions

Microemulsions are thermodynamically stable, clear solutions containing two immiscible liquids in close contact with each other by the formation of droplets of one of the liquids (typically between 10-100nm in size)[31] within a continuous phase of the other, *via* the use of surfactants.[32]

Oil-in-water or water-in-oil microemulsions consist of the two immiscible liquids, and a surfactant and co-surfactant. The latter stabilise the droplets by reducing the interfacial tension between the two liquids.[32] The surfactant phase is initially situated between the oil and water phases, however as the concentration of surfactant increases, the phase incorporates the oil and water into a single phase, giving the microemulsion. The solubilisation of water compared to oil by the surfactant can be given by the Winsor Ratio, R (**Equation 2.1**), which ultimately decides the type of microemulsion formed (**Figure 2.8**).[31,33]

$$R = \frac{A_{CO} - A_{OO} - A_{ll}}{A_{CW} - A_{WW} - A_{hh}}$$

Equation 2.1 Winsor Ratio of Microemulsion systems, where A is the interaction strength per unit area between the respective components. C = surfactant, O = oil, W = water, l = lipophilic portion of surfactant, h = hydrophilic proportion of surfactant.

If the interaction strength between the surfactant and oil is high (A_{CO}) then more water is solubilised by the surfactant, and *vice versa*. A_{OO} and A_{WW} represent the self-interaction strengths between the molecules in the same phase, and so as these increase, solubilisation of that phase is reduced. A_{ll} and A_{hh} represent the self-interaction strengths of the different parts of the surfactant.[33]

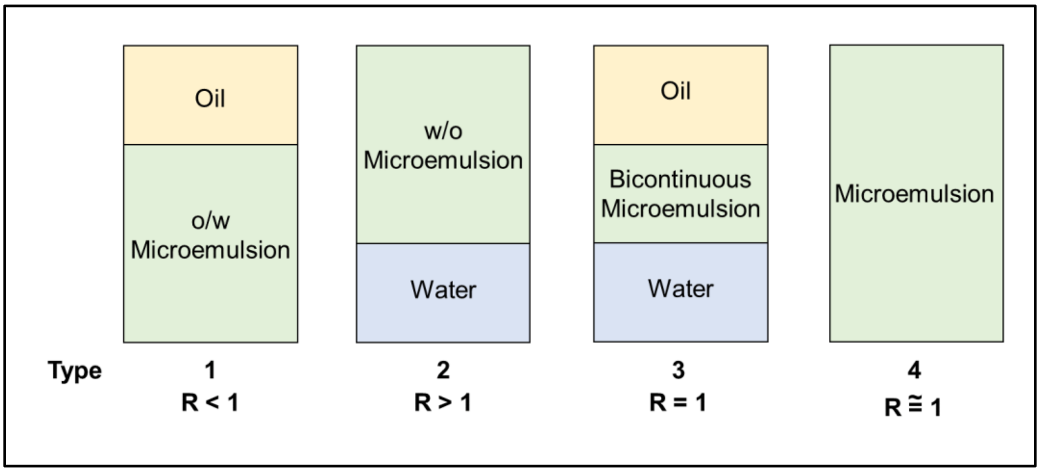

Figure 2.8 Diagrams depicting the different types of systems, as defined by the Winsor ratio, R.

As shown in **Figure 2.8**, if R is much less than 1 then oil is solubilised more than water and a Type 1 system occurs, however if it exceeds 1, then water is more solubilised and a Type 2 system is formed. When R is equal to 1, a type 3 system occurs, where there are 3 phases, however when the denominator or numerator are slightly higher than each other, a type 4 system occurs, forming a one-phase system (microemulsion). If the denominator is higher, than the surfactant solubilises oil more readily than water, and *vice versa.*[33]

2.3.1 Surfactants in Microemulsions

Surfactants, short for Surface-Active Agents, consist of a hydrophobic tail, which interacts with the oil phase, and a hydrophilic headgroup, which interacts with water (**Figure 2.9**). The headgroup is often charged, as described below, and the tail is often long to reduce interfacial tension. In fact, the most stable microemulsions form when the number of carbon atoms in the tail is equal to the number of carbon atoms in the oil and the co-surfactant.[32]

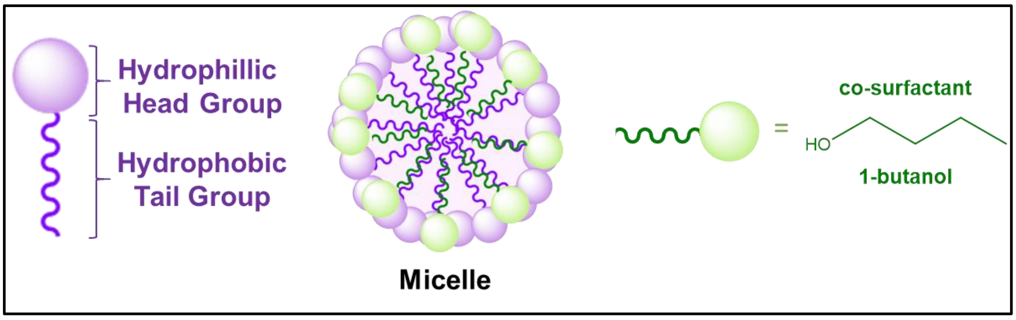

Figure 2.9 Schematic of a micelle, containing (*left*) surfactant, with a hydrophilic head group and hydrophobic tail group, and (*right*) the co-surfactant, commonly 1-butanol.

The co-surfactant is commonly a polar compound with an alkyl chain. However, the chain is not as long as the surfactant, as long chains on polar compounds are known to form liquid crystalline structures, which can increase the viscosity of the system.[31] A common co-surfactant, and one that is used in this work, is 1-butanol (**Figure 2.9**).

Surfactant examples can be split between different hydrophobic tails, and hydrophilic heads.

For hydrophilic headgroups, there are four main types; Anionic (carboxylic acid and sulfonate salts), Cationic (long chain amine and ammonium salts), Zwitterionic (amino acids and sulfobetaines), and Non-ionic (long chain fatty acids and polyoxyethylenated alcohols).[34]

For hydrophobic tails, there are a range of different types, including long straight alkyl or branched chains between eight and twenty carbons, and alkylbenzenes with chain lengths between eight and fifteen carbons long. Other examples include polyoxypropylene and polyoxyethylene polymers.[34]

Changes to the hydrophobic group greatly affect the resultant microemulsion, as it directly affects the interfacial tension.[34] As the length of the chain increases, the hydrophobic nature increases and therefore the solubilization of water is decreased. If the surfactant has an ionic head group, the increase in chain length can cause it to precipitate by forming counterionic salts. The surfactant molecules will also pack closer together, forming aggregates. Increasing the branching of the chain or the unsaturation increases the solubility in both solvents, causing looser packing at the surface. Branching also increases the thermal instability, and unsaturation can change the colour of the microemulsion and lead to oxidation. If an aromatic group is used, *i.e*. an alkylbenzene, looser packing at the surface results and biodegradability decreases. When polypropylene oxide structures are used, there is an increase in the hydrophobicity of the tail, and its solubility in organic solvents, however if ethylene units are used instead of propylene the hydrophilicity is increased instead (polyoxyethylene structures are used as hydrophilic head groups).[34]

2.3.1.1 Critical Micelle Concentration (CMC)

The critical micelle concentration is the concentration at which surfactant molecules form micelles. When surfactants are dissolved in water, there is an increase in the free energy of the system due to the distortion between the hydrophobic tail of the surfactant and the aqueous phase.[35] To reduce this, the surfactants go to the surface with the hydrophobic groups pointing away from the water. The distortion and therefore free energy can also be reduced by surfactant aggregation into micelles with the hydrophobic tails pointing towards each other, protected from the aqueous phase. Therefore, as the concentration of surfactants increase, and there is less space for the surfactants to aggregate at the surface, they instead form micellular structures, at which point the CMC is reached.[35]

Almost all parameters involved in the formation of micelles see a change in the trend in values at the point the CMC is reached, as shown for conductivity and for the surface tension in **Figure 2.10**.[35] In the case of surface tension, a measurement used frequently in the calculation of the CMC in a system, once micelles form the surface tension decreases very little due to the fact that monomers are surface active however micelles are not.[36]

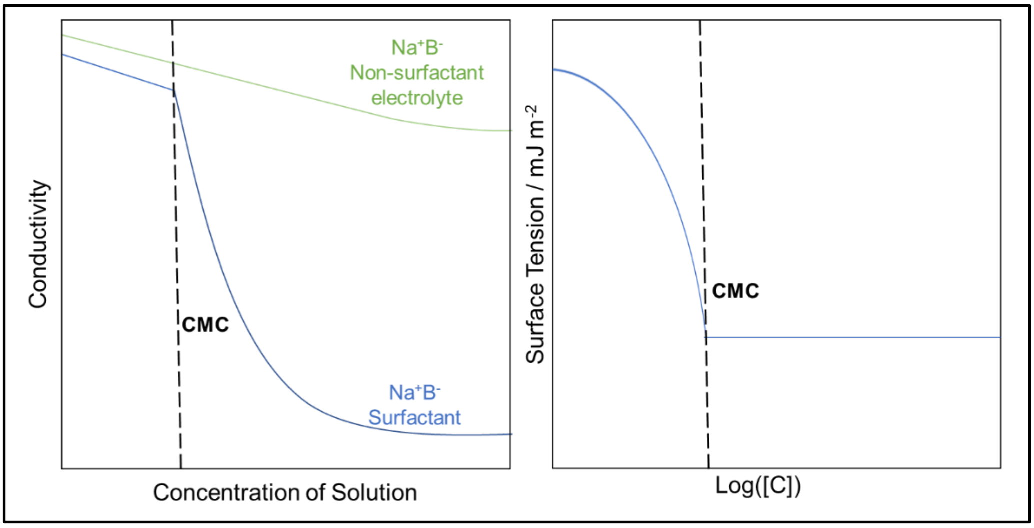

Figure 2.10 Conductivity (*Left*) and Surface Tension (*Right*) plots showing the change in trend once the Critical Micelle Concentration is reached. Adapted from *Surfactants and Interfacial Phenomena.*[33,35].

However, there are many factors that control the CMC, mainly revolving around the structure of the surfactant. In general, as the number of carbon atoms increases in the hydrophobic tail, the CMC decreases due to the unfavourable interaction with water. However, when the number of carbons is more than 16, the CMC value does not change as rapidly, due to the chains coiling in water.[37] If the tail is branched, the CMC does not decrease as rapidly with increase of carbon atoms, and in fact when the tail is unsaturated the CMC is higher as a result of steric hindrance within the micelle between the tails. This is also true with bulky tails and heads. If the hydrophobic tail has a polar group, the CMC increases greatly compared to an un-polar equivalent due to the favourable interactions with water. CMCs are also larger when there is more than one hydrophilic group in the surfactant compared to a single group.[35] Pyridinium cationic heads have smaller CMCs than trimethylammonium salts, due to their planarity and therefore less steric hindrance in micelle formation.[35]

2.4 Liquid Scintillation Cocktails and Sample Preparation

As introduced in **Chapter 1**, liquid scintillation cocktails are divided into two groups, those formulated from “classical” components, and those that utilise more environmentally friendly and less harmful components, particularly in terms of the solvent. However, the components that were once considered “safer” are now under investigation, and as will be shown in the following section, it is a difficult balance between a “safer” solvent that provides a higher flash point and low vapour pressure, with the environmental implications that they bring. Cocktails can also be divided into “organic” and “emulsifying” formulations. As the formulation used in the work herein is based upon an oil-in-water microemulsion, only emulsifying cocktails (water-in-oil microemulsions) will be considered herein, containing three main components; solvent, scintillator(s), and surfactants, all of which will be described herein.

2.4.1 Solvent

As discussed in **Chapter 1**, the decaying radioisotope releases a beta particle which activates and excites the nearby solvent molecules, which then transfers this energy to the scintillant(s), leading to emission of light. Therefore, although the scintillants used need to be carefully selected, the solvent is also a large component of the scintillation mechanism, as it is responsible for the primary energy transfer and makes up between 60-99% of the cocktail.[38] There are two classes of LSC cocktails used based upon which solvents are used; “Classic” and “Safer”. “Classic” cocktails contain toluene, xylene or pseudocumene whereas “Safer” cocktails are those made from di-isopropylnaphthalene (DIN), phenylxylylethane (PXE) or dodecyl benzene (linear alkyl benzene, LAB)[29] shown in **Figure 2.11**. “Safer” solvents benefit from high flash points (the temperature at which a liquid can ignite in air) and low vapour pressures as shown in **Table 2.1**, and are also less toxic compared to “Classic” solvents.

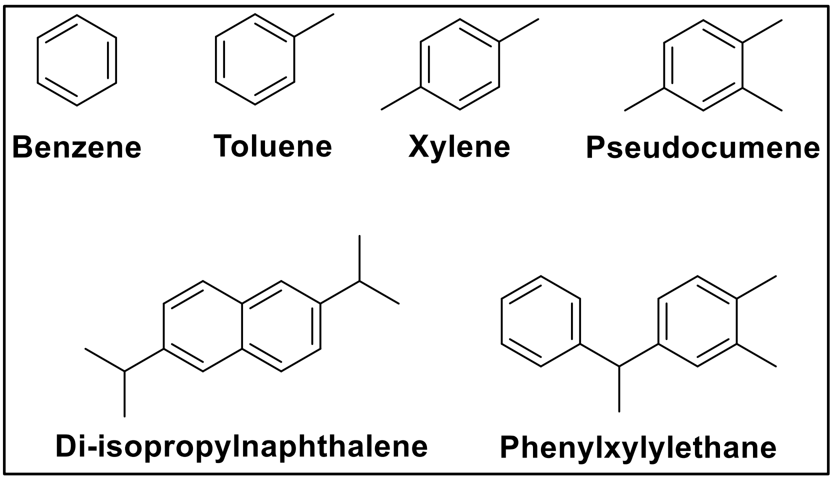

Figure 2.11 Solvents used in both “Classic” (*Top*) and “Safer” (*Bottom*) cocktails.

As the solvent is in such excess compared to the scintillants, and therefore the emitted beta particle will come into contact with the solvent molecules first, it is important that the solvent selected can efficiently absorb and transfer the energy without losing energy by an alternative pathway. Therefore, highly aromatic solvents are used as these have a high density of π-electrons. The more substituted the aromatic ring is, the higher the electron ring density, and so pseudocumene-containing formulations tend to performs better than those containing solvents such as benzene.[29] DIN and PXE, the safer solvents, have a higher counting efficiency than classic solvents.

Table 2.1 Flash points and vapor pressures for a selection of solvents used in scintillation cocktails, adapted from J. Thomson.[29]

Solvent	**Flash Point / °C**	**Vapor pressure at 25°C / mmHg**
“Classical”		
Toluene	4	28
Xylene	25	8
Pseudocumene	50	2
“Safer”		
Di-isopropylnaphthalene	140	<1
Phenylxylyethane	149	<1

Even though DIN and PXE are increasingly being used as the safer option, of the classical solvents pseudocumene is still widely used due to its high flash point, low vapour pressure and low diffusion into plastics (as some scintillation vials are made of plastic instead of glass).[28,29]

As well as this, despite DIN being listed as a “safer” alternative, it is also a potential candidate for removal in new REACH regulations.[39] REACH regulations came into effect in 2007, and aim to remove harmful chemicals that are used in large quantities, and instead force a change to safer alternatives. DIN was listed on the Community Rolling Action Plan in 2013, due to it being suspected of being persistent, bioaccumulating and toxic, and its wide use in industry. Persistent chemicals accumulate in the environment due to their lack of degradation, and thus it is currently under evaluation with further tests required. If moved to the Candidate List, where substances are then aimed to be phased out over a 3-5 year period, it will require authorisation to continue its use, which is costly to the industry.[39] A further implication of REACH regulations is discussed in **Section 2.4.3**, in regards to one of the most popular surfactants.

2.4.2 Primary and Secondary Scintillants

As discussed **Chapter 1**, there are certain characteristics that are required of the primary and secondary scintillants in order to gain maximum efficiency. The photophysical overlap of absorption and emission spectra for the primary and secondary scintillants respectively, as well as short lifetimes and large quantum yields, are important to gain the highest efficiency.[27–29] However, another parameter is the concentration at which the scintillants are loaded. If the concentration is too high, excimer formation can lead to concentration based self-quenching, reducing the photon yield.[29] That being said, if the scintillant is not completely planar a higher concentration can be used as excimers are less likely to form.[29]

The use of oxazole based scintillants was briefly discussed in **Chapter 1** and in **Section 2.2.2,** however the focus was on DPO and POPOP and it is important to mention other successful scintillators used in industrial formulations. For example, as POPOP suffers from solubility issues in organic solvents, there are other secondary scintillants more commonly used such as bis-MSB (**Figure 2.12**) which has a slightly higher wavelength shift but a similar quantum yield (94 *vs* 93 %[30]). There are many other primary scintillants available,[27,29,38] as shown in **Figure 2.12**, however unlike POPOP, DPO is still the main primary scintillant used[38] due to its high quantum yield, short lifetime and low cost.

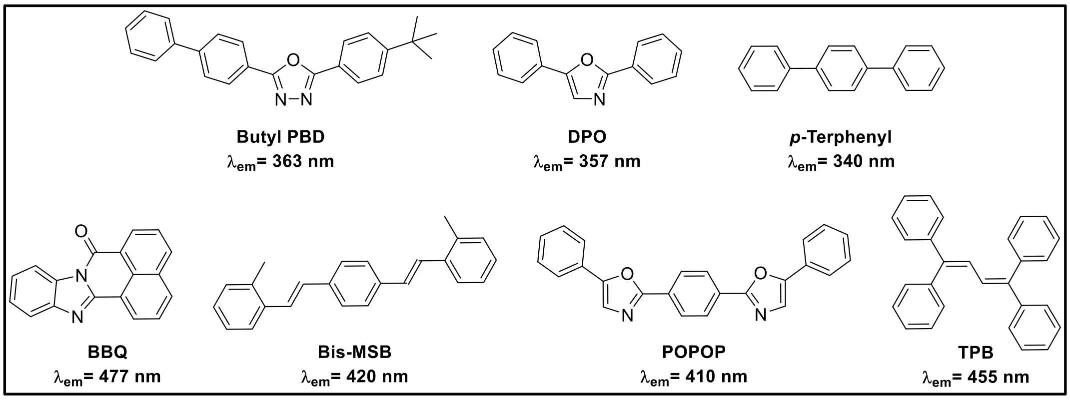

Figure 2.12 Primary (Top) and Secondary (Bottom) Scintillants commonly used in liquid scintillation counting. Emission data retrieved from National Diagnostics[38] and I. B. Berlman.[30]

2.4.3 Surfactants

As most samples that require scintillation analysis are aqueous, particularly environmental samples, surfactants are present in cocktails so that the aqueous sample and organic solvent can be in close contact, *via* a water-in-oil microemulsion formation. There are four different types of surfactants; non-ionic, anionics, cationic and amphoteric, however as discussed below, the main classes used are non-ionic and anionics, typically in conjunction to form stable water-in-oil droplet systems.[29]

Ethoxylates are the most common form of non-ionic surfactants used in commercial formulations. The chain length of ethoxylates can be varied to give different properties for different samples, which makes them useful for a range of cocktails. Alkyl phenol ethoxylates and alcohol ethoxylates are the most used (**Figure 2.13**) however alkyl phenol ethoxylates, particularly 4-nonyl phenol ethoxylates (NPE's) are now heavily restricted due to safety concerns.[29,40]

Alkyl phenol ethoxylates biodegrade to give endocrine disruptors, known to cause sexual dysfunctional issues in aquatic life, and evidence suggests they can also affect both wildlife and humans.[40,41] NPE's were added to the REACH candidate list and labelled as a Substance of Very High Concern (SVHC) in 2017, and from January 2021 NPE's could only be used within the EU if authorisation or exemptions were granted.[39] Authorisation of the use of NPE's is only temporary, and costs £250K, while an alternative is found. Exemptions only apply for research and development situations where only small volumes (less than 1 tonne per year) are used. As NPE's are some of the most effective surfactants they were used widely in scintillation cocktails, meaning that 57 LSC cocktails from leading manufacturers Perkin Elmer, National Diagnostics, Zinsser and Meridian will no longer be able to be used. [39] Alternative cocktails that are NPE-free have been formulated and will be discussed in **Section 2.4.4,** along with those that are currently restricted.

Alcohol ethoxylates can replace alkyl phenol ethoxylates, as these do not biodegrade to give harmful side products. However, they do not form microemulsions as successfully and also result in a lower counting efficiency as they are not aromatic.[29]

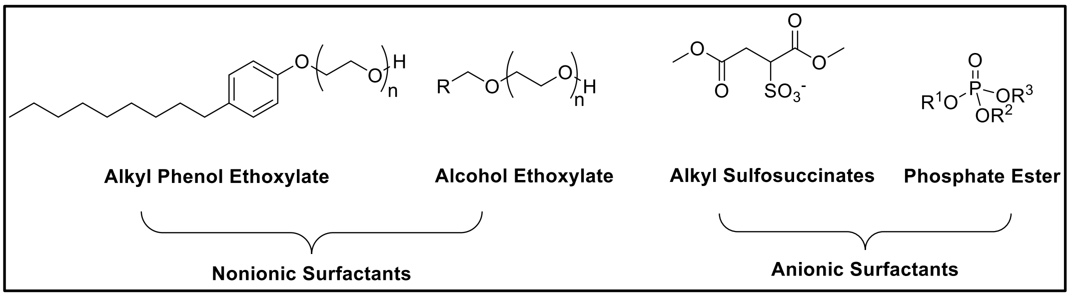

Figure 2.13 Non-ionic and Anionic Surfactants are the two most commonly used types of surfactants in liquid scintillation cocktails, particularly a combination of alky phenol ethoxylates and alkyl sulfosuccinates.[29]

There are many examples of anionic surfactants, however the two most used are alkyl sulfosuccinates and phosphate esters (**Figure 2.13**). The former are combined with non-ionic ethoxylates to yield larger microemulsions, and increase the stability.[29] Phosphate esters are not as common due to their tendency to react with samples if the pH is not controlled. In the acid form, phosphate esters protonate DPO, and can react with metals and the solvent in the sample forming coloured solutions and leading to degradation of the cocktail. However, the neutral form shows resistance to chemiluminescence and can form microemulsions with more challenging samples, making them useful in specific cocktails if the pH is carefully controlled.[29]

Cationic and amphoteric surfactants are the least used due to distinct reasons. For cationic surfactants, the positive charge in the hydrophobic region reacts with anionic surfactants which are the most commonly used and are more successful in conjunction with non-ionic surfactants.[29] As cationic surfactants are inherently basic, chemiluminescence can also occur.[29] Amphoteric surfactants, having both positive and negative centres, are coloured and have poor solubility in scintillant solvents, and are therefore rarely used commercially.[29]

2.4.4 Examples of Cocktails

To the best of the authors knowledge, there are currently no known oil-in-water microemulsion systems used in scintillation counting, however the majority of liquid scintillation cocktails are synthesised to produce water-in-oil microemulsions, due to the fact that samples are typically aqueous. As discussed in **Chapter 1** and in **Section 2.4.5** below, this leads to high disposal costs and environmentally unfriendly techniques. Not only this, but as discussed in detail above, many of the components of liquid scintillation cocktails are toxic, even those that are classified as “safer”. In this section, a range of different cocktails will be discussed, with their components compared.

Table 2.2 shows a comparison between the composition of traditionally “Classical” and “Safer” cocktails based on the solvent flash point and flammability, giving insight into the various components used in liquid scintillation, and overlaps between the formulations. For example, despite Ultima Gold XR being the “safer” cocktail due to the solvent having a high flash point, DIN may have many detrimental effects on the environment, as discussed previously. As well as this, both formulations used alkylphenol ethoxylates, with Ultima Gold XR specifically containing an NPE. Therefore, the once “safer” cocktail is now restricted in use, with formulations using traditional solvents becoming more popular, as will be discussed below.

Table 2.2 Comparisons between “Safer” formulation Ultima Gold XR[42], and “Classical” cocktail Hionic-Fluor[43].

	Hionic-Fluor “Classical”	***Ultima Gold XR “Safer”***
Solvent	Pseudocumene	Diisopropyl naphthalene isomers
Surfactants	• Phosphoric acid, butyl ester, with 2,2'-iminobis(ethanol) • 2-Ethylhexyl phosphate diethanolamine salt • Alkylphenol polyglycolether • Triethyl phosphate • Alkylphenol Polyglycolether • Sodium dioctyl sulphosuccinate	• Ethoxylated nonylphenol • Docusate Sodium • Triethyl phosphate • Bis(2-ethylhexyl) hydrogen phosphate • 3,6-dimethyloct-4-yne-3,6-diol
Primary Scintillant	2,5-Diphenyl oxazole	2,5-Diphenyl oxazole,
Secondary Scintillant	1,4-Bis-(2-methylstyryl)-benzene	1,4-Bis-(2-methylstyryl)-benzene

Dependent on composition, liquid scintillation cocktails can have a variety of properties for different methods of sampling or different concentrations of sample. For example, Gold Star (**Table 2.3**) is particularly useful for concentrated aqueous samples, and has a high chemiluminescence resistance (due to the use of phosphate esters as one of the surfactants). Ultima Gold (**Table 2.4**) is a multi-purpose cocktail, however is particularly useful for samples that can lead to increased quenching. However, due to the restriction on use of NPEs, many cocktails that were efficient for particular sample compositions can no longer be used industrially. Since the restriction, Meridian has developed a series of cocktails in their “ProSafe” range, which replace the NPE surfactants with alkyl ethoxylates, with some cocktails shown in **Table 2.3-2.4** that can be direct substitutes for the restricted compositions.

Table 2.3 Comparisons between Gold Star[44] formulation and ProSafe HC+[45]

	Gold Star	***ProSafe HC+***
Solvent	Diisopropyl naphthalene isomers	Diisopropyl naphthalene isomers
Surfactants	• Ethoxylated nonylphenol • Phosphate ester • 2-(2-butoxyethoxy)ethanol	• Alcohol, secondary C11-15 ethoxylated • Docusate Sodium • Phosphate ester

However, the ProSafe range may also be restricted in the future due to their use of DIN as a solvent. This will again reduce the amount of possible scintillation cocktails available.

Table 2.4 Comparisons between Ultima Gold[46] and ProSafe+[47]

	Ultima Gold	***ProSafe+***
Solvent	Diisopropyl naphthalene isomers	Diisopropyl naphthalene isomers
Surfactants	• Ethoxylated nonylphenol • Bis(2-ethylhexyl) hydrogen phosphate • Dioctyl sodium sulfosuccinate • Triethylphosphate	• Alcohol, secondary C11-15 ethoxylated • 2-(2-butoxyethoxy) ethanol • Phosphate ester

Although Meridian has developed a large range of NPE-free cocktails, Perkin Elmer has also developed NPE-free compositions, including Pico-fluor, the composition of which is presented in **Table 2.5**. Unlike the ProSafe range, Pico-Fluor uses 1,2,4-trimethylbenzene as a solvent. Although this was a traditionally unsafe solvent due to it's lower flash point, due to the restrictions that may come into play with DIN, it may in fact be the safer option environmentally.

Table 2.5 Components of Pico-Fluor Plus scintillation cocktail.[48]

	Pico-Fluor Plus
Solvent	1,2,4-trimethylbenzene
Surfactants	• Isotridecylalcohol • Phosphoric acid, 2-ethylhexyl ester • 2-(2-butoxyethoxy)ethanol • Sodium dioctyl sulphosuccinate • 2,2'-iminodiethanol • Fatty alcohol polyglycolether

2.4.5 Disposal

65% of organic radioactive waste is from liquid scintillation cocktails, however as the radioactivity in most cases is low the disposal issues in fact arise from the components of the cocktails themselves.[29] Currently, there are three different methods for disposal; incineration, chemical oxidation and steam reforming, however the first is by far the most common. Despite being the most common form of disposal, there are many risks associated with its use. Firstly, the transportation from the location the cocktail was used to an off-site incineration facility poses its own risk due to flammability, toxicity and of course the low radioactivity of samples. By incinerating CO_2 is released into the atmosphere, which is a disadvantage in itself, however this is also paired with the potential of radioactive release into the atmosphere. The ash generated from incineration will also be radioactive, and this adds more cost to an already high cost procedure.[29]

Pair these issues with the harmful degradation products that form from phenol ethoxylates[41] and DIN[39], discussed earlier, and it is clear to see that even with “Safer” cocktails, there is an urgent need for a method that is greener, low cost and easier to dispose of.

By using an oil-in-water system, the organic content is substantially reduced and therefore the total organic waste is easier to dispose of, making up a fraction of organic content currently used in liquid scintillation cocktails. This, paired with the use of a non-NPE surfactant, makes the oil-in-water cocktail formulation described herein a possible alternative to the scintillation cocktails that are used today, and which may be removed from industrial use in the near future.

2.5 Results and Discussion

2.5.1 Synthesis and Characterisation of Oxazoles

2.5.1.1 Synthesis of Mono-Substituted Oxazoles

There are various methods for the synthesis of oxazoles, as discussed in **Section 2.2.1**. However most suffer from low yields,[5] problematic reaction conditions such as gaseous HCl[10] or strong cyclodehydrating agents,[7–9] and are therefore less suitable for a large scale industrial setting, particularly when formulating greener equivalents to liquid scintillation cocktails. As well as this, most methods yield di-substituted oxazoles, despite mono-substituted oxazoles being ideal fluorophores in themselves and also building blocks for further functionalisation. However as discussed in **Section 2.2.1**, work by A. M. van Leusen *et al*[11] provides a straight-forward, high yielding and one-pot reaction utilising tosylmethylisocyanide (TosMIC) to form mono-substituted derivatives.

Therefore, a selection of aromatic aldehydes were refluxed with TosMIC and K_2CO_3 in MeOH (and THF depending on reactant solubility[49]) for 24 hours (**Figure 2.14a**). Aldehydes were chosen based upon their resultant fluorescent properties, and thus R-groups containing anthracene, phenanthrene, pyrene and fluorene were chosen (**Figure 2.14b**). Despite previous reports that called for column purification, it was shown that following removal of solvent, addition of water to the crude solid followed by a dichloromethane extraction gave the desired oxazole products in moderate to excellent yields.

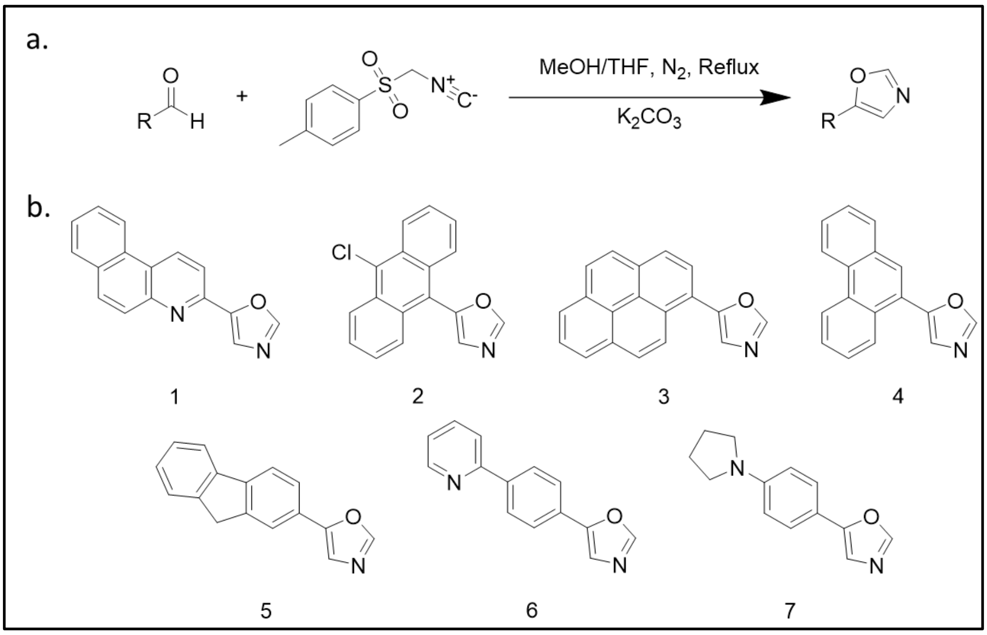

Figure 2.14 a) Reaction conditions of the van Leusen oxazole synthesis[49]; b) Structures of the aryl-substituted oxazoles (**1-7**).

^{1}H NMR spectroscopy provided clear evidence for the formation of the oxazole species *via* the absence of the aldehydic proton of the relevant starting material and the appearance of two new aromatic singlets between 8.5-7.9 and 7.9-7.1 ppm corresponding to the two proton environments for the 2- and 4- position respectively in the oxazole ring. ^{13}C {^{1}H} NMR spectroscopy also showed the absence of the aldehydic carbon and appearance of three carbon resonances corresponding to the oxazole ring.

Aryl oxazoles **1**, **2** and **7** were crystallised *via* slow evaporation of diethyl ether for structural studies, with all three examples showing the anticipated structures (**Figure 2.15** and **Figure 2.16**). Oxazoles **1** and **7** show co-planarity between the oxazole ring and aryl substituent, however oxazole **2** shows an orthogonality with a torsion angle of 50.23° between the oxygen of the oxazole ring and anthracene R-group. As well as this, **2** shows π-π interactions of 3.866 Å between anthracene units (**Figure 2.15**), however there are no significant intermolecular interactions in the packing of **1** and **7**. The crystal structure of **7** shows two conformations of the terminal pyrrolidine group (**Figure 2.16**). In **Chapter 5,** this is further suggested with photophysical measurements recorded at 77 K showing two separate emissive bands for ligand **19** within ***fac*****-[Re(19)(CO)3Br],** which is likely due to the frozen conformation decoupling the different chromophoric components of the ligand resulting in distinguishable emission from each.

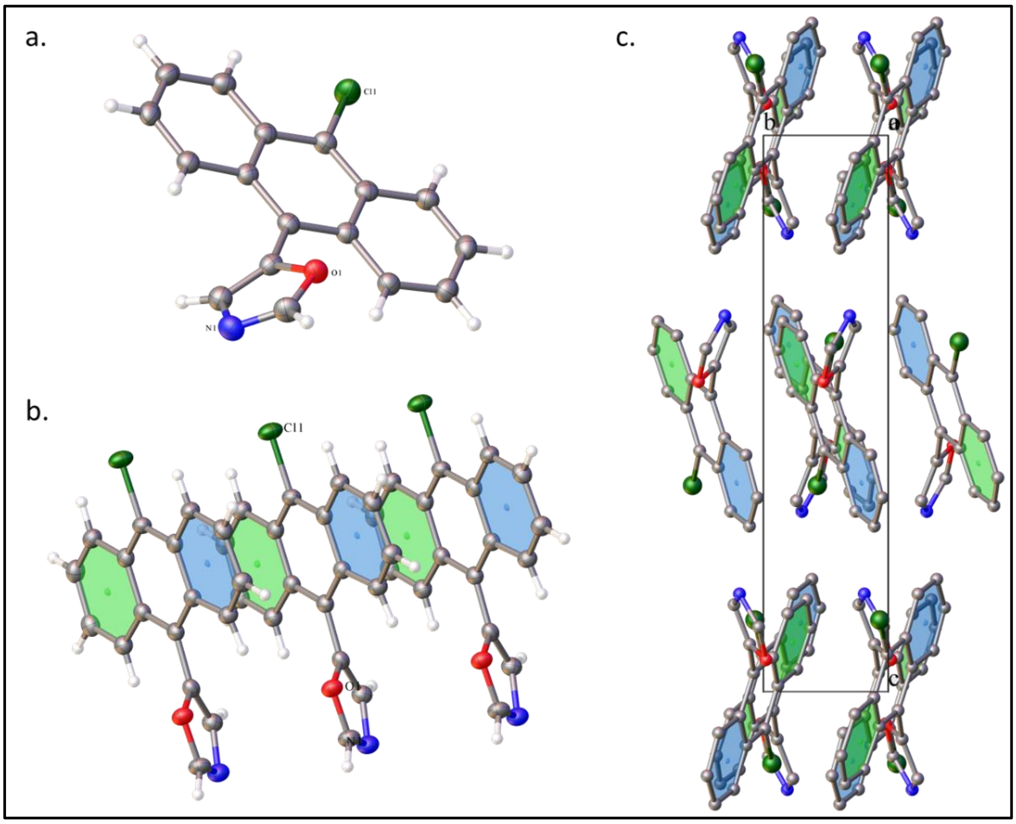

Figure 2.15 a) X-ray crystal structure of **2**, showing the oxazole ring orthogonal to the anthracene unit; b) π-π interactions between the anthracene R-groups, with a centroid-centroid distance of 3.866 Å; c) Packing diagram of **2**, showing the oxazole units anti-parallel to each other; Crystal Data: $C_{17}H_{10}ClNO$, M_r = 279.71, monoclinic, $P2_1/n$ (No. 14), a = 18.1934(8) Å, b = 3.8659(2) Å, c = 19.1544(8) Å, β = 115.941(5)°, $\alpha = \gamma$ = 90°, V = 1211.46(11) Å^3, T = 100(2) K, Z = 4, Z' = 1, $\mu(CuK_\alpha)$ = 2.725 mm^{-1}, 9872 reflections measured, 2223 unique (R_{int} = 0.0851) which were used in all calculations. The final wR_2 was 0.2121 (all data) and R_1 was 0.0740 (I > 2(I)).

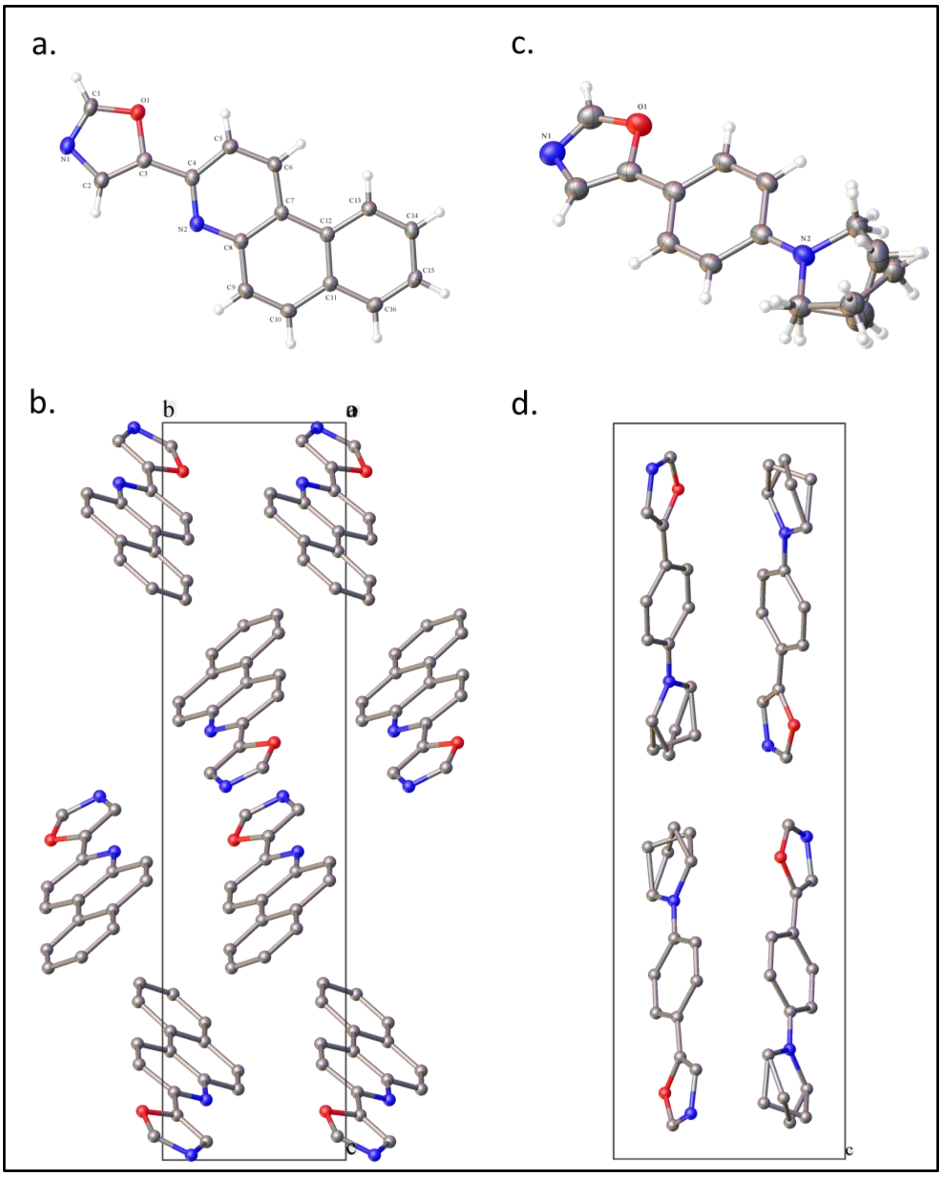

Figure 2.16 a) X-ray crystal structure of **1**, showing the oxazole ring co-planar with the R-group; b) packing structure of 1; c) X-ray crystal structure of **7**, showing co-planarity between oxazole ring and R-group; d) packing structure of **7**; Crystal Data of **1**. $C_{16}H_{10}N_2O$, $M_r = 246.26$, monoclinic, $P2_1/c$ (No. 14), $a = 8.7924(2)$ Å, $b = 5.64640(10)$ Å, $c = 23.1073(5)$ Å, $\beta = 99.918(2)°$, $\alpha = \gamma = 90°$, $V = 1130.03(4)$ Å^3, $T = 100(2)$ K, $Z = 4$, $Z' = 1$, $\mu(\mathrm{MoK}_\alpha) = 0.093$ mm^{-1}, 14529 reflections measured, 2912 unique ($R_{int} = 0.0356$) which were used in all calculations. The final wR_2 was 0.1186 (all data) and R_1 was 0.0439 (I > 2(I)); Crystal Data of **7**. $C_{13}H_{14}N_2O$, $M_r = 214.26$, orthorhombic, $P2_12_12_1$ (No. 19), $a = 6.41320(10)$ Å, $b = 7.34060(10)$ Å, $c = 23.2065(3)$ Å, $\alpha = \beta = \gamma = 90°$, $V = 1092.49(3)$ Å^3, $T = 100(2)$ K, $Z = 4$, $Z' = 1$, $\mu(\mathrm{CuK}_\alpha) = 0.669$ mm^{-1}, 11764 reflections measured, 1997 unique ($R_{int} = 0.0315$) which were used in all calculations. The final wR_2 was 0.0715 (all data) and R_1 was 0.0281 (I > 2(I)).

2.5.1.2 Di-Substituted Oxazoles

Coupling to the 2-position of the oxazole ring was achieved in moderate yields using a modified Ullmann method.[50] Although not a high yielding reaction, the Ullmann method had the advantage over other coupling methodologies typically employing a Palladium catalyst, as CuI (the catalyst used) is significantly easier to handle due to palladium's inherent instability in air. When a palladium cross-coupling reaction was attempted using $Pd(PPh_3)_4$,[51] the product could not be isolated without considerable loss of yield and thus a copper mediated approach was used.

Using iodo-naphthalene, six novel oxazole derivatives were synthesised using previously synthesised oxazoles in **Section 2.5.1.1** (**Figure 2.17**). Oxazole **6** could not be di-substituted despite numerous attempts, however this is believed to be due to the R-group of the oxazole coordinating to the copper catalyst and thus removing the starting oxazole from the reaction and leading to an inactive copper species.

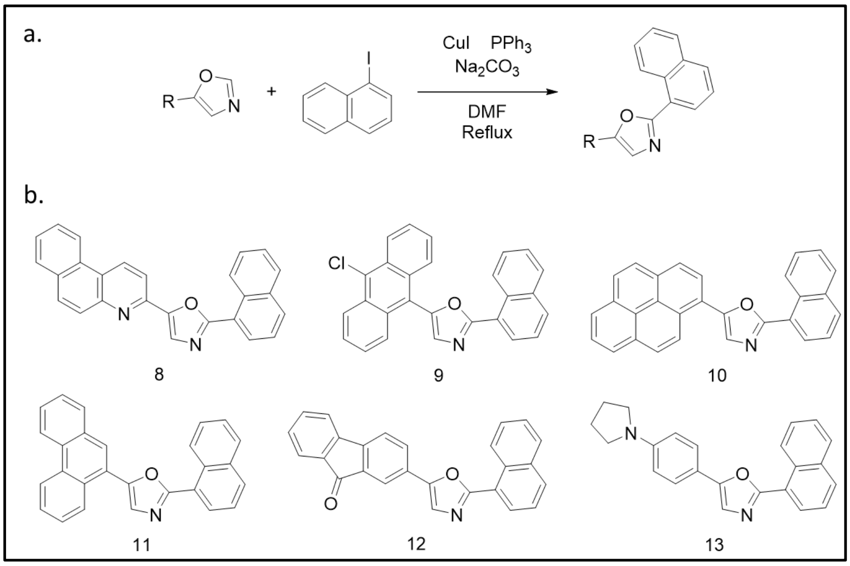

Figure 2.17 a) Reaction conditions of the modified Ullman coupling reaction[50]; b) Structures of the di-substituted oxazoles (**8-13**).

Although reported literature calls for one equivalent of CuI over a 2-hour period, it was found that four equivalents and an excess of the iodo-aryl species was required over 48 hours to yield the desired product in low to moderate yields. After 48 hours, ethylene diamine in water was added to the crude reaction mix, and the product extracted into dichloromethane (DCM). Ethylene diamine in water was then used to wash the organic layer to remove excess copper, and the crude oil obtained *via* evaporation of solvent. This was then triturated in ethanol and filtered to remove excess iodo-naphthalene and triphenyl phosphine oxide to yield the pure product.

^{1}H NMR spectroscopy provided evidence for the coupling of naphthalene to the oxazole ring *via* the absence of the aromatic singlet belonging to the proton of the 2-position of the oxazole ring, and the appearance of aromatic protons indicative of a naphthalene species. ^{13}C {^{1}H} NMR spectroscopy also showed the appearance of 10 new resonances corresponding to the naphthalene ring. ^{31}P NMR spectroscopy was used to ensure all triphenylphosphine oxide, a side product in the reaction, had been removed in purification.

In the case of **12**, the ^{1}H NMR resonance belonging to the aliphatic CH_2 of the fluorene ring was lost, as well as the aliphatic ^{13}C NMR resonance (**Figure 2.18**). A new ^{13}C resonance at 193 ppm was observed, leading to the postulation that due to the oxidising nature of the reaction the CH_2 group in the fluorene ring had oxidised to form a ketone. This was further confirmed *via* HR-MS with a peak at 374.1178 ($[M+H]^+$) instead of 360.1383 for the non-oxidised species.

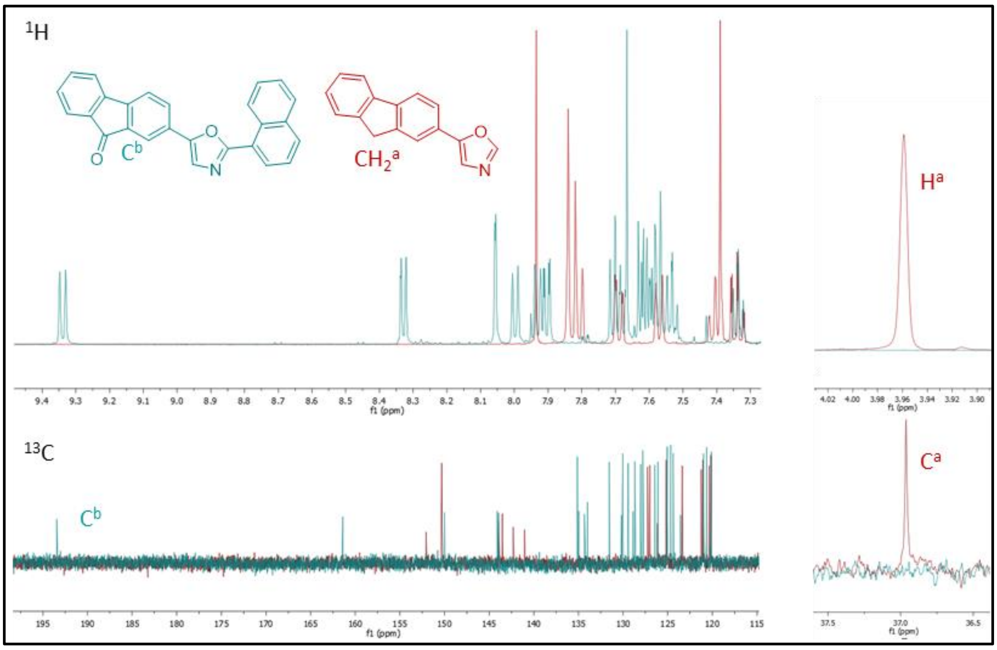

Figure 2.18 ^{1}H (top) and ^{13}C {^{1}H} (bottom) NMR spectra of mono-substituted oxazole **5** and disubstituted oxazole **12**, showing original C^a ^{13}C resonance at 37 ppm shifted to 193 ppm (C^b) upon oxidation to ketone. This is further confirmed by the ^{1}H NMR H^a resonance at 3.96 ppm disappearing following the coupling reaction.

2.5.1.3 Photophysical Studies

2.5.1.3.1 Mono-Substituted Oxazoles

The UV-vis absorption spectra of each oxazole was obtained in acetonitrile (AcN) at room temperature (**Figure 2.19** and **Table 2.6**). Mono phenyl-substituted oxazoles are known to exhibit a peak between 243-267 nm of strong intensity ($\log_{10}(\varepsilon) > 3$), with shifts due to substitution of the phenyl rings,[52] **1-4** all exhibit multiple peaks in this region due to π-π* transitions.

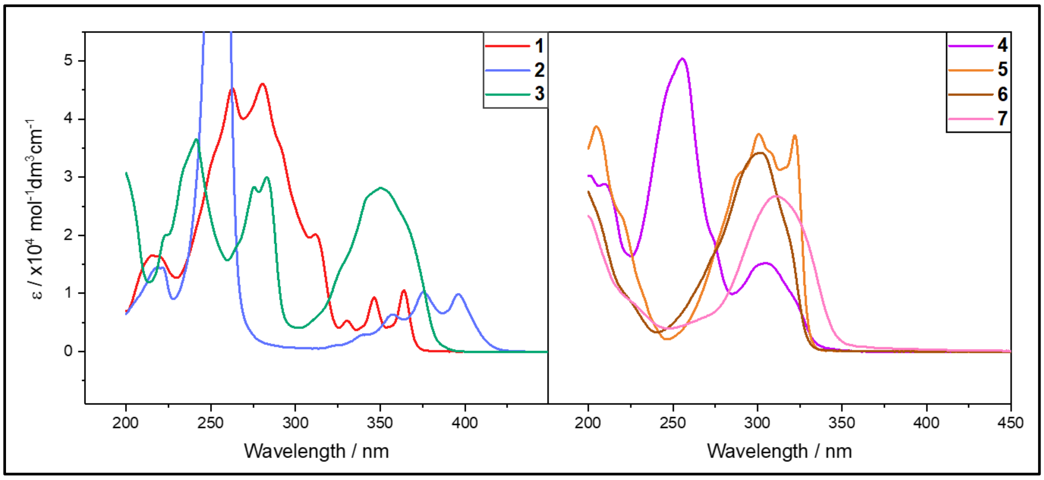

Figure 2.19 UV-vis. absorption spectra (recorded in AcN) for oxazoles **1-7**.

2 exhibited a band centred at 257 nm of high intensity (ε = 149500 mol^{-1}dm^{3}cm^{-1}), and absorption at lower energy with pronounced vibronic structure at 357, 375 and 396 nm. Although there are no known examples of substituted chloro-anthracenes containing a 5-membered ring, bromo-anthracenes bearing either furan or thiophene rings exhibit similar absorption properties to that observed. Both 9-bromo-10-(thien-2-yl)anthracene and 9-bromo-10-(fur-2-yl)anthracene show strong absorption at 255 and 257 nm respectively, with lower energy absorptions between 350 and 400 nm (recorded in MeOH and $CHCl_3$ respectively)[53]. **1** also exhibited vibrational fine structure at 364, 347, 330 nm, whereas **3** exhibited a broad band in this region.

6 showed a single absorption peak at 302 nm, which was red shifted compared to other phenyl pyridine-based systems due to the extended conjugation brought about by the oxazole ring. **7** also showed a single low energy absorption peak at

312 nm, red shifted from 5-phenyloxazole due to the presence of an electron donating amine moiety extending the π-system.

Table 2.6 Absorption and emission data for oxazoles **1-7.** λ_{ex}=295 nm for lifetime measurements.

	λ_{abs} (ε) / nm (mol^{-1}dm^{3}cm^{-1})	λ_{em} / nm	τ_{obs} / ns	ϕ / %
1	364 (10550), 346.5 (9300), 330 (5300), 311.5 (20200), 281 (46000), 263 (45250), 215 (16550)	369, 388, 408 (sh)	5.04 ± 0.50	43 ± 4
2	396 (9900), 375 (10200), 357 (6400), 257 (149500), 222 (14400), 216 (13950)	430 (sh), 448	5.04 ± 0.50	43 ± 4
3	350 (28100), 283 (29950), 275.5 (28300), 241.5 (36550)	393, 411	11.2 ± 1.1	27 ± 3
4	305 (15200), 255.5 (50400), 209 (28850)	372 (sh), 386, 400 (sh)	2.2 ± 0.2 (8.54 %), 12.2 ± 1.2 (91.46%)	4.6 ± 0.5
5	322 (37200), 301 (37400), 205 (38700)	347, 362 (sh)	1.3 ± 0.1	62 ± 6
6	302 (34200)	361	0.26 ± 0.03	16 ± 2
7	311.5 (26750)	376	2.7 ± 0.3	53 ± 5

Fluorescence spectra recorded in aerated AcN showed all oxazoles emit between 330-450 nm, giving a large range of emission from violet to blue fluorescence (**Figure 2.20**). The range of emission wavelengths observed, due to the differing substituents, not only shows that the photophysics is centred upon the substituents and not primarily the oxazole ring, but is also ideal for element-specific scintillation due to the differing signals that can be obtained for each oxazole.

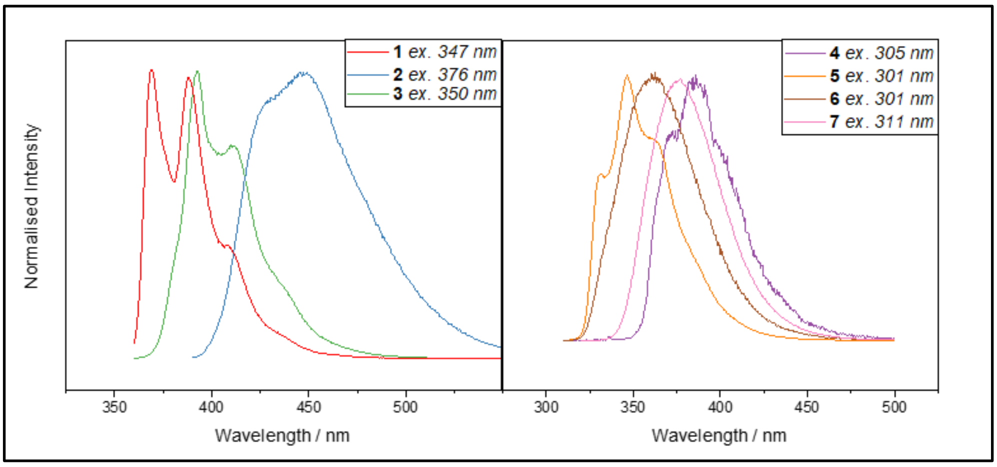

Figure 2.20 Emission spectra (recorded in AcN) for oxazoles **1-7**.

1-3 showed bathochromic shifts due to increased conjugation compared to the latter oxazoles in the series. **1**,**3** and **5** also gave evident vibrational fine structure, similar to that expected from their respective polyaromatic R-groups.

The quantum yields for all seven oxazoles were varied, with **5** and **4** exhibiting the highest and lowest values of 62% and 4.6% respectively. Time-resolved luminescence measurements showed that all oxazoles exhibited short lifetimes of < 15 ns, attributed to the $^1\pi$-π^* dominated $S_1 \rightarrow S_o$ radiative decay process.

All oxazoles with the exception of **6** were further coupled to naphthalene to form di-substituted oxazoles, with all photophysics recorded in $CHCl_3$ due to solubility of the di-substituted product. Therefore, the starting primary oxazoles were also recorded in $CHCl_3$ to compare the changes in photophysical behaviour (**Section 2.5.1.3.2**), however this also showed large variations in the quantum yields recorded as a result of using a less polar solvent, as shown in **Table 2.7**. Both the radiative (k_r) and non-radiative (k_{nr}) rates were calculated in each case, clearly showing an decrease in the rate of non-radiative decay for oxazoles **1**,**2** and **3** on going from a polar to non-polar environment, and an increase for oxazoles **5** and **7**. This is undoubtably a reflection of the solvatochromic nature of these systems, and requires further investigation using a wider range of solvent systems to confirm.

Table 2.7 Photophysical data comparison in AcN and $CHCl_3$ for oxazoles **1-7**.

	AcN			**$CHCl_3$**		
	ϕ	***k_r / x10^7 s^{-1}***	***k_{nr}/ x10^7 s^{-1}***	***ϕ***	***k_r / x10^7 s^{-1}***	***k_{nr} / x10^7 s^{-1}***
1	43	8.53	11.3	57	12.95	9.77
2	43	8.53	11.3	78	12.43	3.51
3	27	2.41	6.52	100	11.4	N/A
4	4.6	0.41	8.41	3	0.37	12.00
5	62	47.69	29.23	21	28.38	106.76
7	53	19.63	17.41	0.8	1.46	181.02

As discussed previously, for effective scintillation the secondary scintillant must have high quantum yields (so that maximum intensity is received), and short lifetimes (to reduce overlap of signal). POPOP is reported to have a quantum yield of 93% (cyclohexane) and lifetime of 1.47 ns.[30] Despite the quantum yields varying, with some oxazoles exhibiting quantum yields exceeding 70% (2 and 3), the lifetimes were all in the nanosecond range, as would be expected from simple fluorescent organic molecules, and thus in combination with these high quantum yields makes them ideal for secondary scintillation.

2.5.1.3.2 Di-substituted Oxazoles

The UV-vis absorption spectra of oxazoles **8-13** were obtained in $CHCl_3$ at room temperature, and compared to their mono-substituted equivalents (**Figure 2.21**). Although mono phenyl-substituted oxazoles are known to exhibit high energy absorbances with strong intensity, di-substituted oxazoles are known to instead exhibit multiple bands of varying intensity, with the high energy bands lower in intensity than the lower energy transitions, the latter of which are due to the extension of the conjugation through the oxazole ring.[4]

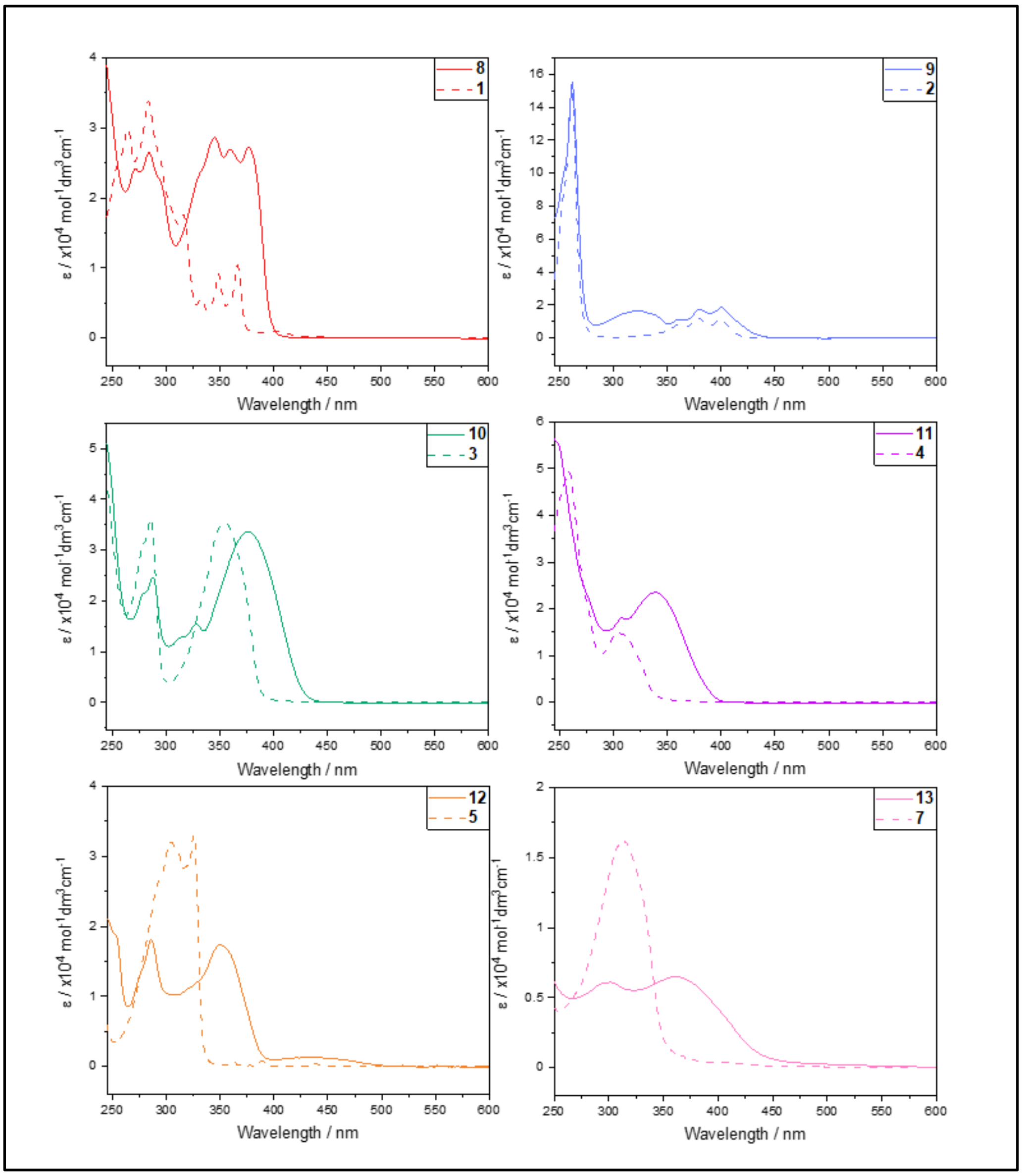

Figure 2.21 UV-vis. absorption spectra (recorded in $CHCl_3$) for oxazoles **8-13** (solid line) and **1-7** (dashed line).

Due to the nature of the original R-group, oxazoles **8-13** all exhibited multiple bands due to a range of π-π* transitions already present within the mono-substituted oxazole. However, in the case of **9** a new high energy band was present at 323 nm, and in the case of **13**, the UV-vis spectra consisted of a high energy band at 301 nm and a low energy band at 362 nm, both with a far smaller extinction coefficient than the original oxazole (**7**). Oxazole **11** showed a new lower energy absorbance at 338 nm, of higher intensity than the original oxazole **4**, and a sharper absorbance at 308 nm. In the case of **10**, the absorption profile was similar to that of the mono-substituted oxazole **3**, with a red shift of absorption of the low energy band by 22 nm, however little shift in the high energy absorption. As expected, the low energy band exhibited an intensity almost double that of the high energy absorbance.[4] Oxazole **8** showed a very similar absorption profile to that of **1**, however the lower energy absorption bands exhibited an intensity of more than double that of mono-substituted oxazole. As well as this, whereas the low energy absorption of **1** showed vibronic fine structure divided into two bands, **8** exhibited a third band of lower energy. Due to the oxidation of the fluorene R-group of **5** into the fluorenone moiety, the absorption spectra of **12** cannot be directly compared to that of **5**. Whereas oxazole **5** consisted of two close bands of high intensity at less than 350 nm, **12** instead exhibited a high energy band at 286 nm, and two low energy bands at 351 nm and 436 nm, the latter of which had a far smaller intensity than the higher energy bands but was similar to that shown by 2-methoxysubstituted fluorenones[54,55].

Table 2.8 Absorption and emission data for oxazoles **1-13**, recorded in $CHCl_3$**.** For oxazole **12** more than one lifetime was recorded, with λ_{em} given in each case, λ_{ex}=295 nm.

	λ_{abs} (ε) / nm ($mol^{-1}dm^{3}cm^{-1}$)	***λ_{em} / nm***	***τ_{obs} / ns (λ_{em})***	***ϕ / %***
8	378 (27300), 360 (26900), 345 (28600), 295 (sh) (22450), 284 (26500), 271 (24150)	484 (sh), 445 (sh), 418, 400	1.50 ± 0.15	74 ± 7
1	403 (900), 367 (10400), 349 (9200), 333 (5600), 316 (17600), 294 (sh) (26100), 284 (33800), 265 (29900)	440 (sh), 412 (sh), 392, 371	4.40 ± 0.44	57 ± 6
9	400 (18650), 380 (17500), 361 (11450), 323 (16500), 262 (155050)	500	3.09 ± 0.31	25 ± 3
2	399 (11800), 378 (12300), 360 (7900), 262 (153300)	451, 428 (sh)	2.31 ± 0.23 (21) 7.33 ± 0.73 (79)	78 ± 8
10	377 (33550), 328 (15400), 313 (12750), 288 (24750), 279 (21500)	496 (sh), 454, 433	2.03 ± 0.20	73 ± 7
3	355 (35500), 286 (36200), 278 (sh) (30800)	438 (sh), 409, 393	2.28 ± 0.23 (12) 9.70 ± 0.97 (88)	100 ± 10
11	339 (23550), 308 (18000), 242 (57600)	452 (sh), 427, 406	2.03 ± 0.20	85 ± 9
4	306 (14800), 259 (49200)	403 (sh), 387, 374 (sh)	3.05 ± 0.31 (25) 9.76 ± 0.98 (75)	3 ± 0.3
12	436 (1255), 351 (17380), 320 (sh) (11180), 286 (18090), 275 (sh) (12860), 254 (18635)	660, 560, 400	2.25[a] ± 0.23 (λ_{560}) 2.10 ± 0.21 (λ_{400})	31[b] ± 3 (λ_{285}) 7 ± 0.7 (λ_{330})
5	325 (33000), 304 (32000)	367 (sh), 349, 333 (sh)	0.74 ± 0.07	21 ± 2
13	362 (6530), 301 (6100)	464, 420, 353 (sh)	2.20 ± 0.22	29 ± 3
7	314 (16200)	397, 362	0.17 ± 0.02 (64) 1.22 ± 0.12 (36)	0.8 ± 0.1

[a] *τ_{obs} is presented at two different emission wavelengths (λ_{em}) due to two different emission maxima*

[b] *ϕ acquired at two different excitation wavelengths (λ_{ex}) due to λ_{ex} dependent emission spectra.*

Fluorescence spectra recorded in aerated $CHCl_3$ showed all oxazoles emitted at a higher wavelength than their mono-substituted equivalents (**Figure 2.22**), showing the increase in conjugation across the oxazole ring, with a broad emission range between 380-600 nm for oxazoles **8-11** and **13**. Oxazole **12**, which will be discussed in more detail below, showed emission up to 700 nm. As with the mono-substituted oxazoles, the large range of emission observed is ideal for element-specific scintillation as all emitted both around and above 420 nm and thus in the ideal range for photomultiplier tube sensitivity, discussed in **Section 2.2.2**.

8, **10** and **11** all gave evident vibrational fine structure, with similar emission profiles to their mono-substituted equivalents, albeit bathochromically shifted by 25, 50 and 40 nm respectively. **13** also gave a similar broad emission to that of the mono-substituted oxazole, with a 68 nm bathochromic shift in emission. These observations suggest that the naphthalene moiety does not affect the vibrational fine structure of the highly aromatic R-group of the mono-substituted oxazole, but instead extends the conjugation of the structure and thus a shift in the emission wavelength results.

The quantum yields for all oxazoles, much like their mono-substituted equivalents, were varied, as shown in **Table 2.8**. **8**, **10** and **11** all gave high quantum yields of 74, 73 and 85 respectively. For **8**, this was only slightly higher than that of **1**, however for **10** the quantum yield was in fact lower, and for **11** the quantum yield was considerably higher than their respective mono-oxazoles. **13** gave a quantum yield of 29%, which despite being low compared to **8**, **10** and **11**, was considerably higher than the quantum yield recorded for the primary oxazole in $CHCl_3$.

Time-resolved luminescence measurements showed that di-substituted oxazoles **8**, **9**, **10** and **11** all exhibited shorter lifetimes than their mono-substituted equivalents. For **12** and **13**, the lifetimes were larger than **5** and **7**, however both were less than 3 ns so can also be attributed, like the mono-substituted equivalents, to the $^1\pi$-π^* dominated S_1 -> S_o radiative decay process.

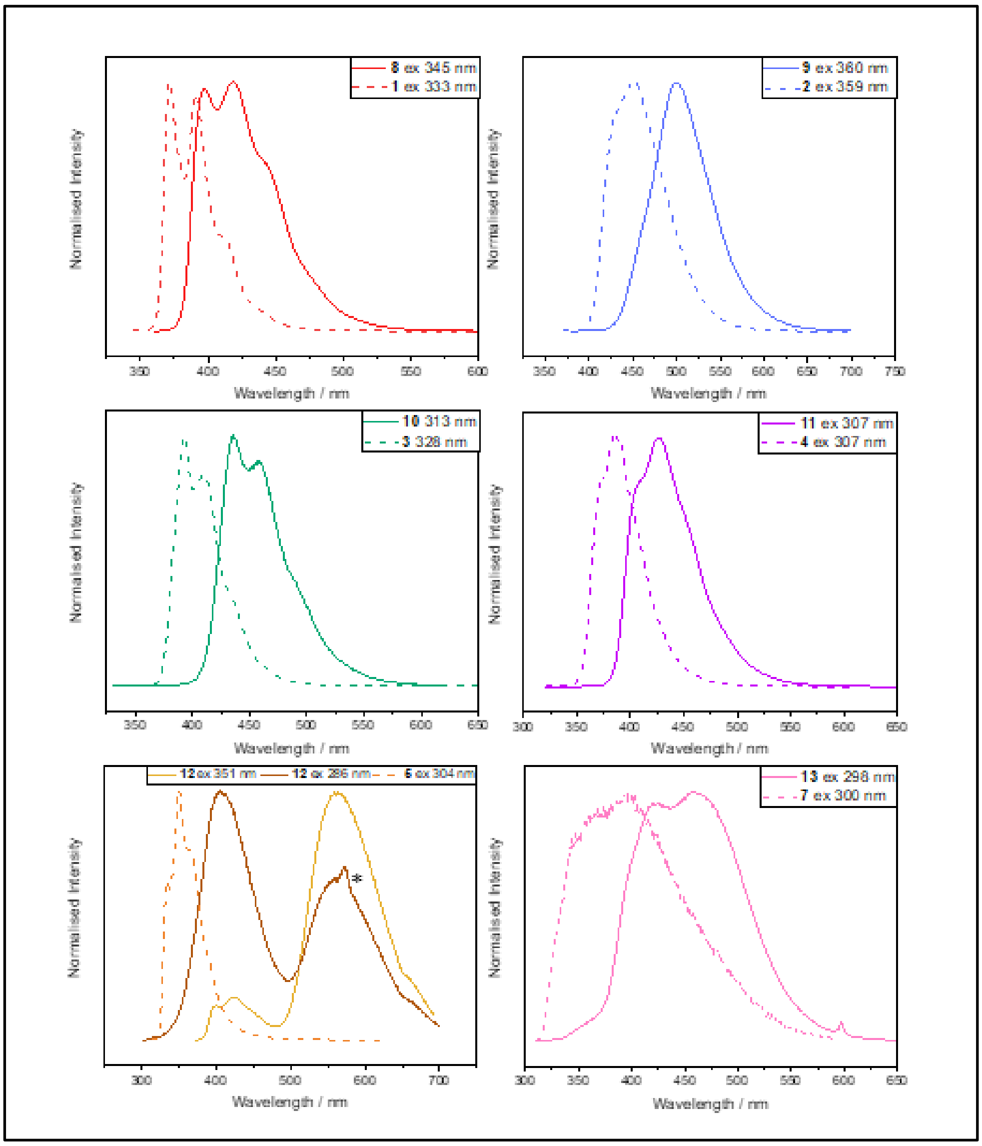

Figure 2.22 Emission spectra (recorded in $CHCl_3$) for oxazoles **8-13** (solid line) and **1-7** (dashed line). *denotes a lamp harmonic associated with the excitation wavelength.

Oxazole **9** posed a more complex emission, with a broad featureless band at 500 nm and small shoulder at 410 nm more evident at lower concentrations (**Figure 2.23**). Although the 500 nm band was originally thought to be an excimer, the emissive lifetime recorded was of the nanosecond scale (with excimer lifetimes typically smaller) and the excitation spectra matched that of the UV-spectra, which both suggested it was not an excimer.[56] As well as this, the fact that the 410 nm emission band did not become a dominating band at concentrations as low as 10^{-7} mol dm^{-3} further showed evidence that this was not the result of excimer emission. However, the emission band at 410 nm did occur at a similar wavelength to that of the mono-substituted oxazole, which is known to be dominated by the chloroanthracene R-group *via* DFT analysis (**Section 2.5.1.4**). *Via* analysis of the excitation acquisition at 410 nm (**Figure 2.23**), the vibrational fine structure of the chloroanthracene absorbance could be observed, further suggesting that the weak emission shown at 410 nm was that of the chloroanthracene group and thus suggesting that the broad, featureless emission at 500 nm was in fact due to charge transfer across the oxazole ring between the naphthalene and chloroanthracene groups.

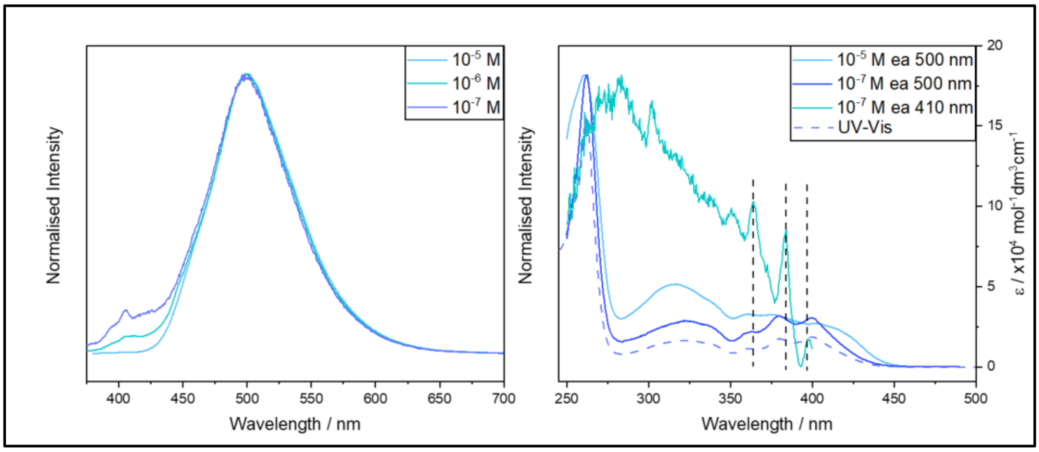

Figure 2.23 *Left:* Emission spectra of **9** recorded at 10^{-5}, 10^{-6} and 10^{-7} M, showing both emission at 500 and 410 nm. *Right:* Excitation acquisitions (solid lines) recorded at 10^{-5} and 10^{-7}, compared to UV-vis (blue dashed). Recorded in $CHCl_3$.

This was also suggested by the reduction in quantum yield, as each energy transfer step would lead to a loss of energy due to non-radiative relaxation to the lowest vibronic state in each singlet excited state. In **Section 2.5.1.4.2**, the LUMO+X states predicted for each transition were made up of π* orbitals localised upon either the chloroanthracene R-group or the naphthalene-oxazole, which also suggests a degree of charge transfer within the fluorophore.

In **Chapter 3**, this was further confirmed when the emission was recorded in water (1% DMSO) and within the polystyrene particle, where energy transfer was found in the latter but dominance of the chloroanthracene emission in the former.

12 also posed a more complex emission due to the oxidation of the fluorene to fluorenone, the latter of which is widely known to have emission properties that are sensitive to solvent[57], temperature[58] and substituents[59]. In non-polar solvents, triplet emission can occur *via* exothermic intersystem crossing (ISC), if the excited singlet state S_1 has n,π* character, to the T_1 or T_2 triplet states (π,π* character). However in polar solvents, where the singlet state possesses π,π* character, intersystem crossing is not possible as the T_3 triplet state (with n,π* character) becomes too high in energy for ISC to occur, leading to radiative and non-radiative relaxation from the singlet state[59] (**Figure 2.24**). This is particularly important when it is a polar protic solvent, as hydrogen bonds formed between the fluorenone carbonyl and solvent lead to non-radiative deactivation from the singlet state[55].

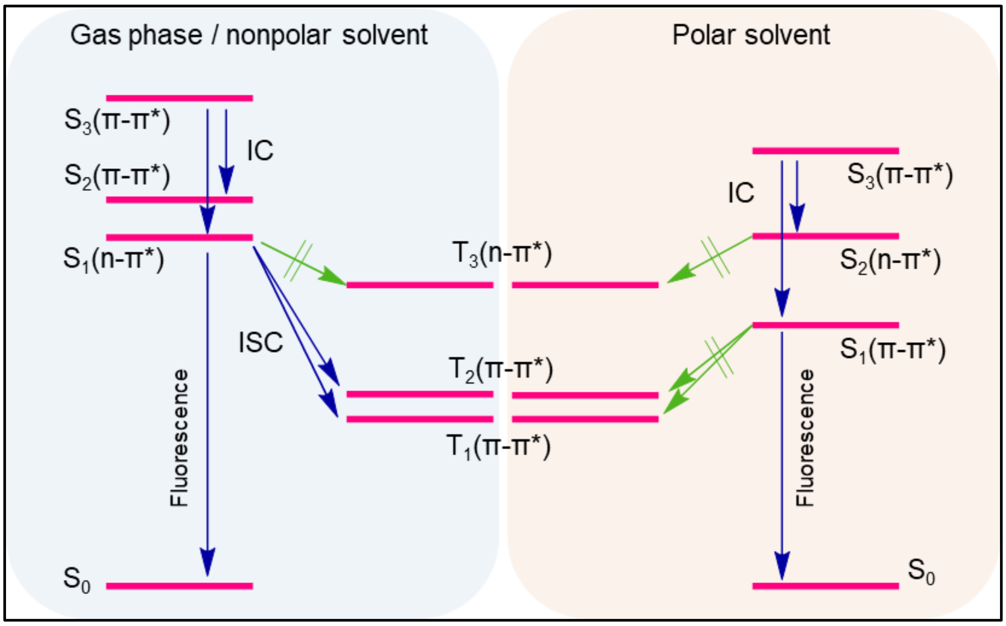

Figure 2.24 Schematic of energy levels involved in fluorenone emission in the gas phase, non-polar and polar solvents. Adapted from T. Gerbich *et al.*[60]

Meta substituents, as with **12**, can greatly influence these pathways, with electron withdrawing groups increasing ISC, whereas electron-donating groups increasing the rate of internal conversion *via* charge transfer to the π,π* singlet state, leading to the oxygen of the carbonyl becoming more basic and therefore a better H-bond acceptor in polar protic solvents[59]. **Figure 2.25** shows the emission spectra of **12** recorded over three wavelengths (*left*), and emission from the proposed charge transfer band at 436 nm (*right*), with excitation at higher energy leading to a duel emitting species. TDA-based TD-DFT, discussed in detail in **Section 2.5.1.4.2**, showed that there are two main excited states; that arising from the fluorenone and that from the entirety of the fluorophore, both π→π* in nature.

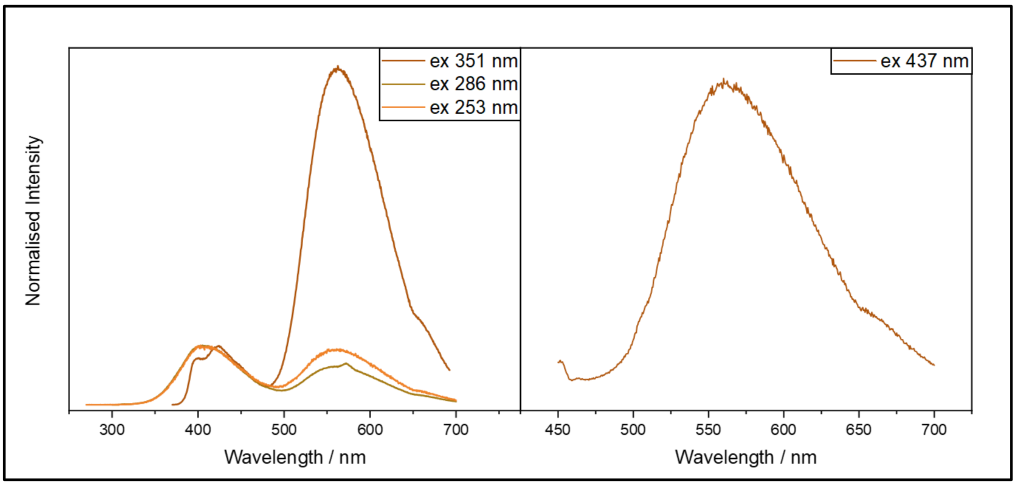

Figure 2.25 Emission spectra of **12** recorded over a range of excitation wavelengths; *Left:* excitation at 351, 286 and 253 nm, *Right:* excitation at 437 nm. Recorded in $CHCl_3$.

The nature of these bands is complex, with the emissive band at 560 nm initially thought to be the result of either excimer formation, triplet emission or singlet emission from the fluorenone R-group.

The wealth of literature surrounding the topic of emission from fluorenone and its derivatives rules out that the low energy emissive band at 560 nm is the result of excimer formation. As well as this, **Figure 2.26** shows no correlation between concentration and emission intensity at 560 nm when normalised to the 430 nm emissive band, with two different trends observed at the two different wavelengths studied.

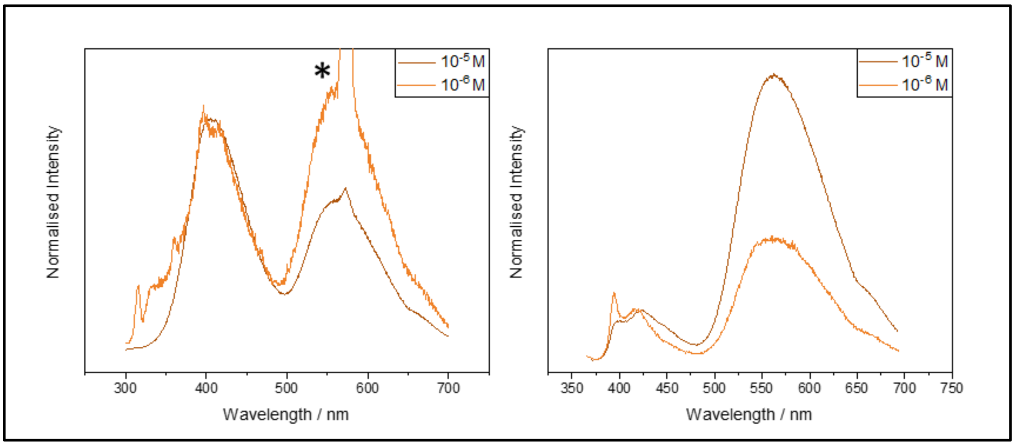

Figure 2.26 Emission spectra for **12**, recorded at 286 nm (*left*) and 350 nm (*right*) in $CHCl_3$ at 10^{-5} and 10^{-6} M. *denotes a lamp harmonic associated with the excitation wavelength.

TDA based TD-DFT analysis, found in **Section 2.5.1.4.2**, predicted that excitation at the low energy absorption band was the result of HOMO→LUMO whereby the HOMO is located across the entirety of the fluorophore, and the LUMO only on the fluorenone. This observation, with the LUMO consistent with that found in the literature,[54,61,62] further confirmed not only that absorption at 436 nm could be assigned to a charge-transfer transition, but also that the emissive band at 560 nm was most probably the result of singlet and/or triplet emission from the fluorenone R-group.

The reasoning behind this postulation is many-fold. Existing literature suggests that in non-polar and relatively non-polar solvents (such as chloroform) ISC between singlet and triplet states, leading to triplet emission, is the dominating factor.[59] However, although the low quantum yields support this (varying dependent on excitation wavelength, with values of 31 and 7% when excited at 285 and 330 nm respectfully), the small lifetime (2.25 ns) does not. Triplet emission could also be ruled out to not be the dominant transition by comparing the predicted HOMO→LUMO transition to that in literature, in that it is predicted to be π→π* in nature,[63] and not n→π*, similar to that of 2-methoxyfluorene in non-polar solvents resulting in fluorescence emission.[59] Therefore, ISC between the π→π* S_1 state and T_1 state cannot occur, with only the T_3 state being n→π* in nature (**Figure 2.24**).

Trends in emissive lifetime were consistent with a singlet state, as shown in **Table 2.9** for toluene, $CHCl_3$ and water (1% DMSO). As the polarity of the solvent increases, the triplet n,π* state is predicted to become more destabilised leading to reduction in ISC, with the π→π* singlet state becoming more stable and leading to an increase in non-radiative decay form the singlet state.[59]

Table 2.9 Differences in λ_{em} of low energy emissive band recorded in three different solvent systems, with the respective emissive lifetime. λ_{ex}=295 nm.

	λ_{em} / nm	τ_{obs} / ns
Toluene	517	6.5 ± 0.7 (84) 1.3 ± 0.1 (16)
Chloroform	562	2.3 ± 0.2
Water (1% DMSO)	559	1.1 ± 0 .1

The shift in emission wavelength when recorded in toluene and chloroform (**Figure 2.27**, and tabulated in **Table 2.9**) was also consistent with literature, as the predicted LUMO state is polar (electron density is situated entirely on the fluorenone) and thus less stable in non-polar solvents, leading to a hypsochromic shift in emission wavelength.[59,63] When normalised to the higher energy emissive band, the intensity of the low energy band also suggested an increase in non-radiative decay upon increasing polarity, with a quenching of the emission when recorded in water (1% DMSO) compared to when in toluene and $CHCl_3$. This was most notable when excited between 280-290 nm, where the low energy emissive band decreased in intensity upon increase in polarity, and was completely quenched in water (1% DMSO).

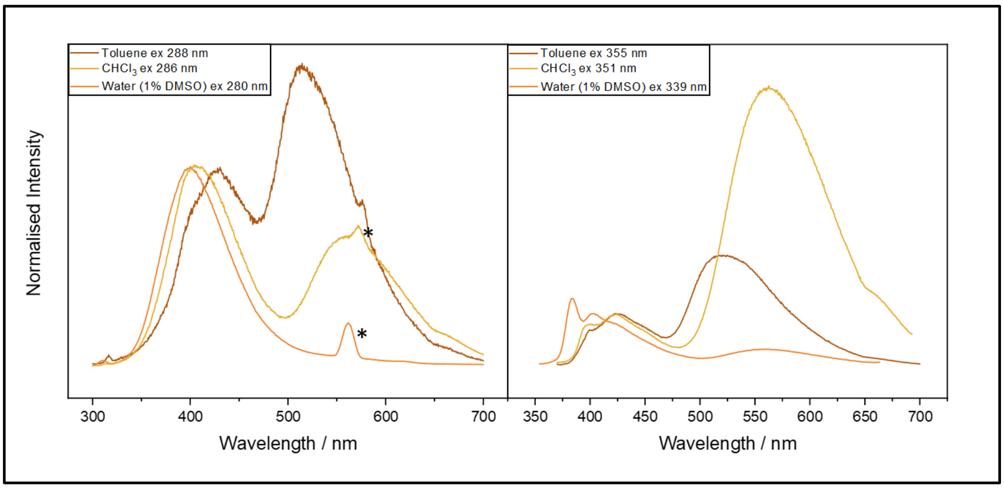

Figure 2.27 Emission spectra of **12** recorded in three different solvent systems at two different excitation wavelengths. *Left*; λ_{ex} = 288 (toluene), 286 ($CHCl_3$), 280 (water, 1% DMSO) nm; *Right;* λ_{ex} = 355 (toluene), 351 ($CHCl_3$), 339 (water, 1% DMSO) nm. *denotes a lamp harmonic associated with the excitation wavelength.

The fact that the emission wavelength of the low energy band recorded in water (1% DMSO) was similar to that recorded in $CHCl_3$ could be explained by the fact that DMSO was required as the fluorophore would not dissolve in water, and thus it could be assumed that there may be more DMSO molecules within the solvation sphere and thus a lower local polarity and less H-bond donors available to stabilise the carbonyl of the excited state.

As discussed previously excimer emission was ruled out partly due to there being no correlation between concentration and relative emission at 560 nm compared to that at 430 nm. When excited at 350 nm, the low energy emissive band dominated the emission relative to the 430 nm emission, particularly at higher concentrations. However when excited at 285 nm, emission at 560 nm was slightly less intense at high concentrations.

It's also shown in **Figure 2.25** that excitation at 350 nm resulted in the 560 nm emissive band dominating the spectra. This somewhat contradicts the predictions of TDA-based TD-DFT discussed in **Section 2.5.1.4.2**, which predicted that excitation around this wavelength lead to a predominantly LUMO+1 state which is π→π* in character across the entirety of the fluorophore, and not localised on the fluorenone.. However, the experimental observation of the dominating 560 nm emissive band may be not just due to direct absorption to the LUMO state, but also a secondary inner filter affect[64] due to the overlap of the charge transfer absorption band with that of the 430 nm emissive band arising from emission from the LUMO+1 excited state (**Figure 2.28**), leading to increased emission at 560 nm.

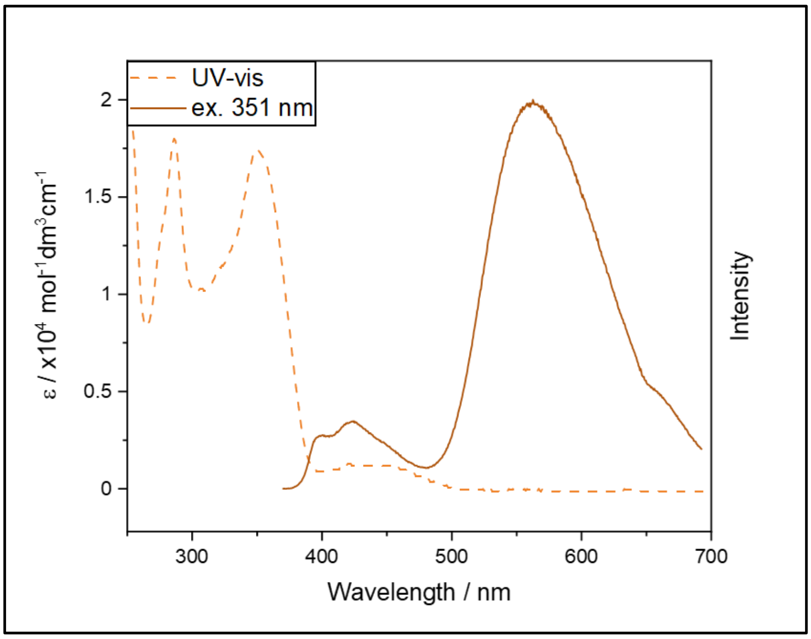

Figure 2.28 Absorption and emission spectra of **12**, showing the overlap of the high energy emissive band with the low energy proposed charge transfer absorption band. Recorded in $CHCl_3$, emission spectra excited at 351nm.

It was also considered beneficial to determine the CIE coordinates of the emission at different excitation wavelengths, especially considering the differences in respective intensities of the two emissive bands. **Figure 2.29** shows the CIE diagram, both with and without the black-body curve. As predicted, the differing intensities of the two bands at different excitation wavelengths lead to different overall colour coordinates (**Table 2.10**), however most interesting is that of excitation at 253 and 286 nm, which result in almost pure white emission.

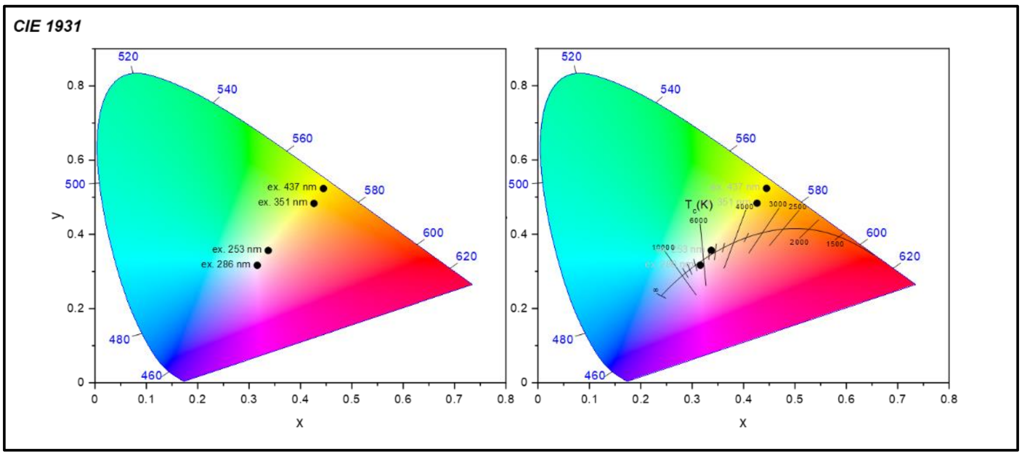

Figure 2.29 *Left*; CIE diagram of **12** excited at four different wavelengths, *Right*; CIE diagram of **12**, including black-body curve. Both spectra plotted using Origin software.

White emission is greatly sought after in OLED devices,[65,66] and thus it would be prudent to further study oxazole **12** to this effect due to its obvious wavelength and concentration dependence on emission, leading to almost pure white emission.

Table 2.10 CIE coordinates of **12** excited at four different wavelengths. Obtained using Origin software.

λ_{ex} / nm	**x**	**y**
437	0.44474	0.52360
351	0.42628	0.48353
286	0.31581	0.31676
253	0.33713	0.35659

CIE graphs were also plotted for **12** in toluene and water (1 % DMSO) and compared to that in $CHCl_3$ at similar excitation wavelengths (**Figure 2.30**). The varying intensities of the two emissive bands in different solvents, and the respective shifts dependent on polarity of the system are clearly shown, suggesting that fluorophore **12** may be a good candidate in sensing applications.

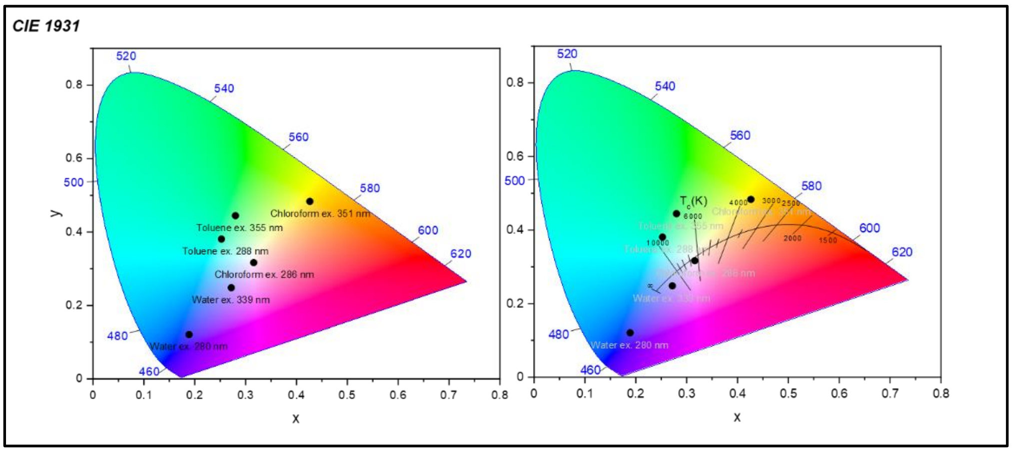

Figure 2.30 *Left*; CIE diagram of **12** excited at different wavelengths in different solvent systems, *Right*; CIE diagram of **12**, including black-body curve. Both spectra plotted using Origin software.

In non-polar solvents such as toluene, the band intensities lead to blue/green emission, whereas in polar solvents such as water (1% DMSO), the resultant emission was more blue/purple. The coordinates of all points are given in **Table 2.11**.

Table 2.11 CIE coordinates of **12** excited at different wavelengths in different solvent systems. Obtained using Origin software.

Solvent (λ_{ex} / nm)	**x**	**Y**
Toluene (288)	0.25234	0.38086
Toluene (355)	0.27990	0.44464
Water, 1% DMSO (280)	0.18878	0.12075
Water, 1% DMSO (339)	0.27168	0.24831
$CHCl_3$ (286)	0.31581	0.31676
$CHCl_3$ (351)	0.42628	0.48353

2.5.1.4 Computational Calculations – DFT Analysis

2.5.1.4.1 Mono-Substituted Oxazoles

To provide further insight into the UV-vis spectroscopy data, and to establish the relative electron density of the multi-chromophoric components within the oxazole structures, DFT calculations were used to investigate the HOMO and LUMO energy levels within each system, which are presented in **Figure 2.31**. TD-DFT was then used to calculate the absorption profile of oxazoles **1-7**, shown in **Figure 2.32**, using B3LYP[67–70] with the 6-311+G(d,p) triple-ζ basis set[71] as this gave the closest agreement with experimental data and crystal structures. Please note that all DFT/TD-DFT calculations of mono-substituted oxazoles were carried out by Dr Benjamin Ward, and those of the di-substituted oxazoles were carried out by the author with the assistance of Dr Benjamin Ward and Owaen Guppy. Complete data sets are given in the **Appendix**.

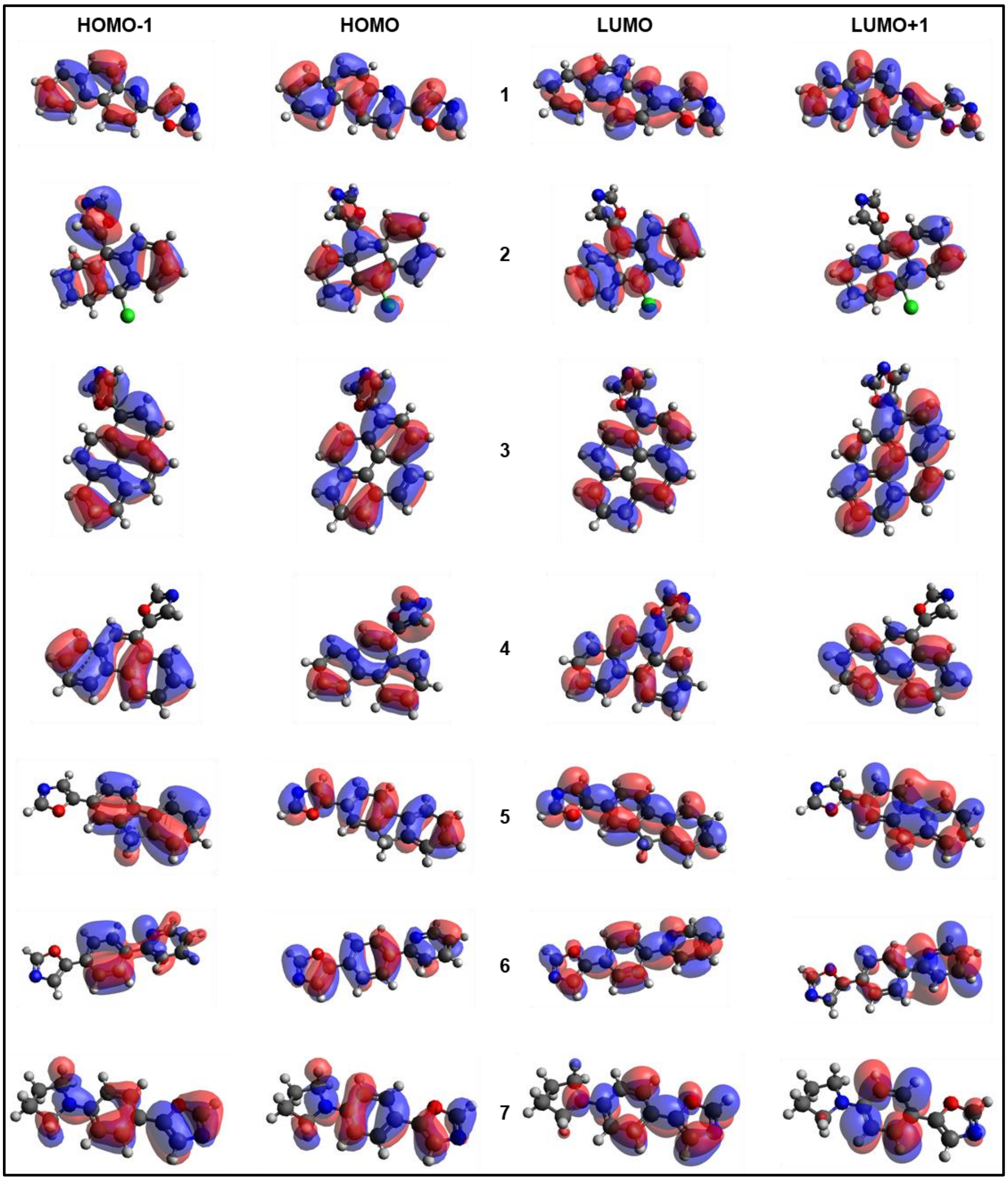

Figure 2.31 Frontier molecular orbitals including H-1 and L+1 of **1-7**, calculated using B3LYP/6-311+G(d,p).

For oxazoles **1-7**, the HOMO→LUMO transition was predicted to be π→π* in nature, with electron density located across the whole fluorophore (**Figure 2.31**). The remaining HOMO-X→LUMO+X transitions were primarily predicted to be

$\pi \rightarrow \pi^*$ in nature, and predominantly derived from the R-group with minor contributions from the oxazole π system. This concurred with the experimental results discussed in **Section 2.5.1.3** in that both the absorption and emission of each oxazole was dominated by the R-group. Exceptions to this were that of **1** and **3**, in which select HOMO-X and LUMO+X states were also predicted to be derived from the whole fluorophore. Oxazoles **2** and **7** were also predicted to display contribution predominantly from the oxazole moiety in the LUMO+2 and HOMO-3 states respectively. Although the lower energy states were predicted to be dominated by $\pi \rightarrow \pi^*$ transitions, there were also $\pi \rightarrow \sigma^*$ and $n \rightarrow \pi^*$ transitions observed at higher energy, albeit low intensity.

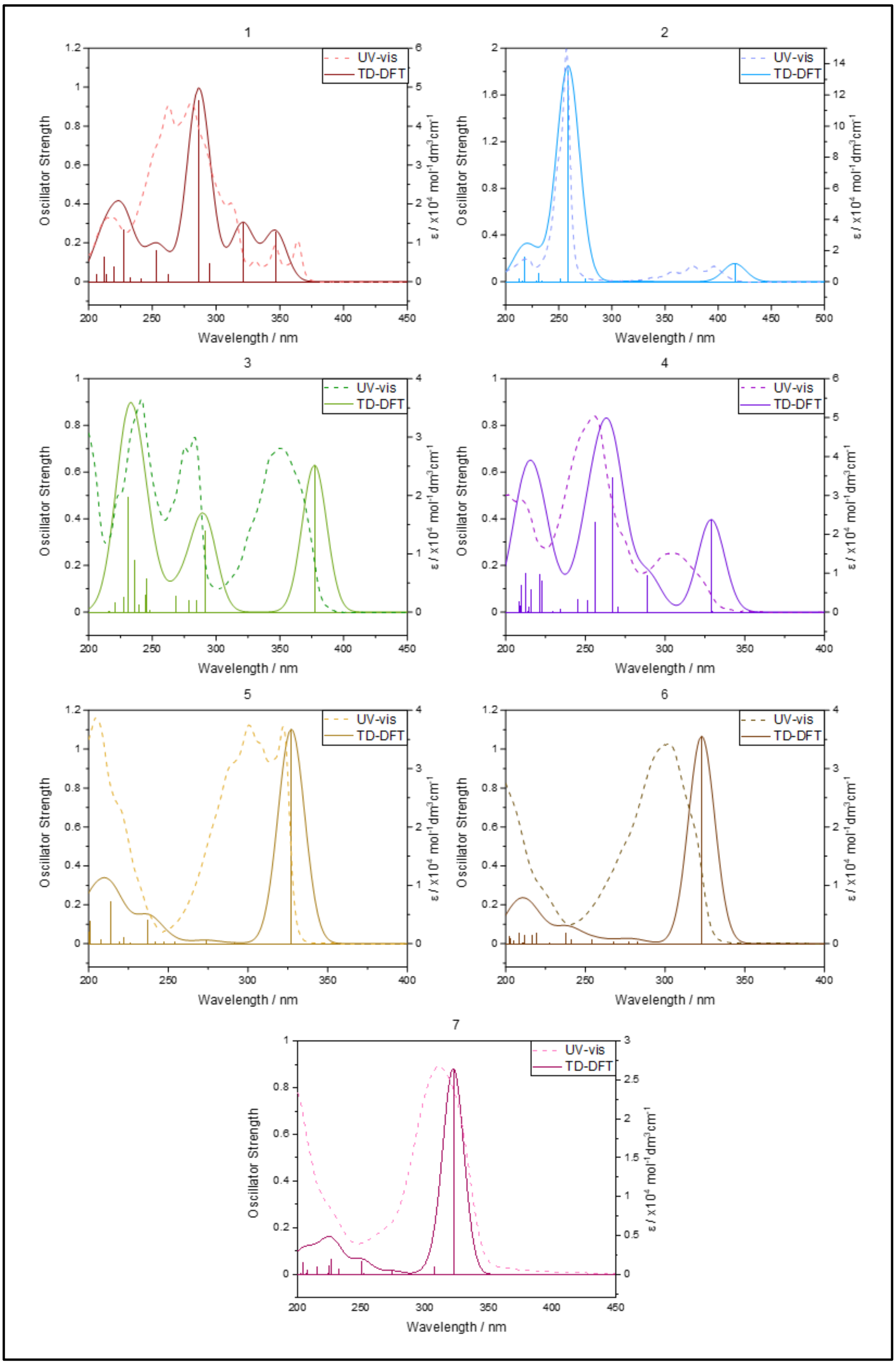

Figure 2.32 TD-DFT calculated transitions of **1-7** (solid line) compared to the absorption spectra (dotted line).

Overall the agreement between simulated and experimental absorption spectra was good, with the TD-DFT components overlapping well with the experimental absorbance maxima, presented in **Figure 2.32**, with only the lower energy transitions slightly differing from experimental values.

2.5.1.4.2 Di-substituted Oxazoles

Unlike oxazoles **1-7**, where B3LYP/6-311+G(d,p) gave good agreement with experimental data, when used for oxazoles **8-13** agreement was poor (**Figure 2.33**). This was surprising, as although there is limited literature surrounding theoretical analysis of oxazole electronic spectra, it is primarily based upon the use of B3LYP (or similar, such as B3LYP5), with the 6-311+G(d,p) or 6-31+G(d,p) basis sets[51,72,73]. However, within the literature it is also clear upon closer inspection that B3LYP/6-311+G(d,p) does not always give good agreement to the experimental evidence, with work by S. Shahab[74], P. Civcir[75], and R. Iliashenko[76] among some examples of an over- or under-estimation of the lowest energy transitions. As well as this many examples are purely theoretical and thus do not have experimental results to offer a comparison[77–79]. A possible reason for this is that B3LYP is poor when predicting charge transfer character, which may be present in some of the disubstituted systems.

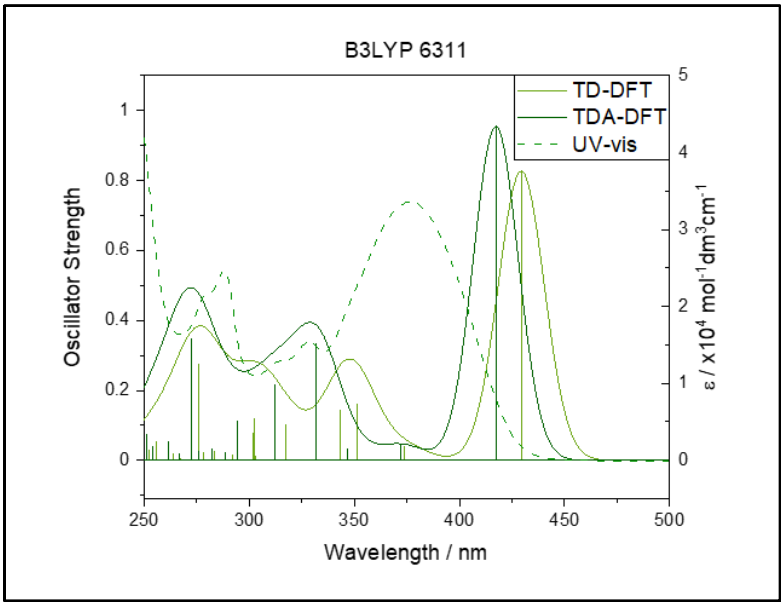

Figure 2.33 TD-DFT and TDA-DFT calculated transitions of **10** (solid green lines) compared to the absorption spectra (dotted green line) using B3LYP/6-311+G(d,p).

In work by P. Civcir *et al*[75], both 6-31G(d,p) and cc-Pvtz were also used as basis sets, and although experimental and theoretical were similar with small molecules, as conjugation increased (shown in **Figure 2.34a**) the less the theoretical results of all three basis sets agreed with experimental observations. M062X was also compared to B3LYP in work by S. Shahab *et al*[74], however whereas B3LYP overestimated the lowest energy transition wavelength, M062X underestimated for the two benzoxazole based compounds being studied (**Figure 2.34b**). A. Chraytech *et al*[80] instead used PBE0, M06-2X, CAM-B3LYP and MN15 functionals to try to predict experimental results, however in all cases the enol form of the structure being analysed, shown in **Figure 2.34c**, was calculated as being more stable than experimentally observed, and thus a more complex analysis was required.

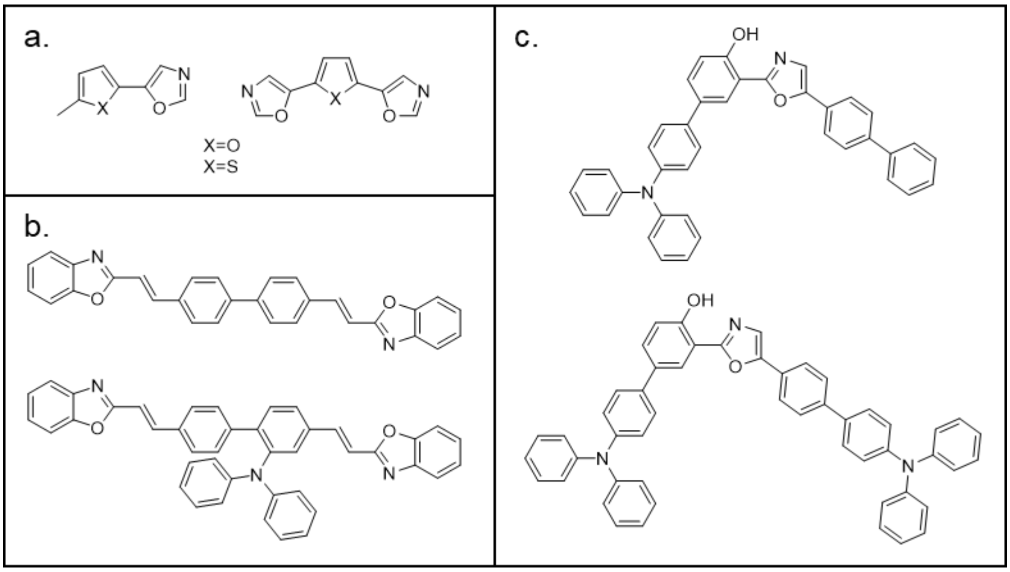

Figure 2.34 a) Select oxazoles analysed in work by P. Civcir *et al,*[75] where the mono-oxazole (*left*) was accurately described by 6-31G(d,p) and cc-Pvtz basis sets, but di-oxazole structures (*right*) were not; b) benzo[d]oxazole derivatives studied in work by S. Shahab *et al*[74]*;* c) 2-(2'-hydroxyphenyl)oxazole derivatives studied by A. Chraytech *et al.*[80]

With this in mind, TD-DFT was used with a range of different functional and basis sets to attempt to find a better agreement to experimental absorption than that shown by B3LYP/6-311+G(d,p). In all cases, both pure TD-DFT and that based upon the Tamm-Dancoff Approximation (TDA) were carried out, with the latter predicting more similar results to those observed experimentally. The functional and basis sets tested were compared based upon their similarity to the overall experimental spectra of **10**, however particular attention was given to the low energy absorption, as this was heavily overestimated when using B3LYP/6-311+G(d,p). The simulated absorption spectra for each combination of functional and basis sets are presented in **Figure 2.35**, overlayed with the experimental absorption spectra. **Table 2.12** shows the shift in the predicted wavelength for the lowest energy transition from the experimental value for each basis set and functional combination used in both TD-DFT and TDA based TD-DFT.

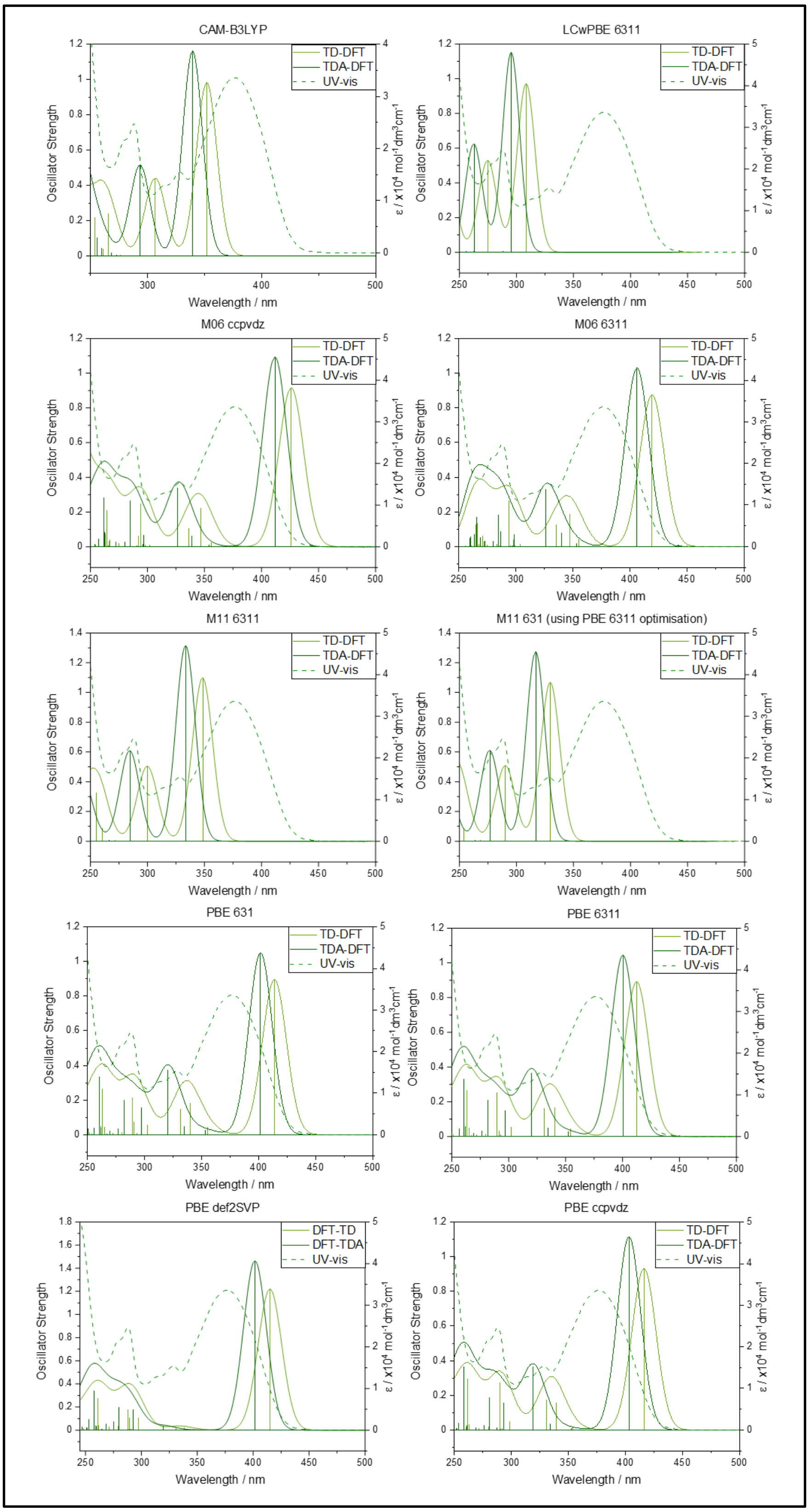

Figure 2.35 TD-DFT and TDA-DFT calculated transitions of **10** (solid green line) compared to the absorption spectra (dotted green line) using a range of different functional and basis sets.

Shown in **Figure 2.35**, both LC-wHPBE[81] and CAM-B3LYP[82] failed to predict the low energy absorbance observed experimentally, with both predicting higher energy bands below 350 nm,, despite CAM-B3LYP proving to be the better choice in work by L. Abegão *et al*[83]. M06[84] and M11[85] functionals were attempted due to their versatility across the periodic table, however M06 yielded an overestimation of the lowest energy absorption wavelength, and M11 heavily underestimated. The M06 functional was used with both ccpvdz[86] and 6-311+G(d,p)[71] basis sets, however there was very little difference between the two.

Table 2.12 Shift in low energy absorption for different functional and basis sets, using both TD-DFT and TDA-DFT.

Functional and Basis Set	**Shift in 376 nm absorption / nm**	
	TD	TDA
B3LYP 6-311	+ 53	+ 41
CAM-B3LYP[82] 6-311	- 24	- 37
LCwPBE[81] 6-311	- 67	- 80
M06[84] ccpvdz[86]	+ 50	+ 36
M06 6-311	+ 43	+ 30
M11[85] 6-311	- 28	- 42
M11 6-31[87–96]	- 46	- 59
PBE[97,98] def2SVP[99]	+ 39	+ 26
PBE ccpvdz	+ 40	+ 27
PBE 6-31	+ 38	+ 26
PBE 6-311	+ 37	+ 24

PBE functionals[97,98] using TDA-based TD-DFT proved to be most in agreement with experimental results, with the lowest energy absorption wavelength overestimated by between 24-27 nm for the four different basis sets used. Although PBE/6-311+G(d,p) gave the better agreement compared to PBE/def2SVP, the former was not able to calculate oxazole **13** without prior geometry optimisation utilising a different functional (much like M11/6-31+G(d,p) with oxazole **10** shown in **Figure 2.35**), and also predicted the proposed charge-transfer band of oxazole **12** too low in energy (shown in **Figure 2.36**, compared to PBE/def2SVP). However, PBE/def2SVP had reasonable agreement with all oxazoles **7-13**, as well as disubstituted oxazoles **14-19** and their resultant Re(I) complexes (presented in **Chapter 5**). Although agreement is not perfect, it is clear to see that PBE-based functionals gave the closest result to experimental observations when compared to the broad range of basis set and functional combinations tested, and that due to a lack of literature surrounding the topic it may be that these oxazole-based systems have reached the limit of DFT capabilities without a new set of parameters for these particular systems, for example a specialised basis set, which is beyond the scope of this work.

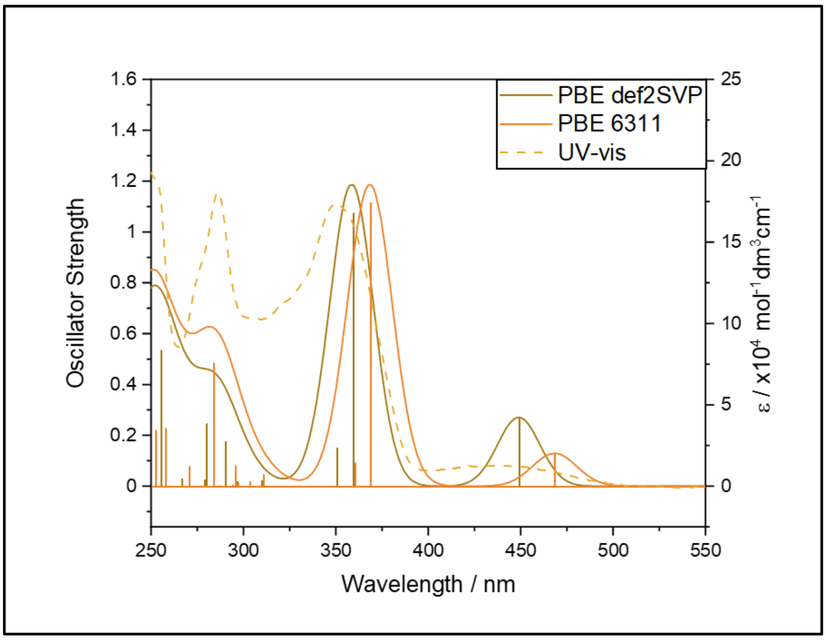

Figure 2.36 TDA based TD-DFT calculated transitions of **12** using PBE/def2SVP (solid brown line) and PBE/6-311+G(d,p) (solid orange line) compared to the absorption spectra (dotted orange line).

Using PBE/def2SVP, disubstituted oxazoles **8**, **12** and **13** were all predicted to be planar, similar to the equivalent mono-oxazoles **1**, **5** and **7**, with oxazole **13** predicted to have a twisted pyridyl terminus also observed in the crystal structure of oxazole **7**. However, oxazoles **9**, **10** and **11**, like their parent mono-oxazoles, were all predicted to have a twist in the R-group relative to the oxazole-naphthalene unit, which is planar. The torsion angles were calculated to be (looking down the R-C bond and starting at the oxazole oxygen) -57.8°, -27.8° and 153.4° for **9**, **10** and **11** respectively, and are presented in **Figure 2.37**. For oxazole **11**, this is similar to the parent oxazole **4**, however for **9** and **10**, the R-group was predicted to be significantly affected by the naphthalene group, with oxazoles **2** and **3** showing torsion angles of -108.3° and 139.6° respectively. It should be noted however that oxazole **2** presented a more twisted structure than that shown in the crystal structure in **Section 2.5.1.1**, although this may be due to differences between solid state and solution-based configurations.

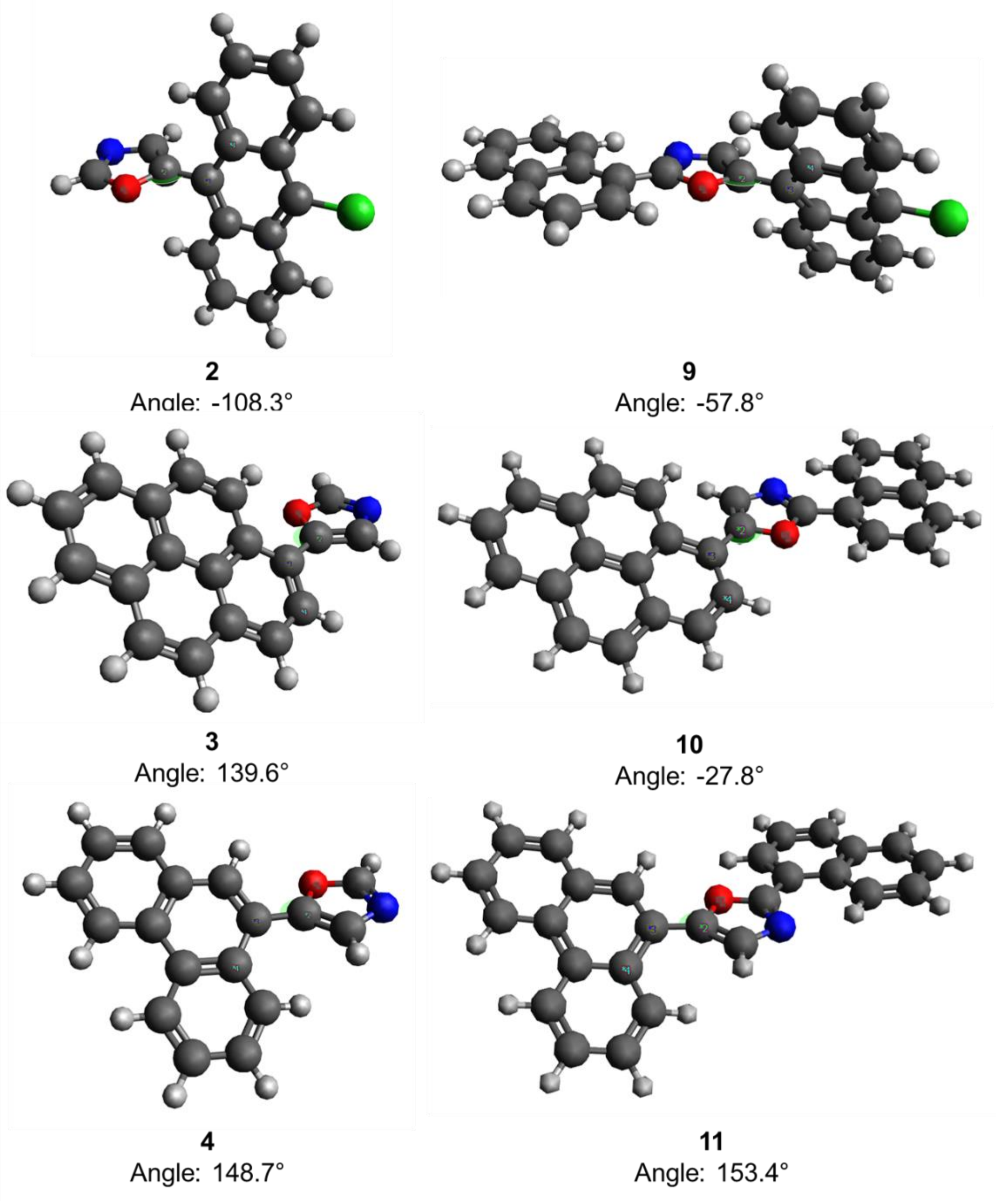

2
Angle: -108.3°

9
Angle: -57.8°

3
Angle: 139.6°

10
Angle: -27.8°

4
Angle: 148.7°

11
Angle: 153.4°

Figure 2.37 Predicted structures of **2**, **3**, **4** and their disubstituted oxazoles **9**, **10**, **11** with dihedral angles.

In oxazoles **8**, **10** and **11**, the HOMO→LUMO transition was predicted to be predominantly π→π* across the entirely of the fluorophore, with oxazole **11** exhibiting slightly more contribution from the naphthalene-oxazole unit in the LUMO. However, in the cases of **9**, **12** and **13**, the HOMO→LUMO transition was predicted to be more complex. In oxazoles **9** and **12**, the LUMO state was dominated by orbitals centred upon the R-group and oxazole and thus the HOMO→LUMO transition shows the excitation of an electron from the entirety of the fluorophore to the R-oxazole unit. In the case of **13**, the electron density on the

HOMO was located across the fluorophore, with slightly more contribution seen from orbitals on the R-group. However, the electron density of the LUMO was predominantly centred on the naphthalene-oxazole unit of the fluorophore, which is in contrast to the other oxazoles in the series.

Both TD-DFT and TDA based TD-DFT were carried out to simulate UV-vis absorption spectra of the disubstituted oxazoles, which were in good general agreement with experimental values. Although both DFT methods were compared, and in some cases both showed similarities to the experimental spectra, overall TDA-DFT gave the best result. In all cases, a large number of absorption transitions were predicted, with varying oscillator strengths. Therefore, only those of particular interest are discussed herein, with transitions of highest contribution discussed. A full list of states and all of their respective transitions is found in the **Appendix**.

The simulated absorption spectra of fluorophores **8**, **10** and **11** all showed reasonable agreement with experimental observations (**Figure 2.38**, along with the respective molecular orbitals involved in the dominating transitions), however for oxazole **8** the series of lower energy transitions were not found with a single absorption predicted instead. All low energy absorptions, found at 369, 402 and 366 nm for oxazoles **8**, **10** and **11** respectively, were predicted to be due to HOMO→LUMO, π→π* transition across the entirety of the fluorophore, with the exception of **10**, with the electron density of the LUMO predominantly centred on the pyrene. The same was largely true for higher energy transitions, however the HOMO-1 state for oxazole **8** showed no electron density from the oxazole π orbitals, and the LUMO+1 and +2 states of oxazole **10** was predicted to contain more contribution from the naphthalene-oxazole unit than the pyrene R-group, and localised solely on the pyrene R-group respectively. For **11**, all transitions were predicted to originate from π orbitals across the fluorophore, however for HOMO-4, the orbitals are located across the side of the phenanthrene R-group closest to the oxazole-naphthalene unit, which may indicate the polarity across the phenanthrene unit as a result of the oxazole-naphthalene substituent.

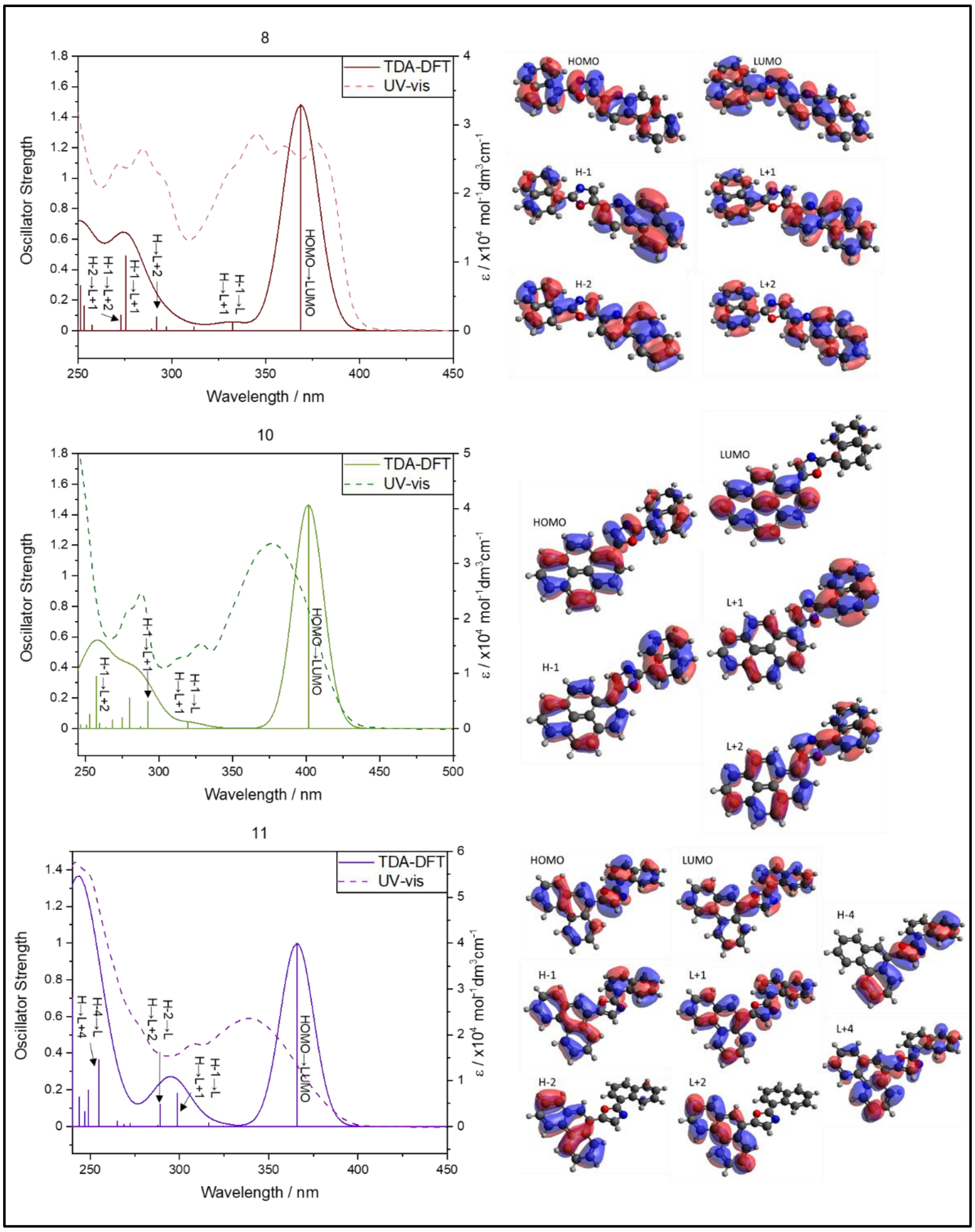

Figure 2.38 *left*: TDA-DFT calculated transitions of **8**, **10**, **11** (solid lines) with dominating transitions labelled, compared to the absorption spectra (dotted line); *right:* Molecular orbitals involved in the dominating transitions.

The simulated absorption spectra for oxazole **13** predicted a low energy absorption at 408 nm, showing HOMO→LUMO, π→π* character across the fluorophore. However unlike **8**, **10** and **11**, there was a slight shift in the orbital contribution from the R-group to the naphthalene (**Figure 2.39**). The same was true for the predicted absorption at 309 nm, however the highest energy absorption at 290 nm was predicted to be ascribed to two main transitions, one of which (HOMO→LUMO+3) predicted excitation of the electron to the π* orbitals of the benzene ring of the pyrrolidine R-group.

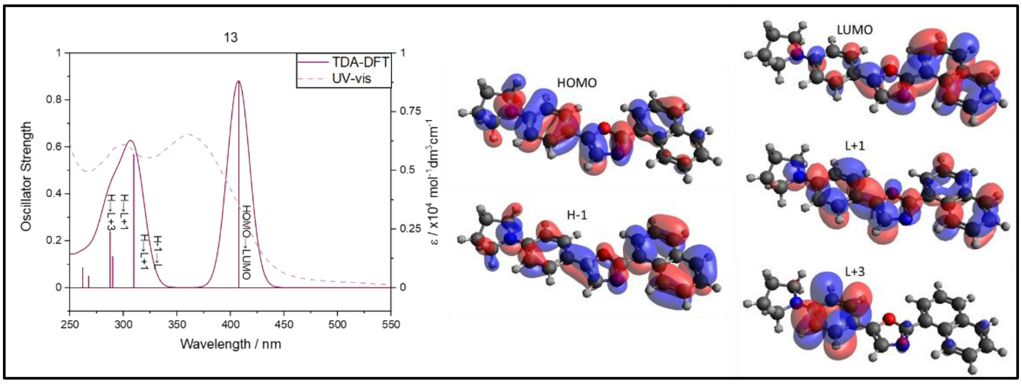

Figure 2.39 *left*: TDA-DFT calculated transitions of **13** (solid pink line) compared to the absorption spectra (dotted pink line); *right:* Molecular orbitals involved in the dominating transitions.

Despite the predicted line-shape differing from that observed, the simulated UV-vis transitions predicted for oxazole **9** showed reasonable agreement with the experimental λ_{abs} maxima (**Figure 2.40**). The lowest energy absorption predicted at 411 nm was assigned predominantly to the HOMO→LUMO, π→π* transition in which the electron is excited from π-orbitals located across the fluorophore into those centred predominantly on the chloroanthracene and oxazole units of the fluorophore. Absorption at 362 nm was predicted to be due to two transitions of almost equal contribution, one of which (HOMO-1→LUMO) showing charge transfer across the oxazole ring from π-orbitals centred predominantly on the oxazole and naphthalene, to the π*-orbitals of the chloroanthracene-oxazole unit. The simulated absorption at 260 nm was made up of multiple transitions, however the main transition was predicted to be due to excitation of the electron from the π-orbitals across the entirety of the fluorophore to the π*-orbitals of the chloroanthracene. However, transitions located at 346 and 305 nm were both predicted to be ascribed to transitions resulting from the excitation of the electron from the π orbitals across the fluorophore to the π* orbitals located primarily on the naphthalene-oxazole unit.

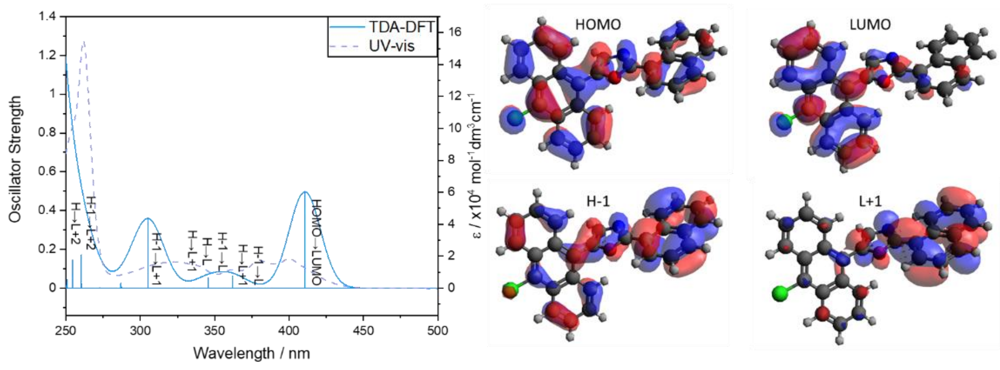

Figure 2.40 *left*: TDA-DFT calculated transitions of **9** (solid blue line) compared to the absorption spectra (dotted blue line); *right:* Molecular orbitals involved in the dominating transitions.

As discussed previously, the simulated spectra recorded using PBE/def2svp gave excellent agreement with the experimental UV-vis spectra of oxazole **12**, particularly for the lower energy transitions (reproduced in **Figure 2.41**, including the predicted molecular orbitals involved in the dominating transitions). The lowest energy transition at 449 nm was predicted to be due to the HOMO→LUMO transition in which the electron is excited from the π orbitals across the fluorophore to the π* orbitals of the fluorenone, thus confirming earlier suggestions that the nature of the low energy emissive band of **12** was a result of charge transfer to the fluorenone, as discussed in the literature.[59] Absorptions at 359 and 351 nm were predicted to be due to the excitation of the electron in a π→π* transition across the entirety of the fluorophore, as well as charge transfer to the π* orbitals of the fluorenone in the case of 351 nm. Those at higher energy, 290 and 280 nm, were predicted to be due to excitation from π orbitals across the fluorophore to the π* orbitals of the fluorenone for the former, and in a π→π* transition across the entirety of the fluorophore and a π→π* transition based solely on the fluorenone.

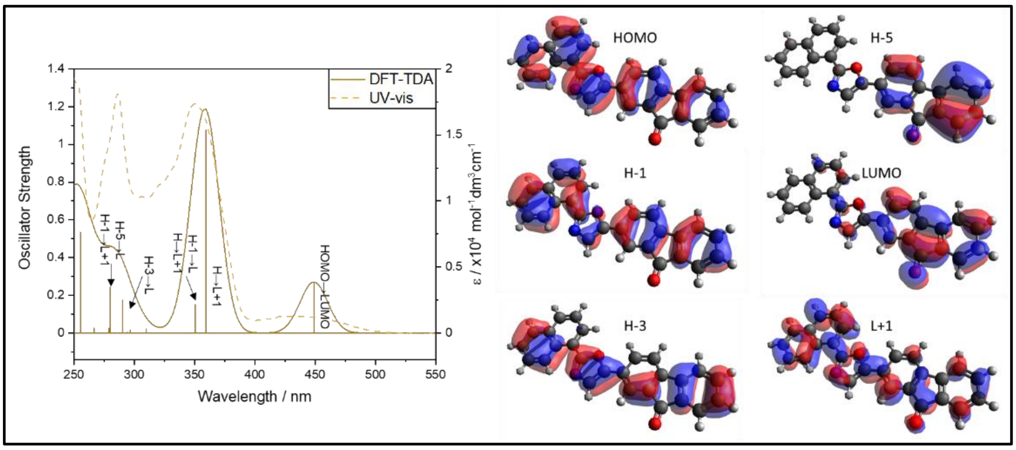

Figure 2.41 *left*: TDA-DFT calculated transitions of oxazole **12** (solid orange line) compared to the absorption spectra (dotted orange line); *right:* Molecular orbitals involved in the dominating transitions.

2.5.2 Incorporation into Oil-in-Water Microemulsions for Scintillation

2.5.2.1 Composition

As described previously, current liquid scintillation cocktails suffer from many disadvantages including high organic solvent content, environmentally harmful surfactants, and time-consuming preparations of aqueous samples before analysis. Oil-in-water microemulsions however have the advantage of a lower overall organic content than commercial cocktails, whilst still being able to solubilise material that would normally be immiscible in organic solvents.

Figure 2.42 shows a schematic representation of the scintillation pathway in an oil-in-water microemulsion. The radionuclide in the aqueous environment releases a beta particle, which then travels a certain distance in the medium before interacting with the oil droplet and exciting the toluene solvent within. This then transfers the energy to the scintillant, which emits this energy as light, *hv*.

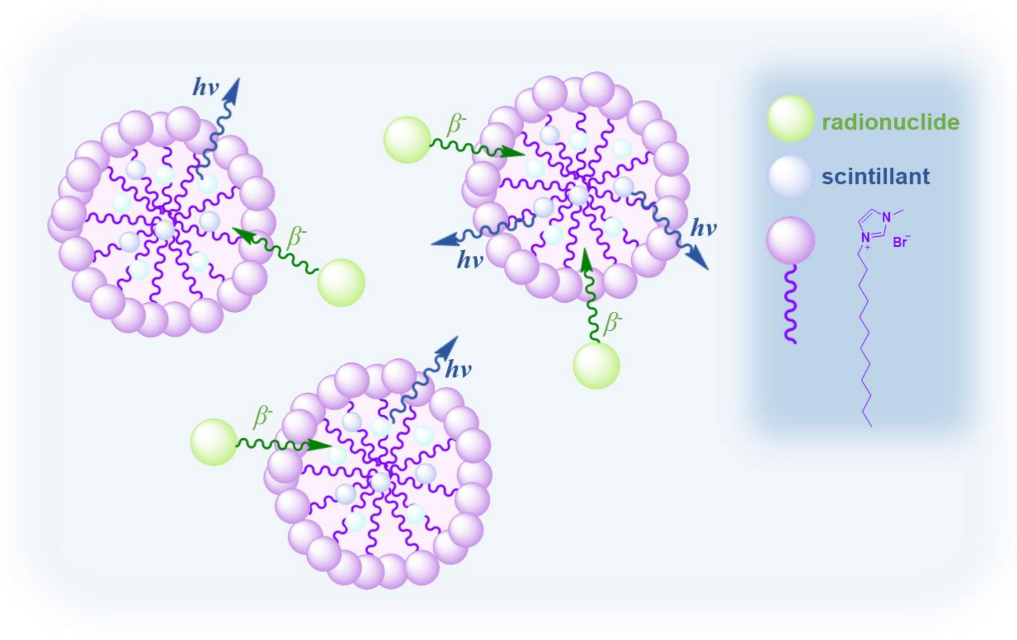

Figure 2.42 Schematic diagram of liquid scintillation in oil-in-water microemulsions. The radionuclide releases a β-particle, which interacts with the toluene present inside the oil droplet. This then transfers the energy to the primary scintillant, DPO, which then transfers it to the secondary scintillant, releasing light *hv.* Inset shows structure of [MeImC$_{12}$]Br.

Mono-oxazoles **1**-**7,** di-substituted oxazoles **8** and **10,** and POPOP were dissolved individually in toluene with DPO at a concentration of 3.4 mmol dm^{-3} and 0.452 mol dm^{-3} respectively. This was then added to a premixed solution of [MeImC$_{12}$]Br (Figure 2.42*),* 1-butanol and ultra-pure water in the ratio 1:1:1:7 and sonicated to give a clear and colourless microemulsion for all except those containing **8** and **10** (discussed in **Section 2.5.2.2.2**).

The surfactant was chosen through extensive research already conducted within the group, *via* the comparison of both the oil-solubilising ability of various chain lengths and counter ions, and the CMC of those systems.[100] A chain length of 12 was found to have the optimum toluene loading of 25% wt., and when in a mixed surfactant system of [MeImC$_{12}$]Br:BuOH, a CMC of 36.5 mmol.

In the systems analysed herein, the oxazoles synthesised are used as the secondary scintillant, with DPO acting as the primary scintillant to provide effective energy transfer. Microemulsions without either scintillant, and those with primary but not secondary (and *vice versa*) were also formulated to test the different contributions to the overall scintillation ability.

2.5.2.2 Scintillation Studies

To analyse the effect of microemulsions in their use as a proximity induced scintillant, both a hard and soft beta emitter were chosen (**Table 2.13**). Sr-90, the hard emitter, has a beta path length in water of millimetres, whereas Ni-63 (the soft emitter) has a beta path length of microns. This means that a signal arising from the presence of Sr-90 would not be affected by its distance from the organic micelle, as there is more than likely a micelle within the beta particle pathlength, however for Ni-63 the distance to the micelle may be more important due to its smaller beta particle path length.

Table 2.13 Radiochemical data for soft emitter Ni-63 and hard emitter Sr-90.[101]

Nuclide (decay)	**Q (average)/ keV**	**$t_{1/2}$ / yr**
Ni-63 (β)	67 (17)	101
Sr-90 (β)	546 (196)	29

Although the author was present during preliminary testing of formulations containing oxazoles **1-7**, all scintillation experiments was carried out by Dr Hibaaq Mohamud at the National Physical Laboratory, Teddington, UK. Please note that the scintillation efficiencies presented here are not absolute values and are for comparison purposes only, due to the scintillation counter not being calibrated to the novel oil-in-water systems (the same is true for the particle suspensions in **Chapter 3**). This, as well as postulated chemiluminescence and secondary interactions, has led to efficiencies of over 1 CPSBq^{-1} in some cases.

2.5.2.2.1 Mono-substituted Oxazoles

All oxazoles showed an inherent ability to scintillate in the presence of Sr-90, with efficiencies ranging between 2.28 CPSBq^{-1} (**1**) and 1.45 CPSBq^{-1} (**2**), as shown in **Figure 2.43.** POPOP containing cocktails exhibited the lowest response of those co-doped, with an efficiency of 1.34 CPSBq^{-1}.

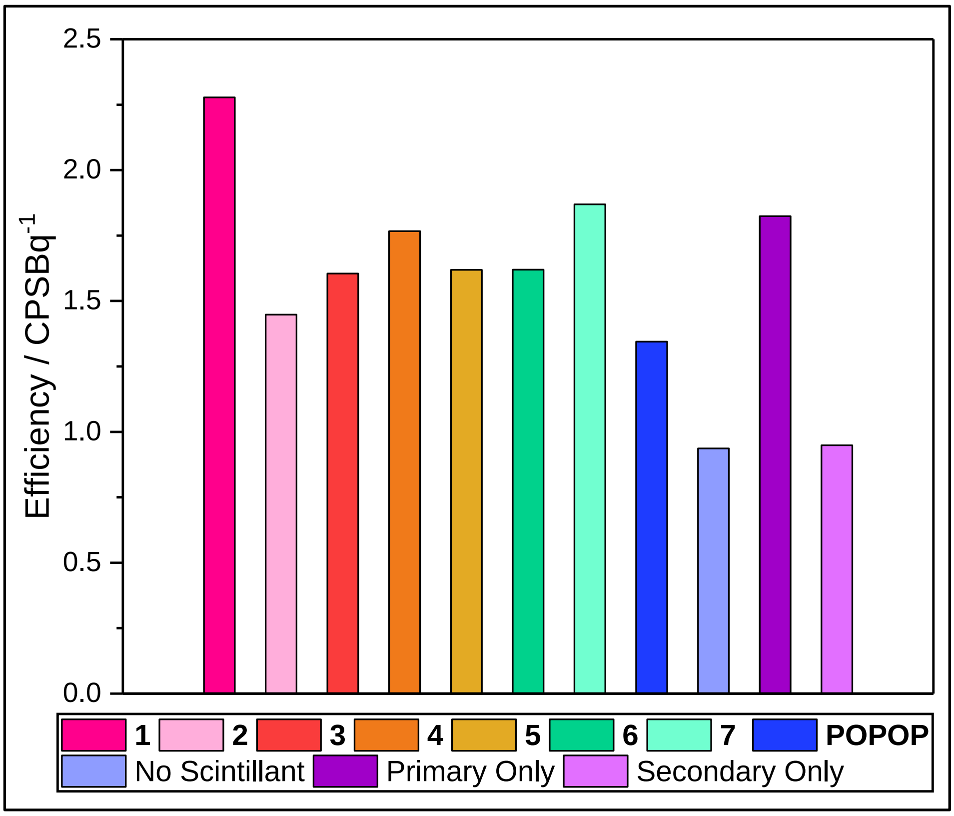

Figure 2.43 Scintillation efficiency of oil-in-water microemulsions in the presence of Sr-90. Counted for 6 minutes with 10 cycles completed in total.

Confirmation that **1**-**7** and POPOP act as secondary scintillants, and hence wavelength shifters only, is confirmed when the primary scintillant is not present. When not present, the cocktail doped with **3** gave a scintillation efficiency of 0.95 CPSBq^{-1}, compared to 1.61 CPSBq^{-1} with both scintillants present. This can also be compared to the scintillation efficiency of the microemulsion without any scintillants present, 0.94 CPSBq^{-1}, showing that the secondary scintillant is only acting as a wavelength shifter for the primary scintillant. As well as this, when the microemulsion was doped only with the primary scintillant DPO, the efficiency (1.82 CPSBq^{-1}) was higher than that when co-doped with both POPOP and some of the oxazoles. Despite this increase in efficiency, co-doping is required to shift the wavelength for DPO emission (approximately 350 nm[102]) to above 400 nm.

The trend in scintillation efficiencies cannot be compared to the emission properties of the oxazoles (**Figure 2.44**). For example, the absorption of POPOP (the industry standard) overlaps with the emission of DPO[103], and therefore would be expected to yield a large energy transfer, however this was the lowest scintillation response observed with the co-doped cocktails. However, both properties can be used in conjunction to assess the suitability of each oxazole for its use as a secondary scintillant. For example, **2** gave the largest wavelength shift, with an emission at 453 nm when excited at 350 nm, however it was the worst performing of the novel oxazoles. Both **5** and **6** have the same efficiency of 1.62 CPSBq^{-1}, however **6** emitted above 400 nm, therefore providing the appropriate shift, whereas **5** emitted between 370-400 nm. **1** however had by far the highest efficiency when co-doped with DPO, and also exhibited emission at 400 nm when excited at 350 nm, therefore making it the ideal secondary scintillant.

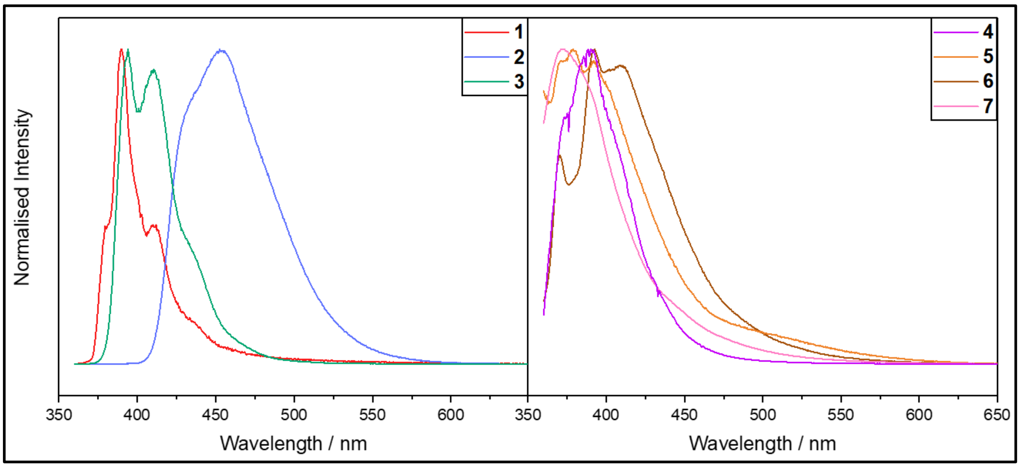

Figure 2.44 Emission spectra (recorded in toluene) for oxazoles **1-7**.

To establish the stability of the microemulsion systems, all samples were re-measured after two months to test their scintillation efficiency after being in the presence of Sr-90 (**Figure 2.45**).

The change in efficiency was minimal, with the largest change being a decrease by 2.6% for **1**, and therefore overall there was not a significant change.

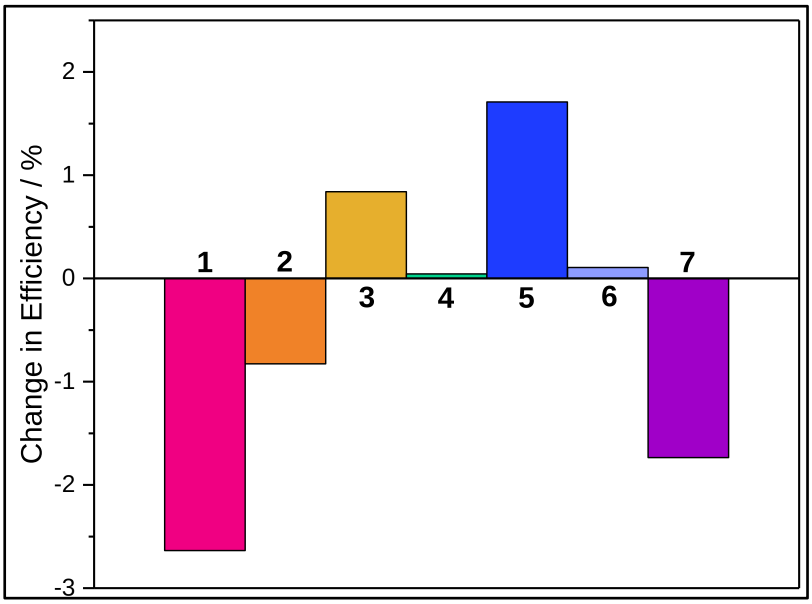

Figure 2.45 Percentage change in scintillation efficiency of oil-in-water microemulsions after 2 months in the presence of Sr-90. Counted for 6 minutes with 10 cycles completed in total.

To understand the need for proximity, the ability of the oxazoles to scintillate when in the presence of Ni-63 was also tested (**Figure 2.46**).

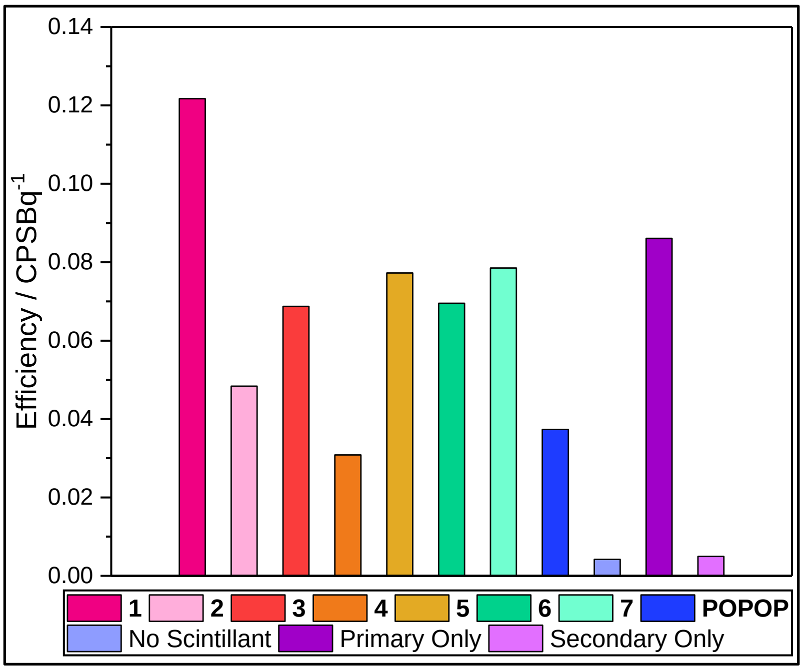

Figure 2.46 Scintillation efficiency of oil-in-water microemulsions in the presence of Ni-63. Counted for 6 minutes with 10 cycles completed in total.

As before with Sr-90, **1** performed the best in the presence of Ni-63, however with an efficiency of 0.122 CPSBq^{-1} compared to 2.28 CPSBq^{-1} in the presence of Sr-

90, whereas **4** (which had an efficiency of 1.77 CPSBq^{-1} in the presence of Sr-90) had the lowest efficiency in the presence of Ni-63 with an efficiency of 0.0308 CPSBq^{-1}. Much like with Sr-90, cocktails without the primary or secondary scintillant performed lowest, with an efficiency of 0.00418 CPSBq^{-1}, however this was as before closely followed by cocktails without the primary scintillant with an efficiency of 0.00496 CPSBq^{-1}. In fact, the same trend in oxazoles efficiency was followed for Sr-90 and Ni-63, with the exception of **4** having the lowest efficiency in the presence of Ni-63.

Results showed a more than ten-fold decrease in scintillation response for all cocktails, including those without one or both scintillants present, as shown in **Figure 2.47.**

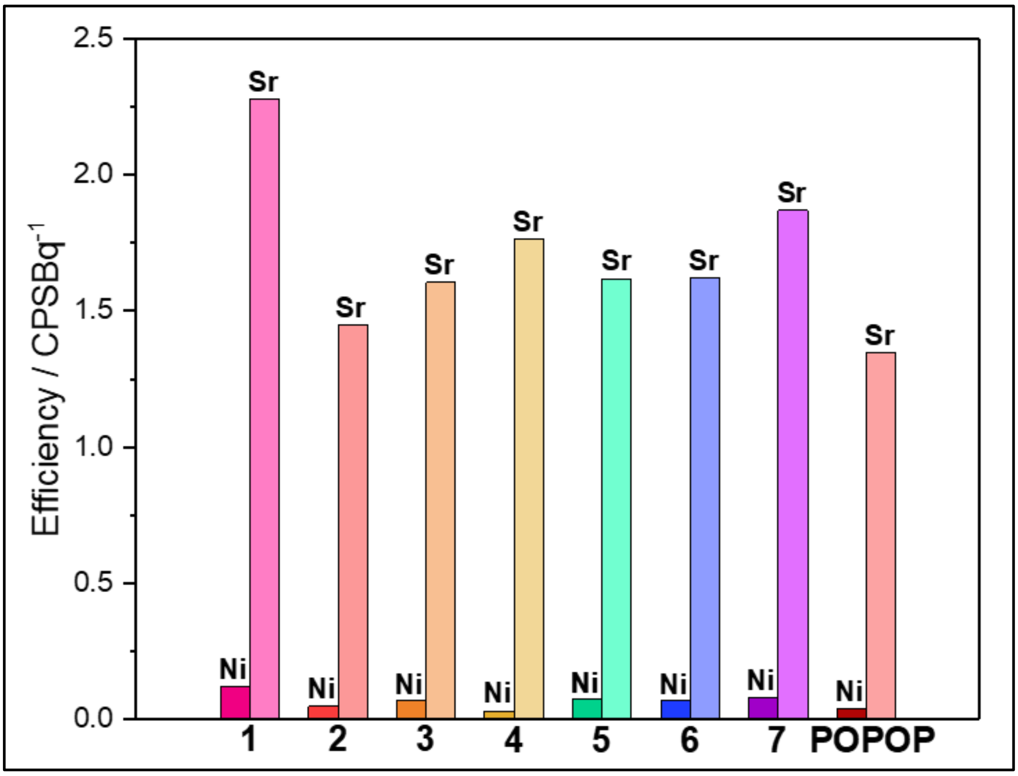

Figure 2.47 Comparison of scintillation efficiency for oil-in-water microemulsions in the presence of Ni-63 and Sr-90.

This shows that there may be proximity effects in the use of oil droplets, as softer emitters will need to be closer to the oil droplet for the emitted beta particle to interact with the scintillants. This in turn suggests that if the surface of the droplet could be functionalised with a metal chelator of choice, selectivity in scintillation could be introduced.

2.5.2.2.2 Di-substituted Oxazoles

For reasons outside of both the authors and NPL's control, only oxazoles **8** and **10** could be analysed for their scintillation efficiency. However, the emission in toluene of all of the disubstituted oxazoles is still an interesting factor to consider (**Figure 2.48**). All showed a shift in emission compared to the primary oxazole, which although cannot be postulated to enhance scintillation due to the reasons discussed previously, these shifts if coupled with an increase in scintillation efficiency would make them a better choice of scintillant due to the available collection window.

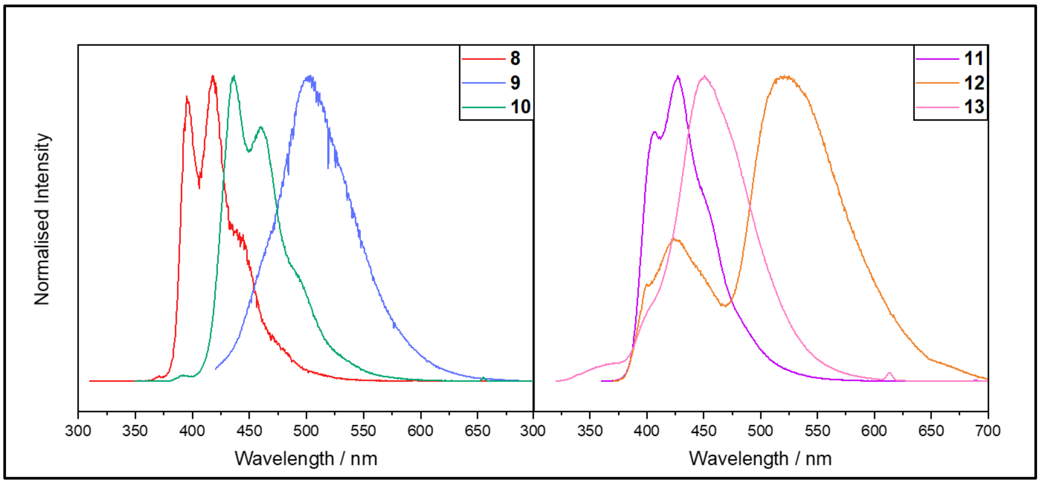

Figure 2.48 Emission spectra (recorded in toluene) for oxazoles **8-13**.

As well as this both **9** and **12**, as discussed previously, exhibited interesting photophysical properties which may provide opportunities to analyse the effect of more complex energy transfer pathways.

Oxazoles **8** and **10** were both dissolved individually in toluene with DPO, which was then added to a premixed solution of [MeImC$_{12}$]Br, 1-butanol and ultra-pure water in the ratio 1:1:1:1. Before analysis, 6 g of water was added to yield the final ratio of 1:1:1:7 and sonicated to form a clear microemulsion.

Despite the higher quantum yield (in the case of oxazole **8**) and shorter emission lifetime, both oxazoles suffered a decrease in efficiency when compared to their mono-substituted counterparts, as shown in **Figure 2.49**. This was particularly evident when in the presence of Ni-63, with a drop in efficiency of 76 and 80 % for oxazoles **8** and **10** respectively when compared to cocktails doped with **1** and **3**.

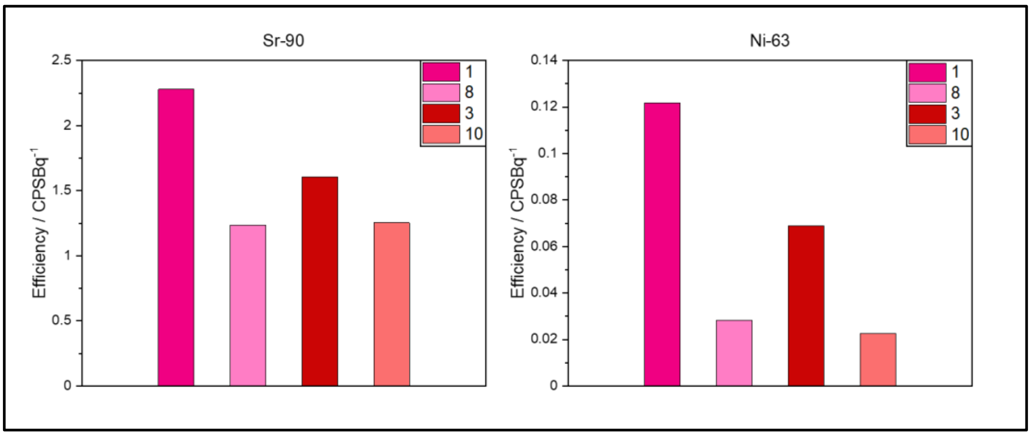

Figure 2.49 Comparison of scintillation efficiency for oil-in-water microemulsions doped with **1**, **8**, **3** and **10** in the presence of Sr-90 (*left*) and Ni-63 (*right*). Cocktails containing **1** and **3** counted for 30 minutes, and those containing **8** and **10** counted for 30 minutes with 10 cycles completed in total for all samples.

However when formulated before analysis, the final microemulsions doped with **8** and **10** were coloured at the concentrations used for oxazoles **1-7**, therefore a significant colour quenching could have occurred during detection. Thus these low efficiency values may not be the true efficiency compared to cocktails containing oxazoles **1** and **3**, and repeats are required beyond the scope of this thesis at a lower concentration to establish whether a higher efficiency can be obtained.

2.6 Conclusion

Seven novel mono-substituted oxazoles were synthesised with a broad range of photophysical properties. Six of these were then successfully extended into di-substituted species *via* the use of 1-iodonaphthalene, giving rise to a greater breadth of conjugation and therefore higher wavelength emission, with **9** and **12** giving more complex photophysical properties. Further photophysical analysis in a range of solvents is required to further confirm their possible solvatochromic properties, and Excitation Emission Matrix (EEM) measurements would be useful for oxazole **12** to further elucidate the dual emissive nature.

DFT analysis was used to further inform on the observed photophysical characteristics of all oxazoles, with an in-depth evaluation of different basis sets and functional combinations used for di-substituted oxazoles.

The first seven oxazoles were co-doped with the primary scintillant, DPO, into oil-in-water microemulsions to test their ability to act as a secondary scintillant in the scintillation counting of both hard- and soft-beta emitting radionuclides. Scintillation data in the presence of Sr-90, a hard emitter, shows that all oxazoles have a higher efficiency than POPOP co-doped with DPO, with **1** being by far the best candidate for secondary scintillation.

Stability studies in the presence of Sr-90 over two months show relatively little change in scintillation efficiency and therefore are stable against a hard radionuclide.

Preliminary scintillation experiments of cocktails doped with disubstituted oxazoles **8** and **10** showed that the disubstituted oxazoles exhibited a lower scintillation efficiency than the respective mono-oxazole doped cocktails. However, both exhibited higher wavelength emission, thus moving more into the sensitivity window of PMT detectors, possibly removing the requirement to adapt the equipment to the microemulsion. As both of these samples were coloured, a lower concentration should also be tested to investigate whether an increase in efficiency can be achieved with the removal of possible colour quenching.

By comparing the scintillation efficiency of the microemulsions in the presence of Sr-90 and Ni-63, results show that there is more than a ten-fold decrease in efficiency for Ni-63, suggesting that the oil-in-water microemulsions give rise to a proximity effect when detecting softer emitters.

2.7 Experimental

2.7.1 General Procedure for the Preparation of Oxazoles 1-7, Adapted from Kotha *et al*[49]

Aldehyde (1 eq.) and K_2CO_3 (2.5 eq.) were added to methanol or a mixture of methanol and THF (dependent on solubility of the aldehyde), followed by TosMIC (1.2 eq.). The reaction was stirred at reflux under N_2, with the progress monitored *via* NMR sampling. Once NMR data showed the absence of aldehyde proton, the reaction was allowed to cool, and the product extracted in DCM and washed three times with water. The DCM layer was dried over magnesium sulphate, filtered and the solvent removed *in vacuo* to yield the desired oxazole.

2.7.1.1 Synthesis of 5-(benzo[f]quinolin-3-yl)oxazole (1)

Following the general procedure, using benzo[f]quinoline-3-carbaldehyde (196 mg, 0.95 mmol) in a solvent mixture of methanol (10 mL) and THF (10 mL). The reaction mixture was refluxed for 4 hours to yield 5-(benzo[f]quinolin-3-yl)oxazole as a brown solid (0.154 g, 66%). ^1H NMR (400 MHz, $CDCl_3$): δ= 9.03 (1H, d, J = 8.7 Hz, Ar-H), 8.63 (1H, d, J = 7.9 Hz, Ar-H), 8.07 (1H, s, OCHN), 8.03 (2H, s, Ar-H), 7.95 (1H, d, Ar-H, J = 8.7 Hz), 7.95 (1H, dd, Ar-H, J = 1.5, 7.8 Hz), 7.89 (1H, s, NCH), 7.76-7.65 (2H, m, Ar-H) ppm; $^{13}C\{^1H\}$ NMR (101 MHz, $CDCl_3$): δ= 151.6, 151.3, 148.2, 146.4, 131.8, 131.8, 131.8, 129.4, 128.9, 128.0, 127.6, 127.4, 125.8, 124.8, 122.7, 117.59 ppm. ES-MS (positive ion mode): found m/z 247.0866 [M+] $C_{16}H_{10}N_2O + H^+$; UV-vis (MeCN) λ_{max} (ε / $mol^{-1}dm^3cm^{-1}$) 364 (10550), 347 (9300), 330 (5300), 311.5 (20200), 281 (46000), 263 (45250), 215 (16550) nm; IR ν_{max} / cm^{-1}: 3092, 3053, 2980, 1584, 1558, 1506, 1485, 1462, 1408, 1327, 1364, 1285, 1272, 1251, 1225, 1198, 1107, 1089, 1076, 1036, 995, 950, 923.

2.7.1.2 Synthesis of 5-(10-chloroanthracen-9-yl)oxazole (2)

Following the general procedure, using 10-chloro-9-anthraldehyde (200 mg, 0.83 mmol) in a solvent mixture of methanol (12 mL) and THF (15 mL). The reaction mixture was refluxed for 3.5 hours to yield 5-(10-chloroanthracen-9-yl)oxazole as a bright yellow solid (0.178 g, 77%). ^1H NMR (400 MHz, $CDCl_3$): δ= 8.60 (2H, ddd, Ar-H, J = 0.8, 1.3, 8.9 Hz), 8.24 (1H, s, OCHN), 7.82 (2H, ddd, Ar-H, J = 0.8, 1.3, 8.9 Hz), 7.62 (2H, ddd, Ar-H, J = 1.2, 6.6, 9.0 Hz), 7.53 (2H, ddd, Ar-H, J = 1.2, 6.6, 9.0 Hz), 7.43 (1H, s, NCH); $^{13}C\{^1H\}$ NMR (101 MHz, $CDCl_3$): δ= 152.0, 147.3, 132.1, 128.5, 128.3, 127.0, 126.9, 125.9, 125.2, 121.0 ppm. ES-MS (positive ion mode): found m/z 280.0525 [M+] $C_{17}H_{10}ClNO + H^+$; UV-vis (MeCN) λ_{max} (ε / $mol^{-1}dm^3cm^{-1}$) 396 (9900), 375 (10200), 357 (6400), 257 (149500), 222 (14400), 216 (13950) nm; IR v_{max} / cm^{-1}: 3645, 3129, 3084, 2983, 2888, 1500, 1463, 1446, 1392, 1342, 1264, 1154, 1109, 1092, 1029, 971, 942, 916, 870, 832, 787, 758, 692, 641, 622, 607, 590, 470, 429, 396.

2.7.1.3 Synthesis of 5-(pyrene-1-yl)oxazole (3)

Following the general procedure, using pyrene-1-carbaldehyde (509 mg, 2.15 mmol) in a solvent mixture of methanol (15 mL) and THF (15 mL). The reaction mixture was refluxed overnight to yield 5-(pyrene-1-yl)oxazole as a yellow solid (0.401 g, 67%). ^1H NMR (400 MHz, $CDCl_3$): δ= 8.53 (1H, d, Ar-H, J = 9.4 Hz), 8.02-8.25 (9H, m, Ar-H and OC(H)N), 7.60 (1H, s, NCH) ppm. $^{13}C\{^1H\}$ NMR (101 MHz, $CDCl_3$): δ= 151.5, 151.2, 131.9, 131.5, 130.8, 128.9, 128.5, 128.1, 127.4, 126.5, 126.1, 126.1, 125.7, 125.4, 125.0, 124.7, 124.1, 122.1 ppm; ES-MS (positive ion mode): found m/z 270.0914 [M+] $C_{19}H_{13}NO + H^+$; UV-vis (MeCN) λ_{max} (ε / $mol^{-1}dm^3cm^{-1}$) 350 (28100), 283 (29950), 275.5 (28300) 241.5 (36550) nm; IR v_{max} / cm^{-1} 3126, 3051, 2978, 2886, 1670, 1584, 1495, 1429, 1381, 1278, 1240, 1178, 1099, 1065, 1017, 951, 923, 844, 761, 720, 686, 631, 507.

2.7.1.4 Synthesis of 5-(phenanthren-9-yl)oxazole (4)

Following the general procedure, using phenanthrene-9-carbaldehyde (500 mg, 2.42 mmol) in a solvent mixture of methanol (12 mL) and THF (15 mL). The reaction mixture was refluxed overnight to yield 5-(phenanthren-9-yl)oxazole as a beige solid (0.413 g, 69%). 1H NMR (400 MHz, $CDCl_3$): δ= 8.79 (1H, dd, Ar-H, J = 0.7, 8.2 Hz), 8.71 (1H, ap. d, Ar-H, J = 8.2 Hz), 8.26 (1H, dd, Ar-H, J = 1.2, 8.2 Hz), 8.11 (1H, s, OCHN), 8.02 (1H, s, Ar-H), 7.94 (1H, dd, Ar-H, J = 7.9, 1.4 Hz), 7.60-7.77 (4H, m, Ar-H), 7.50 (1H, s, NCH) ppm. $^{13}C\{^1H\}$ NMR (101 MHz, $CDCl_3$): δ= 151.1, 131.1, 130.9, 130.8, 129.3, 129.2, 128.6, 127.9, 127.4, 127.3, 127.2, 125.8, 125.3, 124.0, 123.4, 122.8 ppm. ES-MS (positive ion mode): found m/z 246.0915 [M+] $C_{17}H_{11}NO + H^+$; UV-vis (MeCN) λ_{max} (ε / $mol^{-1}dm^3cm^{-1}$) 305 (15200), 256 (50400), 209 (28850) nm;. IR v_{max} / cm^{-1} 3140, 3105, 3056, 2981, 1658, 1604, 1563, 1499, 1449, 1434, 1396, 1310, 1252, 1209, 1145, 1125, 1106, 1094, 1041, 965, 951, 906, 893, 860, 845, 830, 769, 748, 720, 680, 633, 598, 507, 443, 427, 409.

2.7.1.5 Synthesis of 5-(fluorene-2-yl)oxazole (5)

Following the general procedure, using fluorene-2-carbaldehyde (200 mg, 1.03 mmol) in a solvent mixture of methanol (8 mL) and THF (6 mL). The reaction mixture was refluxed for 5 hours to yield 5-(fluorene-2-yl)oxazole as a yellow solid (0.217 g, 90%). ^{1}H NMR (400 MHz, $CDCl_3$): δ= 7.93 (1H, s, OCHN), 7.84 (1H, s, Ar-H), 7.82 (2H, t, Ar-H, J = 8.0 Hz), 7.69 (1H, dd, Ar-H, J = 1.6, 8.0 Hz), 7.57 (1H, dt, Ar-H, J = 1.0, 7.5 Hz), 7.41 (2H, ap. t, Ar-H, J = 7.5 Hz), 7.39 (1H, s, NCH), 7.34 (1H, td, Ar-H, J =1.2, 7.5 Hz), 3.96 (2H, s, C-H) ppm; ^{13}C NMR (101 MHz, $CDCl_3$): δ= 152.2, 150.4, 144.0, 143.6, 142.4, 141.1, 127.35, 127.1, 126.2, 125.3, 123.5, 121.3, 121.1, 120.5, 120.3, 37.1 ppm; ES-MS (positive ion mode): found m/z 236.0913 [M+] $C_{17}H_{11}NO + H^+$; UV-vis (MeCN) λ_{max} (ε / mol^{-1}dm^{3}cm^{-1}) 322 (37200), 301 (37400), 205 (38700) nm; IR v_{max} / cm^{-1} 3650, 3104, 2979, 2892, 1404, 1257, 1157, 1114, 1090, 1042, 947, 882, 861, 844, 823, 771, 737, 642, 482, 422.

2.7.1.6 Synthesis of 5-(4-(pyridin-2-yl)phenyl)oxazole (6)

Following the general procedure, using 4-(pyridin-2-yl)benzaldehyde (200 mg, 1.09 mmol) dissolved in methanol (15 mL). The reaction mixture was refluxed overnight to yield 5-(4-(pyridin-2-yl)phenyl)oxazole as a bright yellow solid (0.168 g, 69%). ^{1}H NMR (400 MHz, d_6-DMSO): δ= 8.70 (1H, ddd, Ar-H, J = 0.9, 1.9, 4.8 Hz), 8.50 (1H, s, OCHN), 8.20-8.25 (2H, m, Ar-H), 8.04 (1H, dt, Ar-H, J = 8.0, 0.9 Hz), 7.91 (1H, td, Ar-H, J = 1.9, 7.6 Hz), 7.89-7.84 (2H, m, Ar-H), 7.80 (1H, s, NCH), 7.39 (1H, ddd, Ar-H, J = 7.6, 4.8, 1.0 Hz) ppm; ^{13}C{^{1}H} NMR (101 MHz, d_6-DMSO): δ= 155.1, 152.1, 150.2, 149.7, 138.6, 137.3, 127.9, 127.2, 124.4, 122.9, 122.7, 120.3 ppm; ES-MS (positive ion mode): found m/z 223.0864 [M+] $C_{14}H_{10}N_2O + H^+$; UV-vis (MeCN) λ_{max} (ε / mol^{-1}dm^{3}cm^{-1}) 302 (34200) nm; IR v_{max} / cm^{-1} 3675, 3650, 3091, 3056, 2982, 2888, 1586, 1506, 1485, 1458, 1431, 1405, 1392, 1330, 1299, 1276, 1264, 1192, 1157, 1115, 1092, 1061, 1047, 1012, 987, 956, 941, 920, 871, 849, 822, 780, 739, 723, 664, 645, 617, 553, 482, 468, 447, 424.

2.7.1.7 Synthesis of 5-(4-(pyrrolidin-1-yl)phenyl)oxazole (7)

Following the general procedure, using 4-(pyrrolidin-1-yl)benzaldehyde (500 mg, 2.85 mmol) dissolved in solvent mixture of methanol (25 mL) and THF (10 mL). The reaction mixture was refluxed overnight to yield 5-(4-(pyrrolidin-1-yl)phenyl)oxazole as an orange solid (0.447 g, 73%). ^{1}H NMR (500 MHz, $CDCl_3$): δ= 7.81 (1H, s, OCHN), 7.52-7.48 (2H, m, Ar-H), 7.12 (1H, s, NCH), 6.60-6.58 (2H, m, Ar-H), 3.36-3.29 (4H, m, CH_2), 2.07-1.97 (4H, m, CH_2) ppm; ^{13}C{^{1}H} NMR (126 MHz, $CDCl_3$): δ= 152.7, 149.3, 148.1, 125.9, 118.4, 115.2, 111.8, 47.7, 25.6 ppm; ES-MS (positive ion mode): found m/z 215.12 [M+] $C_{13}H_{14}N_2O + H^+$; UV-vis

(MeCN) λ_{max} (ε / $mol^{-1}dm^3cm^{-1}$) 311.5 (26750) nm; IR v_{max} / cm^{-1} 3129, 3106, 2967, 2890, 2869, 2843, 1611, 1591, 1555, 1520, 1488, 1457, 1428, 1381, 1284, 1273, 1252, 1228, 1192, 1161, 1121, 1098, 1088, 1044, 1000.

2.7.2 General Procedure of Ullmann-based Coupling for the Synthesis of Oxazoles 8-13, adapted from Yoshizumi *et al*[50]

Oxazole (1 eq.), Na_2CO_3 (2 eq.), PPh_3 (0.2 eq.), CuI (4 eq.) and iodo-napthalene (1.2 eq) were added to degassed DMF (4 mL), and the reaction was stirred in the dark for 48 hrs at 110°C under N_2. The reaction mixture was then allowed to cool, before being stirred with ethylene diamine (10 mL) in water (10 mL) for 10 minutes. The crude product was extracted into DCM (100 mL), which was then washed with ethylene diamine (10 mL) in water (100 mL) until the aqueous layer was clear, followed by washing with water (3 x 100 mL). The DCM layer was dried over magnesium sulphate, filtered and the solvent removed *in vacuo* to yield crude product. The crude product was triturated in ethanol and the solid filtered to yield the desired product.

Please note that oxazoles were initially synthesised by the author, however some NMR, IR, MS and photophysical data was collected from samples synthesised by Laura McLauchlan (supervised project student).

2.7.2.1 Synthesis of 5-(benzo[f]quinolin-3-yl)-2-(naphthalen-1-yl)oxazole (8)

Following the general procedure, using 1 (0.2g, 0.812 mmol) to yield an orange solid (0.112 g, 43%); ^1H NMR (500 MHz, $CDCl_3$): δ= 9.40 (1H, d, J = 8.6 Hz, Ar-H), 9.07 (1H, d, J = 8.6 Hz, Ar-H), 8.66 (1H, d, J = 8.3 Hz, Ar-H), 8.43 (1H, d, J = 7.3 Hz, Ar-H), 8.15 (1H, s, Ar-H), 8.10 (1H, d, J = 8.6 Hz, Ar-H), 8.05 (2H, s, Ar-H), 8.02 (1H, d, J = 8.2 Hz, Ar-H), 7.28 (2H, t, J = 7.5 Hz), 7.77-7.57 (5H, m, Ar-H) ppm; $^{13}C\{^1H\}$ NMR (126 MHz, $CDCl_3$): 162.3, 151.0, 148.5, 146.9, 134.2, 131.9, 131.8, 131.8, 131.8, 130.5, 129.7, 129.0, 128.8, 128.4, 128.3, 127.9, 127.9, 127.6, 127.5, 126.6, 126.3, 125.2, 124.8, 123.9, 122.8, 117.7 ppm; ES-MS (positive ion mode): found m/z 373.1344 [M+] $C_{26}H_{16}N_2O + H^+$; UV-vis ($CHCl_3$) λ_{max} (ε / $mol^{-1}dm^3cm^{-1}$) 378 (27300), 360 (26900), 345 (28600), 295 (sh) (22450), 284 (26500), 271 (24150) nm; IR v_{max} / cm^{-1} 3048, 2362, 2336, 1742, 1715, 1696, 1651, 1615, 1575, 1557, 1543, 1507, 1494, 1471, 1447, 1421, 1375, 1360, 1338, 1317, 1247, 1214, 1156, 1144, 1105, 1064, 1042, 1023, 955, 840, 748, 723, 668, 617, 604, 555, 527, 505, 472, 420.

2.7.2.2 Synthesis of 5-(10-chloroanthracen-9-yl)-2-(naphthalen-1-yl)oxazole (9)

Following the general procedure, using 2 (0.2 g, 0.715 mmol) to yield a yellow solid (0.135 g, 53%); ^{1}H NMR (500 MHz, $CDCl_3$): δ= 9.48 (1H, d, J = 8.5 Hz, Ar-H), 8.64 (2H, d, J = 8.8 Hz, Ar-H), 8.32 (1H, dd, J = 7.3, 1.0 Hz, Ar-H), 8.07 (2H, d, J = 8.7 Hz, Ar-H), 8.00 (1H, d, J = 8.1 Hz, Ar-H), 7.95 (1H, d, J = 8.1 Hz, Ar-H), 7.71-7.64 (4H, m, Ar-H), 7.62-7.54 (4H, m, Ar-H) ppm; $^{13}C\{^1H\}$ NMR (126 MHz, $CDCl_3$): δ= 162.7, 146.7, 134.1, 132.2, 132.1, 131.5, 130.2, 130.2, 128.7, 128.7, 128.1, 127.8, 127.1, 127.00, 126.4, 126.3, 126.3, 125.3, 125.1, 123.8, 121.6 ppm; ES-MS (positive ion mode): found m/z 406.1005 [M+] $C_{27}H_{16}ClNO + H^+$; UV-vis ($CHCl_3$) λ_{max} (ε / $mol^{-1}dm^3cm^{-1}$) 400 (18650), 380 (17500), 361 (11450), 323 (16500), 262 (155050) nm; IR ν_{max} / cm^{-1} 3100, 3057, 3044, 2960, 2922, 2852, 2366, 2324, 1942, 1912, 1834, 1800, 1737, 1716, 1620, 1588, 1577, 1528, 1503, 1480, 1437, 1388, 1337, 1322, 1261, 1241, 1212, 1183, 1149, 1132, 1099, 1063, 1030, 1003, 989, 956, 938, 878, 870, 848, 816, 799, 754, 722, 686, 660, 639, 625, 605, 587, 560, 532, 466, 434, 416.

2.7.2.3 Synthesis of 5-(3a1,5a1-dihydropyren-1-yl)-2-(naphthalen-1-yl)oxazole (10)

Following the general procedure, using 3 (0.1g, 0.371 mmol) to yield a yellow solid (92 mg, 63% yield): ^{1}H NMR (400 MHz, $CDCl_3$): δ= 9.46 (1H, d, J = 8.6 Hz, Ar-H), 8.73 (1H, d, J = 9.3 Hz, Ar-H), 8.43 (1H, dd, J = 7.4, 1.0 Hz, Ar-H), 8.39 (1H, d, J = 8.0, Ar-H), 8.29-8.21 (4H, m, Ar-H), 8.13 (2H, m, Ar-H), 8.06 (2H, m, Ar-H), 7.96 (1H, d, J = 8.1 Hz, Ar-H), 7.85 (1H, s, NCH), 7.72 (1H, ddd, J = 8.6, 6.7, 1.2 Hz, Ar-H), 7.66-7.58 (2H, m, Ar-H) ppm; $^{13}C\{^1H\}$ NMR (126 MHz, $CDCl_3$): δ= 161.8, 151.0, 134.2, 131.8, 131.5, 131.5, 130.9, 130.4, 129.0, 128.8, 128.5, 128.1, 128.0, 127.8, 127.5, 127.3, 126.5, 126.5, 126.4, 126.0, 126.0, 125.7, 125.3, 125.2, 125.2, 124.8, 124.3, 124.0, 122.5 ppm; ES-MS (positive ion mode): found m/z 396.1383 [M+] $C_{29}H_{17}NO + H^+$; UV-vis ($CHCl_3$) λ_{max} (ε / $mol^{-1}dm^3cm^{-1}$) 377 (33550), 328 (15400), 313 (12750), 288 (24750), 279 (21500) nm; IR ν_{max} / cm^{-1} 3095, 3042, 3010, 2358, 2337, 2158, 1918, 1747, 1732, 1716, 1680, 1649, 1597, 1576, 1541, 1520, 1508, 1489, 1457, 1435, 1418, 1397, 1369, 1345, 1316, 1292, 1263, 1244, 1218, 1197, 1181, 1162, 1129, 1075, 1028, 988, 974, 947, 903, 834, 819, 798, 767, 754, 738, 709, 679, 660, 627, 604, 579, 566, 541, 506, 497, 464, 430, 415.

2.7.2.4 Synthesis of 2-(naphthalen-1-yl)-5-(phenanthren-9-yl)oxazole (11)

Following the general procedure, using 4 (0.2 g, 0.815 mmol) to yield a yellow solid (0.147 g, 49 %); ^{1}H NMR (500 MHz, $CDCl_3$): δ= 9.43 (1H, d, J = 8.6 Hz, Ar-H), 8.82 (1H, ap d, J = 8.1, Ar-H), 8.74 (1H, ap d, J = 8.3 Hz, Ar-H), 8.46 (1H, dd, J = 8.0, 1.3 Hz, Ar-H), 8.39 (1H, dd, J = 7.3, 1.2 Hz, Ar-H), 8.16 (1H, s, Ar-H), 8.01 (1H, ap d, J = 8.1, Ar-H), 7.99 (1H, ap d, J = 7.7, Ar-H), 7.95 (1H, ap d, J = 8.2 Hz, Ar-H), 7.78-7.66 (6H, m, Ar-H), 7.65-7.58 (2H, m, Ar-H) ppm; $^{13}C\{^1H\}$ NMR (126 MHz, $CDCl_3$): 161.6, 150.3, 134.1, 131.4, 131.2, 130.9, 130.7, 130.3, 129.2, 129.2, 128.7, 128.1, 128.0, 127.9, 127.7, 127.4, 127.2, 127.2, 127.1, 126.4, 126.3, 125.9, 125.1, 124.3, 124.0, 123.3, 122.7 ppm; ES-MS (positive ion mode): found m/z 372.1378 [M+] $C_{27}H_{17}NO + H^+$; UV-vis ($CHCl_3$) λ_{max} (ε / $mol^{-1}dm^3cm^{-1}$) 339 (23550), 308 (18000), 242 (57600) nm; IR v_{max} / cm^{-1} 3128, 3054, 2932, 2364, 2328, 1942, 1668, 1590, 1557, 1519, 1490, 1445, 1430, 1384, 1347, 1299, 1250, 1212, 1171, 1144, 1130, 1068, 1030, 993, 974, 943, 910, 884, 859, 840, 802, 760, 745, 715, 671, 660, 618, 604, 536, 501, 464, 444, 416.

2.7.2.5 Synthesis of 2-(2-(naphthalen-1-yl)oxazol-5-yl)-9H-fluoren-9-one (12)

Following the general procedure, using 5 (0.1g, 0.429 mmol), to yield a bright orange solid (27 mg, 17% yield): 1H NMR (400 MHz, $CDCl_3$): δ= 9.34 (1H, d, J= 8.8 Hz, Ar-H), 8.33 (1H, dd, J = 7.3, 1.1, Ar-H), 8.06 (1H, ap. d, J = 1.2 Hz, Ar-H), 8.00 (1H, d, J = 8.1 Hz, Ar-H), 7.93 (1H, d, J = 8.2, Ar-H), 7.90 (1H, dd, J = 7.8, 1.6 Hz, Ar-H), 7.72-7.68 (2H, m, Ar-H), 7.67 (1H, s, NCH), 7.64-7.56 (4H, m, Ar-H), 7.56-7.51 (1H, m, Ar-H), 7.36-7.31 (1H, m, Ar-H) ppm; $^{13}C\{^1H\}$ NMR (126 MHz, $CDCl_3$): δ= 193.3, 161.3, 149.9, 144.0, 139.9, 135.0, 134.9, 134.2, 133.9, 131.4, 130.1, 129.9, 129.3, 128.8, 128.6, 127.9, 127.7, 126.3, 126.0, 124.9, 124.6, 124.3, 123.4, 120.9, 120.5, 120.0 ppm; ES-MS (positive ion mode): found m/z 374.1178 [M+] $C_{26}H_{15}NO + H^+$; UV-vis ($CHCl_3$) λ_{max} (ε / $mol^{-1}dm^3cm^{-1}$) 436 (1255), 351 (17380), 320 (sh) (11180), 286 (18090), 275 (sh) (12860), 254 (18635) nm; IR v_{max} / cm^{-1} 3333, 3053, 2960, 2928, 2858, 2364, 2341, 1920, 1833, 1712, 1670, 1618, 1598, 1577, 1558, 1522, 1511, 1456, 1394, 1378, 1361, 1288, 1270, 1255, 1186, 1149, 1122, 1073, 1028, 972, 951, 919, 902, 884, 864, 842, 822, 798, 762, 732, 686, 665, 640, 628, 582, 566, 536, 521, 505, 474, 432, 416.

2.7.2.6 Synthesis of 2-(naphthalen-1-yl)-5-(4-(pyrrolidin-1-yl)phenyl)oxazole (13)

Following the general procedure, using 7 (0.1g, 0.467 mmol), to yield a dark yellow oil (91 mg, 57% yield): ^{1}H NMR (400 MHz, $CDCl_3$): δ= 9.35 (1H, ddd, J = 8.6, 2.2, 0.9 Hz, Ar-H), 8.28 (1H, dd, J = 7.3, 1.2 Hz, Ar-H), 7.94 (1H, ap. d, J = 8.2 Hz, Ar-

H), 7.91 (1H, ap. d, J = 8.2 Hz, Ar-H), 7.66-7.62 (3H, m, Ar-H), 7.59-7.53 (2H, m, Ar-H), 7.37 (1H, s, NCH), 6.63 (2H, d, J = 8.8 Hz, Ar-H), 3.39-3.33 (4H, m, CH_2), 2.08-2.02 (4H, m, CH_2) ppm; $^{13}C\{^1H\}$ NMR (126 MHz, $CDCl_3$): δ= 159.8, 156.2, 152.3, 148.1, 134.2, 130.7, 130.3, 128.6, 127.5, 127.5, 126.5, 126.3, 125.9, 125.2, 124.5, 120.5, 115.4, 111.9, 47.7, 25.6 ppm; ES-MS (positive ion mode): found m/z 341.1650 [M+] $C_{23}H_{20}N_2O + H^+$; UV-vis ($CHCl_3$) λ_{max} (ε / $mol^{-1}dm^3cm^{-1}$) 362 (6530), 301 (6100) nm; IR ν_{max} / cm^{-1} 3047, 2961, 2837, 2362, 2338, 1608, 1588, 1522, 1504, 1480, 1457, 1434, 1373, 1351, 1226, 1175, 1121, 1072, 986, 961, 946, 863, 805, 771, 740, 719, 685, 660, 641, 570, 538, 518, 474, 452, 420.

2.7.3 General Procedure for the Formulation of Microemulsions

Stock solutions of oxazole **1-8**, **10** and POPOP with DPO were prepared as 3.4 mM and 0.452 M respectively in toluene. $[MeImC_{12}]Br$ was synthesised previously within the group.

Oil-in-water microemulsions were prepared as 1:1:1:1 w/w/w/w $[MeImC_{12}]Br$: 1-butanol: toluene (with scintillant): ultra-pure H_2O and sonicated to give a clear microemulsion. Before analysis, a further 6 g of water was added to bring the total ratio to 1:1:1:7, and thoroughly mixed.

Prior to scintillation analysis, radionuclide sample was spiked into the cocktail (Ni-63 (2.0 kBq/g) prepared in 0.1 mol dm^{-3} HCl, or Sr-90 (96.99 Bq/g) prepared in 1 mol dm^{-3} HNO_3), and the sample agitated. Sources contained 100 μg g^{-1} of inactive nickel and 50 μg g^{-1} inactive strontium and yttrium, respectively.

2.8 References

1. J. W. Conforth and R. H. Conforth, *J. Chem. Soc.*, 1947, 96–102.
2. D. J. Brown and P. B. Ghosh, *J. Chem. Soc. B Phys. Org.*, 1969, 270–276.
3. Paul. Haake and W. B. Miller, *J. Am. Chem. Soc.*, 1963, **85**, 4044–4045.
4. I. J. Turchi and M. J. S. Dewar, *Chem. Rev.*, 1975, **75**, 389–437.
5. I. J. Turchi, *Ind. Eng. Chem. Prod. Res. Dev.*, 1981, **20**, 32–76.
6. R. H. Wiley, *Chem. Rev.*, 1945, **37**, 401–442.
7. R. Robinson, *J. Chem. Soc. Trans.*, 1909, **95**, 2167–2174.
8. S. Gabriel, *Berichte Dtsch. Chem. Ges.*, 1910, **43**, 134–138.
9. S. Gabriel, *Berichte Dtsch. Chem. Ges.*, 1910, **43**, 1283–1287.
10. E. Fischer, *Berichte Dtsch. Chem. Ges.*, 1896, **29**, 205–214.
11. A. M. van Leusen, B. E. Hoogenboom and H. Siderius, *Tetrahedron Lett*, 1972, **13**, 2369–2372.
12. J. W. Cornforth and R. H. Cornforth, *J. Chem. Soc. Resumed*, 1949, 1028–1030.
13. G. E. Schiltz, in *Comprehensive Organic Synthesis II*, ed. P. Knochel, Elsevier, Amsterdam, 2nd edn., 2014, pp. 555–572.
14. H. H. Wasserman and F. J. Vinick, *J. Org. Chem.*, 1973, **38**, 2407–2408.
15. O. H. Oldenziel, D. Van Leusen and A. M. Van Leusen, *J. Org. Chem.*, 1977, **42**, 3114–3118.
16. A. M. Van Leusen, J. Wildeman and O. H. Oldenziel, *J. Org. Chem.*, 1977, **42**, 1153–1159.
17. S. Kakkar and B. Narasimhan, *BMC Chem.*, , DOI:10.1186/s13065-019-0531-9.
18. H.-Z. Zhang, Z.-L. Zhao and C.-H. Zhou, *Eur. J. Med. Chem.*, 2018, **144**, 444–492.
19. Ditazole, https://www.drugbank.ca/drugs/DB08994, (accessed 11 February 2020).
20. Compound Summary Ditazole, https://pubchem.ncbi.nlm.nih.gov/compound/Ditazole, (accessed 11 February 2020).
21. Oxaprozin, https://medlineplus.gov/druginfo/meds/a693002.html, (accessed 11 February 2020).

22. Ageroplas, pubchem.ncbi.nlm.nih.gov/compound/Ageroplas, (accessed 11 February 2020).
23. L. W. McKeen, in *Fatigue and Tribological Properties of Plastics and Elastomers (Third Edition)*, ed. L. W. McKeen, William Andrew Publishing, Norwich, NY, 2016, pp. 45–64.
24. E. Smulders and E. Sung, in *Ullmann's Encyclopedia of Industrial Chemistry*, ed. Wiley-VCH Verlag GmbH & Co. KGaA, Wiley-VCH Verlag GmbH & Co. KGaA, Weinheim, Germany, 2011, p. o15_o13.
25. M. A. Fourati, T. Maris, W. G. Skene, C. G. Bazuin and R. E. Prud'homme, *J. Phys. Chem. B*, 2011, **115**, 12362–12369.
26. F. N. Hayes, B. S. Rogers and D. G. Ott, *J. Am. Chem. Soc.*, 1955, **77**, 1850–1852.
27. D. R. Edler, 2015.
28. M. F. L'Annunziata and M. J. Kessler, in *Handbook of Radioactivity Analysis (Third Edition)*, ed. M. F. L'Annunziata, Academic Press, Amsterdam, 2012, pp. 423–573.
29. J. Thomson, in *Handbook of Radioactivity Analysis (Third Edition)*, ed. M. F. L'Annunziata, Academic Press, Amsterdam, 2012, pp. 575–623.
30. I. B. Berlman, in *Handbook of Fluorescence Spectra of Aromatic Molecules*, Elsevier, Amsterdam, 2nd edn., 1971, pp. 107–415.
31. In *Surfactants and Interfacial Phenomena*, John Wiley & Sons, Inc., Hoboken, NJ, USA, 2012, pp. 336–367.
32. E. McEvoy, S. Donegan, J. Power, K. Altria and A. Marsh, in *Encyclopredia of Separation Science*, Elsevier Science Ltd., Amsterdam, 2000, pp. 1–10.
33. In *Surfactants and Interfacial Phenomena*, John Wiley & Sons, Inc., Hoboken, NJ, USA, 2012, pp. 235–271.
34. In *Surfactants and Interfacial Phenomena*, John Wiley & Sons, Inc., Hoboken, NJ, USA, 2012, pp. 1–38.
35. In *Surfactants and Interfacial Phenomena*, John Wiley & Sons, Inc., Hoboken, NJ, USA, 2012, pp. 123–201.
36. P. Mukerjee and K. J. Mysels, *Critical micelle concentrations of aqueous surfactant systems*, NBS, US, 1971.
37. P. Mukerjee, *Adv. Colloid Interface Sci.*, 1967, **1**, 242–275.
38. National Diagnostic Laboratory Staff, 2004.
39. V. Binns and J. Thomson, 24.

40. L. Ye, J. Guo and R.-S. Ge, in *Vitamins & Hormones*, Elsevier, Amsterdam, 2014, vol. 94, pp. 349–390.
41. Endocrine Disrupting Chemicals (EDCs), https://www.who.int/ceh/risks/cehemerging2/en/, (accessed 10 February 2020).
42. Ultima Gold XR LSC Cocktail Safety Data Sheet, https://www.sigmaaldrich.com/MSDS/MSDS/DisplayMSDSPage.do?country=GB&language=en&productNumber=L8411&brand=SIGMA&PageToGoToURL=https%3A%2F%2Fwww.sigmaaldrich.com%2Fcatalog%2Fproduct%2Fsigma%2Fl8411%3Flang%3Den, (accessed 11 February 2020).
43. Hionic-Fluor PerkinElmer Safety Data Sheet, https://apps.wku.edu/sds/uploads/docs/4884.pdf, (accessed 11 February 2020).
44. Gold Star SDS, https://cdn.website-editor.net/d756dd1269b5433bbe6aec36ab1b1b9a/files/uploaded/Gold%2520Star%2520version%25206.5%2520DEC2019.pdf, (accessed 3 December 2021).
45. ProSafe HC+ SDS, https://cdn.website-editor.net/d756dd1269b5433bbe6aec36ab1b1b9a/files/uploaded/ProSafe%2520HC%252B%2520version%25206.4%2520DEC2019.pdf, (accessed 3 December 2021).
46. Ultima Gold^{TM} LSC Cocktail For aqueous and non-aqueous samples | Sigma-Aldrich, http://www.sigmaaldrich.com/, (accessed 6 December 2021).
47. ProSafe+ SDS, https://cdn.website-editor.net/d756dd1269b5433bbe6aec36ab1b1b9a/files/uploaded/ProSafe%252B%2520version%25206.4%2520DEC2019.pdf, (accessed 3 December 2021).
48. Pico-Fluor Plus MSDS, https://www.perkinelmer.com/Content/MSDSDatabase/MSDS_6013691_Pico-Fluor_Plus_(GB).pdf, (accessed 3 December 2021).
49. S. Kotha and V. Shah, *Synthesis*, 2007, 3653–3658.
50. T. Yoshizumi, T. Satoh, K. Hirano, D. Matsuo, A. Orita, J. Otera and M. Miura, *Tetrahedron Lett.*, 2009, **50**, 3273–3276.
51. M. S. Skorotetcky, O. V. Borshchev, N. M. Surin, Y. Odarchenko, S. A. Pisarev, S. M. Peregudova, K. W. Törnroos, D. Chernyshov, D. A. Ivanov and S. A. Ponomarenko, *Dyes Pigments*, 2017, **141**, 128–136.

52. C. A. Maryanoff, in *Chemistry of Heterocyclic Compounds: A Series Of Monographs*, ed. I. J. Turchi, John Wiley & Sons, Inc., Hoboken, NJ, USA, 2008, pp. 343–360.
53. S. Kotha, A. K. Ghosh and K. D. Deodhar, *Synthesis*, 2004, 549–557.
54. S. J. Ananthakrishnan, E. Varathan, E. Ravindran, N. Somanathan, V. Subramanian, A. B. Mandal, J. D. Sudha and R. Ramakrishnan, *Chem. Commun.*, 2013, **49**, 10742–10744.
55. G.-J. Zhao and K.-L. Han, *J. Phys. Chem. A*, 2007, **111**, 9218–9223.
56. F. M. Winnik, *Chem. Rev.*, 1993, **93**, 587–614.
57. C.-W. Chang, T. I. Sølling and E. W.-G. Diau, *Chem. Phys. Lett.*, 2017, **686**, 218–222.
58. L. Biczok and T. Berces, *J. Phys. Chem.*, 1988, **92**, 3842–3845.
59. I. Ghosh, A. Mukhopadhyay, A. L. Koner, S. Samanta, W. M. Nau and J. N. Moorthy, *Phys. Chem. Chem. Phys.*, 2014, **16**, 16436–16445.
60. T. Gerbich, J. Herterich, J. Köhler and I. Fischer, *J. Phys. Chem. A*, 2014, **118**, 1397–1402.
61. T. Chen, Z.-Q. Chen, W.-L. Gong, C. Li and M.-Q. Zhu, *Mater. Chem. Front.*, 2017, **1**, 1841–1846.
62. M.-S. Yuan, X. Du, F. Xu, D.-E. Wang, W.-J. Wang, T.-B. Li, Q. Tu, Y. Zhang, Z. Du and J. Wang, *Dyes Pigments*, 2015, **123**, 355–362.
63. K. Yoshihara and D. R. Kearns, *J. Chem. Phys.*, 1966, **45**, 1991–1999.
64. Granite, What is the Inner Filter Effect?, https://www.edinst.com/blog/inner-filter-effect/, (accessed 7 April 2021).
65. F. Zhao and D. Ma, *Mater. Chem. Front.*, 2017, **1**, 1933–1950.
66. S. Reineke, M. Thomschke, B. Lüssem and K. Leo, *Rev. Mod. Phys.*, 2013, **85**, 1245–1293.
67. A. D. Becke, *J. Chem. Phys.*, 1993, **98**, 5648–5652.
68. C. Lee, W. Yang and R. G. Parr, *Phys. Rev. B*, 1988, **37**, 785–789.
69. S. H. Vosko, L. Wilk and M. Nusair, *Can. J. Phys.*, , DOI:10.1139/p80-159.
70. P. J. Stephens, F. J. Devlin, C. F. Chabalowski and M. J. Frisch, *J. Phys. Chem.*, 1994, **98**, 11623–11627.
71. R. Krishnan, J. S. Binkley, R. Seeger and J. A. Pople, *J. Chem. Phys.*, 1980, **72**, 650–654.
72. V. Botti, F. Elisei, F. Faraguna, Ž. Marinić, U. Mazzucato, I. Šagud, M. Šindler-Kulyk and A. Spalletti, *J. Photochem. Photobiol. Chem.*, 2016, **329**, 262–272.

73. V. Patil, N. Sekar, V. S. Padalkar, J. Rajput, S. R. Patil and S. V. Patil, *J. Mol. Struct.*, 2020, **1199**, 126984.
74. S. Shahab, M. Sheikhi, L. Filippovich, R. Alnajjar, Z. Ihnatovich, K. Laznev, A. Strogova, M. Atroshko and M. Drachilovskaya, *J. Mol. Struct.*, 2020, **1202**, 127352.
75. P. Ü. Civcir, G. Kurtay and K. Sarıkavak, *Struct. Chem.*, 2017, **28**, 773–790.
76. R. Y. Iliashenko, O. O. Borodin, M. Wera and A. O. Doroshenko, *J. Photochem. Photobiol. Chem.*, 2015, **298**, 68–77.
77. D. R. Sherin and T. K. Manojkumar, *Mater. Today Proc.*, 2020, **33**, 1229–1233.
78. M. Megala and B. J. M. Rajkumar, *J. Comput. Electron.*, 2019, **18**, 1128–1138.
79. F. De Carvalho, M. D. Coutinho Neto, F. H. Bartoloni and P. Homem-de-Mello, *Molecules*, 2018, **23**, 1231.
80. A. Chrayteh, C. P. Ewels and D. Jacquemin, *Phys. Chem. Chem. Phys.*, 2020, **22**, 25066–25074.
81. T. M. Henderson, A. F. Izmaylov, G. Scalmani and G. E. Scuseria, *J. Chem. Phys.*, 2009, **131**, 044108.
82. T. Yanai, D. P. Tew and N. C. Handy, *Chem. Phys. Lett.*, 2004, **393**, 51–57.
83. L. M. G. Abegão, R. D. Fonseca, T. N. Ramos, F. Mahuteau-Betzer, S. Piguel, J. Joatan R., C. R. Mendonça, S. Canuto, D. L. Silva and L. De Boni, *J. Phys. Chem. C*, 2018, **122**, 10526–10534.
84. Y. Zhao and D. G. Truhlar, *Theor. Chem. Acc.*, 2008, **120**, 215–241.
85. R. Peverati and D. G. Truhlar, *J. Phys. Chem. Lett.*, 2011, **2**, 2810–2817.
86. T. H. Dunning, *J. Chem. Phys.*, 1989, **90**, 1007–1023.
87. R. Ditchfield, W. J. Hehre and J. A. Pople, *J. Chem. Phys.*, 1971, **54**, 724–728.
88. W. J. Hehre, R. Ditchfield and J. A. Pople, *J. Chem. Phys.*, 1972, **56**, 2257–2261.
89. P. C. Hariharan and J. A. Pople, *Theor. Chim. Acta*, 1973, **28**, 213–222.
90. P. C. Hariharan and J. A. Pople, *Mol. Phys.*, 1974, **27**, 209–214.
91. M. S. Gordon, *Chem. Phys. Lett.*, 1980, **76**, 163–168.
92. M. M. Francl, W. J. Pietro, W. J. Hehre, J. S. Binkley, M. S. Gordon, D. J. DeFrees and J. A. Pople, *J. Chem. Phys.*, 1982, **77**, 3654–3665.
93. R. C. Binning and L. A. Curtiss, *J. Comput. Chem.*, 1990, **11**, 1206–1216.

94. J.-P. Blaudeau, M. P. McGrath, L. A. Curtiss and L. Radom, *J. Chem. Phys.*, 1997, **107**, 5016–5021.
95. V. A. Rassolov, J. A. Pople, M. A. Ratner and T. L. Windus, *J. Chem. Phys.*, 1998, **109**, 1223–1229.
96. V. A. Rassolov, M. A. Ratner, J. A. Pople, P. C. Redfern and L. A. Curtiss, *J. Comput. Chem.*, 2001, **22**, 976–984.
97. C. Adamo and V. Barone, *J. Chem. Phys.*, 1999, **110**, 6158–6170.
98. M. Ernzerhof and G. E. Scuseria, *J. Chem. Phys.*, 1999, **110**, 5029–5036.
99. F. Weigend and R. Ahlrichs, *Phys. Chem. Chem. Phys.*, 2005, **7**, 3297–3305.
100. E. C. Stokes, PhD Thesis, Cardiff University, 2017.
101. Livechart - Table of Nuclides - Nuclear structure and decay data, https://nds.iaea.org/relnsd/vcharthtml/VChartHTML.html, (accessed 5 April 2021).
102. . J. R. Lakowicz, *Principles of fluorescence spectroscopy*, Springer, New York, 3rd ed., 2006.
103. M. Taniguchi and J. S. Lindsey, *Photochem. Photobiol.*, 2018, **94**, 290–327.

3 Incorporation of Oxazole-Based Fluorophores Within Nanoparticle Constructs for use in Scintillation Proximity Assay

3.1 Overview

Following from the results of **Chapter 2**, in which oxazoles **1-7, 8** and **10** were shown to scintillate in the presence of both Sr-90 and Ni-63, the aim of the following chapter was to encapsulate both mono-substituted and di-substituted oxazoles **1-13** within a particle suitable for use in a Scintillation Proximity Assay (SPA). By incorporating these fluorophores into a polystyrene/silica core/shell particle, they were to be tested for their scintillation viability against a hard emitter, Sr-90, and a soft emitter, Ni-63, to further look at developing greener and low-cost alternatives for radionuclide analysis. By encapsulating fluorophores with a broad range of emissive wavelengths, it was hoped that an element specific system could be realised, in which a range of different particles could be added to a sample, or a cartridge such as one shown in **Figure 3.1**, following functionalisation (**Chapter 4**), resulting in element specific analysis in a complex mixture of radionuclides.

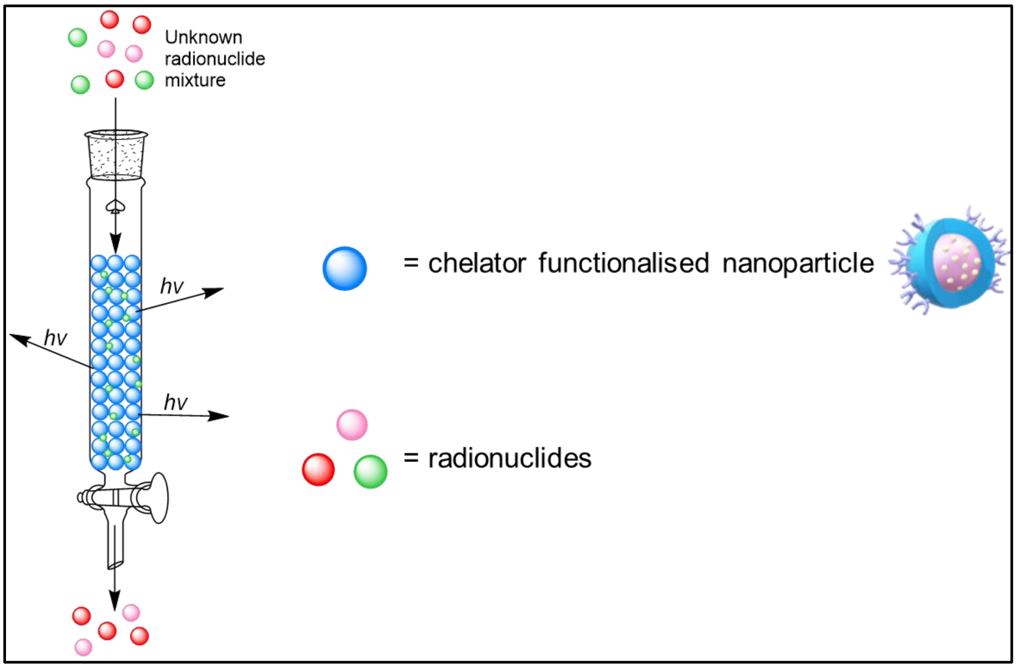

Figure 3.1 Schematic of element specific scintillant particles.

3.2 The Scintillation Proximity Assay

The Scintillation Proximity Assay (SPA) is a method employed frequently in biology for the analysis of radio-labelled substrates. There, scintillant nanoparticles are decorated with specific receptors on their surface, such as antibodies, for the radio-labelled substrate of choice and introduced within the aqueous medium.[1] When the particles are not present in the medium, the radio-labelled substrate releases a beta-particle which travels a certain distance in water before being absorbed, with no signal observed.[2] As shown in **Figure 3.2**, when the particles are introduced the radio-labelled substrate binds to the surface of the scintillant particle *via* the receptor ligands, and so when a beta particle is released it instead interacts directly with the bead, leading to emission of light.[2,3]

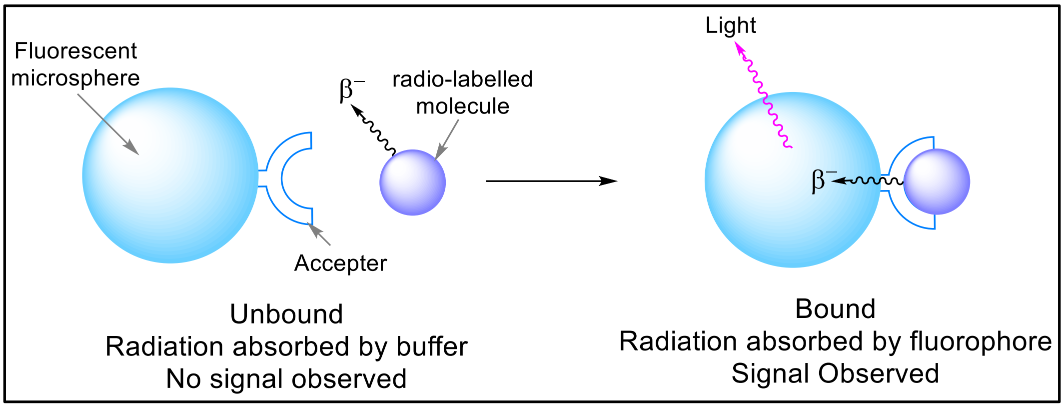

Figure 3.2 Schematic of the Scintillation Proximity Assay. Adaped from Bosworth *et al*[1].

This technique therefore relies upon there being little to no signal observed for unbound radionuclide, and thus is more suitable for radionuclides with smaller beta-path distances so that when unbound the beta-particle will be absorbed quickly by the buffer before it comes into contact with the particle. For this reason, most early literature surrounding the topic has been in the detection of ^{3}H and ^{125}I labelled biological targets, as discussed below. ^{125}I emits two Auger electrons with a path length of 1 μM and 17 μm respectively,[4] however although the latter is an order of magnitude higher than that of ^{3}H β-particles it is still within range to give a low background signal, and radiolabelling with ^{125}I is less complex and widely studied.[5] The gamma emission that also results from ^{125}I has a much higher path length of 15 cm,[1] and is far too energetic to be absorbed by the beads, therefore does not impinge upon the reading. ^{14}C, ^{35}S and ^{33}P have also been utilised,[5] however their longer path lengths (50, 65 and 125 μm respectively[4]) result in higher background signals, and are therefore not always ideal due to "non-proximity effects"[3] shown in **Figure 3.3**.

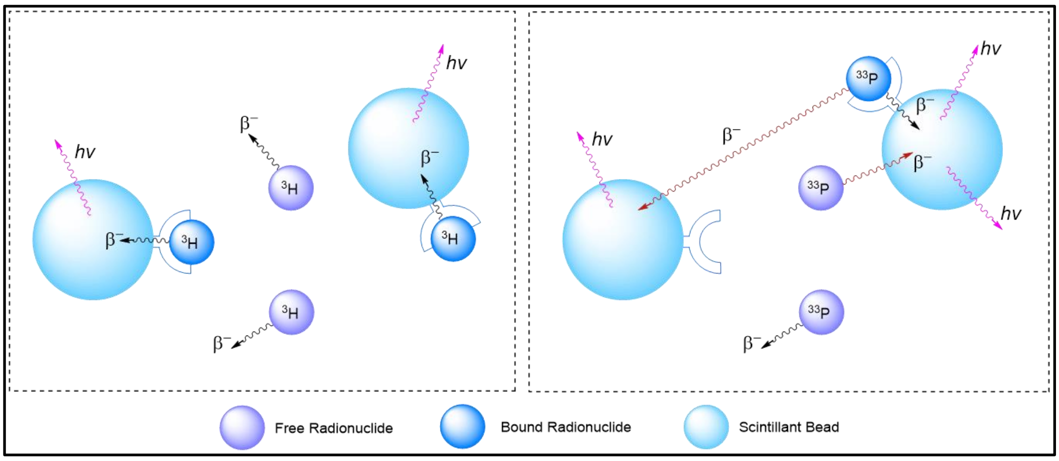

Figure 3.3 Schematic of non-proximity effect, using ^{3}H and ^{33}P radionuclides as an example. Adapted from X. Khawaja *et al*.[3]

3.2.1 Early Development

Before the use of SPA, ligand-binding assays and radioimmunoassays (RIA) relied upon time consuming physical separation of bound *vs* free ligand, and the hazards associated with handling both radioactive and biologically active samples were always present.[1] The use of liquid scintillation, as discussed in **Chapter 2,** also posed its own risks. There was also variability in results, due to the termination of the assay being either precipitation, filtration or centrifugation.[3] The use of beads not only reduced the amount of human manipulation required, but also paved the way for automation at a lower cost.

The first recorded use of a proximity assay was in 1970 by Hart and Greenwald,[6] however it was far from the SPA technology that is in use today. In their work, two beads were synthesised; a polystyrene bead labelled with ^{3}H and functionalised with an antigen, and the second a scintillant encapsulated polystyrene latex bead also with the antigen covalently attached. When dispersed in dilute solution, the beads were not close enough to yield successful transfer of beta-emission from the tritium-labelled bead to the scintillant bead. However, when the antibody was added, agglutination occurred leading to particles being in closer contact and therefore the beta-emission from ^{3}H in the first bead resulted in excitation of the scintillant in the second bead. Despite this success, it involved two types of beads as well as the antibody, and as the kinetics of ternary reactions are slow, incubation times were long.[3]

However in 1985, S. Udenfriend *et al*[5] reported the first SPA as is used today, following from the initial research by Hart and Greenwald[6], and utilising ^{125}I instead of ^{3}H. Instead of multiple beads, they functionalised a commercially available scintillant-encapsulated polystyrene bead with a suitable receptor (a range of antibody and antigens were used). These were introduced to the aqueous medium with a ^{125}I-labelled ligand (antibody or antigen), giving a scintillant signal when the ligand bound to the bead surface. By adding un-labelled ligand after the measurement was taken, the radio-labelled ligand was displaced and the scintillant signal reduced, allowing the IC_{50} to be calculated and giving the same values as traditional RIA methods. They also found that by adding glycerol, up to a volume of 12%, the particles were kept in suspension which in turn enhanced counting efficiency and no longer relied on shaking during incubation.

3.2.2 Commercial Beads

There are now a wide range of beads available for use in the scintillation proximity assay, including both organic and inorganic materials. Organic, or plastic, beads are made up of polyvinyl toluene (PVT) or polystyrene (PS), whereas inorganic beads are made of either yttrium silicate (YSi) or yttrium oxide (YO_x). For plastic beads, scintillation occurs *via* the incorporation of diphenyl anthracene (DPA) or europium for PVT and PS beads respectively. DPA emits between 400-450 nm, whereas europium emits between 550 to 700 nm. For the inorganic beads, europium is also within the YO_x lattices, however, for YSi, naturally occurring cerium ions within the lattice act as scintillators.[4] The fluorescence spectra of these are shown in **Figure 3.4**.

YSi are the more efficient of the beads, however they are also denser and so do not remain in solution which therefore makes them incompatible for automation.[3] Plastic beads, which will be the primary focus of the work herein, can remain dispersed in aqueous medium for a longer time period, despite their bigger size (5-8 μm *vs* average of 2.5μm).[4]

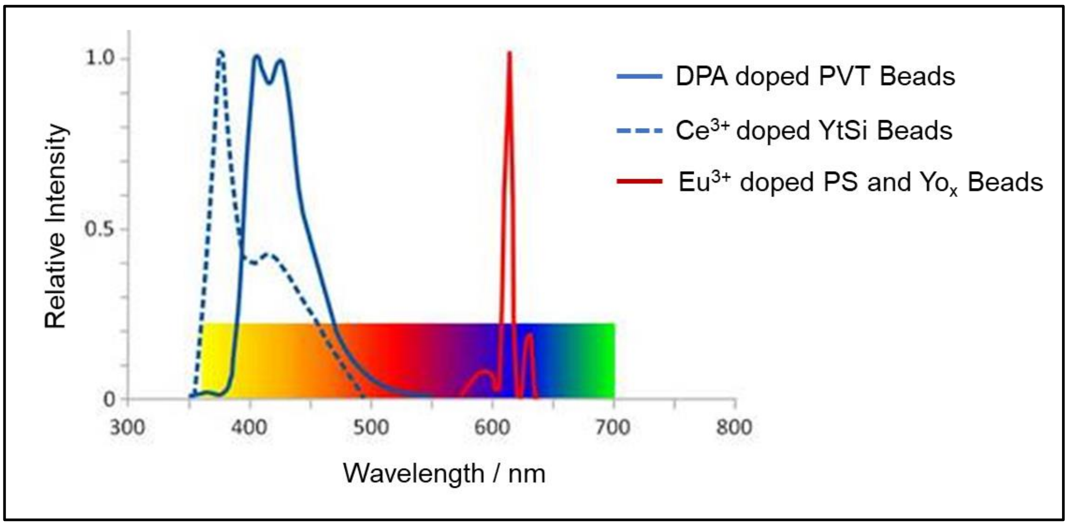

Figure 3.4 Luminescence spectra of the four commercially available scintillant beads, taken and modified from "SPA Bead Technology" by Perkin Elmer[4].

SPA is now widely used within the biological sector, with a range of commercially available beads pre-functionalised for particular assays, including those for antibodies, proteins, peptides and membranes, most of which are available as both YSi or PVT.[4] There are now also varied uses for this technology, including Flash Plates[7] and Immobilised Metal Affinity Chromatography (IMAC)[8].

Flash Plates are microwell plates that can be precoated with polystyrene impregnated with scintillant, and can be functionalised in much the same way as scintillant beads but also come unfunctionalized.[7] Flash Plates are therefore fully automated, as there is not the disadvantage of particle suspensions requiring agitation during the assay, and also have increased sensitivity and signal strength, despite a lower surface to volume ratio[3].

Immobilised Metal Affinity Chromatography is the process of separating various radio-labelled biomolecules according to their metal-binding affinity *via* the use of a matrix functionalised with various metals, such as Ni^{2+} and Co^{2+}, selective to the biomolecule of interest.[9] Once separated, this is traditionally followed by liquid scintillation *via* the use of LSC cocktails described in **Chapter 2**.

However, work by J. J. Liu *et al*,[8] showed that by impregnating the matrix with a scintillant as well as functionalising with a suitable metal, both selective isolation of assay mixtures and SPA scintillation output could be achieved in one-step. Using PVT beads functionalised with iminodiacetic acid, a range of hard Lewis metal ions were bound to the surface. These were then used to separate [^{3}H]-labelled inositol phosphates from inositol after a phosphoinositide hydrolysis, as inositol phosphates coordinated to the metal whereas inositol would not (**Figure 3.5**). This not only gave separation, but also yielded an assay output without need for a second step involving liquid scintillation medium.

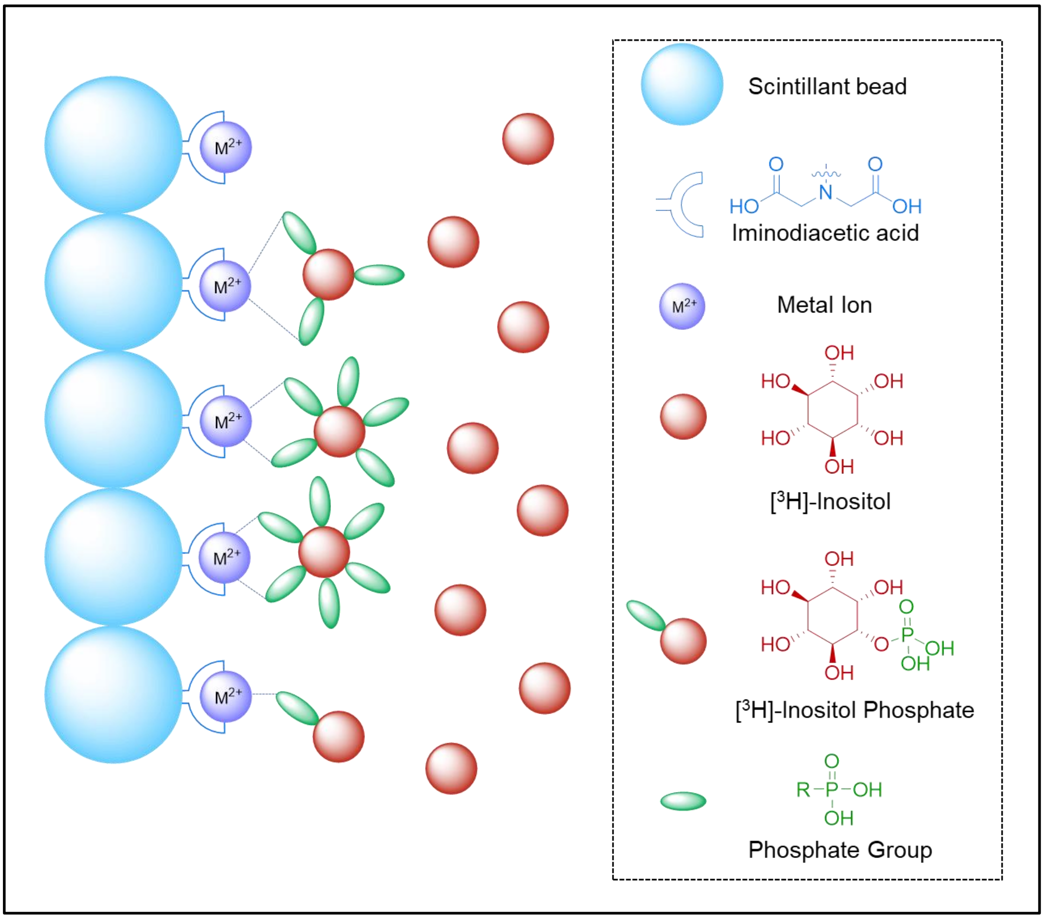

Figure 3.5 Schematic of Immobilised Metal Infinity Column, adapted from E. Sulkowski[10], using the immobilisation of [^{3}H]-Inositol Phosphate versus [^{3}H]-Inositol as an example.[8]

3.2.3 Applications

SPA has a variety of biological applications, replacing traditional low-throughput assays due to its ability to be automated and the reduction in preparation and workup steps.[1,2]

The most common use of SPA is in competitive binding assays, which can be used to calculate the binding affinities of a variety of inhibitors. S. Sun *et al*[11] developed a binding assay for Peroxisome Proliferator-activated Receptors (PPAR) which enabled binding affinities to be calculated for both tight and loose binding ligands.

This had previously not been possible in other SPA assays. PPAR's are involved in regulating the metabolism of lipids and glucose, and therefore are primary drug targets for a range of illnesses, including diabetes. The SPA beads chosen were YSi, and unlike other methods, relied on electrostatic interactions between the surface and PPAR *via* coating with positively charged polylysine. This both reduced the number of experimental steps (due to the particles not needing to be functionalised), and also reduced non-specific binding between ligands and uncoated particles. PPAR was added to the particle suspension at the same time as the radio-labelled ligands, and when the radio-labelled ligand bound to the ligand-binding domain of PPAR, a scintillation signal was observed (**Figure 3.6**). For binding affinity calculations, non-radiolabelled ligands were then added, and the drop in signal observed. By using the starting concentrations of both radio-labelled ligand and inhibitor (un-radiolabelled ligand), as well as the concentration of inhibitor when 50% of the radioligand is reduced, IC_{50}, calculations for both tightly bound and non-tightly bound ligands could be formed.

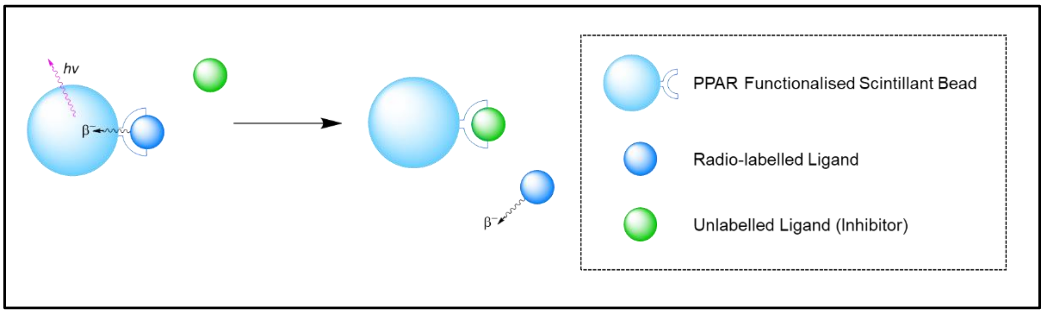

Figure 3.6 Schematic of the use of SPA beads in competitive binding assays, using work by S. Sun *et al*[11] as an example.

Another example where SPA technology has been used for high throughput drug screening is antibiotic screening. An example of this is the screening of coumarin and cyclothialidine based antibiotics for the inhibition of DNA GyraseB (GyrB)[12]. DNA gyrase, consisting of two GyrA units and two GyrB units, catalyses DNA negatively supercoiling *via* breaking and reforming a DNA strand, using ATP hydrolysis.[13] GyrB contains the domain responsible for the ATPase reaction,[14] and so inhibitors for this domain are greatly sought after. As SPA does not require multiple steps (including separation) and can be automated, an assay based on this greatly increases the number of possible antibacterials that can be screened. M. Gevi *et al*[12] used commercially available streptavidin coated SPA beads, which were introduced to both a 43 kDa fragment of GryB labelled with biotin, and ^3H labelled dihydronovobiocin. The biotin attached to the GryB subunit interacted strongly with streptavidin, and therefore bound the subunit onto the particle surface. [^{3}H]-dihydronovobiocin interacted with the ATPase domain, and due to its close proximity to the SPA bead led to a scintillation signal (**Figure 3.7**). Various non-radiolabelled inhibitors were then introduced to displace [^{3}H]-dihydronovobiocin, and as with previous work mentioned[11] the scintillation signal decreased as more un-labelled inhibitor bound to the ATPase domain.

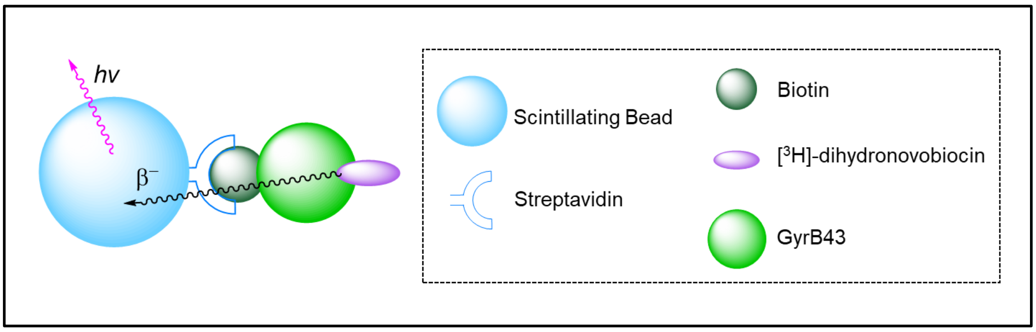

Figure 3.7 Schematic of the use of SPA beads in drug screening, adapted from M. Gevi *et al.*[12]

These results were then used to calculate the IC$_{50}$, taking into account both non-proximity effects and non-specific binding. The former was taken into account by running a parallel assay without the biotin-labelled GyrB subunit, so that any binding between [^{3}H]-dihydronovobiocin and the particle surface could be established, and the latter was resolved by also using a large excess of non-radiolabelled dihydronovobiocin.

Both examples previously mentioned rely upon the radio-labelled ligand binding to a domain on the surface of the particle, however a slightly different method exists for high throughput screening for inhibitors of enzyme reactions. R. Macarrón *et al*[15] developed an assay for the incorporation of radio-labelled amino acids into tRNA *via* the enzyme aminoacyl-tRNA synthetase (aaRS), and therefore an assay to test a range of inhibitors of the enzyme *via* a high throughput plate format (**Figure 3.8**). Unlike previous examples, it is the starting substrate and end-product that are radio-labelled, not the ligand that binds to a domain attached to the bead.

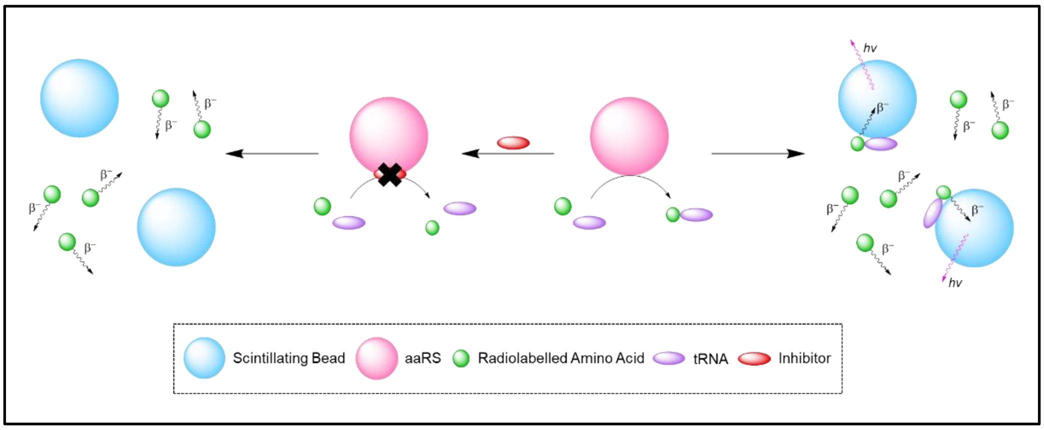

Figure 3.8 Schematic of SPA beads in enzyme inhibition assays. When aaRS is uninhibited, the reaction proceeds to form radiolabelled tRNA which can interact with the scintillant bead and lead to a signal. When inhibited, the reaction does not proceed and a signal is not observed. Example taken from the work of R. Macarrón *et al.*[15]

Under acidic conditions, YSi SPA beads were found to non-specifically associate with the radio-labelled tRNA aggregates, however not with the starting radio-labelled amino acids. Using this method, a signal was observed after formation of the tRNA aggregate using the radio-labelled amino acids, as the tRNA aggregate was then bound to the bead surface. This allowed the calculation of steady-state kinetic constants of the enzyme catalysed reaction, and inhibitor binding constants for a large range of known inhibitors for a range of different aaRS enzymes, as the inhibitors would stop the formation of the tRNA and therefore the signal would decrease.[15] All SPA assays were compared to standard assays, involving precipitation and filtration of assay products, and gave similar results.

To the best of the author’s knowledge, there are no known examples of the capture and scintillation-based analysis of radionuclide’s on the surface of particles for metal-ions commonly found in low-level radioactive waste, including but not limited to nickel, cobalt, and iron[16]. All known SPA-based assays are used within a biological setting with the capture of biological substrates.

3.3 Core-Shell Particles

3.3.1 Types of Particle

Core-Shell particles have increased in popularity in recent years, with over 1356 publications regarding the subject in 2019, compared to 53 in 2000[17]. This increase is due to many factors, including the rise of a variety of applications that can make use of their bespoke properties, in medicine, catalysis and electronics to name but a few[18]. Both the core and shell of the particle construct can be varied to yield different properties, which will be described below.

Much like there are a range of different nanoparticle shapes, there are also a range of possible core-shell structures, shown in **Figure 3.9**. These include spherical, which will be the focus of the following work, however it is also useful to examine other structures and their uses.

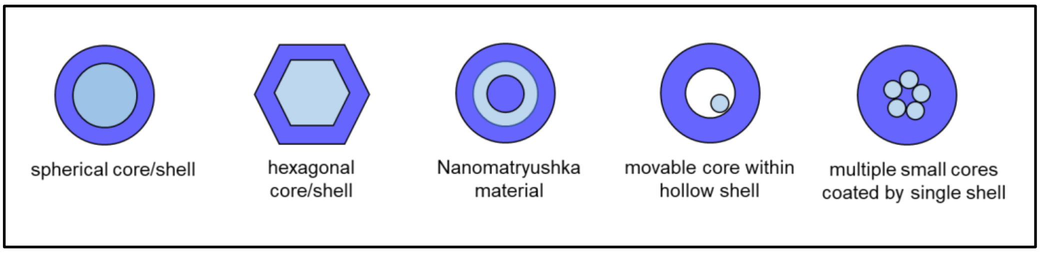

Figure 3.9 Different types of Core-Shell particles. Adapted from R. Chaudhuri *et al.*[18]

H. Chauhan *et al*[19] synthesised CdSe/CdS hexagonal particles *via* a hot injection method, forming a CdSe "seed" and then utilising oleylamine as a surfactant which successfully promoted grown of the shell in the x and y axis, but inhibited growth along the z-axis. Promoting growth in 2D is advantageous in photovoltaic devices as this leads to free movement of the charge carriers in the x-y plane, which is parallel to the semiconductor layer, but perpendicular movement is minimised. Extensive photophysical and photoelectronic analysis was carried out, showing that the CdSe/CdS particles could yield polarized emission and thus are interesting alternatives in photovoltaic materials.[19]

Another type of core-shell particle is the Nanomatryushka particle system, as shown in **Figure 3.9**. These particles are made of metallic cores, surrounded by a nanometre sized insulation layer (containing Raman active dyes), and then a metallic shell.[20–22] The presence of these dyes forms SERs (surface-enhanced

Raman scattering) hotspots, first observed in 1974[23], leading to strong Raman signals ideal for bioimaging applications.[22] In work by L. Lin *et al*[22], the first example of multiple layered Nanomatryushka particles were presented, with gold metallic core and layers, and different Raman active dyes in each insulation layer. L. Lin *et al*[22] found that the double shell (compared to single and triple) gave the best averaged SERs signal, with the dye in the outer-most insulation layer dominating the signal. Overall, these particles were found to possess high tunability, with the signal intensity being modified by the number of metallic and insulator layers, and the position of the signal modified by interchanging the Raman dyes in each layer.

Similar to spherical core-shell particles, constructs involving multiple cores within the same shell are also of interest, particularly those based upon iron oxide nanoparticles. An example of such work is demonstrated by C. Blanco-Andujar *et al*,[24] who used a microwave method to form multi-core iron oxide particles with a citric acid shell for possible use in hyperthermic treatment. By changing both the size and number of iron oxide particles in each shell, the magnetic properties could be tuned, with some performing better than commercial formulations.

One of the more interesting core-shell constructs is that of shells with moving cores, or “yolk/shell” structures. These are of great interest in catalysis, as the shells reduce aggregation that occurs in supported metal particles, and provide a homogenous environment which leads to a higher catalytic activity compared to that of bulk catalysts due to an increased interaction between the substrate and catalyst[25]. There are multiple ways of forming these particles, including removal of a “middle” layer to yield the core and shell[26], however work by J. Lee *et al*[27] used etching techniques to form yolk/shell particles of Au/SiO_2. By first forming gold nanoparticles and coating in silica, KCN could be used to selectively etch the gold core leading to complete control of the “yolk” size (**Figure 3.10**).

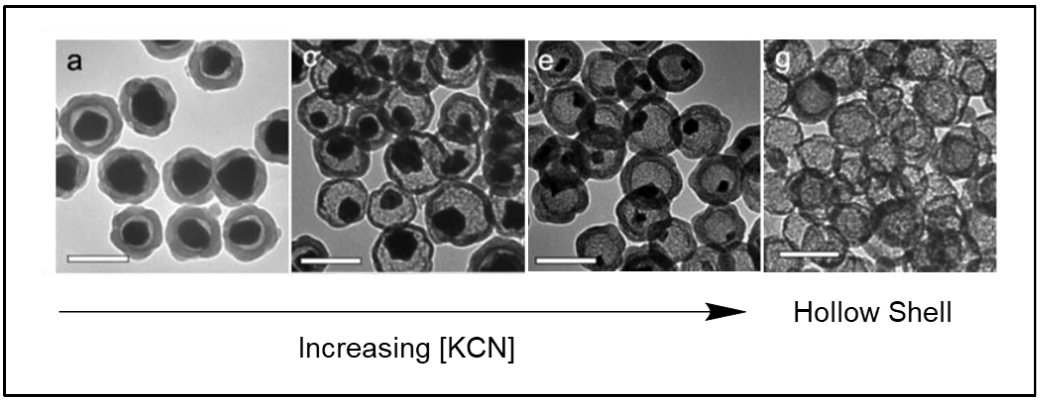

Figure 3.10 Au/SiO_2 yolk/shell particles, with the Au “yolk” decreasing in size as the etching agent, [KCN], increases. Taken from J. Lee *et al.*[27]

Not only are there a variety of particle shapes, but the core-shell composition can have a variety of combinations, dependent on their use. These can be broken down into 4 main groups; Inorganic/Inorganic, Inorganic/Organic, Organic/Inorganic and Organic/Organic.[18]

Inorganic/Inorganic particles have a variety of uses, particularly in photovoltaics[28], catalysis[29] and bioimaging[30]. Although the main constituents can be metal or metal oxides, one of the most common shells for its enhanced biocompatibility and pore structures is silica[31,32]. The use of silica has many advantages, including increasing the dispersibility of particle suspensions and increasing the stability due to silica’s chemical inertness[33]. Not only have metals such as gold[34] and silver[28] been coated in a silica shell, but also oxides such as Fe_3O_4. Silica coating of iron oxides has become a popular area of research, with multiple reviews covering the topic[35,36] due to their use in biological applications, in particular MRI imaging agents[37] and drug delivery systems.[38] Silica coating iron oxides has many advantages, including reducing aggregation and increasing biocompatibility.[36,39,40]

Inorganic/Organic particles contain a metallic compound as the core, and frequently a polymer-based molecule as the shell. This increases the stability of the core due to its protection by the polymer shell and also increases the biocompatibility *via* the use of polymers such as Dextran[41] or Starch[42]. Much like with silica coated inorganic particles, Fe_3O_4 can be coated with polymers, increasing their biocompatibility and stability and allowing their use in imaging and drug delivery applications.[36]

Organic/Organic particles are those containing two separate polymer systems of different properties, with uses in bio-applications[43,44], coatings[45], catalysis[46,47] and sensing[48]. The advantages of having two different polymers is that the physical properties can be combined, for example mixing hydrophobic and hydrophilic polymers together, with the latter being able to be easily functionalised (for example *via* hydroxyl groups), and the former being more rigid.[49]

Despite the breadth of literature surrounding the previous examples, the following sections and the work presented herein is of the use of polymer cores coated with a silica shell, *i.e*. Organic/Inorganic.

3.3.2 Polymer Core, Silica Shell Particles

Polymer core, silica shell particles combine the flexibility and low density of polymers with the rigidity and thermal stability of silica.[50] As well as this, silica shells allow further functionalisation of the surface *via* known and well established methodology, whereas polymers alone require specific monomers and the chemistry, particularly post-modification, is less straight forward.[51]

The vast majority of literature concerning these constructs, with a selection discussed in the following section, is in fact using polymers as the template with the final step being the removal of the core *via* calcination, yielding hollow silica particles. There are also examples that utilise both the core and shell for these applications, and also as hosts for assays. Both of these concepts will be discussed below, as all show varied methods for the synthesis of the core-shell structure.

3.3.2.1 Synthesis

In one of the first examples of polystyrene core, silica shell particles, F. Caruso *et al*[52] focused on the use of layer-by-layer (LbL) self-assembly to form silica coated polystyrene (**Figure 3.11**). The polymer core was pre-coated with a 3-layer film in a polyelectrolyte solution to yield a positive surface charge on the core surface, which interacted electrostatically with the silica shell. Layers of SiO_2 and poly(diallyldimethylammonium) chloride (PDADMAC) were sequentially added, alternating the surface charge from negative to positive and thus allowing further layers to be added. By layering with PDADMAC, hollow layers could then be formed following calcination or introduction of organic solvent, as shown in further work by F. Caruso *et al*[53], for use in a variety of applications including “capsule agents” for medicinal uses.

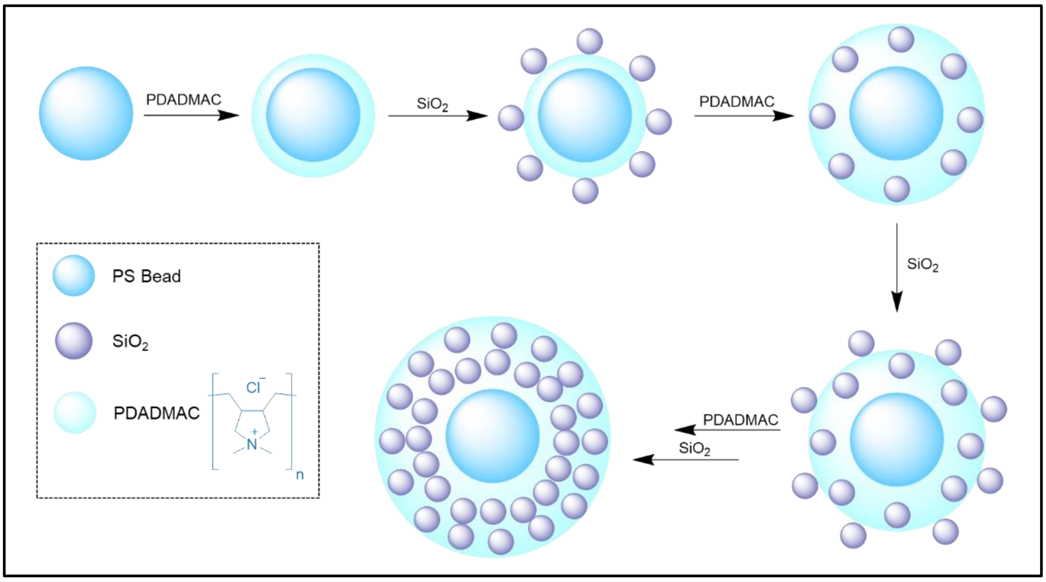

Figure 3.11 Schematic of LbL assembly using PDADMAC and SiO_2 beads, adapted from F. Caruso *et al.*[52]

Dependent on polymer synthesis, the resulting core can have either a positive, negative or neutral net surface charge, however if negative or neutral a pre-coating step is required for silica coating. Despite the thickness control that comes from LbL coating, it suffers from multiple steps, including this step. Work by C. Graf *et al*[54] removed this step, by forming polystyrene beads using polyvinylpyrrolidone (PVP) as both a stabilizer and coating in one step. PVP increased the stability of the polystyrene beads by decreasing agglomeration, and could interact favourably with the silica hydroxyl groups, increasing silica formation on the surface. J. Hong *et al*[55] also used PVP to stabilise the organic core and increase silica loading, however their work also included the use of electrolytes (NaCl) to increase the size of the polymer core by promoting aggregation, forming larger particles. The advantage of the use of PVP is shown in **Figure 3.12**, where silica particles form a homogeneous coating on PVP-stabilised polymers (**a**), compared to when no stabiliser is present (**b**). When poly(acrylic acid) (PAA) was used instead of PVP, the interaction between silica and the surface was weaker (as PAA is acidic) and therefore coating was less homogenous with free silica particles observed (**c**).

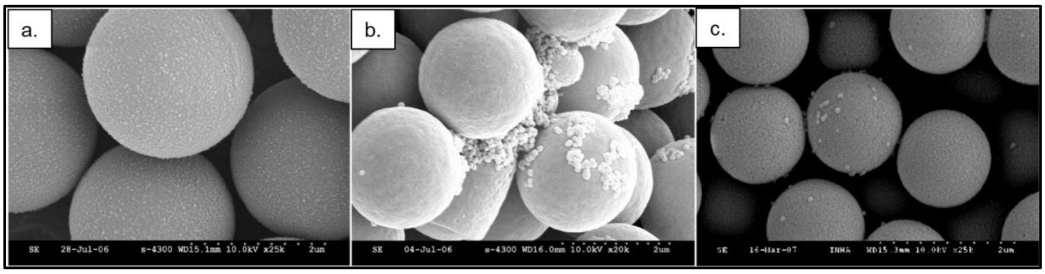

Figure 3.12 SEM images of core-shell particles with a) PVP as stabiliser, b) no stabiliser, c) PAA as stabiliser. Taken from J. Hong *et al.*[55]

M. Chen *et al*[56] used a similar method, however instead of using PVP, they instead used 2-(methacryloyl)ethyltrimethylammonium chloride (MTC) as a cationic auxiliary monomer to form methyl methacrylate (MMA) polymer beads, leading to the core-shell structure forming in one step. By imparting a positive charge on the surface of the beads, without the need for stabilizers, pre-formed silica particles could be added at the same time as bead formation and interact electrostatically with the cationic surface monomer, stabilising the polymer core.

Despite work by J. Hong *et al*[55] showing that PAA was a less successful stabilizer for the enhancement of silica shell growth, Z. Qian *et al*[57] showed that it could yield well covered polymer beads, with the concentration of PAA inversely proportional to the diameter of the silica particles that result on the surface. After formation of the core-shell particles, they were deposited on a glass substrate, and then further modified with dodecyltrichlorosilane to form a superhydrophobic layer (**Figure 3.13a**), being one of the few examples of coatings that do not first remove the polymer core.

The use of both hollow and polymer-core silica shell particles as both superhydrophobic and superhydrophillic surfaces originates from the roughness of the surface structure. Silica particles formed from the sol-gel Stöber synthesis first form small "seed" particles after polymerisation of TEOS, that are then attracted to the polymer core, where they grow in size and new particles form side-by-side.[58] This forms so-called "raspberry-like" particles with rough surfaces and high surface area. By careful design of the surface functionalisation, this can lead to superhydrophobic materials with a similar water contact angle to natural self-cleaning coatings such as the lotus leaf (>150°C, **Figure 3.13a**), and superhydrophilic materials with a water-contact angle of 0°, making them ideal antifogging agents[59] (**Figure 3.13b**).

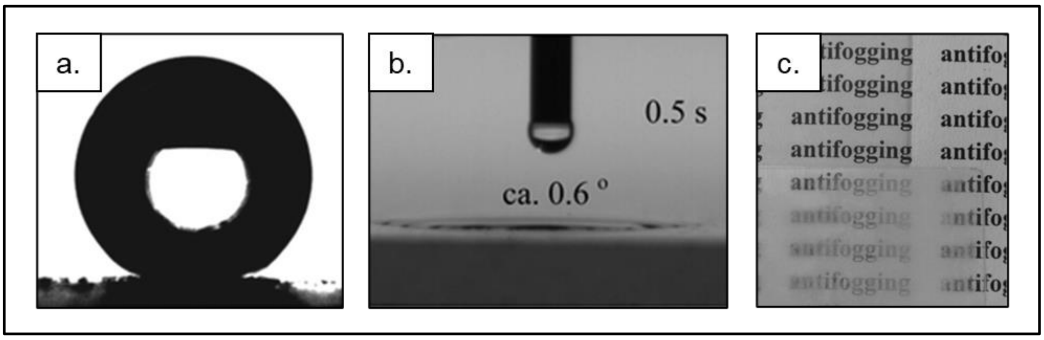

Figure 3.13 Water droplet on a) superhydrophobic and b) superhydrophilic coating; c) demonstration of anti-fogging properties of core-shell particles (top plate) *vs* glass substrate (bottom plate). Taken from Z. Qian *et al*[57] (a) and X. Du *et al*[60] (b and c).

X. Lui *et al*[61] utilised LbL assembly to form core-shell particles, which were then calcined to yield superhydrophilic hollow spheres with antifogging properties. Unlike work by F. Caruso *et al*[52], X. Lui used PVP to stabilise the polystyrene beads and form a net-negatively charged surface, using potassium persulfate as an initiator[61]. A three-component electrolyte layer, much like work by F. Caruso, was used before the introduction of silica nanoparticles, and the process repeated to yield two layers of silica particles. These beads were then deposited on a substrate and calcined to yield hollow silica spheres without polyelectrolytes or core, with SEM showing that those with two layers of silica tended to remain intact *vs* those with a single layer.

A rather novel method for the formation of core-shell particles with a reportedly improved silica coating to PVP stabilised particles is that reported by X. Du *et al*[60]. In their work, the polystyrene particles were formed using PVP as a stabiliser, however they were then treated with oxygen plasma, yielding hydroxy groups on the surface due to interactions between the surface atoms and active oxygen species (**Figure 3.14**). This then increased the silica surface coating by providing numerous sites on the polymer core in which the silica monomers could hydrogen bond. After core-shell formation, these were deposited *via* LbL assembly onto a glass substrate coated with polyelectrolyte, and calcined to remove both polymer and polyelectrolytes and yielding superhydrophilic hollow spheres.

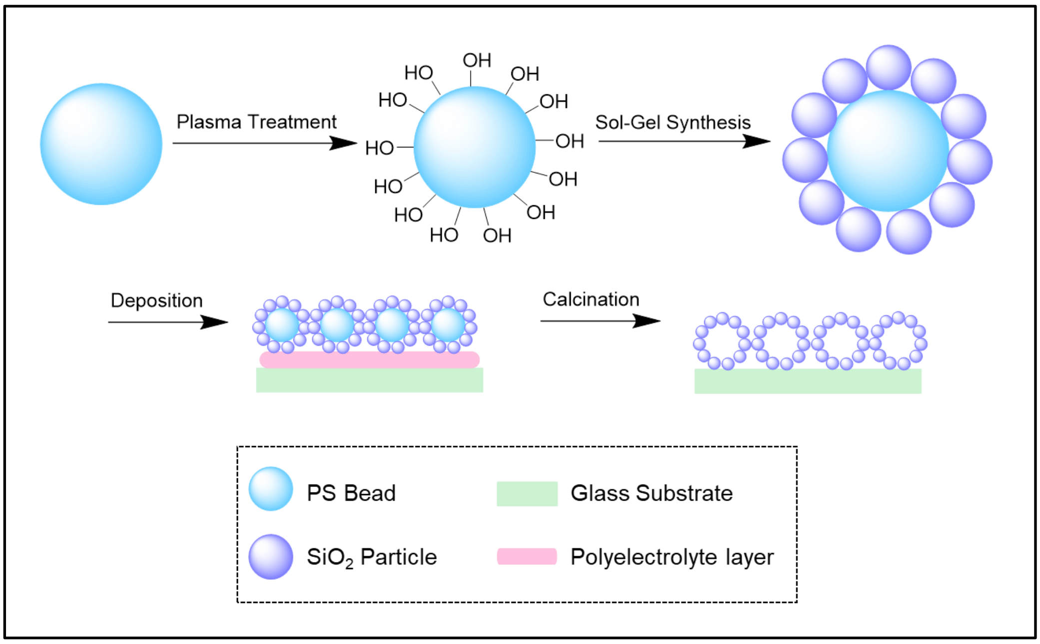

Figure 3.14 Schematic of formation of core-shell films *via* plasma treatment. Adapted from X. Du *et al.*[60]

Another interesting method for the formation of core-shell particles comes from the use of droplet formation in a microfluidic system. In this system (**Figure 3.15**), D. Kim *et al*[58] used 1,10-decanediol dimethacrylate (DDMA) as the polymer core, polymerised with 3-(trimethyoxysilyl) propyl methacrylate (TPM) to form silanol groups on the surface, and thus removing the need to add stabilizers or a pre-coating step before silica addition. As shown in **Figure 3.15**, both monomers and Darocur 1173 (photo-initiator) were introduced to a PVA solution, creating a shear force leading to formation of the droplets. Once droplets were formed, photopolymerisation of the droplets took place *via* UV irradiation, followed by hydrolysis to form hydroxyl groups at the particle surface before introduction of TEOS for silica particle formation at the surface. Although more complex in that it relies upon a novel apparatus, this synthesis removed the need for multiple steps, and components could easily be modified to change core size and shell thickness to form highly monodisperse particles.

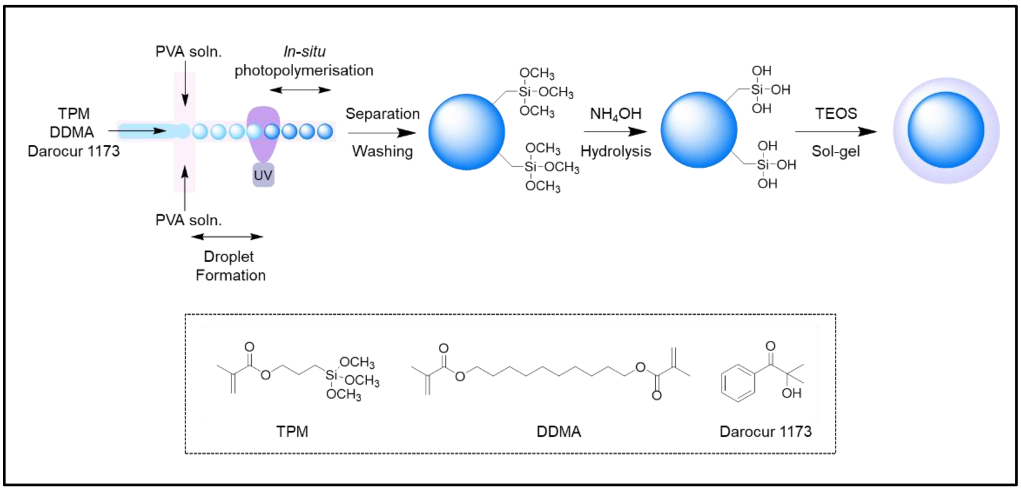

Figure 3.15 Schematic of synthesis of core-shell particles *via* a microfluidic system. Adapted from D. Kim *et al.*[58]

Despite the differences in polymer bead and shell synthesis in the previous examples, the formation of silica particles has followed the same sol-gel approach first used by Stöber in 1968[62]. Here, monodisperse silica particles were formed from a range of tetraalkyl silicates *via* ammonia catalysed hydrolysis (**Figure 3.16**). Since then, it has been cited over 10,000 times,[63] and is the standard protocol for the synthesis of silica particles due to the simplicity of the one-pot reaction, without the need for toxic solvents or surfactants, and the uniform sizes of the resultant particles.[64] However, over this time various modifications to the synthesis have been found to yield a range of particle sizes.[64]

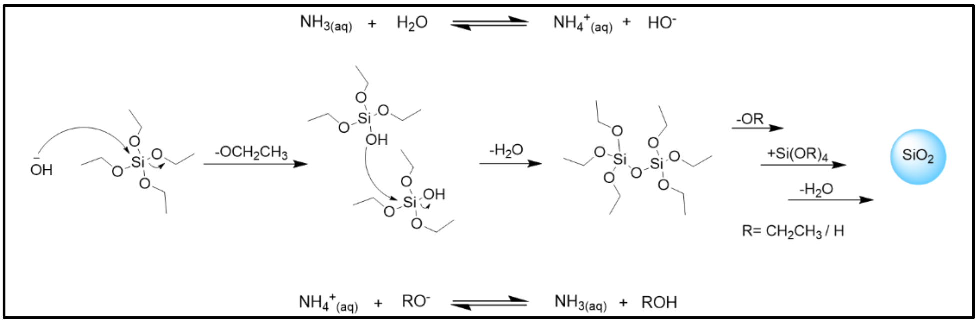

Figure 3.16 Stöber synthesis reaction scheme, adapted from P. Ghimire *et al.*[65]

The same can be shown in shell synthesis, with the concentration of TEOS controlling shell thickness due to its influence on hydrolysis and growth on the polymer surface.[31] Work by F. Dong *et al*[66] also showed that increasing TEOS concentration led to larger particles on the surface, forming “flower-like” particles instead of “raspberry-like”. (**Figure 3.17**). This is further confirmed by X. Du *et al*[60], who found increase in TEOS concentration led to larger SiO_2 particles on the surface, with a larger overall coverage on the polystyrene particles. X. Zhou *et al*[50] also found that increasing the concentration of ammonia catalyst led to more silica particles on the polymer surface, with an increase in the silica particle diameter. However, there were also more unbound silica particles, as the nucleation rate is faster with increase in ammonia concentration as well as TEOS.[65,67,68]

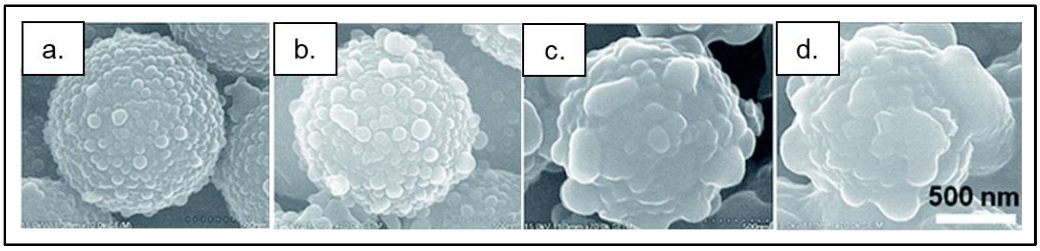

Figure 3.17 SEM images showing progression from “raspberry” to “flower”-like particles with increased TEOS concentration. Taken from F. Dong *et al.*[66]

3.3.2.2 Further Applications

As discussed in **Section 3.3.2.1**, polymer/silica core/shell particles are effective in both hydrophilic and hydrophobic coatings due to the raspberry-like structure of the silica shell and the ability to be further functionalised or calcined, however there are a range of other uses.

Suspension Array Technologies (SATs) are cytometric assays used for a variety of biological substrates.[69] Traditionally, a range of differently functionalised polymer or silica particles doped with different fluorophores are used to coordinate to analytes of interest.[70] These then flow through a channel after coordination of the analyte of interest, where the fluorophore within the bead is excited, causing emission of light. The particles are then separated based on the fluorescence signal obtained, which also causes separation of the analytes. A simplified example is shown in **Figure 3.18**, with only two types of functionalised particle. Although both sets of particles can be prepared in bulk[70] and both have their distinctive advantages, combining both polymer and silica removes many of the disadvatantages[51]. For example, incorporation of fluorophores into polymer beads is straightforward, unlike in silica particles where silyl-derivatives would need to be synthesised. Also, whereas there are a range of functionalisation protocols for silica particles, surface functionalisation of polymer beads is more complex, with it normally being dependent on the starting monomer.[51]

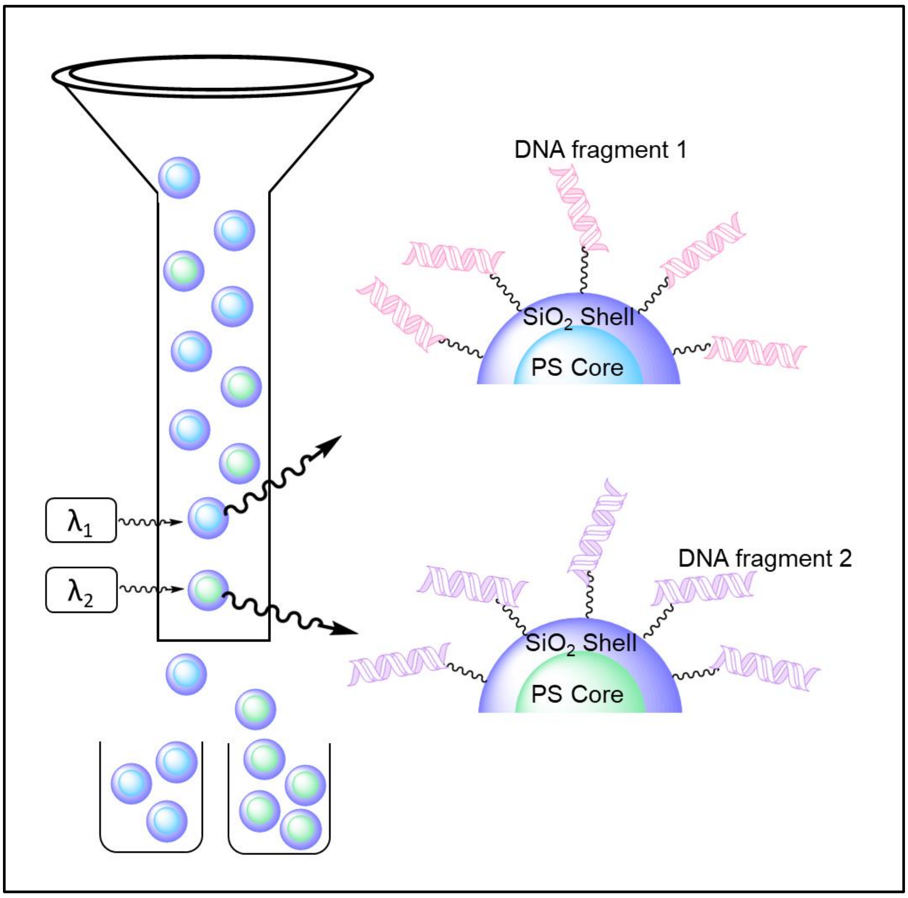

Figure 3.18 Schematic of core-shell particles in Suspension Array Technology assays. Two sets of particles with different fluorophore dopants and functionalised surfaces are separated based on their resultant fluorescence signal, allowing the separation of the two types of DNA fragments bound to the surface. Adapted from D. Sarma *et al.*[51]

Therefore, by combining both of these into a core-shell structure, D. Sarma *et al*[51] formed beads that were easily surface functionalised, with a range of possible fluorophores available for impregnation of the core (**Figure 3.18**). As in previous methods described, polystyrene beads were formed with PVP as a stabiliser, however the molecular weight of the polymer was varied, finding that with smaller molecular weights the silica coating was smoother. This led to a smaller surface area, however gave the highest sensitivity in measurements compared to raspberry-like coatings (which exhibited larger steric hindrance).

Although highlighting previously that one of the main properties of core-shell thin films were that of their superhydrophobic/hydrophilic properties, there are also other properties that the core-shell structure imparts. X. Zhou *et al*[50] synthesised poly(styrene-*co*-butyl acrylate) beads functionalised with poly-acrylic acid, which were then coated with silica *via in-situ* formation of silica beads from TEOS in a sol-gel process. These beads were then used to form films, and tested for a range of different properties. Studies showed that an increased silica content led to an increase in both the thermal stability and the fire-retardancy. Uncoated polymer particles would become molten in the presence of extreme heat, which could spread the fire, however by fully coating the particles with silica, this is prevented.. It was found that these constructs prevented any molten material from spreading, with only the silica shell remaining after the fire was consumed, and thus have potential use in fire-retardant materials. The tensile strength of the material also increased with increase in silica content, as did the rigidity. Those with a high silica content also demonstrated a lower water absorption (10% *vs* 50% for uncoated polymer particles),[50] which is beneficial for uses in electrical insulation, and also in reducing degradation.[58]

One of the most interesting applications for polymer/silica core/shell constructs, and the basis of the work described herein, is that of their use as scintillant particles as discussed in **Section 3.2.3**. C. Janczak *et al*[71] formulated scintillant doped polymer/silica core/shell particles (nanoSCINT) without the need for pre-coating, stabilizers or covalent attachment *via* the polymerisation of polystyrene with 2,2'-Azobis(2-methylpropionamidine) Dihydrochloride (AIBA) as initiator. AIBA, unlike other initiators such as 2,2′-Azobis(2-methylpropionitrile) (AIBN), gives the resultant polystyrene beads a net positive surface charge,[72] and so negative silica particles and oligomers are electrostatically attracted to the surface. As discussed in **Section 3.2**, polystyrene acts as the solvent traditionally used in LSC, and *via* swelling and deswelling of the polymer core (initiated by the presence of organic solvents) both a primary and secondary scintillant could be doped into the core. The silica shell, being hydrophilic, allows the particles to be easily dispersed in aqueous media. They found that the beads synthesised were effective across a range of pH values, with the scintillation response in the presence of [^{3}H] not changing between pH 3-9.5. As well as this, the scintillation response was a linear increase with both an increase in [^{3}H] (**Figure 3.19a**) and an increase in particle concentration. Although the scintillation response was less than LSC, it was still sensitive enough to quantify nCi to mCi amounts of [^{3}H], with far less fluorophore than the LSC equivalent. The scintillation response for ^{33}P and ^{35}S were also linear, as shown in **Figure 3.19b**, with the scintillation response higher for ^{33}P *vs* both ^{35}S and ^{3}H.

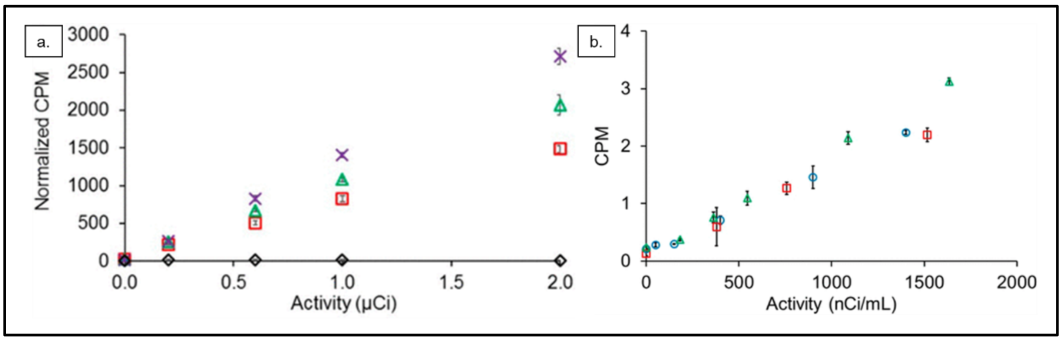

Figure 3.19 Scintillation response of a) nanoSCINT (square) scintillant polystyrene cores (cross), water (diamonds) and recovered nanoSCINT from previous exposure (triangles) with increasing ^{3}H activity and b) nanoSCINT with increasing activity of ^{3}H (circles), ^{35}S (squares) and ^{33}P (triangles). Taken from C. Janczak *et al.*[71]

By utilising this method, core-shell particles can be formed with a range of possible fluorophores suitable for scintillation encapsulated within. The silica shell provides both stability, and a surface that can be easily functionalised to provide specific analysis in an aqueous environment.

3.4 Results and Discussion

3.4.1 Synthesis and Characterisation of Nanoparticles

3.4.1.1 Synthesis

As discussed in **Section 3.3.1**, there are numerous methods for the synthesis of core-shell particles, however multiple parameters need to be considered for the formation of particles suitable for scintillation. Firstly, the core should ideally be able to act as the solvent in classical cocktails, and therefore polystyrene was the ideal choice due to its aromaticity and likeness to toluene. Secondly, the incorporation of the fluorophore cannot be “spontaneous” unlike traditional silica based particles (*i.e*. entrapment of dopants as the particles are being made), and lastly the shell must be able to protect the core from leaching of fluorophore, therefore providing consistent scintillation results as well as structural integrity and the ability to further functionalise to introduce selectivity. Therefore, a polystyrene-silica core-shell system was chosen, with synthesis of particles and encapsulation of fluorophore achieved *via* a method developed by C. Janczak *et al*[71], of which results were discussed in **Section 3.3.2.2**.

Un-doped polystyrene beads were formed first *via* the polymerisation of styrene, initiated by AIBA in water and stirred for 5 hours at 70°C. Excess styrene was then removed *in vacuo* to yield an aqueous stock solution of particles. Oxazoles **1-13** were then added in a 1:9 solvent mixture of isopropanol (iPrOH) and $CHCl_3$ respectively, leading to swelling of the beads and incorporation of the fluorophore within the bead matrix (**Figure 3.20**). Unlike the original method,[71] which called for initial sonication followed by stirring for at least one hour, higher loading was observed when the reaction was stirred for 3.5 hours, with sonication occurring every hour. After this time, the particles were de-swelled *via* removal of the organic solvent *in vacuo*, thus trapping the fluorophore within the bead.

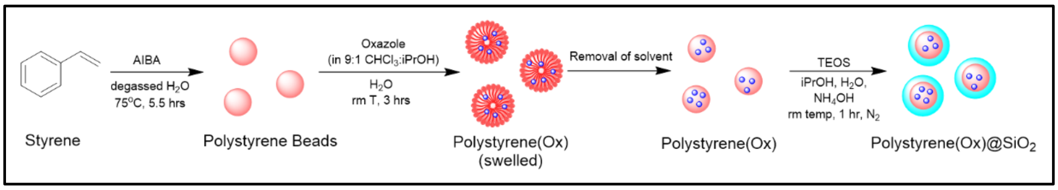

Figure 3.20 Particle synthesis reaction scheme.

Silica coating was achieved *via* a Stöber approach using ammonia as a catalyst to initiate the polymerisation of TEOS in the presence of water, with isopropanol used as solvent.[71] The polystyrene beads were dispersed in isopropanol, water and ammonia with vigorous stirring, before addition of TEOS. After one hour of stirring at room temperature, the beads were then collected *via* centrifugation, and washed repeatedly with water and ethanol to remove unreacted TEOS and leached fluorophore, before being dried in a desiccator overnight.

3.4.1.2 Particle Morphology

Both polystyrene beads before oxazole doping and core-shell particles (**PS(Ox)@SiO$_2$** where Ox = **1-7**) were analysed *via* SEM, STEM and EDX to confirm morphology.

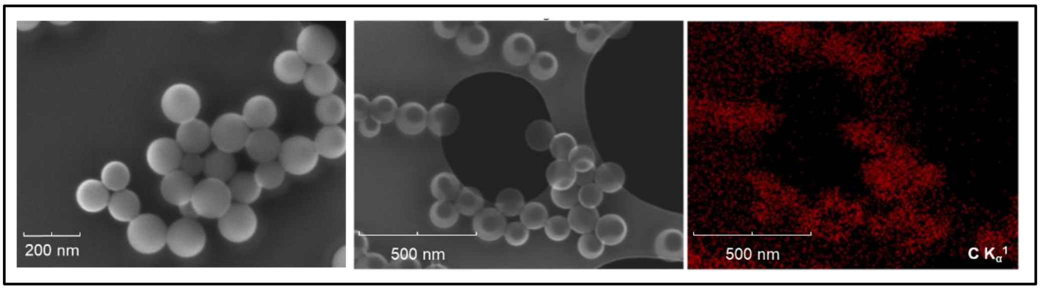

Figure 3.21 SEM (left, middle) and EDX (right) images of polystyrene beads before oxazole doping.

SEM images confirmed that the polystyrene beads were monodisperse, with EDX data confirming their carbon composition (**Figure 3.21**). Once encapsulated, SEM images showed that the silica shell of **PS(Ox)@SiO$_2$** was amorphous, appearing to be an aggregation of small silica particles on the surface of the polystyrene core as opposed to a smooth shell (**Figure 3.22** ***left***). Despite this, there appeared to be almost complete coverage of polymer beads with the silica shell, keeping structural integrity despite multiple washes *via* both sonication and centrifuge.

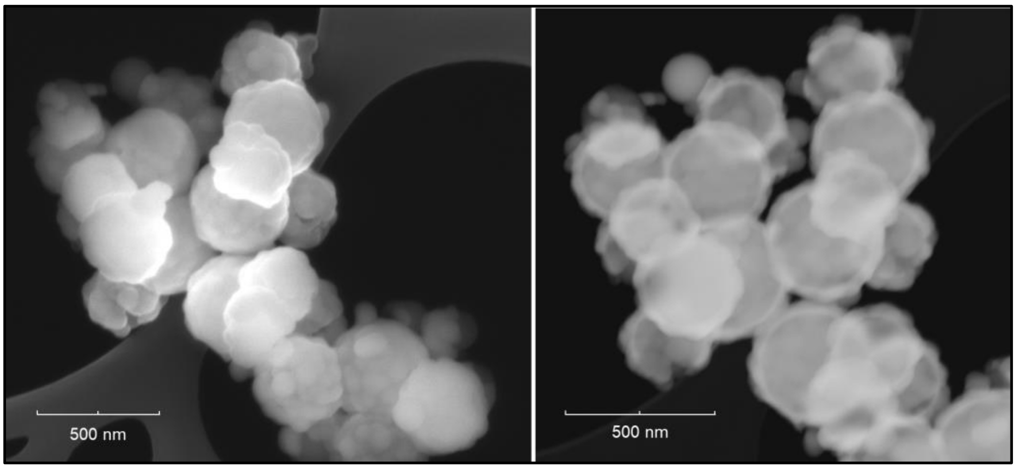

Figure 3.22 SEM (*left*) and STEM (*right*) image of **PS(Ox)@SiO₂** showing both the mottled silica surface and the core-shell structure.

STEM images were obtained for all **PS(Ox)@SiO₂,** showing the contrast of the dense silica shell compared to the polystyrene core and hence successful coating of the polymer beads (**Figure 3.22 *right***). As shown in **Figure 3.23**, EDX further confirmed the core-shell structure, with K_α emission observed for silicon and oxygen, particularly on the peripheral of the particles, and for carbon in the core of the constructs.

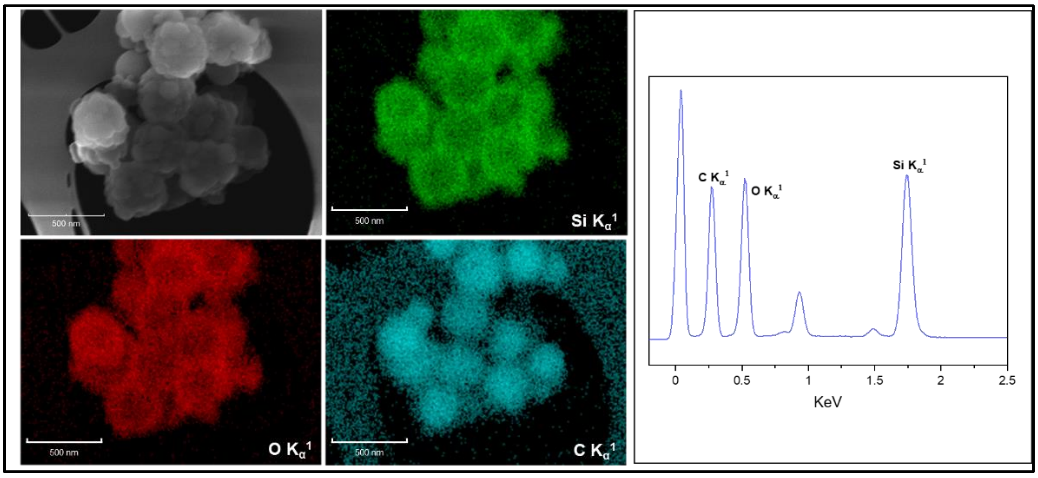

Figure 3.23 EDX images (*left*) and spectra (*right*) of **PS(Ox)@SiO₂**, showing both the polymer core and silica shell made of carbon and silica and oxygen respectively.

Size analysis using SEM images for polystyrene beads and STEM images for all **PS(Ox)@SiO₂** samples were obtained (**Table 3.1**), showing an average shell thickness and core diameter of 45 nm and 276 nm respectively for **PS(Ox)@SiO₂.** However, polystyrene beads before oxazole doping showed a much smaller diameter, with a lower standard deviation and hence a more monodisperse sample. This is expected to be due to incomplete de-swelling in the polymer core after doping leading to a slightly larger range of sizes, and a larger diameter on average. C. Janczak *et al*[71] measured the particle sizes after doping but before silica coating, and found on average the particle diameter to be 190 +/- 3 nm, which further confirms that it is the doping of fluorophore, and not conditions of the silica coating step, that causes the increase in particle size.

Table 3.1 Calculated diameter of polystyrene beads and core and shell thickness of **PS(Ox)@SiO$_2$;** particle sizes were calculated using ImageJ software.

	Min / nm	**Max / nm**	**Mean / nm**	**SD / nm**
Polystyrene Bead	106 ± 3	145 ± 3	127 ± 3	13
PS(Ox)@SiO$_2$ Core	200 ± 8	550 ± 8	276 ± 8	66
PS(Ox)@SiO$_2$ Shell	20 ± 1	75 ± 1	45 ± 1	10

The shell thickness is slightly larger than that published by Janczak *et al*,[71] who observe a shell thickness of 30 nm (with a range between 25 and 35 nm) however the core size (270 nm) is consistent. Although the same method was used, the difference in shell size is most probably due to the sensitivity of silica particle formation to subtle changes in reaction conditions,[68] as discussed in **Section 3.3.2.1**.

For encapsulation of disubstituted oxazoles **8-13**, the mean particle size and standard deviation were increased, the latter of which was due to a large variation of particle sizes between different samples. Although **PS(Ox)@SiO$_2$** where Ox = **5** were a lot higher than other samples, the remaining primary oxazoles all shared similar size ranges. However, for disubstituted oxazoles the particle size ranges were too varied to give a total range (as in **Table 3.1**) and instead have been tabulated per sample (**Table 3.2**).

Table 3.2 Calculated diameter of polystyrene core of **PS(Ox)@ SiO_2**; particle sizes were calculated using ImageJ software.

	Min / nm	Max / nm	Mean / nm	SD / nm
PS(8)@SiO_2	143 ± 29	1537 ± 29	431 ± 29	280
PS(9)@SiO_2	209 ± 33	1142 ± 33	353 ± 33	173
PS(10)@SiO_2	115 ± 15	273 ± 15	201 ± 15	42
PS(11)@SiO_2	157 ± 10	446 ± 10	238 ± 10	64
PS(12)@SiO_2	282 ± 16	408 ± 16	338 ± 16	45
PS(13)@SiO_2	177 ± 14	316 ± 14	259 ± 14	45

For **PS(Ox)@SiO_2** where Ox= **8** and **9**, the standard deviation was a lot larger than for **10-13**, with particles ranging from 143 nm to over 1 µm and standard deviations of 280 and 173 nm, in comparison to a standard deviation of less than 70 nm for **10-13**. **Figure 3.24** shows the difference in size variation between **PS(8)@SiO_2** and **PS(13)@SiO_2**, with the former having a much larger distribution of particles. Larger particles are more beneficial for the scintillation proximity assay, as discussed in **Section 3.2**, however the reasoning for this greater variation of size is hard to determine. Results in **Chapter 6** showed even larger particle sizes, with an increased size distribution, indicating that the dopant species encapsulated has an effect on the de-swelling of the particle pores, perhaps interacting with the polystyrene environment and leading to incomplete de-swelling, leading to larger particle cores.. The fact that the encapsulation of more conjugated oxazoles **8-13** leads to a larger average core size than when the more simple oxazoles **1-7** are encapsulated, suggests that it could be an electronic interaction, for example π-stacking, between the highly aromatic oxazole and the polystyrene within the core.

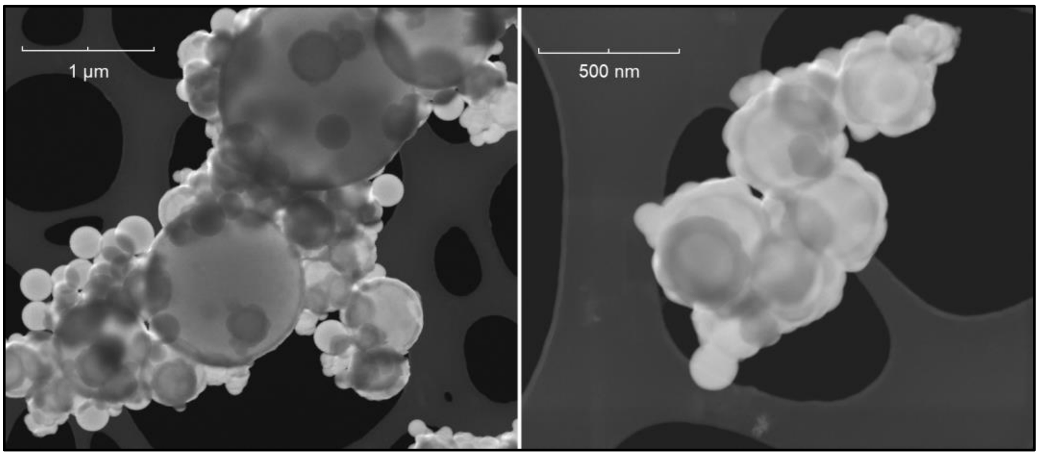

Figure 3.24 STEM images of **PS(Ox)@SiO$_2$** where Ox = **8** (*left*) and **13** (*right*), showing the broad range of particle sizes observed between samples.

Interestingly, despite the greater variation of core size, the shell thickness remained consistent across **PS(8-13)@SiO$_2$** (**Table 3.3**) and similar to that shown for samples **PS(1-7)@SiO$_2$** (**Table 3.1**). This further suggests that the increase in particle size is due to the dopant, and not an external factor such as the silica-capping step, as well as showing that the size of the particle core does not affect the silica coating thickness.

Table 3.3 Calculated shell thickness of **SiO$_2$@PS(8-13);** sizes were calculated using ImageJ software.

	Min / nm	**Max / nm**	**Mean / nm**	**SD / nm**
PS(8)@SiO$_2$	31 ± 1	96 ± 1	50 ± 1	11
PS(9)@SiO$_2$	34 ± 1	64 ± 1	45 ± 1	8
PS(10)@SiO$_2$	34 ± 5	81 ± 5	49 ± 5	14
PS(11)@SiO$_2$	35 ± 1	66 ± 1	47 ± 1	9
PS(12)@SiO$_2$	30 ± 3	54 ± 3	42 ± 3	8
PS(13)@SiO$_2$	46 ± 4	90 ± 4	56 ± 4	12

3.4.1.3 IR Spectroscopy

FT-IR spectroscopy showed peaks that can be assigned to both the silica shell and the polystyrene core. The IR-spectra, shown in **Figure 3.25**, is dominated by the silica shell, with a strong peak at 1070 cm^{-1} assigned to the asymmetric Si-O-Si asymmetric vibration, and further peaks at 956 cm^{-1} and 796 cm^{-1} being assigned to the Si-OH asymmetric vibration and Si-O symmetric vibration respectively.[73]

Medium intensity peaks at 754 and 698 cm^{-1} can be assigned to the out-of-plane C-H bend, and broad weak bands centred at 1676 and 1496 cm^{-1} are assigned to aromatic C=C vibrations of the phenyl ring.[74] Very weak bands at 2923 and 3027 cm^{-1} are assigned to the methylene groups of the polystyrene backbone,[74,75] however the domination of the silica bands in the spectra make these assignments tentative due to their weakness.

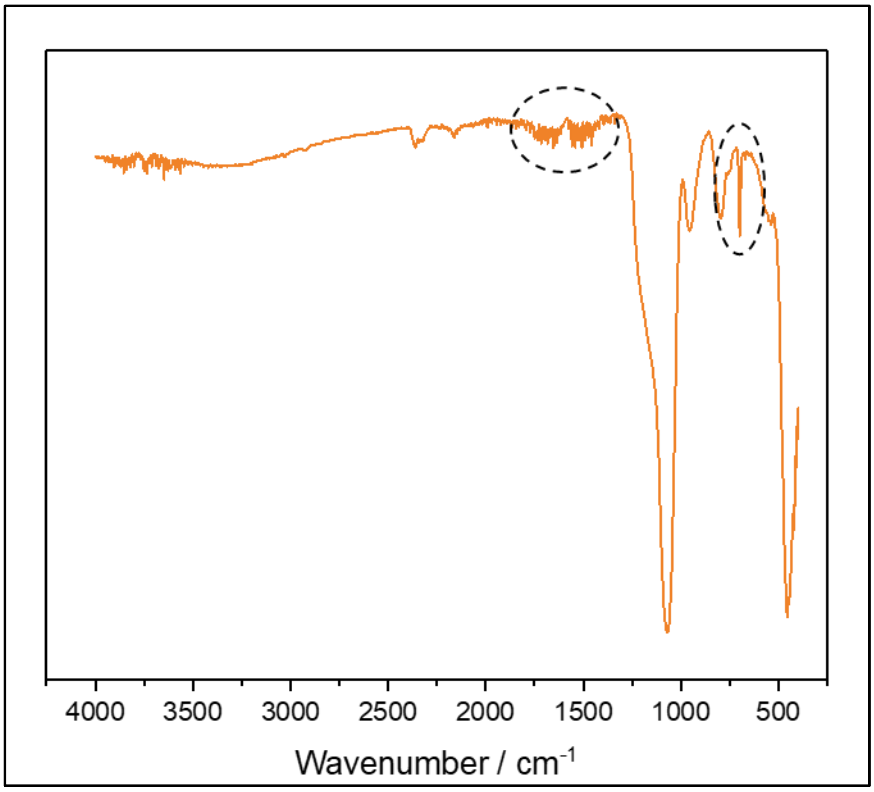

Figure 3.25 ATR-FT-IR Spectra of **PS(Ox)@SiO$_2$** showing the dominant Si-O vibrations as well as weaker C=C and C-H stretches of the polystyrene core (circled).

3.4.1.4 Photophysical Studies

3.4.1.4.1 PS(Ox)@SiO$_2$ where Ox= 1-7

3.4.1.4.1.1 Solid State UV-Vis

The Diffuse Reflectance spectra of **PS(Ox)@SiO$_2$**, where Ox= **3,4,5** and **7**, were obtained in solid state as absorption bands could not be observed in solution due to particle scatter.

All spectra showed the successful encapsulation of the oxazole, with the absorption bands matching those of the native oxazole (**Figure 3.26**). Due to the nature of the equipment the sample was excited during the reflectance scan, as the charge coupled device does not sweep from high to low wavelength, and instead pulses all wavelengths in the same instance. Therefore emission is also observed from the particle, which also corresponded to the emission of the native oxazole.

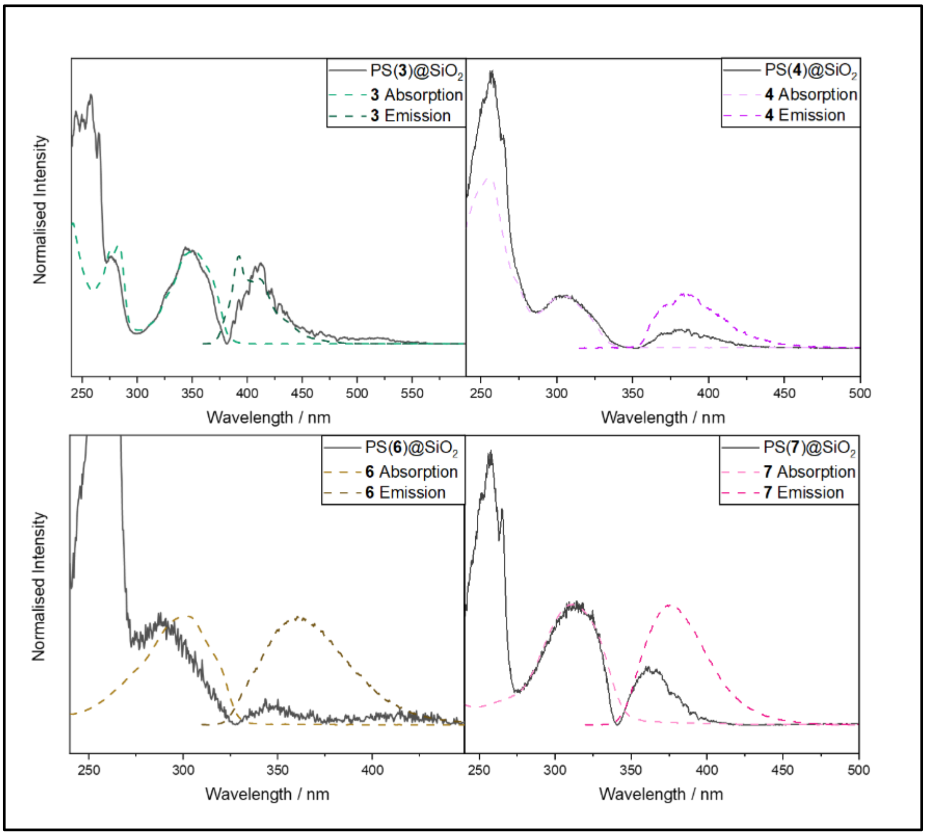

Figure 3.26 Solid-state diffuse reflectance spectra of a range of **PS(Ox)@SiO$_2$** particles showing agreement with the oxazole solution UV-Vis, with a new absorption at 260 nm. Solid-state diffuse reflectance spectra were plotted according to the Kubelka-Munk transformation[76], with the absorption and emission spectra normalised.

All particles showed a new absorption at approximately 260 nm, which is due to the π→π* transition within the polystyrene, however for **PS(4)@SiO$_2$** the new absorption at 260 nm observed for the other particles was overlayed with that of an existing absorption for oxazole **4**.

3.4.1.4.1.2 Luminescence

Once incorporated within the nanoparticle, all oxazoles exhibited a shift in emission wavelength when compared to free in solution (**Figure 3.27**). **PS(Ox)@SiO$_2$** where **Ox= 2, 3, 4** and **5** all showed a slight red shift in emission, whereas **Ox= 1, 6** and **7** showed a blue shift in emission, with the most pronounced being **7**, similar to that observed by **POPOP** (**Figure 3.27**).

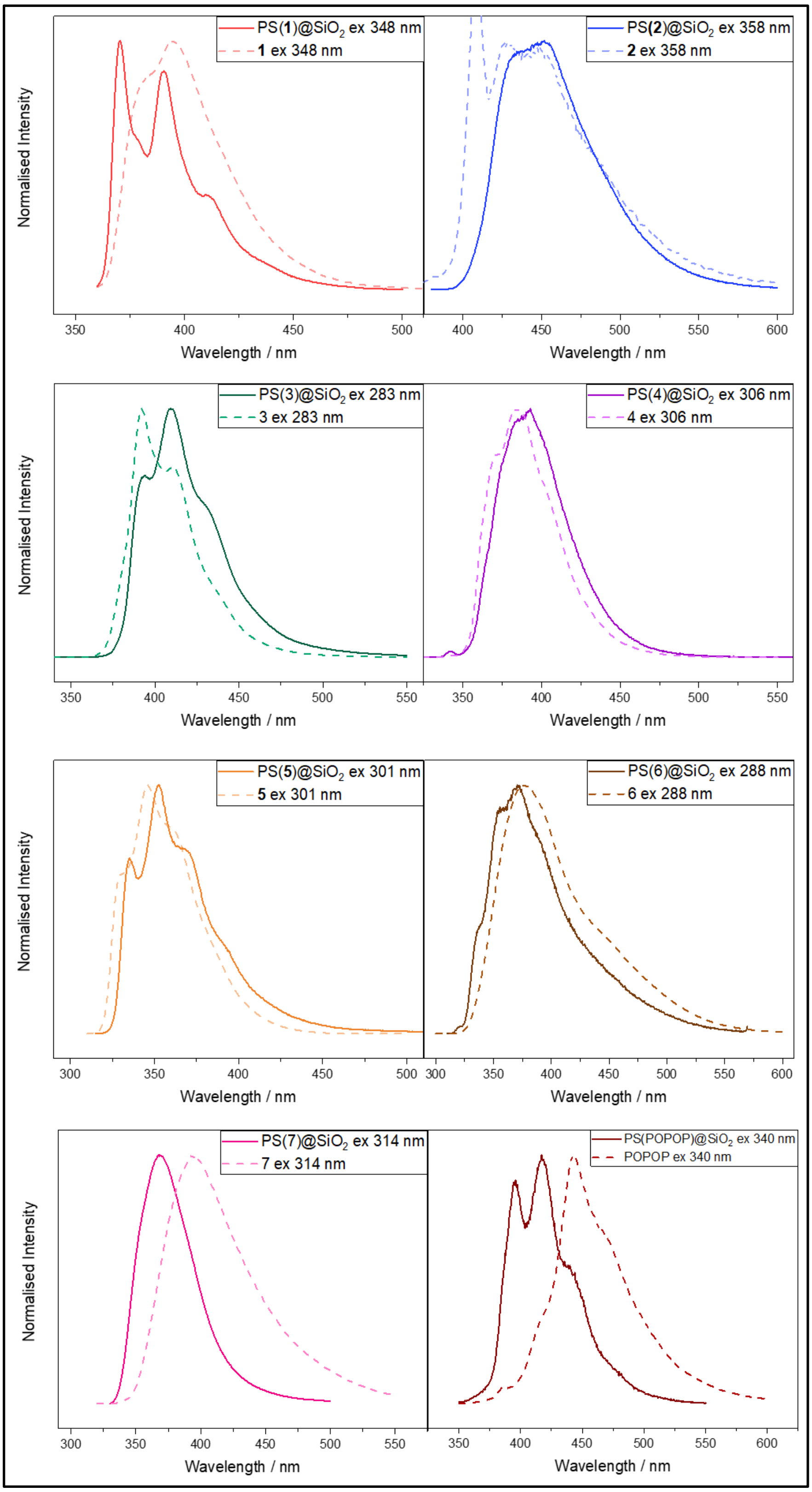

Figure 3.27 Emission spectra for **PS(Ox)@SiO$_2$** where Ox = **1-7** and **POPOP** (bold line), compared to oxazole= **1-7** and POPOP (dashed line). Particles recorded as a water suspension (0.04 % wt), oxazoles and POPOP recorded in water (1% AcN).

These shifts in emission are not fully understood. Work by S. Chakraborty *et al*[77], who analysed the photoluminescence properties of a range of fluorophores (including both DPO and POPOP) in polystyrene films, attributes the red shift in emission to a concentration dependent Stokes shift, known as the inner filter effect, with both solvatochromic effects and excimer formation within the films responsible.

Although **PS(3)@SiO$_2$** exhibits only a small shift in emission compared to **3** in solution, the intensities of the vibrational bands are inverted, with the emission at 410 nm being higher than that at 393 nm. The solvent dependence of pyrene emission bands has been the subject of much research, linking the intensity of the vibronic band transitions and the solvent polarity due to vibronic coupling of the states[78,79], also known as the Ham effect.[80] Although with wavelengths slightly shifted compared to the literature values (most probably due to the oxazole moiety), it can be assumed that emissive bands found at 392 and 410 nm can be assigned to the first and third vibronic bands due to their sensitivity to the environment.[79,81] When encapsulated within the particle, a highly hydrophobic environment, the emission band at 410 is considerably higher than that at 393 nm, with the ratio between the two bands inverted when compared to that in water, a polar environment. This sensitivity to the environment of the two bands is in line with that observed by vibronic bands one and three of pyrene emission when in hydrophobic and polar environments respectively.[79,80]

The fluorescence lifetimes of all particles were measured and compared to oxazoles **1-7** in water (spiked into water using 1% AcN), with all showing bi-exponential decay when encapsulated *vs* mono-exponential in water, with the exception of **2** and **3**, which also displayed bi-exponential decay in water (**Table 3.4**). The bi-exponential character of the lifetime measurement has many possible explanations; firstly, the polymer matrix and thus “pore” that the fluorophores sit within will not all be the same size, and therefore the fluorophores will be exposed to a range of environments. Some of these “pores” may contain more solvent from the encapsulation reaction than others, some may be considerably larger, whereas others may have multiple fluorophores stacked in a smaller space. For this reason, the lifetimes may appear biexponential as an average of more than one environment. Another explanation, bought about by the work of S. Chakraborty *et al*[77] is that the local environment may lead to high concentrations of fluorophores in the same space, which can increase the likelihood of singlet-singlet annihilation, leading to bi-exponential decay profiles. Lastly, for the cases of **PS(6)@SiO$_2$** and

PS(5)@SiO$_2$, where one of the components is less than 1 ns, the biexponential character could be due to decay from both the fluorophore (the larger component) and polystyrene, with an emission wavelength of approximately 330 nm (in cyclohexane)[82], which lies within a similar region to the oxazoles. Examples of mono- and bi-exponential fits to the lifetime data are given in the **Appendix**.

Table 3.4 Fluorescence lifetime measurements of Ox = **1-7** in water and encapsulated within **PS(Ox)@SiO$_2$**. λ_{ex}=295 nm.

	τ_{obs} / ns	
	Water	**PS(Ox)@SiO$_2$**
1	6.8 ± 0.7	1.8 ± 0.2 (34), 5.1 ± 0.5 (66)
2	1.5 ± 0.2 (56), 6.0 ± 0.6 (44)	2.8 ± 0.3 (30), 7.6 ± 0.8 (70)
3	4.8 ± 0.5 (6), 28.2 ± 2.8 (94)	4.1 ± 0.4 (79), 10.3 ± 1.0 (21)
4	25.3 ± 2.5	10.0 ± 1.0 (11), 32.0 ± 3.2 (89)
5	1.4 ± 0.1	0.4 ± 0.04 (17), 1.3 ± 0.1 (83)
6	0.7 ± 0.1	0.1 ± 0.01 (17), 0.7 ± 0.07 (83)
7	0.4 ± 0.04	1.2 ± 0.1 (31), 3.0 ± 0.3 (69)

To probe energy transfer between the polymer core and the encapsulated oxazole, emission was also recorded when excited at 268 nm, the absorption maxima for polystyrene.[83] **7** does not exhibit strong absorption at 268 nm, however when encapsulated within a particle exhibits strong emission at this excitation wavelength (**Figure 3.28**). This suggests that energy transfer between the polystyrene core and the oxazole species is present, which is paramount for efficient scintillation.

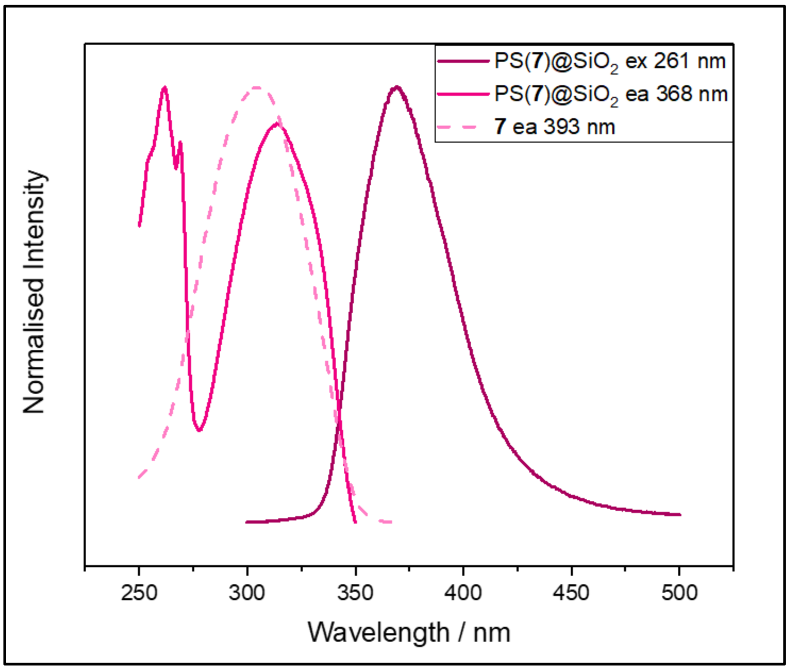

Figure 3.28 Emission and Excitation Spectra of **PS(7)@SiO₂** and **7** (particles recorded in water, 1% AcN in water required for **7**).

3.4.1.4.2 Co-Doping of Nanoparticles with DPO

As discussed in **Chapter 2**, a primary scintillant is required in both traditional and novel cocktail systems to yield a higher scintillant response. Therefore, despite the close-proximity between the polystyrene and oxazole appearing to yield successful energy transfer, co-doping of particles with DPO as well as the novel oxazole was also attempted.

Co-doping was successful for two of the seven oxazoles, **2** and **7**, shown in **Figure 3.29** with two emissive bands in the steady state luminescence spectra showing good agreement with that of **PS(DPO)@SiO₂** and the respective **PS(Ox)@SiO₂**, and the excitation spectra also overlapping with that of **PS(DPO)@SiO₂** and **PS(Ox)@SiO₂.** Attempted co-doping of other oxazoles showed either mono-doped **PS(DPO)@SiO₂** or **PS(Ox)@SiO₂** emission within the core, with only the respective dopant observed in the excitation acquisition. This may to be due to unfavourable interactions between the two fluorophores, however the differences between the oxazoles and their interactions with DPO is not understood.

For **2**, the oxazole emission could be seen solely when excited at 358 nm, however when exciting at 304 nm (for DPO), emission from both DPO and **2** was observed in equal intensity. The excitation spectra for each emission peak was the same as the mono-doped variants.

For **7**, the emission and excitation acquisition of each component were similar, leading to challenging deconvolution of the spectra (**Figure 3.29**). However both the emission and excitation spectra of the co-doped particles shows broadness over both peaks of the mono-doped variants, and so it was assumed that co-doping was successful.

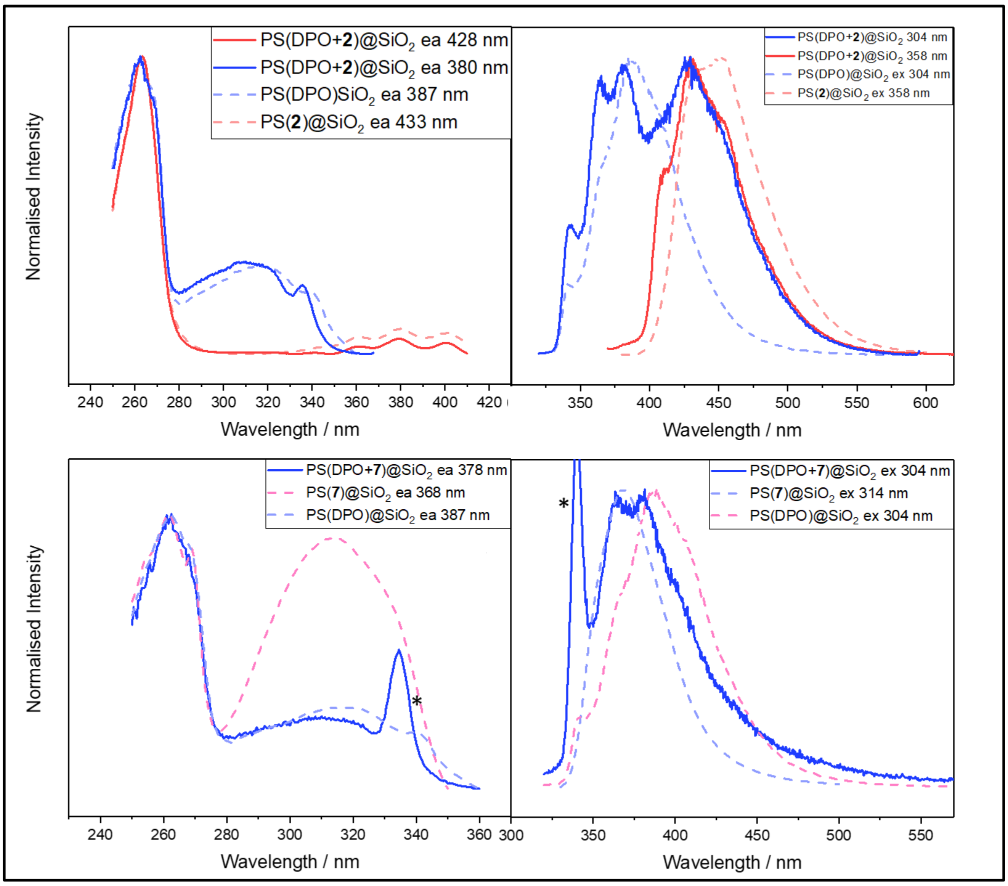

Figure 3.29 Excitation (left) and emission (right) spectra of **PS(DPO+2)@SiO$_2$** and **PS(DPO+7)@SiO$_2$** co-doped particles (recorded in water). *denotes a lamp harmonic associated with the excitation wavelength.

The morphology and core/shell sizes of these particles was also examined (**Table 3.5** and **Table 3.6**), and showed observations similar to that of **PS(8-13)@SiO$_2$**.

Table 3.5 Calculated diameter of polystyrene core of **PS(DPO+Ox)@SiO_2**; particle sizes were calculated using ImageJ software.

	Min / nm	Max / nm	Mean / nm	SD / nm
Small PS(DPO+2)@SiO_2	150 ± 29	480 ± 29	281 ± 29	93
Large PS(DPO+2)@SiO_2	1010 ± 172	1846 ± 172	1392 ± 172	344
PS(2)@SiO_2	*215 ± 14*	*368 ± 14*	*287 ± 14*	*45*
PS(DPO+7)@SiO_2	135 ± 6	415 ± 6	183 ± 6	52
PS(7)@SiO_2	*219 ± 10*	*298 ± 10*	*247 ± 10*	*32*

The average core size for **PS(DPO+7)@SiO_2** was similar (and in fact slightly smaller) to that observed for **PS(7)@SiO_2**, however the standard deviation was higher. For **PS(DPO+2)@SiO_2** there appeared to be both small particles of similar size yet considerably more distribution than that of **PS(2)@SiO_2**, and also a range of much larger particles, (shown in **Figure 3.30**, compared with **PS(DPO+7)@SiO_2**) consistent with results discussed in **Section 3.4.1.2** for disubstituted oxazoles **8-13**, as a result of incomplete deswelling due to the larger dopant size.

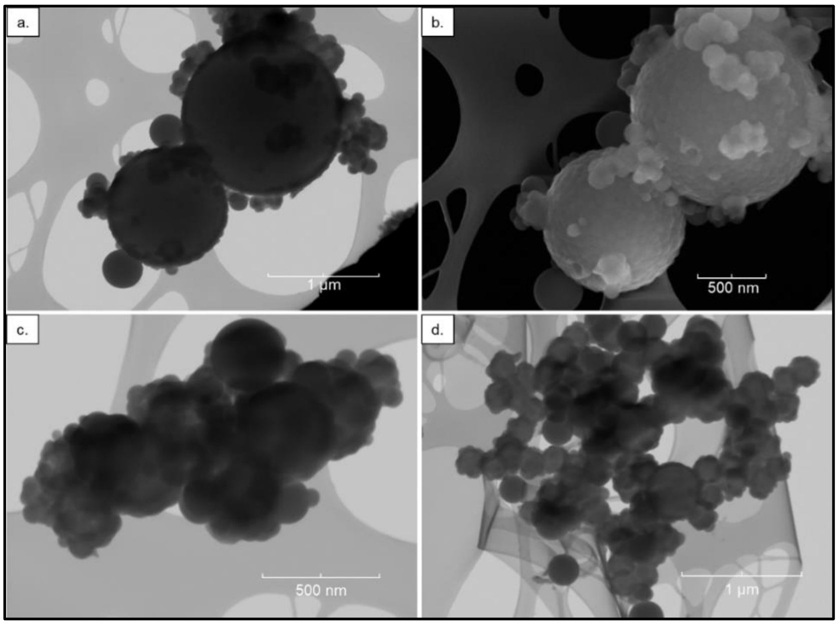

Figure 3.30 a) STEM and b) SEM images of larger **PS(DPO+2)@SiO_2** particles; c) STEM image of smaller **PS(DPO+2)@SiO_2** particles; d) STEM image of **PS(DPO+7)@SiO_2** particles.

As with **PS(8-13)@SiO$_2$**, despite differences in core size, the shell thickness remained consistent (**Table 3.6**) with that shown for samples **PS(1-7)@SiO$_2$** (**Table 3.1**).

Table 3.6 Calculated shell thickness of **PS(DPO+Ox)@SiO$_2$**; sizes were calculated using ImageJ software.

	Min / nm	**Max / nm**	**Mean / nm**	**SD / nm**
PS(DPO+2)@SiO$_2$	44 ± 2	71 ± 2	60 ± 2	8
PS(DPO+7)@SiO$_2$	20 ± 2	79 ± 2	43 ± 2	13

3.4.1.4.3 PS(Ox)@SiO$_2$ where Ox = 8-13

All oxazoles, with the exception of **8**, exhibited a shift in emission wavelength when compared to free in solution (**Figure 3.31**). **PS(Ox)@SiO$_2$** where **Ox= 9, 10,** and **12** all showed a slight red shift in emission, whereas for **11** a large blue shift was observed in contrast to the primary oxazole which showed a slight red shift. Interestingly, both **8** and **13** showed almost no shift in emission wavelength, the latter also in contrast with the primary oxazole **7** which showed a large blue shift, and **8** showing a more pronounced vibrational fine structure in the particle compared to in water.

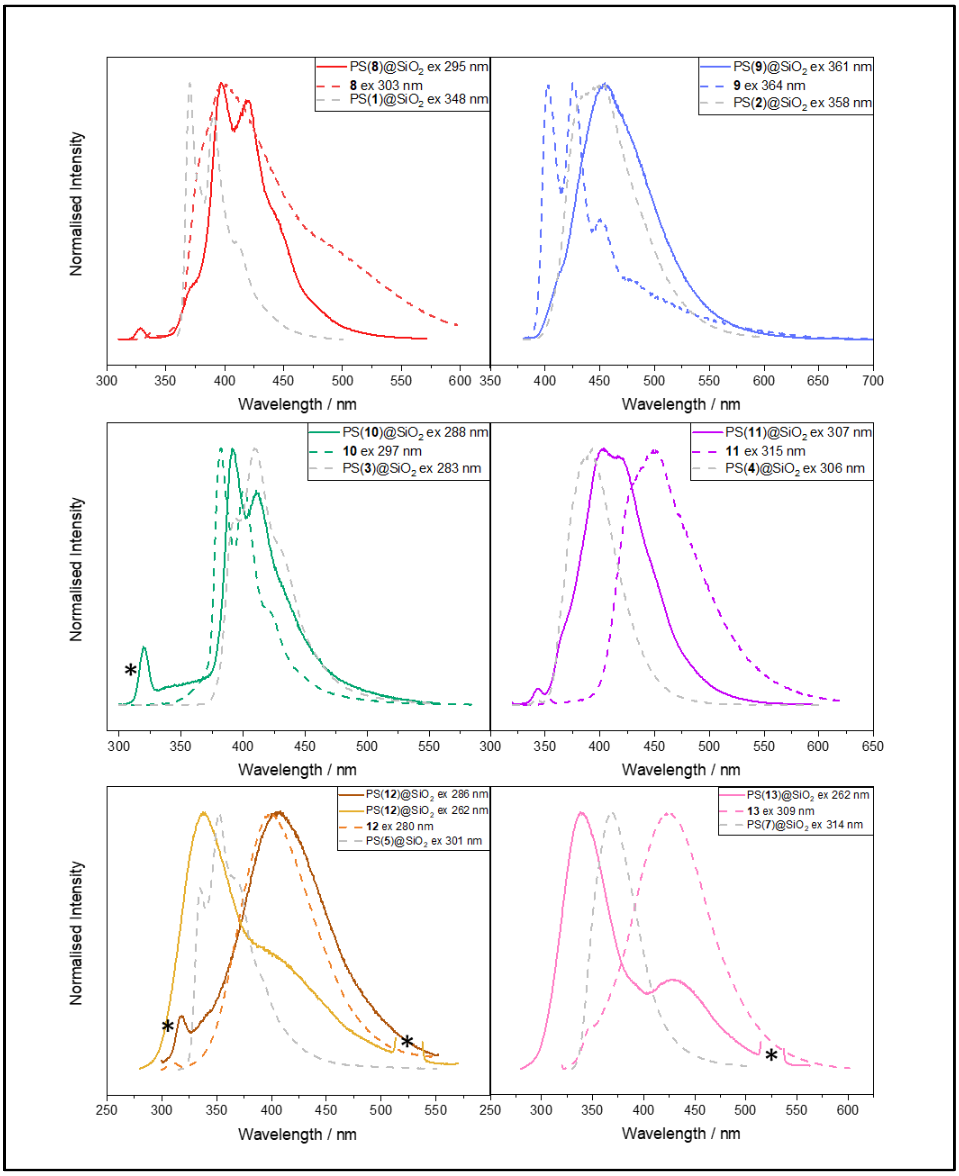

Figure 3.31 Emission spectra for **PS(Ox)@SiO₂** where Ox = **8-13**, compared to **8-13** in water, and **PS(Ox)@SiO₂** where Ox = **1-5** and **7**. Particles recorded in water, **Ox** recorded in water containing 1% DMSO. *denotes a lamp harmonic associated with the excitation wavelength, some of which have been removed from the spectra.

The emission spectra of both **PS(13)@SiO₂** and **PS(12)@SiO₂**, of which the latter will be discussed in more detail below, contained a strong emissive band at 338 nm, corresponding to polystyrene emission. The excitation spectra of both confirms this, with an intense band at 268 nm (**Figure 3.32**). Unlike previous examples shown, this suggests a reduction in energy transfer from the polystyrene core to the oxazole (thus leading to polystyrene emission). That being said, the excitation spectra of **PS(13)@SiO₂** at 430 nm suggests some evidence of energy transfer, with the absorption at 268 nm dominating the oxazole-based bands.

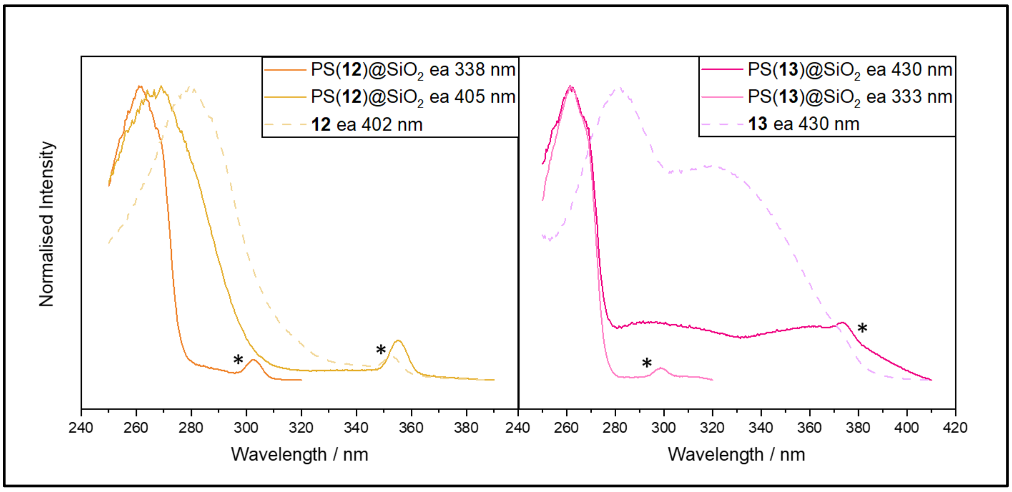

Figure 3.32 Excitation Spectra of **PS(Ox)@SiO₂**, where Ox = **11** (*left*) and **13** (*right*), compared to free oxazole. Particles recorded in water, **9** recorded in water containing 1% DMSO. *denotes a lamp harmonic associated with the excitation spectra

As with oxazoles **1-7**, fluorescence lifetimes of all particles were measured and compared to oxazoles **8-13** (1% DMSO spike in water), presented in **Table 3.7**. With the exception of **13** and **12** (at 490 nm), all showed bi-exponential decay, however unlike the majority of mono-substituted oxazoles, **8-11** also showed bi-exponential decay in water. This may in part be due to the extended aromatic system forming more aggregates in the polar solvent, and therefore more than one environment is present overall in the system. An interesting observation is that the lifetime of both **8** and **10** decreased when encapsulated, as did **1** and **3**; with **13** and **7** both increasing. The fluorescence lifetimes of **9**, **11** and **12** did not show a large change in fluorescence lifetime, similar to **2**, **4** and **5**.

Table 3.7 Fluorescence lifetime measurements of Ox = **8-13** in water (1% DMSO) and encapsulated within **PS(Ox)@SiO$_2$**. λ_{ex}=295 nm.

	Water		**PS(Ox)@SiO$_2$**	
	λ_{em} / nm	**τ_{obs} / ns**	**λ_{em} / nm**	**τ_{obs} / ns**
8	398	0.74 ± 0.07 (17), 6.26 ± 0.63 (83)	398	0.6 ± 0.1 (19), 1.8 ± 0.2 (81)
9	485 454 426 403	0.4 ± 0.04 (30), 3.8 ± 0.4 (70) 0.9 ± 0.1 (25), 5.0 ± 0.5 (75) 1.35 ± 0.14 (20), 5.13 ± 0.51 (80) 1.7 ± 0.17 (38), 6.5 ± 0.65 (62)	455 407	1.42 ± 0.14(42), 3.98 ± 0.40 (58) 0.84 ± 0.08 (48), 4.0 ± 0.4 (52)
10	400	1.2 ± 0.1 (19), 34 ± 3.4 (81)	410	1.8 ± 0.2 (63), 5.7 ± 0.6 (37)
11	451	1.04 ± 0.10 (51), 3.53 ± 0.35 (49)	420	1.73 ± 0.17 (68), 4.45 ± 0.45 (32)
12	556 402	1.05 ± 0.11 0.98 ± 0.10 (92), 4.70 ± 0.47 (8)	490 405	1.9 ± 0.19 1.3 ± 0.13 (73), 3.65 ± 0.37 (27)
13	430	0.73 ± 0.07 (25), 2.08 ± 0.21 (75)	430	1.9 ± 0.19

As discussed in **Chapter 2**, both **9** and **12** showed more complex emission, which is further confirmed herein. In **Chapter 2**, it was suggested that **9** displayed evidence of energy transfer, or “donor-acceptor” behaviour, between the two R-groups of the oxazole ring due to a large featureless emission band at 500 nm and a smaller component at 410 nm thought to be due to chloroanthracene emission. This was also suggested in the DFT analysis, in which the LUMO and LUMO+1 were dominated by either the chloroanthracene and naphthalene R-groups respectively. When recorded in water (1% DMSO), the higher energy peak dominated the emission spectra, suggesting that charge transfer is quenched. The fluorescence lifetimes also showed a change in emissive species with increasing wavelength, as shown in **Table 3.7**, with the emission lifetime of **9** in water at 403 and 426 nm being similar to that of **2** in water. When encapsulated, the emissive wavelength at 455 nm was similar to that of the suggested charge transfer band, and not of **PS(2)@SiO$_2$** at a similar wavelength, thus suggesting that the emissive peak observed in **PS(9)@SiO$_2$** was a result of the low energy charge transfer and not that of chloroanthracene.

The excitation spectra, shown in **Figure 3.33**, clearly demonstrate a shift in the contribution between the chloroanthracene bands and the 300 nm component for **9** in water (1% DMSO). Where the excitation spectra is recorded at 403 nm, the former dominates, however this contribution is overshadowed by the 300 nm component when recorded at 450 nm.

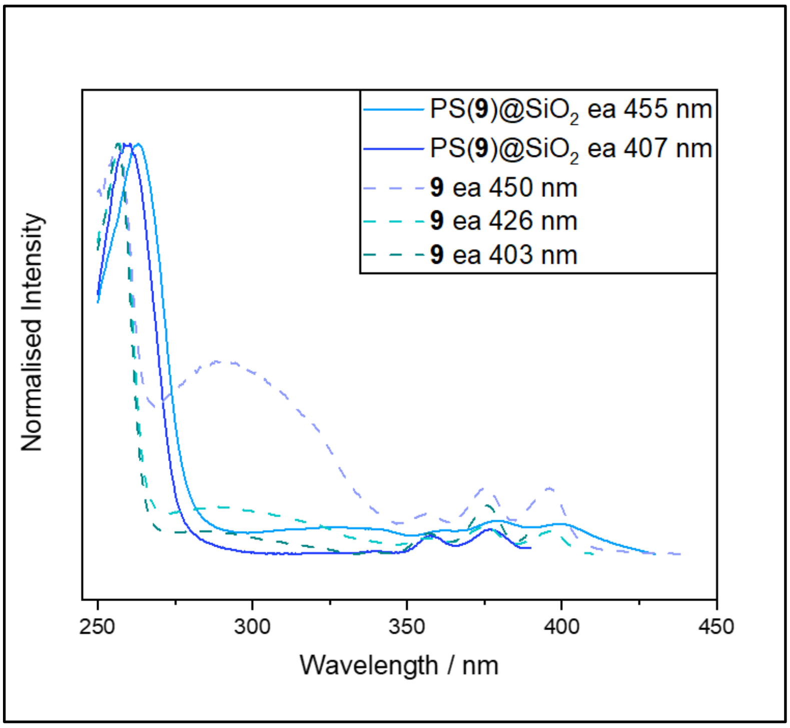

Figure 3.33 Excitation Spectra of **PS(9)@SiO$_2$**, compared to free oxazole. Particles recorded in water, **9** recorded in water containing 1% DMSO.

When encapsulated, the excitation spectra at 455 nm shows both components at equal intensity, similar to that shown in the excitation spectra of **9** in CHCl$_3$ at a concentration of 10^{-7} M in **Chapter 2**, however at 407 nm only the chloroanthracene absorption bands are observed.

In **Chapter 2**, the dual emissive characteristics of **12** were discussed in detail, with the low energy emissive band at 560 nm being assigned to singlet emission originating from the fluorenone R-group, and higher energy emission at 400 nm due to π→π* emission from the entirety of the fluorophore. When recorded in water (1% DMSO), as discussed in **Chapter 2**, the emission from the low energy state is greatly reduced compared to the emission at 402 nm (**Figure 3.34**). This is consistent with the literature, as when the polarity of the solvent increases the T_3 triplet state (with n,π* character) becomes too high in energy, the π→π* singlet state becomes more stable and thus ISC cannot occur, leading solely to relaxation from the singlet state[84]. However, in polar protic solvent systems, hydrogen bonds can form between the fluorenone carbonyl and solvent, which lead to an increase in non-radiative decay.[85]

More interestingly, when encapsulated within the nanoparticle the low energy emissive band is almost entirely quenched with incredibly weak emission at 500 nm (**Figure 3.34**), heavily blue shifted from the 560 nm emission observed in water.

This gives further evidence that the low energy band is due to emission from the fluorenone, which is incredibly sensitive to solvent. The polystyrene core, similar to toluene, would produce a non-polar environment for the dopant, leading to a destabilisation of the polar LUMO state (electron density situated entirely on the fluorenone R-group) and thus resulting in a hypsochromic shift in emission wavelength[86] (as discussed for toluene in **Chapter 2**).

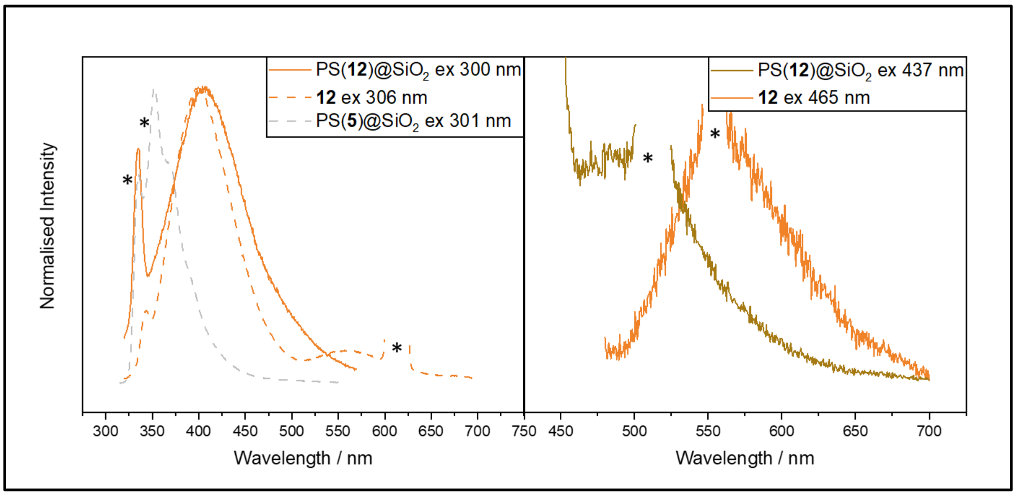

Figure 3.34 Emission spectra recorded in water for *Left*: **PS(12)@SiO$_2$** compared to **12**, and **PS(5)@SiO$_2$** recorded at 301 nm**;** *Right:* **PS(12)@SiO$_2$** compared to **12**, recorded at 437 and 465 nm respectively. Particles recorded in water, **12** recorded in water containing 1% DMSO. *denotes a lamp harmonic associated with the excitation wavelength, some of which have been removed from the spectra.

The excitation spectra of **12** both in water and encapsulated are shown in **Figure 3.35**, and lead to interesting observations. The excitation spectra of **12** in water at 556 nm shows both the high energy bands at approximately 338 and 284 nm and the low energy charge transfer absorption at 464 nm, similar to that found for **12** in $CHCl_3$ (**Chapter 2**). At 402 nm (emission resulting from the entirety of the fluorophore) the excitation spectra shows that the higher energy absorption at 284 nm dominates over that at 338 nm. When encapsulated however, both excitation spectra recorded at 405 and 490 nm are dominated by an even higher energy band at 268 nm, which is indicative of polystyrene. Also, the excitation spectra recorded at 490 nm does not show evidence of the charge transfer band between 450-500 nm, thus further confirming quenching of the low energy emissive band when encapsulated.

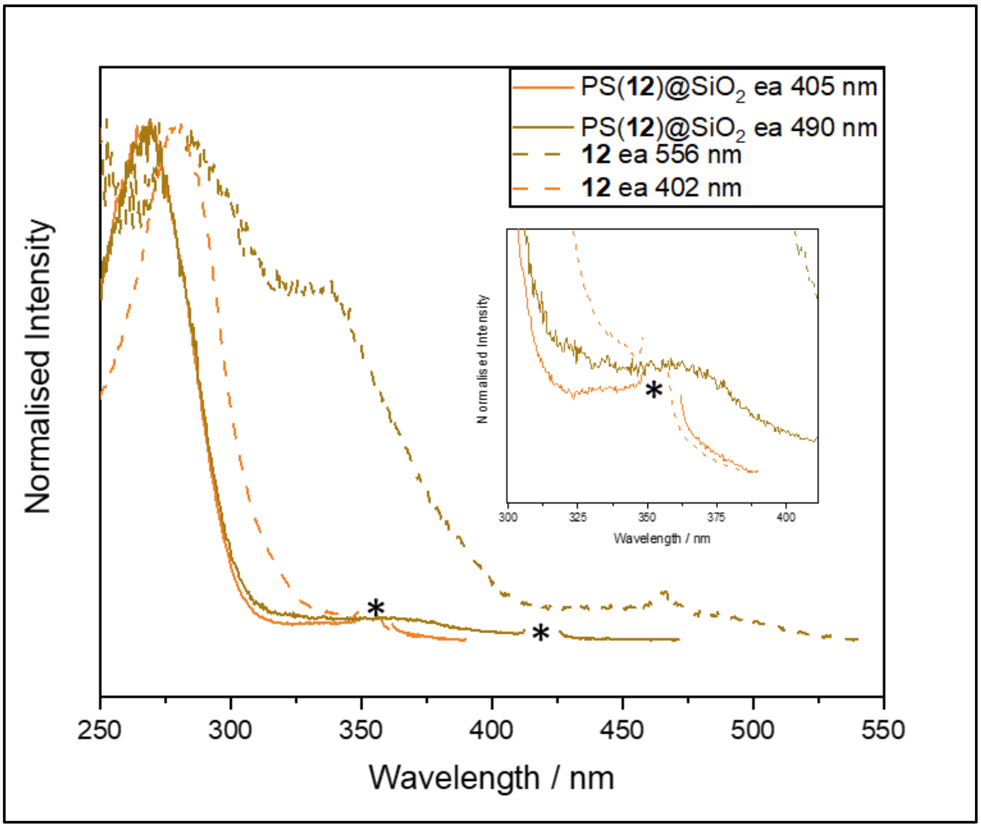

Figure 3.35 Excitation Spectra of **PS(12)@SiO₂**, compared to free oxazole. Particles recorded in water, **12** recorded in water containing 1% DMSO. *denotes a lamp harmonic associated with the excitation wavelength that have been removed from the spectra.

3.4.1.5 Scintillation

The ability of the nanoparticles to act as proximity induced scintillants was analysed using both a hard and soft emitter, Sr-90 and Ni-63 (**Table 3.8**). As discussed previously, beta particles arising from Sr-90 decay have a long path length, and so proximity to the scintillant is not a limiting factor on the consequent scintillation response, and in fact can lead to “non-proximity effects” (**Figure 3.3**). However, beta particles from Ni-63 have a much shorter path length, and so proximity to the bead is fundamental to gain a scintillant response. Therefore, it was expected that a strong scintillant response would be observed in the presence of Sr-90, but a much weaker response for Ni-63, as the particles are unfunctionalized and thus the radionuclides would not strongly interact with the silica surface.

Table 3.8 Radiochemical data for soft emitter Ni-63 and hard emitter Sr-90[87], originally reported in **Chapter 2.**

Nuclide (decay)	**Q (average)/ keV**	**$t_{1/2}$ / yr**
Ni-63 (β)	67 (17)	101
Sr-90 (β)	546 (196)	29

Although the author was present during preliminary testing of particles containing oxazoles **1-7**, and **POPOP**, all scintillation experiments were carried out by Dr Hibaaq Mohamud at the National Physical Laboratory, Teddington, UK. As noted in **Chapter 2**, the scintillation efficiencies presented here are not absolute values and are for comparison purposes only, due to the scintillation counter not being calibrated to the novel particle suspensions.

3.4.1.5.1 PS(Ox)@SiO_2 where Ox = 1-7

As with oil-in-water microemulsions, all particles showed an inherent ability to scintillate in the presence of Sr-90 (**Figure 3.36**), however both **PS(4)@SiO_2** and **PS(5)@SiO_2** were similar to that of the un-doped particle, **PS@SiO_2** (0.593, 0.604 and 0.582 CPSBq^{-1} respectively). This differs to the oil-in-water microemulsions, where those doped with **4** showed one of the highest efficiencies (1.767 CPSBq^{-1}). This may be due to a decreased energy transfer between the polystyrene core and **4** and **5** compared to the other oxazoles, and therefore although the beta particle interacts with the polystyrene core, there is not efficient energy transfer between the polystyrene and oxazoles **4** and **5**, therefore resulting in a much weaker scintillant response, similar to the undoped particle, as the signal would be derived mainly from the polystyrene. As absorption of oxazole occurs in a similar range to that of polystyrene, it is hard to differentiate energy transfer *via* polystyrene excitation from emission *via* direct oxazole excitation in these cases.

Unlike in oil-in-water microemulsions, **PS(POPOP)@SiO$_2$** gave the highest scintillant efficiency of 0.871 CPSBq^{-1}, followed by **PS(7)@SiO$_2$** which was also the second highest scintillant response for microemulsions (0.765 CPSBq^{-1} and 1.869 CPSBq^{-1} for particles and microemulsions respectively). The reason for this high response may be due to the evident energy transfer between the polystyrene and **7**, shown in **Figure 3.28**. In contrast, **PS(1)@SiO$_2$** had a relatively poor response when compared to the other dopants with an efficiency of 0.649 CPSBq^{-1}, despite being by far the best scintillant for microemulsions (2.278 CPSBq^{-1}).

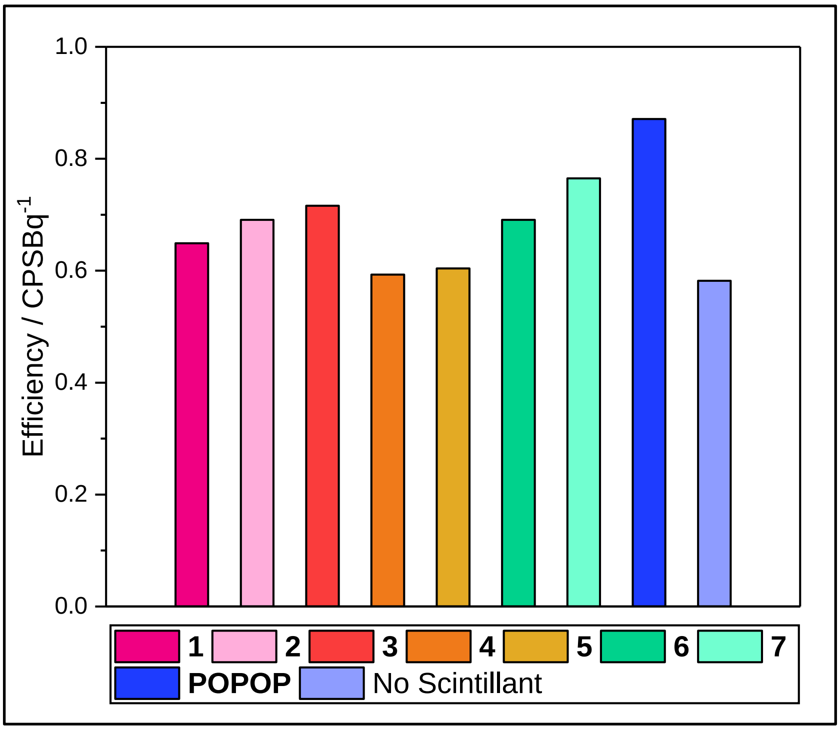

Figure 3.36 Scintillation efficiency of **PS(Ox)@SiO$_2$** in the presence of Sr-90. Counted for 6 minutes with 10 cycles completed in total.

As with microemulsions, the stability of these systems after two months in the presence of Sr-90 was tested and is presented in **Figure 3.37**. Although most samples showed a decrease in efficiency, it should be noted that the change was minimal, with all but **PS(2)@SiO₂** experiencing a < 1% change. This is similar to the microemulsions, which showed a maximum decrease in efficiency of 2.5 % (those doped with **1**).

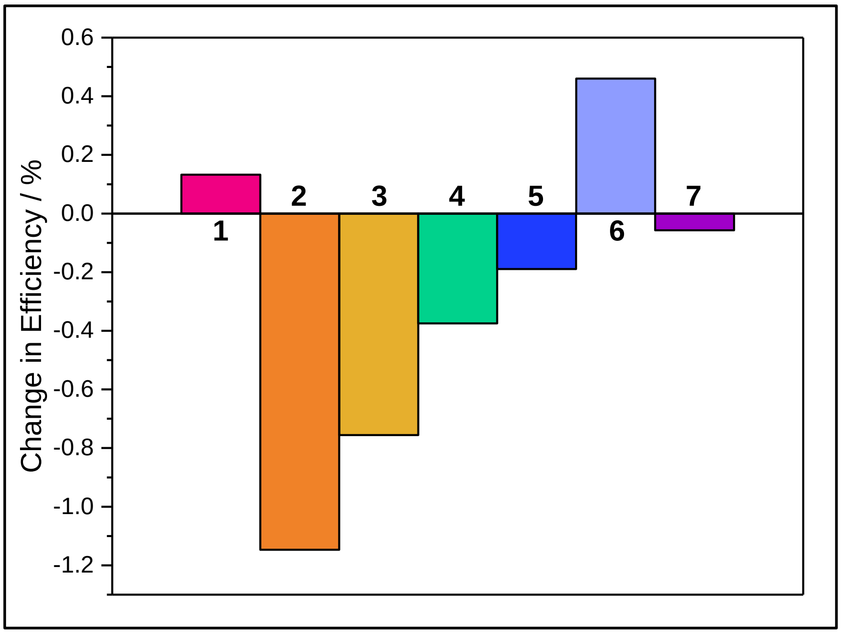

Figure 3.37 Percentage change in scintillation efficiency of **PS(Ox)@SiO₂** after 2 months in the presence of Sr-90. Counted for 6 minutes with 10 cycles completed in total.

To be able to analyse the proximity effect, the ability of these systems to scintillate in the presence of Ni-63 was also tested, with the results shown in **Figure 3.38**.

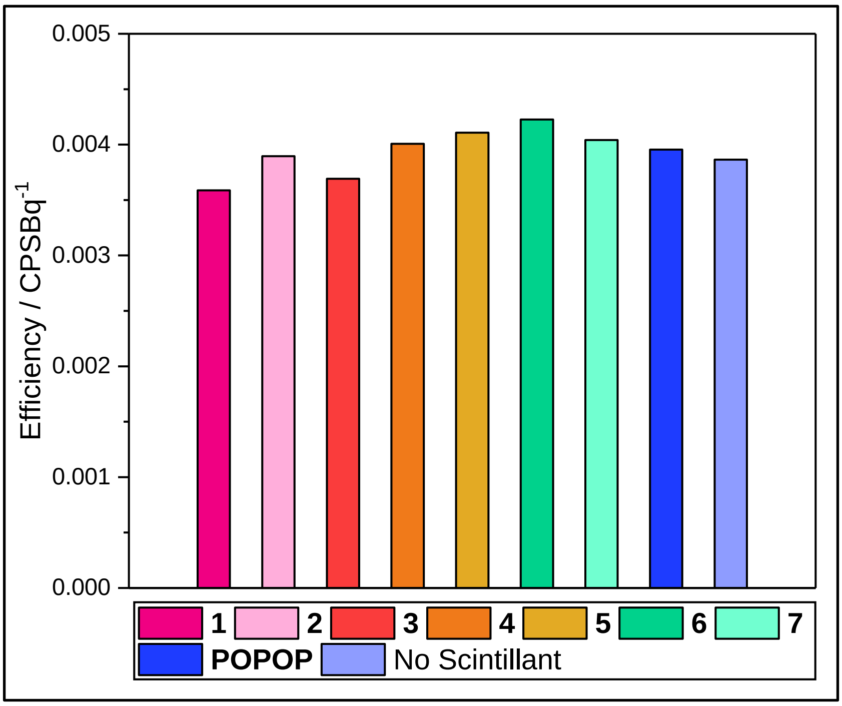

Figure 3.38 Scintillation efficiency of **PS(Ox)@SiO$_2$** in the presence of Ni-63. Counted for 6 minutes with 10 cycles completed in total.

Unlike in the presence of Sr-90, **PS(6)@SiO$_2$** showed the highest efficiency of 0.00423 CPSBq^{-1}, with **1** and **3** giving a scintillant response lower than the undoped particle with an efficiency of 0.00386 CPSBq^{-1}. However, when looking at the efficiency values per scan, it was clear to see that all measurements are within error and therefore although plotted as their average value, are all of too similar values to be compared individually. This lack of signal is further shown by comparison to the values obtained with Sr-90 (**Figure 3.39**), which confirms the possible need for proximity for soft-emitters such as Ni-63 for a measurable interaction between the beta particle and scintillant. This suggests that the efficiency in the presence of Ni-63 could be increased *via* functionalisation of the particle surface with a Ni-chelator, which could also lead to selectivity in a mixed radionuclide sample.

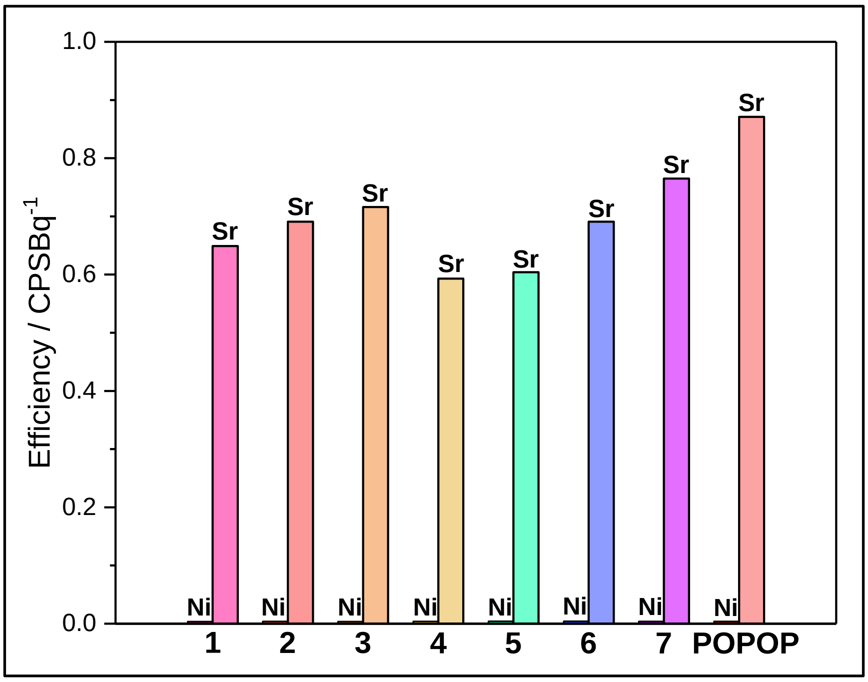

Figure 3.39 Comparison of scintillation efficiency for **PS(Ox)@SiO$_2$** in the presence of Ni-63 and Sr-90. Counted for 6 minutes with 10 cycles completed in total.

3.4.1.5.2 Co-doped particles with DPO

It was found with microemulsions that the presence of DPO as the primary scintillant was fundamental in the energy transfer pathway in order to yield high efficiencies for each oxazole. Therefore, the co-doped particles were tested for their efficiency in the presence of Sr-90 and Ni-63.

In the case of Sr-90, **PS(2+DPO)@SiO$_2$** and **PS(4+DPO)@SiO$_2$** showed an increase in efficiency of 4 and 19 % respectively, however **PS(7+DPO)@SiO$_2$** showed a decrease of 8 % (**Figure 3.40**). When observing the values however, the efficiency of the co-doped particles is similar across all three samples, unlike the mono-doped equivalents that show variation across the series. This leads to the presumption that when co-doped, unlike the microemulsions that showed variation across the different oxazoles, the ability of the particle to scintillate is dominated by DPO, and therefore may not involve the secondary scintillant despite photophysical measurements indicating possible energy transfer between the polystyrene, DPO and oxazole.

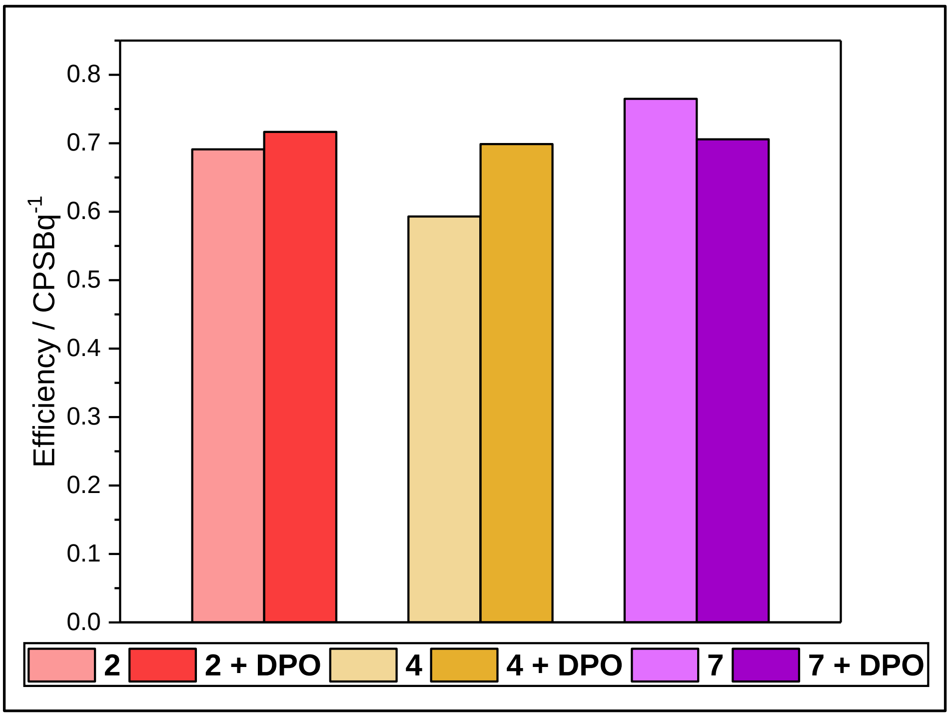

Figure 3.40 Comparison of scintillation efficiency for **PS(Ox)@SiO$_2$** and **PS(Ox+DPO)@SiO$_2$** in the presence of Sr-90. Counted for 6 minutes with 10 cycles completed in total.

In the case of Ni-63, all co-doped particles show an increase in efficiency between 46 and 58% of the mono-doped efficiency (**Figure 3.41**). However as in the case of Sr-90, the values are very similar and therefore it can again be presumed that unlike in cocktails, where there is an interaction between the primary and secondary scintillants, that the signal observed here is in fact solely for DPO.

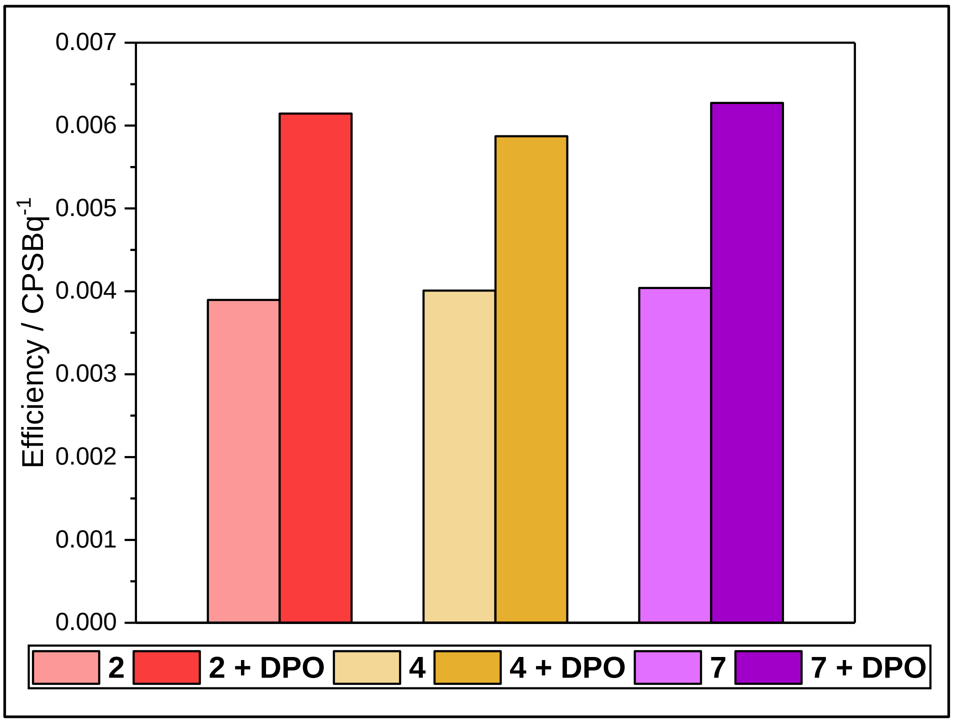

Figure 3.41 Comparison of scintillation efficiency for **PS(Ox)@SiO$_2$** and **PS(Ox+DPO)@SiO$_2$** in the presence of Ni-63. Counted for 6 minutes with 10 cycles completed in total.

3.4.1.5.3 PS(Ox)@SiO$_2$ where Ox = 8-13

As in **Chapter 2,** for reasons outside of both the author's and NPL's control only particles doped with oxazoles **8** and **10** could be analysed for their scintillation efficiency. The majority of the di-substituted oxazoles emitted at a similar range to the mono-substituted equivalents, as discussed in **Section 3.4.1.4.3**, however all had shorter emissive lifetimes. This, coupled with the photophysical data in **Chapter 2** suggesting that the quantum yields are also larger in the majority of cases, led to the postulation that the disubstituted oxazoles would yield a higher scintillation response, particularly as DPO (a disubstituted oxazole) appeared to dominate the energy pathway in the co-doped particles discussed in **Section 3.4.1.5.2**.

However, both **PS(8)@SiO$_2$** and **PS(10)@SiO$_2$** gave a lower scintillation efficiency than their mono-substituted equivalents, **PS(1)@SiO$_2$** and **PS(3)@SiO$_2$** respectively (**Figure 3.42**). In the presence of Sr-90, there was an ~3 and 13%

reduction in efficiency for **PS(8)@SiO$_2$** and **PS(10)@SiO$_2$** respectively compared to their mono-oxazole equivalents.

The reduction in efficiency was particularly noticeable in the presence of Ni-63. **PS(8)@SiO$_2$** and **PS(10)@SiO$_2$** gave scintillation efficiencies of 8.91x10^{-4} and 7.61x10^{-4}, compared to 0.00359 and 0.00369 for **PS(1)@SiO$_2$** and **PS(3)@SiO$_2$**, yielding an ~75 and 79% reduction in scintillation efficiencies respectively.

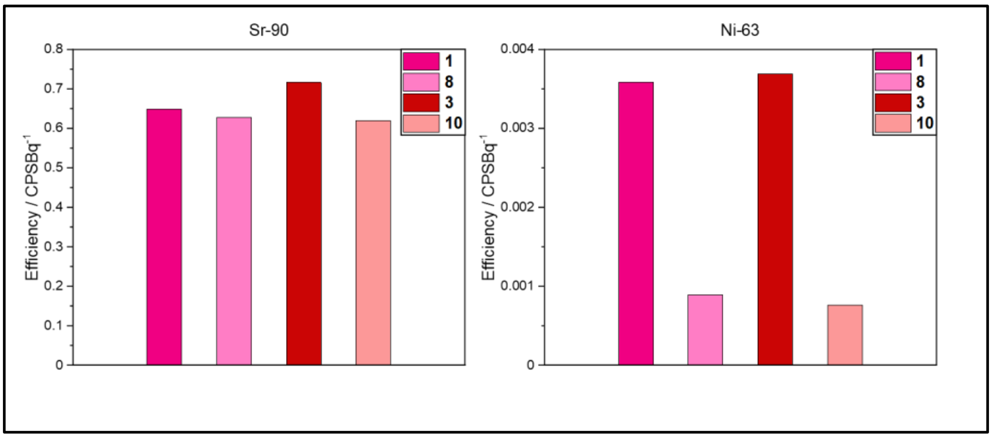

Figure 3.42 Scintillation efficiency of **PS(Ox)@SiO$_2$** (where Ox= **1, 3, 8, 10**) in the presence of Sr-90 (*left*) and Ni-63 (*right*). Counted for 30 minutes with 10 cycles completed in total.

What is also noticeable from the scintillation data is that the efficiency was found to be lower than that of the un-doped particle in the presence of Ni-63, shown in **Figure 3.38**, and only slightly higher than that of the undoped particles in the presence of Sr-90 (**Figure 3.36**). This was surprising, as even in the scintillation cocktails discussed in **Chapter 2**, the efficiency was still higher than that of the undoped cocktails. It may be due to a number of reasons, including low fluorophore concentration reducing the signal, or too high a fluorophore concentration leading to aggregation-based quenching. Quenching pathways brought about due to the fluorophore's more complex photophysics could also be a factor to consider, however investigations into this require further study. It is also notable to point out that these samples, as with cocktails doped with oxazoles **8** and **10** in **Chapter 2**, were recorded almost a year after synthesis (due to reasons outside of the authors control), and thus degradation may also be a factor.

3.4.1.6 Disposal of Samples

As discussed in **Chapter 2**, disposal of radioactive scintillant cocktails is one of the major issues both economically and environmentally in characterisation of low-level waste in the nuclear industry. However, the advantage of particles is that they can be removed from the aqueous sample *via* filtration or similar separating methods to be used again with a different sample.

Another advantage of polystyrene based particles is that the organic component can be combusted *via* heating, leaving only the silica shell. SEM and STEM imaging showed that by furnace heating at 700°C for 3 hours under compressed air, the polymer core was removed either by leaving the semi-porous silica shell intact or by breakage of the surface (**Figure 3.43**).

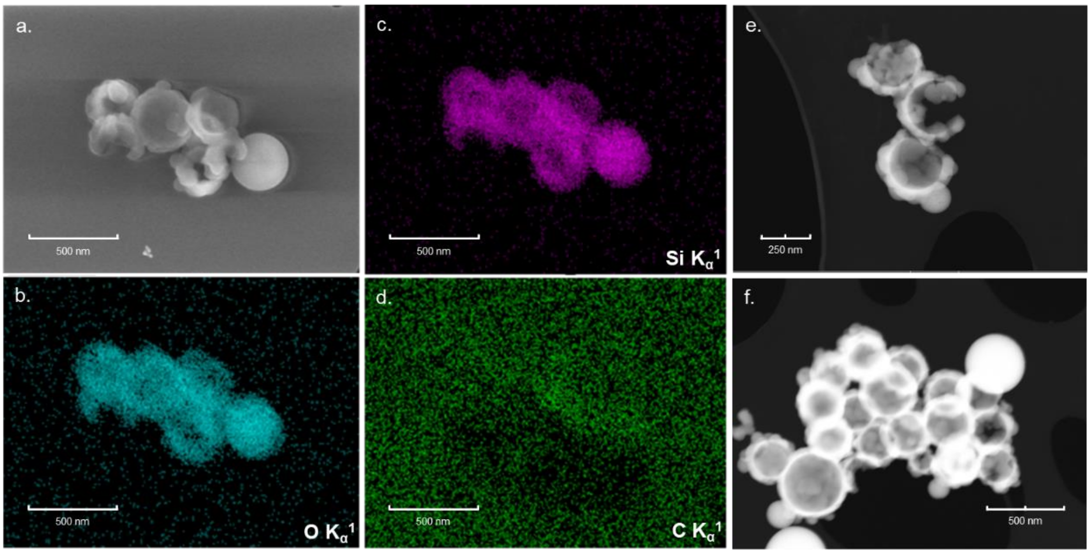

Figure 3.43 a) SEM and b,c,d) EDX images after furnace treatment of **PS(Ox)@SiO₂** showing the removal of the polystyrene core; e and f) STEM images showing both intact and broken silica spheres.

For unfunctionalized particles described within this chapter, pre-treatment may not be required, as the radionuclide is not believed to interact strongly with the surface. However, for functionalised particles discussed in **Chapter 4**, where radionuclides are believed to coordinate to the particle surface, pre-treatment involving a stronger chelator or a change in pH to strip the particles of radionuclides would be required prior to combustion.

3.5 Conclusion

A series of fluorescent particles were synthesised using a range of novel secondary scintillants, with evident core-shell structure as shown *via* microscopic techniques.

Scintillation studies of **PS(1-7)@SiO$_2$** in the presence of both a hard and soft emitter showed their ability to scintillate, as well as the need for proximity for softer emitters. This was evidenced by the more than 10-fold decrease of efficiency between scintillation in the presence of the hard beta emitter and soft beta emitter, thus suggesting the proximity effect could be used for radionuclide samples.

Although the efficiency was less than that of the microemulsion counterparts examined in **Chapter 2**, the benefits of reusability, disposal and lack of organic solvent make these a more environmentally friendly approach. Due to their ease of formation and ability to be made in bulk, they also have an economic advantage.

PS(8)@SiO$_2$ and **PS(10)@SiO$_2$** were also tested for their scintillation ability. Despite promising photophysical results compared to their mono-oxazole counterparts **PS(1)@SiO$_2$** and **PS(3)@SiO$_2$**, both performed poorly, particularly in the presence of Ni-63. It is however notable to point out that these samples were recorded almost a year after synthesis (due to reasons outside of the author's control).

Select systems were co-doped with a known primary scintillator, however unlike the oil-in-water microemulsions which showed the presence of energy transfer between the primary and secondary scintillants, the primary scintillator appeared to dominate the scintillation pathway and therefore these systems would not be viable.

Stability studies in the presence of Sr-90 for **PS(1-7)SiO$_2$** were similar to the microemulsion counterparts, showing less than a 1.2% change in scintillation efficiency, and so therefore are stable against hard radionuclides.

Future work should be focused on the measurement of the remaining particles containing di-substituted oxazoles, as well as repeat measurements of **PS(8)@SiO$_2$** and **PS(10)@SiO$_2$** to rule out degradation of the particles. It would also be prudent to record the scintillation efficiency of DPO doped particles so that a comparison can be made to those that are co-doped.

3.6 Experimental

3.6.1 Synthesis of the polystyrene microsphere[71]

Styrene (3.3 mL) was added to rapidly stirring, degassed H_2O (100 mL), heated to 75 °C under N_2. AIBA (10 mg) dissolved in H_2O (200 μL) was added, and the reaction mixture was heated at 75 °C for 5.5 hours with vigorous stirring *via* stirrer bar. Once cool, excess styrene was removed *in vacuo*, and small aliquots of the aqueous polystyrene mixture removed and lyophilized to determine mg/mL of nanoparticle solution. Polystyrene beads (14 mg/mL) were stored at room temperature in the dark until further use.

3.6.2 General procedure for encapsulation of fluorescent dyes, adapted from C. Janczak *et al*[71]

Oxazole (0.06 mmol) was dissolved in iPrOH:$CHCl_3$ (0.1:0.9 mL) and added to the aqueous polystyrene solution (5 mL). The reaction mixture was sonicated to disperse the organic droplets for 10 minutes, and then stirred rapidly for 3 hours under N_2, sonicating every hour for 10 minutes to re-disperse organic droplets. Organic solvents were removed *in vacuo* and the nanoparticle solution stored at 4°C in the dark until further use.

3.6.3 General procedure for silica coating, adapted from C. Janczak *et al*[71]

PS(Ox) (4 mL, approx. 56 mg of particles) was dispersed in iPrOH (200 mL), H_2O (38 mL), and NH_4OH (5 mL) under N_2. The reaction mixture was stirred rapidly with dropwise addition of TEOS (2 mL, 8.96 mmol) over several minutes, and then stirred for a further hour. After this time the nanoparticles were collected *via* centrifugation (30 minutes, 4.4 rpm), washed several times with water and ethanol until washings no longer fluoresced under a UV lamp, before being dried under vacuum in a desiccator to yield **PS(Ox)@SiO_2.**

3.6.4 General Procedure for Preparation of Nanoparticle Samples for Scintillation Studies

Particle samples were suspended in aqueous solution at a concentration of 0.02 % wt/v, before addition of radionuclide sample (Ni-63 (2.0 kBq/g) prepared in 0.1 mol dm^{-3} HCl, or Sr-90 (96.99 Bq/g) prepared in 1 mol dm^{-3} HNO_3). Sources contained 100 µg g^{-1} of inactive nickel and 50 µg g^{-1} inactive strontium and yttrium, respectively. Samples were agitated prior to analysis.

3.7 References

1. N. Bosworth and P. Towers, *Nature*, 1989, **341**, 167–168.
2. N. D. Cook, *Drug Discov. Today*, 1996, **1**, 287–294.
3. X. Khawaja, J. Dunlop and D. Kowal, *Expert Opin. Drug Discov.*, 2008, **3**, 1267–1280.
4. PerkinElmer, SPA Bead Technology, https://www.perkinelmer.com/lab-products-and-services/application-support-knowledgebase/radiometric/spa-beads.html, (accessed 13 May 2020).
5. S. Udenfriend, L. D. Gerber, L. Brink and S. Spector, *Proc. Natl. Acad. Sci. U. S. A.*, 1985, **82**, 8672–8676.
6. H. E. Hart and E. B. Greenwald, *J. Nucl. Med.*, 1979, **20**, 1062–1065.
7. FlashPlates PerkinElmer, https://www.perkinelmer.com/lab-products-and-services/application-support-knowledgebase/radiometric/flashplates.html, (accessed 15 May 2020).
8. J. J. Liu, D. S. Hartman and J. R. Bostwick, *Anal. Biochem.*, 2003, **318**, 91–99.
9. J. W. Wong, R. L. Albright and N.-H. L. Wang, *Sep. Purif. Methods*, 1991, **20**, 49–106.
10. E. Sulkowski, *BioEssays*, 1989, **10**, 170–175.
11. S. Sun, J. Almaden, T. J. Carlson, J. Barker and M. R. Gehring, *Metab. Eng.*, 2005, **7**, 38–44.
12. M. Gevi and E. Domenici, *Anal. Biochem.*, 2002, **300**, 34–39.
13. J. H. M. Cabral, A. P. Jackson, C. V. Smith, N. Shikotra, A. Maxwell and R. C. Liddington, *Nature*, 1997, **388**, 903–906.
14. D. B. Wigley, G. J. Davies, E. J. Dodson, A. Maxwell and G. Dodson, *Nature*, 1991, **351**, 624–629.
15. R. Macarrón, L. Mensah, C. Cid, C. Carranza, N. Benson, A. J. Pope and E. Díez, *Anal. Biochem.*, 2000, **284**, 183–190.
16. M. L. Carboneau and J. P. Adams, *National Low-Level Waste Management Program Radionuclide Report Series. Volume 10, Nickel-63*, U.S. Department of Energy Office of Scientific and Technical Information, 1995.
17. SciFinder Results for ‘Core Shell Particle’ Topic Search, https://scifinder.cas.org/scifinder/view/scifinder/scifinderExplore.jsf, (accessed 13 May 2020).

18. R. Ghosh Chaudhuri and S. Paria, *Chem. Rev.*, 2012, **112**, 2373–2433.
19. H. Chauhan, Y. Kumar and S. Deka, *Nanoscale*, 2014, **6**, 10347–10354.
20. R. Bardhan, S. Mukherjee, N. A. Mirin, S. D. Levit, P. Nordlander and N. J. Halas, *J. Phys. Chem. C*, 2010, **114**, 7378–7383.
21. V. Kulkarni, E. Prodan and P. Nordlander, *Nano Lett.*, 2013, **13**, 5873–5879.
22. L. Lin, H. Gu and J. Ye, *Chem. Commun.*, 2015, **51**, 17740–17743.
23. M. Fleischmann, P. J. Hendra and A. J. McQuillan, *Chem. Phys. Lett.*, 1974, **26**, 163–166.
24. C. Blanco-Andujar, D. Ortega, P. Southern, Q. A. Pankhurst and N. T. K. Thanh, *Nanoscale*, 2015, **7**, 1768–1775.
25. R. Purbia and S. Paria, *Nanoscale*, 2015, **7**, 19789–19873.
26. K. Kamata, Y. Lu and Y. Xia, *J. Am. Chem. Soc.*, 2003, **125**, 2384–2385.
27. J. Lee, J. C. Park and H. Song, *Adv. Mater.*, 2008, **20**, 1523–1528.
28. H. Choi, J.-P. Lee, S.-J. Ko, J.-W. Jung, H. Park, S. Yoo, O. Park, J.-R. Jeong, S. Park and J. Y. Kim, *Nano Lett.*, 2013, **13**, 2204–2208.
29. D. M. Fouad and M. B. Mohamed, *Nanotechnology*, 2011, **22**, 455705.
30. M. Bruchez Jr., *Science*, 1998, **281**, 2013–2016.
31. A. M. El-Toni, M. A. Habila, J. P. Labis, Z. A. ALOthman, M. Alhoshan, A. A. Elzatahry and F. Zhang, *Nanoscale*, 2016, **8**, 2510–2531.
32. T. Zhao, N.-T. Nguyen, Y. Xie, X. Sun, Q. Li and X. Li, *Front. Chem.*, 2017, **5**, 118.
33. S. Foglia, M. Ledda, D. Fioretti, G. Iucci, M. Papi, G. Capellini, M. G. Lolli, S. Grimaldi, M. Rinaldi and A. Lisi, *Sci. Rep.*, 2017, **7**, 46513.
34. J. Fokkema, J. Fermie, N. Liv, D. J. van den Heuvel, T. O. M. Konings, G. A. Blab, A. Meijerink, J. Klumperman and H. C. Gerritsen, *Sci. Rep.*, 2018, **8**, 13625.
35. B. K. Sodipo and A. A. Aziz, *J. Magn. Magn. Mater.*, 2016, **416**, 275–291.
36. M. A. Agotegaray and V. L. Lassalle, in *Silica-coated Magnetic Nanoparticles*, Springer International Publishing, NYC, 2017, pp. 9–26.
37. F. Ye, S. Laurent, A. Fornara, L. Astolfi, J. Qin, A. Roch, A. Martini, M. S. Toprak, R. N. Muller and M. Muhammed, *Contrast Media Mol. Imaging*, 2012, **7**, 460–468.
38. N. An, H. Lin, C. Yang, T. Zhang, R. Tong, Y. Chen and F. Qu, *Mater. Sci. Eng. C*, 2016, **69**, 292–300.
39. A.-H. Lu, E. L. Salabas and F. Schüth, *Angew. Chem. Int. Ed.*, 2007, **46**, 1222–1244.

40. S. Laurent, D. Forge, M. Port, A. Roch, C. Robic, L. Vander Elst and R. N. Muller, *Chem. Rev.*, 2008, **108**, 2064–2110.
41. M. Peng, H. Li, Z. Luo, J. Kong, Y. Wan, L. Zheng, Q. Zhang, H. Niu, A. Vermorken, W. Van de Ven, C. Chen, X. Zhang, F. Li, L. Guo and Y. Cui, *Nanoscale*, 2015, **7**, 11155–11162.
42. T. T. Dung, T. M. Danh, L. T. M. Hoa, D. M. Chien and N. H. Duc, *J. Exp. Nanosci.*, 2009, **4**, 259–267.
43. I. Brigger, C. Dubernet and P. Couvreur, *Adv. Drug Deliv. Rev.*, 2002, **54**, 631–651.
44. C.-F. Lee, M.-L. Hsu, C.-H. Chu and T.-Y. Wu, *J. Polym. Sci. Part Polym. Chem.*, 2014, **52**, 3441–3451.
45. A. K. Khan, B. C. Ray and S. K. Dolui, *Prog. Org. Coat.*, 2008, **62**, 65–70.
46. W.-H. Li and H. D. H. Stöver, *Macromolecules*, 2000, **33**, 4354–4360.
47. M. D. Besteti, F. G. Souza, D. M. G. Freire and J. C. Pinto, *Polym. Eng. Sci.*, 2014, **54**, 1222–1229.
48. C. D. Jones and L. A. Lyon, *Macromolecules*, 2003, **36**, 1988–1993.
49. M. Gosecka and M. Gosecki, *Colloid Polym. Sci.*, 2015, **293**, 2719–2740.
50. X. Zhou, H. Shao and H. Liu, *Colloid Polym. Sci.*, 2013, **291**, 1181–1190.
51. D. Sarma, K. Gawlitza and K. Rurack, *Langmuir*, 2016, **32**, 3717–3727.
52. F. Caruso, H. Lichtenfeld, M. Giersig and H. Möhwald, *J. Am. Chem. Soc.*, 1998, **120**, 8523–8524.
53. F. Caruso, *Science*, 1998, **282**, 1111–1114.
54. C. Graf, D. L. J. Vossen, A. Imhof and A. van Blaaderen, *Langmuir*, 2003, **19**, 6693–6700.
55. J. Hong, H. Han, C. K. Hong and S. E. Shim, *J. Polym. Sci. Part Polym. Chem.*, 2008, **46**, 2884–2890.
56. M. Chen, S. Zhou, B. You and L. Wu, *Macromolecules*, 2005, **38**, 6411–6417.
57. Z. Qian, Z. Zhang, L. Song and H. Liu, *J. Mater. Chem.*, 2009, **19**, 1297.
58. D.-Y. Kim, S. H. Jin, S.-G. Jeong, B. Lee, K.-K. Kang and C.-S. Lee, *Sci. Rep.*, 2018, **8**, 8525.
59. L. Feng, S. Li, Y. Li, H. Li, L. Zhang, J. Zhai, Y. Song, B. Liu, L. Jiang and D. Zhu, *Adv. Mater.*, 2002, **14**, 1857–1860.
60. X. Du, X. Liu, H. Chen and J. He, *J. Phys. Chem. C*, 2009, **113**, 9063–9070.
61. X. Liu, X. Du and J. He, *ChemPhysChem*, 2008, **9**, 305–309.
62. W. Stöber, A. Fink and E. Bohn, *J. Colloid Interface Sci.*, 1968, **26**, 62–69.

63. PlumX Metrics for ‘Controlled Growth of Monodisperse Silica Spheres in the Micron Size Range’, https://plu.mx/plum/a/?doi=10.1016/0021-9797(68)90272-5&theme=plum-sciencedirect-theme&hideUsage=true.
64. L. M. Rossi, L. Shi, F. H. Quina and Z. Rosenzweig, *Langmuir*, 2005, **21**, 4277–4280.
65. P. P. Ghimire and M. Jaroniec, *J. Colloid Interface Sci.*, 2021, **584**, 838–865.
66. F. Dong, H. Xie, Q. Zheng and C.-S. Ha, *RSC Adv.*, 2017, **7**, 6685–6690.
67. Y. Han, Z. Lu, Z. Teng, J. Liang, Z. Guo, D. Wang, M.-Y. Han and W. Yang, *Langmuir*, 2017, **33**, 5879–5890.
68. M. A. Bourebrab, D. T. Oben, G. G. Durand, P. G. Taylor, J. I. Bruce, A. R. Bassindale and A. Taylor, *J. Sol-Gel Sci. Technol.*, 2018, **88**, 430–441.
69. S. A. Dunbar, *Clin. Chim. Acta*, 2006, **363**, 71–82.
70. J. P. Nolan and L. A. Sklar, *Trends Biotechnol.*, 2002, **20**, 9–12.
71. C. M. Janczak, I. A. C. Calderon, Z. Mokhtari and C. A. Aspinwall, *ACS Appl. Mater. Interfaces*, 2018, **10**, 4953–4960.
72. B. Liu, Y. Wang, M. Zhang and H. Zhang, *Polymers*, 2016, **8**, 55.
73. K. Panwar, M. Jassal and A. K. Agrawal, *Particuology*, 2015, **19**, 107–112.
74. W.-C. Liaw, Y.-L. Cheng, M.-K. Chang, W.-F. Lien and H.-R. Lai, *Polym. J.*, 2016, **48**, 91–99.
75. X. Fan, L. Zheng, J. Cheng, S. Xu, X. Wen, Z. Cai, P. Pi and Z. Yang, *Surf. Coat. Technol.*, 2012, **213**, 90–97.
76. What is Kubelka-Munk, https://mmrc.caltech.edu/FTIR/Literature/Diff%20Refectance/Kubelka-Munk.pdf, (accessed 19 November 2021).
77. S. Chakraborty, K. Harris and M. Huang, *AIP Adv.*, 2016, **6**, 125113.
78. D. S. Karpovich and G. J. Blanchard, *J. Phys. Chem.*, 1995, **99**, 3951–3958.
79. K. Hara and W. R. Ware, *Chem. Phys.*, 1980, **51**, 61–68.
80. A. Nakajima, *Bull. Chem. Soc. Jpn.*, 1971, **44**, 3272–3277.
81. G. K. Bains, S. H. Kim, E. J. Sorin and V. Narayanaswami, *Biochemistry*, 2012, **51**, 6207–6219.
82. Spectrum [Polystyrene] | AAT Bioquest, https://www.aatbio.com/fluorescence-excitation-emission-spectrum-graph-viewer/polystyrene, (accessed 20 November 2021).
83. T. Li, C. Zhou and M. Jiang, *Polym. Bull.*, 1991, **25**, 211–216.

84. I. Ghosh, A. Mukhopadhyay, A. L. Koner, S. Samanta, W. M. Nau and J. N. Moorthy, *Phys. Chem. Chem. Phys.*, 2014, **16**, 16436–16445.
85. G.-J. Zhao and K.-L. Han, *J. Phys. Chem. A*, 2007, **111**, 9218–9223.
86. K. Yoshihara and D. R. Kearns, *J. Chem. Phys.*, 1966, **45**, 1991–1999.
87. Livechart - Table of Nuclides - Nuclear structure and decay data, https://nds.iaea.org/relnsd/vcharthtml/VChartHTML.html, (accessed 5 April 2021).

4 Surface Functionalisation of Nanoparticles: Towards Element Specificity

4.1 Overview

The aim of the following chapter was to surface functionalise scintillant nanoparticles synthesised in **Chapter 3** with TMS-EDTA, a commercially available silyl-modified metal chelator. By functionalising with a chelating agent such as EDTA, it was hoped that Ni-63 could be sequestered by the particles, and possibly lead to an increase in scintillation efficiency, thus demonstrating the need for proximity with weak beta emitters. Functionalisation of scintillant particles could pave the way for further explorations using metal-specific chelators, leading to element specific systems. For example, a range of different functionalised particles could be added to a sample with the different radionuclides resolved *via* their emission spectra. Alternatively a cartridge of one type of metal specific particle could lead to element specific sequestration and analysis of one radionuclide from a complex mixture.

4.2 Surface Functionalisation: Methods and Uses

The functionalisation of nanoparticles is well established, with a variety of different applications including those in biology, such as drug delivery[1,2] and bioimaging[3,4], and those in catalysis, such as the functionalisation with inorganic catalysts[5] or organic moieties for tandem reactions[6]. However, another use of functionalised nanoparticles is in the sequestering of metal cations in waste-water from a range of different industries, including mining, paper and pesticides[7]. Due to its relevance with the work herein, focus will be on the functionalisation of nanoparticles for this use.

There is already a range of different techniques in use for the sequestering of metal cations in waste-streams.[8] Chemical precipitation is the process of allowing the metal cations to precipitate as hydroxides or sulfides, and has the advantages of being suitable for high concentrations of metal ions and is relatively inexpensive, unlike other techniques with high initial costs.[7] However, other contaminants in the waste-water (such as chelators) can stop precipitation, and the precipitates can form a “sludge” as with other methods, which is harder to separate from the bulk liquid. As well as this, the use of sulfide precipitation requires strict pH control to avoid the formation of H_2S fumes. Coagulation-flocculation is more advantageous than chemical precipitation as the sludge is easier to remove, however the volume of sludge is higher.[7] Ion exchange and membrane filtration both suffer with high cost due to resins and membranes requiring regeneration or replacement and overall high running cost.[8] Electrochemical and flotation methods are also used however they have the disadvantage of high initial cost, as well as maintenance[8]. Despite this, the flotation technique has a high selectivity and efficiency, and electrochemical methods are rapid and produce less sludge.[7] Lastly, the adsorption technique, of which functionalised particles is based on, can be used for low metal concentrations. However, the efficiency is entirely reliant on the adsorbent used[7] of which some, such as activated carbon, are expensive. There has been some advancement in adsorption with the use of biological adsorbents including bacteria[9] and algae[10], however for the purpose of this work, only silica-containing constructs will be discussed.

When designing a synthetic route for surface functionalisation, there are three different interactions to consider; covalent bond formation with the particle surface using alkoxysilanes, physical adsorption, and electrostatic interaction between a charged surface and an oppositely charged substrate[11], of which there are advantages and disadvantages for each. Adsorption and electrostatic functionalisation are used predominantly with biological functionalisation, for the incorporation of charged species such as antibodies and proteins. However, these interactions are pH, ionic strength and concentration dependent, which may prove advantageous in drug delivery, but can be considered “unstable” across a broad pH range.[11] Covalent bond formation on the other hand is far less directed by these factors, however suffers from steric hindrance if the particles are over-loaded. Despite this, covalent bond formation is common due to well-known silyl chemistry and a wide range of commercially available alkoxy silanes which can be used independently or further functionalised.

4.2.1 Functionalised Mesoporous Silica

One of the most extensive studies using functionalised particles in waste-water sequestration is the use of mesoporous silica. Mesoporous silica are low cost silica constructs with high surface area and uniform pore size[12], formed *via* a templating agent that directs the silica polymerisation[13], of which a simplified schematic is shown in **Figure 4.1**. The particle size and overall morphology of the constructs can be controlled in the usual ways of silica growth such as pH, however the pore size is controlled by the template, additives and co-solvents[13,14]. One of the more popular examples is SBA-15, a 2D hexagonal construct with pore sizes between 46-300 Å[15] and shown in **Figure 4.1**.

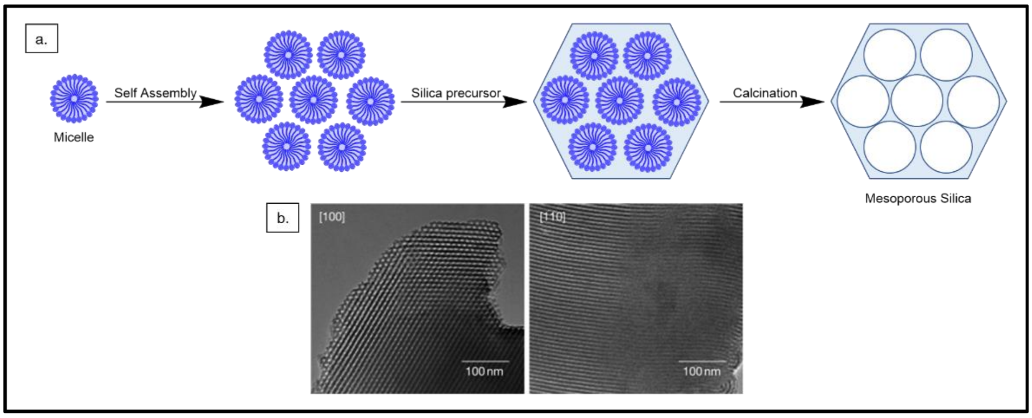

Figure 4.1 a) Schematic of mesoporous silica formation; b) TEM images of 2D SBA-15 along [100] and [110] planes, taken from T. Kimura *et al*[16].

Functionalised SBA-15 has been studied extensively for its use in metal sequestration, with primary examples utilising di-, tri- and tetra-amine metal chelators such as triethylenetetramine (TETA), ethylenediaminetetraacetic acid (EDTA) and diethylenetriamine pentaacetate (DTPA) shown in **Figure 4.2**, of which will be discussed below. Although mesoporous silica was not used in the work herein, the functionalisation of such constructs and the consequent adsorption properties are useful to analyse and understand as the same surface modification can be applied to particles.

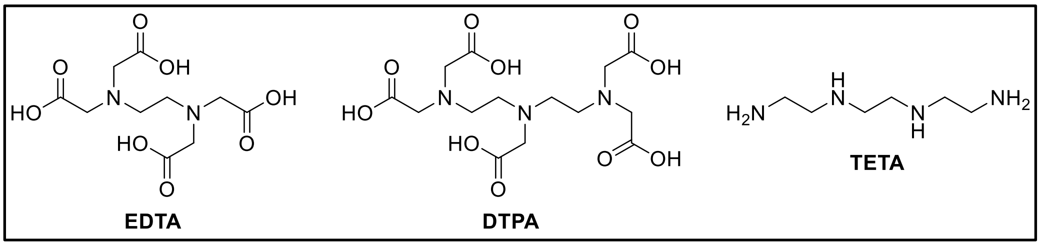

Figure 4.2 EDTA, DTPA and TETA are all commonly used chelators in metal sequestration.

An example of such functionalisation is provided by J. Lachowicz *et al*[12] who utilised triethylenetetramine (TETA) functionalised SBA-15 for the sequestration of Cu^{2+} and Zn^{2+}, commonly found in mine water. The silica surface was coated using a method by Mahmoud *et al*[17], who used a two-step approach shown in **Figure 4.3**. Firstly, the hydroxy-silica surface was modified with (3-chloropropyl)trimethoxysilane (CPTMS) *via* refluxing with toluene overnight. SBA-

Cl was then isolated, and again refluxed in toluene overnight with triethylenetetramine (TETA) to form SBA-TETA, with IR spectroscopy showing the presence of TETA on the particle surface with an NH_2 bend at 1650 cm^{-1} (**Figure 4.3**).

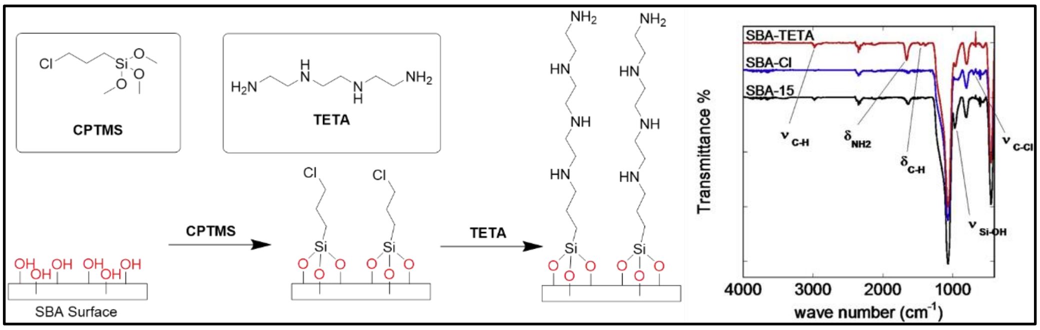

Figure 4.3 *Left:* Reaction scheme showing functionalisation of silica surface with CPTMS, followed by TETA addition, adapted from J. Lachowicz *et al*[12]; *Right:* IR spectra showing successful functionalisation with CPTMS and TETA, taken from J. Lachowicz *et al*[12].

Adsorption studies of these particles were carried out in the presence of Cu^{2+} and Zn^{2+} at pH 4 to avoid metal hydroxide formation. Although adsorption of Zn^{2+} was faster than that of Cu^{2+} (taking 3 and 8 hrs respectively to reach equilibrium), once equilibrium was reached twice the amount of Cu^{2+} was bound. Therefore, this showed that TETA on the particle surface had a great affinity to Cu^{2+}, which was confirmed in the literature for the free ligand[18].

Y. Shirashi *et al*[19] studied the adsorption differences between three different types of adsorbents; a silica gel, a mesoporous molecule sieve (MCM-41) and aluminium oxide, all functionalised with either EDTA and DTPA. In their work, they also used a two-step approach for surface functionalisation, shown in **Figure 4.4**, however (3-aminopropyl)triethoxysilane (APTES) was used to first functionalise the hydroxy surface instead of CPTES, forming primary amine groups on the surface. In the second step EDTA-anhydride was added with ethanol and acetic acid, to yield an EDTA functionalised surface, which was confirmed *via* IR spectroscopy showing a characteristic amide stretch between 1650-1700 cm^{-1}.

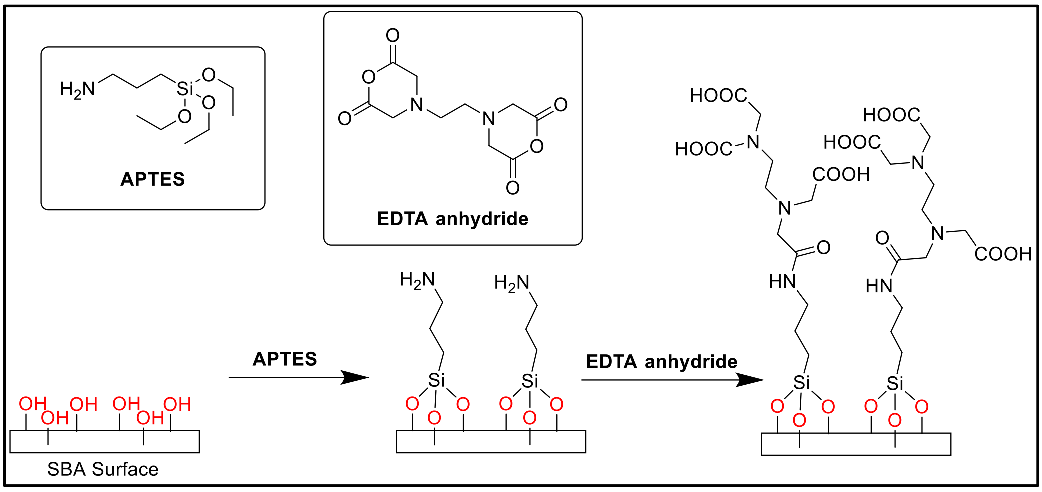

Figure 4.4 Reaction scheme showing the functionalisation of the SBA surface with APTES, followed by the addition of EDTA-anhydride to give EDTA-functionalised SBA, adapted from Y. Shirashi *et al*[19].

Adsorption studies showed that as the pH increased, the ability of the surface-ligand to sequester metal ions decreased, unlike the ligand free in solution, which they suggested was due to electrostatic interactions between the particle surface and the EDTA ligand (however, metal hydroxide formation at high pH could not be discounted) and so experiments were performed in aqueous HCl solution. Of the adsorbents tested, silica gel functionalised with EDTA (silicaED) performed the best, and was found to be able to separate Cu^{2+} from Ni^{2+}, VO^{2+}, Zn^{2+}, Co^{2+}, and Mn^{2+}, as well as VO^{2+} and Ni^{2+} from Mn^{2+}, Co^{2+} and Zn^{2+} *via* varying the pH of the solution. The increased adsorption of silicaED was thought to be due to a larger amount of EDTA on the surface compared with MCM-41 and aluminium oxide, which was confirmed *via* elemental analysis. It was found that there were more DTPA units on the adsorbent surface, however metal binding was not as successful compared to EDTA, unlike in solution where DTPA-metal complexes have a higher stability constant than EDTA complexes. As DTPA is a larger chelate unit, it was hypothesised that this was due to steric hindrance on the surface. Reusability of silicaED was tested *via* stripping bound metals from the surface with 1 M HCl and then repeating the adsorption process, showing no change in the amount absorbed.

For the nature of the work herein, the stability of the sequestering moiety in the presence of radiation is of utmost importance to allow longevity and reproducibility of scintillation results. S. Iqbal *et al*[20] synthesised EDTA-functionalised mesoporous silica for the adsorption of metal cations formed during the corrosion of nuclear reactor coolants, with particular interest in the adsorbent's stability in the presence of gamma radiation. As in previous examples, the SBA-15 surface was first functionalised with APTES under reflux in toluene, however an extra purification step using Soxhlet extraction was utilised. Instead of EDTA-anhydride being used, $SOCl_2$ was used to form acyl-chlorinated EDTA from EDTA, which was then reacted with the amine-functionalised SBA-15, to form EDTA-SBA-15 (**Figure 4.5**).

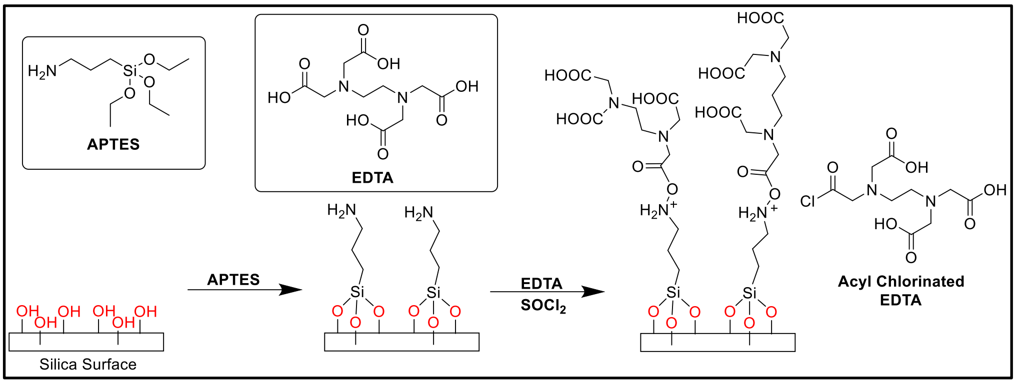

Figure 4.5 Reaction scheme showing the functionalisation of the SBA surface with APTES, followed by the addition of EDTA and $SOCl_2$ to yield EDTA-functionalised SBA *via* acyl-chlorinated EDTA, adapted from S. Iqbal *et al*[20].

The pH was varied to find the optimum conditions (**Figure 4.6a**), and it was found that a pH of 2.5 prevented metal hydroxide formation and silica leaching, as well as preventing protonation of the amine moieties and so was used for further measurements.

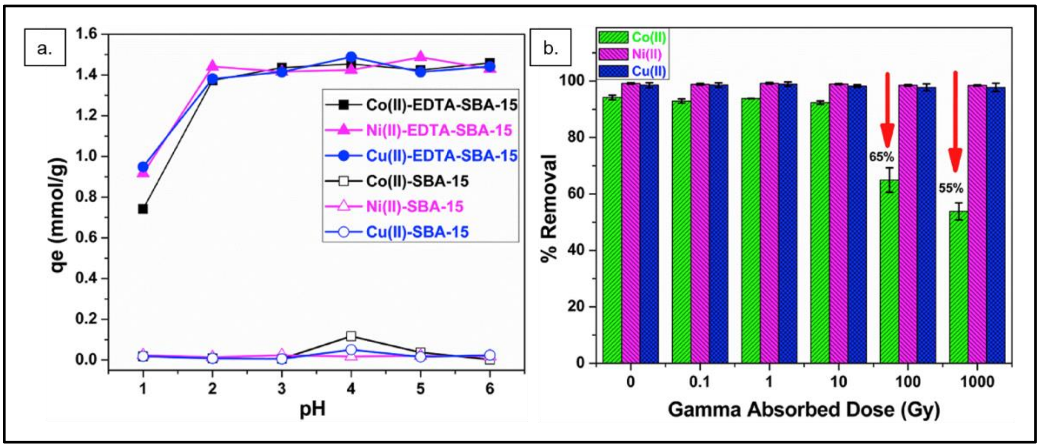

Figure 4.6 a) pH dependency of adsorption of metal ion (qe), also showing enhanced adsorption of EDTA functionalised SBA-15 *vs* SBA-15; b) Effect of gamma irradiation on metal-sequestration at pH 2.5, taken from S. Iqbal *et al*[20].

The stability and effectiveness of EDTA-SBA-15 in the presence of gamma radiation was tested up to 1000 Gy (1000 J kg^{-1}), and showed that up to 10 Gy, more than 95% sequestration was observed for Cu^{2+}, Ni^{2+} and Co^{2+} (**Figure 4.6b**). Between 10–1000 Gy, the sequestration of Cu^{2+} and Ni^{2+} remained relatively unchanged, with the biggest drop being in the chelation of Co^{2+}. This latter decrease is said to be due to the chemical deposition of EDTA in the presence of gamma radiation, which was shown by K. Krapfenbaur *et al*[21] to degrade into CO_2, N,N'-methylacetylethylenediamine, N-hydroxy methyliminodiacetic acid, ammonia and iminodiacetic acid when exposed to 6 kGy of gamma radiation. Despite this, and as mentioned in the work of Iqbal,[20] the pipes in which the corrosion products are formed are exposed to 0.1-0.2 Gy/hr and therefore much less than the doses given in both Iqbal's work and the degradation dose.

4.2.2 Functionalised Silica Nanoparticles

Although functionalised mesoporous silica has been the subject of much research for waste water treatment and gives insight into various functionalisation synthetic strategies, due to the nature of the work herein it is of importance to examine the use of particles, particularly core shell constructs, that also have use in sequestration of metal ions.

Much like Y. Shirashi *et al*[19], who as described previously examined the differences in absorption ability of two different chelators and a range of substrates, P. Shao *et al*[22] examined a range of different commercially available alkoxysilanes (**Figure 4.7**) for their metal binding ability.

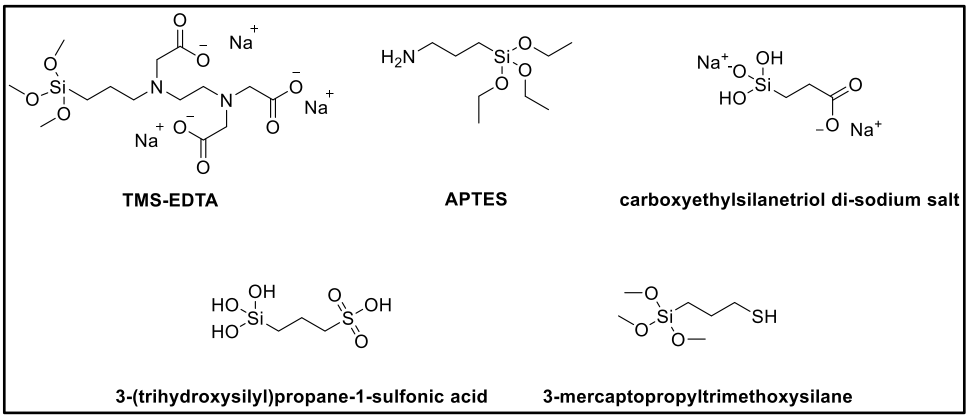

Figure 4.7 Alkoxysilanes used to functionalise the silica surface by P. Shao *et al*[22].

The functionalisation was performed at reflux for 12 hrs, however the solvent used varied dependent on alkoxysilane used; for APTES ethanol was used, however for TMS-EDTA and 3-(trihydroxysilyl)propane-1-sulfonic acid toluene was used as solvent. For 3-mercaptopropyltrimethoxysilane and carboxyethylsilanetriol di-sodium salt, a mixture of methanol, DMF and water was used in a 55:15:2 ratio. It should also be noted that unlike previous methods described for EDTA functionalisation, in which a two-step approach was utilised, TMS-EDTA was used directly on the silica surface. Successful functionalisation was confirmed *via* EDS and XPS analysis, as well as TGA to calculate the amount of chelator bound to the surface. Despite EDTA-functionalised particles showing the least functionalisation, they in fact exhibited the highest adsorption of Pb^{2+}, and also the highest selectivity for Pb^{2+} when in a mixture of different metal ions (Pb^{2+}, Cu^{2+}, Ni^{2+}, Zn^{2+}, and Cd^{2+}) as shown in **Figure 4.8a**. P. Shao also found that increasing the pH between 3-7 increased the adsorption of Pb(II) for EDTA-functionalised particles (**Figure 4.8b**), unlike previous reports using acidic conditions to prevent metal hydroxide formation. Although metal hydroxide formation is more prevalent at pH 7, the chelation of Pb(II) to EDTA is dominant due to the full deprotonation of the EDTA carboxylate groups.

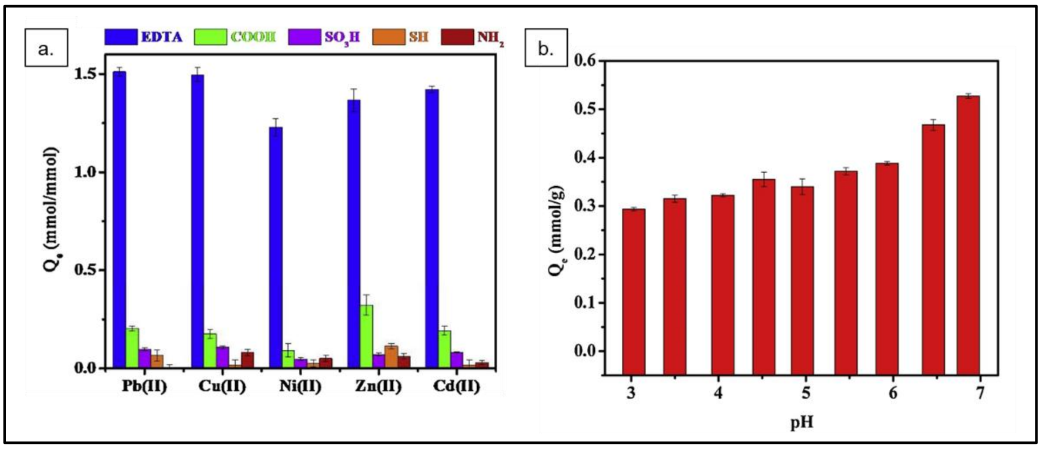

Figure 4.8 a) Normalised adsorption capacity, with respect to number of groups grafted to surface, for a range of metal ions; b) pH dependency of adsorption capacity of Pb^{2+} for EDTA functionalised particles, taken from P. Shao *et al*[22].

The results reviewed thus far suggest that EDTA is by far the most suitable chelating agent for sequestration of metal ions, even providing some level of selectivity dependent on conditions. D. Dupont *et al*[23] used EDTA as the chelating agent whilst evaluating the differences between three different particle structures; SPIONs (Super Paramagnetic Iron Oxide Nanoparticles consisting of Fe_3O_4), SiO_2 nanoparticles and TiO_2 nanoparticles, and their ability to change the sequestration of certain metal ions due to steric crowding on the particle surface. SPIONs have the added advantage of being able to be magnetically separated from the bulk solution and thus easier to reuse, however they also suffer from lack of stability and are prone to aggregation[24]. To covalently attach EDTA to the particle surface, TMS-EDTA was utilised in a one-step reaction using methanol as solvent and acetic acid as catalyst for the silyl-polymerisation. Functionalisation was confirmed *via* IR spectroscopy, and the amount of EDTA groups on the surface was calculated *via* both TGA and CHN elemental analysis, showing that silica particles had the largest density of EDTA, followed by TiO_2 and lastly Fe_3O_4 particles. By measuring the adsorption across a broad pH range, they found that as the pH increased so did the adsorption of Gd^{3+} due to the deprotonation of the EDTA carboxylate groups. However, as the pH was increased the formation of metal hydroxide complexes also increased, and so the optimum pH was found to be 6.5 (**Figure 4.9a**). Due to the larger content of EDTA on the surface, the adsorption of Gd^{3+} was highest with SiO_2 particles and lowest for Fe_3O_4. The stability of the particles through a range of pH values was also tested, and it was found that all particles were stable between a pH of 2.5-10, allowing metals to be stripped from the surface at pH 2.75 with no loss of stability of the particles for further adsorption experiments (**Figure 4.9b**). Selectivity studies were carried out with a range of different lanthanide ions (**Figure 4.9c**), with silica particles showing better selectivity for smaller ions due to the denser EDTA coating on the surface causing unfavourable steric hindrance for larger metal ions. Although TiO_2 and Fe_3O_4 particles showed the same pattern, it was by far the most notable for SiO_2-EDTA particles, and thus despite the magnetic advantages of Fe_3O_4 particles, SiO_2 particles showed both the highest adsorption and the best selectivity between small and large lanthanide ions.

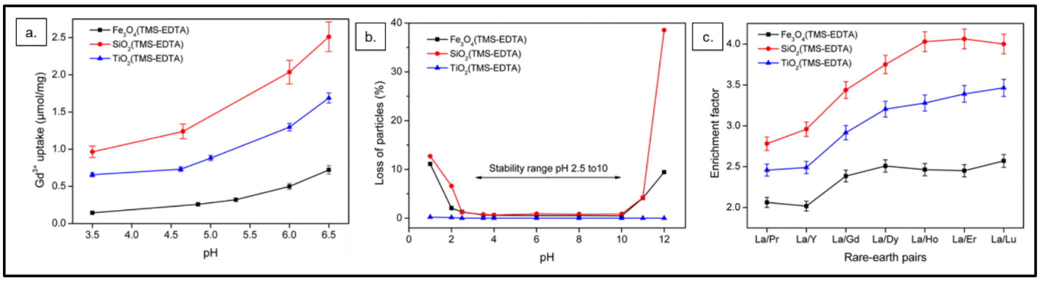

Figure 4.9 a) pH dependency of Gd^{3+} adsorption; b) pH dependency of particle stability and c) separation of $La^{3+}/L_n{}^{3+}$ pairs at pH 6.5, for EDTA-functionalised Fe_3O_4, SiO_2, and TiO_2, taken from D. Dupont *et al*[23].

Following from these results, D. Dupont *et al*[25] continued this work by analysing Fe_3O_4 core-silica shell particles functionalised with EDTA, to provide the advantages of the SPION core and the dense EDTA layer brought about by the use of a silica shell. As with previous work, adsorption was measured at a range of pH values, with pH 6 showing optimum adsorption of Nd^{3+}, above which precipitation of $Nd(OH)_3$ occurred (**Figure 4.10a**). The stability range of the core-shell constructs was larger compared to SPIONs or silica particles, with a lower pH limit of 1.5 giving a metal stripping efficiency of 94%. The core-shell particles also showed selectivity based on metal ion size (**Figure 4.10b**), as with the silica-EDTA particles in the previous work, due to the steric hindrance of the EDTA groups on the particle surface.

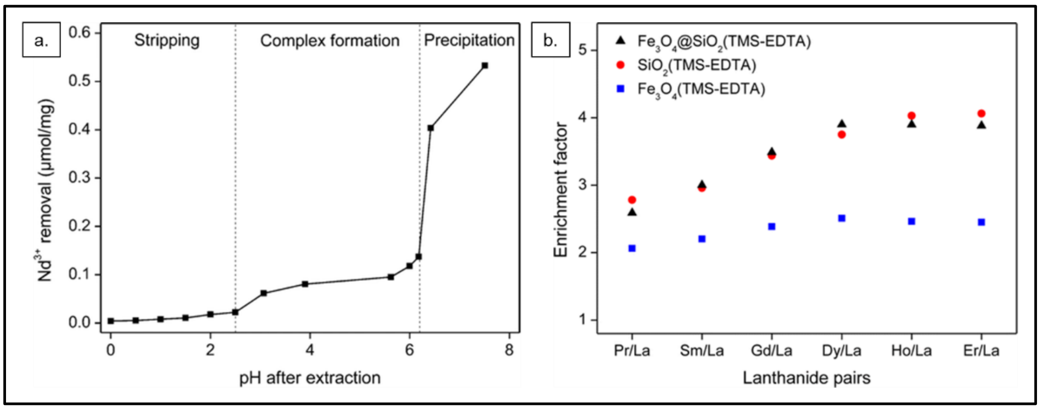

Figure 4.10 a) pH dependency on removal of Nd^{3+} from solution in the presence of $Fe_3O_4@SiO_2$(TMS-EDTA), with removal above 6 being due to precipitation of $Nd(OH)_3$; b) Separation of La^{3+}/Ln^{3+} pairs at pH 6.0 for $Fe_3O_4@SiO_2$(TMS-EDTA), compared with SiO_2(TMS-EDTA) and Fe_3O_4(TMS-EDTA) from previous studies[23]. Taken from D. Dupont *et al*[25].

A very recent example of $Fe_3O_4@SiO_2$ core-shell particles functionalised with EDTA is that of N. Kobylinska *et al*[26], who used core-shell particles to sequester metal ions in waste water and then stripped them into fresh solution to “pre-concentrate” the ions, allowing more accurate determination of metal ion concentration using ICP-OES. Core-shell particles were functionalised using TMS-EDTA, much like work by D. Dupont *et al*[23,25], however the reaction was carried out at reflux in a water:methanol solution of 1:1 ratio, instead of acidic conditions, and as in all other examples confirmed *via* IR spectroscopy. Elemental analysis was also employed to determine the number of EDTA groups on the surface, which was found to be 0.53 mmol g^{-1}. As with previous studies, the particles were found to be stable over a large pH range, ranging between 1-8.5, and shown *via* comparison to be far more stable than bare Fe_3O_4. Unlike other studies, N. Kobylinska also analysed the effects of the sample matrix in metal adsorption by looking at the effect of common pollutants found in waste water. Both organic (humic acid) and inorganic (Na$^+$, Ca^{2+}, K$^+$ *etc*.) pollutants caused relatively little difference in metal-uptake. Even competing ions, such as Fe^{3+} and Mg^{2+}, which form EDTA complexes did not affect the metal uptake, as the optimum pH for metal adsorption lies within the range that the counter ions form hydroxide species. To further remove Fe^{3+} from the final eluent solution, NH_4F (a masking agent of NaOH) was added prior to removal of particles from the bulk sample. The particles were tested against real-world environmental and tap water samples that were spiked with different concentrations of metals to be analysed, and were found to be suitable for the preconcentration of trace metal ions (with a recovery over 94%), which could then be analysed successfully by ICP-OES.

By reviewing the previous work, it can be clearly shown that EDTA could be used to successfully bring radionuclides closer to the nanoparticle surface, thus potentially increasing the scintillation response observed by the particle in the presence of soft beta emitters, and allowing sequestration of the radionuclide. As well as this it could be regenerated for further analysis *via* change in sample conditions. The ease of synthesis (either using a two-step approach or TMS-EDTA) and stability across a range of pH values mean that EDTA was identified as the candidate for a proof of concept study in the enhancement of the scintillation signal.

4.3 Results and Discussion

4.3.1 Synthesis

For the initial proof-of-concept study on the proximity effect for nanoparticles synthesised in **Chapter 3**, functionalisation of the particle surface with an EDTA-based chelator was attempted. The reasoning behind this decision was three-fold; firstly, EDTA (**Figure 4.11**) is an industrially used nickel chelator, used in industrial, medicinal, cosmetic and laboratory settings, and therefore was ideal to test the proximity theory in terms of Ni-63; secondly, EDTA can also chelate to many other commonly found metals in low level waste, including Co, Cu, and Ca, and thus competition studies could be performed; and lastly, TMS-EDTA (**Figure 4.11**) is a commercially available silyl-based agent, making it potentially applicable to a larger scale industry setting. As discussed earlier, these reasonings were further confirmed by the extensive literature on the use of EDTA for metal sequestration in waste-water.

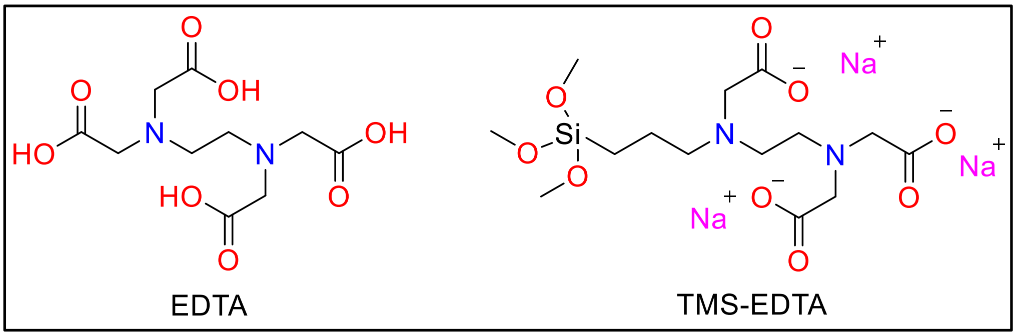

Figure 4.11 Ethylenediaminetetraacetic acid (EDTA) and TMS-EDTA, where one carboxylate is replaced with a silyl-linker.

As discussed in **Section 4.2**, functionalisation of the silica surface is well known, with a variety of methods available to yield a range of different properties. However, the work-up for some of these methods (frequently filtering without excessive washing) casts doubt over whether there has been a genuine covalent surface interaction, an electrostatic interaction, or more simply a mixture of particles and unreacted silyl-agent. Many of the methods for functionalisation described in **Section 4.2** utilise toluene as solvent, however this is incompatible with the polystyrene core of the nanoparticles used herein, leading to leaching of fluorophore and styrene and therefore not viable in the system chosen.

Inspired by the work of D. Dupont *et al*[23,25], who functionalised Fe_3O_4@SiO_2 and SiO_2 particles with TMS-EDTA utilising acidic conditions (to both catalyse silyl-group polymerisation and deprotonation of the particle surface), **PS(Ox)@SiO_2** were sonicated for 4 hours with TMS-EDTA added halfway through reaction time with acetic acid. The resultant particles were filtered, instead of precipitated, and washed with water and acetone. Upon analysis, no functionalisation was observed *via* IR spectroscopy where it would be expected to find symmetric and asymmetric carboxyl stretches between 1400-1600 cm^{-1} , associated with the carboxylic acid of the EDTA chelator [23]. It should be noted that acetone could partially dissolve the polystyrene and cause leaching of the fluorophore, however this would not cause a lack of functionalisation of the silica surface.

Protocols in Bioconjugate Techniques[27] discuss how functionalisation of the silica surface first yields hydrogen bond formation, which then requires a curing step to cause condensation at the particle surface and lead to covalent bond formation **(Figure 4.12).** Without this step, the silyl agent can easily leave the particle surface, particularly after excessive centrifugation and sonication, thus giving unfunctionalized particles after drying.

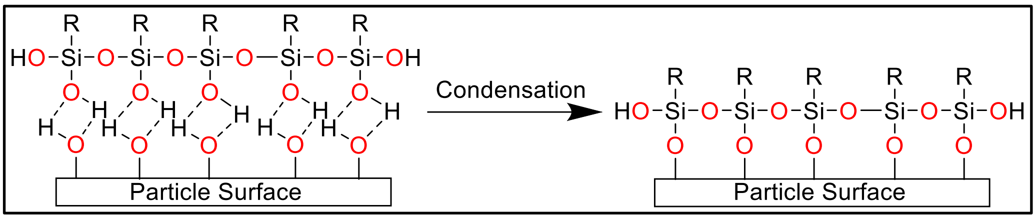

Figure 4.12 Surface functionalisation is reported to require a condensation step, aided by curing, to form covalent bonds between the surface and silyl-functionalised chelator. Adapted from Bioconjugate Techniques[27].

With this in mind, a second method was investigated from Bioconjugate Techniques[27]. This alternative method did not require the use of sonication and added the particles to an acidic mixture of the functional silane, followed by oven curing after stirring overnight. However, this method proved unsuccessful as the TMS-EDTA polymerised far too quickly in the acidic media before the particles could be added, evidenced by the cloudy and incredibly viscous solution that formed almost instantly upon introduction of TMS-EDTA. This was repeated, instead suspending the nanoparticles in the acidic ethanol and then adding TMS-EDTA, however this also proved unsuccessful with no evidence of functionalisation after curing.

It became evident that the surface of the particles may not be as reactive as expected. Therefore surface functionalisation was attempted in the same step as surface coating of the polystyrene beads in the hope that a mixture of both TEOS and TMS-EDTA would co-polymerise at the polystyrene core under basic conditions (**Figure 4.13**).

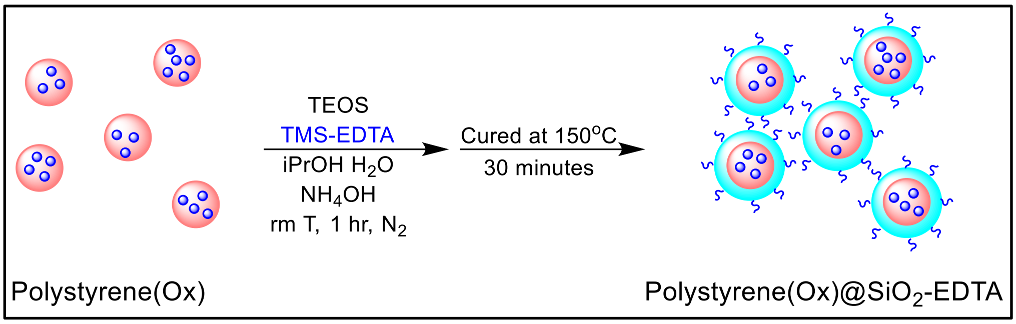

Figure 4.13 Reaction scheme of surface functionalisation, showing the addition of TMS-EDTA and a further curing step to yield **PS(Ox)@SiO₂-EDTA**.

After one hour of stirring, instead of purification *via* centrifuge as with the original **PS(Ox)@SiO₂** particles, the functionalised particles were filtered and washed with copious ethanol and water to ensure removal of excess TEOS and functional silane. These were then cured in an oven for 30 minutes, showing successful functionalisation *via* IR spectroscopy and EDX analysis of proof-of-concept metal binding experiments.

4.3.2 Characterisation

4.3.2.1 IR Spectroscopy

Successful functionalisation of the particle surface was shown initially *via* IR spectroscopy, with weak absorptions at 1600 and 1405 cm^{-1} assigned to the COO$^-$ (symmetrical) and CH_2-COO$^-$ (asymmetrical) vibrations of the EDTA unit respectively, similar to those described for pure silica particles functionalised with EDTA at 1591 and 1408 cm^{-1} [23]. Despite the vibrations associated with EDTA normally being intense, vibrations associated with the silica shell dominate with the asymmetric Si-O vibration at 1070 cm^{-1} and peaks at 956 and 796 cm^{-1} assigned to Si-OH asymmetric vibration and Si-O symmetric vibration respectively,[28] which are also found in **PS(Ox)@SiO₂**. Absorbances at 700 and 760 cm^{-1} are assigned to phenyl C-H stretches within the core, as in **Chapter 3**.[29]

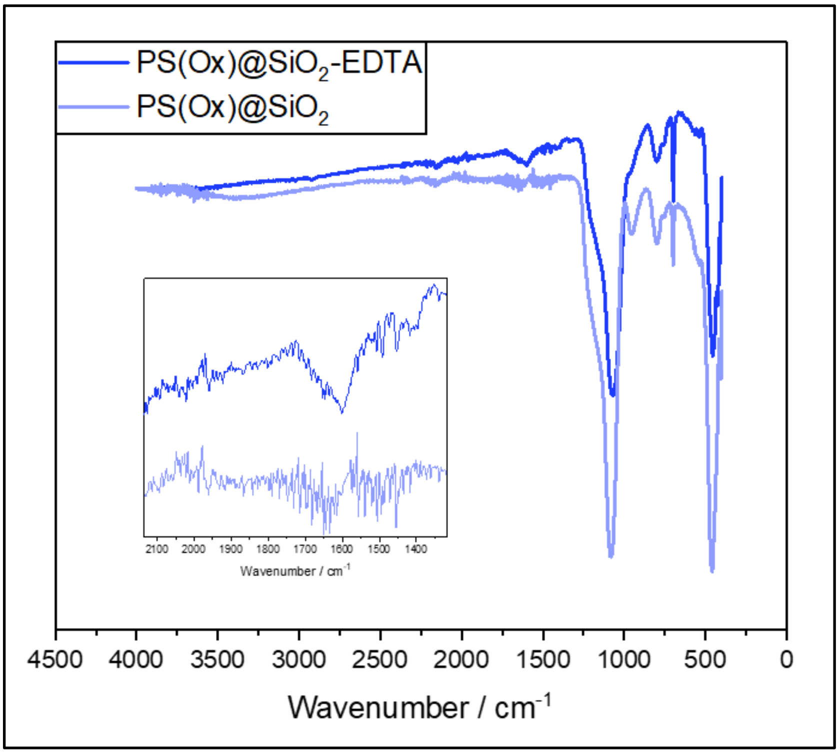

Figure 4.14 ATR-FT-IR Spectrum of **PS(Ox)@SiO₂** and **PS(Ox)@SiO₂-EDTA**, the latter containing C=O stretches of the EDTA unit (*inset*).

4.3.2.2 Particle Morphology

SEM images showed increased aggregation of functionalised particles compared to non-functionalised particles. Whereas **PS(Ox)@SiO₂** showed relatively mono-disperse core-shell constructs, **PS(Ox)@SiO₂-EDTA** aggregated making STEM analysis redundant. Despite this, the mottled surfaces of the particles could be observed *via* SEM, with EDX confirming the carbon cores (**Figure 4.15**).

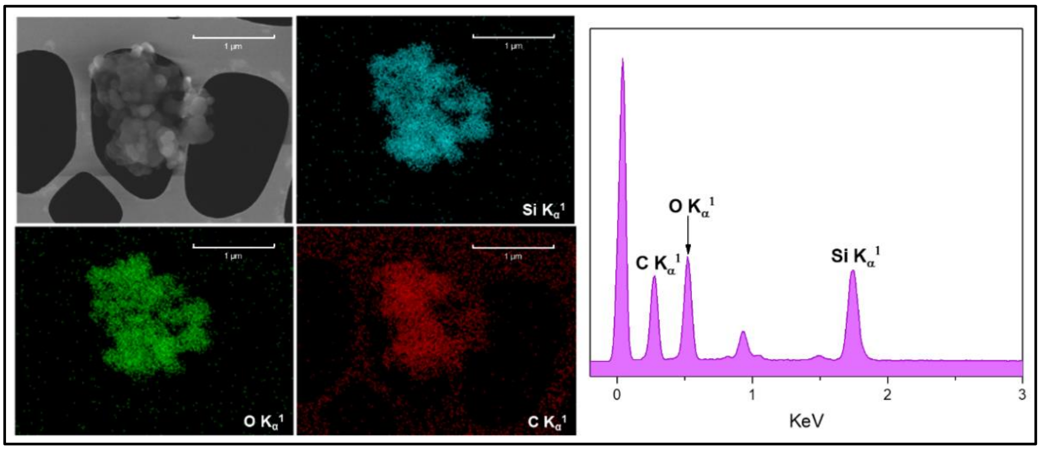

Figure 4.15 *Left*: SEM image showing the mottled particle surface of **PS(Ox)@SiO$_2$-EDTA**, and corresponding EDX images showing the presence of Si, O, and C; *Right*: EDX Spectrum of **PS(Ox)@SiO$_2$-EDTA**.

Unlike the unfunctionalized particles, with an average particle size of 366 nm, **PS(Ox)@SiO$_2$-EDTA** are more than double the size and far more poly-disperse, ranging between 615 to 970 nm in diameter. This increase in size can be seen as an advantage however, as commercially available particles are between 5 and 8 µm to allow a more effective proximity effect.[30,31]

4.3.2.3 Photophysical Studies

As in **Chapter 3**, photophysical studies provide fundamental information on the success of encapsulation of the fluorophore within the particle. **PS(2)@SiO$_2$-EDTA** showed a similar emission profile to **2** in water, slightly blue-shifted compared to **PS(2)@SiO$_2$** (**Figure 4.16**). The red shift originally observed for **PS(2)@SiO$_2$** compared to **2** in water was thought to be due to the high local concentration leading to a concentration dependent Stokes shift (both solvatochromic and excimer based)[32], or due to the increased rigidity of the environment. However, the larger particle size of **PS(2)@SiO$_2$-EDTA** may cause less restriction and a lower local concentration and therefore the emission would appear less red-shifted.

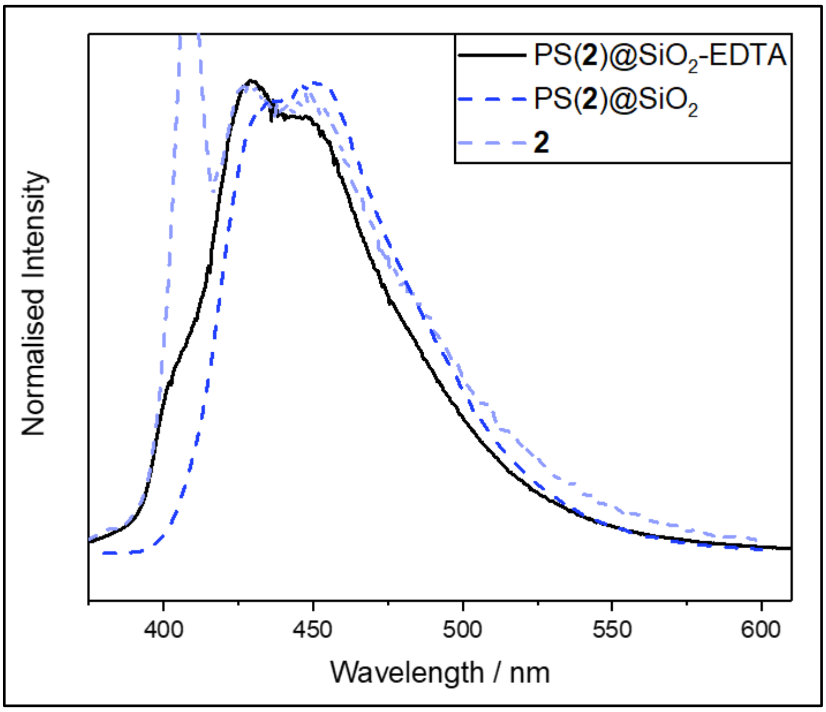

Figure 4.16 Emission Spectra of **PS(2)@SiO$_2$-EDTA** (black) excited at 357nm, showing similarities to both **PS(2)@SiO$_2$** (dotted dark blue) and **2** (dotted light blue), postulated to be due to encapsulation within a larger particle. All spectra recorded in water, 0.04% w/v and 1x10^{-5}M (1% AcN doped) for particles and **2** respectively.

As will be discussed further in **Chapter 6,** the silica shell is semi-permeable which allows solvent to enter the core. Therefore, a larger particle may have a larger water content, and the emission of **2** in **PS(2)SiO$_2$-EDTA** will be more similar to that of **2** in water than in the smaller **PS(2)@SiO$_2$** particles.

Despite the similarity in emission profile between **PS(2)@SiO$_2$-EDTA** and **2** in solution, the lifetime of **PS(2)@SiO$_2$-EDTA** was larger than **2** in water and similar to that of **PS(2)@SiO$_2$** (**Table 4.1**). This gives further evidence of encapsulation, and also shows that although morphology plays a part in the differences in emission profile, the same non-radiative decay pathways remain when encapsulated despite the differences in core size.

Table 4.1 Time-resolved lifetime measurements of **PS(2)@SiO$_2$-EDTA**, **PS(2)@SiO$_2$** and **2** in water (1% AcN for **2**). λ_{em}=448 nm, λ_{ex}=295 nm.

	τ (%) / ns
PS(2)@SiO$_2$-EDTA	2.2 ± 0.22 (34), 8.7 ± 0.87 (66)
PS(2)@SiO$_2$	2.8 ± 0.28 (30), 7.6 ± 0.76 (70)
2	1.5 ± 0.15(56), 6.0 ± 0.60 (44)

4.3.3 Metal Binding Studies

To analyse the ability of the functionalised particles to bind radionuclides of interest, a series of proof-of-concept experiments were carried out using stable Ni^{2+} to compare functionalised and unfunctionalized particles. Commonly found metal ions in low level waste, Ni^{2+}, Co^{2+} and Ca^{2+} (present in tap water), were used to compare the two sets of particles providing further evidence, in conjunction with IR spectroscopy, that the particles were successfully surface functionalised.

Particles were suspended in water, before addition of an aqueous solution of M(OH$_2$)$_6$ (where M= Co^{2+} or Ni^{2+}. Ca^{2+} was added as tap-water). In one set of studies, the binding assays were carried out with no additive so that the natural binding ability could be established, however a second study was also carried out in which triethylamine (TEA) was also added to aid deprotonation of the EDTA carboxylate groups and prevent protonation of the amine bridge. The suspension was then stirred overnight, centrifuged and washed repeatedly to remove excess M^{2+} complexes, before being dried in a desiccator.

The two different environments were studied so that it could be established whether selective binding or removal of metal ions could occur by changing the pH of the environment. This was based on work by N. El-Ashgar *et al*[33] in which it was showed that Co^{2+}, Ca^{2+} and Ni^{2+} could be selectively removed from a silica gel containing EDTA *via* the use of buffers at various pH values.

4.3.3.1 EDX Analysis

EDX analysis was used to analyse the particle surface and investigate the presence of sequestered metal ions. Both functionalised and unfunctionalized particles were tested for comparison, with the unfunctionalized particle surface also expected to show affinity to the metal ion albeit to a lesser extent, due to its ability to scintillate in the presence of Ni-63 (shown in **Chapter 3**) despite the limited beta path length of decaying nuclei. All spectra are normalised to the Si K_α^1 peak, and all percentage bindings are calculated *via* % wts made relative to Silicon. Please note that the percentages given are not quantitative, and are instead given to provide comparison between different samples.

4.3.3.1.1 Without Additive

PS(Ox)@SiO_2-EDTA was shown to successfully bind both Ni^{2+} and Co^{2+}, as shown in **Figure 4.17**. **PS(Ox)@SiO_2** showed no such binding of either metal ion, therefore confirming the presence of EDTA on the surface of **PS(Ox)@SiO_2-EDTA**.

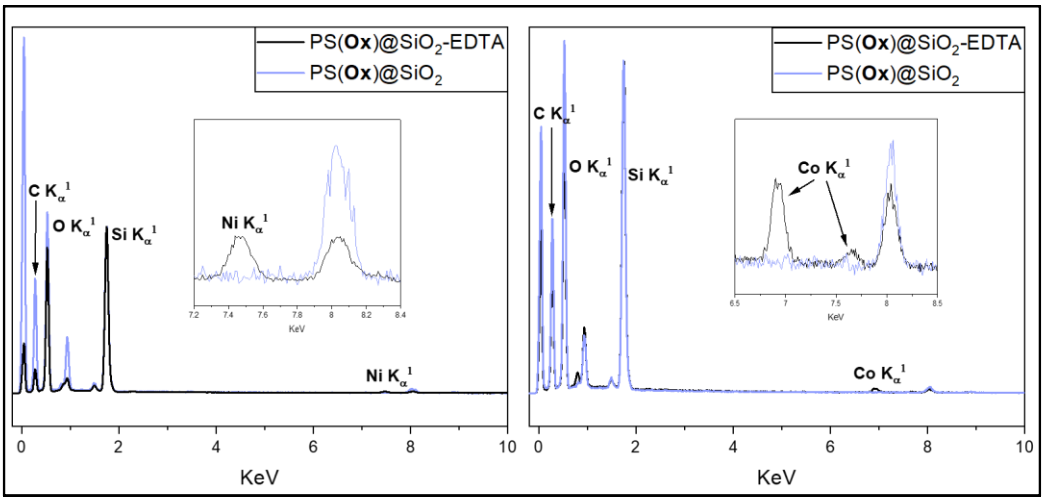

Figure 4.17 EDX spectrum of **PS(Ox)@SiO_2-EDTA** and **PS(Ox)@SiO_2** after the presence of Ni^{2+} (*left*) and Co^{2+} (*right*). All spectra normalised to Si K_α^1 peak.

To investigate any potential selectivity on the particle surface, both Co^{2+} and Ni^{2+} were added as competing metal ions. As shown in **Figure 4.18**, both ions bound to the particle surface in equal proportions, however both also showed a reduction in binding when compared to the mono-doped cases, with more than a 50% decrease in Co^{2+} binding and a ~ 33 % reduction in Ni^{2+} binding. As both metals were added in large excess, it can be assumed that the particles may be saturated with the ions when co-doped. As with the mono-doped cases, **PS(Ox)@SiO_2** showed no evidence of metal binding.

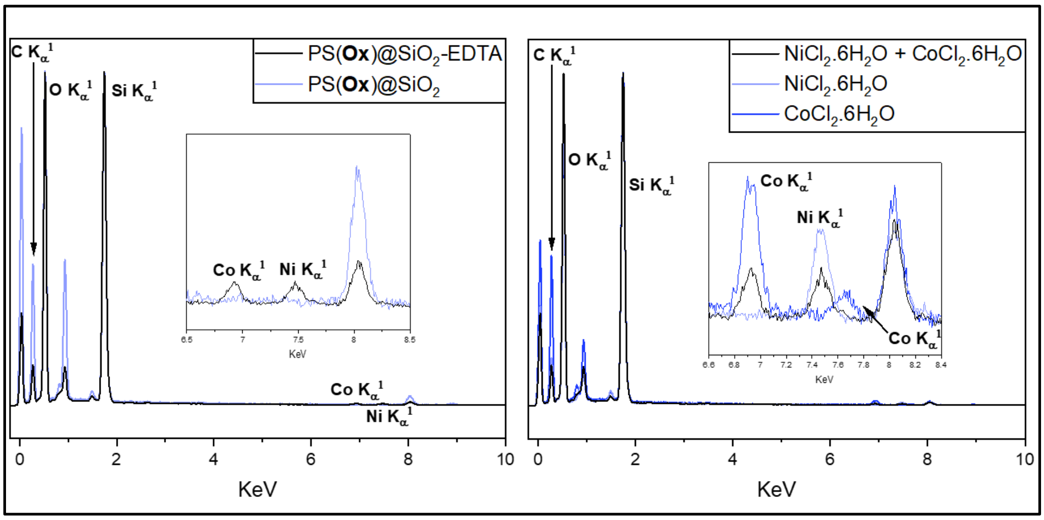

Figure 4.18 EDX spectrum of **PS(Ox)@SiO$_2$-EDTA** and **PS(Ox)@SiO$_2$** after the presence of Ni^{2+} and Co^{2+} (*left*), and **PS(Ox)@SiO$_2$-EDTA** after the presence of Ni^{2+} and Co^{2+} compared to when mono-doped (*right*). All spectra normalised to Si K_α^1 peak.

The almost equal binding of Co^{2+} and Ni^{2+} when co-doped is unexpected, as although there is a smaller reduction in Ni^{2+} binding of the surface, and a slight increase in Ni^{2+} binding over Co^{2+}, it would be assumed that overall more Ni^{2+} would be bound due to the higher formation constant for $[Ni(EDTA)]^{2-}$ *vs* $[Co(EDTA)]^{2-}$ (**Table 4.2**).

Table 4.2 Stability constant, $\log K_f$, for $M^{2+} + EDTA \rightleftharpoons [M(EDTA)]^{2-}$. Recorded at 25°C with 0.1 M ionic strength.[34]

M^{2+}	$\log K_f$
Co^{2+}	16.45
Ni^{2+}	18.40
Ca^{2+}	10.65

As one of the carboxylate arms has been replaced by the silyl group it was thought that this change in selectivity may be due to the surface “EDTA” being a pentadentate ligand instead of hexadentate (**Figure 4.19**), however there are numerous reports to suggest that both Ni^{2+} and Co^{2+} form $[M(EDTAH)(H_2O)]$.[35–37]

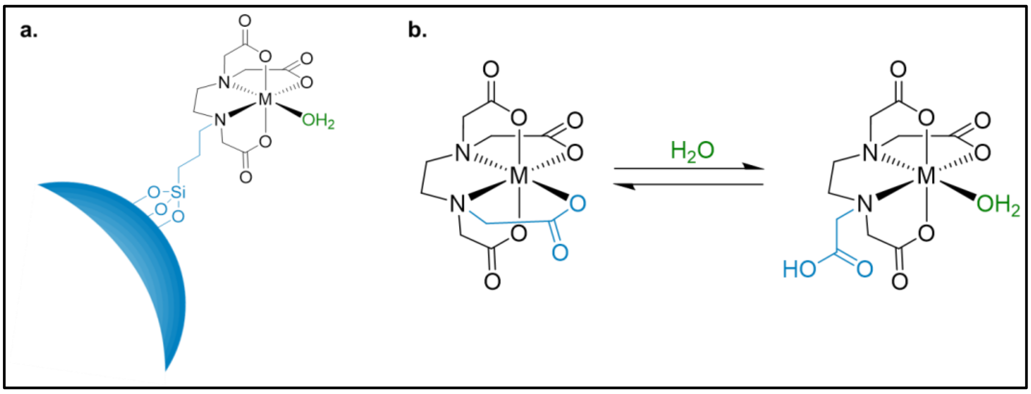

Figure 4.19 *a.* Schematic of $[M(EDTA\text{-}Si)(H_2O)]^-$ complex on the surface of the particle surface; *b.* Reaction scheme for equilibrium between $[M(EDTA)]^{2-}$ and $[M(EDTAH)(H_2O)]^-$.

However, the formation constants for these complexes can only be found *via* first the formation of [M(EDTA)],[35,37] which would not be the pathway in this case due to the lack of carboxylate arm. A free carboxylate arm in $[M(EDTA)(OH_2)]$ would drastically change the entropy and therefore the formation dynamics, which makes comparison of these values an inaccurate representation. Therefore the reason for the binding of both Co^{2+} and Ni^{2+} is hard to determine as a complex mix of factors are in play, namely individual reaction kinetics and the particle surface, which is by its nature difficult to characterise.

To further establish competition between metal ions in solution, doping experiments were carried out in tap water co-doped with Ni^{2+}, and in tap water without external dopants. For **PS(Ox)@SiO$_2$-EDTA** (shown in **Figure 4.20**), Ca^{2+} showed a relatively weak complexation to the surface compared to Ni^{2+} and Co^{2+}, with negligible Ca^{2+} present when in the presence of Ni^{2+}, which concurs with the large difference in stability constants of $[Ni(EDTA)]^{2+}$ and $[Ca(EDTA)]^{2+}$ respectively (**Table 4.2**).

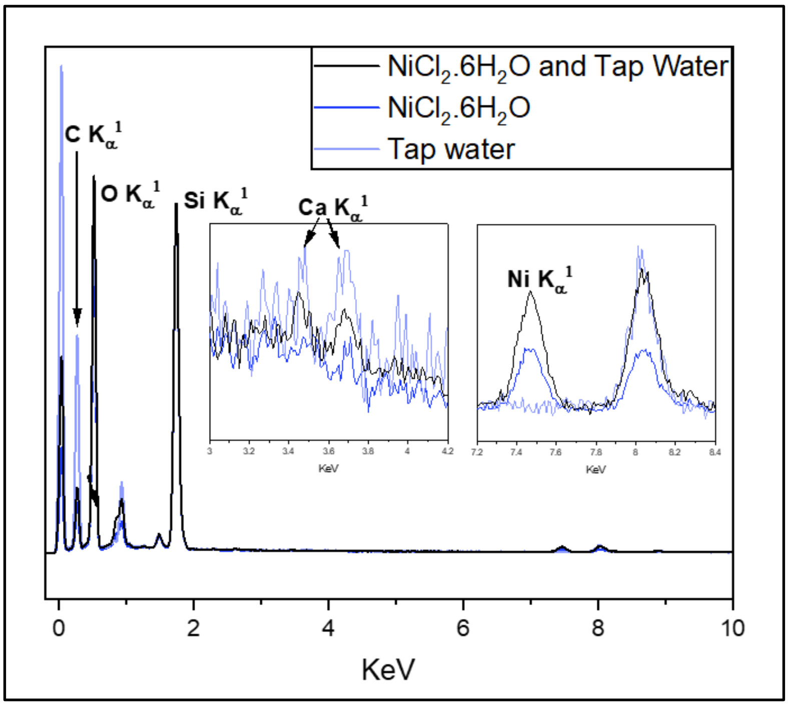

Figure 4.20 EDX spectrum of **PS(Ox)@SiO₂-EDTA** comparing the intensity changes in M^{2+} peaks after the presence of Ni^{2+}, Ca^{2+}, and both M^{2+}. All spectra normalised to Si K_α^1 peak.

An interesting observation is that Ni^{2+} showed an increase in surface binding when in the presence of Ca^{2+}. This sheds light on the binding dynamics at the surface as Ca^{2+} in sodium calcium edetate ([Ca(EDTA)]2Na) is known to easily trans metalate with harmful divalent metal ions in the body, forming stable complexes of the latter with EDTA[38,39]. Therefore this increase in Ni^{2+} binding may suggest that the trans metalation of Ca^{2+} for Ni^{2+} is more stable than that of Ni^{2+} coordinating to free ligand on the particle surface.

As shown in **Figure 4.21**, for **PS(Ox)@SiO₂** there was minimal binding of Ca^{2+} to the particle surface, however when co-doped there was a small increase in Ni^{2+}.

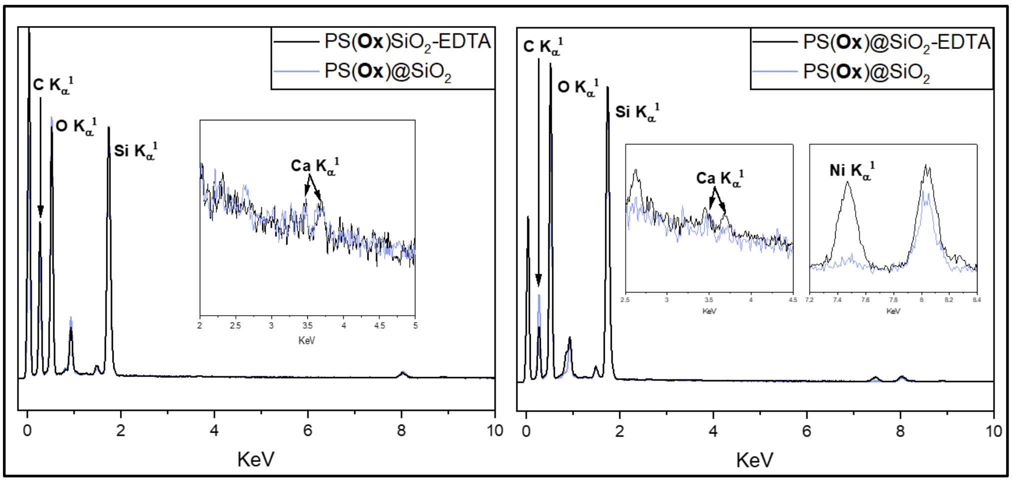

Figure 4.21 EDX spectrum of **PS(Ox)@SiO₂-EDTA** and **PS(Ox)@SiO₂** after the presence tap water containing Ca^{2+} (*left*) and after the presence of tap water and Ni^{2+} (*right*). All spectra normalised to Si K_α^1 peak.

4.3.3.1.2 In the Presence of Additive

In the presence of TEA, **PS(2)@SiO₂-EDTA** successfully bound Ni^{2+} with a 3-fold increase compared to **PS(2)@SiO₂**, and bound Co^{2+} approximately double the amount shown for **PS(2)@SiO₂** (**Figure 4.22**).

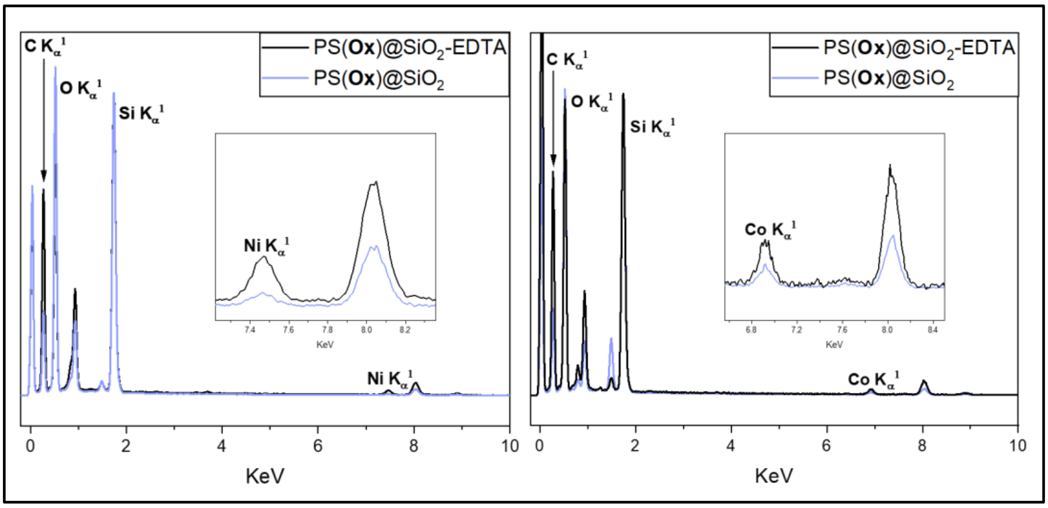

Figure 4.22 EDX spectrum of **PS(Ox)@SiO₂-EDTA** and **PS(Ox)@SiO₂** after the presence of Ni^{2+} (*left*) and Co^{2+} (*right*). All spectra normalised to Si K_α^1 peak.

As in **Section 4.3.3.1.1**, co-doping studies were also carried out to investigate the selectivity of EDTA on the particle surface, with both Co^{2+} and Ni^{2+} added as competing metal ions (**Figure 4.23**). For both functionalised and unfunctionalized particles there was a higher Co^{2+} loading than Ni^{2+}, with loading of both more for functionalised particles as with the mono-doped cases.

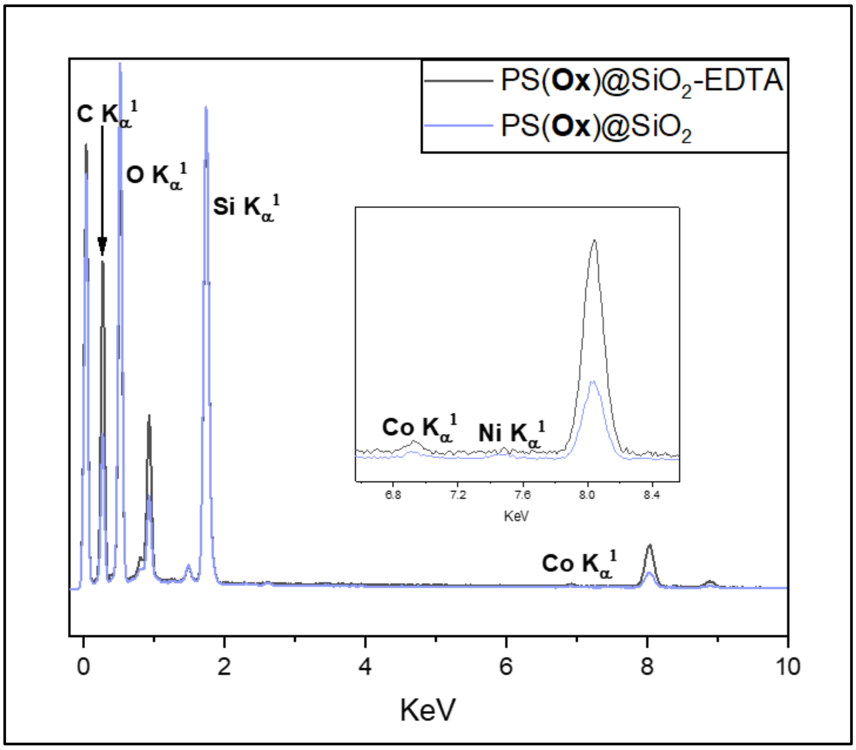

Figure 4.23 EDX spectrum of **PS(Ox)@SiO_2-EDTA** and **PS(Ox)@SiO_2** after the presence of Ni^{2+} and Co^{2+}. All spectra normalised to Si K_α^1 peak.

There is a reduction of metal binding of both Ni^{2+} and Co^{2+} when in competition with each other, when compared to the respective mono-doped cases (**Figure 4.24**). This is most prominent with particles functionalised with EDTA, with Ni^{2+} and Co^{2+} binding decreasing by 64 % and 55 % respectively, compared to the mono-doped cases. This large reduction of Ni^{2+} binding when in competition with Co^{2+} leads to almost exclusive Co^{2+} binding at the surface.

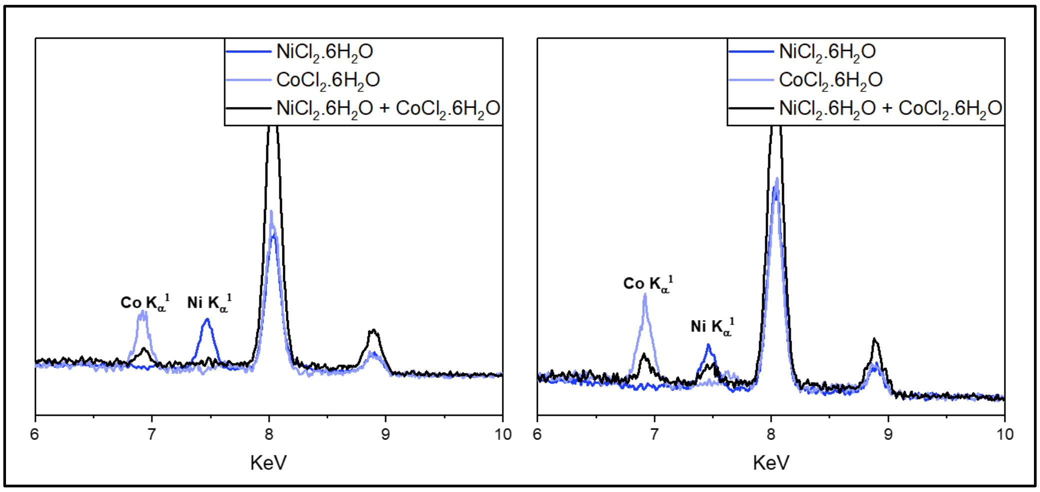

Figure 4.24 EDX spectrum of **PS(Ox)@SiO$_2$-EDTA** (*left*) and **PS(Ox)@SiO$_2$** (*right*) comparing the intensity changes in M^{2+} peaks after the presence of Ni^{2+}, Co^{2+}, and both M^{2+}. All spectra normalised to Si K_α^1 peak.

This is unexpected due to the higher formation constant for $[Ni(EDTA)]^{2-}$ than $[Co(EDTA)]^{2-}$ (**Table 4.2**), as discussed previously, and differs from the trend observed without triethylamine present.

To further establish competition between metal ions in solution, doping-experiments were carried out in tap water with and without Ni^{2+} present, to introduce a Ca^{2+} source. Ca^{2+} was found to bind exclusively to functionalised particles, with no binding observed for unfunctionalized particles, as shown in **Figure 4.25**.

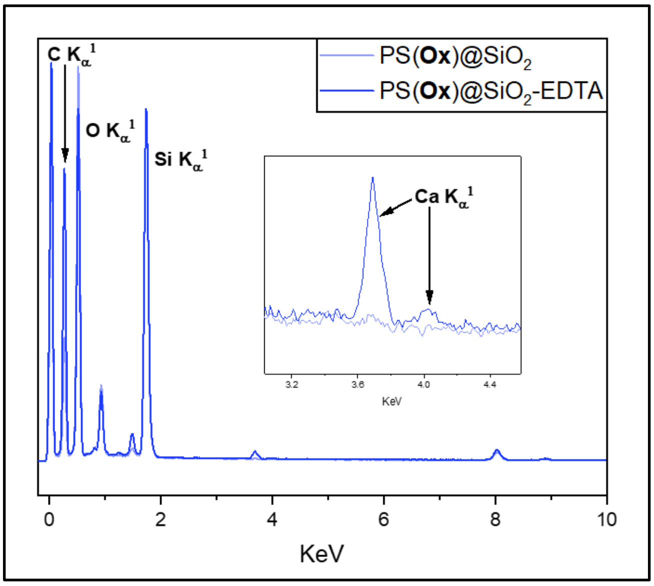

Figure 4.25 EDX spectrum of **PS(Ox)@SiO$_2$-EDTA** and **PS(Ox)@SiO$_2$** after the presence of tap water containing Ca^{2+}. All spectra normalised to Si K_α^1 peak.

When in tap water, **PS(2)@SiO₂-EDTA** found a 60% decrease in Ni-binding compared to Ni^{2+} alone (**Figure 4.26**), with only a 10% decrease in Ca^{2+} between tap water alone and Ni^{2+} doped tap water.

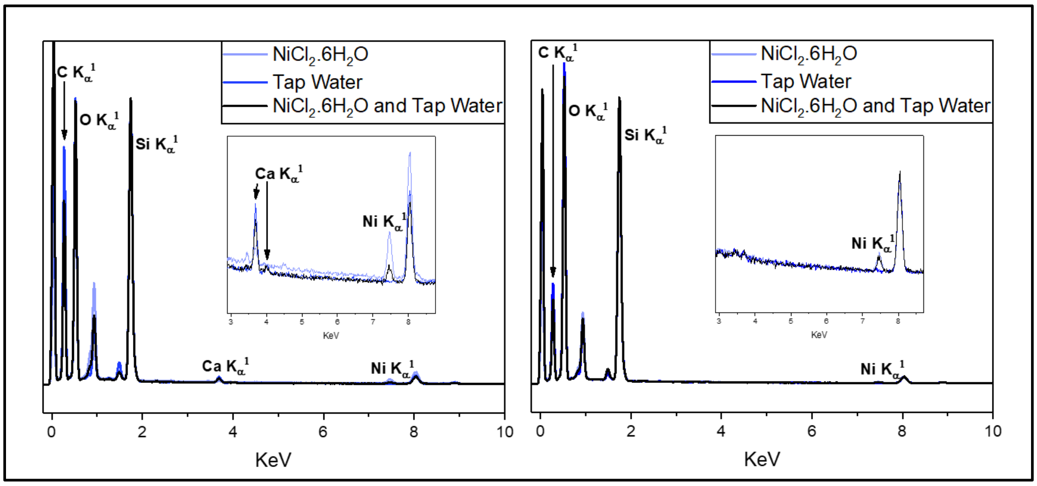

Figure 4.26 EDX spectrum of **PS(Ox)@SiO₂-EDTA** (*left*) and **PS(Ox)@SiO₂** (*right*) comparing the intensity changes in M^{2+} peaks after the presence of Ni^{2+}, Ca^{2+}, and both M^{2+}. All spectra normalised to Si K_α^1 peak.

This may appear surprising, considering the results found in **Section 4.3.3.1.1**, however due to the addition of TEA to aid deprotonation of the carboxylate arms and prevent protonation of the amine bridge of EDTA, the metal hydroxides of Ca^{2+}, Ni^{2+} and Co^{2+} may have formed as a result. The solubility of $Co(OH)_2$ and $Ni(OH)_2$ in water are within the same order of magnitude (**Table 4.3**) and therefore the differences in surface binding of these is not due to varying precipitation. However, $Ca(OH)_2$ has a much larger solubility than $Ni(OH)_2$ and is a known flocculator, and so whilst some Ni^{2+} may precipitate out as a hydroxide, Ca^{2+} will remain in solution and can therefore bind to the particle surface more effectively, despite the lower formation constant compared to Ni^{2+}.

Table 4.3 Solubility products ($pK_{sol} = -logK_{sol}$) of $M(OH)_2$ at 25°C[40].

Hydroxide	**pK_{sol}**
$Ni(OH)_2$	15.2
$Co(OH)_2$	14.9
$Ca(OH)_2$	5.19

For unfunctionalized particles, there was no noticeable change in Ni^{2+} binding, with no Ca^{2+} observed on the surface of the particles in both tap water and Ni^{2+} doped tap water (**Figure 4.26**).

As expected, the addition of TEA impacted the binding of the dopants to the particle surface, summarised in **Table 4.4**, however it was not expected to yield a higher binding. In the case of Ni^{2+}, the addition of TEA doubled the metal binding, and a 32% increase in binding was observed for Co^{2+}. Despite this, when co-doped with both Co^{2+} and Ni^{2+} , the overall percentage of M^{2+} on the surface was similar suggesting that maximum loading had been achieved. As well as this, the percentage of Co^{2+} present was similar with and without additive, however there was an increase in Ni^{2+} binding when TEA was not present in the co-doped examples.

Table 4.4 Percentage of M^{2+} present on functionalised particles. Calculated *via* % wts made relative to silicon.

	M^{2+} relative to Si / %		
Dopant (additive)	**Ni**	**Co**	**Ca**
Ni^{2+} (TEA)	21.6 ± 0.6	-	-
Ni^{2+}	11.7 ± 1.0	-	-
Co^{2+} (TEA)	-	18.6 ± 1.2	-
Co^{2+}	-	12.8 ± 2.0	-
Ni^{2+} + Co^{2+} (TEA)	3.5 ± 0.1	5.6 ± 0.7	-
Ni^{2+} + Co^{2+}	5.8 ± 1.3	4.9 ± 0.8	-
Tap water (TEA)	-	-	4.9 ± 0.2
Tap water	-	-	0.6 ± 0.1
Ni^{2+} + Tap water (TEA)	7.0 ± 0.6	-	3.6 ± 0.2
Ni^{2+} + Tap water	20.8 ± 2.3	-	< 0

In the presence of tap water, the binding of Ni^{2+} decreased by 68 % when TEA was present, however Ni^{2+} binding increased by 44 % without TEA, as described previously. As well as this, there was considerably more Ca^{2+} present when TEA was added in both mono-doped and co-doped cases with Ni^{2+}.

It should also be noted that in the presence of TEA, unfunctionalized particles also saw an increase in metal binding, which could be due to the deprotonation of the hydroxy groups on the particle surface.

The differences observed for **PS(Ox)@SiO$_2$-EDTA** are positive in terms of sequestering metals of interest. Whereas it was originally postulated that a stronger chelating agent could be used to strip particles of the attached radionuclides, instead the pH could be changed using various buffers to selectively remove metals. In the case of Ni^{2+} in tap water, increase in pH could potentially strip the particle surface of Ni^{2+}. This increase in pH also applies to reduction of Ni^{2+} binding compared to Co^{2+} (and potentially similar M^{2+} ions). Work by N. El-Ashgar *et al*[33] showed that Co^{2+}, Ca^{2+} and Ni^{2+} could be selectively removed from a silica gel containing EDTA *via* the use of buffers at various pH's. Therefore, this could be a direct method for the recycling of radionuclide bound particles (as well as retrieval of radionuclide), therefore making them re-usable without the use of more expensive chelating moieties.

4.3.3.2 Photophysical Studies

Due to the silica shell of the core-shell particle, the closest contact between the bound metal at the surface and the encapsulated fluorophore would be at least 20 nm, and therefore the encapsulated fluorophore was predicted to be insensitive to binding events at the surface. That being said, photophysical studies of metal-bound functionalised particles yielded interesting results both with and without TEA, as shown in **Figure 4.27**. After metal binding, neither set of particles showed a shift in emission, with those without TEA showing negligible change in emission line-shape, however those in the presence of the additive showed a marked change, particularly those with Ca^{2+}.

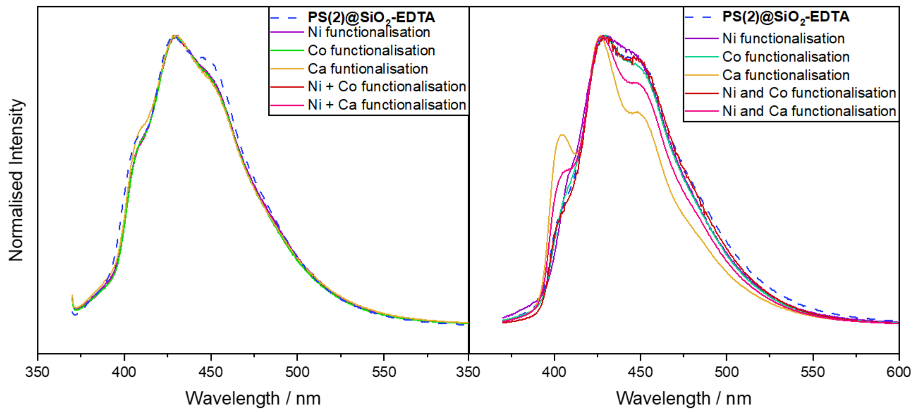

Figure 4.27 Emission Spectra of **PS(2)@SiO$_2$-EDTA** after metal binding studies with (*right*) and without (*left*) TEA, excited at 357 nm. All spectra recorded in water, 0.04% w/v. **PS(2)@SiO$_2$-EDTA** recorded in water in both cases as reference.

The reasoning for the change in emission intensity after calcium binding is hard to determine. All three metal ions (Ni^{2+}, Co^{2+} and Ca^{2+}) are known fluorescence quenchers, however as stated previously the distance between the encapsulated fluorophore and the metal bound to the particle surface is far too large for an interaction to occur. Therefore, the difference in emission profile upon binding of Ca^{2+} cannot be determined, however could be the result of re-absorption of the fluorophore due to the scattering of light brought about by the particles.

The change in emission line-shape could also be a result of the basic environment slightly degrading the silica shell, which could cause more solvent to enter the polystyrene core and hence change the local environment for the fluorophore, and hence the line-shape. This reasoning is further confirmed by that of the unfunctionalized particles in the presence of TEA which also showed a change in line-shape (**Figure 4.28**), despite experiencing lower metal binding. This disruption of local environment of the unfunctionalized particles was further confirmed *via* SEM analysis, showing a slight decrease in particle size after the metal-binding assay (**Table 4.5**), which could be due to a disturbance in the polystyrene structure.

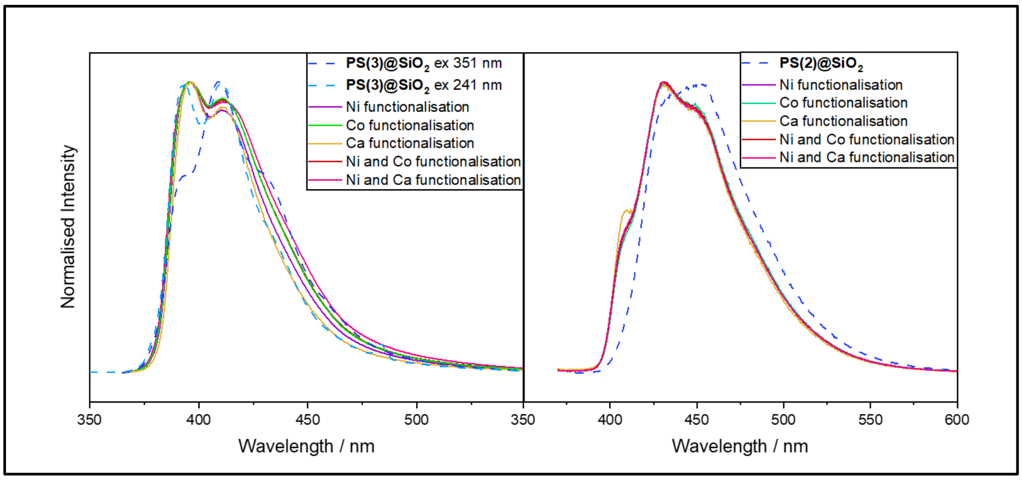

Figure 4.28 Emission Spectra of **PS(Ox)@SiO$_2$** after metal binding studies with (*right)* and without (*left*) TEA, excited at 357 and 351 nm respectively for oxazoles **2** and **3**. All spectra recorded in water, 0.04% w/v. **PS(Ox)@SiO$_2$** recorded in water in both cases as reference, for **PS(3)@SiO$_2$** spectra also recorded at 241 nm for line-shape comparison.

The line-shape of the emission profile for unfunctionalized particles (**PS(3)@SiO$_2$**) without TEA present also changed following the metal functionalisation experiments (**Figure 4.28** ***left***). However, this is most probably due to a statistical phenomenon as the line shape observed was identical to that of **PS(3)@SiO$_2$** when excited at higher energy, and could be due to relatively small changes in internal environment which pyrene-based ligands are extremely sensitive to, as discussed in **Chapter 3**. SEM also helped to confirm this, as the particle size did not change upon metal-binding, which is expected due to the negligible metal binding observed and absence of TEA.

Table 4.5 Calculated diameter of **PS(Ox)@ SiO$_2$** before and after introduction of metal ion, where **PS(2)@SiO$_2$** were used with additive, and **PS(3)@SiO$_2$** without; particle sizes were calculated using ImageJ software.

	Before		**After**	
	PS(3)@SiO$_2$	***PS(2)@SiO$_2$***	***PS(3)@SiO$_2$***	***PS(2)@SiO$_2$***
Average / nm	362 ± 12	323 ± 7	369 ± 4	236 ± 7
Min / nm	285 ± 12	212 ± 7	304 ± 4	168 ± 7
Max / nm	423 ± 12	441 ± 7	538 ± 4	354 ± 7
SD / nm	43	44	46	41

The change in emission lifetimes is also difficult to explain, with results shown in **Table 4.6** and **Table 4.7** . Upon metal binding in the presence of TEA, the emission lifetimes of functionalised particles slightly decrease. For unfunctionalized particles, the lifetimes increase, with a mono-exponential character instead of biexponential, with the exception of those treated with Ni^{2+} and Ca^{2+} simultaneously where the emission lifetimes are both biexponential and longer than the original emission lifetime.

Table 4.6 Time-resolved lifetime measurements of **PS(2)@SiO$_2$-EDTA** and **PS(2)@SiO$_2$** before and after metal binding studies with TEA. All measurements recorded in water, 0.04% w/v. λ_{em}=430, λ_{ex}=295 nm.

	PS(2)@SiO$_2$-EDTA	***PS(2)@SiO$_2$***
Before	1.8 ± 0.18 (32), 8.1 ± 0.81 (68)	2.2 ± 0.22 (41), 10.7 ± 1.07 (59)
Ni^{2+}	0.8 ± 0.08 (28), 5.8 ± 0.058 (72)	6.9 ± 0.69
Co^{2+}	1.9 ± 0.19 (27), 7.5 ± 0.75 (73)	7.3 ± 0.73
Ca^{2+}	1.7 ± 0.17 (27), 7.5 ± 0.75 (73)	6.3 ± 0.63
Ni^{2+} + Co^{2+}	0.8 ± 0.08 (17), 6.7 ± 0.67 (83)	7.5 ± 0.75
Ni^{2+} + Ca^{2+}	1.3 ± 0.13 (22), 6.4 ± 0.64 (78)	2.1 ± 0.21 (11), 8.7 ± 0.87 (89)

For **PS(2)@SiO$_2$-EDTA** without the presence of TEA (**Table 4.7**), the emission lifetimes show an overall negligible decrease, however a larger decrease was observed in the presence of Co^{2+} and Ca^{2+} (of which the latter was mono-exponential). Again, for unfunctionalized particles a mono-exponential character instead of biexponential was observed.

Table 4.7 Time-resolved lifetime measurements of **PS(2)@SiO$_2$-EDTA** and **PS(3)@SiO$_2$** before and after metal binding studies, without TEA. All measurements recorded in water, 0.04% w/v. λ_{em}=430 and 412 nm for Ox = **2** and **3** respectively, λ_{ex}=295 nm.

	PS(2)@SiO$_2$-EDTA	***PS(3)@SiO$_2$***
Before	1 ± 0.10 (42), 6.9 ± 0.69 (58)	4.1 ± 0.41 (79), 10.3 ± 1.03 (21)
Ni^{2+}	1.7 ± 0.17 (56), 6.6 ± 0.66 (44)	4.7 ± 0.47
Co^{2+}	1.3 ± 0.13 (64), 3.8 ± 0.38 (36)	4.0 ± 0.40
Ca^{2+}	1.7 ± 0.17	4.0 ± 0.40
Ni^{2+} + Co^{2+}	1.3 ± 0.13 (56), 6.2 ± 0.62 (44)	4.0 ± 0.40
Ni^{2+} + Ca^{2+}	1.3 ± 0.13 (56), 5.7 ± 0.57 (44)	4.2 ± 0.42

Although it would be interesting for a clear pattern to emerge between metal binding and consequent emission lifetimes, due to the relatively small changes observed the lack of clear reasoning may in fact be the result of either error inherent to the recording or the polydisperse nature of the particle core between samples, as opposed to a result of the metal binding. An example of this is shown when comparing the initial luminescent lifetime of **PS(2)@SiO$_2$-EDTA** used in both binding studies; the luminescent lifetime of the particles used in studies containing TEA is slightly larger than that used for studies without TEA, despite synthetic technique being identical.

4.3.4 Scintillation

To assess whether functionalisation of the surface could lead to an increased scintillant response from Ni-63 compared to unfunctionalized particles, scintillation experiments were carried out and compared to those of **Chapter 3**.

Preliminary results, presented in **Figure 4.29**, show that when functionalised the scintillation response is on average slightly higher than unfunctionalized particles in the presence of Ni-63. However, as the difference between the two separate runs for **PS(2)@SiO$_2$-EDTA** is large, these results require further substantiation with continued study to ascertain whether an increase in scintillation is observed.

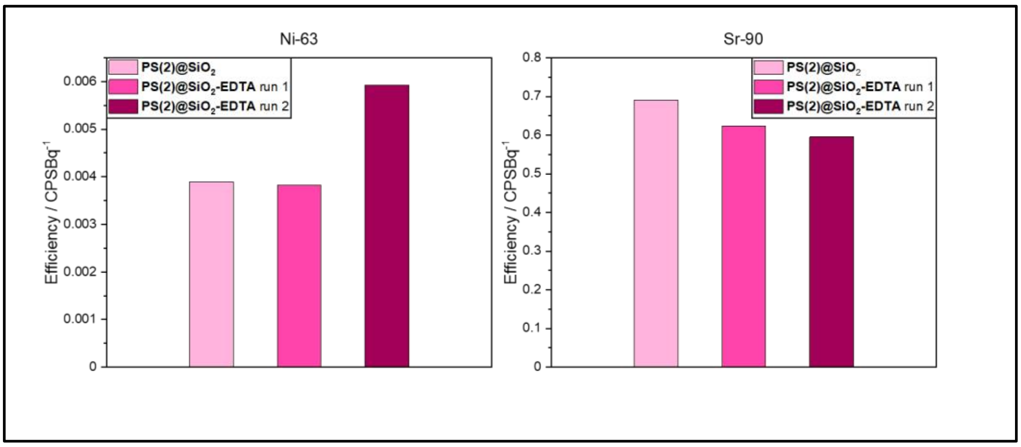

Figure 4.29 Scintillation efficiency of **PS(2)@SiO$_2$** and **PS(2)@SiO$_2$-EDTA** in the presence of Ni-63 (*left*) and Sr-90 (*right*). Counted for 30 minutes with 10 cycles completed in total.

In the presence of Sr-90, the scintillation efficiency slightly decreased when particles are functionalised (**Figure 4.29**). Both HEDTA[41] and EDTA[42,43] can coordinate to strontium, however due to the long path length of the beta-particles emitted from Sr-90 it was not thought that a large change in scintillation efficiency would be observed by complexation as scintillation would be observed without coordination to the surface (as shown in **Chapter 3**). It is also important to note that both tests yielded slightly different results, and so further substantiation is also needed in this case as the decrease in scintillation efficiency cannot be explained.

4.4 Conclusion

PS(Ox)@SiO$_2$ was successfully functionalised with TMS-EDTA to yield **PS(Ox)@SiO$_2$-EDTA**, shown *via* IR spectroscopy. Metal binding studies utilising EDX for analysis showed that functionalised particles successfully chelated Ni^{2+}, Co^{2+} and Ca^{2+} to the particle surface to a greater extent than unfunctionalized, giving further evidence of successful surface functionalisation. The existence of Ni^{2+} on the surface of unfunctionalized particles, albeit at a far lesser extent, could explain why a scintillation response was still observed for **PS(Ox)@SiO$_2$** in **Chapter 3**.

The differences in metal binding observed *via* the addition of TEA provide both evidence that the particles can be recycled *via* a change in pH, and also that metals can be selectively sequestered in the presence of different buffers. To further confirm this, it is suggested that metal binding studies at a range of pH values be carried out.

When in the presence of Ni-63, the scintillation efficiency was on average improved compared to unfunctionalized particles. However, due to the differences in the two experimental runs further analysis is required. In the presence of Sr-90, the scintillation efficiency slightly decreased with respect to unfunctionalized particles, however a large change in efficiency was not predicted due to the longer beta path length of Sr-90. The slight decrease in efficiency could be a result of degradation of particles as, similar to select examples in **Chapters 2** and **3**, the particles were recorded almost a year after synthesis (due to reasons outside of the authors control), and thus degradation may have occurred.

Despite preliminary scintillation results showing that functionalised particles only gave a slight increase (on average) in efficiency when in the presence of Ni-63, EDX analysis support the hypothesis that an increased loading of Ni-63 is observed for functionalised nanoparticles. Therefore, these particles if functionalised with element-specific ligands, provide an opportunity for sequestration of lower energy radionuclides of interest within a mixture, which could then be analysed independently to reduce domination of signal from stronger beta emitters such as Sr-90.

4.5 Experimental

The synthesis of the polystyrene microsphere and subsequent fluorophore encapsulation followed that of **Chapter 3**.

4.5.1 General Procedure for silica coating and surface functionalisation

Polystyrene(Ox) (4 mL, approx. 56 mg of particles) was dispersed in iPrOH (200 mL), H_2O (38 mL), and NH_4OH (5 mL) under N_2. The reaction mixture was stirred rapidly with dropwise addition of TEOS (2 mL, 8.96 mmol) and TMS-EDTA (1.14 mL, 40 % soln in water) and then stirred for a further hour. After this time, the nanoparticles were collected *via* filtration, washed several times with water and ethanol, before being cured in an oven for 30 minutes at 150^{o}C to yield **PS(Ox)@SiO$_2$-EDTA**.

4.5.2 General Procedure for Metal-Binding Studies

PS(Ox)@SiO$_2$-EDTA (10 mg) was suspended in water (9 mL) before addition of $MCl_2.6H_2O$ (M= Ni^{2+}, Co^{2+} or both) in water (0.23 M, 1 mL) and TEA (5 drops) if required. The suspension was stirred overnight and the particles collected *via* centrifugation (30 minutes, 4.4 rpm), washed several times with water and ethanol, before being dried under vacuum in a desiccator.

4.5.2.1 Metal binding studies involving Ca^{2+}

PS(Ox)@SiO$_2$-EDTA (10 mg) was suspended in tap water (9 mL), before addition of TEA (5 drops) if required. For competitive studies, $NiCl_2.6H_2O$ in tap water (0.23 M, 1 mL) was added before addition of TEA. The suspension was stirred overnight, and the particles collected *via* centrifugation (30 minutes, 4.4 rpm) and washed several times with water and ethanol, before being dried under vacuum in a desiccator.

4.5.3 General Procedure for Preparation of Nanoparticle Samples for Scintillation Studies

Particle samples were suspended in aqueous solution at a concentration of 0.02 % wt/v, before addition of radionuclide sample(Ni-63 (2.0 kBq/g) prepared in 0.1 mol dm^{-3} HCl, or Sr-90 (96.99 Bq/g) prepared in 1 mol dm^{-3} HNO_3). Sources contained 100 μg g^{-1} of inactive nickel and 50 μg g^{-1} inactive strontium and yttrium, respectively. Samples were agitated prior to analysis.

4.6 References

1. W. Xu, X. Gao, P. Ge, F. Jiang, X. Zhang and J. Xie, *Int. J. Pharm.*, 2018, **553**, 349–362.
2. A. A. Ansari, M. A. Siddiqui, A. Khan, N. Ahmad, M. Alam, A. M. El-Toni and A. A. Al-Khedairy, *Colloids Surf. Physicochem. Eng. Asp.*, 2019, **573**, 146–156.
3. A. M. G. Mutti, J. A. O. Santos, D. G. S. M. Cavalcante, A. S. Gomes, A. E. Job, A. M. Pires and S. A. M. Lima, *Opt. Mater.*, 2019, **90**, 57–63.
4. D. R. Hristov, L. Rocks, P. M. Kelly, S. S. Thomas, A. S. Pitek, P. Verderio, E. Mahon and K. A. Dawson, *Sci. Rep.*, 2015, **5**, 17040.
5. M. Esmaeilpour and S. Zahmatkesh, *Inorg. Nano-Met. Chem.*, 2019, **49**, 267–276.
6. R. Jin, D. Zheng, R. Liu and G. Liu, *ChemCatChem*, 2018, **10**, 1739–1752.
7. F. Fu and Q. Wang, *J. Environ. Manage.*, 2011, **92**, 407–418.
8. C. F. Carolin, P. S. Kumar, A. Saravanan, G. J. Joshiba and Mu. Naushad, *J. Environ. Chem. Eng.*, 2017, **5**, 2782–2799.
9. V. Javanbakht, S. A. Alavi and H. Zilouei, *Water Sci. Technol.*, 2014, **69**, 1775–1787.
10. E. Da'na, *Microporous Mesoporous Mater.*, 2017, **247**, 145–157.
11. M. C. Gomes, Â. Cunha, T. Trindade and J. P. C. Tomé, *J. Innov. Opt. Health Sci.*, 2016, **09**, 1630005.
12. J. I. Lachowicz, G. R. Delpiano, D. Zanda, M. Piludu, E. Sanjust, M. Monduzzi and A. Salis, *J. Environ. Chem. Eng.*, 2019, **7**, 103205.
13. I. I. Slowing, J. L. Vivero-Escoto, B. G. Trewyn and V. S.-Y. Lin, *J. Mater. Chem.*, 2010, **20**, 7924.
14. D. Zhao, J. Sun, Q. Li and G. D. Stucky, *Chem. Mater.*, 2000, **12**, 275–279.
15. D. Zhao, *Science*, 1998, **279**, 548–552.
16. T. Kimura and K. Kuroda, in *Comprehensive Inorganic Chemistry II (Second Edition)*, eds. J. Reedijk and K. Poeppelmeier, Elsevier, Amsterdam, 2013, pp. 133–150.
17. M. E. Mahmoud, M. S. Abdelwahab and E. M. Fathallah, *Chem. Eng. J.*, 2013, **223**, 318–327.
18. V. M. Nurchi, G. Crisponi, M. Crespo-Alonso, J. I. Lachowicz, Z. Szewczuk and G. J. S. Cooper, *Dalton Trans*, 2013, **42**, 6161–6170.

19. Y. Shiraishi, G. Nishimura, T. Hirai and I. Komasawa, *Ind. Eng. Chem. Res.*, 2002, **41**, 5065–5070.
20. S. Iqbal and J.-I. Yun, *Microporous Mesoporous Mater.*, 2017, **248**, 149–157.
21. K. Krapfenbauer and N. Getoff, *Radiat. Phys. Chem.*, 1999, **55**, 385–393.
22. P. Shao, D. Liang, L. Yang, H. Shi, Z. Xiong, L. Ding, X. Yin, K. Zhang and X. Luo, *J. Hazard. Mater.*, 2020, **387**, 121676.
23. D. Dupont, W. Brullot, M. Bloemen, T. Verbiest and K. Binnemans, *ACS Appl. Mater. Interfaces*, 2014, **6**, 4980–4988.
24. B. K. Sodipo and A. A. Aziz, *J. Magn. Magn. Mater.*, 2016, **416**, 275–291.
25. D. Dupont, J. Luyten, M. Bloemen, T. Verbiest and K. Binnemans, *Ind. Eng. Chem. Res.*, 2014, **53**, 15222–15229.
26. N. Kobylinska, L. Kostenko, S. Khainakov and S. Garcia-Granda, *Microchim. Acta*, 2020, **187**, 289.
27. G. T. Hermanson, *Bioconjugate techniques*, Elsevier/AP, London ; Waltham, MA, 3rd edn., 2013.
28. K. Panwar, M. Jassal and A. K. Agrawal, *Particuology*, 2015, **19**, 107–112.
29. W.-C. Liaw, Y.-L. Cheng, M.-K. Chang, W.-F. Lien and H.-R. Lai*, Polym. J.*, 2016, **48**, 91–99
30. PerkinElmer, SPA Bead Technology, https://www.perkinelmer.com/lab-products-and-services/application-support-knowledgebase/radiometric/spa-beads.html, (accessed May 13, 2020).
31. N. Bosworth and P. Towers, *Nature*, 1989, **341**, 167–168.
32. S. Chakraborty, K. Harris and M. Huang, *AIP Adv.*, 2016, **6**, 125113.
33. N. M. El-Ashgar, I. M. El-Nahhal, M. M. Chehimi, F. Babonneau and J. Livage, *Int. J. Environ. Anal. Chem.*, 2009, **89**, 1057–1069.
34. D. C. Harris, *Quantitative Chemical Analysis*, W. H. Freeman, USA, 8th edn., 2010.
35. N. E. Boland and A. T. Stone, *Geochim. Cosmochim. Acta*, 2017, **212**, 176–195.
36. G. S. Smith and J. L. Hoard, *J. Am. Chem. Soc.*, 1959, **81**, 556–561.
37. S. Harada, Y. Funaki and T. Yasunaga, *J. Am. Chem. Soc.*, 1980, **102**, 136–139.
38. L. Gerhardsson and J. Aaseth, in *Chelation Therapy in the Treatment of Metal Intoxication*, eds. J. Aaseth, G. Crisponi and O. Andersen, Academic Press, Boston, 2016, pp. 313–341.

39. L. Gerhardsson and G. Kazantzis, in *Handbook on the Toxicology of Metals*, eds. G. F. Nordberg, B. A. Fowler and M. Nordberg, Academic Press, San Diego, 4th edn., 2015, pp. 487–505.
40. F. Scholz and H. Kahlert, *ChemTexts*, 2015, **1**, 7.
41. A. R. Felmy, M. J. Mason and O. Qafoku, *J. Solut. Chem.*, 2003, **32**, 301–318.
42. B. C. Sinha and S. K. Roy, *Analyst*, 1973, **98**, 289–292.
43. M. Friedman and Z. Hirschfeld, *J. Oral Rehabil.*, 1982, **9**, 327–333.

5 Photophysical Investigations into Rhenium Tricarbonyl Complexes of Functionalised 2-Pyridyl Oxazole Ligands

5.1 Overview

In **Chapter 2** the breadth of applications of the oxazole unit were discussed, focussing primarily on their ability to scintillate due to favourable photophysical characteristics. However, a further application for these heterocycles is as bidentate ligands, utilising the nitrogen-donor of the oxazole ring, and shown in **Figure 5.1**. Although there are many examples of benzoxazole-pyridine ligands, as discussed herein, there are relatively few examples of oxazole-pyridine diimine units (py-oxazole). In the following discussion, examples of benzoxazoles, oxazoles and oxazolines (due to their structural similarity) as ligands in bidentate systems are presented. This is followed by applications of rhenium complexes, concluding with the few examples of rhenium complexes utilising benzoxazole and oxazoline systems. To the best of the author's knowledge, there are no known examples of rhenium complexes with oxazole-based ligands in the bidentate unit, with the exception of those comprising a benzoxazole unit (**Figure 5.1**, and discussed in **Section 5.1.3**) and thus the aim of this chapter was to synthesise a range of novel oxazole-based rhenium(I) tricarbonyl complexes with a broad range of photophysical properties, with DFT analysis to further support the proposed electronic assignments.

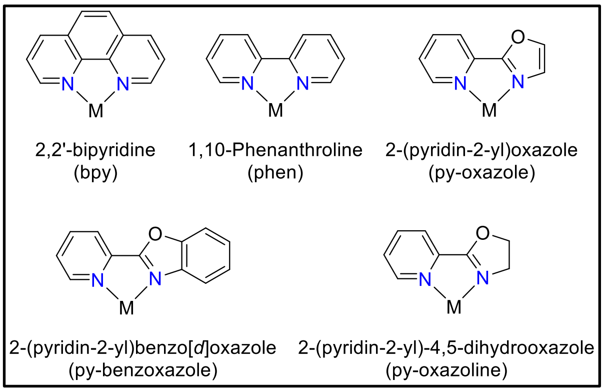

Figure 5.1 Schematic representation of common bidentate ligands 2,2'-bipyridine and 1,10-phenanthroline, as well as those based on oxazole, benzoxazole and oxazoline moieties.

5.1.1 Bidentate ligands utilising the oxazole-based heterocycle

Iridium complexes are known for their strong phosphorescent emission and long emissive lifetimes, with their use in both bioimaging and OLED applications extensively studied.[1–3] Traditionally, heteroleptic iridium complexes are typified by three bidentate ligands. Tuning of emission can be achieved *via* modification of the cyclometallating ligands, due to the fact that the LUMO is localised on the pyridyl-unit of the ligand, whereas the iridium d-orbitals and the phenyl-unit make up the HOMO level.[2] However, chromophoric ancillary ligands can also play a role in tuning the complex emission, due to changes that such a ligand can bring to the electronic levels within the complex. Two examples of the utilisation of an oxazole- and benzoxazole- based auxiliary ligand are presented by H. Benjamin *et al*[2] and Y. You *et al*[4] respectively.

Work by H. Benjamin *et al*[2] focused on colour tuning of the iridium complex emission *via* the introduction of electron withdrawing substituents on the 2-phenoxyoxazole ancillary ligand, shown in **Figure 5.2**. They found that substitution of 2-phenoxyoxazoline (**Ir-1**) with 2-phenyoxyoxazole gave a 6 nm blue shift. Further functionalisation of the phenyl-pyridine ligand with fluorines, and the 2-phenyoxyoxazole with methanesulfonyl on the phenyoxy ring, shifted emission further between 20-45 nm, with emission bands at 476 and 501 nm. Despite **Ir-2** (**Figure 5.2**), demonstrating the highest quantum yield and lifetime, when doped into an OLED device it gave a lower brightness (26150 cd m^{-2}) than the unfunctionalized complex and the oxazoline complex, **Ir-1** (**Figure 5.2**).

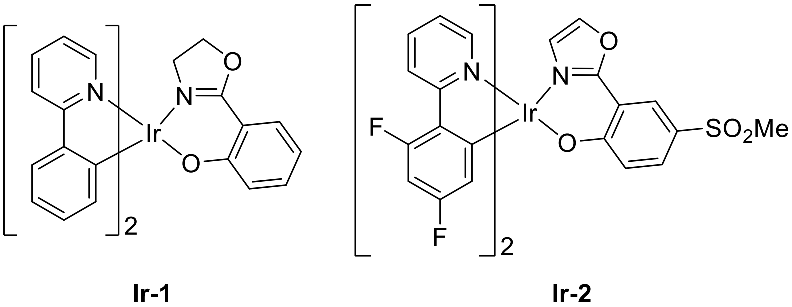

Ir-1

λ_{em} = 527 nm
ϕ = 0.55
τ = 0.34 μs

Ir-2

λ_{em} = 476, 501 nm
ϕ = 0.73
τ = 3.01 μs

Figure 5.2 Ir-1 and **Ir-2** complexes based upon oxazoline and oxazole units, and their respective photophysical data (recorded in DCM, degassed for Φ), adapted and taken from H. Benjamin *et al.*[2]

Y. You *et al*[4] also used the oxazole and benzoxazole systems as ancillary ligands to tune the emission of iridium complexes, finding that for each fused ring added to the oxazole ligand, a shift of 25 nm results (**Figure 5.3**). By examining the photophysics of these systems, two excitation pathways were predicted (shown in **Figure 5.3**), with excitation of both the cyclometallating and ancillary ligand resulting in the ancillary ligand emission. The emission spectra showed vibronic structure in all complexes, suggesting a large contribution from ligand-centred transitions, and the emission maxima did not vary with solvent or show evidence of rigidochromism, suggesting that there was little ^{3}MLCT character in the emission observed (particularly for **Ir-5**). Despite promising photophysical results, when **Ir-5** was doped into an OLED device both the emission efficiency and brightness were lower than expected.

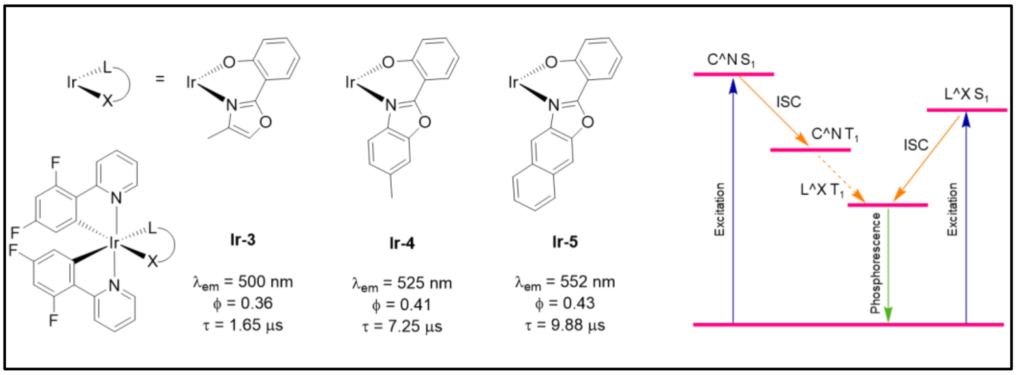

Figure 5.3 Ir-3, **Ir-4** and **Ir-5** subunits and their respective photophysical data, recorded in Ar-saturated toluene, adapted and taken from Y. You *et al*.[4] Jablonski diagram of emission contribution from both ligand systems, adapted from Y. You *et al*[4].

Whereas both of the previous examples focussed on the photophysics of the resulting oxazole-based complexes, complexes bearing oxazole-based ligands can also be used in catalytic reactions. M. Poyatos *et al*[5] coordinated benzoxazole based ligands to silver, palladium, platinum and rhodium (**Figure 5.4a**), with **Pd-2** able to catalyse Suzuki cross-coupling reactions, and **Rh-1** and **Pt-1** able to catalyse hydrosilation reactions. Z. Wu *et al*[5] coordinated benzoxazole based ligands to rhodium (**Figure 5.4b**), with **Rh-2** having catalytic use in the alkylation of isatin molecules via the activation of terminal alkynes.

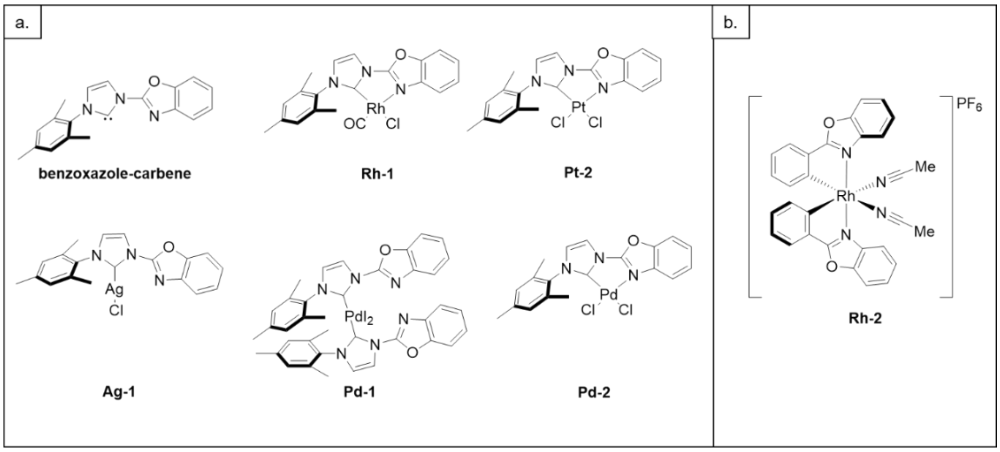

Figure 5.4 a) Benzoxazole--carbene ligand, with **Rh-1**, **Pt-2**, **Ag-1**, **Pd-1** and **Pd-2** complexes formed from the complexation of benzoxazole-carbene[5],[5]; b) **Rh-2** complex formed from a similar benzoxazole ligand[6]

5.1.2 Rhenium(I) tricarbonyl complexes : Synthesis, Photophysics and Applications

Rhenium is located in the third row of the transition metals in the periodic table and is therefore referred to as a “heavy” atom. Rhenium(I) has a d^6 configuration, and its carbonyl-diimine complexes of the type *fac*-[Re(diimine)$(CO)_3$X] were first discovered to be emissive in 1974, with long phosphorescent lifetimes.[7] This, along with their thermal and photochemical stability[8], as well as their ease of synthesis, has made them ideal for a variety of applications detailed below.

Another advantage of *fac*-[Re(diimine)$(CO)_3$X] is their ease of modification and stepwise addition of ligands, with a range of possible diimine and axial ligands. The most common synthetic route to *fac*-[Re(diimine)$(CO)_3$X] (where X=halide) is shown in **Figure 5.5**. Re$(CO)_5$X is initially formed *via* slow addition of X_2 into a solution of $Re_2(CO)_{10}$[9] (DCM is used in **Figure 5.5**, in line with experimental procedure carried out, however hexane is used in reference 10). Once isolated, this is then reacted with the diimine of choice (for **Figure 5.5**, 2,2’-bipyridine) to form *fac*-[Re(diimine)$(CO)_3$X][10]. Halide abstraction can then occur using $AgBF_4$ or $AgPF_6$ to yield a range of different axial ligands and vary the complex solubility.

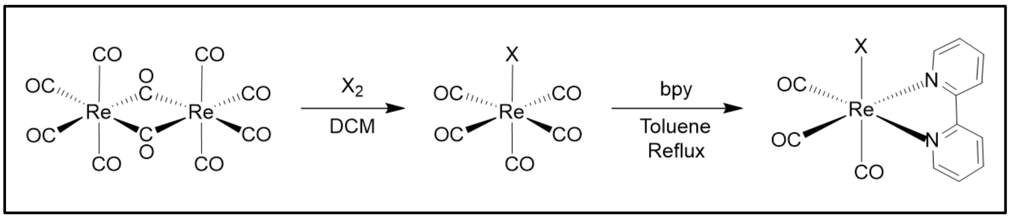

Figure 5.5 Reaction scheme for the synthesis of *fac*-[Re(bpy)(CO)$_3$X].

The photophysical properties of *fac*-[Re(diimine)(CO)$_3$X] are dominated by visible absorption and phosphorescent emission assigned to the ^{1}MLCT and ^{3}MLCT states. These correspond to charge transfer between 5d(Re) and the diimine π* orbitals[8] and thus can be fine-tuned *via* change in ligand aromaticity. Although ^{1}IL absorption states are often observed in the UV region, and thus are well separated from ^{1}MLCT, the corresponding triplet states are often in close proximity allowing a mixing of states.[8] In fact, it is more commonly found that these low energy bands are a combination of MLCT, XLCT or IL(diimine), schematics of which are shown in **Figure 5.6**.

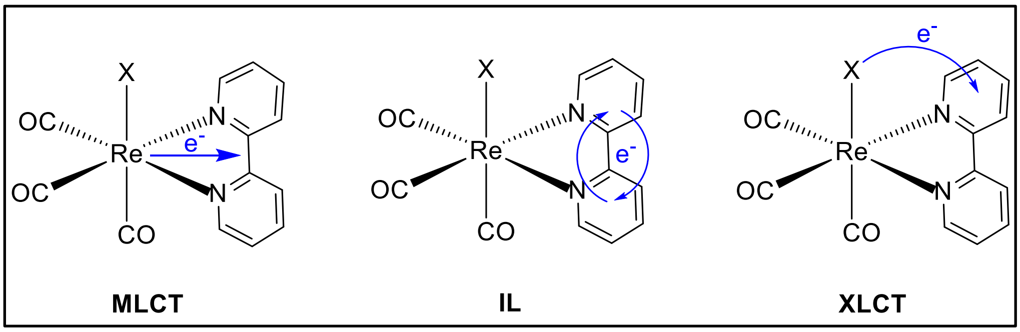

Figure 5.6 Schematic representation of MLCT, IL and XLCT states. SBLCT (sigma bond-to-metal charge transfer) is not shown as it is only observed for X ligands with high-lying sigma orbitals, such as alkyl or benzyl ligands. Adapted from A. Vlček[8].

Evidence of a high ^{3}MLCT character is shown by "rigidochromism", first described by M. Wrighton *et al*[7] in 1973. At low temperature (where the solvent forms a solid "glass") or in solid state emission, the excited ^{3}MLCT state cannot be stabilised by the rearrangement of the dipoles of surrounding solvent molecules, and therefore the state becomes destabilised and hence higher in energy.[7,8,11] This increase in energy results in a blue shift in emission to that of solution state, and is indicative of a ^{3}MLCT state as π→π* transitions (*i.e.* ^{3}LC) do not lead to a large enough change in dipole moment.

As discussed previously, *fac*-[Re(diimine)$(CO)_3X$] complexes possess a host of advantages that make them ideal for a range of applications, utilising the diverse photophysics as well as carbonyl fingerprints and inherent electrochemical properties.

5.1.2.1 Bioimaging

One of the most common applications of luminescent rhenium(I) tricarbonyl complexes is that of bioimaging, due to a large Stokes shift and long emissive lifetimes[12], that are far longer than autofluorescence (despite oxygen quenching of the triplet ^{3}MLCT state), as well as commonly showing high photostability[13] and kinetic inertness meaning that metal-DNA interactions do not occur.[14]

Rhenium(I) tricarbonyl species also have multimodal properties due to the advantageous characteristic IR bands of the carbonyl ligands. As discussed below, S. Clède *et al*[15] and I. Chakraborty *et al*[16] both utilise these bands in bioimaging applications.

The first example of the use of rhenium(I) tricarbonyl complexes with ^{3}MLCT emission was demonstrated by A. Amoroso *et al*[14] in the cell imaging of *Spironucleus vortens*. Both functionalised bathophenanthroline and bipyridine were used with pyridine derivatives as the axial ligand to form charged lipophilic and hydrophilic complexes (**Figure 5.7a**). ^{3}MLCT emission occurred at *ca.* 555 nm and 565 nm for bipyridine and bathophenanthroline derivatives respectfully and excitation was far enough in the visible range to prevent tissue damage. **Re-2** and **Re-3** were the most effective imaging agents (**Figure 5.7a** shows confocal fluorescence microscopy image using **Re-3**), however **Re-2** suffered from a high toxicity, as did derivatives of **Re-1**. The toxicity however was ascribed to the ligands chosen, with the highly lipophilic derivatives of Re-1 disrupting the cell membrane and leading to lysis at high concentration, and the polar sulfonated Re-2 also leading to cell death. Therefore,this paved the way for future complexes with more biologically relevant coordinated ligands.

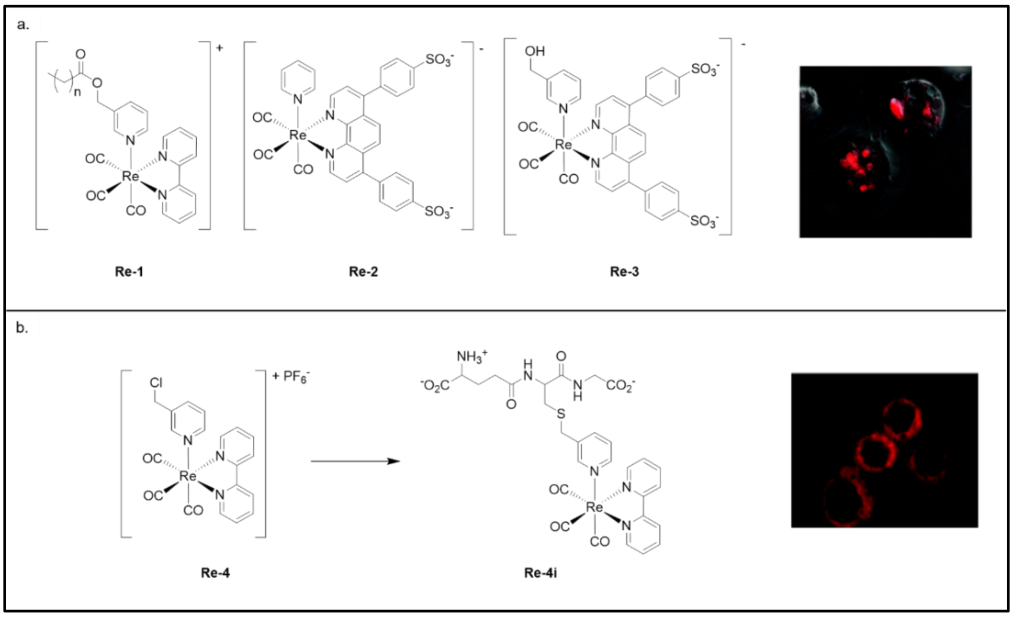

Figure 5.7 a. Rhenium(I) tricarbonyl complexes **Re-1** (n = 6, 12, or 16), **Re-2** and **Re-3** (*left*) with confocal fluorescence microscopy image of **Re-3** (*right*), adapted and taken from A. Amoroso *et al*[14]; **b. Re-4** reacted with glutathione to form a glutathione-rhenium conjugate, **Re-4i**, with similar photophysical properties (*left*) and showed mitochondrial localisation *via* confocal fluorescence microscopy imaging (*right*), adapted and taken from A. Amoroso *et al*[17].

Following from this work, A. Amoroso *et al*[17] synthesised rhenium(I) tricarbonyl complexes bearing an axial pyridine ligand functionalised with chloromethyl for a mitochondria selective, thiol-reactive imaging agent (**Re-4**, **Figure 5.7b**). **Re-4** demonstrated emission at 551 nm and was shown to react with glutathione to form a water-soluble fluorescent complex (**Re-4i**) with similar photophysical characteristics. When incubated with MCF-7 cells, localisation of the complex was evident (**Figure 5.7b**) which was further confirmed to be mitochondrial *via* co-incubation with a known mitochondrial tracker, as both imaging agents emitted from the same regions within the cells.

S. Clède *et al*[15] utilised a rhenium(I) tricarbonyl complex for use as a Single Core Multimodal Probe for Imaging (SCoMPI), shown in **Figure 5.8**. In the design of **Re-5**, the bidentate triazole-based ligand was functionalised with a long alkyl chain with a terminal azide, the latter to promote uptake within the cells and the former to allow comparison of N_3 IR stretches (2096 cm^{-1}) to that of CO, which fall within the cell tissue transparency window.

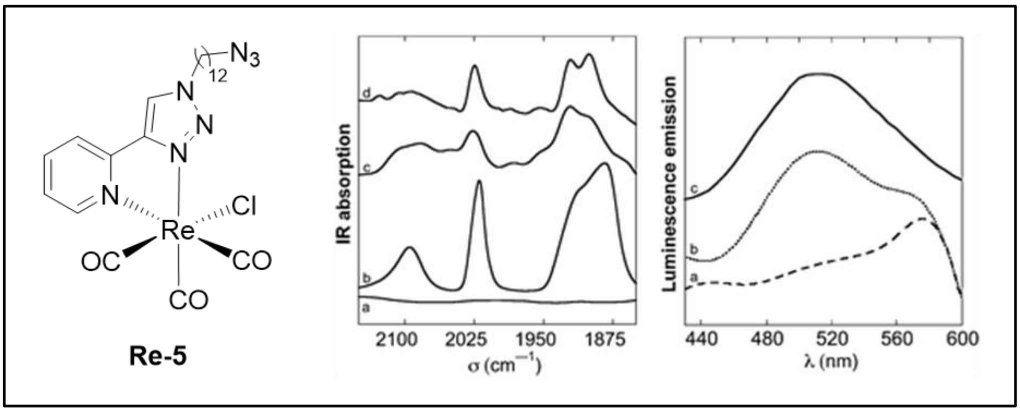

Figure 5.8 *Left*: Structure of **Re-5**; *Middle*: FTIR-spectra of a) control cells on nitrocellulose membrane, b) solid **Re-5**, c) cells incubated with **Re-5**, on a nitrocellulose membrane, d) SR-FTIR-SM on a single cell incubated with **Re-5**; *Right*: Emission spectra of a) single control cell, b) single cell incubated with **Re-5**, c) **Re-5** in H_2O:EtOH (6×10^{-5} M). All spectra ex. 350 nm, taken from S. Clède *et al*[15].

Figure 5.8 shows both the IR- and emission spectra of MDA-MB-231 cells incubated with the complex, compared to the solid complex and the non-incubated cells, with IR-stretches at 1920 and 2025 cm^{-1} for the carbonyl ligands (the authors propose C_{3v} symmetry, and thus the stretches observed are assigned to the E and A_1 bands respectively) and emission at 520 nm assigned to the ^{3}MLCT state. The resultant synchrotron radiation FTIR SpectroMicroscopy (SR-FTIR-SM) mappings of a single cell are shown in **Figure 5.9**. Results showed that the SR-FTIR maps overlayed with the fluorescence microscopy images, and that the complex accumulated within the Golgi apparatus.

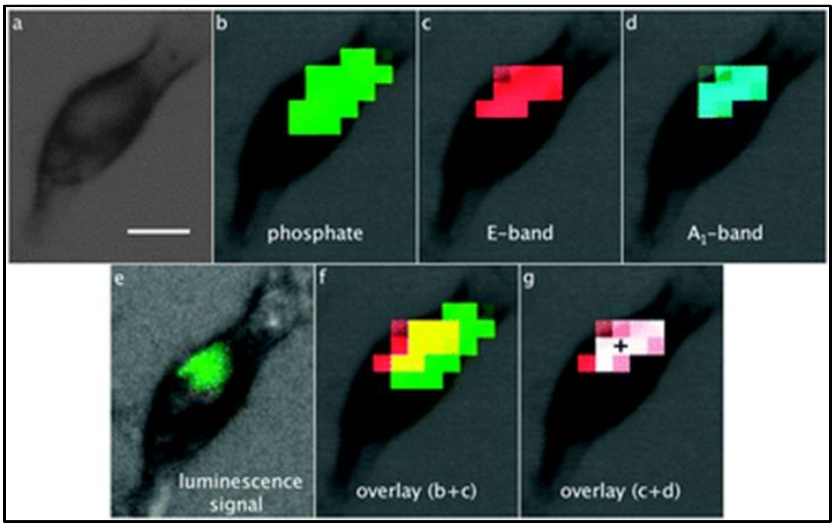

Figure 5.9 a) Bright field image of MDA-MB-231 cells inclubated with **Re-5**, scale bar = 10 µm. b-d) various SR-FTIR maps of relevant IR-stretches; e) epifluorescence image showing **Re-5** localisation; f-g) overlays of relavant SR-FTIR mappings. Taken from S. Clède *et al*[15].

Another example of triazole-based ligands in bioimaging applications comes from H. Bertrand *et al*[18], who examined structural variations of benzothiadiazole-triazole ligands, in particular 4-(2-pyridyl)-1,2,3-triazole (Pyta) and the relatively unexplored regioisomer 1-(2-pyridine)-1,2,3-triazole (Tapy). Both ligands coordinated to Re(I) tricarbonyl complexes to form **Re-6** and **Re-7**, and are presented in **Figure 5.10**, with those functionalised with long chain alkyl groups focused upon in this discussion due to the focus on bioimaging.

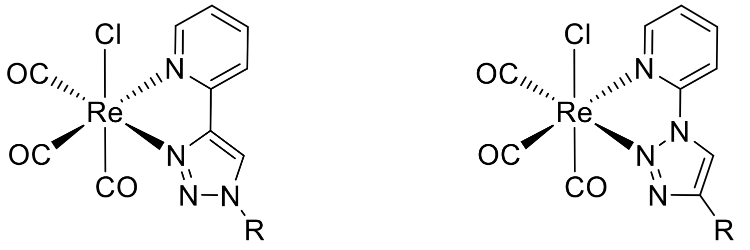

Re-6
(Re-Pyta)

$R=C_{12}H_{25}$
AcN λ_{em}= 522 nm
H_2O:DMSO (98:2) λ_{em}= 512 nm

Re-7
(Re-Tapy)

$R=C_{12}H_{25}$
AcN λ_{em}= 569 nm
H_2O:DMSO (98:2) λ_{em}= 554 nm

Figure 5.10 Structures of **Re-6** and **Re-7**. Information taken, and structures adapted, from H. Bertrand *et al*[18].

Photophysical and DFT data (using hybrid B3LYP functional, and 6311G** and LANL2DZ for the ligands and the Re centre respectively) showed no change when the R-group was modified, however **Re-7** exhibited lower energy emission than **Re-6**, with a 30-35 nm shift in water (2% DMSO). This was further suggested by DFT, which showed **Re-7** complexes possessed lower energy orbitals and a smaller band gap than **Re-6** (**Figure 5.11**). **Re-7** complexes bearing long-chain alkyl groups exhibited a higher quantum yield in water when compared to acetonitrile, thought to be due to the alkyl-chain surrounding the complex in aqueous solvent and thus reducing solvent-based quenching, however this was not observed in **Re-6** complexes. MDA-MB-231 was incubated with both **Re-6** and **Re-7**, with the fluorescence intensity presented in **Figure 5.11**, showing that the intensity of the **Re-7** complex was stronger than that of the **Re-6** analogue.

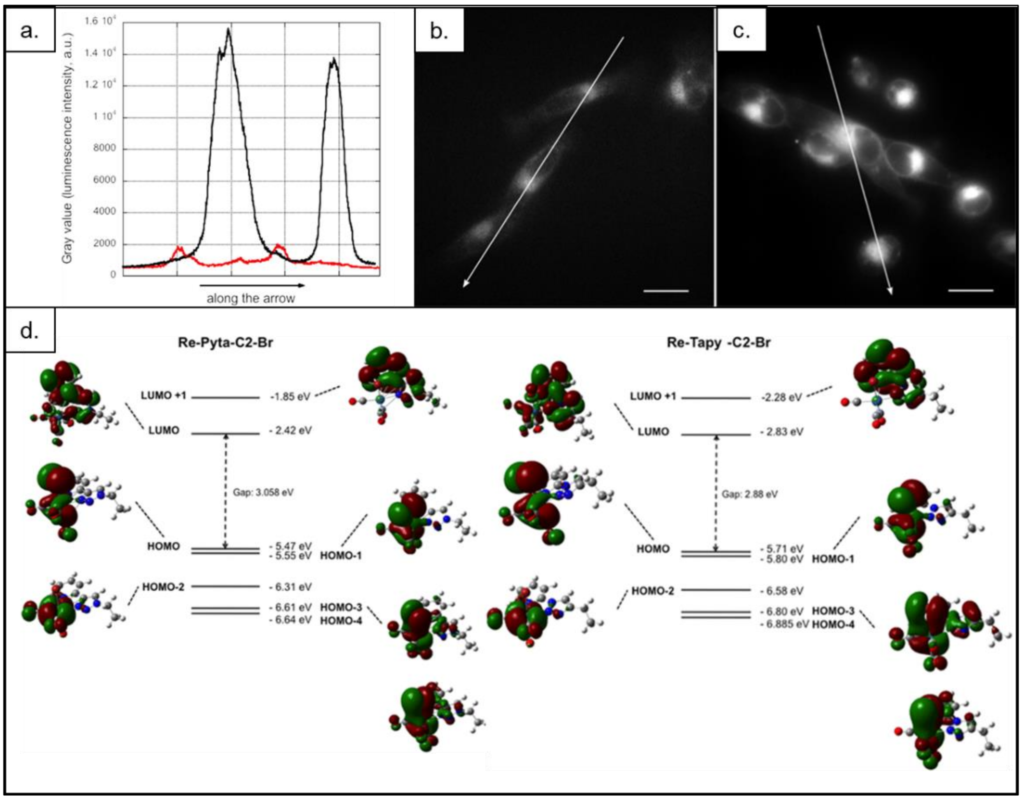

Figure 5.11 a) Intensity profile along white arrow of images (b) and (c); b) Luminescence signal for MDA-MB-231 cells incubated with **Re-6** where R=$C_{12}H_{25}$; c) MDA-MB-231 cells incubated with **Re-7** where R=$C_{12}H_{25}$; d) Frontier orbital diagrams generated from DFT analysis for **Re-6** and **Re-7**, where the axial Cl is replaced with Br. Note that for image (b) brightness and contrast were increased to allow imaging of the cells. Taken from H. Bertrand *et al*[18].

Interestingly, work by I. Chakraborty *et al*[16] showed a unique photoactivatable property of a rhenium(I) tricarbonyl species that led to the release of CO within the cells for the potential use in cancer treatment. Although CO gas is known to be toxic, it can have a use in the treatment of cancerous tissue. A novel rhenium(I) tricarbonyl complex (**Re-8**) composed of a 2-(2-pyridyl)-benzothiazole bidentate ligand, a triphenylphosphine monodentate ligand, and a triflate counter ion, were encapsulated within Al-MCM-41 silica nanoparticles, shown in **Figure 5.12**. The complex showed minimal leaching from the particles due to the favourable electrostatic interactions with the negatively charged walls of the composite, with ICP-OES analysis showing 0.97 +/- 0.1 wt% Re within the particles.

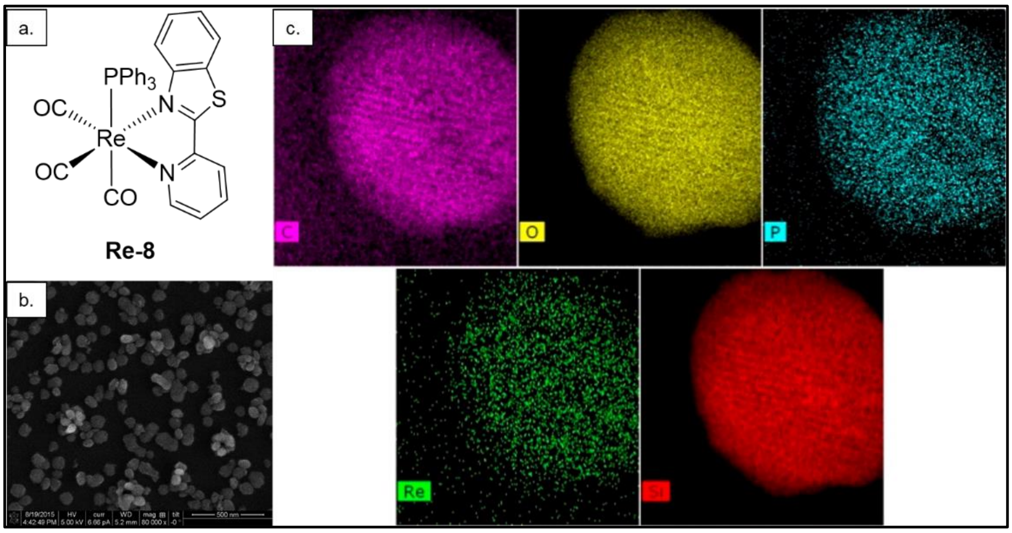

Figure 5.12 a) Structure of **Re-8**; b) SEM of Al-MCM-41 encapsulated with **Re-8**; EDX maps of Al-MCM-41 encapsulated with **Re-8**. Taken from I. Chakraborty *et al*[16].

When irradiated at 345 nm, the IR spectra of **Re-8** showed that stretches at 2038, 1953 and 1921 cm^{-1} (assigned to carbonyl stretches) reduced in intensity, with the appearance of two new bands at 1935 and 1861 cm^{-1}, suggesting loss of one CO (**Figure 5.13**). The emission spectra, also presented in **Figure 5.13**, showed emission at 605 nm decreased in intensity when irradiated over the same time as the IR-analysis, showing that a loss of CO can lead to a “turn-off” of luminescence.

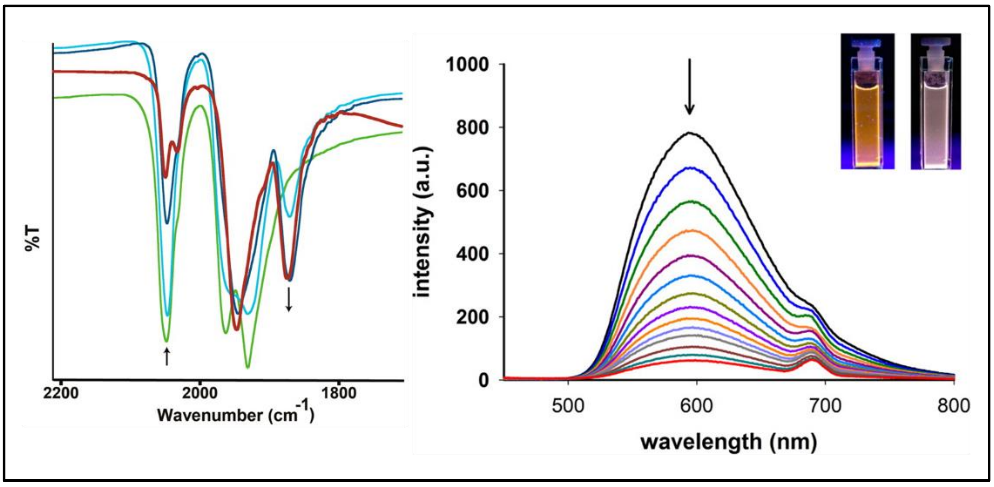

Figure 5.13 Changes in (*left*) FTIR spectra and (*right*) emission spectra, upon illumination at 305 nm, 3 mW cm^{-2} and 345 nm respectively. Emission spectra recorded at 2.7 x10^{-5} M in AcN, *inset* shows visible loss of luminescence upon iradiation. Taken from I. Chakraborty *et al*[16].

These observations were also shown with the encapsulated complex when incorporated into MDA-MB-231 cells, and thus CO release could be tracked *via* the decrease in emission intensity. After irradiation over 15 minutes, 80% of cells were destroyed, shown in the confocal microscopy images presented in **Figure 5.14**, and thus this technology offers an alternative cancer therapy, where a variety of bioconjugates could be added to the particle surface to yield targeted delivery of CO within the body.

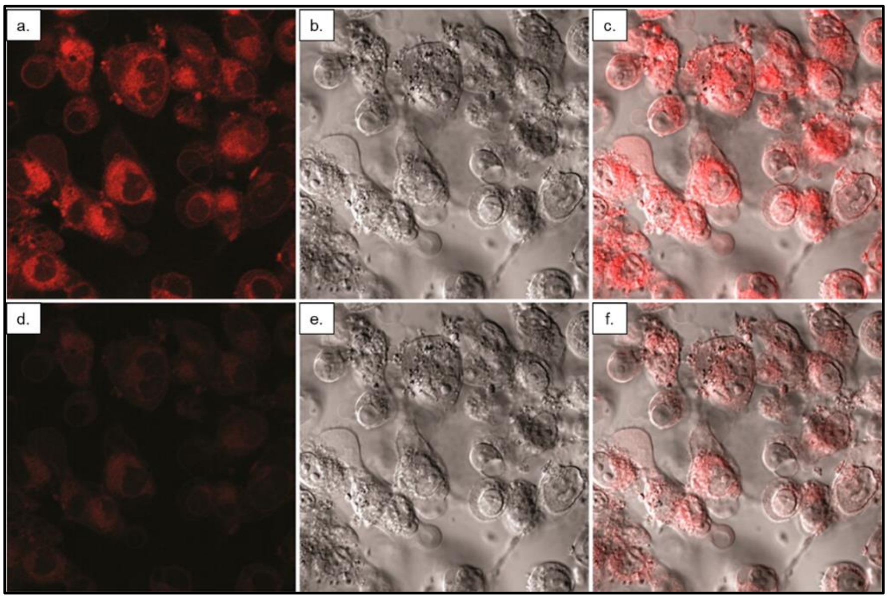

Figure 5.14 Confocal microscopy of MDA-MB-231 cells inclubated with **Re-8** encapsulated Al-MCM-41 over 3 hours. Initial a) fluorescence image; b) bright-field image; c) merged image; d,e,f) after 30 minutes. Taken from I. Chakraborty *et al*[16].

5.1.2.2 CO_2 Reduction Catalysis

Another application for rhenium(I) tricarbonyl complexes is that of catalysts in CO_2 reduction to CO. When uncatalyzed, reduction of CO_2 occurs *via* a monoelectronic pathway, and requires up to –2 V potential due to the high energy intermediate, $CO_2^{\cdot -}$[19]. However *via* catalysis with rhenium(I) tricarbonyl complexes, the reduction can take place at less negative potentials for dielectronic reduction[20], as shown in **Equation 5.1**.

Equation 5.1 Reduction of CO_2 to CO and H_2O, taken from J. Hawecker *et al*[21].

$$CO_2 + 2H^+ + 2e^- \leftrightharpoons CO + H_2O$$

Work by J. Hawecker *et al*[21] in 1983 showed the first known example of rhenium(I) tricarbonyl complexes as viable CO_2 reduction catalysts, using *fac*-[Re(bipy)(CO)$_3$X] (X=Br or Cl, latter presented in **Figure 5.15** as **Re-9**) and yielding selective CO release photochemically (with no H_2 as with multiple-complex systems also described within the publication). This was then expanded in 1984[20], finding that the same complex could catalyse CO_2 reduction electrochemically at a potential of -1.25 V, much lower than required for non-catalysed reduction. In

DMF:water (9:1) solutions containing Et_4NCl, 98 % current efficiency was obtained, with selective CO release and no formate or H_2 produced as with the photoreduction case.

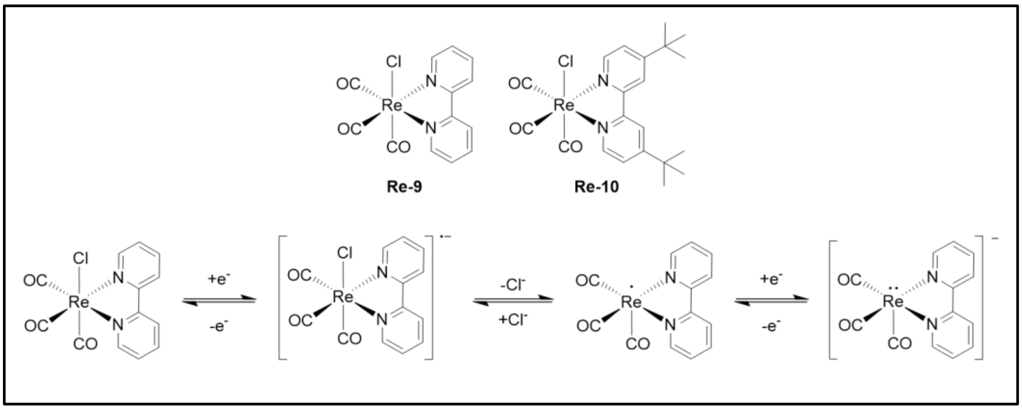

Figure 5.15 Top: Structures of **Re-9** and **Re-10**, adapted from J. Hawecker *et al*[21] and J. Smieja *et al*[22] respectively; Bottom: Proposed reaction pathway for **Re-9** in the reduction of CO_2, adapted from J. Smieja *et al*[22].

A more recent example of CO_2 reduction follows from this initial work, whereby four rhenium complexes containing functionalised bipy ligands were tested for their catalytic activity and compared to *fac*-[Re(bipy)$(CO)_3$Cl][22]. J. Smieja *et al*[22] showed that out of the four complexes tested (where bipy was functionalised with carboxy, methyl, methoxy and tert-butyl groups) it was *fac*-[Re(bipy-tBu)$(CO)_3$Cl], **Re-9**, that showed the most promise in CO_2 reduction (**Figure 5.15**). Compared to *fac*-[Re(bipy)$(CO)_3$Cl], it showed a 3.5-fold increase in catalytic activity and a Faradaic efficiency of 99 +/- 2 % in acetonitrile. The proposed catalytic cycle is presented in **Figure 5.15**.

Tapy and pyta-based rhenium complexes, such as those discussed in **Section 5.1.2.1**, have also been focussed on for their ability to catalyse CO_2 reduction. However, work by H. Ching *et al*[23] showed that tapy-based complexes showed minimal catalytic activity, and although pyta-based complexes (presented in **Figure 5.16**) displayed high stabilities, the catalytic efficiency (even with water or TFE present as proton sources) and CO selectivity could not be compared to that of Re(bipy)$(CO)_3$Cl, the values of which are presented in **Figure 5.16**.

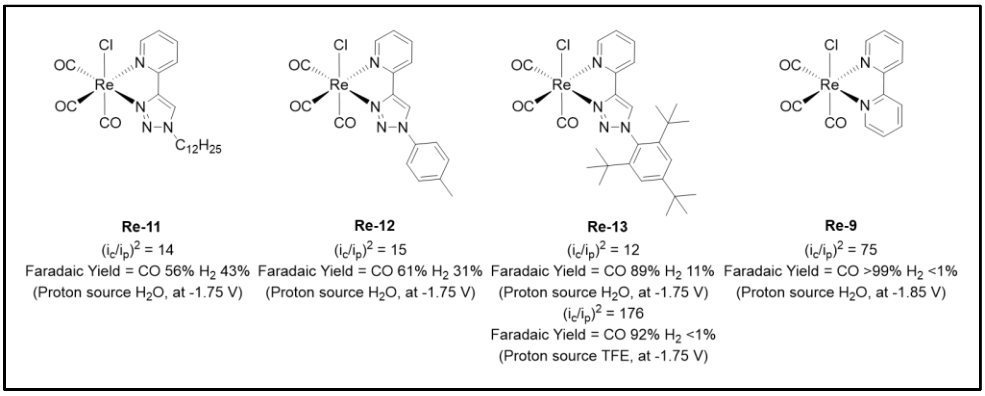

Figure 5.16 Structures of **Re-11**, **Re-12**, and **Re-13**, with **Re-9**[21] as reference. Structures adapted, and information taken from H. Ching *et al*[23].

5.1.2.3 Electrochemical OLED Devices

Phosphorescent complexes have been the focus of much research in their ability to be used in Phosphorescent Light Emitting Diodes (PLEDs), due to their high quantum efficiency and colour tunability.[24] Although rhenium complexes have the disadvantage of being harder to colour tune and exhibiting lower quantum yields then the iridium complex equivalents, they do have the advantage of shorter lifetimes and easier, high yielding synthesis,[25] the latter of which is important in mass produced devices.

Examples of novel rhenium(I) tricarbonyl complexes fabricated into the emissive layer of PLED devices are presented in **Figure 5.17**. Y-X. Hu *et al*[25] used a thiadiazole-functionalised 1,10-phenanthrolene based rhenium complex, **Re-14**, to yield orange-red emission with an efficiency of 16.8 cd/A, and an emissive quantum efficiency of 5.4 % (higher than that of *fac*-[Re(phen)$(CO)_3$Br]). DFT analysis suggested that the LUMO was primarily located on the thiadiazole ring, which supported electrochemical analysis that showed the LUMO was lower in energy in **Re-14** than *fac*-[Re(phen)$(CO)_3$Br], thus showing electronic tunability. The low emissive lifetime for **Re-14** (0.04 µs) was also advantageous, as long lifetimes could lead to an increase in triplet-triplet annihilation, however the complex suffered from a low quantum yield of 4 %.

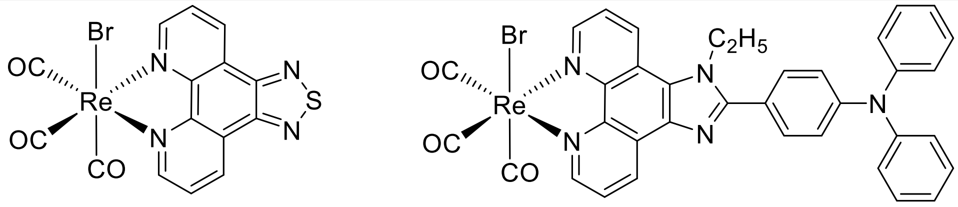

Re-14

λ_{PL} = 621 nm
λ_{EL} = 590 nm
Max. Luminance = 3982 cd/m
Max. Current efficiency = 16.8 cd/A
Max. Power efficiency = 5.8 lm/W

Re-15

λ_{PL} = *ca*. 545 nm
λ_{EL} = 550 nm
Max. Brightness = 6483 cd/m^2
Max. Current efficiency = 17.6 cd/A
Max. Power efficiency = 9.2 lm/W

Figure 5.17 Structures of **Re-14** and **Re-15**. Adapted, and information taken from, Y-X. Hu *et al*[25] and C. Liu *et al*[26] respectively.

Using (3-ethyl-2-(4'-triphenylamino)imidazo[4,5-f] 1,10-phenanthroline) (TPIP) as the cyclometallation ligand, C. Liu *et al*[26] presented a novel complex, Re(TPIP)(CO)$_3$Br, **Re-15**, with an emissive lifetime of 0.2 µs and yellow-green emission at 552 nm (**Figure 5.17**). When fabricated within the emissive layer of the PLED, the triphenyl-amine moiety acted as a hole transport group, leading to increased charge trapping and triplet exciton confinement, resulting in enhanced electrophosphorescence. This yielded a brightness of 6483 cd m^{-2} and current efficiency of 17.6 cd/A, higher than that of **Re-14**. A further advantage of this system was that by using a low dopant amount of complex in the emissive layer, holes in the *N,N'*-di-1-naphthyl-*N,N'*-diphenylbenzidine (NPB) layer formed excitons with electrons that had not formed excitons in the emissive layer, leading to dual emission from both Re(TPIP)(CO)$_3$Br and NPD, and yielding white emission.

Although the photophysical characteristics and PLED parameters are not as favourable as those for other transition metal systems[24], the ease of synthesis of rhenium complexes (*vs* those of iridium for example), and the short emissive lifetimes, make the complexes interesting for alternative PLED devices[25].

5.1.3 Rhenium(I) tricarbonyl complexes containing oxazole-based bidentate ligands

As discussed previously, there are relatively few examples of the use of oxazole-based ligands in rhenium coordination chemistry. However, there are examples based upon benzoxazole and oxazoline, of which a selection will be discussed herein.

The first investigation into benzoxazole as a viable ligand for rhenium(I) tricarbonyl complexes was reported by R. Czerwieniec *et al*[27], shown in **Figure 5.18** and referred to as **Re-16** and **Re-18**. For **Re-16**, absorbance at 382 nm was assigned to the ^{1}MLCT state, red shifted compared to that of complexes bearing the analogous 2-(2-pyridyl)-N-methyl-benzimidazole (MPBI, **Re-17**), and blue shifted compared to that bearing 2-(2-pyridyl)benzothiazole (PBT) due to the respective electron-donating abilities of the different heteroatoms. When the halide was substituted for acetonitrile, forming positively charged complexes (**Re-18** and **Re-19)**, the ^{1}MLCT band of all three complexes was blue shifted as charge transfer between the rhenium centre and ligand is less favourable in cationic complexes.

At low temperature, the broad and featureless emissive band of **Re-16** and **Re-17** indicated that the emission is dominated by the ^{3}MLCT state, further confirmed by the rigidochromism also observed compared to room temperature emission. Whereas for **Re-18** and **Re-19**, the vibronic structure showed evidence of the ^{3}IL state, with the rigidochromism observed showing that the emissive state may be an admixture of both ^{3}MLCT and ^{3}IL states.

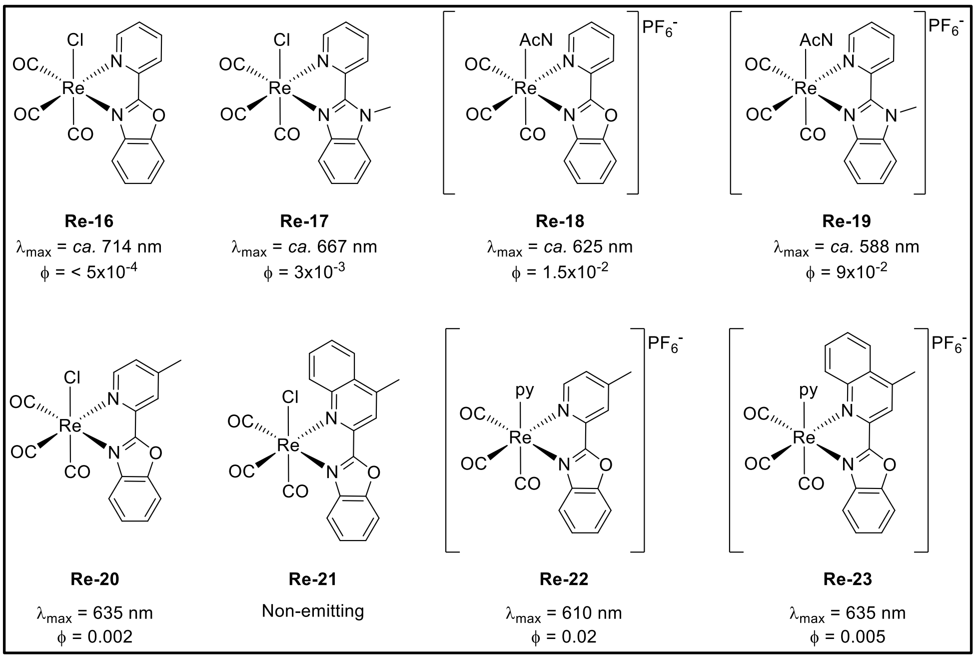

Figure 5.18 Top: Structures and photophysical properties of **Re-(16-19)**, adapted and taken from R. Czerwieniec *et al*[27]; Bottom: Structures and photophysical properties of **Re-(20-23)**, adapted and taken from A. Albertino *et al*[12].

A. Albertino *et al*[12] continued this study by comparing more conjugated ligand derivatives; 2-(4-methylpyridin-2-yl)benzo[*d*]-X-azole and 2-(benzo[*d*]-X-azol-2-yl)-4-methylquinoline, where X= O, S or N-CH_3. [Re(2-(4-methylpyridin-2-yl)benzo[*d*]-O-azole)$(CO)_3$Cl] (**Re-20**) and [Re(2-(benzo[*d*]-O-azol-2-yl)-4-methylquinoline)$(CO)_3$Cl] (**Re-21**) showed ^{1}MLCT absorption bands at 380 and 400 nm respectively, the latter red shifted with respect to **Re-16** due to the increase in conjugation across the ligand. Those with chloride ligands were weakly emissive compared to cationic complexes bearing a pyridine, with **Re-20** showing an emissive band at 635 nm with a quantum yield of 0.002, **Re-21** non-emitting. However, the cationic complexes **Re-22** and **Re-23** showed emission at 610 and 635 nm, with **Re-22** exhibiting a higher quantum yield of 0.02.

Surprisingly, despite there being no known examples of the oxazole unit being used as part of a bidentate ligand system with rhenium(I), there are many examples of oxazoline rings being utilised, despite their lack of aromaticity compared to the oxazole. They are known to be better σ-donors than pyridine, and thus present a useful addition to a bidentate ligand. A. Świtlicka *et al*[11] utilised the oxazoline-quinoxaline ligand to yield the novel [Re(quinox)$(CO)_3$Cl] (**Re-24**), shown in **Figure 5.19**. The lower energy absorption band, located at 406 nm in acetonitrile, was assigned to a ^{1}MLLCT state (metal ligand to ligand charge transfer, *i.e.*, a mixture of ^{1}MLCT and ^{1}LC states) due to DFT analysis predicting the contributing HOMO orbitals to be centred on the rhenium core, carbonyl and chloride ligands (**Figure 5.19**). Luminescence measurements showed emission at 780 nm in acetonitrile, and 764 nm in $CHCl_3$, thus demonstrating that polar solvents stabilised the excited state more effectively. In the solid state, the emission was heavily blue shifted to 655 nm. This is reasoned by the stabilisation of the ^{3}MLCT state in different solvents, with the charge transfer from the rhenium centre to the ligand causing a change in dipole moment, which is more stabilised in polar solvents, such as acetonitrile, due to the solvent being able to reorient to stabilise the change. In the solid state, this stabilisation of the excited state does not occur, and thus the emission is shifted to a higher energy. Emission lifetimes were recorded in acetonitrile, chloroform and in the solid-state, giving short biexponential lifetimes indicative of ligand-centred emission for acetonitrile (2.5 ns (94.2%), 14.0 ns (5.8%)) and chloroform (2.8 ns (96.1%), 10.1 (4.0%)) with χ^2 of 1.011 and 1.085 respectively, and a long mono exponential lifetime (38.6 ns, χ^2 = 0.923) in the solid state indicative of phosphorescent ^{3}MLCT state.

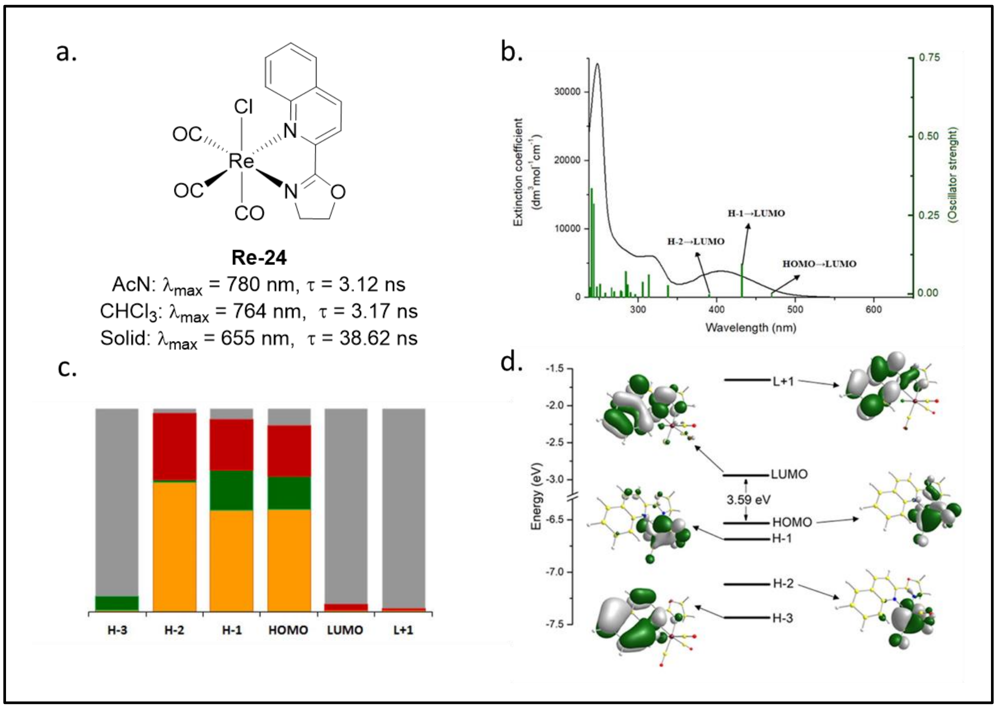

Figure 5.19 a) Structure and photophysical properties of **Re-24**: b) absorption spectra (black line) compared to DFT calculated transitions (green lines); c) frontier orbitals relative contribution, grey= oxazoline ligand, green = Cl ligand, red = carbonyl ligands, orange = Re centre; d) Frontier orbital diagram generated from DFT analysis of **Re-24**. All taken from A. Świtlicka *et al*[11].

Oxazoline-pyridine complexes have also been analysed for the use of CO_2 reduction catalysts in work by J. Nganga *et al*[28], the structures of which are presented in **Figure 5.20**. Although the oxazoline lacks the same aromaticity as the oxazole ring, the pyridine is in conjugation with the C=N of the ring, and thus there is still an aromatic system available to stabilise the negative charge before reduction of CO_2. The relative turnover frequency of **Re-26** was in fact higher than that of *fac*-[Re(bipy)(CO)$_3$Cl] (**Re-9**)[21,23], suggested to be due to the enhanced σ-donor ability of the oxazoline ligand. However, despite the increase in turnover efficiency, the Faradaic efficiency and stability of the complexes was far lower, with complexes **Re-25** and **Re-26** yielding a 55 % efficiency, and **Re-27** yielding a 30 % efficiency. That being said the stability could be modified with adaptions to the ligand design, and therefore oxazoline based systems could indeed be used for CO_2 reduction catalysis.

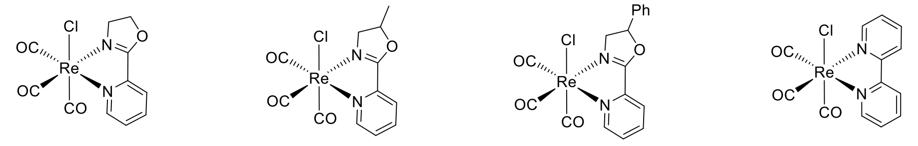

Re-25	**Re-26**	**Re-27**	**Re-9**
$(i_c/i_p)^2$ = 66	$(i_c/i_p)^2$ = 85	$(i_c/i_p)^2$ = 11	$(i_c/i_p)^2$ = 75
Faradaic Yield = CO 55% H_2 <3%	Faradaic Yield = CO 55% H_2 <3%	Faradaic Yield = CO 30% H_2 <3%	Faradaic Yield = CO >99% H_2 <1%

Figure 5.20 Structures and properties of **Re-25-27**, with **Re-9** as reference. Information for **Re-(25-27)** taken from J. Nganga *et al*[28], information for **Re-9** was supplied by J. Nganga et al, however differed to previous properties given by H. Ching *et al*[23], and thus information presented here is taken from H. Ching *et al*[23] for continuality with previous discussion.

5.2 Results and Discussion

5.2.1 Synthesis

In **Chapter 2**, a series of mono-substituted oxazoles (**1-7**) were synthesised with varying R-groups, leading to a diverse range of photophysical characteristics. These were further functionalised with naphthalene moieties in the 2-position of the oxazole ring, leading to six novel di-substituted oxazole species (**8-13**), which showed both higher emission wavelengths and evidence of charge transfer across the oxazole ring. Within this chapter, a further six novel di-substituted oxazole species were synthesised following the same method (adapted from T. Yoshizumi *et al*[29]), resulting in 2-pyridyl di-substituted oxazole species using the original mono-substituted oxazoles **1-5** and **7**, yielding suitable N-N cyclometallation units for coordination to rhenium.

Coupling to the 2-position of the oxazole ring was achieved in moderate yields *via* the modified Ullmann method[29] discussed in **Chapter 2**, using 2-iodopyridine to yield six novel oxazole derivatives (**Figure 5.21**). Unlike oxazoles **8-12**, where purification of all crude products could be achieved *via* trituration, **18** and **19** required column chromatography with 1:1 and 9:1 petroleum ether : ethyl acetate respectively.

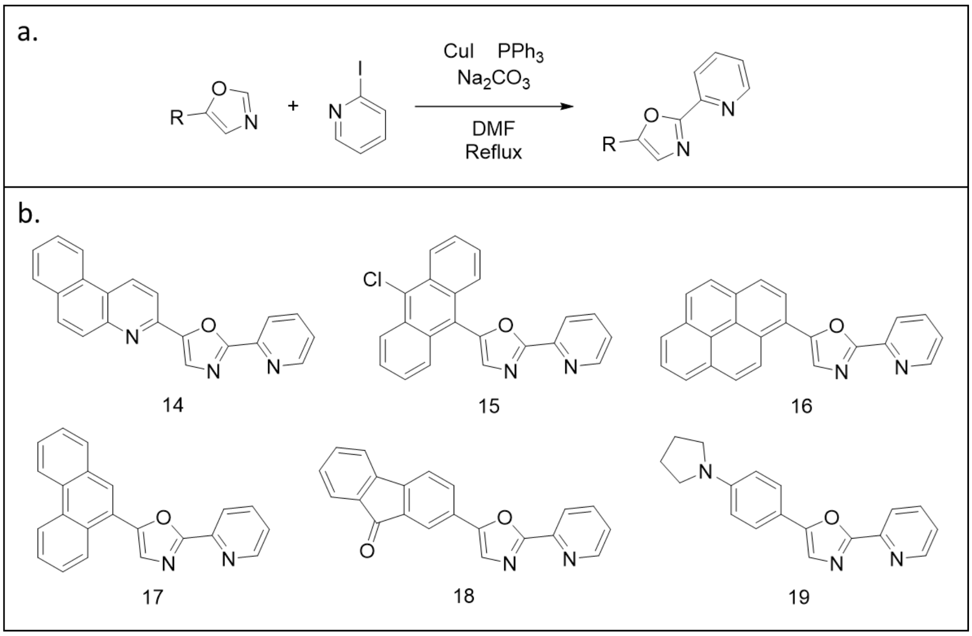

Figure 5.21 a) Reaction conditions of the modified Ullman coupling reaction[29]; b) Structures of the di-substituted oxazoles (**14-19**).

Coupling of pyridine to the oxazole ring was shown *via* ^{1}H NMR spectroscopy with the absence of the aromatic singlet of the 2-position of the oxazole ring, and the appearance of four new aromatic proton environments indicative of pyridine. ^{13}C {^{1}H} NMR spectroscopy also showed new resonances corresponding to the pyridine ring.

As with the synthesis of **12**, the fluorene R-group of oxazole **5** oxidised to fluorenone in the synthesis of **18**, which was confirmed *via* the loss of the ^{1}H NMR resonance belonging to the aliphatic CH_2 of the fluorene ring, and the corresponding aliphatic ^{13}C {^{1}H} NMR resonance (**Figure 5.22**). A new ^{13}C {^{1}H} NMR resonance was found belonging to that of the ketone of the fluorenone at 193 ppm, and HR MS further confirmed the oxidation with a peak at 325.0978 ($[M+H]^+$) instead of that of the non-oxidised species.

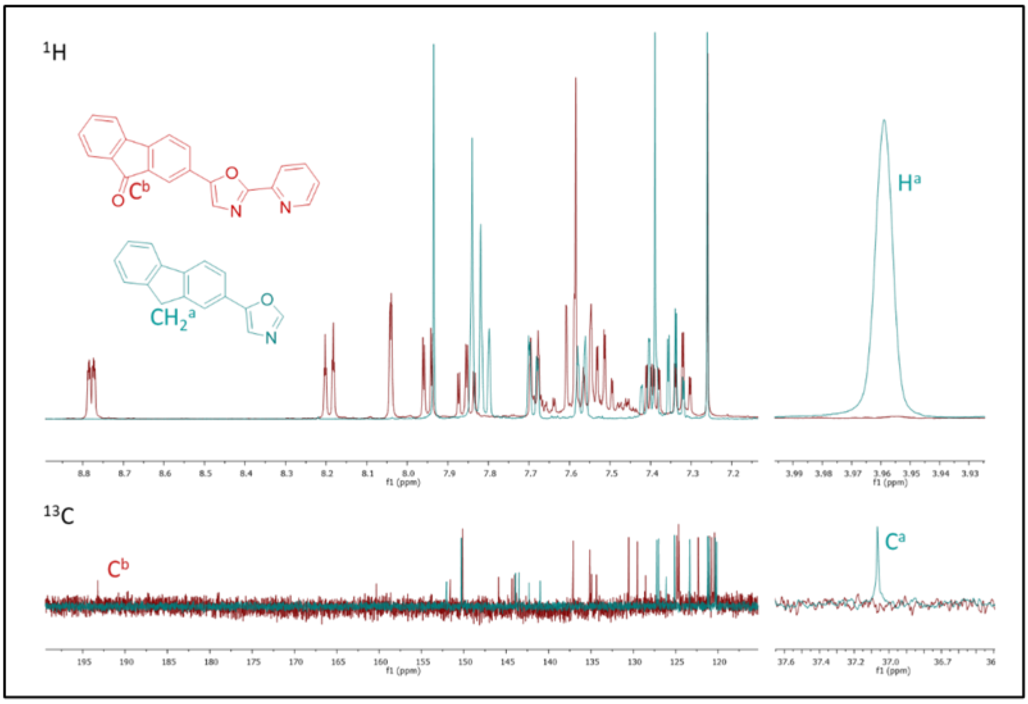

Figure 5.22 ^{1}H (top) and ^{13}C {^{1}H} (bottom) NMR spectra of mono-substituted oxazole **5** and disubstituted oxazole **18**, showing original C^a ^{13}C {^{1}H} resonance at 37 ppm shifted to 193 ppm (C^b) upon oxidation to ketone. This is further confirmed by the ^{1}H NMR H^a resonance at 3.96 ppm disappearing following the coupling reaction.

Ligands **14-19** were coordinated to rhenium to form rhenium tricarbonyl species with an axial bromide ligand, presented in **Figure 5.23**. In this method, $Re(CO)_5Br$ and ligand were dissolved in toluene and heated to reflux until the product precipitated. The precipitate was filtered and washed with toluene and ether, to yield the desired complex in moderate yield.

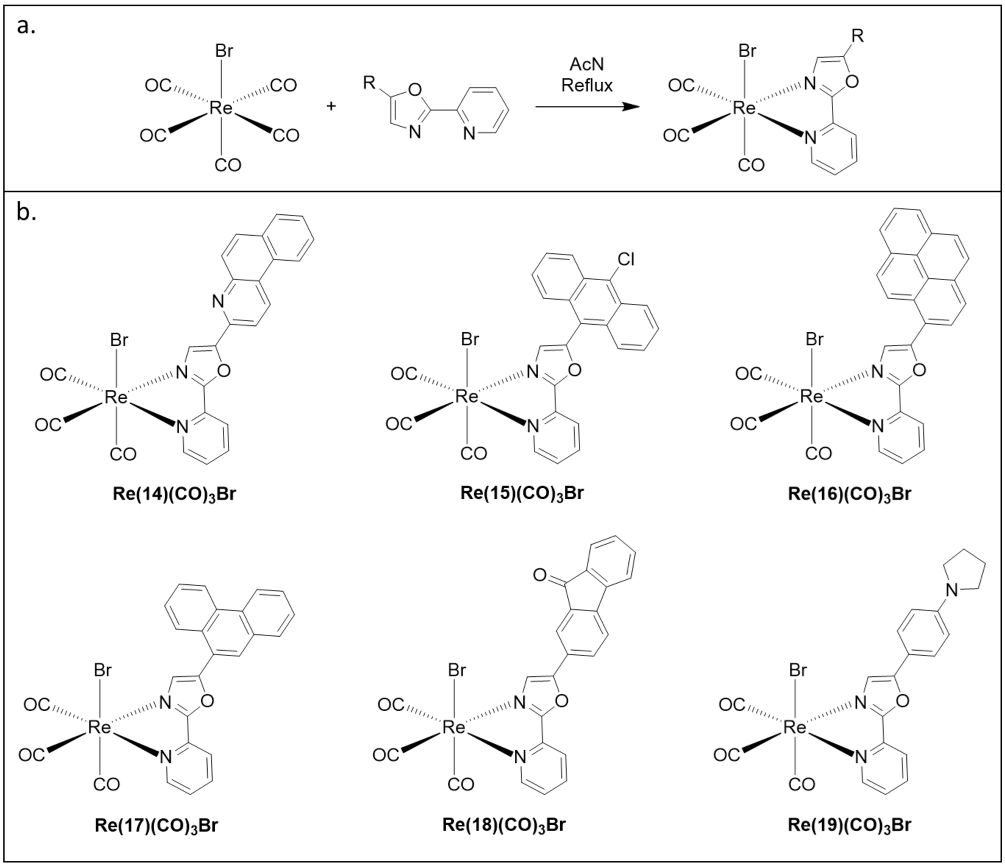

Figure 5.23 a) Reaction conditions for the synthesis of ***fac*-[Re(L)(CO)$_3$Br]**; b) Structures of the resultant ***fac*-[Re(L)(CO)$_3$Br]** complexes, where **L=14-19**.

The complexes were found to be poorly soluble in all solvents, however were characterised by ^{1}H NMR, IR spectroscopies and HR MS, and where possible (due to poor solubility) ^{13}C {^{1}H} NMR spectroscopy in d6-DMSO. The photophysical properties were extensively characterised *via* both UV-vis and luminescence spectroscopy in $CHCl_3$ using a 1% DMSO spike (due to poor solubility), and DFT analysis was carried out on all ligands and complexes.

Despite the limited solubility, ^{1}H NMR spectra of all complexes except ***fac*-[Re(18)(CO)$_3$Br]** were able to be recorded in $CDCl_3$ for direct comparison to the free ligand. This comparison gave greater insight into the coordination of the ligand to the metal, by comparing the shift in the Ox-H proton upon coordination, of which an example spectra is given in **Figure 5.24**, and shifts for all complexes except ***fac*-[Re(18)(CO)$_3$Br]** are given in **Table 5.1**.

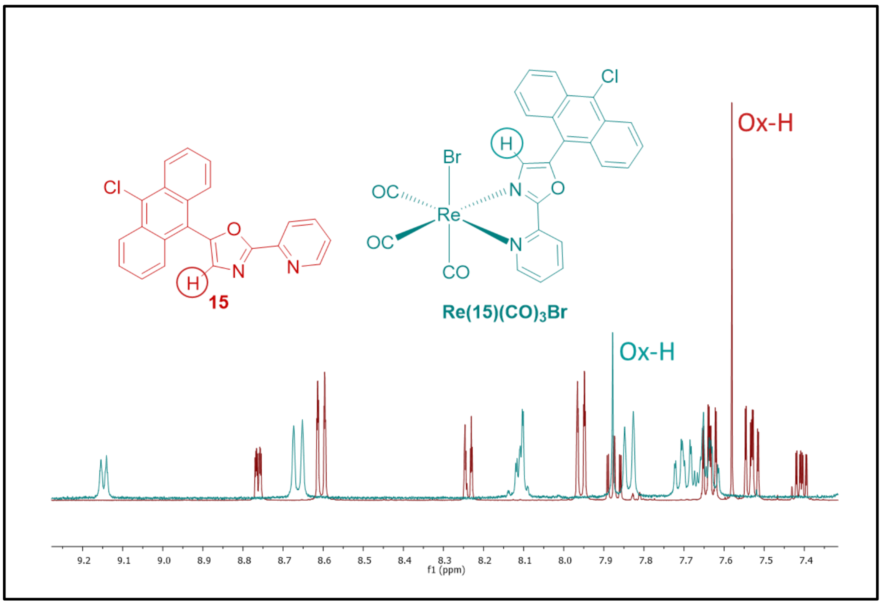

Figure 5.24 ^{1}H NMR spectra of ligand **15** (red) and ***fac*-[Re(15)(CO)$_3$Br]** (blue), showing the shift in Ox-H upon complexation. ^{1}H NMR spectra recorded in CDCl$_3$.

The Ox-H resonance of coordinated ligand was deshielded by between 0.2 and 0.3 ppm compared to free ligand, with the largest shift coming from ***fac*-[Re(15)(CO)$_3$Br]**, of which the spectra is shown in **Figure 5.24**.

The more deshielded the proton, the more π-density being drawn to the rhenium centre from the oxazole nitrogen.

Table 5.1 Ox-H downfield ^{1}H shift upon complexation. ^{1}H NMR spectroscopy data recorded in CDCl$_3$.

	Δ^{1}H δ$_{Ox-H}$ / ppm
Re(14)(CO)$_3$Br	0.25
Re(15)(CO)$_3$Br	0.30
Re(16)(CO)$_3$Br	0.24
Re(17)(CO)$_3$Br	0.27
Re(19)(CO)$_3$Br	0.24

^{13}C {^{1}H} NMR spectroscopy of all complexes with the exception of ***fac*-[Re(14)(CO)$_3$Br]** and ***fac*-[Re(18)(CO)$_3$Br]** were recorded in d$_6$-DMSO, showing three down-field peaks between 187 and 197 ppm, corresponding to the carbonyl ligands. As shown in **Table 5.2**, there was little difference between peak positions, despite differences in the Ox-H proton shift.

Table 5.2 $^{13}C\ \{^{1}H\}$ NMR positions assigned to carbonyl ligands in ***fac*-[Re(L)(CO)$_3$Br]** where **L = 15-17** and **19**. Recorded in d$_6$-DMSO.

	$^{13}C\ \delta_{co}$ / ppm		
***fac*-[Re(15)(CO)$_3$Br]**	188.2	195.7	196.7
***fac*-[Re(16)(CO)$_3$Br]**	188.0	195.7	196.6
***fac*-[Re(17)(CO)$_3$Br]**	188.0	195.7	196.6
***fac*-[Re(19)(CO)$_3$Br]**	187.9	195.9	196.6

IR spectroscopy of all complexes were recorded showing the presence of bands not present in the free oxazole ligands between 1850 and 2050 cm^{-1}, corresponding to the carbonyl ligand C≡O stretching frequencies and presented in **Figure 5.25**. As the complexes possess pseudo C_s symmetry, the number of IR active stretches observed should be three corresponding to A', $A'^{(2)}$ and A'' for the symmetric in- and out-of-phase vibrations, and the asymmetric vibration of the equatorial ligands respectively[8]. The latter occur at a similar energy and are assigned to the lower energy vibronic bands between 1850-1950 cm^{-1} (A'' being the higher frequency of the two), with A' assigned to the single, higher energy band between 2000-2050 cm^{-1}.

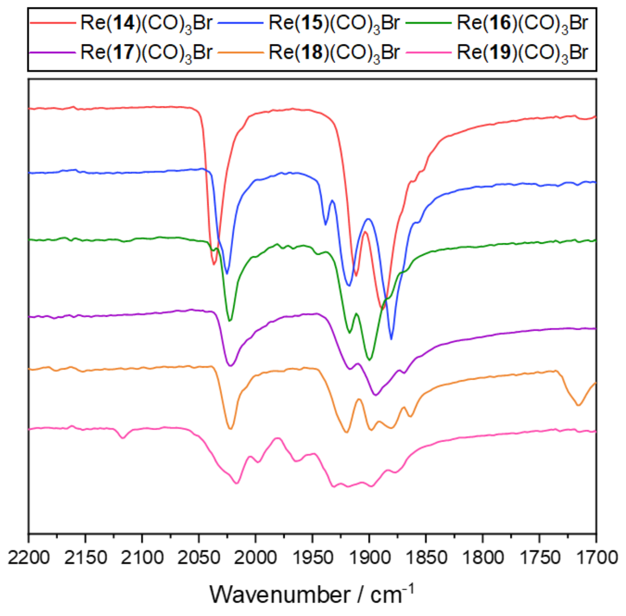

Figure 5.25 ATR-FT-IR-Spectra of the carbonyl region for ***fac*-[Re(14-19)(CO)$_3$Br]**. Note that the band at 1716 cm^{-1} for ***fac*-[Re(18)(CO)$_3$Br]** is assigned to the fluorenone ketone of ligand **18**.

***fac*-[Re(L)$(CO)_3$Br]** where L = **14-17** showed three clearly defined bands, and are tabulated in **Table 5.3**, whereas ***fac*-[Re(18)$(CO)_3$Br]** and ***fac*-[Re(19)$(CO)_3$Br]** both showed broader stretches in the lower frequency region and thus make assignment of A'' and A'$^{(2)}$ challenging. The more complex IR-spectra of ***fac*-[Re(18)$(CO)_3$Br]** and ***fac*-[Re(19)$(CO)_3$Br]** is not understood.

Table 5.3 IR *v*(CO) stretches for ***fac*-[Re(14-19)$(CO)_3$Br]**.

	***v*(CO) A' / cm^{-1}**	***v*(CO) A'' and A'$^{(2)}$ / cm^{-1}**
Re(14)$(CO)_3$(Br)	2037	1912, 1889
Re(15)$(CO)_3$(Br)	2025	1918, 1880
Re(16)$(CO)_3$(Br)	2023	1917, 1900
Re(17)$(CO)_3$(Br)	2022	1918, 1894
Re(18)$(CO)_3$(Br)	2022	1920, 1906-1844 (br)
Re(19)$(CO)_3$(Br)	2017	1946-1847 (br)

An increase in electron density across the Re-N bond leads to a more electron rich Re(I) centre, and therefore more back donation into the π^* orbital of the CO ligands. This increase of electron density in the π^* orbital leads to a weaker C≡O bond, and hence should give rise to a lower IR stretching frequency. Unfortunately, a clear trend is not evident from the vibrational frequencies given in **Table 5.3**, despite A" bands being most affected by an increase in back-bonding. This is due to the resolution of the equipment (4 cm^{-1}) encompassing the range in which the peaks are observed. The only caveat was that ***fac*-[Re(15)$(CO)_3$Br]** exhibited the lowest frequency A'$^{(2)}$ vibronic band, in line with the largest Ox-H shift observed in **Table 5.1**, however no such pattern was observed in the A' bands.

All complexes with the exception of ***fac*-[Re(14)$(CO)_3$Br]** exhibited similar vibronic stretching frequencies, with the latter exhibiting the highest A' by more than 10 cm^{-1}, and the lowest A'' by 5 cm^{-1}, despite showing one of the smallest Ox-H proton shifts. However more intricate electronic factors may be in play, as ***fac*-[Re(14)$(CO)_3$Br]** also exhibited different photophysical characteristics from the remaining complexes, with both a more intense ^{3}MLCT and the highest quantum yield recorded, as discussed in **Section 5.2.2**.

5.2.2 Photophysical Studies

The UV-vis absorption spectra of ligands **14-19** and the respective complexes were recorded in $CHCl_3$ with 1% DMSO at room temperature (presented in **Figure 5.26** and **Table 5.4**). Di-substituted oxazoles, as discussed in detail in **Chapter 2**, exhibit multiple bands of varying intensity, with the lower energy transitions at a higher extinction coefficient than the higher energy transitions, the former of which a result of the conjugation through the oxazole ring.[30]

As with oxazoles **8-13**, ligands **14-19** all exhibited multiple bands assigned to π-π* transitions within the varying R-group, with similar spectral line-shapes to that of **8-13**, and showing the same variations when compared to mono-substituted oxazoles **1-5** and **7**. Notable examples are that of **15**, with a high energy band at 301 nm similar to that of **9** (323 nm) but absent in **2**, and in the case of the oxidation of the fluorene R-group of **5** into the fluorenone-substituted oxazole **18**, with a low intensity band at 430 nm confirming a degree of intramolecular charge transfer (ICT)[31,32] and similar to that shown by both **12** and other 2-methoxysubstituted fluorenones[32,33].

The correlation between ligand and complex absorbance did not follow a similar trend, and therefore ***fac*-[Re(14-19)(CO)$_3$Br]** complexes are discussed independently. However, all showed a red-shift in absorption bands of varying amounts, and all showed a broadness of the lowest energy absorption, which is confirmed *via* DFT to be assigned largely to the metal-to-ligand charge transfer (^{1}MLCT) transition.

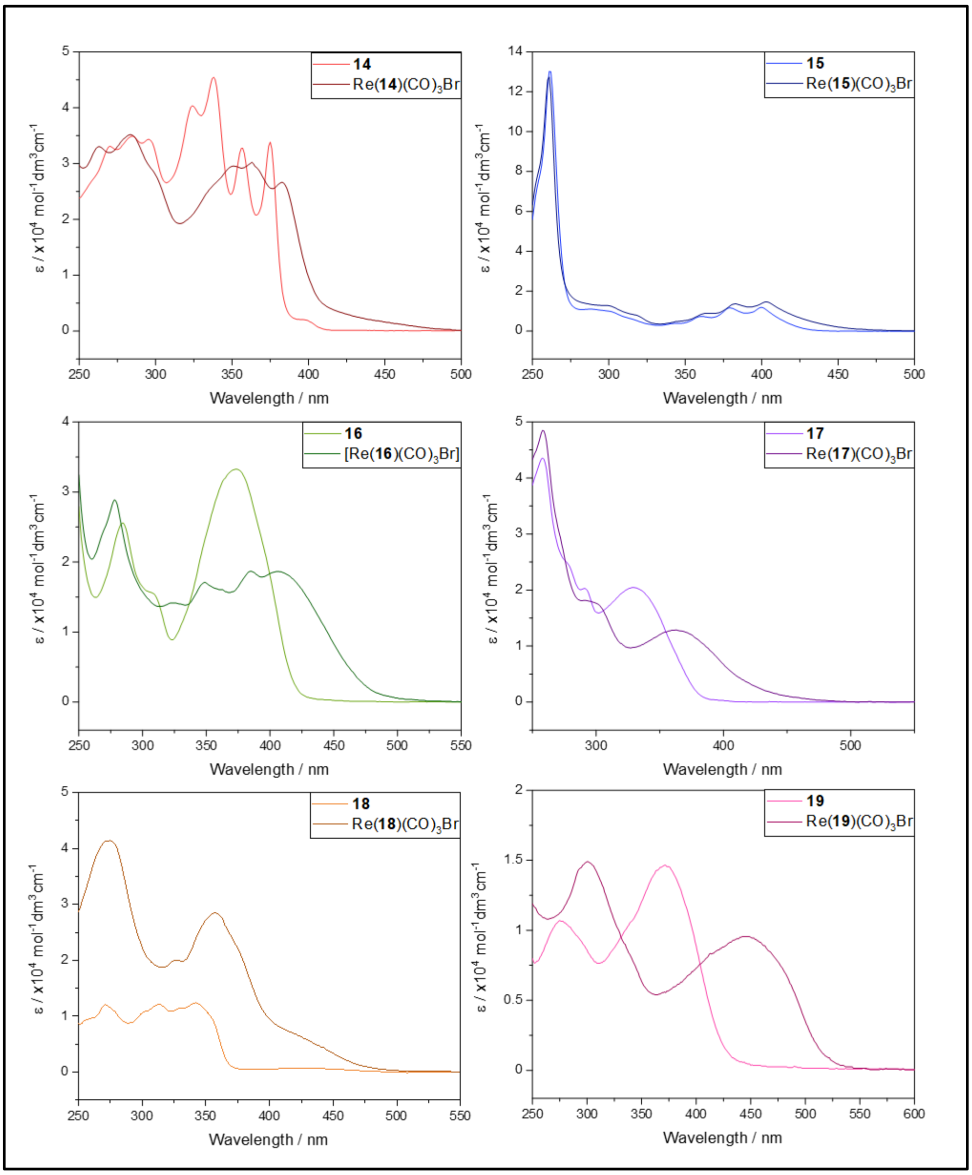

Figure 5.26 UV-vis. absorption spectra (recorded in $CHCl_3$ with 1% DMSO) for ligands **14-19** and the respective ***fac*-[Re(L)(CO)$_3$Br]** complexes.

The UV-vis absorption spectra of ***fac*-[Re(15)(CO)$_3$Br]** was almost identical to that of **15**, with a slight red shift and a broadening of the low energy absorbance from 400 to 450 nm, likely a result of the ^{1}MLCT band. For both ***fac*-[Re(14)(CO)$_3$Br]** and ***fac*-[Re(16)(CO)$_3$Br]**, the general line-shape and intensity were similar to their respective ligands. However, π→π* bands at 315 and 342 nm in the spectra of **14** were no longer present in the complex, and ***fac*-[Re(16)(CO)$_3$Br]** also showed much more structured absorbance between 350-400 nm compared to the free ligand. A broadness from 390 to 475 nm and 350-475 nm for ***fac*-[Re(14)(CO)$_3$Br]** and ***fac*-[Re(16)(CO)$_3$Br]** respectfully suggest ^{1}MLCT absorbance, with the latter appearing to overlap with more structured ligand π→π* bands that are not evident in the free ligand spectra.

For ***fac*-[Re(17)(CO)$_3$Br]**, the high energy absorbances were similar to free ligand, with a slight red shift. However, a red shift of approximately 30 nm was found for the lower energy absorption, the resultant band being considerably broader than that of the free ligand, most likely due to overlap with the ^{1}MLCT band.

The absorption spectra of ***fac*-[Re(19)(CO)$_3$Br]** was heavily red shifted compared to the free ligand, with a 26 and 74 nm shift observed for the high and low energy absorptions respectively. The low energy absorbance, as with ***fac*-[Re(17)(CO)$_3$Br]**, was considerably broader than the free ligand, suggesting overlap with the ^{1}MLCT band. The intensity of the two absorption bands were inverted with respect to the free ligand.

Both the spectral line-shape and absorption intensity of ***fac*-[Re(18)(CO)$_3$Br]** was markedly different from that of free ligand, with two distinct bands at 364 and 258 nm, and a broader shoulder between 400 and 500 nm, likely a combination of ^{1}MLCT and the existing ICT band of the ligand[33].

Table 5.4 Absorption and emission data for oxazoles **14-19**, recorded in $CHCl_3$ (1 % DMSO). For ligands **18** and **19** more than one lifetime was recorded, with λ_{em} given in each case. λ_{ex}=295 nm.

	λ_{abs} (ε) / nm ($mol^{-1}dm^3cm^{-1}$)	λ_{em} / nm	τ_{obs} / ns (λ_{em})	ϕ (λ_{ex}) / %
14	399 (1972), 375 (33790), 356 (32690), 338 (45320), 323 (40380), 296 (34280), 285 (34890)	381, 403, 426 (sh), 457 (sh)	2.2 ± 0.2	76 ± 8
15	400 (11860), 379 (16650), 360 (7302), 342 (3785), 315 (6011 sh),301 (9836 sh), 288 (11060), 262 (130300), 252 sh (68870)	405 (sh), 487	3.5 ± 0.4	34 ± 3
16	374 (33190), 310 (15500), 285 (25400),	428, 444	1.8 ± 0.2	38 ± 4
17	331 (20480), 291 (20250), 278 (24660), 258 (43370)	410	1.6 ± 0.2	62 ± 6
18	430 (725), 343 (12400), 330 (11400 sh), 314 (12120), 301 (10710 sh), 271 (12050), 257 (9420)	407, 543,	1.5 ± 0.2 (λ_{406})[a] 3.6 ± 0.4 (λ_{542})	0.57 ± 0.06 (λ_{295})[b] 1.41 ± 0.14 (λ_{330})
19	372 (14600), 276 (10670)	399 (sh), 469	1.2 ± 0.1 (λ_{398})[a] 2.2 ± 0.2 (λ_{470})	43 ± 4

[a] *τ_{obs} is presented at two different emission wavelengths (λ_{em}) due to two different emission maxima*

[b] *ϕ acquired at two different excitation wavelengths (λ_{ex}) due to λ_{ex} dependent emission spectra*

The emission spectra of ligands **14-19** were recorded in aerated $CHCl_3$ containing 1% DMSO, and are presented in **Figures 5.27-5.31**, with the corresponding mono-substituted (**1-7**) and di-substituted naphthyl based oxazoles (**8-13**) for comparison. As with oxazoles **8-13**, ligands **14-19** all emitted at a higher wavelength than their mono-substituted equivalents due to an increase in conjugation across the oxazole ring. All ligands except **18** emitted across a broad range between 350 – 600 nm. Ligand **18**, much like oxazole **12**, showed a more complex emission up to 700 nm, and is discussed in more detail below.

As with the naphthyl-based equivalent, ligand **14** gave evident vibrational fine structure similar to oxazoles **1** and **8**, however was not as bathochromically shifted as oxazole **8** with respect to the parent oxazole **1**, due to the less conjugated pyridine *vs* naphthalene (**Figure 5.27**). The line shape observed, as discussed in **Chapter 2** for the naphthalene moiety, suggests that the pyridine substituent does not affect the vibrational fine structure of the highly aromatic R-group of **1**, instead simply extending conjugation of the structure and thus causing a bathochromic shift in the emission wavelength. When measured at 77 K (**Figure 5.27**), the spectra showed similar features to that observed at room temperature, however as they are recorded in solvents of varying polarity, it is difficult to ascertain any small differences.

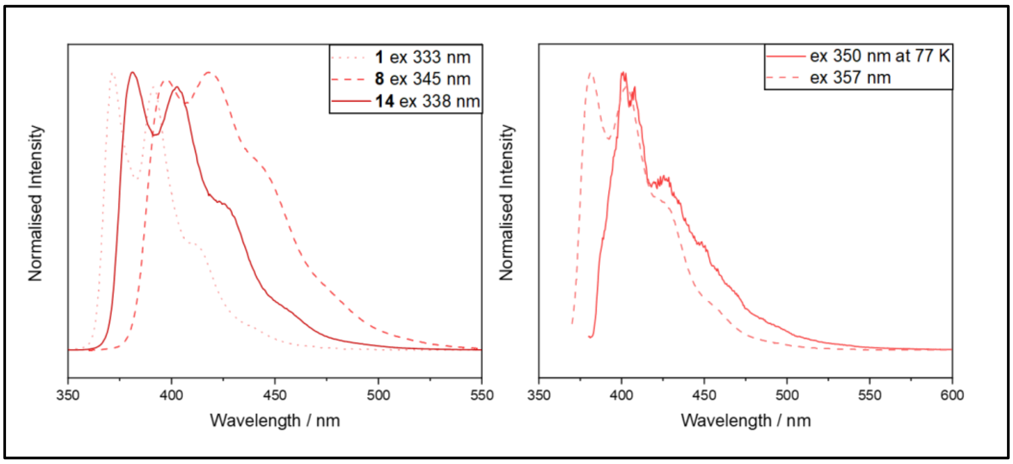

Figure 5.27 *Left:* Emission spectra (recorded in $CHCl_3$, 1 % DMSO) for ligand **14** (solid line) *vs* **8** (dashed line) and **1** (dotted) (both recorded in $CHCl_3$); *Right:* Emission spectra recorded at 77 K of ligand **14** (recorded in EtOH:MeOH) *vs* room temperature measurement (dashed line, recorded in $CHCl_3$, 1 % DMSO).

Unlike oxazoles **10** and **11**, which also gave the same vibrational fine structure observed by the mono-substituted oxazoles **3** and **4**, ligands **16** and **17** possessed a broader and less defined line shape, bathochromically shifted from the mono-oxazoles by 33 and 24 nm respectively (**Figure 5.28**), the former being similar to the shift observed for oxazole **10**. Ligand **19** also shifted by a similar amount to its naphthyl-oxazole equivalent **13**, showing a bathochromic shift of 70 nm compared to the mono-oxazole **7**. However, unlike the naphyl-oxazole **13**, which showed a broad emission band with two peaks of similar intensity at 420 and 464 nm, ligand **19** instead showed a main emissive band at 469 nm, and a smaller shoulder at 399 nm, the latter of which occurring at the same wavelength as the mono-oxazole highest wavelength emissive band (**Figure 5.28**). The emission spectra recorded at 77 K of ligands **17** and **19** were almost identical to that recorded at room temperature, however when recorded at 77K, **16** gave a 34 nm bathochromic shift compared to the room temperature spectra, speculated to be due to the restricted matrix causing the ligand adopting a more planar structure, and thus conjugation was extended (**Figure 5.28**). However, as the spectra recorded at 77 K was measured in a solvent of differing polarity to that of room temperature measurements, it cannot be ruled out that this is simply a result of the different solvent environment.

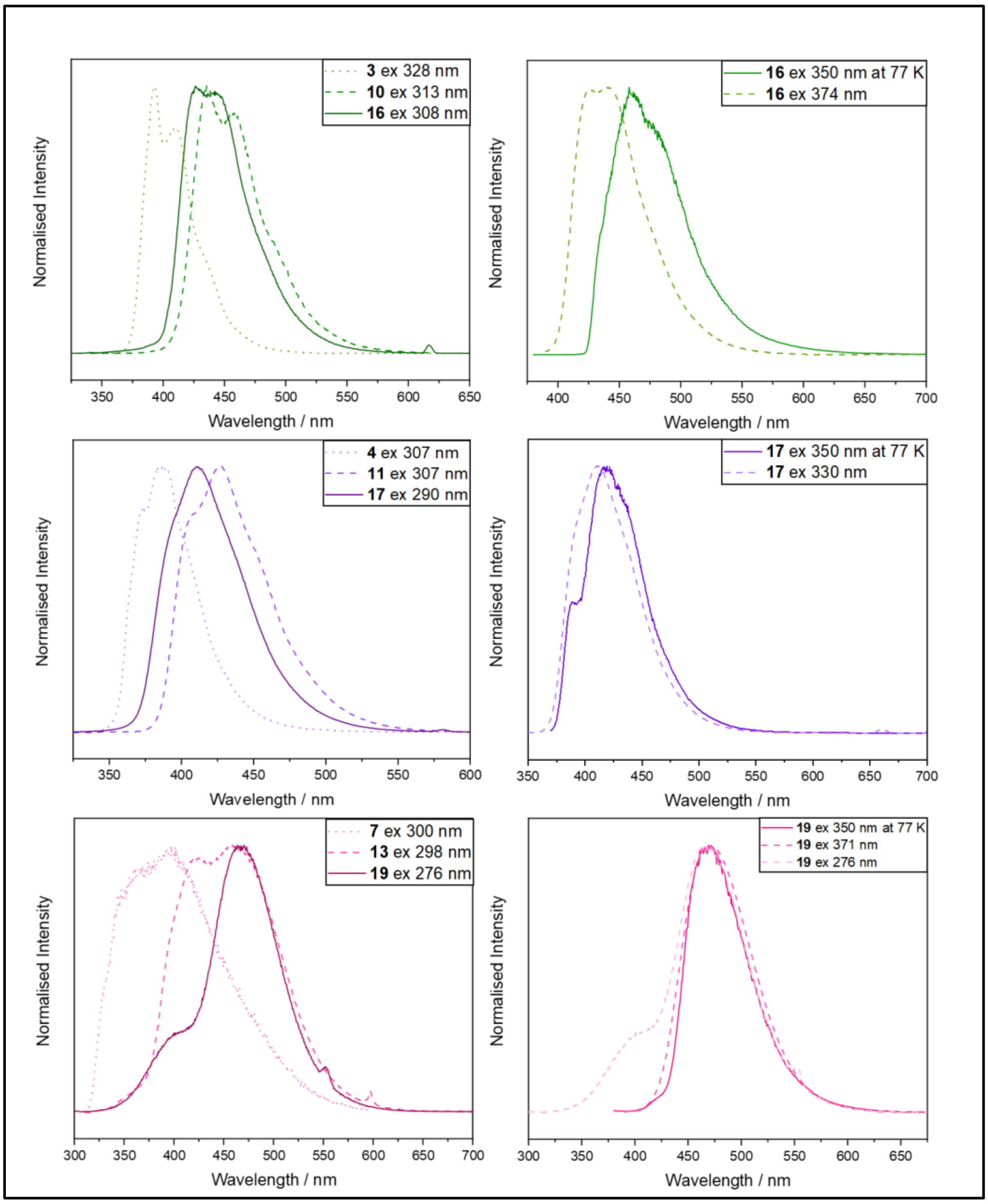

Figure 5.28 *Left:* Emission spectra for ligand **16, 17** and **19** (solid line, recorded in $CHCl_3$, 1 % DMSO) *vs* **10, 11** and **13** (dashed line) and **3, 4** and **7** (dotted), recorded in $CHCl_3$; *Right:* Emission spectra recorded at 77 K of ligands **16, 17** and **19** (recorded in EtOH:MeOH) *vs* room temperature measurement (dashed line, recorded in $CHCl_3$, 1 % DMSO).

Ligand **15** possessed similar photophysical characteristics to that of oxazole **9**, with a broad featureless emissive band at 487 nm (**Figure 5.29**). As discussed in detail in **Chapter 2**, spectra recorded at a range of concentrations suggested this was not the result of an excimer. The emission lifetime was of the nanosecond scale, whereas excimer lifetimes are typically smaller, and the excitation spectra matched that of the UV-vis spectra.[34] When excited at 293 nm, a shoulder is present at 405 nm, occurring at a similar (slightly blue-shifted) wavelength to that of the mono-oxazole **2**, and following the same trend as that observed with **9**. DFT analysis in **Chapter 2** suggested that the photophysics of oxazole **2** is dominated by the chloroanthracene R-group, and the excitation acquisition of **15**, as with oxazole **9**, showed the vibrational fine structure of the chloroanthracene moiety thus further suggesting that the weak emission observed at 405 nm is that of the chloroanthracene group.

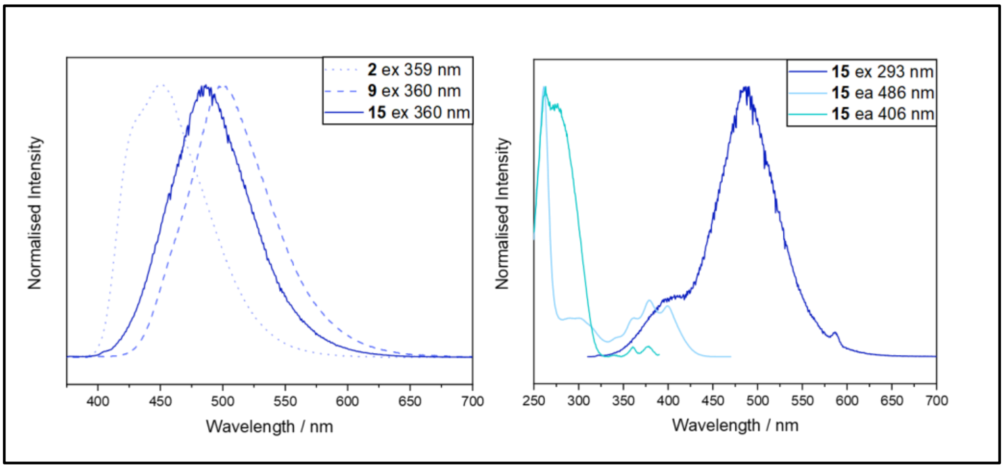

Figure 5.29 *Left:* Emission spectra (recorded in $CHCl_3$, 1 % DMSO) for ligand **15** (solid line) *vs* **9** (dashed line) and **2** (dotted) (both recorded in $CHCl_3$); *Right:* Excitation acquisition of ligand **15** overlayed with room temperature emission showing shoulder at 405 nm when excitation at 293 nm.

Emission spectra recorded at 77 K of ligand **15** showed emission only at 428 nm, identical to that of oxazole **2** at room temperature, with no evidence of the low energy emissive band (**Figure 5.30**). Therefore, one can speculate that the broader high intensity band at 487 nm is, as with oxazole **9**, a result of charge transfer between the chloroanthracene and pyridine groups, which may not occur at low temperature. This is further suggested in the DFT analysis, discussed in **Section 5.2.3**, indicating that charge transfer occurs across the oxazole ring between the naphthalene and chloroanthracene groups, with the LUMO+X states predicted for each transition made up of π* orbitals localised upon either the chloroanthracene-oxazole or the pyridine-oxazole groups.

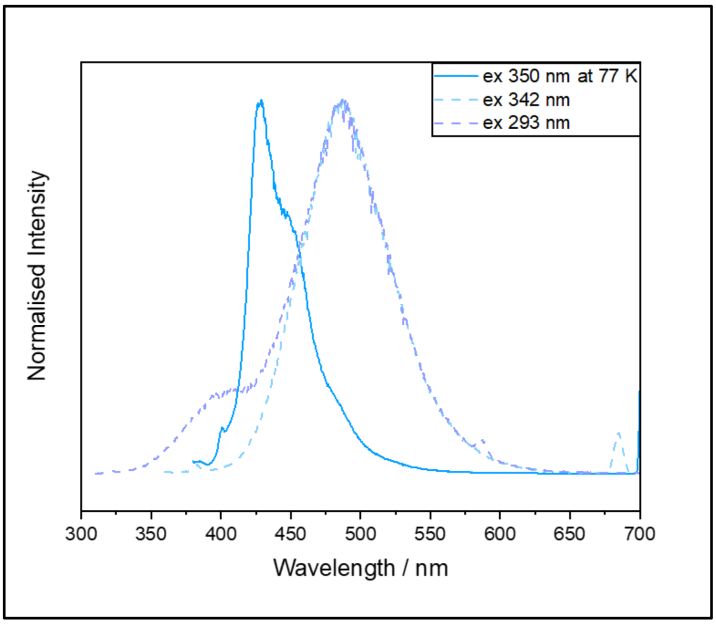

Figure 5.30 Emission spectra recorded at 77 K of ligand **15** (recorded in EtOH:MeOH) *vs* room temperature measurement (dashed line, recorded in $CHCl_3$, 1 % DMSO).

Ligand **18**, as with oxazole **12**, showed dual emission at 407 and 543 nm (**Figure 5.31**). The former emissive band was slightly red shifted by 7 nm to that of **12**, however the latter was blue shifted by 17 nm. As discussed in **Chapter 2**, the high wavelength emissive band was assigned to singlet emission from the fluorenone moiety, as a result of ICT between the pyridine-oxazole unit (or naphthalene-oxazole in the case of **12**) and the fluorenone R-group[34]. TDA based TD-DFT analysis, found in **Section 5.2.3** and similar to that of oxazole **12,** predicted that excitation at the low energy absorption band leads to an intramolecular charge transfer, leading to localisation on the fluorenone (LUMO). This observation, with the LUMO consistent with that found in the literature, confirmed that the absorption at 430 nm is the result of ICT, and that the emissive band at 543 nm (as with oxazole **12**), is the result of singlet emission from the fluorenone R-group, when the short emissive lifetime is also taken into account. This is further confirmed by measurements recorded at 77 K, shown in **Figure 5.31**. The emissive band at 407 nm was unchanged, however at low energy the spectra showed two vibronically structured features, blue shifted compared to the room temperature emission at 543 nm. These low energy bands are likely due to both singlet and triplet emission of the fluorenone. Lifetime measurements at 77K would be required to categorically assign these features. Also, as the spectra recorded at 77 K was measured in a solvent of differing polarity to that of room temperature measurements, it cannot be ruled out that any shifts in emission wavelength observed is simply a result of the different solvent environment.

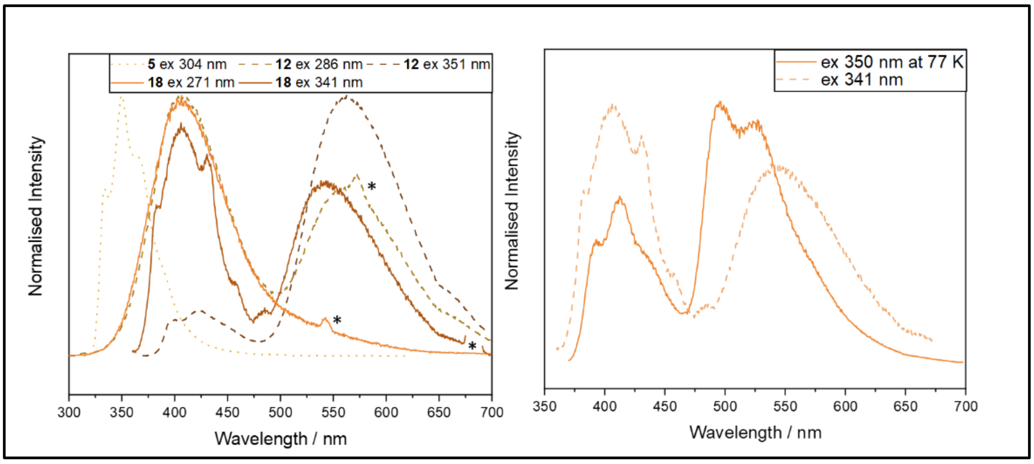

Figure 5.31 *Left:* Emission spectra (recorded in $CHCl_3$, 1 % DMSO) for ligand **18** (solid line) *vs* **12** (dashed line) and **5** (dotted) (both recorded in $CHCl_3$); *Right:* Emission spectra recorded at 77 K of ligand **18** (recorded in EtOH:MeOH) *vs* room temperature measurement (dashed line, recorded in $CHCl_3$, 1 % DMSO). *denotes a lamp harmonic associated with the excitation wavelength.

As with oxazoles **1-13**, the quantum yields for ligands **14-19** were varied, as shown in **Table 5.4**. Ligands **15** and **19** exhibited an increase in quantum yield compared to oxazoles **9** and **13**, whereas both **16** and **18** showed a decrease compared to **10** and **12**. Considering the similarities in emission spectra between **16** and **10**, the large decrease in quantum yield (50 %) was unexpected. However, although there was a reduction in quantum yield for **18**, both **12** and **18** exhibited low quantum yields, which are indicative of fluorenone derivatives[33].

Time-resolved luminescence measurements showed that ligands **14-19** all exhibited similar short lifetimes to that of the naphthalene-oxazoles **8-13** and are attributed to the $^1\pi$-π^* dominated $S_1 \rightarrow S_0$ radiative decay process.

The emission spectra of ***fac*-[Re(L_{14-19})$(CO)_3$Br]** were recorded in aerated $CHCl_3$ containing 1% DMSO, and are presented in **Figures 5.32-5.36** with the photophysical parameters tabulated in **Table 5.5**. The spectra revealed emission profiles that were typically multiple component, and thus more complicated than the benchmark Re(I) diimine examples discussed earlier in the introduction.

Table 5.5 Absorption and emission data for ***fac*-[Re(14-19)(CO)$_3$Br]**, recorded in CHCl$_3$ (1 % DMSO). For lifetime measurements, λ_{em} is given in each case, λ_{ex}=295 nm.

***fac*-[Re(L)(CO)$_3$Br]**	***λ_{abs} (ε) / nm (mol^{-1}dm^{3}cm^{-1})***	***λ_{em} / nm***	***τ_{obs} / ns (λ_{em})***	***ϕ / %***
L = 14	426 (2844), 383 (26580), 363 (30230), 350 (29440), 334 (25210), 300 (28230), 283 (35140), 263 (33090)	381 (sh), 407, 432, 456 (sh), 495, 610	1.2 ± 0.1 (λ_{407}) 41 ± 4 (λ_{616})	3.5 ± 0.4
L = 15	403 (14680), 382 (13600), 363 (8927), 345 (4796), 318 (8013), 300 (12690), 261 (127100)	405, 486 (sh)	1.2^a ± 0.1 (λ_{405}) 1.7 ± 0.2 (λ_{486})	0.15 ± 0.02
L = 16	407 (18710), 385 (18640), 349 (17100), 323 (14070), 279 (28940)	360, 375, 392, 415, 465, 490, 546	1.7^a ± 0.2 (λ_{409}) 1.2 ± 0.1 (λ_{463}) 1.5 ± 0.2 (λ_{490})	2.24 ± 0.22
L = 17	364 (12770), 301 (17690), 258 (48500)	417, 614, 671	1.2 ± 0.1 (λ_{417})	0.33 ± 0.03
L = 18	432 (5474), 358 (28460), 327 (20030), 273 (41270)	410, 510, 529, 607, 665	1.3^a ± 0.1 (λ_{410}) 1.7 ± 0.2 (77), 8.4 ± 0.8 (23) (λ_{510}) 1.8 ± 0.2 (66), 7.1 ± 0.7 (34) (λ_{530})	N/A
L = 19	448 (9542), 301 (14880)	406, 556, 671 (sh)	1.2 ± 0.1 (λ_{406})	1.38 ± 0.14

[a] *τ_{obs} is presented at two different emission wavelengths (λ_{em}) due to multiple emission maxima.*

For ***fac*-[Re(14)(CO)$_3$Br]**, two emission bands were exhibited, with the higher energy band assigned to ligand centred emission, and the broader, lower energy band centred at 610 nm (**Figure 5.32**). The emission lifetime of the ligand centred emission was less than that of the free ligand, most probably due to the heavy atom effect of the Re(I) centre, and the lifetime of the 610 nm band was 41 ns, consistent with a ^{3}MLCT transition. The low energy band observations are similar to that of *fac*-[Re(bpy)(CO)$_3$Cl], which showed emission at 612 nm with a lifetime of 50 ns in degassed DCM[35], and that of **Re-16** (containing a benzoxazole ligand, **Figure 5.18**) which showed emission at 635 nm in acetonitrile[12], both assigned to ^{3}MLCT. However the band is blue shifted with respect to **Re-12** (**Figure 5.18**, also containing a benzoxazole ligand) which showed emission at 714 nm in acetonitrile[27]. Unlike ***fac*-[Re(14)(CO)$_3$Br]**, and the rest of the complexes described below, these benchmark complexes did not show ligand-centred emission at higher energy.

Emission spectra recorded at 77 K showed a similar ligand centred emission (**Figure 5.32**), as well as a relatively intense structured emission band between 537 – 688 nm, with prominent peaks at 550 and 579 nm, and shoulders at 600 and 637 nm, unlike at room temperature where only a broad band was observed. This increase in vibronic structure suggests ligand-centred contribution (^{3}LC) to the low energy bands, and it can be speculated that the intense peak at 579 nm is a result of ^{3}LC due to it not being present in the room temperature emission spectra. The lack of bathochromic shift of the lower energy bands compared to room temperature measurements further suggests evidence of a ^{3}LC contribution. However, as the spectra recorded at 77 K was measured in different solvent to that of room temperature measurements, it cannot be ruled out that this is simply a result of the different solvent environment.

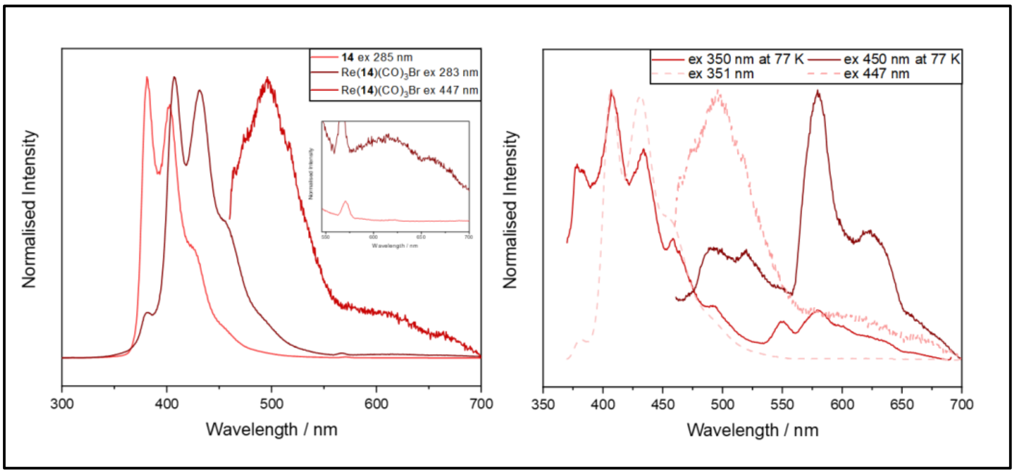

Figure 5.32 *Left:* Emission spectra of ***fac*-[Re(14)(CO)$_3$Br]** *vs* **14** (both recorded in CHCl$_3$, 1 % DMSO); *Right:* Emission spectra recorded at 77 K of ***fac*-[Re(14)(CO)$_3$Br]** (recorded in EtOH:MeOH) *vs* room temperature measurement (dashed line, recorded in CHCl$_3$, 1 % DMSO).

***fac*-[Re(17)(CO)$_3$Br]** also showed two emission bands (**Figure 5.33**), assigned to a ligand centred emission, and a much weaker and broad low energy band centred at 614 nm. The quantum yield was markedly lower than that of ***fac*-[Re(14)(CO)$_3$Br]** (0.33 *vs* 3.5 %). Measurements taken at 77 K showed ligand-centred emission very similar to that at room temperature, with the exception of increased vibronic fine structure (**Figure 5.33**). The low energy band found at 614 nm in the room temperature emission was bathochromically shifted when recorded at 77 K by approximately 50 nm, suggesting rigidochromism within the complex consistent with ^{3}MLCT character. However, as the spectra recorded at 77 K was measured in a solvent of different polarity to that of room temperature measurements, both the vibronic fine structure of the ligand-centred emission and bathochromic shift of the low energy band could also be the result of differing solvent environments.

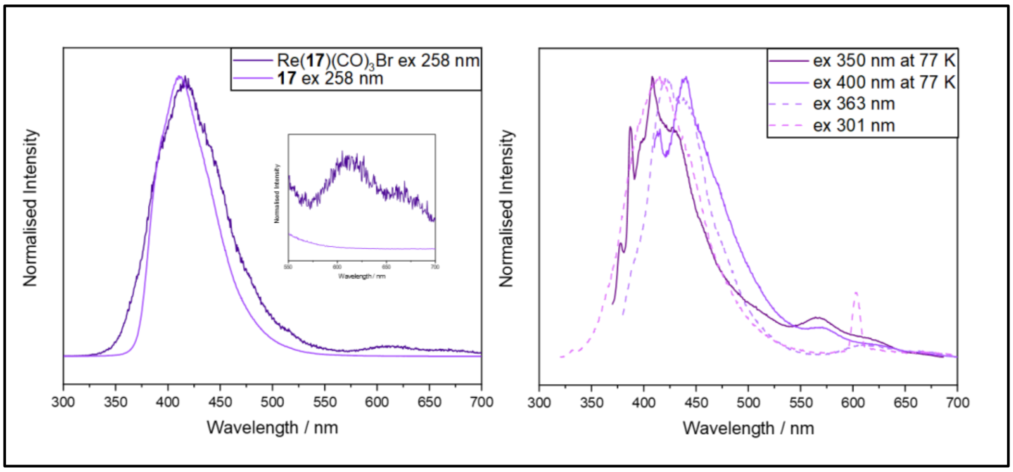

Figure 5.33 *Left:* Emission spectra of ***fac*-[Re(17)(CO)$_3$Br]** *vs* **17** (both recorded in CHCl$_3$, 1 % DMSO); *Right:* Emission spectra recorded at 77 K of ***fac*-[Re(17)(CO)$_3$Br]** (recorded in EtOH:MeOH) *vs* room temperature measurement (dashed line, recorded in CHCl$_3$, 1 % DMSO).

***fac*-[Re(18)(CO)$_3$Br]**, like ligand **18** and oxazole **12**, demonstrated many photophysical spectral features (**Figure 5.34**). The postulated dual-emissive nature of ligand **18** appears to be still present within the complex, with ligand-centred bands observed at 410 and 529 nm, the latter assigned to ICT between the pyridine-oxazole and the fluorenone R-group due to its similarities with ligand emission (blue shifted by 14 nm) and proposed DFT assignments (**Section 5.2.3**). However, the latter emissive band appeared to blue-shift further to 510 nm when excited > 400 nm. That this is the same band shifted, and not two separate bands, is evidenced by the similarities in emission lifetime.

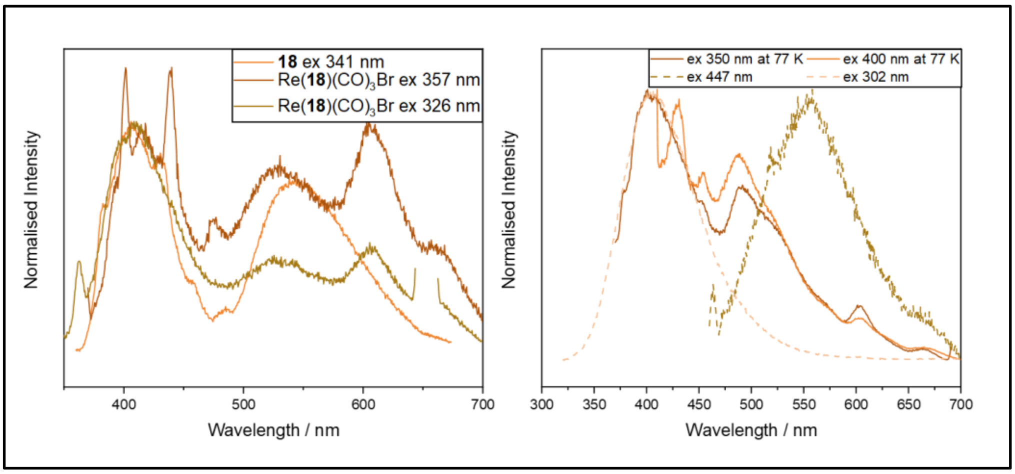

Figure 5.34 *Left:* Emission spectra of ***fac*-[Re(18)(CO)$_3$Br]** *vs* **18** (both recorded in $CHCl_3$, 1 % DMSO); *Right: Emission spectra recorded at 77 K* of ***fac*-[Re(18)(CO)$_3$Br]** (recorded in EtOH:MeOH) *vs* room temperature measurement (dashed line, recorded in $CHCl_3$, 1 % DMSO). *denotes a lamp harmonic associated with the excitation wavelength.

Similar to ligand **18**, when excited at < 300 nm, only the peak at 410 nm was observed, due to ligand $^1(\pi \rightarrow \pi^*)$ emission. As well as ligand centred bands, a lower energy band at 607 nm was assigned to ^{3}MLCT transitions. The emission in general was weak compared with other complexes, with the quantum yield not being able to be recorded, or a lifetime of the proposed ^{3}MLCT state. An emission lifetime of 1.3 ns was recorded at 410 nm, similar to that of the free ligand at 406 nm. At 510 and 530 nm, slightly longer biexponential lifetimes were recorded. Emission spectra recorded at 77 K spectra of ***fac*-[Re(18)(CO)$_3$Br]** showed many features (**Figure 5.34**), but mainly these are attributed to both singlet and triplet ligand based processes (as with ligand **18**). Additional weak low energy shoulder features were present > 600 nm and may be assigned to ^{3}MLCT emission.

The emission spectra for complexes ***fac*-[Re(15,16,19)(CO)$_3$Br]** were dominated by ligand-centred bands, with no ^{3}MLCT emission observed, with the exception of ***fac*-[Re(16)(CO)$_3$Br]** when recorded at 77 K.

For ***fac*-[Re(15)(CO)$_3$Br]** (**Figure 5.35**), a low energy ^{3}MLCT transition was not observed, however two high energy bands were present, dependent on wavelength. When excited at 403 nm, a ligand centred emission overlapping with that of the free ligand was observed at 486 nm, with a lifetime of 1.7 ns, similar to that of **15**. However, when excited at higher energy the dominating emissive band was that of the shoulder observed in the free ligand, centred at 405 nm, with an emission lifetime of 1.2 ns. Using evidence presented in **Chapter 2** for the disubstituted oxazole **10** *via* both photophysical observations and those predicted *via* DFT, paired with the similar observations for free ligand **15**, it can be speculated that the intense emission band at 403 nm is the result of a twist in the oxazole ligand at the oxazole-anthracene bond preventing through-bond conjugation, and thus resulting in chloroanthracene-only emission at 403 nm. The origin of the band centred at 486 nm is therefore unknown, but can be tentatively assigned to a charge transfer transition between the pyridine-oxazole and chloroanthracene unit that although dominates in the spectra of the free ligand, is reduced when coordinated to the rhenium centre. Emission spectra recorded at 77 K overlayed with that of the room temperature emission for higher energy ligand-centred bands, and like ***fac*-[Re(14)(CO)$_3$Br]**, showed increased vibrational fine structure however this could also be attributed to the change of solvent and not temperature. Interestingly, two of the emissive bands were identical to that observed by **15** when recorded at 77 K, but no ^{3}MLCT band was observed (**Figure 5.35**). The lack of ^{3}MLCT emission may be a result of energy transfer, whereby the ^{3}MLCT excited state is quenched by lower lying triplet states of the anthracene unit, demonstrated by N. Shavaleev *et al*.[36] However, one would then expect to observe the chloroanthracene triplet state, (located at 690 nm for anthracene[36,37]) which appears to be absent. The postulated charge transfer band at 486 nm in the room temperature spectra is also absent, similar to that observed for ligand **15**.

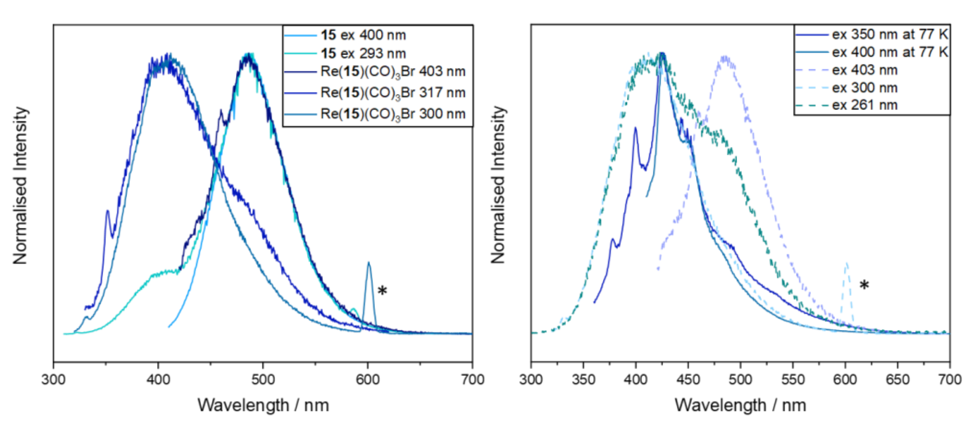

Figure 5.35 *Left:* Emission spectra of ***fac*-[Re(15)(CO)$_3$Br]** *vs* **15** (both recorded in CHCl$_3$, 1 % DMSO); *Right:* Emission spectra recorded at 77 K of ***fac*-[Re(15)(CO)$_3$Br]** (recorded in EtOH:MeOH) *vs* room temperature measurement (dashed line, recorded in CHCl$_3$, 1 % DMSO). *denotes a lamp harmonic associated with the excitation wavelength.

In the case of ***fac*-[Re(16)(CO)$_3$Br]** and ***fac*-[Re(19)(CO)$_3$Br]**, both show multi-component emission dependent on wavelength with low energy bands at 546 and 556 nm respectively (**Figure 5.36**). However, an emissive lifetime was unable to be obtained for these bands, which makes these unlikely to be a result of a ^{3}MLCT transition.

***fac*-[Re(16)(CO)$_3$Br]** exhibited two ligand-based emission bands, much like ***fac*-[Re(15)(CO)$_3$Br]**. The lower energy band, and the more intense of the two, was attributed to the red-shifted ligand-centred band. However, the highly structured emission bands between 360 and 415 nm were indicative of pyrene emission. Discussed in more detail in **Section 5.2.3**, this may be in part due to inefficient through-bond conjugation between the pyrene and oxazole-pyridine units leading to multicomponent emission, similar to that described for the chloroanthracene-based ligand **15**. Measurements recorded at 77 K showed the shoulder observed between 350 and 430 nm in the room temperature measurements as the primary band, with vibronic fine structure indicative of that of pyrene (**Figure 5.36**). The ligand centred emission at 465 and 490 nm observed in room temperature emission were absent in the emission spectra recorded at 77 K, following the same trend observed with ***fac*-[Re(15)(CO)$_3$Br]**. Therefore, the higher energy bands observed at room temperature are tentatively assigned to pyrene emission, due to the fine structure observed, and further supported by DFT analysis (**Section 5.2.3**), and the low energy band assigned to charge transfer between the pyridine-oxazole moiety and the pyrene. When excited at 400 nm directly into the ^{1}MLCT band at 77 K, the emission spectra shows a broad band at 650 nm, which appears consistent with an ^{3}MLCT emission rather than a triplet pyrene phosphorescence. As described by N. Shavaleev *et al*[36], pyrene triplet states are known to quench the ^{3}MLCT state if they lie below the latter. The quantum yield for ***fac*-[Re(16)(CO)$_3$Br]** was the second highest recorded at 2.24 %, with a ligand centred lifetime varying from 1.7 ns for the higher energy transition, and 1.2 ns for the main low energy emission band.

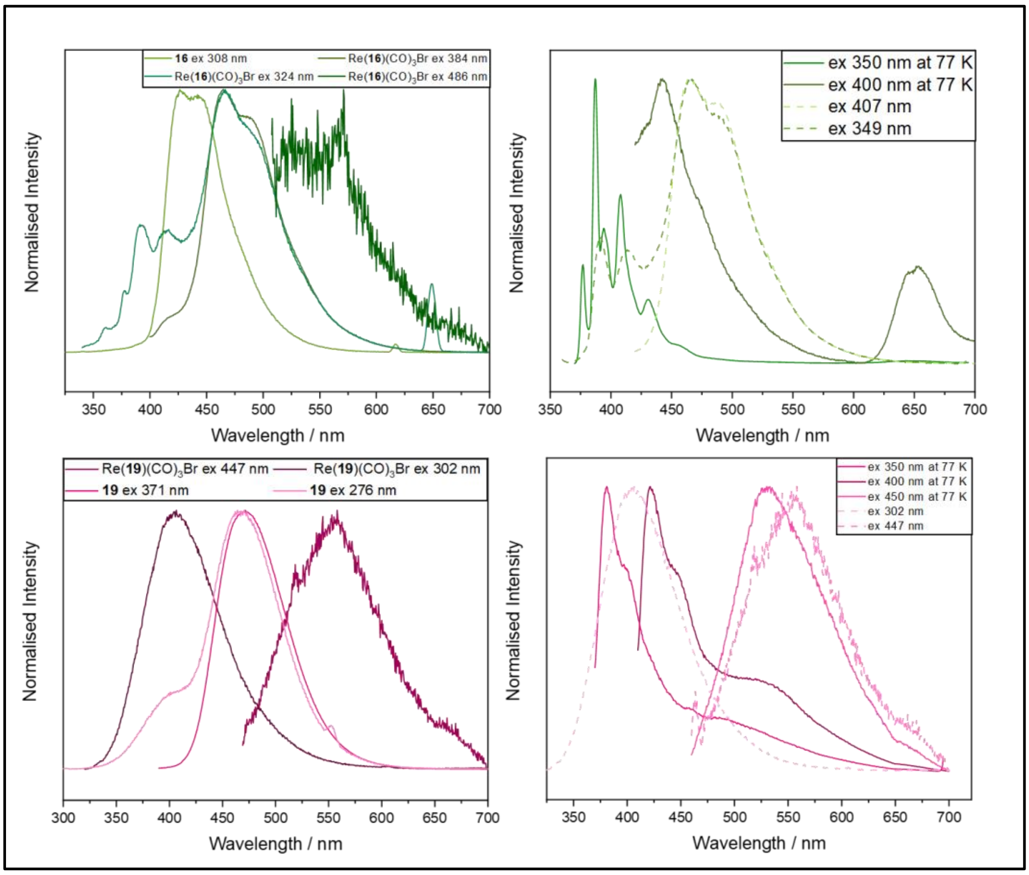

Figure 5.36 *Left:* Emission spectra of ***fac*-[Re(16)(CO)$_3$Br]** *vs* **16** (top) and ***fac*-[Re(19)(CO)$_3$Br]** *vs* **19** (bottom), all recorded in $CHCl_3$, 1 % DMSO; *Right:* Emission spectra recorded at 77 K of ***fac*-[Re(16)(CO)$_3$Br]** (top) and ***fac*-[Re(19)(CO)$_3$Br]** (bottom), both recorded in EtOH:MeOH *vs* room temperature measurement (dashed line, recorded in $CHCl_3$, 1 % DMSO).

For ***fac*-[Re(19)(CO)$_3$Br]**, the band at 405 nm was assigned to a ligand-centred transition, overlaying with the shoulder observed for free ligand **19**, as opposed to 469 nm where the main emissive band of **19** was found. The emissive lifetime however was identical to that of the free ligand. Emission spectra recorded at 77 K presented a more complicated picture (**Figure 5.36**), with spectral features dependent on excitation wavelength. Vibronically structured shorter wavelength features, which are attributed to ligand-based singlet emission, overlapped with a broader feature at around 500 nm which is likely to comprise some charge transfer character (due to the donor-accepter, push-pull character of **19**). At 77 K, it is likely that a frozen conformation decouples the different chromophoric components of the ligand resulting in distinguishable emission from each. DFT analysis (discussed in **Section 5.2.3**) also predicts charge transfer within the ligand, which could help explain the evident lack of emission centred upon the entirety of the ligand system.

Emission spectra recorded at 77 K showed no evidence of a long wavelength band consistent with a ^{3}MLCT feature, implying that any MLCT excited state is quenched. Further studies, including electrochemical assessments, are required to elucidate the origin of the quenching which may involve the terminal pyrrolidine group. The quantum yield of ***fac*-[Re(19)(CO)$_3$Br]** was recorded to be 1.4 %, higher than that of ***fac*-[Re(15)(CO)$_3$Br].**

5.2.3 Theoretical Studies using DFT/TDA-DFT

To provide further insight into the electronic states and the geometries of both the ligands and Re(I) complexes, DFT analyses was utilised using the PBE functional[38,39] and Def2SVP basis set[40], as with the di-substituted fluorophores in **Chapter 2**. As discussed in **Chapter 2**, a range of different functional and basis sets were tested to find the best fit to experimental absorption spectra of oxazoles **8-13**, and thus this was used for the ligands and complexes discussed herein. Def2SVP was also able to effectively characterise the rhenium centre as well as the lighter elements associated with the ligand, unlike other systems where an auxiliary basis set is required. Custom solvent conditions were also carried out (due to photophysical measurements being carried out in a $CHCl_3$-DMSO 99:1 solvent system) however yielded negligible differences to the orbital energies and thus for ease the SCRF was set to chloroform parameters. Please note that all calculations were run by the author, with the guidance of Dr Benjamin Ward and Owaen Guppy.

Ligands **14**, **18** and **19** were all predicted to be planar, with **19** displaying a twisted pyridyl terminus similar to that observed in the crystal structure of oxazole **7**. However, ligands **15**, **16** and **17** were all predicted to contain a twist in the R-group to oxazole unit, with the pyridine planar to the oxazole (**Figure 5.37**). The torsion angles were calculated to be (on going clockwise, looking from the R-C bond and starting at the oxazole oxygen) -122.7°, -148.3° and -153.2° for **15**, **16** and **17**, respectively. Ligands **15**, **16** and **17** in ***fac*-[Re(15)(CO)$_3$Br]**, ***fac*-[Re(16)(CO)$_3$Br]** and ***fac*-[Re(17)(CO)$_3$Br]** respectively displayed non-planarity, the most notable found in ***fac*-[Re(16)(CO)$_3$Br]**, where the pyrene R-group was rotated by approximately 180°C compared to that of the free ligand, with respect to the oxazole-pyridine component (**Figure 5.37**).

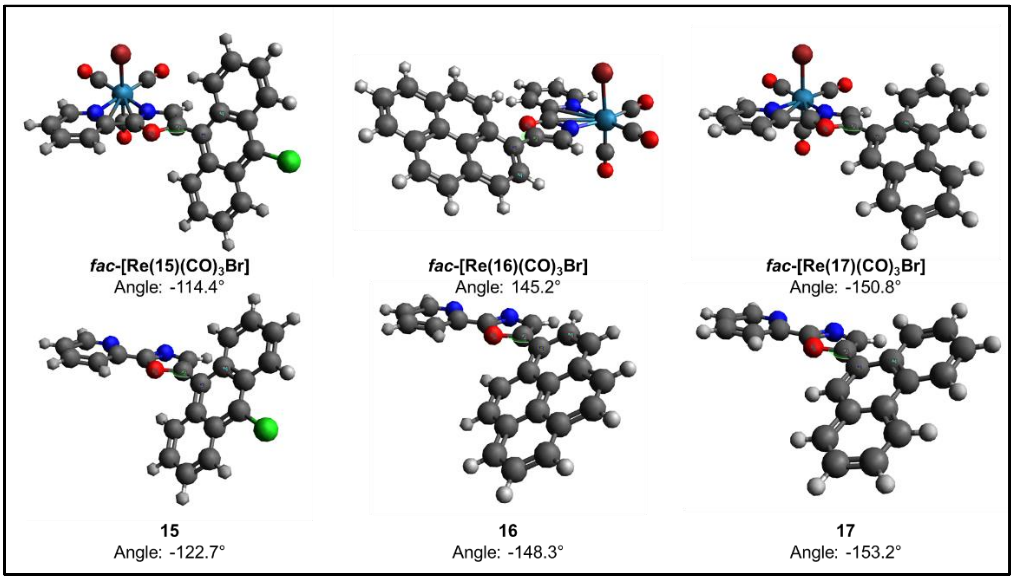

Figure 5.37 Predicted structures of ligands **15-17** and their respective ***fac*-[Re(15-17)(CO)$_3$Br]** complexes with dihedral angles.

For ***fac*-[Re(14)(CO)$_3$Br]** and ***fac*-[Re(19)(CO)$_3$Br]** each maintained planarity, however were slightly puckered with respect to the rhenium core. In the case of ***fac*-[Re(18)(CO)$_3$Br]**, the ligand also displayed slight puckering, but more interestingly the fluorenone R-group was flipped compared to the free ligand, with the carbonyl group pointing away from the complex as opposed to the same direction of the chelating unit.

As discussed in previous works, the bond lengths between rhenium and the chelating unit are indicators of the degree of electron donation from each side of the ligand.[11] Distorted octahedral rhenium complexes are common, due to the chelating unit forming a five membered ring with the rhenium centre.[11,18,27] This distortion is commonly shown not just by the N-Re-N bite angle, but also the N-Re-Cl angle[27]. Theoretical bond angles and lengths for all complexes are presented in **Table 5.6**. In all complexes, the Re-N(ox) bond length was predicted to be shorter than that of Re-N(py), suggesting that the oxazole component is more electron donating than pyridine. This is similar to the oxazoline being more electron donating than pyridine in work by A. Świtlicka *et al*[11], and concurring with similar results of R. Czerwieniec *et al*[27] (the crystal structure of *fac*-[Re(PBO)(CO)$_3$Cl] exhibited Re-N lengths of 2.206(4) and 2.171(3) for Re-N(py) and Re-N(ox) respectively). However, across the complexes the bond lengths were similar, suggesting that the R-group does not greatly affect the degree of electron donation which also concurs with the experimental carbonyl stretches discussed in **Section 5.2.1**, which showed no obvious trend. The predicted N-Re-N bond angle was also similar to that described by R. Czerwieniec *et al*[27] (74.56(13)°) in the crystal structure of *fac*-[Re(CO)$_3$(PBO)Cl].

Table 5.6 Predicted bond lengths and torsion angles of ***fac*-[Re(L)(CO)$_3$Br]** generated from DFT analysis.

	Re-N(ox) / Å	**Re-N(py) / Å**	**N-Re-N / °**	**N(ox)-Re-Br / °**
Re(14)(CO)$_3$Br	2.197	2.242	74.1	83.6
Re(15)(CO)$_3$Br	2.196	2.242	74.0	82.9
Re(16)(CO)$_3$Br	2.197	2.242	74.1	83.8
Re(17)(CO)$_3$Br	2.197	2.243	74.0	83.7
Re(18)(CO)$_3$Br	2.198	2.242	74.1	83.9
Re(19)(CO)$_3$Br	2.195	2.241	74.2	84.1

All equatorial Re-CO bond lengths were calculated to be 1.922 Å, longer than the axial Re-CO (1.912-1.913 Å). These lengths were in line with X-ray analysis results using the PBO ligand discussed by R. Czerwieniec *et al*[27]. It is however unusual for both equatorial bond lengths to be the same, but this may be a limitation of the DFT calculation. Re-Br bond lengths varied between 2.642-2.645 Å, longer than that observed in the crystal structure of fac-[Re(PBO)(CO)$_3$Cl] (2.4837(10) Å), but shorter than that observed in the crystal structures of Re-pyta and Re-tapy based complexes (2.678 and 2.675 Å respectively) bearing bromide axial ligands described in the work by H. Bertrand *et al*[18]. C-Re-N bond angles were also calculated, with C-Re-N(py) slightly smaller than C-Re-N(ox), and angles ranging between 97.8-98.0 and 98.3-98.5° respectively.

In terms of electronic characteristics, in ligands **14**, **16** and **17**, the dominant HOMO→LUMO transition was predicted to possess $\pi \rightarrow \pi^*$ and involve orbitals across the entirety of the ligand. However, in the cases of **15**, **18** and **19**, the HOMO→LUMO descriptions were more complex. For **15**, both the HOMO and LUMO states were predicted to be dominated by orbitals centred upon the chloroanthracene and oxazole. However, for **18** and **19** a degree of intra-ligand charge transfer was predicted. For ligand **19**, the HOMO→LUMO transition showed excitation from predominantly the oxazole-phenyl to the pyridine-oxazole groups. Ligand **18** is predicted to display charge transfer, with the electron density in the HOMO across the entirely of the ligand with the exception of the carbonyl, however in the LUMO the electron density was predicted to be on the fluorenone, similar to work described by F. Xu *et al.*[41] This, along with the TDA-DFT results discussed below, sheds light on the dual emissive nature observed in the experimental emission spectra.

Frontier orbital diagrams for ***fac*-[Re(14-19)(CO)$_3$Br]** are presented in **Figure 5.38**. The band gaps varied considerably across the series, with ***fac*-[Re(19)(CO)$_3$Br]** exhibiting the smallest band gap, whereas ***fac*-[Re(17)(CO)$_3$Br]** exhibited the largest band gap.

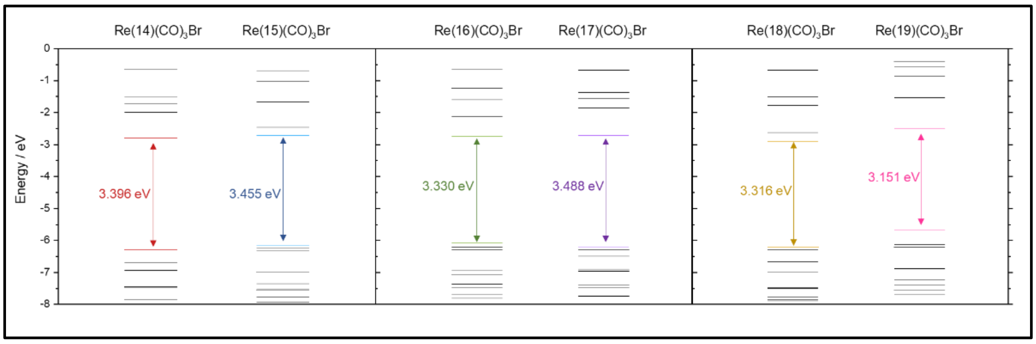

Figure 5.38 Frontier orbital diagrams with band-gaps of ***fac*-[Re(L)(CO)$_3$Br]** generated from DFT analysis.

***fac*-[Re(14)(CO)$_3$Br]**, ***fac*-[Re(17)(CO)$_3$Br]** and ***fac*-[Re(18)(CO)$_3$Br]** were all predicted to contain a high % d-orbital contribution to their HOMO and H-1 states (**Table 5.7**), whereas ***fac*-[Re(15)(CO)$_3$Br]**, ***fac*-[Re(16)(CO)$_3$Br**] and ***fac*-[Re(19)(CO)$_3$Br]** contain negligible d-character, with the HOMO containing orbitals centred almost entirely upon the oxazole and R-group (chloroanthracene, pyrene and phenyl pyrrolidine respectively), with little contribution from the pyridine of the ligand. This concurs with photophysical results discussed in **Section 5.2.2** , where ***fac*-[Re(14,17,18)(CO)$_3$Br]** all show ^{3}MLCT emission, whereas ***fac*-[Re(15,16,19)(CO)$_3$Br]** show ligand centred emission only.

Table 5.7 Predicted % contribution of rhenium d-orbitals, calculated by DFT.

***fac*-[Re(L)(CO)$_3$Br]**	**%d orbital contribution**					
	H-2	H-1	HOMO	LUMO	L+1	L+2
L=14	0.10	31.5	35	0.58	0.57	0.26
L=15	32	33	3.1	0.56	0.25	0.39
L=16	31	32	5.5	0.50	0.57	0.26
L=17	0.76	31	35	0.62	0.53	0.13
L=18	0.20	31	35	0.24	0.48	0.70
L=19	32	34	0.78	0.73	0.50	0.99

For all complexes, the LUMO+X orbitals were predicted to be predominantly ligand centred, with varying contributions across the ligand. For example, in ***fac*-[Re(14)(CO)$_3$Br]**, ***fac*-[Re(17)(CO)$_3$Br]** and ***fac*-[Re(19)(CO)$_3$Br]**, the LUMO state showed predominantly oxazole-pyridine character, with little contribution from the R-group, however for ***fac*-[Re(15)(CO)$_3$Br**], ***fac*-[Re(16)(CO)$_3$Br]** and ***fac*-[Re(18)(CO)$_3$Br]**, the first LUMO state covered the entirety of the ligand. ***fac*-[Re(15)(CO)$_3$Br]**, ***fac*-[Re(16)(CO)$_3$Br]** and ***fac*-[Re(17)(CO)$_3$Br]** all exhibited LUMO+3 states with predominantly R-group only character.

Both TD-DFT and TDA based TD-DFT were carried out to simulate the UV-vis spectra of both oxazoles **8-13** (**Chapter 2**), ligands **14-19** and Re(I) complexes. Whilst both methods provided good general agreement with experimental values, TDA based TD-DFT gave the best agreement and was used for all theoretical investigations. In all cases, a large number of absorption transitions were predicted, with varying oscillator strengths. Therefore, only those of high oscillator strengths and of particular interest are discussed herein, with a full list of states and their respective transitions (only those of the highest contribution are discussed here) found in the **Appendix.**

Ligands **14**, **16** and **17** were all predicted to demonstrate relatively straight forward electronic transitions, with the predicted absorption spectra presented in **Figure 5.39** including the corresponding transitions and states. Both ligands **14** and **17** were predicted to exhibit HOMO→LUMO transitions due to the excitation of the electron from the π-orbitals encompassing the entirety of the ligand to the equivalent π* orbitals. For **16** this is also the case, however there was little contribution from the pyridyl π orbitals in the HOMO. The simulated absorption spectra of ligand **14**, although showing good agreement at higher energies, failed to successfully predict the lower energy bands despite doing so for the equivalent complex discussed below. That being said, it is also the case for the naphthalene-oxazole **8**, and thus is in good agreement across the two fluorophores. Although the low energy HOMO→LUMO transition was centred on the entirety of the ligand, the higher energy transition at 280 nm was dominated by orbitals centred upon the benzoquinoline of the ligand. The predicted electronic transitions of ligand **16** were primarily based upon the π and π* orbitals over the entirety of the ligand, however as with the HOMO state, LUMO+2 also had little contribution from the pyridyl group. At higher energy absorptions there was some evidence of charge transfer, which was particularly evident at 266 nm, where the dominant transition (82%) was to the LUMO+3 state, which is centred upon the pyridyl group. Another interesting observation is that the HOMO-2 state of **17**, similar to that of the HOMO-4 state predicted for oxazole **11**, showed localisation across the side of the phenanthrene R-group closest to the oxazole-pyridine, indicating polarity across the phenanthrene as a result of this coupling.

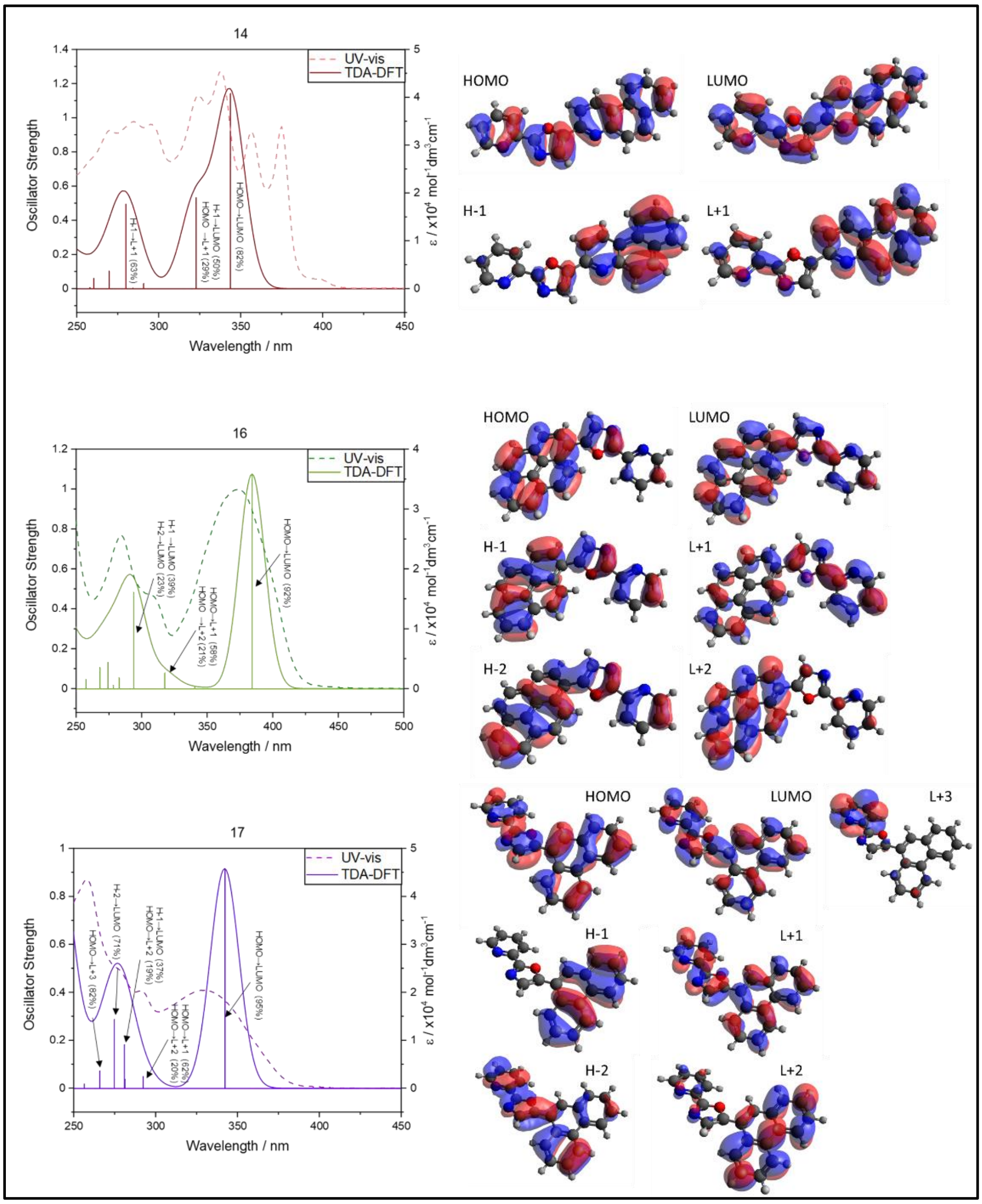

Figure 5.39 *left*: TDA-DFT calculated transitions of **14**, **16**, **17** (solid lines) with dominating transitions labelled, compared to the absorption spectra (dotted line); *right:* Molecular orbitals involved in the dominating transitions.

TDA based DFT of ligand **19** predicted charge transfer across the structure, with the HOMO→LUMO transition showing a transfer of electron density from the phenyl-oxazole unit of the HOMO to the oxazole-pyridine of the LUMO, presented in **Figure 5.40**, most likely due to the donor-accepter, push-pull character of the pyrrolidine donor. Higher energy transitions also followed this trend, with the exception of those to the LUMO+3, which was more localised on the phenyl than the oxazole-pyridine group.

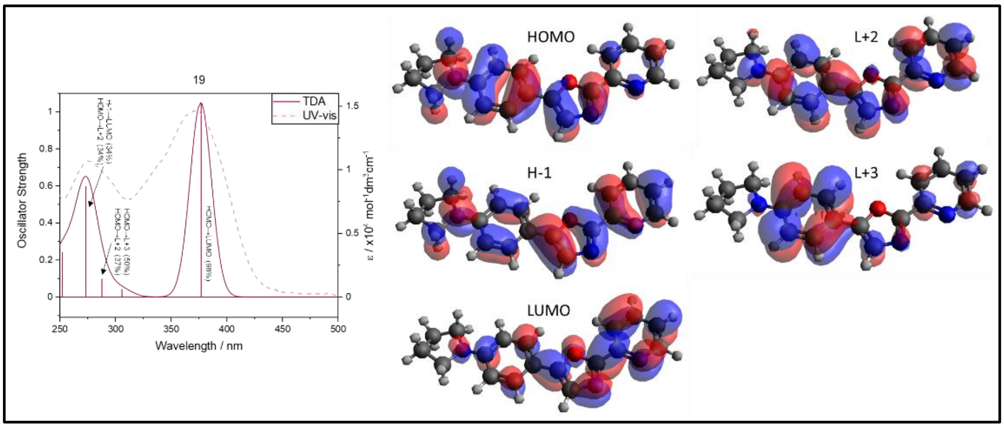

Figure 5.40 *left*: TDA-DFT calculated transitions of **19** (solid line) with dominating transitions labelled, compared to the absorption spectra (dotted line); *right:* Molecular orbitals involved in the dominating transitions.

Both ligands **15** and **18** demonstrated more complex photophysics compared to the other ligands in the series, as shown in **Section 5.2.2**, with charge-transfer postulated for the broad emission observed in **15**, and dual emission observed in **18** as a result of the fluorenone R-group.

For ligand **15**, both the HOMO and LUMO were predicted to be centred predominantly on the π and π* orbitals respectively of the chloroanthracene-oxazole unit (**Figure 5.41**), thus the absorption at 396 nm correlates to a discrete π→π* transition in this area of the fluorophore. Higher energy absorptions showed evidence of charge transfer across the oxazole, with absorption at 335 nm predicted to be dominated by charge transfer from the chloroanthracene to the pyridine, and for 323 nm, the pyridine to the chloroanthracene. Predictions of charge transfer correlate with the luminescence spectra of **15**, which showed a broad, lower energy band thought to be a result of charge transfer between the R-groups of the oxazole. The highest energy absorption shown in **Figure 5.41** at 259 nm was predicted to be dominated by π and π* orbitals localised primarily on the oxazole-pyridine unit. This was not expected, as this absorption is traditionally assigned to the chloroanthracene due to existing literature of anthracenes discussed in **Chapter 2**, and the TDA-DFT results of the naphthalene-oxazole **9** which predicted excitation to the chloroanthracene π* orbitals. Absorption at 256 nm, at a much lower oscillator strength, described the expected transition to the chloroanthracene π* orbitals (LUMO) from π orbitals located primarily on the pyridine (HOMO-3), and so this discrepancy from the expected result may be the case of poor agreement between the simulated and experimental spectra, as discussed for Ligand **14**.

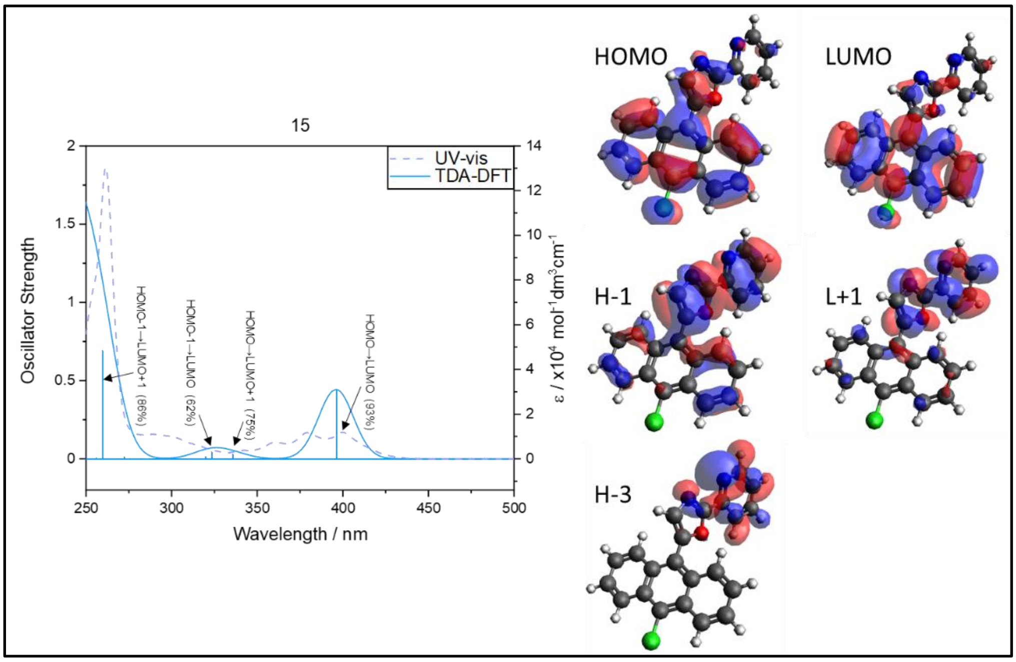

Figure 5.41 *left*: TDA-DFT calculated transitions of **15** (solid line) with dominating transitions labelled, compared to the absorption spectra (dotted line); *right:* Molecular orbitals involved in the dominating transitions.

The absorption spectra of **18** was characterised by both the high energy transitions typical of a highly conjugated aromatic fluorophore, as well as a broad low energy transition centred at 430 nm. The latter was assigned to a charge transfer transition to the fluorenone moiety, as discussed in depth in **Chapter 2**, and in **Section 5.2.2** herein. TDA-DFT effectively predicted this transition, as shown in **Figure 5.42**, with the HOMO→LUMO dominating the absorption (93%) and describing the excitation of an electron from π orbitals across **18** to π* orbitals centred on the fluorenone, including the carbonyl bond, and similar to that observed in literature[33,41]. Higher energy transitions were primarily dominated by transitions located on, or charge transfer to, the fluorenone, with the exception of absorption at 333 nm, which was predicted to be dominated by the HOMO→LUMO+1 describing excitation of the electron from the π-orbitals encompassing the entirety of the ligand to the equivalent π* orbitals. A further exception was the highest energy transition shown in **Figure 5.42** at 265 nm, which was predicted to contain a small contribution from the HOMO→LUMO+3 transition (34%), describing charge transfer from the entirety of the ligand to the π*-orbitals of the pyridine unit only.

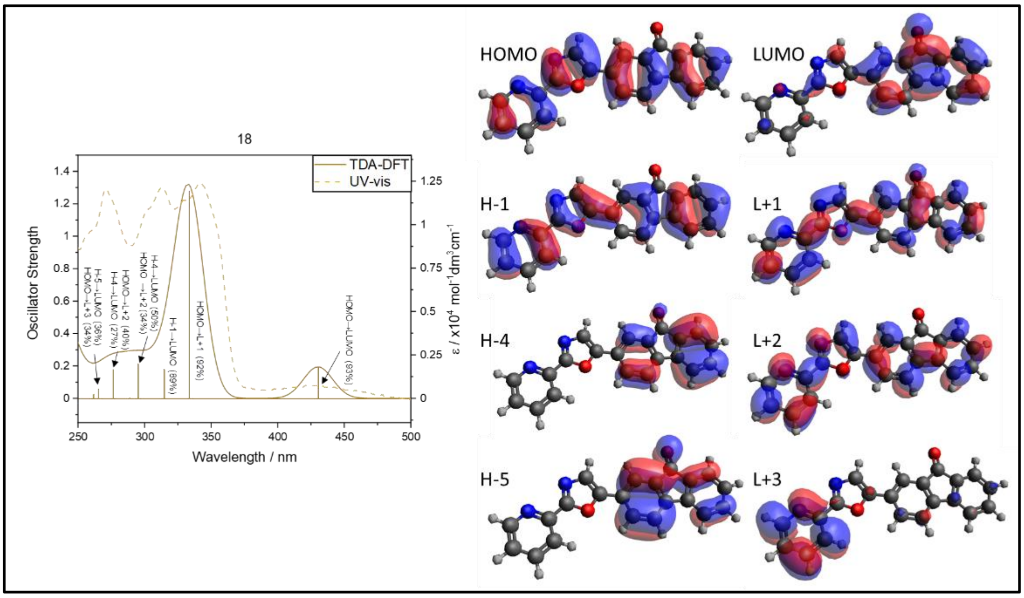

Figure 5.42 *left*: TDA-DFT calculated transitions of **18** (solid lines) with dominating transitions labelled, compared to the absorption spectra (dotted line); *right:* Molecular orbitals involved in the dominating transitions.

***fac*-[Re(14,17,18)(CO)$_3$Br]** all exhibited proposed ^{3}MLCT luminescence in the emission spectra discussed in **Section 5.2.2**, with DFT analysis predicting high % d orbital contribution within the HOMO states compared to ***fac*-[Re(15,16,19)(CO)$_3$Br]**. The lowest energy absorption predicted by TDA-DFT for ***fac*-[Re(14)(CO)$_3$Br]** was found at 493 nm, far above that of the experimental value. However, the oscillator strength for this transition was incredibly low, at 0.0038, and thus is only discussed here due to the fact that it represents the HOMO→LUMO transition, shown in **Figure 5.43**. The same was true for both ***fac*-[Re(17)(CO)$_3$Br]** and ***fac*-[Re(18)(CO)$_3$Br]** at 480 and 493 nm respectively. However, in all three cases the slightly higher energy transitions predicted at 426, 452 and 461 nm respectively were all predicted to be dominated by the HOMO-1→LUMO transition, which by inspecting the %d orbital contributions in **Table 5.7**, can also be assigned to ^{1}MLCT states. Shown in **Table 5.8**, both the HOMO and HOMO-1 also contained a high % contribution of bromide p-orbitals, thus suggesting that the ^{1}MLCT state is mixed with ^{1}XLCT. Interestingly, whereas both ***fac*-[Re(14)(CO)$_3$Br]** and ***fac*-[Re(17)(CO)$_3$Br]** were predicted to have LUMO states localised predominantly on the oxazole-pyridine chelating unit, the LUMO of ***fac*-[Re(18)(CO)$_3$Br]** instead showed contribution from the π* orbitals across the entirety of the ligand, which may be the result of mixing of the ^{1}MLCT band with the charge transfer band of the ligand to the fluorenone. Unlike free ligand **18**, complex ***fac*-[Re(18)(CO)$_3$Br]** did not show transitions only to the fluorenone ring despite the dual emission shown in **Figure 5.34**.

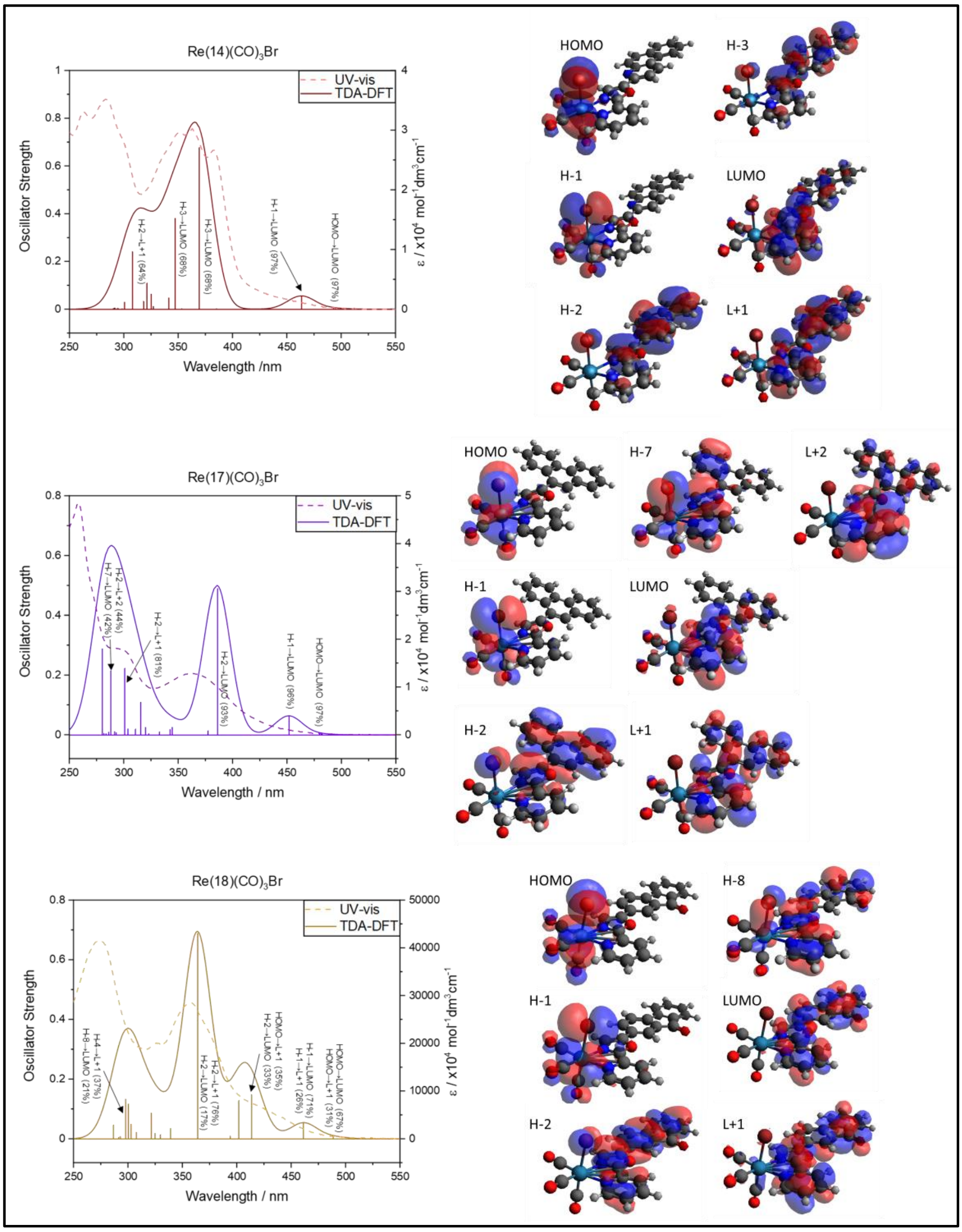

Figure 5.43 *left*: TDA-DFT calculated transitions of ***fac*-[Re(14,17,18)(CO)$_3$Br]** (solid lines) with dominating transitions labelled, compared to the absorption spectra (dotted line); *right:* Molecular orbitals involved in the dominating transitions.

Higher energy bands for all three complexes were predominantly ligand based, with the exception of the HOMO-4 state in the 298 nm absorption band of ***fac*-[Re(18)(CO)$_3$Br]**, which had a larger 23% d-orbital contribution. One notable difference between the complexes was that the ligand based transitions were centred upon the entirety of the ligand for ***fac*-[Re(18)(CO)$_3$Br]**, however in the case of ***fac*-[Re(14)(CO)$_3$Br]** and ***fac*-[Re(17)(CO)$_3$Br]** appeared to show slight charge transfer, with the HOMO-3/-2 and HOMO-2 respectively being centred upon the R-group and oxazole, and the LUMO states being centred predominantly upon the oxazole-pyridine unit. For all three complexes there was a noticeable % component of bromide p-orbitals to the HOMO-X states (**Table 5.8**), most notable in ***fac*-[Re(17)(CO)$_3$Br]** and ***fac*-[Re(18)(CO)$_3$Br]**, and thus a small degree of ^{1}XLCT was also assigned to both the higher energy transitions and the predicted ^{3}MLCT states.

Table 5.8 Predicted % contribution of Br p-orbitals, calculated by DFT. Individual contributions (p_x, p_y, p_z) found in the appendix, LUMO+X orbitals not presented but all contributions < 2 %.

***fac*-[Re(L)(CO)$_3$Br]**	**%Br p-orbital contribution**			
	H-3	H-2	H-1	HOMO
L=14	2.7	3.8	46	43
L=15	0.78	45	42	2.5
L=16	0.76	47	42	4.4
L=17	0.067	5.7	46	42
L=18	0.76	6.2	47	42
L=19	0.71	47	44	0.25

***fac*-[Re(15)(CO)$_3$Br]**, ***fac*-[Re(16)(CO)$_3$Br]** and ***fac*-[Re(19)(CO)$_3$Br]** presented a more complex picture in their analysis. As discussed previously, all possessed HOMO states in which the predominant contribution was that of the antenna R-group in the ligand, whether that be chloroanthracene, pyrene or phenyl pyrrolidine respectively.

For ***fac*-[Re(15)(CO)$_3$Br]** and ***fac*-[Re(16)(CO)$_3$Br]** the lowest energy absorption was predicted to be dominated by the HOMO-1→LUMO transition, whereas for ***fac*-[Re(19)(CO)$_3$Br]**, it contributed almost equally with the HOMO→LUMO (**Figure 5.44**). In all cases, the HOMO-1→LUMO transition described an ^{1}MLCT transition to the pyridine-oxazole chelating unit, with a large HOMO-1 % d-orbital component (**Table 5.7**) as well as bromide p-orbital contribution (**Table 5.8**), and thus can be assigned as a mixed state of ^{1}XLCT/^{1}MLCT. Photophysical measurements in **Section 5.2.2** showed that for ***fac*-[Re(15)(CO)$_3$Br]** and ***fac*-[Re(19)(CO)$_3$Br]** no ^{3}MLCT emission was observed, suggested to be due to quenching by chloroanthracene and pyrrolidine respectfully. In the case of ***fac*-[Re(16)(CO)$_3$Br]**, ^{3}MLCT emission was only observed when the emission spectra was recorded at 77 K. The HOMO→LUMO transition (which is predicted to contribute strongly in the lower energy absorptions) was ligand centred originating from the R-group and oxazole, with the LUMO predominantly centralised on the oxazole-pyridine unit. With the exception of ***fac*-[Re(19)(CO)$_3$Br]**, there was a small bromide component, and therefore the HOMO→LUMO transition can be assigned as a ^{1}ILCT with a small ^{1}XLCT contribution for ***fac*-[Re(15)(CO)$_3$Br]** and ***fac*-[Re(16)(CO)$_3$Br]**. Higher energy transitions were also predominantly ligand centred, either localised across the entirety of the ligand system or from the π-orbitals of the R-group and oxazole into the π* orbitals of the pyridine-oxazole unit. In some cases, particularly at the highest energy transitions, the Re(I) d-orbitals and bromide p-orbitals also contributed to the HOMO-X states, particularly the HOMO-2 of both ***fac*-[Re(16)(CO)$_3$Br]** and ***fac*-[Re(17)(CO)$_3$Br]**.

In the case of ***fac*-[Re(19)(CO)$_3$Br]**, the push-pull donor-acceptor characteristic of the pyrrolidine was evident, and correlated well with photophysical observations. The lack of charge transfer predicted from the pyridine-oxazole to the chloroanthracene or chloroanthracene-localised transitions, unlike the free ligand, also correlated well with photophysical observations for ***fac*-[Re(15)(CO)$_3$Br]**.

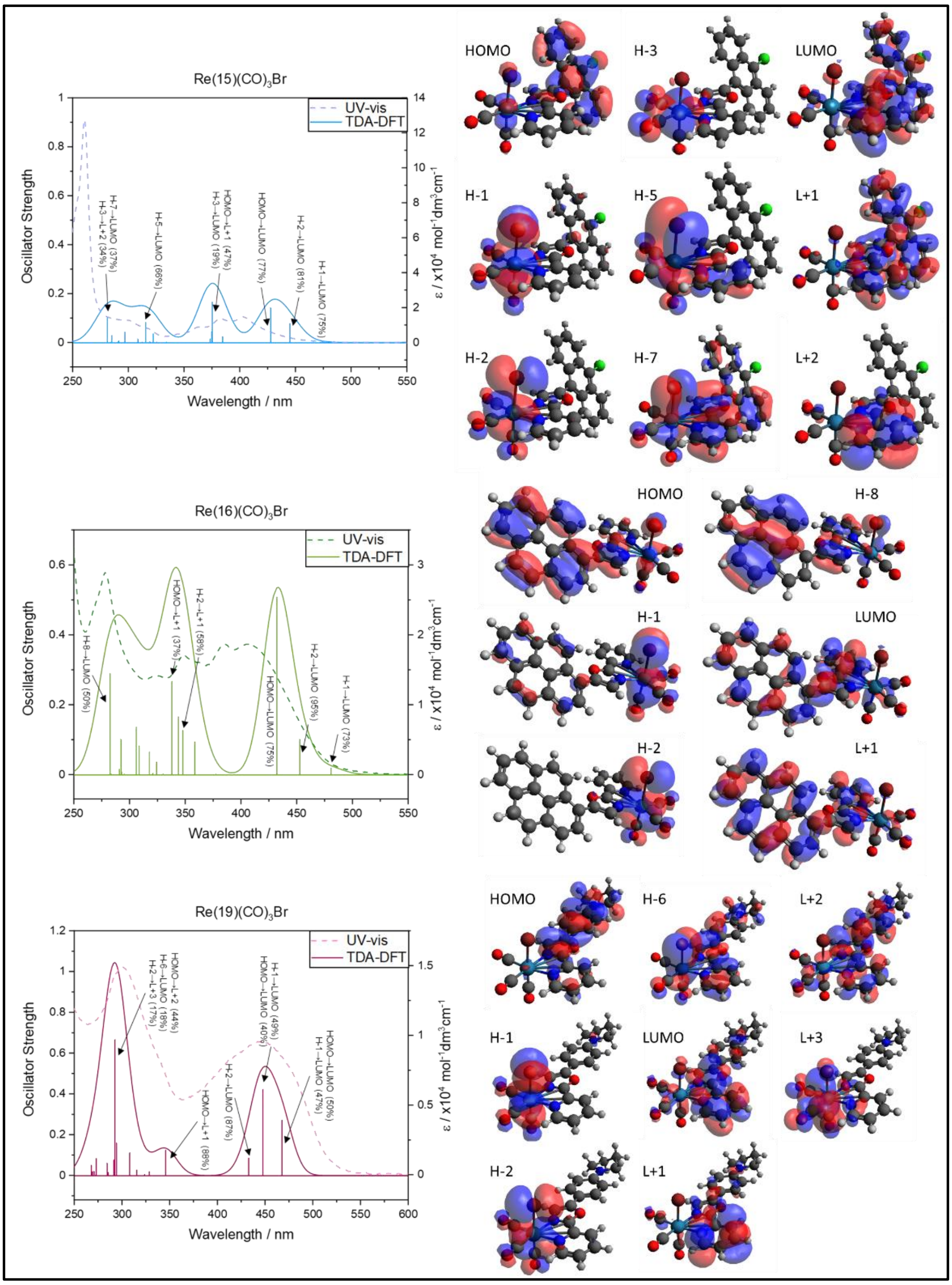

Figure 5.44 *left*: TDA-DFT calculated transitions of ***fac*-[Re(15,16,19)(CO)$_3$Br]** (solid lines) with dominating transitions labelled, compared to the absorption spectra (dotted line); *right:* Molecular orbitals involved in the dominating transitions.

5.3 Conclusion

Six novel pyridine-oxazole based chelating ligands were synthesised based upon the oxazoles discussed in **Chapter 2**, and were then used to synthesise six novel rhenium(I) tricarbonyl complexes.

Both complexes and ligands displayed a varied range of photophysical characteristics and were studied in-depth, with DFT and TDA-DFT analysis used to further inform experimental observations. Complex emission was characterised by combinations of ligand and MLCT based states. In all cases ligand-based emission was observed, typically involving the pendant fluorophore. In a minority of cases the MLCT emitting state was observed at *ca.* 610 nm, consistent with benchmark diimine[35] (including benzoxazole[12]) cases. However, they generally appeared weakly emissive, and in some cases it is possible that additional quenching pathways are available *via* low lying triplet states, particularly those baring pendant chloroanthracene and pyrene fluorophores. Both ligand **18** and ***fac*-[Re(18)(CO)$_3$Br]** exhibited dual emission arising from emission of the fluorenone R-group as well as across the ligand, which was further confirmed *via* TDA-DFT and correlates well with oxazole **12** in **Chapter 2**. As with oxazole **12** in **Chapter 2**, Excitation Emission Matrix (EEM) measurements would be useful to further elucidate the dual emissive nature of ligand **18** and the associated complex.

Due to the varied photophysical characteristics observed, and thus the ability to fine-tune emission, it would be advantageous to attempt to improve the solubility of these complexes *via* halide abstraction, as well as further analysis of the push-pull nature of ligand **19** in ***fac*-[Re(19)(CO)$_3$Br].**

5.4 Experimental

5.4.1 Ligand Synthesis

All primary oxazoles synthesised as described in **Chapter 2.**

5.4.1.1 General Procedure of Ullmann-based Coupling, adapted from Yoshizumi *et al*[29]

Oxazole (1 eq.), Na_2CO_3 (2 eq.), PPh_3 (0.2 eq.), CuI (4 eq.) and iodo-pyridine (1.2 eq) were added to degassed DMF (4 mL), and the reaction was stirred in the dark for 48 hrs at 110°C under N_2. The reaction mixture was then allowed to cool, before being stirred with ethylene diamine (10 mL) in water (10 mL) for 10 minutes. The crude product was extracted into DCM (100 mL), which was then washed with ethylene diamine (10 mL) in water (100 mL) until the aqueous layer was clear, followed by washing with water (3 x 100 mL). The DCM layer was dried over magnesium sulphate, filtered and the solvent removed *in vacuo* to yield crude product. The crude product was triturated in ethanol and the solid filtered to yield the desired product, unless otherwise stated.

5.4.1.1.1 Synthesis of 5-(benzo[f]quinolin-3-yl)-2-(pyridin-2-yl)oxazole (**14**)

As general procedure, using oxazole **1**, to yield product as a dark solid (26mg, 20% yield). ^{1}H NMR (400 MHz, $CDCl_3$) δ= 9.03 (1H, d, J = 8.7 Hz, Ar-H), 8.81 (1H, ddd, J = 4.8, 1.8, 0.9 Hz, Ar-H), 8.64 (1H, d, J = 8.3 Hz, Ar-H), 8.28 (1H, dt, J = 4.9, 1.1 Hz, Ar-H), 8.15 (1H, d, J = 8.6 Hz, Ar-H), 8.08 (1H, s, Ar-H), 8.03 (2H, s, Ar-H), 7.96-7.93 (1H, m, Ar-H), 7.88 (1H, td, J = 7.7, 1.8 Hz, Ar-H), 7.75-7.64 (2H, m, Ar-H), 7.42 (1H, ddd, J = 7.6, 4.8, 1.2 Hz, Ar-H) ppm; $^{13}C\{^1H\}$ NMR (101MHz, $CDCl_3$) 161.0, 152.3, 150.3, 149.2, 148.4, 146.5, 146.1, 137.2, 132.0, 131.83, 131.81, 129.6, 129.0, 128.1, 128.0, 127.7, 127.5, 125.0, 122.9, 122.7, 118.0 ppm; ES-MS (positive ion mode): found m/z 324.1147 [M^+] $C_{21}H_{14}N_3O$; UV-vis ($CHCl_3$-DMSO 99:1) λ_{max} (ε / $mol^{-1}dm^3cm^{-1}$) 399 (1972), 375 (33790), 356 (32690), 338 (45320), 323 (40380), 296 (34280), 285 (34890) nm; IR ν_{max} / cm^{-1} 3040, 1682, 1584, 1482, 1455, 1450, 1434, 1415, 1362, 1328, 1301, 1279, 1244, 1196, 1148, 1125, 1080, 1045, 996, 988, 972, 949, 885, 869, 852, 842, 830, 789, 747, 741, 706, 682, 640, 615, 558, 538, 506, 476, 459, 434, 406.

5.4.1.1.2 Synthesis of 5-(10-chloroanthracen-9-yl)-2-(pyridin-2-yl)oxazole (**15**)

As general procedure, using oxazole **2**, to yield pure product as a yellow solid (51mg, 40%). ^{1}H NMR (500 MHz, $CDCl_3$) δ= 8.76 (1H, ddd, J = 4.8, 1.8, 1.0 Hz, Ar-H), 8.61 (2H, ddd, J = 8.9, 1.3, 0.8 Hz, Ar-H), 8.24 (1H, dt, J = 7.9, 1.1 Hz, Ar-H), 7.96 (2H, ddd, J = 8.8, 1.3, 0.8 Hz, Ar-H), 7.87 (1H, td, J = 7.8, 1.8 Hz, Ar-H), 7.64 (1H, dd, J = 8.8, 1.1 Hz, Ar-H), 7.63 (1H, dd, J = 8.9, 1.2 Hz, Ar-H), 7.58 (1H, s, Ar-H), 7.54 (1H, dd, J = 8.8, 1.2 Hz, Ar-H), 7.52 (1H, dd, J = 8.9, 1.2 Hz, Ar-H), 7.41 (1H, ddd, J = 7.6, 4.8, 1.2 Hz, Ar-H) ppm; ^{13}C{^{1}H} NMR (101 MHz, $CDCl_3$) 150.4, 137.2, 132.4, 130.7, 128.7, 127.3, 127.1, 126.3, 125.3, 125.0, 122.2, 121.2, 119.8, 117.6, 117.4, 115.6 ppm; ES-MS (positive ion mode): found m/z 357.0799 [M^+] $C_{22}H_{14}N_2OCl$; UV-vis ($CHCl_3$-DMSO 99:1) λ_{max} (ε / mol^{-1}dm^{3}cm^{-1}) 400 (12917), 379 (12738), 359 (8330), 343 (5103), 282 (49199), 261 (165450) nm; IR ν_{max} / cm^{-1} 3083, 3049, 1590, 1537, 1454, 1435, 1338, 1265, 1149, 1134, 1100, 1043, 1031, 993, 933, 871, 842, 794, 756, 740, 713, 688, 635, 618, 606, 581, 488 cm^{-1}.

5.4.1.1.3 Synthesis of 5-(pyren-1-yl)-2-(pyridin-2-yl)oxazole (**16**)

As general procedure, using oxazole **3**, to yield yellow solid (90 mg, 35 % yield). ^{1}H NMR (500 MHz, $CDCl_3$) 8.82 (1H, ddd, J = 4.82, 1.80, 0.94 Hz, Ar-H), 8.65 (1H, d, J = 9.3 Hz, Ar-H), 8.40 (1H, d, J = 8.0 Hz, Ar-H), 8.28 (1H, dt, J = 8.0, 1.1 Hz, Ar-H), 8.25-8.19 (4H, m, Ar-H), 8.16-8.03 (3H, m, Ar-H), 7.89 (1H, td, J = 7.8, 1.8 Hz, Ar-H), 7.78 (1H, s, Ar-H), 7.42 (1H, ddd, J = 7.6, 4.8, 1.2 Hz, Ar-H) ppm; ^{13}C{^{1}H} NMR (126 MHz, $CDCl_3$) 160.7, 152.3, 150.4, 146.4, 137.2, 132.0, 131.5, 130.9, 129.1, 128.6, 128.2, 127.8, 127.5, 126.5, 126.3, 126.0, 125.7, 125.2, 125.1, 124.8, 124.79, 124.1, 122.3, 122.1 ppm; ES-MS (positive ion mode): found m/z 347.1177 [M^+] $C_{24}H_{15}N_2O$; UV-vis ($CHCl_3$-DMSO 99:1) λ_{max} (ε / mol^{-1}dm^{3}cm^{-1}) 374 (33190), 310 (15500), 285 (25400) nm; IR ν_{max} / cm^{-1} 3110, 3039, 1587, 1560, 1543, 1504, 1453, 1435, 1276, 1242, 1195, 1174, 1142, 1101, 1074, 1043, 1024, 989, 974, 956, 941, 837, 823, 787, 751, 735, 716, 708, 676, 631, 616, 605, 532, 508, 432, 411.

5.4.1.1.4 Synthesis of 5-(phenanthren-9-yl)-2-(pyridin-2-yl)oxazole (**17**)

As general procedure, using oxazole **4**, to yield yellow solid (35 mg, 27 % yield). ^{1}H NMR (500 MHz, $CDCl_3$) 8.81 (1H, ddd, J = 4.9, 1.7, 0.9 Hz, Ar-H), 8.80-8.77 (1H, m, Ar-H), 8.70 (1H, ap. d, J = 8.2 Hz, Ar-H), 8.40-8.36 (1H, m, Ar-H), 8.26 (1H, dt, J = 8.00, 1.1 Hz, Ar-H), 8.19 (1H, s, Ar-H), 7.98-7.95 (1H, m, Ar-H), 7.87 (1H, td, J = 7.8, 1.8 Hz, Ar-H), 7.75-7.62 (4H, m, Ar-H), 7.67 (1H, s, Ar-H), 7.40 (1H, dd, J = 4.9, 1.2 Hz, Ar-H); $^{13}C\{^1H\}$ NMR (126 MHz, $CDCl_3$) 160.5, 151.7, 150.3, 146.4, 137.1, 131.1, 130.9, 130.8, 129.4, 129.1, 128.6, 127.9, 127.7, 127.5, 127.3, 127.1, 125.7, 124.8, 123.9, 123.4, 122.7, 122.3 ppm; ES-MS (positive ion mode): found m/z 323.1191 [M$^+$] $C_{22}H_{14}N_2O$; UV-vis ($CHCl_3$-DMSO 99:1) λ_{max} (ε / mol^{-1}dm^{3}cm^{-1}) 331 (20480), 291 (20250), 278 (24660), 258 (43370); IR ν_{max} / cm^{-1} 3057, 2953, 2919, 2871, 2851, 1693, 1586, 1557, 1530, 1521, 1496, 1456, 1436, 1401, 1303, 1286, 1250, 1150, 1133, 1103, 1086, 1040, 993, 947, 907, 849, 792, 765, 747, 717, 709, 674, 619, 598, 540, 505, 485, 440, 420.

5.4.1.1.5 Synthesis of 2-(2-(pyridin-2-yl)oxazol-5-yl)-9H-fluoren-9-one (**18**)

As general procedure, using oxazole **5**, with crude product purified *via* column chromatography (1:1 PE:EA) to yield a yellow solid (58 mg, 42 % yield). ^{1}H NMR (400 MHz, $CDCl_3$) δ= 8.78 (1H, ddd, J = 4.8, 1.8, 0.9 Hz, Ar-H), 8.19 (1H, dt, J =7.9, 1.0 Hz, Ar-H), 8.04 (1H, dd, J = 1.7, 0.5 Hz, Ar-H), 7.95 (1H, dd, J = 7.8, 1.6 Hz, Ar-H), 7.85 (1H, td, J = 7.8, 1.7 Hz, Ar-H), 7.69 (1H, dt, J = 7.3, 0.8 Hz, Ar-H), 7.62-7.57 (1H, m, Ar-H), 7.58 (1H, s, Ar-H), 7.57-7.49 (2H, m, Ar-H), 7.40 (1H, dd, J = 7.6, 1.2 Hz, Ar-H), 7.32 (1H, td, J = 7.3, 1.3 Hz, Ar-H) ppm; $^{13}C\{^1H\}$ NMR (126 MHz, $CDCl_3$) 193.2, 160.3, 151.6, 150.2, 145.9, 144.3, 144.0, 137.1, 135.1, 134.9, 134.4, 130.5, 129.5, 128.5, 124.9, 124.7, 124.6, 122.3, 121.0, 120.7, 120.4 ppm; AP-MS (positive ion mode): found m/z 325.0978 [M$^+$] $C_{21}H_{13}N_2O_2$; UV-vis ($CHCl_3$-DMSO 99:1) λ_{max} (ε / mol^{-1}dm^{3}cm^{-1}) 430 (725), 343 (12400), 330 (11400 sh), 314 (12120), 301 (10710 sh), 271 (12050), 257 (9420); IR ν_{max} / cm^{-1} 3114, 3061, 2922, 1710, 1648, 1617, 1601, 1587, 1564, 1537, 1480, 1455, 1437, 1368, 1338, 1292, 1244, 1185, 1150, 1135, 1115, 1102, 1084, 1041, 997, 971, 920, 836, 791, 764, 732, 718, 709, 692, 665, 644, 619, 585, 570, 540, 473, 461, 451, 443, 436, 431, 424, 419, 412.

5.4.1.1.6 Synthesis of 2-(pyridin-2-yl)-5-(4-(pyrrolidin-1-yl)phenyl)oxazole (**19**)

As general procedure, using oxazole **7**, with crude product purified *via* column chromatography (9:1 PE:EA) to yield an orange solid (35mg, 26% yield). ^{1}H NMR (400 MHz, $CDCl_3$) δ= 8.74 (1H, ddd, J = 4.8,1.8 Hz, Ar-H) , 8.13 (1H, dt, J = 8.0, 1.0 Hz, Ar-H), 7.80 (1H, td, J= 7.7, 1.7, Ar-H), 7.65 (2H, d, J= 8.9, Ar-H), 7.32 (1H, ddd, J= 7.6, 4.8, 1.1 Hz, Ar-H), 7.30 (1H, s, Ar-H), 6.59 (2H, d, J= 8.9, Ar-H), 3.34 (4H, m, CH_2), 2.03 (4H, m, CH_2) ppm; ^{13}C{^{1}H} NMR (126 MHz, CDCl3): δ= 158.8, 154.0, 150.1, 148.4, 146.7, 136.9, 126.3, 124.1, 121.8, 120.9, 115.0, 111.8, 47.7, 25.7 ppm; ES-MS (positive ion mode): found m/z 292.1450 [M+] C18H18N3O; UV-vis ($CHCl_3$-DMSO 99:1) λ_{max} (ε / mol^{-1}dm^{3}cm^{-1}) 372 (14600), 276 (10670) nm; IR v_{max} / cm^{-1} 3121, 3054, 2960, 2917, 2849, 1645, 1612, 1594, 1569, 1552, 1505, 1485, 1463, 1427, 1385, 1339, 1317, 1298, 1257, 1247, 1228, 1194, 1180, 1156, 1120, 1099, 1082, 1057, 1041, 1025, 1000, 988, 963, 951, 935, 914, 887, 866, 808, 800, 790, 747, 719, 710, 681, 667, 640, 621, 580, 540, 522, 512.

5.4.2 Complex Synthesis

5.4.2.1 Synthesis of $Re(CO)_5Br$

$Re_2(CO)_{10}Br$ (1g, 1.53 mmol) was dissolved in DCM (40 mL), before slow addition of Br_2 (0.5 mL). The solvent was removed *in vacuo*, and the crude solid recrystalised in acetone to yield $Re(CO)_5Br$ as a white solid (520 mg, 84% yield) .

5.4.2.2 General Synthesis of $Re(L)(CO)_3Br$

$Re(CO)_5Br$ (1 eq) and ligand (1.2 eq) were added to toluene and refluxed under N_2 until precipitation occurred. The reaction mixture was cooled to room temperature, filtered and the solid washed with toluene and diethyl ether to yield the desired complex.

5.4.2.2.1 Synthesis of ***fac*-[Re(14)(CO)$_3$Br]**

As general procedure using **14** (10 mg) to yield ***fac*-[Re(14)(CO)$_3$Br**] as a yellow solid (10 mg 55 % yield). ^{1}H NMR (500 MHz, d6-DMSO): δ= 9.55 (1H, d, J= 8.8, Ar-H), 9.12 (1H, ddd, J= 5.4, 1.4, 0.9, Ar-H), 9.00 (1H, d, J= 8.3, Ar-H), 8.96 (1H, s, Ar-H), 8.61 (1H, ddd, J= 7.9, 1.3, 0.8), 8.48-8.41 (2H, m, Ar-H), 8.25 (1H, d, J= 9.1, Ar-H), 8.16-8.11 (1H, m, Ar-H), 8.03 (1H, d, J= 9.1, Ar-H), 7.88 (1H, ddd, J= 7.7, 5.4, 1.4, Ar-H), 7.86-7.77 (2H, m, Ar-H); ES-MS (positive ion mode): found m/z 673.9720 [M$^+$] $C_{24}H_{14}N_3O_4BrRe$; UV-vis ($CHCl_3$-DMSO 99:1) λ_{max} (ε / mol^{-1}dm^{3}cm^{-1}) 426 (2844), 383 (26580), 363 (30230), 350 (29440), 334 (25210), 300 (28230), 283 (35140), 263 (33090) nm; IR ν_{max} / cm^{-1} 3165, 3094, 3072, 3041, 3007, 2037, 1912, 1889, 1600, 1580, 1517, 1486, 1473, 1456, 1439, 1427, 1413, 1402, 1359, 1340, 1320, 1303, 1289, 1252, 1216, 1197, 1167, 1158, 1127, 1091, 1076, 1055, 1031, 1019, 995, 979, 957, 911, 887, 872, 853, 846, 828, 794, 754, 730, 714, 700, 650, 643, 626, 567, 554, 531, 524, 490, 464, 428, 411.

5.4.2.2.2 Synthesis of ***fac*-[Re(15)(CO)$_3$Br]**

As general procedure using **15** (30 mg) to yield ***fac*-[Re(15)(CO)$_3$Br**] as a yellow solid (36 mg, 70% yield). ^{1}H NMR (500 MHz, d6-DMSO): δ= 9.16 (1H, ddd, J = 5.5, 1.3, 0.8, Ar-H), 8.62 (2H, ddd, J = 8.9, 1.1, 0.8 Hz, Ar-H), 8.60 (1H, s, Ar-H), 8.40 (1H, ddd, J= 7.9, 1.4, 0.8 Hz, Ar-H), 8.35 (1H, ap. td, J= 7.7, 1.4 Hz, Ar-H), 8.05 (2H, d, J= 8.8 Hz, Ar-H), 7.89-7.82 (3H, m, Ar-H), 7.78 (2H, ddd, J= 8.8, 6.6, 1.2 Hz, Ar-H) ppm; ^{13}C{^{1}H} NMR (126 MHz, d6-DMSO): δ= 196.6, 195.7, 188.0, 165.8, 154.3, 149.7, 143.4, 140.8, 132.4, 131.7, 131.1, 128.4, 128.2, 127.7, 125.8, 124.7, 124.4, 118.4 ppm; ES-MS (negative ion mode): found m/z 703.9276 [M$^-$] $C_{25}H_{13}N_2O_4ClBrRe$; UV-vis ($CHCl_3$-DMSO 99:1) λ_{max} (ε / mol^{-1}dm^{3}cm^{-1}) 403 (14680), 382 (13600), 363 (8927), 345 (4796), 318 (8013), 300 (12690), 261 (127100) nm; IR ν_{max} / cm^{-1} 2025, 1939, 1918, 1880, 1617, 1575, 1548, 1527, 1519, 1475, 1444, 1406, 1334, 1302, 1261, 1181, 1171, 1155, 1138, 1094, 1053, 1033, 1021, 987, 965, 934, 895, 878, 862, 840, 778, 766, 751, 732, 721, 702, 688, 650, 642, 634, 604, 594, 546, 529, 508, 495, 481, 419.

5.4.2.2.3 Synthesis of ***fac*-[Re(16)(CO)$_3$Br]**

As general procedure using **16** (40 mg) to yield ***fac*-[Re(16)(CO)$_3$Br**] as a yellow solid (32 mg, 47% yield); ^{1}H NMR (500 MHz, d6-DMSO): δ= 9.13 (1H, ddd, J = 5.4, 1.3, 0.8 Hz, Ar-H), 8.82 (1H, s, Ar-H), 8.78 (1H, d, J= 9.3 Hz, Ar-H), 8.63 (1H, d, J= 8.2 Hz, Ar-H), 8.60 (1H, ddd, J= 7.9, 1.2, 0.8 Hz, Ar-H), 8.51-8.41(5H, m, Ar-H), 8.37 (1H, d, J= 8.9, Ar-H), 8.31 (1H, d, J= 8.9, Ar-H), 8.19 (1H, t, J= 7.6, Ar-H), 7.87 (1H, ddd, J= 7.7, 5.5, 1.3 Hz, Ar-H) ppm; ^{13}C{^{1}H} NMR (126 MHz, d6-DMSO): δ= 196.6, 195.7, 188.0, 164.2, 154.3, 154.3, 143.0, 140.8, 132.5, 130.8, 130.2, 129.7, 129.3, 128.9, 127.7, 127.5, 127.3, 127.0, 126.8, 126.7, 126.3, 125.3, 124.4, 124.1, 123.8, 123.5, 119.0 ppm; ES-MS (positive ion mode): found m/z 695.9686 [M$^+$] $C_{27}H_{14}N_2O_4BrRe$; UV-vis (CHCl$_3$-DMSO 99:1) λ_{max} (ε / mol^{-1}dm^{3}cm^{-1}) 407 (18710), 385 (18640), 349 (17100), 323 (14070), 279 (28940) nm; IR v_{max} / cm^{-1} 2023, 1917, 1900, 1622, 1596, 1581, 1562, 1557, 1530, 1502, 1480, 1455, 1433, 1414, 1403, 1377, 1359, 1311, 1299, 1276, 1256, 1246, 1236, 1206, 1179, 1155, 1097, 1080, 1050, 1022, 987, 973, 948, 902, 851, 830, 816, 801, 784, 766, 752, 740, 719, 700, 684, 669, 650, 643, 628, 596, 582, 577, 566, 528, 508, 490, 476, 467, 449, 435, 426, 409.

5.4.2.2.4 Synthesis of ***fac*-[Re(17)(CO)$_3$Br]**

As general procedure using **17** (40 mg) to yield ***fac*-[Re(17)(CO)$_3$Br**] as a yellow solid (26 mg, 37% yield); ^{1}H NMR (500 MHz, d6-DMSO): δ= 9.11 (1H, ddd, J= 5.4, 1.4, 0.9 Hz, Ar-H), 9.03 (1H, ap. d, J= 8.2 Hz, Ar-H), 8.95 (1H, ap. d, J= 8.2 Hz, Ar-H), 8.67 (1H, s, Ar-H), 8.55 (1H, s, Ar-H), 8.53 (1H, ddd, J= 7.9, 1.3, 0.9 Hz, Ar-H), 8.48 (1H, dd, J= 8.0, 1.3 Hz, Ar-H), 8.41 (1H, ap. td, J= 7.8, 1.5 Hz, Ar-H), 8.16 (1H, ap. d, J= 8.0 Hz, Ar-H), 7.89-7.75 (5H, m, Ar-H) ppm; ^{13}C{^{1}H} NMR (126 MHz, d6-DMSO): δ= 196.6, 195.7, 188.0, 164.2, 154.3, 153.8, 143.1, 140.8, 130.6, 130.3, 130.2, 130.2, 129.5, 129.0, 128.9, 128.0, 127.8, 127.8, 127.6, 125.7, 124.3, 123.8, 123.2, 121.1 ppm; ES-MS (positive ion mode): found m/z 692.9553 [M$^+$] $C_{25}H_{14}N_2O_4BrRe$ + Na; UV-vis (CHCl$_3$-DMSO 99:1) λ_{max} (ε / mol^{-1}dm^{3}cm^{-1}) 364 (12770), 301 (17690), 258 (48500) nm; IR v_{max} / cm^{-1} 3100, 3064, 2954, 2915, 2848, 2022, 1918, 1894, 1869, 1620, 1592, 1570, 1557, 1532, 1518, 1493, 1478, 1449, 1413, 1367, 1315, 1300, 1260, 1249, 1240, 1179, 1164, 1152, 1096, 1052, 1037, 1025, 1001, 986, 968, 955, 906, 860, 853, 830, 784, 764, 747, 723, 700, 671, 652, 645, 627, 617, 601, 549, 540, 531, 506, 491, 474, 465, 453, 443, 434, 424, 414.

5.4.2.2.5 Synthesis of ***fac*-[Re(18)(CO)$_3$Br]**

As general procedure using **18** (20 mg) to yield ***fac*-[Re(18)(CO)$_3$Br**] as a yellow solid (17mg, 49% yield). ^{1}H NMR (400 MHz, d6-DMSO): δ= 9.07 (1H, ddd, J= 5.4, 1.3, 0.8 Hz, Ar-H), 8.81 (1H, s, Ar-H), 8.66 (1H, ddd, J= 7.9, 1.2, 0.7 Hz, Ar-H), 8.41 (1H, ap. td, J= 7.9, 1.4 Hz, Ar-H), 8.33-8.27 (2H, m, Ar-H), 8.07 (1H, dd, J= 7.9, 0.5 Hz, Ar-H), 7.95-7.91 (1H, m, Ar-H), 7.84 (1H, ddd, J= 7.8, 5.5, 1.4 Hz, Ar-H), 7.73-7.66 (2H, m, Ar-H), 7.49-7.44 (1H, m, Ar-H) ppm; ES-MS (negative ion mode): found m/z 671.9459 [M$^-$] $C_{24}H_{12}N_2O_5BrRe$; UV-vis ($CHCl_3$-DMSO 99:1) λ_{max} (ε / mol^{-1}dm^{3}cm^{-1}) 432 (5474), 358 (28460), 327 (20030), 273 (41270) nm; IR v_{max} / cm^{-1} 3104, 3069, 3034, 2022, 1920, 1898, 1880, 1863, 1715, 1618, 1603, 1568, 1557, 1537, 1525, 1506, 1480, 1460, 1431, 1407, 1360, 1299, 1262, 1247, 1224, 1190, 1174, 1160, 1117, 1094, 1051, 1018, 1000, 983, 962, 924, 911, 855, 849, 832, 806, 798, 785, 767, 757, 734, 721, 700, 688, 667, 660, 644, 626, 588, 571, 556, 530, 509, 492, 472, 463, 450, 441, 426.

5.4.2.2.6 Synthesis of ***fac*-[Re(19)(CO)$_3$Br]**

As general procedure using **19** (24 mg) to yield ***fac*-[Re(19)(CO)$_3$Br**] as a red solid (9 mg, 19 % yield). ^{1}H NMR (500 MHz, $CDCl_3$): δ= 9.02 (1H, ap. dt, J= 5.4, 1.1 Hz, Ar-H), 8.08-8.04 (2H, m, Ar-H), 7.58 (2H, d, J= 8.9 Hz, Ar-H), 7.54 (1H, s, Ar-H), 7.53-7.49 (1H, m, Ar-H), 6.62 (2H, d, J= 8.9 Hz, Ar-H), 3.38 (4H, m, CH_2), 2.07 (4H, m, CH_2) ppm; ^{13}C{^{1}H} NMR (126 MHz, d6-DMSO): δ= 196.6, 195.9, 187.9, 161.6, 156.0, 154.0, 148.8, 143.0, 140.6, 127.9, 126.4, 123.3, 121.1, 111.9, 111.4, 47.3, 25.0 ppm; ES-MS (negative ion mode): found m/z 638.9915.9276 [M$^-$] $C_{21}H_{17}N_3O_4BrRe$; UV-vis ($CHCl_3$-DMSO 99:1) λ_{max} (ε / mol^{-1}dm^{3}cm^{-1}) 448 (9542), 301 (14880) nm; IR v_{max} / cm^{-1} 2114, 2017, 1999, 1964, 1914, 1604, 1502, 1480, 1392, 1195, 1160, 810, 790, 749, 724, 697, 681, 665, 646, 629, 594, 576, 535, 516, 500, 480, 462, 444, 427, 415.

5.5 References

1. R. Wang, D. Liu, H. Ren, T. Zhang, H. Yin, G. Liu and J. Li, *Adv. Mater.*, 2011, **23**, 2823–2827.
2. H. Benjamin, J. Liang, Y. Liu, Y. Geng, X. Liu, D. Zhu, A. S. Batsanov and M. R. Bryce, *Organometallics*, 2017, **36**, 1810–1821.
3. S. Lamansky, P. Djurovich, D. Murphy, F. Abdel-Razzaq, H.-E. Lee, C. Adachi, P. E. Burrows, S. R. Forrest and M. E. Thompson, *J. Am. Chem. Soc.*, 2001, **123**, 4304–4312.
4. Y. You, J. Seo, S. H. Kim, K. S. Kim, T. K. Ahn, D. Kim and S. Y. Park, *Inorg. Chem.*, 2008, **47**, 1476–1487.
5. M. Poyatos, A. Maisse-François, S. Bellemin-Laponnaz and L. H. Gade, *Organometallics*, 2006, **25**, 2634–2641.
6. Z. Wu, Z. Zhang, L. Ding, M. Xiang and S. Luo, *Tetrahedron Lett.*, 2020, **61**, 152577.
7. M. Wrighton and D. L. Morse, *J. Am. Chem. Soc.*, 1974, **96**, 998–1003.
8. A. Vlček, in *Photophysics of Organometallics*, ed. A. J. Lees, Springer, Berlin, Heidelberg, 2010, pp. 115–158.
9. S. P. Schmidt, W. C. Trogler, F. Basolo, M. A. Urbancic and J. R. Shapley, in *Inorganic Syntheses*, John Wiley & Sons, Ltd, USA, 1990, pp. 160–165.
10. R. O. Bonello, I. R. Morgan, B. R. Yeo, L. E. J. Jones, B. M. Kariuki, I. A. Fallis and S. J. A. Pope, *J. Organomet. Chem.*, 2014, **749**, 150–156.
11. A. Świtlicka, K. Choroba, A. Szlapa-Kula, B. Machura and K. Erfurt, *Polyhedron*, 2019, **171**, 551–558.
12. A. Albertino, C. Garino, S. Ghiani, R. Gobetto, C. Nervi, L. Salassa, E. Rosenberg, A. Sharmin, G. Viscardi, R. Buscaino, G. Croce and M. Milanesio, *J. Organomet. Chem.*, 2007, **692**, 1377–1391.
13. L. C.-C. Lee, K.-K. Leung and K. K.-W. Lo, *Dalton Trans.*, 2017, **46**, 16357–16380.
14. A. J. Amoroso, M. P. Coogan, J. E. Dunne, V. Fernández-Moreira, J. B. Hess, A. J. Hayes, D. Lloyd, C. Millet, S. J. A. Pope and C. Williams, *Chem. Commun.*, 2007, 3066–3068.
15. S. Clède, F. Lambert, C. Sandt, Z. Gueroui, M. Réfrégiers, M.-A. Plamont, P. Dumas, A. Vessières and C. Policar, *Chem. Commun.*, 2012, **48**, 7729–7731.

16. I. Chakraborty, S. J. Carrington, J. Hauser, S. R. J. Oliver and P. K. Mascharak, *Chem. Mater.*, 2015, **27**, 8387–8397.
17. A. J. Amoroso, R. J. Arthur, M. P. Coogan, J. B. Court, V. Fernández-Moreira, A. J. Hayes, D. Lloyd, C. Millet and S. J. A. Pope, *New J. Chem.*, 2008, **32**, 1097–1102.
18. H. C. Bertrand, S. Clède, R. Guillot, F. Lambert and C. Policar, *Inorg. Chem.*, 2014, **53**, 6204–6223.
19. J. Schneider, H. Jia, J. T. Muckerman and E. Fujita, *Chem. Soc. Rev.*, 2012, **41**, 2036–2051.
20. J. Hawecker, J.-M. Lehn and R. Ziessel, *J. Chem. Soc. Chem. Commun.*, 1984, 328–330.
21. J. Hawecker, J.-M. Lehn and R. Ziessel, *J. Chem. Soc. Chem. Commun.*, 1983, 536–538.
22. J. M. Smieja and C. P. Kubiak, *Inorg. Chem.*, 2010, **49**, 9283–9289.
23. H. Y. V. Ching, X. Wang, M. He, N. Perujo Holland, R. Guillot, C. Slim, S. Griveau, H. C. Bertrand, C. Policar, F. Bedioui and M. Fontecave, *Inorg. Chem.*, 2017, **56**, 2966–2976.
24. Y. Chi and P.-T. Chou, *Chem. Soc. Rev.*, 2010, **39**, 638–655.
25. Y.-X. Hu, G.-W. Zhao, Y. Dong, Y.-L. Lü, X. Li and D.-Y. Zhang, *Dyes Pigments*, 2017, **137**, 569–575.
26. C. Liu, J. Li, B. Li, Z. Hong, F. Zhao, S. Liu and W. Li, *Appl. Phys. Lett.*, 2006, **89**, 243511.
27. R. Czerwieniec, A. Kapturkiewicz, J. Lipkowski and J. Nowacki, *Inorganica Chim. Acta*, 2005, **358**, 2701–2710.
28. J. K. Nganga, C. R. Samanamu, J. M. Tanski, C. Pacheco, C. Saucedo, V. S. Batista, K. A. Grice, M. Z. Ertem and A. M. Angeles-Boza, *Inorg. Chem.*, 2017, **56**, 3214–3226.
29. T. Yoshizumi, T. Satoh, K. Hirano, D. Matsuo, A. Orita, J. Otera and M. Miura, *Tetrahedron Lett.*, 2009, **50**, 3273–3276.
30. I. J. Turchi and M. J. S. Dewar, *Chem. Rev.*, 1975, **75**, 389–437.
31. S. J. Ananthakrishnan, E. Varathan, E. Ravindran, N. Somanathan, V. Subramanian, A. B. Mandal, J. D. Sudha and R. Ramakrishnan, *Chem. Commun.*, 2013, **49**, 10742–10744.
32. G.-J. Zhao and K.-L. Han, *J. Phys. Chem. A*, 2007, **111**, 9218–9223.
33. I. Ghosh, A. Mukhopadhyay, A. L. Koner, S. Samanta, W. M. Nau and J. N. Moorthy, *Phys. Chem. Chem. Phys.*, 2014, **16**, 16436–16445.
34. F. M. Winnik, *Chem. Rev.*, 1993, **93**, 587–614.

35. K. Kalyanasundaram, *J. Chem. Soc. Faraday Trans. 2 Mol. Chem. Phys.*, 1986, **82**, 2401–2415.
36. N. M. Shavaleev, Z. R. Bell, T. L. Easun, R. Rutkaite, L. Swanson and M. D. Ward, *Dalton Trans.*, 2004, 3678–3688.
37. K. S. Schanze, D. Brent MacQueen, T. A. Perkins and L. A. Cabana, *Coord. Chem. Rev.*, 1993, **122**, 63–89.
38. C. Adamo and V. Barone, *J. Chem. Phys.*, 1999, **110**, 6158–6170.
39. M. Ernzerhof and G. E. Scuseria, *J. Chem. Phys.*, 1999, **110**, 5029–5036.
40. F. Weigend and R. Ahlrichs, *Phys. Chem. Chem. Phys.*, 2005, **7**, 3297–3305.
41. F. Xu, H. Wang, X. Du, W. Wang, D.-E. Wang, S. Chen, X. Han, N. Li, M.-S. Yuan and J. Wang, *Dyes Pigments*, 2016, **129**, 121–128.

6 Encapsulation of Lanthanide complexes Within Core-Shell Nanostructures

6.1 Overview

In **Chapter 3** it was demonstrated that the photophysical properties of a fluorophore are affected upon encapsulation into the core-shell particle. To further investigate the environment and hence role of the internal particle matrix on the photophysics of the fluorophore, dopants with photophysical properties known to be sensitive to the immediate environment are required to gain greater insight into these observations. In the following chapter a range of known lanthanide complexes have been encapsulated to investigate the core environment and the encapsulated solvent.

A further advantage to investigating the encapsulation of lanthanide complexes is that there is little literature surrounding the topic, with the exception of those based upon europium. Even in examples given in the following section, the photophysical measurements are rarely discussed in detail, and thus as far as the author is aware, the encapsulation and subsequent analysis of particle morphology and photophysics for a range of lanthanide complexes is presented for the first time.

6.2 Lanthanide Luminescence

The lanthanides, known as “rare earth elements” and located in the f-block of the periodic table, make up some of the most interesting elements in the periodic table due to their incredibly shielded valance elections, located in the 4f orbitals. This shielding of the 4f electrons by the $5s^2 5p^6$ subshells impacts the reactivity, oxidation number, geometry, bonding and more importantly the spectroscopic characteristics. Unlike the transition metals which show varied reactivity across the row, the reactivity of the ions from lanthanum to lutetium remains remarkably similar.[1] The prime oxidation state of each ion is +3 as the first three ionisation enthalpies are low in comparison with the fourth, leading to highly electropositive ions that form readily in complexes, aqueous solution and solid oxides.[1] **Table 6.1** shows the electronic configurations and term symbols for the lanthanide series.

Table 6.1 Electronic configurations of both the atom and Ln^{3+} ion, and term symbols of ground and excited States.

Name	**Electronic Configuration**		**Ground State Term Symbol**
	Atom	M^{3+}	
Lanthanum	$[Xe]5d6s^2$	$[Xe]$	$^1S_0$
Cerium	$[Xe]4f^15d^16s^2$	$[Xe]4f^1$	$^2F_{5/2}$
Praseodymium	$[Xe]4f^36s^2$	$[Xe]4f^2$	$^3H_4$
Neodymium	$[Xe]4f^46s^2$	$[Xe]4f^3$	$^4I_{9/2}$
Promethium	$[Xe]4f^56s^2$	$[Xe]4f^4$	$^5I_4$
Samarium	$[Xe]4f^66s^2$	$[Xe]4f^5$	$^6H_{5/2}$
Europium	$[Xe]4f^76s^2$	$[Xe]4f^6$	$^7F_0$
Gadolinium	$[Xe]4f^75d6s^2$	$[Xe]4f^7$	$^8S_{7/2}$
Terbium	$[Xe]4f^96s^2$	$[Xe]4f^8$	$^7F_6$
Dysprosium	$[Xe]4f^{10}6s^2$	$[Xe]4f^9$	$^6H_{15/2}$
Holmium	$[Xe]4f^{11}6s^2$	$[Xe]4f^{10}$	$^5I_8$
Erbium	$[Xe]4f^{12}6s^2$	$[Xe]4f^{11}$	$^4I_{15/2}$
Thulium	$[Xe]4f^{13}6s^2$	$[Xe]4f^{12}$	$^3H_6$
Ytterbium	$[Xe]4f^{14}6s^2$	$[Xe]4f^{13}$	$^2F_{7/2}$
Lutetium	$[Xe]4f^{14}5d6s^2$	$[Xe]4f^{14}$	$^1S_0$

Another characteristic arising from the shielding of the 4f electrons is that the chemical environment does not affect the electrons, and therefore crystal field effects that normally dominate transition metal chemistry are much smaller when compared to spin-orbit coupling (2000 *vs* 100 cm^{-1}).[2] Therefore, coordination number and the resultant geometry in complexes is not controlled by the crystal field and instead by steric effects, which due to their large ionic radii leads to complexes with high coordination numbers. This also leads to small splittings of the degenerate states (approx 100 cm^{-1}), as shown in **Figure 6.1**, and thus lanthanides are characterised by their sharp absorption bands for f-f transitions, unlike d-d transitions.[2]

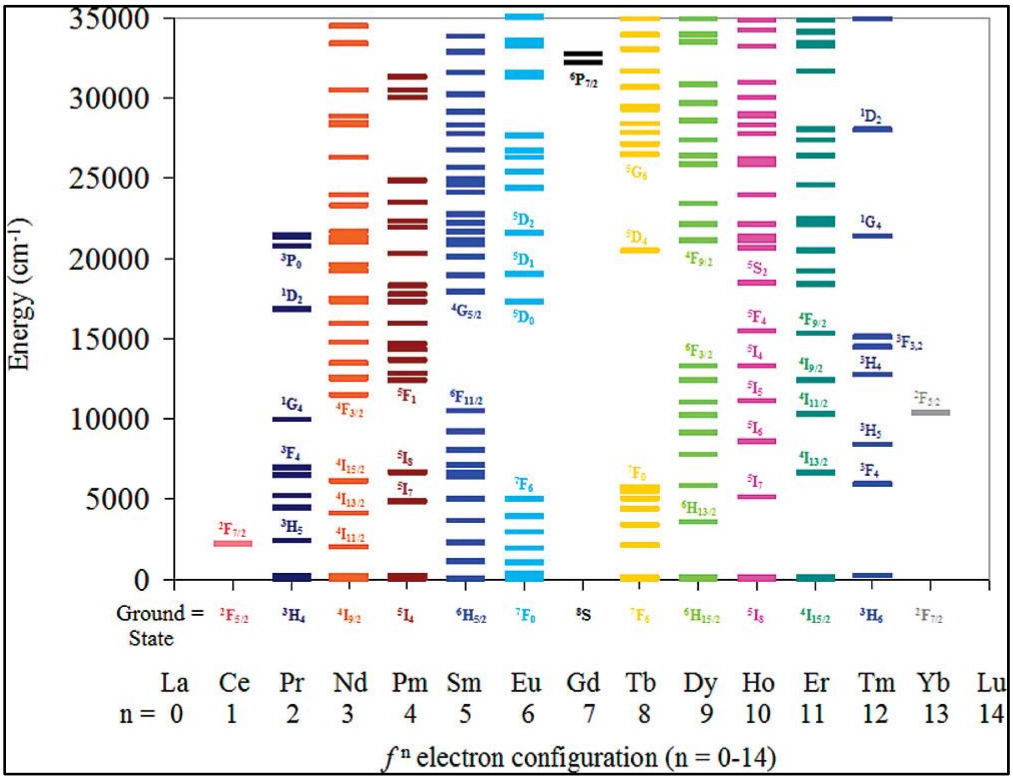

Figure 6.1 Energy level diagrams for lanthanide ions in aqueous environment, where the blue line represents the ground state, and the red line represents the main excited states. Taken from E. G. Moore *et al*[3]

Similar to d-d transitions in transition metal complexes, f-f transitions in lanthanide complexes are parity forbidden.[2] The crystal field is far more dominant in transition metal complexes and leads to a distortion of symmetry of the metal ion causing a relaxation of the rule. However lanthanide complexes, which have a far smaller crystal field contribution due to the 4f electrons being shielded, and thus cannot undertake this distortion and therefore the colours are less intense.[2] Despite being less intense, they tend to have long emission lifetimes[4] (as f-f transitions are parity forbidden) which is advantageous for a variety of biological applications[5,6].

Although the low contribution from the crystal field renders lanthanide absorption bands independent of environment, there are some transitions that show a dependence on the ligands and environment which they are in. Although electric dipole transitions are formally forbidden, due to the parity of the f-f transition not changing, electronic states of opposite parity can mix into the 4f wavefunctions as a result of non-centrosymmetric interactions, which relaxes the parity rule and the transition can therefore take place as “induced” electric dipole transitions.[4] These “hypersensitive” bands are sensitive to changes in the metal-ion environment and follow the electric quadrupole rules. Magnetic dipole transitions still occur as expected as these, like electric quadrupole transitions, are parity allowed.[7]

Emission from lanthanide ions can also occur from transitions other than those originating from the 4f orbitals, including Ligand to Metal Charge Transfer (LMCT, discussed in detail in **Chapters 1** and **5**), 4f-5d transitions and energy transfer *via* sensitisation of the antenna ligands.[7]

4f-5d transitions, as the name suggests, are transitions in which a 4f electron is transferred to a 5d subshell. These transitions are intense as they are parity allowed, however with the exception of Ce^{3+}, Pr^{3+} and Tb^{3+}, are rarely observed due to their high energies of more than > 50000 cm^{-1}.[8]

6.2.1 Sensitisation

The sensitisation of lanthanide emission bought about by the coordinated ligand was first demonstrated by S. Weissman in 1942.[9] He demonstrated that the characteristic Eu^{3+} emission bands could be observed by exciting the coordinated ligand in a variety of different complexes and conditions, with brighter emission observed due to the transition being parity allowed.

As shown by the simplified Jablonski diagram in **Figure 6.2**, sensitisation occurs *via* a series of energy transfer steps. The singlet state of the ligand is excited, and due to the close proximity of the lanthanide ion, spin-orbit coupling occurs which allows intersystem crossing (ISC) to the lower lying triplet state. This triplet state, which lies slightly above the excited level of the lanthanide ion, then transfers this energy to excite the 4f states of the lanthanide ion, leading to emission. The most efficient sensitisation occurs when the singlet and triplet state of the ligand are separated by approximately 5000 cm^{-1}, as this results in the most efficient ISC,[7] and the triplet state is between 2500-3500 cm^{-1} higher in energy than the accepting lanthanide state.[7] The latter prevents back-transfer of energy, which would lead to a reduction of quantum yield.

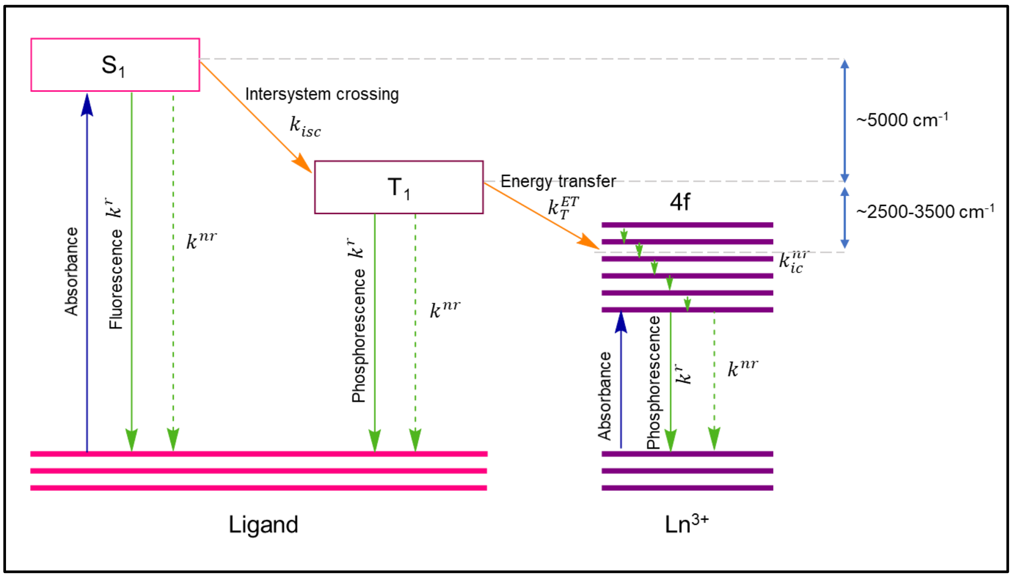

Figure 6.2 Simplified Jablonski diagram showing the various transitions occurring within a lanthanide complex, and the sensitisation pathway. k^{nr} = non-radiative decay rate, k^r = radiative decay rate, isc = intersystem crossing, ET = energy transfer, ic = internal conversion. Adapted from S. Eliseeva *et al.*[7]

6.2.2 Quantum Yield and the Judd-Ofelt Parameters

Also shown in **Figure 6.2** are the various non-radiative deactivation pathways present, which need to be minimised to lead to high quantum yields. The overall quantum yield is given by **Equation 6.1**, whereby it can be seen to be directly related to the quantum yield arising from direct excitation (also known as the intrinsic quantum yield), and the sensitisation efficiency.[10] The sensitisation efficiency is made up of the energy transfer efficiency to the Ln(III) ion, and the efficiency of the population of the "feeding level" (e.g. T_1 in **Figure 6.2**) by the initially excited state (S_1).[11]

$$Q_{Ln}^{L} = \eta_{pop}^{D}\eta_{et}Q_{Ln}^{Ln} = \eta_{sens}Q_{Ln}^{Ln}$$

$$where\ Q_{Ln}^{L} = overall\ quantum\ yield, Q_{Ln}^{Ln} = intrinsic\ quantum\ yield,$$

$$\eta_{pop}^{D} = population\ efficiency,\ \eta_{et} = energy\ transfer\ efficiency$$

$$\eta_{sens} = sensitisation\ efficiency$$

Equation 6.1 Calculation to determine the quantum yield.[11]

The energy gap between the lowest level excited state and the ground state of the lanthanide is directly related to the intrinsic quantum yield. If the gap is small, non-radiative deactivation can dominate, such as *via* vibrational quenching from high energy O-H, N-H or C-H vibrational overtones of coordinated ligands, and thus cause a decrease in quantum yield.[4] In fact, one of the main non-radiative deactivation routes shown in **Equation 6.2** is that caused by vibrational processes (k^{vibr})[10] . **Equation 6.2** also shows the difficulty in determining the true radiative decay rate, k^r, and hence radiative lifetime, due to the number of different non-radiative deactivation pathways that occur in the deactivation of the lanthanide complex ($k^{'nr}$ represents the other deactivation routes).

$$\frac{1}{\tau_{obs}} = k_{obs} = k^r + \sum_n k_n^{nr} = k^r + \sum_i k_i^{vibr}(T) + \sum_i k_i^{pet}(T) + \sum_k k_k^{\prime nr}$$

Equation 6.2 Sum of the multiple deactivation routes involved in an electronic transition.[10]

To calculate the intrinsic quantum yield, both the observed and radiative lifetimes (or rate constants) are required, as shown in **Equation 6.3**.

$$Q_{Ln}^{Ln} = \frac{\tau_{obs}}{\tau_{rad}} = \frac{k^r}{k_{obs}}$$

Equation 6.3 Calculation to determine the intrinsic quantum yield[4]

In the case of lanthanide ions, the absorption spectrum can be used to calculate the radiative lifetime using **Equation 6.4**:

$$\frac{1}{\tau^{rad}} = 2303 \times \frac{8\pi c n^2 \tilde{v}^2 (2J' + 1)}{N_A (2J + 1)} \int \varepsilon(\,v)\, d\tilde{v}$$

$$where\ J = quantum\ number\ for\ initial\ state$$

$$J' = quantum\ number\ for\ final\ state$$

$$c = speed\ of\ light\ in\ vacuo\ (cm\ s^{-1}), \tilde{v} = frequency\ of\ the\ transition\ (cm^{-1}),$$

$$n = refractive\ index,\ N_A = avogadro's\ constant,$$

$$\varepsilon(v) = molar\ extinction\ coefficient\ (mol^{-1} dm^3 cm^{-1})$$

Equation 6.4 Strickler-Berg equation to determine the radiative lifetime from the absorption spectrum.[12,13]

Alternatively, for Eu^{3+} complexes a more straight-forward method is achieved owing to the $^5D_0 \rightarrow {}^7F_1$ transition, which can act as a "constant" due to it's magnetic, and hence environmentally independent, nature. **Equation 6.5** gives the reciprocal of the radiative lifetime as a function of the ratio of the intensity of the total emission spectrum (I_{tot}) to the intensity of the $^5D_0 \rightarrow {}^7F_1$ transition (I_{MD}), with the Einstein coefficient $A_{MD,0}$ equal to 14.65 s^{-1}. The Einstein coefficient is defined as the spontaneous emission probability of the transition in a vacuum.

$$\frac{1}{\tau^{rad}} = A_{MD,0} \times n_0^3 (\frac{I_{tot}}{I_{MD}})$$

$$where\ n_0 = refractive\ index\ of\ the\ solution,$$

$$A_{MD,0} = \ Einstein\ coefficient\ for\ the\ \ {}^5D_0 \rightarrow \ {}^7F_1\ transition,$$

$$I_{tot} = \ intensity\ of\ entire\ spectra,\ I_{MD} = intensity\ of\ the\ \ {}^5D_0 \rightarrow \ {}^7F_1\ transition$$

Equation 6.5 Calculation to determine the radiative lifetime using the Eu^{3+} emission spectrum.[12]

The intrinsic quantum yield is frequently referred to as the emissive quantum efficiency, η, which in Judd-Ofelt theory is related to the radiative and non-radiative decay using A_{rad}, k_{nrad} and A_{tot} to define the radiative, non-radiative, and total decay rates, respectively.

$$\eta = \frac{\tau_{obs}}{\tau_{rad}} = \frac{A_{rad}}{A_{tot}} = \frac{A_{rad}}{A_{rad} + \ k_{nrad}}$$

Equation 6.6 Calculation to determine the Emissive Quantum Efficiency, or Intrinsic Quantum Yield.[14]

A_{tot} can be calculated, as **Equation 6.6** represents, from the inverse of the observed lifetime, and A_{rad} can be calculated either by using **Equation 6.6** or from the sum of the coefficients of spontaneous emission ($A_{0 \rightarrow J}$), which is given by the following:

$$A_{0 \rightarrow J} = \left(\frac{\sigma_{0 \rightarrow J}}{S_{0 \rightarrow 1}}\right)\left(\frac{S_{0 \rightarrow J}}{\sigma_{0 \rightarrow 1}}\right) A_{0 \rightarrow 1}$$

Equation 6.7 Calculation to determine the sum of the coefficients of spontaneous emission[14]

With σ and S corresponding to the energy barycentre of the transition and the area under the curve in the spectrum respectively. $A_{0\rightarrow1}$ represents the coefficient of spontaneous emission for the $^5D_0 \rightarrow {}^7F_1$ transition, equal to 50 s^{-1}.[15]

The emissive quantum efficiency can also be used to calculate the efficiency of energy transfer, η_{ET}, given in **Equation 6.8**, if the total quantum yield is known. The triplet quantum yield of the ligand (Q_T) can be assumed to be one due to lanthanides ions possessing high spin-orbit coupling.[16]

$$Q_{Ln}^{L} = \ Q_T \, \eta_{ET}\eta$$

$$where \ Q_{Ln}^{L} = overall \ quantum \ yield,$$

$$Q_T \ = triplet \ formation \ quantum \ yield,$$

$$\eta_{ET} = energy \ transfer \ efficiency, \eta = emissive \ quantum \ efficiency$$

Equation 6.8 Relationship between the total quantum yield, triplet formation quantum yield, emissive quantum efficiency and energy transfer efficiency. Adapted from A. Beeby *et al.*[16]

Not only can the coefficients of spontaneous emission be used in the calculation of the decay rates and efficiency, but also in the calculation of the experimental Judd-Ofelt intensity parameters, Ω_J:

$$A_{0\rightarrow J} = \frac{4e^2\omega^3}{3\hbar c^3}\frac{1}{2J+1}\chi \sum_{\lambda=2,4,6} \Omega_\lambda \langle\, {}^5D_0 \| U^{(\lambda)} \| \, {}^7F_J \rangle^2$$

Equation 6.9 Calculation to determine the Judd-Ofelt Intensity Parameters.[17]

The $\langle\, {}^5D_0 \| U^{(\lambda)} \| \, {}^7F_J \rangle^2$ matrix has known values of 0.0032 and 0.0023 for J = 2 and 4 respectively.[17] The Lorentz local field correction, χ, is calculated from the refractive index, n_0 of the sample:

$$\chi = \frac{n_0({n_0}^2 + 2)^2}{9}$$

Equation 6.10 Calculation to determine the Lorentz local field correction.[17]

The Judd-Ofelt intensity parameters can be used to give insight into how the chemical environment affects the europium complex and its hypersensitive transitions. When combined with analysis of the composition of the transition bands, they can also lend insight into the symmetry of the complex.

6.2.3 Solvation Number, q, of the Lanthanide Complex

As mentioned previously, one of the main non-radiative deactivation pathways is that of vibrational quenching from high energy O-H vibrational overtones of coordinated ligands, such as coordinated water[4,10]Although this causes a decrease in quantum yield and thus is something to be avoided in the design of novel complexes, it can also be used in sensing applications to investigate both the local environment and if there are coordinated water ligands present.[4] To calculate the number of water molecules in the local coordination sphere of the lanthanide ion, q, both the lifetimes measured in water and D_2O are required (**Equation 6.11**), as it is assumed that O-D vibrations are negligible and that the remaining deactivation paths are not affected by the change in solvent.[4]

$$q = A \times \left(\left(\frac{1}{\tau_{H_2O}} - \frac{1}{\tau_{D_2O}} \right) - B \right) - C$$

Equation 6.11 General calculation to determine the solvation number of a lanthanide complex,[4] with the exception of Nd^{3+}.

Correction parameters, A, B and C, are also used with values dependent on lanthanide ion being studied. Correction parameter A accounts for the inner sphere contribution, B for other vibrations present (*i.e.* as a result of coordinated ligands with N-H or C-H bonds) and C for the outer sphere contribution.[4] In the case of Nd^{3+}, a separate equation is required (**Equation 6.12**), however solvation values calculated for Nd^{3+} should be taken with caution, as they are known to be unreliable.[7]

$$q = 130 \left(\frac{1}{\tau_{H_2O}} - \frac{1}{\tau_{D_2O}} \right) - 0.4 \; in \; ns$$

Equation 6.12 Calculation to determine the solvation number of a neodymium complex.[18]

6.3 Nanoparticles incorporating lanthanide complexes

Current literature surrounding the encapsulation of lanthanide complexes into nanoparticle constructs is predominantly based upon europium and terbium complexes, with very rare examples of the use of ytterbium and gadolinium. To the best of the author's knowledge, no such literature exists on the encapsulation of neodymium and erbium complexes. That is not to say that there is no literature surrounding the use of these latter ions in particles, however they are not encapsulated as complexes, and instead oxides or more complex crystalline structures and thus not within the scope of this work.

Therefore, the following review focusses on the use of europium complexes, both encapsulated within silica and polymer matrixes, and is followed by an example of gadolinium and ytterbium complexes. Examples of terbium encapsulation are not noted since they are not relevant to the work described herein.

6.3.1 Europium Doped Silica Based Particles

As discussed in **Chapters 3** and **4**, silica-based particles have multiple advantages, most notably stability, non-toxicity, and ability to be functionalised. These factors all play a role when designing an imaging agent; stability ensures that the heavy metal does not enter the body, the fact that the particles are non-toxic reduces the side-effects commonly experienced with, for example, MRI contrast agents, and functionalisation of the surface allows a specialist approach to the area of interest.

One of the first examples of not just the synthesis, but also the application of lanthanide-encapsulated particles in bioassays is that of Z. Ye *et al*,[19] who used a water-in-oil microemulsion to synthesise silica particles encapsulating a BHHT-Eu^{3+} chelate (BHHT = 4,4'-bis(1",1",1",2",2",3",3"-heptafluoro-4",6"-hexanedion-6"-yl)-*o*-terphenyl, shown in **Figure 6.3a**). By changing the co-surfactants the size of the particles could be varied, with a smaller particle formed when the carbon chain of the surfactant was increased (**Figure 6.3c**). As one of the main components of the synthesis is the aqueous phase, by using D_2O instead of water a longer fluorescence lifetime of the Eu^{3+}-chelate was achieved due to less water molecules within the coordination sphere of the complex. Both the emission and excitation spectra of the particles were similar to that of the pure complex, showing minimal interaction between the particle core and the complex (**Figure 6.3b**). Photostability was improved upon encapsulation, with particles formed using n-octanol photobleaching to 70% of the initial signal, compared to 50% for the pure complex. This is rationalised by a decrease in photodecomposition once the complex is encapsulated, as it is then protected from free radicals formed from solvent molecules.

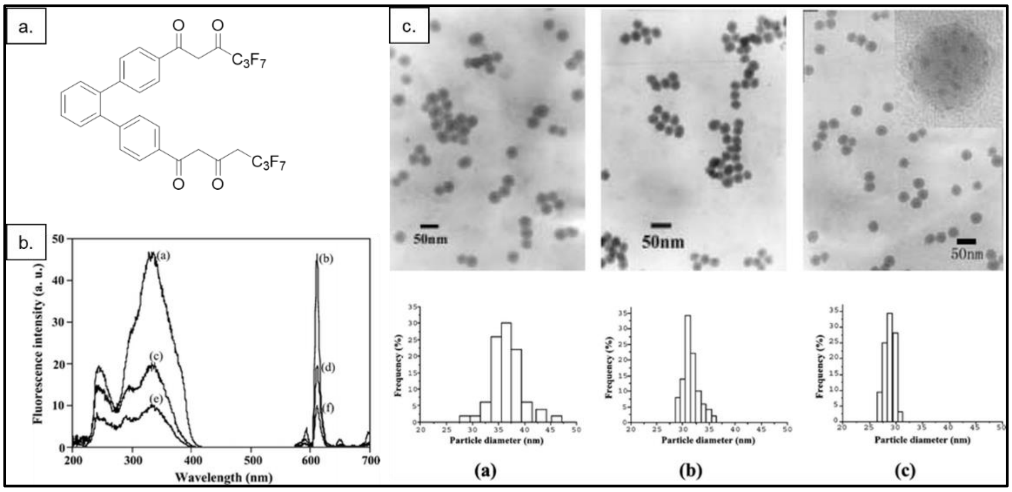

Figure 6.3 a) BHHT ligand; b) Emission spectrum of free complex (a, b), and particles using n-octanol and n-hexanol in D_2O as surfactant (c,d and e,f respectively) in 0.05 M Tris-HCl buffer (pH 7.8) with Triton X-100 (0.05%); c) TEM images and particle size distribution of particles using n-hexanol, n-heptanol and n-octanol in D_2O (a, b and c respectively). Taken from Z. Ye *et al*.[19]

The particles were functionalised with streptavidin in a multi-step process. Firstly, the surface was functionalised with APTES, yielding surface primary amine groups that could then react with 2,4,6-trichloro-1,3,5-triazine, giving reactive chloride groups which could then react with streptavidin (SA) amino groups to form the functionalised particles. By carrying out an immunoassay to quantitatively analyse a human hepatitis B surface antigen, results showed that the SA-functionalised particles encapsulated with HBBT-Eu^{3+} were suitable for the use as probes in fluorescence bioassays.

An example of the use of a core-shell construct of the encapsulation of lanthanide complexes is shown in work by H. Härmä *et al*,[20] using Eu:NTA:TOPO as the core (NTA = naphtoyltrifluoroacetone, TOPO = trioctylphosphine oxide, **Figure 6.4a**) with a polyvinylpyrrolidine inner shell and silica as the outer shell (**Figure 6.4b**). NTA was chosen as the antenna ligand, whereas TOPO minimised water in the inner coordination sphere, thus reducing non-radiative deactivation *via* water. TEM images of the particles, shown in **Figure 6.4c**, clearly showed the core-shell structure with different contrast showing the agglomerated complex *vs* polyvinylpyrrolidone in the core, which was found to be ~ 71 nm in diameter, with an 11 nm silica shell.

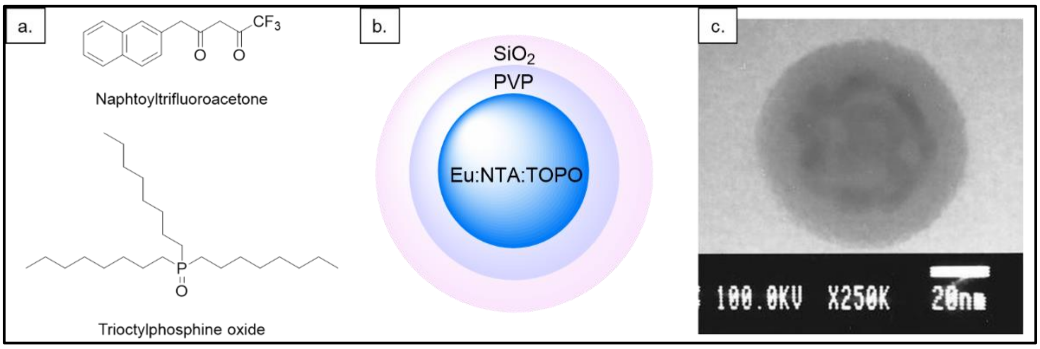

Figure 6.4 a) Chemical structures of naphtoyltrifluoroacetone (NTA) and trioctylphosphine oxide (TOPO); b) Schematic of core-shell particle; c) TEM image of core-shell particle. Adapted and taken from H. Härma *et al.*[20]

Both the complex and the particles gave similar emission and excitation spectra, with the exception of the latter having excitation contributions below 300 nm. The observation of contributions to the excitation spectrum below 300 nm could not be explained by the author. However, *via* comparison with previous work within this thesis, it may be the interaction between polyvinylpyrrolidine and the agglomerated complex, similar to that observed between polystyrene and the dopant in the particles synthesised within this work, which lead to a band at 268 nm in the excitation spectra. The emission lifetime of the complex in the particle was less than that of the complex in DMSO, however this was attributed to the possible presence of water in the core due to the synthesis conditions, much like that observed in work by Z. Ye *et al*[19].

Although most encapsulation procedures concern the use of doping into the “core” of the particle, an interesting example involving the doping of the lanthanide complex into the shell of the particle is provided by J. Yang *et al*.[21] In their work, a commercially available amino-polystyrene bead was used as the core template, in which the silica shell was added *via* a sol-gel reaction with TMOS (tetramethyl orthosilicate) and $Eu(NO_3)_3$ as dopant. The positively charged amine groups on the surface of the polystyrene beads promoted silica shell formation *via* electrostatic interactions with the negative TMOS, and ethanol was used as solvent to slow the silica shell formation, allowing time for $Eu(NO_3)_3$ to be encapsulated. The core-shell particles were then calcinated to remove the polystyrene core, leaving the solid shell and an empty core, shown in **Figure 6.5**. The empty core has future advantages in drug encapsulation, and the silica shell can be easily functionalised. They found that high doping of Eu^{3+} gave particles which were irregular in size, and thus the 8-10 nm shell was doped with < 3 % (mole fraction). The work focussed on the synthesis and the particles' ability to perform in bioimaging applications, however gave little information on the luminescence properties of the material. The emission data shown and discussed demonstrated that the dominant emissive band was that at 615 nm, assigned to the $^5D_0 \rightarrow ^7F_2$ transition, with unfortunately no emissive lifetime recorded or extensive discussion.

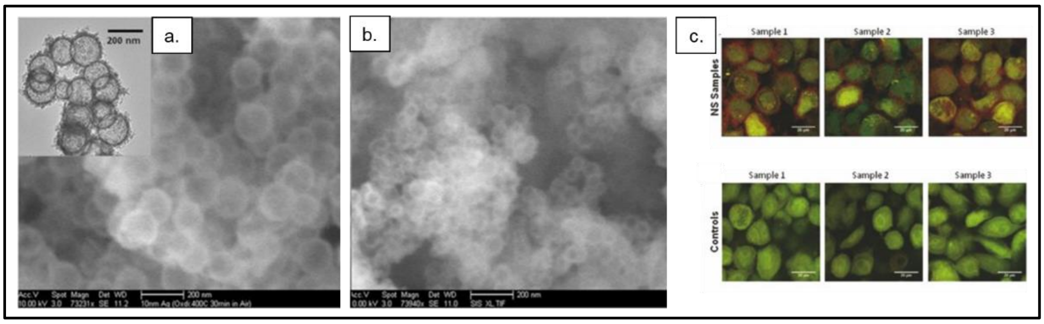

Figure 6.5 a) SEM image (*inset* TEM) of nanoshells using 200 nm template; b) SEM image using 100 nm template; c) Imaging of nanoshell adhesion to HeLa cells (*top*) *vs* control (*bottom*). Taken from J. Yang *et al.*[21]

Despite lack of photophysical discussion, the bioimaging capabilities of the particles were studied in detail and showed great promise. The particles' surface was functionalised with poly(ethylenimine) which prevented aggregation of particles by introducing a positive charge, and helped the particles to bind to and penetrate cells. The particles showed strong luminescence on the outside of the HeLa cells (**Figure 6.5c**), however as they did not possess appropriate functionalised groups on the surface, did not show a strong signal when internalised. That being said, with the appropriate receptors on the surface, and impregnation of drug molecules into the empty core, the possibility of a dual-functioning bioimaging particle could be imagined using this approach.

Although the previous two examples gave rather novel approaches to the encapsulation of lanthanide complexes, simple methods can still be used for biologically relevant particles, which is shown by A. Lourenço *et al.*[22] In their work, $Eu(TTA)_3(H_2O)_2$ (TTA = thenoyltrifluoroacetone), a well-studied complex also used in the work herein, was encapsulated within a silica nanoparticle during the particles synthesis using TEOS *via* the Stöber method. The particle surface was then further functionalised with APTES, to allow introduction of a "spacer" group containing reactive aldehyde groups which were then able to bind anti-oxLDL antibodies *via* imine bond formation (the full scheme is shown in **Figure 6.6a**).

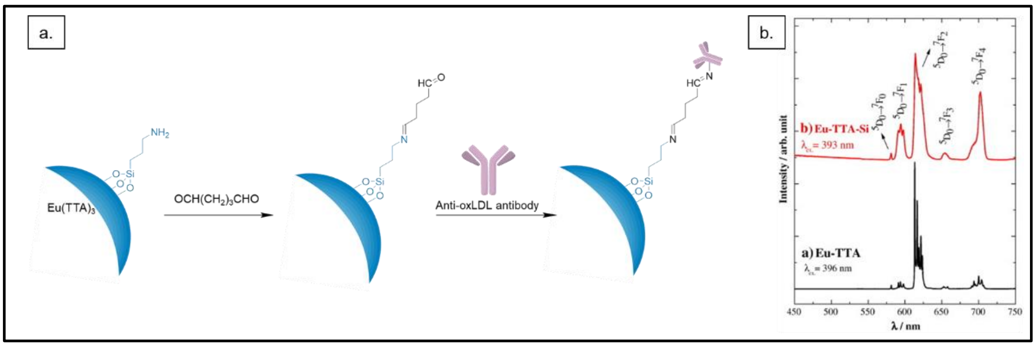

Figure 6.6 a) schematic of particle functionalisation; b) emission spectra of nanoparticle (top) and free complex (bottom) at 77 K. Adapted and taken from A. Lourenço *et al.*[22]

Unlike the previous example by J. Yang *et al,*[21] the photophysical properties of the particles were extensively studied; the emission spectra showed $^5D_0\rightarrow{}^7F_J$ transitions where J = 0, 1, 2, 3 and 4, but was dominated by the $^5D_0\rightarrow{}^7F_2$ hypersensitive transition, shown in **Figure 6.6b**. When encapsulated, this transition intensity decreased compared to $^5D_0\rightarrow{}^7F_1$, which suggested that the complex was in a higher symmetry state when encapsulated. This is further confirmed by the Judd-Ofelt Parameters where Ω_4 was larger than the free complex, which also indicates higher symmetry.[23] The emission spectra compared to the complex was also shown to be broader, which shows inhomogeneity of the Eu^{3+} sites within the particle, further confirmed by the biexponential emission lifetime observed. The average lifetime increased compared to the free complex, which was rationalised by considering that the complex will be more rigid within the silica particle, and less water molecules would be within the coordination sphere to bring about non-radiative deactivation *via* the vibrations of O-H bonds. Despite the increase in lifetime, the emissive quantum efficiency was smaller than that of the free complex, due to a decrease in the radiative rate despite also a decrease in the non-radiative rate *vs* that of the complex. By carrying out an antibody-antigen assay between HRP-oxidized LDL (HRP = horseradish peroxidase, LDL = low density lipoprotein) and the anti-oxLDL antibody on the surface of the particle, it was shown that the particles interacted well with biomolecules, and thus may be able to be used in bioimaging studies.

6.3.2 Europium Doped Polymer Based Particles

Although silica appears to be the particle material of choice in terms of ease of modification, stability and biocompatibility, there are still numerous reports of lanthanide encapsulation into a polymer matrix, with a range of different synthetic routes and polymers to choose from to suit different dopants and applications.

J. Desbiens *et al.*[24] synthesised polystyrene based particles using a miniemulsion technique, which had the advantage that both dopants and monomer were mixed before the emulsion was formed, and therefore hydrophobic dopants do not need to come into contact with the aqueous phase. $Eu(TTA)_3phen$ was used as the lanthanide dopant (**Figure 6.7a**) and a range of % weights were used to establish the effect on the polymerisation and stability of the resultant particles in the presence of increasing concentration of Eu^{3+}. They found that 2 % weight of Eu^{3+} gave the best yield, similar to that of the silica shell in work by J. Yang *et al*,[21] as increased concentration of the complex lead to destabilisation during synthesis and a decreased conversion of monomer to polystyrene. As well as this, the total amount of the europium complex encapsulated varied considerably when the initial concentration was more than 2 %. Even at 2% loading, the polydispersity index was larger for doped than undoped polymer particles. To aid increased stability in the presence of organic solvents, and thus try to prevent dopant leakage, divinylbenzene was used as a cross linker during particle synthesis, however europium loss was not completely removed, particularly with the higher doped materials, as shown in **Figure 6.7b**. This is a prime example of the disadvantages of uncoated polymer particles, in that slight changes to solvent can lead to swelling and thus leakage of the dopant, which can be particularly problematic in terms of biological applications.

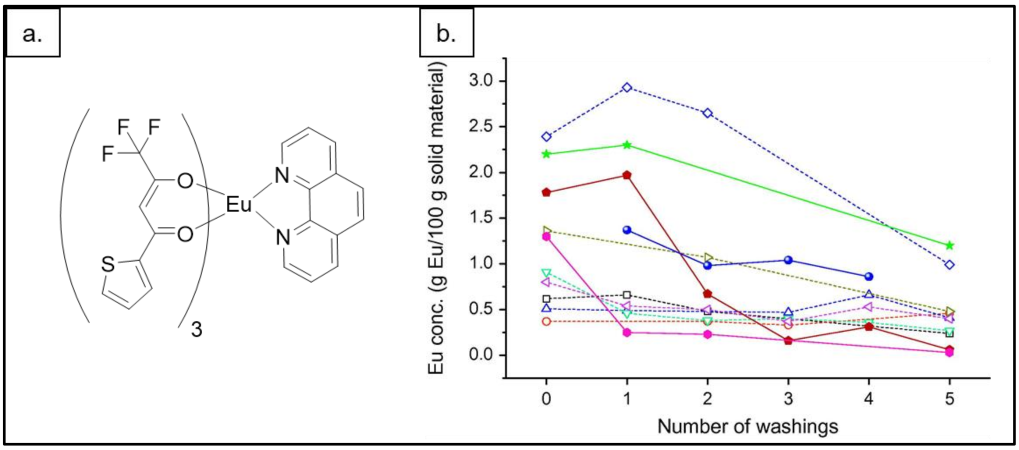

Figure 6.7 a) Eu(TTA)$_3$phen complex; b) Eu^{3+} concentration within particles as a function of washing steps (Open symbols = crosslinked, filled symbols = non-crosslinked). Adapted and taken from J. Desbiens *et al.*[24]

Luminescence results showed the intensity ratio between $^5D_0 \rightarrow {}^7F_2$ and $^5D_0 \rightarrow {}^7F_1$ of the encapsulated complex was similar to the complex in THF, however instead of attributing this to no change in local symmetry in the complex, the reasoning used is that as the intensity of the $^5D_0 \rightarrow {}^7F_2$ has not changed, the complex has not degraded upon particle formation. Although this may be the case, the lack of change in intensity is most likely to be due to similarities in environment between the polystyrene core and THF, perhaps lending insight into pore structures within the material. The emissive lifetime was also similar, with only a slight increase from 707 to 720 μs between the free and encapsulated complex, respectively. This again lends evidence to the similarities of the environment.

Another example of the miniemulsion technique in the synthesis of polystyrene particles is that of T. Aikawa *et al.,*[25] however in this case further stabilisation *via* surface functionalisation was also achieved. Poly(ethylene glycol) monomethoxy methacrylate and Bovine Serum Albumin (BSA) were used as surfactants, the latter of which also stabilised the resultant droplets *via* adsorbing onto the surface which ultimately lead to BSA-coated polystyrene particles. This yielded an array of different functional groups for the particle surface, which then lead to the attachment of N-(6-maleimidocaproyloxy)succinimide, of which the terminal succinimide could then react with thiol groups in antibody fragments to yield bio-functionalized particles.

Two similar complexes were compared as dopants, Eu(TTA)$_3$(H$_2$O)$_2$ and Eu(TTA)$_3$(TOPO)$_2$, the former of which has been described previously. However, Eu(TTA)$_3$(TOPO)$_2$ is far more soluble and therefore a higher doping level could be achieved as $Eu(TTA)_3(H_2O)_2$ had a lower solubility and therefore destabilised the droplets during synthesis, similar to previous works described here.[24] Up to 15 % of $Eu(TTA)_3(TOPO)_2$ could be doped within the polystyrene particle before particles suffered from aggregation and precipitation from solution, much higher than previous examples using silica.

The excitation and emission spectra of the encapsulated complex was similar to that of the free complex in THF, showing that the polystyrene had not interacted with the complex, with $^5D_0 \rightarrow {}^7F_J$ transitions where J = 0, 1, 2, 3 clearly visible. The functionalised particles were tested for their ability to detect human α-fetoproteins *via* both a time-resolved fluoroimmunoassay and an immunochromatographic assay, giving detection limits of 3.3 pg/mL and 2 ng/mL respectively.

The method of nano-precipitation for the synthesis of polymer particles is demonstrated by M. Cardoso Dos Santos *et al*.[26] whereby pre-formed methyl methacrylate-based polymers and varying amounts of $Eu(tta)_3phen$ were prepared in acetonitrile, before being precipitated and suspended in water. The polymers contained sulfonate or carboxylate groups, which helped in controlling the resultant particle size of 10, 20 and 30 nm in diameter for PMMA polymers with sulfonate loadings of 3 and 1 % and carboxylate loadings of 10 % respectively. A slight increase in these values was observed with higher loading of $Eu(tta)_3phen$, however at the highest doping of 40 wt %, the particle sizes retained narrow size distributions and average diameters of 13, 23 and 34 nm. Doping with the lanthanide complex was shown *via* TEM, where a higher contrast was observed for particles doped with the complex compared to undoped particles.

The photophysical properties were analysed in-depth compared to previous examples. The absorbance spectrum of the loaded particles in water showed no differences from the free complex, with an increase in absorbance at higher loadings. The emission spectrum also showed clearly the $^5D_0 \rightarrow {}^7F_J$ transitions with J = 0, 1, 2, 3, and 4 clearly visible (shown in **Figure 6.8a**), and the quantum yield also increased with increase in dopant up to 20 wt % loading, to a maximum of 0.25. The emission lifetime was fitted to a biexponential decay, with values varying between different dopant loadings, indicating two different environments within the particles. As the shorter lifetime was similar to that of the free complex in acetonitrile, it was suggested that the environment responsible was closer to the particle surface, whereas the longer lifetime may be the result of an environment deeper within the core. No concentration quenching was observed at high dopant levels, and using the increase in emission intensity as a function of concentration of dopant it was calculated that for the highest loading (40 wt %), 5000 complexes were encapsulated per particle, yielding a brightness of 4.2x10^7 mol^{-1} dm^3 cm^{-1}.

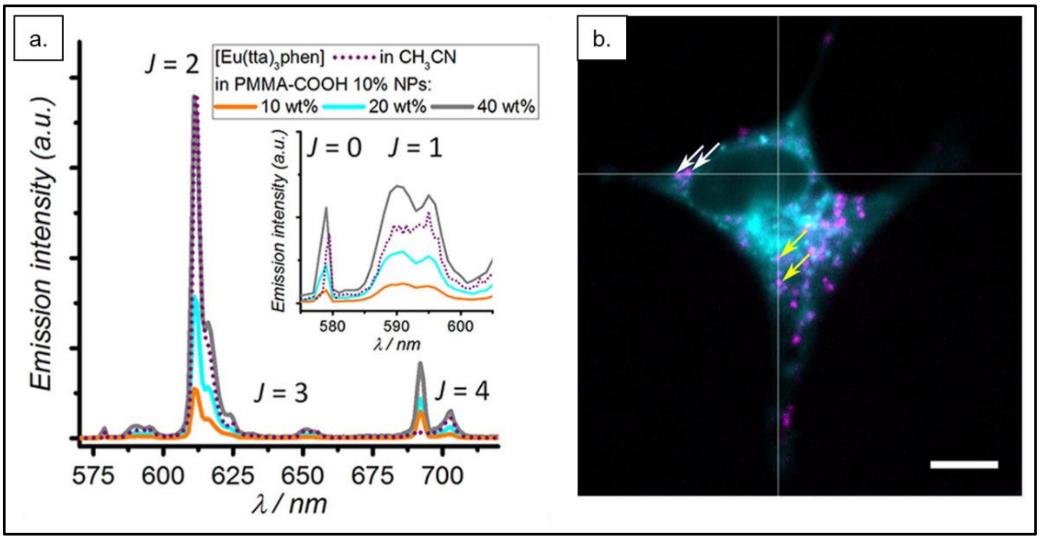

Figure 6.8 a) Emission spectra of PMMA-COOH particles with different complex loadings in aqueous solution, compared to that of the free complex in AcN, *inset*: $^5D_0\rightarrow{}^7F_J$ transitions; b) x/y-optical section of HeLa cell (turquoise) with PMMA-COOH particles with 40 % complex loading (magenta). Arrows point to particles in endosomes and lysosomes respectively, white bar = 10 µm. Taken from M. Cardoso Dos Santos *et al*.[26]

Due to the brightness calculated, time-gated imaging at the single particle level was attempted using HeLa cells, with the particles successfully being able to be imaged inside the cells (**Figure 6.8b**) using excitation intensities as low as 0.24 W cm^{-2}. Although not functionalised in this case, further functionalisation of the surface could be achieved, thus making them even more specific in future imaging applications.

A method similar to the work described herein for the encapsulation of lanthanide complexes into polymer particles is demonstrated by S. Qi *et al*.[27] In their work, Eu(DBM)$_3$phen (**Figure 6.9a**) was dissolved in DCM, and added to pre-formed polystyrene particles in water. However, unlike the work described in this thesis, adapted from the protocol published by C. Janczak *et al*.[28], the reaction mixture is instead stirred for 24 hrs to allow slow evaporation of organic solvent leading to encapsulation of the hydrophobic dopant within the polymer core.

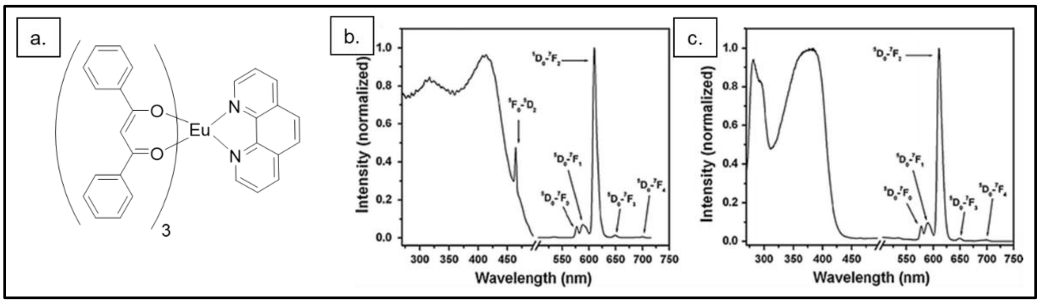

Figure 6.9 a) Eu(DBM)$_3$phen complex; b) excitation and emission spectra of Eu(DBM)$_3$phen; c) excitation and emission spectra of Eu(DBM)$_3$phen doped particles, swelled with DCM. Adapted and taken from S. Qi et al[27].

Unlike previous examples that have noted no shift in excitation or emission wavelength of the particles *vs* free complex, S. Qi *et al.*[27] instead notes that the π→π* transition in the excitation spectrum due to the DBM ligand blue shifts compared to the free complex, and also splits into two peaks. This indicates that the encapsulation has affected the local symmetry of the complex, which is further confirmed by the absence of the $^7F_0 \rightarrow {}^5D_2$ transition in the excitation spectra (due to non-radiative energy transfer to a defect level, shown in **Figure 6.9b/c**). In the emission spectra, $^5D_0 \rightarrow {}^7F_J$ transitions where J = 0, 1, 2, 3, and 4 are clearly observed, with $^5D_0 \rightarrow {}^7F_2$ dominating. An intense $^5D_0 \rightarrow {}^7F_2$ transition is indicative of Eu^{3+} being in a highly polarized environment. The ratio of the intensity of the $^5D_0 \rightarrow {}^7F_2$ compared to the $^5D_0 \rightarrow {}^7F_1$ transitions was compared to the free complex and found to have decreased. However, unlike A. Lourenco *et al.*,[22] they attribute this to a decrease in symmetry of the complex. Although the previous evidence of blue-shift of π→π* transition and lack of $^7F_0 \rightarrow {}^5D_2$ transition in the excitation spectrum indicates that there is a decrease in symmetry upon encapsulation, an increase in the intensity ratio compared to the free complex is actually known to be a sign of an increased symmetry, with examples by both by A. Lourenco *et al*[22] and H. Zhang *et al*[29]. Despite this confusion, the emission lifetime was calculated to be longer than that of the free complex, which is attributed to be due to the rigid environment of the polystyrene core, which reduces non-radiative deactivation by preventing vibration of the complex. The particles were also found to increase the stability of the complex under UV radiation, and this effect is attributed to the same reasoning. Due to the intense emission, long emission lifetime and stability, these particles could therefore find an application in biological assays once functionalised.

6.3.3 Ytterbium and Gadolinium Doped Particles

As discussed previously, there are limited examples of particles doped with lanthanide complexes other than those of europium. However, there are three of interest; one detailing the encapsulation of an ytterbium cyanoporphyrazine complex,[30] and the others being interesting studies on the change in relaxivity upon encapsulation of Magnevist,[31] a known Gd^{3+}-based MRI agent, and its encapsulation and targeted release to the imaging site.[32]

L. G. Klapshina *et al.*[30] doped a previously reported ytterbium complex[33] (**Figure 6.10a**) into a silica shell surrounding a polyethylene glycol (PEG) based core. Unlike previous examples that used the Stöber method with TEOS, the silica shell was instead formed *via* a fluorinated organosilicon oligomer (**Figure 6.10b**), which was added to the reaction mixture at the same time as the ytterbium complex to PEG. The organosilicon oligomer coordinated to the ytterbium complex *via* the primary amide groups, and hydrogen-bonded to the cyano-groups of the macrocycle. The affinity for the oligomer compared to PEG for the ytterbium complex was confirmed *via* energy-dispersive X-ray spectroscopy (EDAX), which showed that in the core-shell particle (**Figure 6.10c**) the core contained predominantly carbon and oxygen (1.29 % and 0.39 % fluorine and silica also present respectively), with ytterbium only present in the shell.

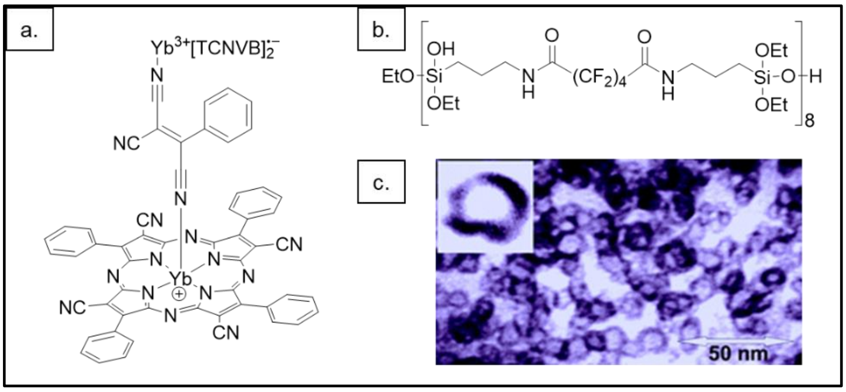

Figure 6.10 a) Ytterbium cyanoporphyrazine complex; b) fluorinated silicon oligomer; c) TEM image of doped particles, *inset:* 3 x magnification. Adapted and taken from L. G. Klapshina *et al.*[30]

The photophysical analysis of the particles is unexpected, as only the ligand emission is discussed and shown, despite mention of luminescence up to 1000 nm. That being said, the porphyrazine macrocycle exhibits a higher quantum yield and fluorescence enhancement factor when in the nanoparticle and dispersed in physiological fluids (e.g. human albumin solution and serum) compared to the free complex. This is thought to be due to aggregation of the particles with the various biomolecules (such as proteins) present in the physiological fluids (due to the hydrophobic nature of the surface) limiting water from entering the ytterbium coordination sphere and thus reducing non-radiative decay. *In vivo* imaging of tumours was carried out, however using a different composite not mentioned in this discussion (involving the interaction between the ytterbium complex and PEG, forming a macromolecular aggregate suspension with similar photophysics), and showed effective accumulation at the cancer site. Therefore, it is hoped that the core-shell particles would also demonstrate a similar level of imaging.

Despite the extensive use of gadolinium complexes as MRI agents, relatively few examples exist of the complexes encapsulated within a particle, even mesoporous varieties, with most concerning either surface functionalisation of particles with the lanthanide ion,[34] or formation of Gd_2O_3[35,36]. However, two poignant examples are mentioned here; one involving an in-depth study on the changes in the relaxivity of a known complex when encapsulated, the other showing how polymeric particles can be utilised for modified release of the complex at the target site.

In MRI, water protons are magnetised with longitudinal and transverse relaxation times. These values vary dependent on environment within the body, and thus contrast between different tissues is found. The gadolinium ion is paramagnetic, with seven unpaired elections, and therefore can increase the contrast by interacting with the nearby water protons and forming a magnetic dipolar interaction. However, Gd^{3+} is toxic and therefore requires strong chelation to prevent leakage into the body. This is possible, however chelation also prevents water molecules from coordinating, and therefore reduces the contrast that can occur.

J. Ananta *et al.*[31] studied the change in relaxivity upon encapsulating gadolfullerenes, gadonanotubes and Magnevist inside silica microparticles (SiMPs) suitable for intravascular injection. Magnevist, also known as gadopentetic acid, is a well-known MRI contrast agent and shown in **Figure 6.11a**. Due to the nature of the work carried out within this chapter, only results relating to encapsulated Magnevist will be discussed.

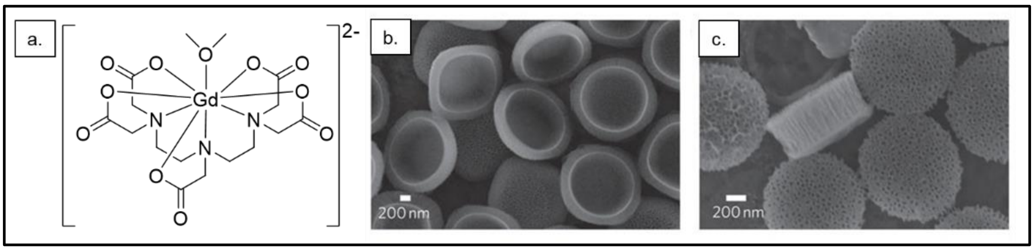

Figure 6.11 a) Magnevist, also known as gadopentetic acid; b) SEM image of H-SiMP particles; c) SEM image of D-SiMP particles. Adapted and taken from J. Ananta *et al.*[31]

The morphology and porosity of the SiMPs, shown in **Figure 6.11**, were controlled *via* the use of photolithography and electrochemical etching, and were doped with Magnevist *via* sequential loading, which achieved a higher loading than doping the full amount in one step. **Figure 6.11** shows the two different morphologies analysed, those that are quasi-hemispherical and those that are discoidal in shape, both of which had pores between 30-40 nm in diameter. Despite the pore size, release of the encapsulated complex could not be detected using ICP-OES.

The longitudinal relaxivity rate of the encapsulated Magnevist *vs* the free complex was studied, with values of 14 $mM^{-1}s^{-1}$ (H-SiMP) and 4 $mM^{-1}s^{-1}$ respectively. This increase in relaxivity can be understood by considering the different factors that make up the relaxivity, including q (discussed in **Section 6.2.3**), the tumbling rate of both the lanthanide ion and the coordinated water molecules, and the residence time of the water molecules within the inner sphere of the complex. When encapsulated, the mobility of both the complex and the water molecules diffused in the pores is restricted, increasing both the correlation time and the tumbling rate, and therefore causing an increase in the overall relaxivity. The increase in the relaxivity shows promise in MRI imaging, not just for the increase in core parameters but also for the much reduced toxicity.

Although J. Ananta *et al*.[31] focussed on the diffusion of water into the particle, and the minimisation of complex leakage, A. Doiron *et al.*[32] instead showed how biodegradable polymer particles could be used as a method for targeted release of complex at the imaging site for the detection of plaque resulting from atherosclerosis. Magnevist was used as the dopant, due to its existing use as an MRI agent and hence well studied relaxivity parameters. Water-in-oil-in-oil double emulsion was used for the encapsulation of the complex within two different polymers; polylactide-poly(ethylene glycol) (PLA-PEG) and poly(lactidie-co-glycolide) (PLGA) the latter resulting in larger particles when sonication power was varied. ICP-MS was used to measure the loading of the particles, with the larger PLGA particles achieving a loading of over 50 % wt, the smaller particles up to 25 % wt and the PLA-PEG particles achieving up to 15 % wt.. *In vitro* release of the complex from the particle core occurred over 5 hours, with over 90 % released in the first hour. This is attributed to both effective diffusion through the polymer matrix, and also due to the biodegradability of the polymer. The larger PLGA particles showed contrast increase in MRI imaging, with an r_1 value similar to that of free complex, thus paving the way for modified release particles, ultimately reducing toxicity.

6.4 Results and Discussion

6.4.1 Synthesis

A range of known lanthanide complexes were chosen to be encapsulated within the polystyrene core to fully investigate both the effect of the particle environment on the complex, and also the effect of the complex on the particle morphology.

Eu(TTA)$_3$ was chosen due to the literature precedent, giving an ideal comparison to help rationalise observations. The TTA complexes are also hydrophobic, and therefore compatible with encapsulation into the organic particle core. **Gd(TTA)$_3$** was encapsulated to investigate the TTA ligand within the polymer core. **Ln(TTA)$_3$** where Ln= Nd, Yb and Er were encapsulated, as the vast majority of literature surrounding the encapsulation of lanthanide complexes is primarily focussed on that of visible emitters such as Eu^{3+} and Tb^{3+} complexes. **Nd(TTA)$_3$(bpy)$_2$** and **Er(TTA)$_3$bpy** were also used due to inadequate emission intensity of **Nd(TTA)$_3$** and **Er(TTA)$_3$**, discussed in more detail in the following sections.

All **Ln(TTA)$_3$** complexes were synthesised by a method proposed by L-Y Zhang *et al*[37], however starting lanthanide complexes differed in some instances and NaOH was used instead of HCl to control the pH of the reaction mixture. Both **Er(TTA)$_3$(bpy)** and **Nd(TTA)$_3$(bpy)$_2$** were synthesised by a method proposed by S. J. Lyle *et al*[38] for the synthesis of $Eu(AA)_3.3H_2O$ (where AA = acetylacetone), in which ammonia was introduced to the reaction mixture *via* tubing to a heated ammonium hydroxide solution. Both protocols resulted in the formation of the precipitate, and either filtration or trituration followed by washing with water and $CHCl_3$ to remove excess complex and ligand. All complexes were analysed *via* mass spectrometry, yielding the predicted molecular ion peak in each case.

In the case of **PS(Ln(TTA)$_3$)@SiO$_2$** where Ln = Gd, Nd and Er, and both **PS(Nd(TTA)$_3$(bpy)$_2$)@SiO$_2$** and **PS(Er(TTA)$_3$bpy)@SiO$_2$**, the synthesis of particles proceeded as described in **Chapter's 3** and **4**. The only caveat was the addition of drops of ethanol to the $CHCl_3$:iPrOH solvent system, to aid dissolution of the erbium and neodymium complexes prior to addition to the polystyrene beads.

However, in the case of **PS(Eu(TTA)$_3$)@SiO$_2$** and **PS(Yb(TTA)$_3$)@SiO$_2$**, adaptions were required. In both cases when the original methodology was undertaken, the polymer bead suspension gradually became clear upon addition of the respective lanthanide complex, and therefore it would appear that the complexes affected the structure of the polymer, possibly causing dissolution of the structure. This was surprising, considering polystyrene beads containing europium are well known industrially, with producers such as PerkinElmer copolymerising europium with polystyrene.[39] Initially the reaction mixture was not sonicated after the first hour to give “milder” reaction conditions, however this continued to yield a clear solution. However, it appeared that the dissolution only started to occur after the first hour, and so the reaction time was instead shortened to prevent dissolution of the polymer beads. In the case of **PS(Eu(TTA)$_3$)@SiO$_2$**, when **Eu(TTA)$_3$** was added, the reaction mixture initially clumped and then became less opaque. With **PS(Yb(TTA)$_3$)@SiO$_2$**, after one hour there appeared to be two layers, and so the more opaque layer (containing intact polymer beads) was separated and organic solvent removed from the suspension. Although a shorter reaction time may have resulted in a smaller uptake of lanthanide complex, the photophysical studies showed that both complexes were able to be doped inside the core at a measurable concentration.

6.4.2 Morphological Studies

All particles were analysed *via* SEM, STEM and EDX to investigate both the particle morphology and composition. Although encapsulations in **Chapter 3** involving larger organic molecules and co-doping led to a larger range of particle sizes, none showed the size range observed for lanthanide particles, presented in **Table 6.2**. As in previous examples, the silica shell thickness did not show as large a variation.

Table 6.2 Calculated diameter of polystyrene core and shell thickness of **PS(Ln)@SiO$_2$**; particle sizes were calculated using ImageJ software.

	Min / nm	Max / nm	Mean / nm	SD / nm
Core Diameter	46 ± 15	1012 ± 15	212 ± 15	153
Shell Thickness	17 ± 2	107 ± 2	49 ± 2	19

Despite this large range of sizes, it should be noted that the larger core diameters observed were of the minority, as shown in the histogram in **Figure 6.12a**. This shows quite clearly that there were a large number of particles between 51-300 nm, and then a smaller number of particles in the larger size ranges with the exception of **PS(Er(TTA)$_2$bpy)@SiO$_2$**, which showed only particles in the smaller size ranges. Both **PS(Yb(TTA)$_3$)@SiO$_2$** (shown in **Figure 6.12c**, compared to **PS(Gd(TTA)$_3$@SiO$_2$** in **Figure 6.12b**) and **PS(Eu(TTA)$_3$)@SiO$_2$** only showed larger particles, however this may be due to the smaller sample size of both as a result of the large amount of silica particles observed. One could speculate whether the small number of core-shell particles observed is a result of the increased particle size, however larger particles were also observed for **PS(Nd(TTA)$_3$)@SiO$_2$** *vs* **PS(Nd(TTA)$_3$(bpy)$_2$)@SiO$_2$,** as discussed below.

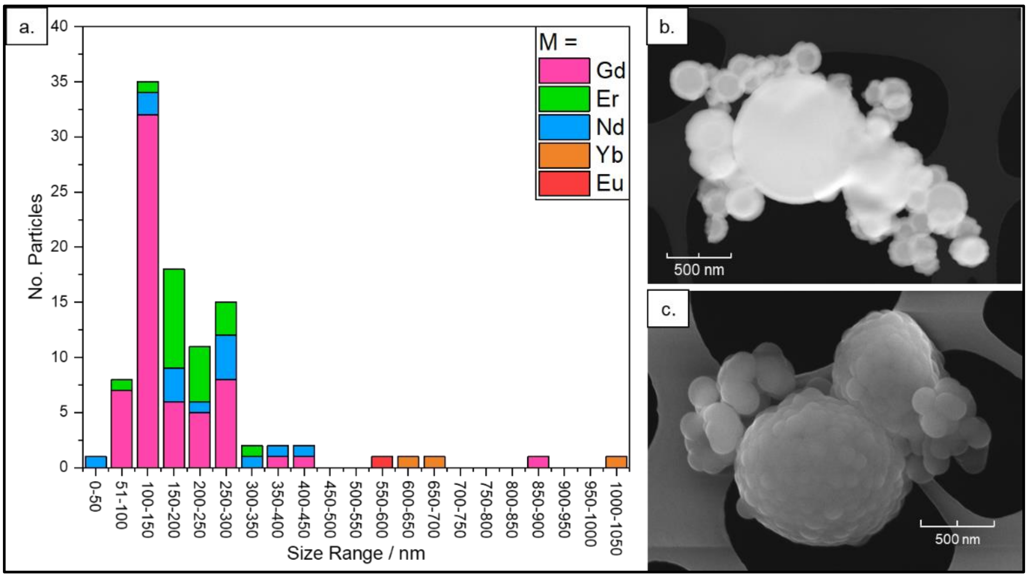

Figure 6.12 a) Histogram showing size distribution of particle cores; b) STEM image of **PS(Gd(TTA)$_3$)@SiO$_2$** compared to c) SEM image of **PS(Yb(TTA)$_3$)@SiO$_2$**.

EDX analysis showed the presence of both ytterbium and gadolinium in their respective particles, however failed to show europium (**Figure 6.13**). In the case of **PS(Yb(TTA)$_3$)@SiO$_2$**, ytterbium was only found in the largest of particles. In the case of **PS(Gd(TTA)$_3$)@SiO$_2$**, gadolinium was present in almost all particles imaged. This variation between particles however does suggest that not all particles were successfully doped, or at least within the sensitivity of EDX, despite photophysical studies (discussed in **Section 6.4.3**) showing the presence of the complexes within the particles. In the case of **PS(Eu(TTA)$_3$)@SiO$_2$**, in-laboratory experiments concerning the doping of particles with iridium complexes (not presented within this work) also showed this result, in which the complex was confirmed to be within the particle *via* photophysical measurement, and yet iridium could not be found *via* EDX. This is undoubtedly a reflection on the relative sensitivities of luminescence *vs* EDX.

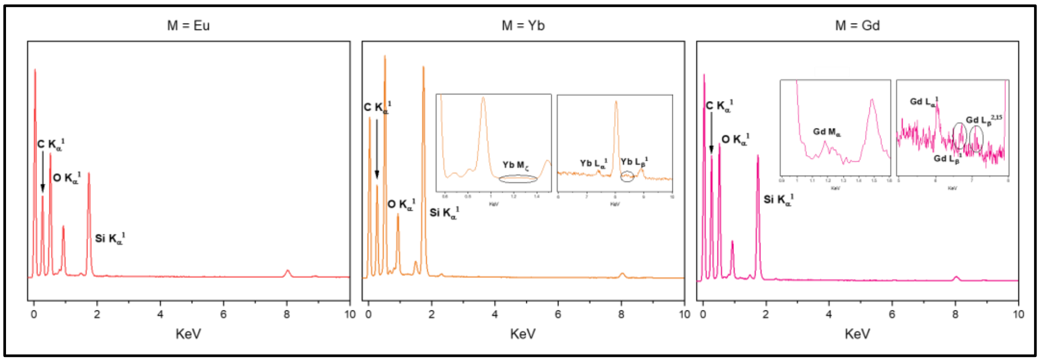

Figure 6.13 EDX spectra of **PS(Eu(TTA)$_3$)@SiO$_2$** (*left*), **PS(Yb(TTA)$_3$)@SiO$_2$** (*middle*), and **PS(Gd(TTA)$_3$)@SiO$_2$** (*right*).

For both **PS(Er(TTA)$_2$bpy)@SiO$_2$** and **PS(Nd(TTA)$_3$(bpy)$_2$)@SiO$_2$**, neither lanthanide was found within the particles *via* EDX. However, as shown in **Figure 6.14**, both **PS(Nd(TTA)$_3$)@SiO$_2$** and **PS(Er(TTA)$_3$)@SiO$_2$** showed the presence of the respective metals, suggesting a higher loading of the latter complexes. This may well be the case, as the coordination of bpy may lead to a larger overall complex, which may not be as compatible with the polystyrene core. This also shows that the marked difference in emission intensity observed for **PS(Nd(TTA)$_3$)@SiO$_2$** *vs* **PS(Nd(TTA)$_3$(bpy)$_2$)@SiO$_2$** is not a result of loading, but is instead entirely due to the coordination of bpy (discussed in **Section 6.4.3**).

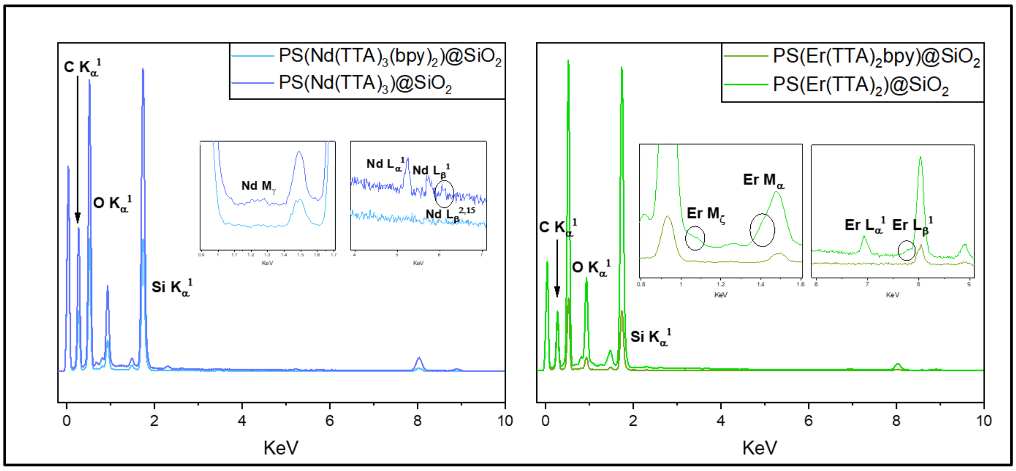

Figure 6.14 EDX spectra of *left*: **PS(Nd(TTA)$_3$)@SiO$_2$** *vs* **PS(Nd(TTA)$_3$(bpy)$_2$)@SiO$_2$** and *right:* **PS(Er(TTA)$_3$)@SiO$_2$** *vs* **PS(Er(TTA)$_3$bpy)@SiO$_2$**.

Another interesting observation on the comparison between **PS(Nd(TTA)$_3$)@SiO$_2$** and **PS(Nd(TTA)$_3$(bpy)$_2$)@SiO$_2$** is the respective particle sizes. **PS(Nd(TTA)$_3$(bpy)$_2$)@SiO$_2$** particles were less than 450 nm in diameter, however as shown in **Figure 6.15**, **PS(Nd(TTA)$_3$)@SiO$_2$** particles were considerably larger (with some in the micron range) much like those of **PS(Yb(TTA)$_3$)@SiO$_2$**.

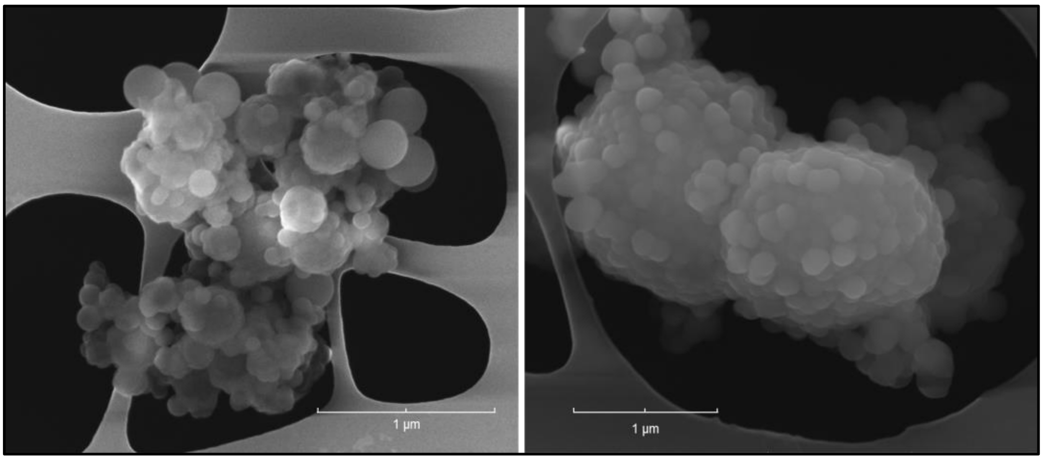

Figure 6.15 SEM images of **PS(Nd(TTA)$_3$(bpy)$_2$)@SiO$_2$** (*left*), and **PS(Nd(TTA)$_3$)@SiO$_2$** (*right*).

6.4.3 Photophysical Studies

6.4.3.1 PS(Eu(TTA)$_3$)@SiO$_2$

Upon excitation of the TTA ligand at 375 nm, **PS(Eu(TTA)$_3$)@SiO$_2$** emission showed the expected $^5D_0 \rightarrow {}^7F_J$ transitions of the europium complex, with J = 0,1,2,3, and 4 at 579, 592, 614, 652 and 701 nm respectively (**Figure 6.16**). The emission spectrum also showed smaller bands at 537 and 555 nm, corresponding to $^5D_1 \rightarrow {}^7F_1$ and $^5D_1 \rightarrow {}^7F_2$ respectively[14] (**Figure 6.16** *inset*). Particles were directly excited *via* the TTA ligand to promote intermolecular charge transfer between ligand and metal, and thus sensitisation, which is evidenced to be efficient due to the lack of excitation transitions for Eu^{3+} ($^7F_{0,1} \rightarrow {}^5D_J$, ^5S_J , ^5H_J, ^5G_J, and ^5L_J) shown in the excitation spectrum (**Figure 6.16**).

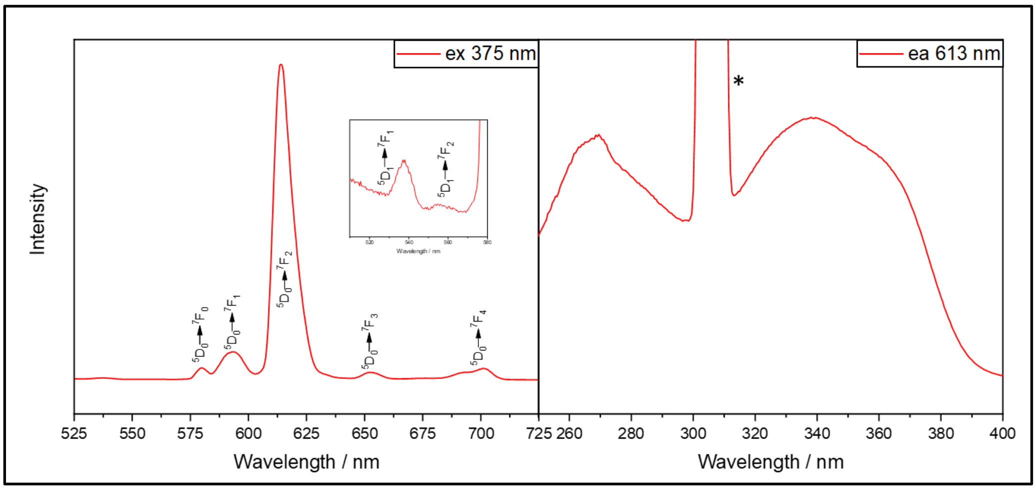

Figure 6.16 Emission (*left*) and excitation (*right*) spectra of **PS(Eu(TTA)$_3$)@SiO$_2$**, recorded in water. For the emission spectra, slit widths were set to 4 and 5 nm for excitation and emision respectively; for the excitation spectra slit widths were set to 5 and 10 nm for excitation and emission respectively. * denotes a lamp harmonic associated with the excitation spectra.

The observation of the $^5D_0 \rightarrow ^7F_0$ transition in the emission spectrum is indicative of a low symmetry environment, as the transition is disallowed (J and J' both equal 0)[40], this reduction in symmetry compared to the free complex is further confirmed by the Judd-Ofelt parameters and intensity ratios discussed below.

The excitation spectrum also showed a possible contribution from the polystyrene core, which absorbs strongly at 268 nm, and thus evidence of energy transfer between the core and the ligand. This was further investigated *via* excitation at 268 nm, shown in **Figure 6.17**. Although excitation at 350 nm (direct excitation of TTA based bands) gave a far more intense emission of the europium complex, excitation at 268 nm also promoted a more intense emission than that of direct excitation of Eu^{3+} at 396 nm.

That excitation at 268 nm promoted emission of the lanthanide species is not unexpected as polystyrene emits weakly at 338 nm, well within the absorbance of the TTA ligand, thus energy transfer between the two species and consequent sensitisation of Eu^{3+} results.

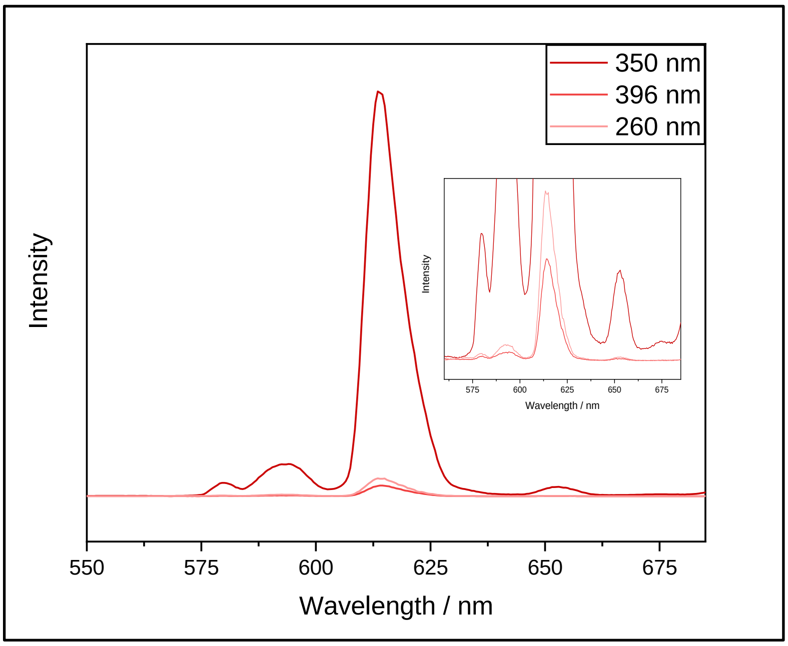

Figure 6.17 Emission spectra of **PS(Eu(TTA)$_3$)@SiO$_2$**, excited at a range of wavelengths. Recorded in water. Slit widths were set to 4 and 5 nm for excitation and emission respectively.

The emission lifetimes of **PS(Eu(TTA)$_3$)@SiO$_2$** in H_2O and D_2O are presented in **Table 6.3**, along with those of **PS(M(TTA)$_3$)@SiO$_2$** where M = Yb and Gd, and **PS(Nd(TTA)$_3$(bpy)$_2$)@SiO$_2$** and **PS(Er(TTA)$_3$bpy)@SiO$_2$**.

Table 6.3 Emissive lifetimes, τ, and solvation numbers, q, for **PS(X)@SiO$_2$.** λ_{ex}=355 nm.

PS(X)@siO$_2$	**τ / μs**		**q**
	H_2O	**D_2O**	
X = Eu(TTA)$_3$	253 ± 25	344 ± 34	1
X = Yb(TTA)$_3$	0.581 ± 0.058 (19) 5.03 ± 0.50 (81)	7.86 ± 0.79	1 (19) 0 (81)
X = Nd(TTA)$_3$(bpy)$_2$	0.196 ± 0.020 (26) 1.16 ± 0.12 (74)	0.286 ± 0.029 (41) 1.20 (59) ± 0.12	0
X = Er(TTA)$_3$(bpy)	N/A	1.08 ± 0.11	N/A

The solvation number, q, for **PS(Eu(TTA)$_3$)@SiO$_2$** was calculated based on the reciprocal of the lifetimes of each sample in both H_2O and D_2O, as shown in

Equation 6.11, with correction factors A = 1.2 ms and B = 0.25 ms^{-2} used to take into account external influences.

PS(Eu(TTA)$_3$)@SiO$_2$ gave a mono-exponential lifetime in both H_2O and D_2O, with the lifetime in the latter being almost 100 µs longer, yielding a solvation number of 1. **Table 6.4** shows that the lifetime in H_2O was slightly shorter, but still comparable to the lifetime of solid **Eu(TTA)$_3$,** indicating limited quenching by the surrounding water in the pore.

To further understand the changes that have occurred to the complex upon encapsulation, the Judd-Ofelt parameters were also calculated. Although other lanthanide complexes would require the use of the absorption spectrum, the parameters were able to be calculated for the europium complex due to the $^5D_0 \rightarrow ^7F_1$ transition, which is a magnetic dipole transition and thus independent of environment. This can then be used as the standard when investigating the other transitions and thus calculating the radiative and non-radiative rate of deactivation (A_{rad} and A_{nrad}), the emission quantum efficiency (η), and the experimental intensity parameters (Ω). These parameters can then be compared to known values for **Eu(TTA)$_3$**.

As discussed in **Section 6.2.2**, the emissive quantum efficiency is related to the radiative and non-radiative decay, in that it is the ratio of the number of photons emitted *vs* absorbed, given by **Equation 6.6** and reproduced below for clarity:

$$\eta = \frac{\tau_{obs}}{\tau_{rad}} = \frac{A_{rad}}{A_{tot}} = \frac{A_{rad}}{A_{rad} + A_{nrad}}$$

Equation 6.13 Calculation for the determination of the emissive quantum efficiency[14]. Reproduced from **Equation 6.6**.

A_{tot} is calculated from the inverse of the observed lifetime, and A_{rad} from **Equation 6.7**. As $^5D_0 \rightarrow ^7F_6$ cannot be observed in the spectrum only two transitions, where J = 2 and 4, are used. $^5D_0 \rightarrow ^7F_6$ transitions are rarely reported experimentally in literature as they occur at a wavelength outside of the range of commercial spectrometers (occurring between 810-840 nm).[41] As well as this, the intensity of the transition is incredibly low, and therefore even a laser array that is sensitive to that particular region cannot always detect the transition.[41] Therefore, calculations of the Judd-Ofelt parameters frequently use only that of J= 2 and 4[14,17,22].

The values for both radiative and non-radiative deactivation, as well as the total deactivation rate and emissive lifetime are shown in **Table 6.4**, and compared to values for the solid complex. The observed emissive lifetime for **PS(Eu(TTA)₃)@SiO₂** was slightly shorter than that of **Eu(TTA)₃**, with the calculated non-radiative deactivation rate larger, most likely due to the presence of water within the core promoting deactivation. However the fact that the encapsulated complex has a similar lifetime to that of the free complex is advantageous considering the particles are suspended in water, and not in the solid state like the free complex.

Table 6.4 Calculated radiative, non-radiative and total decay rates, and emissive lifetime of **PS(Eu(TTA)₃)@SiO₂** suspended in water, compared to free complex in the solid state[17].

	A_{tot} / s^{-1}	A_{rad} / s^{-1}	k_{nrad} / s^{-1}	τ / µs
PS(Eu(TTA)₃)@SiO₂	3952	502	3450	253
Eu(TTA)₃	3846	1110	2730	260

By rearranging **Equation 6.9**, the experimental intensity parameters, Ω_J, can also be calculated:

$$\Omega_\lambda = \frac{A_{0\to J}}{\left(\frac{4e^2\omega^3}{3\hbar c^3}\frac{1}{2J+1}\chi\langle\, {}^5D_0\|U^{(\lambda)}\|\, {}^7F_J\rangle^2\right)}$$

Equation 6.14 Rearrangement of **Equation 6.9** for the calculation of the experimental intensity parameter Ω_J.

Using $\langle\, {}^5D_0\|U^{(\lambda)}\|\, {}^7F_J\rangle^2$ values of 0.0032 and 0.0023 for J = 2 and 4 respectively[17], and calculating the Lorentz local field correction, χ, *via* **Equation 6.10**. In the case of the core-shell particle, the refractive index of silica was used, as the definitive value is well studied and is between that of water (the suspension solvent) and the polystyrene core. For the calculation of these parameters, shown in **Table 6.5** (and those in **Table 6.4**), software developed by A. Ćirić *et al.*[42] was used due to ease of use and minimisation of error associated with integration of the emission profile.

Table 6.5 Calculated emissive quantum efficiency and experimental intensity parameters for **PS(Eu(TTA)$_3$(H$_2$O)$_2$)@SiO$_2$** using JOES software[42,43], compared to free complex[17].

	η / %	Ω$_2$ / x10^{-20} cm^{-2}	Ω$_4$ / x10^{-20} cm^{-2}
PS(Eu(TTA)$_3$)@SiO$_2$	13	15.9	1.74
Eu(TTA)$_3$	29	33	5

The emissive quantum efficiency was calculated to be under half of that of the solid complex. This was not unexpected as, suggested earlier for the increase in non-radiative decay, the presence of water will lead to a lower quantum efficiency.

The Judd-Ofelt parameters, $\Omega_{J=2,4}$, for **PS(Eu(TTA)$_3$)@SiO$_2$** were different from that of **Eu(TTA)$_3$**, confirming the change in environment brought about by encapsulation and the local solvent. In fact, the intensity ratio of the $^5D_0 \rightarrow ^7F_2$ and $^5D_0 \rightarrow ^7F_1$ transitions was higher than that of the pure complex (9.36 *vs* 8.90[44]), which is indicative of a lower symmetry environment[29] and is further supported by the lower value of Ω_4[23].

The smaller Ω_2 compared to that of **Eu(TTA)$_3$** shows that the $^5D_0 \rightarrow ^7F_2$ transition is hypersensitive, and the environment is less polarizable. This corresponds to the respective environments of **PS(Eu(TTA)$_3$)@SiO$_2$** *vs* solid **Eu(TTA)$_3$**, as the encapsulated complex will have a solvated coordination sphere of water (hence the decrease in emission lifetime and increase in non-radiative decay), which although polar is not as polarizable as organic ligands and larger atoms. In contrast, solid **Eu(TTA)$_3$** will not have a solvated coordination sphere and instead will have a more polarizable environment.

6.4.3.2 PS(Gd(TTA)$_3$)@SiO$_2$

Unlike the other lanthanide complexes, **Gd(TTA)$_3$** does not exhibit emission from the Gd^{3+} ion *via* ligand sensitization due to the first excited level of the ion being far higher in energy than the T$_1$ state of TTA. However, spin-orbit coupling between the singlet and triplet levels of the ligand still occurs due to the heavy atom effect, and therefore the TTA triplet state phosphorescence is well characterised at low temperature[17] with the fluorescence emission almost entirely quenched.[45] It appears only one study shows **Gd(TTA)$_3$** ligand triplet emission at room temperature, however it is in a rigid polymer resin as a solid sample.[45]

Therefore, as results presented both in this chapter and in **Chapter 3** suggest the presence of water inside the particle, and emission lifetimes shown in **Table 6.3** also suggest that solvent can pass through the silica shell, it was advantageous to encapsulate **Gd(TTA)$_3$** as the photophysics of the ligand (in particular the triplet excited state) can be analysed both in a rigid matrix and in the presence of solvent.

Although previous investigations on gadolinium complexes have predominantly been carried out at low temperature to observe the ligand triplet state, **Figure 6.18** shows the appearance of both the singlet and triplet states of TTA recorded at room temperature for **PS(Gd(TTA)$_3$)@SiO$_2$** in a water suspension. The singlet state was observed at 386 nm, with two further peaks at 438 and 493 nm, the latter of which is thought to be the triplet state due to its similarities to the literature.[17,45]

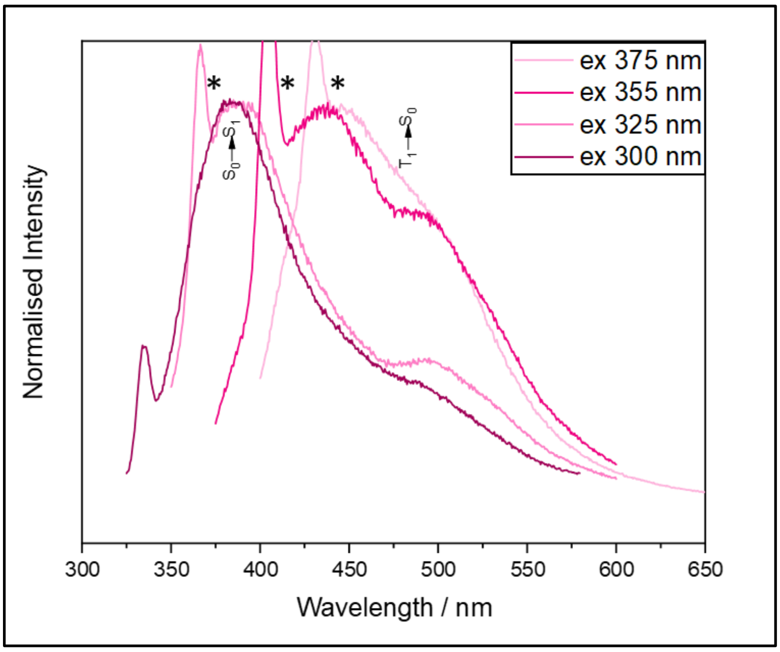

Figure 6.18 Emission spectrum of **PS(Gd(TTA)$_3$)@SiO$_2$**, recorded in water. The slit widths were set to 4 nm for both excitation and emission. *denotes a lamp harmonic associated with the excitation wavelength.

The appearance of the ligand triplet state at room temperature can only suggest that the deactivation pathways commonly found have been reduced without the need of a cryogenic climate. The main environmental causes of deactivation of a triplet state are that of collisional and vibrational quenching, and quenching by molecular oxygen in solution. By analysing the emission lifetimes of the other encapsulated lanthanide complexes presented in **Table 6.3**, it is likely that diffusion of solvent occurs between the bulk solvent and the particle core, due to the differences in lifetime when suspended in D_2O and H_2O. However, as suggested in previous chapters, the particle core may be more restrictive than solution and therefore the appearance of the triplet state of TTA may be due to an interplay of reduced oxygen diffusion (which low temperature measurements also reduce) and both a reduction in collisional and vibrational quenching of the complex in the more restrictive environment.

6.4.3.3 PS(Yb(TTA)$_3$)@SiO$_2$

Upon directly exciting TTA at 355 nm, **PS(Yb(TTA)$_3$)@SiO$_2$** exhibited emission at 978 nm, corresponding to the spin allowed $^2F_{5/2} \rightarrow {}^2F_{7/2}$ transition (shown in **Figure 6.19**). The emission was far more intense when the particles were suspended in D_2O rather than H_2O or in the solid state, which further confirms solvent diffusion between the external solvent and the particle core. Thus, analysis confirms the isolation of a near-IR emitting nanoparticle material.

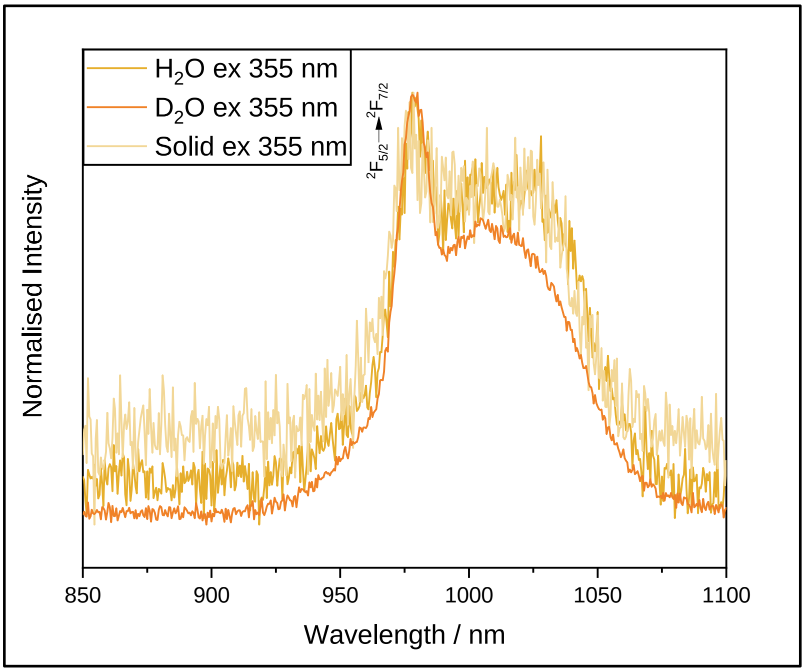

Figure 6.19 Emission spectra of **PS(Yb(TTA)$_3$)@SiO$_2$**, suspended in H_2O, D_2O and as a solid sample. In water and as a solid, the slit widths were set to 10 and 4 nm for excitation and emission respectively, in D_2O slit widths were set to 10 and 3 nm for excitation and emission respectively.

The emission lifetimes recorded for **PS(Yb(TTA)$_3$)@SiO$_2$** presented in **Table 6.3** showed a more complex situation than that of **PS(Eu(TTA)$_3$)@SiO$_2$**, with a bi-exponential lifetime recorded in water, but a mono-exponential lifetime recorded in D_2O. Previous work by M. Cardoso Dos Santos *et al,*[26] discussed in **Section 6.3.2**, attributed the bi-exponential lifetime to two different environments within the particle; one close to the surface and one deeper within the core. This can be rationalised by assuming the shorter lifetime (with a smaller contribution) originates from a species closer to the surface and thus more surrounded by water. It could also be a larger pore, and thus more water is present leading to an increase in non-radiative decay. In D_2O, the water in both cases will be substituted, and thus non-radiative decay will be reduced even in the more extreme case, leading to a mono-exponential environment where the local environment (the solvent) is the same.

The solvation numbers of both the small and large contributions were calculated using **Equation 6.11**, with A = 1 µs and B = 0.2 μs^{-1}. The solvation number for the smaller contribution was calculated as 1, whereas the larger component (and larger emission lifetime in H_2O) yielded a value of 0.

The larger lifetime component was also considerably longer than that of **Yb(TTA)$_3$** recorded in $CHCl_3$. In $CHCl_3$, the emission lifetime was recorded to be 0.85µs[46], which is only slightly larger than the smaller lifetime component of **PS(Yb(TTA)$_3$)@SiO$_2$**, showing that the environment inside the particle gives the complex encapsulated a level of protection from quenching *via* local solvent.

6.4.3.4 PS(Ln(TTA)$_3$)@SiO$_2$ and PS(Ln(TTA)$_3$(bpy)$_x$)@SiO$_2$ where Ln = Nd^{3+} and Er^{3+}

Measurement of both **PS(Nd(TTA)$_3$)@SiO$_2$** and **PS(Er(TTA)$_3$)@SiO$_2$** failed to detect any emission, even when suspended in D_2O. This was surprising due to both Nd^{3+} and Er^{3+} being found *via* EDX analysis (**Section 6.4.2**) and was therefore not a result of poor loading in the particle. Therefore, 2,2'-bipyridine was coordinated to further exclude water from the coordination sphere, in the hope of reducing quenching and hence increase emission intensity.

Thus for the variant **PS(Nd(TTA)$_3$(bpy)$_2$)@SiO$_2$** direct excitation of ligand at 355 nm lead to weak yet observable emission in water, with transitions far more intense in D_2O (**Figure 6.20**) at 904, 1064 and 1335 nm corresponding to $^4F_{3/2} \rightarrow {}^4I_{9/2}$, $^4F_{3/2} \rightarrow {}^4I_{11/2}$ and $^4F_{3/2} \rightarrow {}^4I_{13/2}$ respectively.

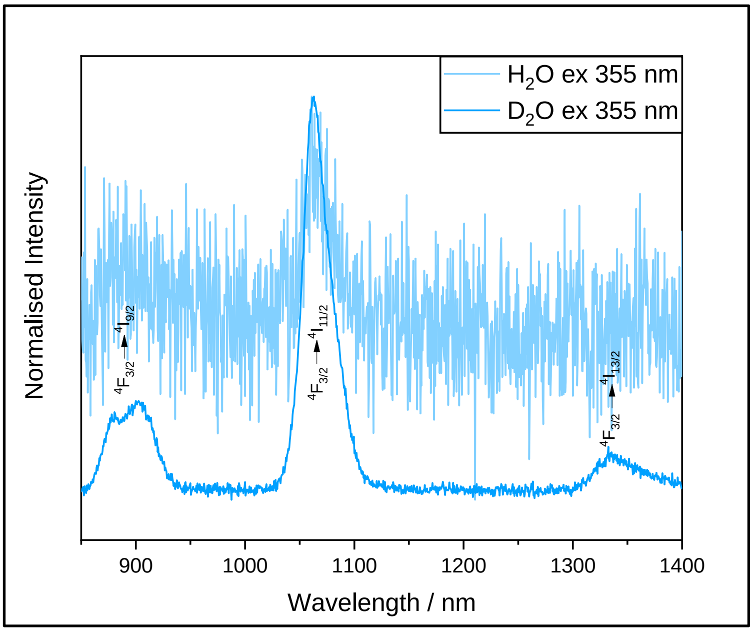

Figure 6.20 Emission spectra of **PS(Nd(TTA)$_3$(bpy)$_2$)@SiO$_2$** recorded in both D_2O and H_2O. Slit widths were set to 10 and 3 nm for excitation and emission respectively.

As expected, excitation of ligand led to singlet ligand emission $S_0 \rightarrow S_1$. Excitation at 262 nm also led to ligand emission, as well as polystyrene emission at 338 nm. However, unlike in the case of **PS(Eu(TTA)$_3$)@SiO$_2$**, excitation at 262 nm cannot suggest energy transfer between the polystyrene and the complex due to 2,2'-bipyridine also displaying absorbance at this wavelength.

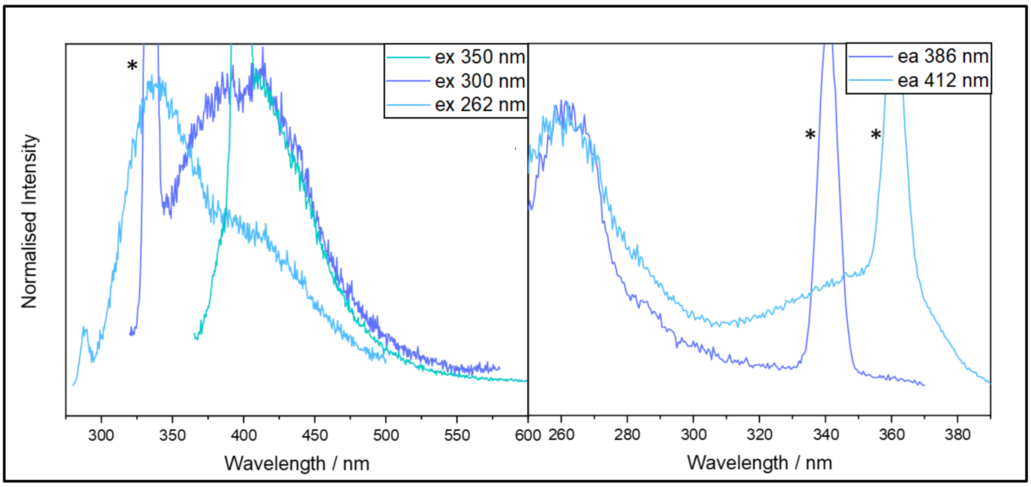

Figure 6.21 Emission (*left*) and excitation (*right*) spectra of **PS(Nd(TTA)$_3$(bpy)$_2$)@SiO$_2$** between 250 – 600 nm, focusing on ligand photophysics. Recorded in water. *denotes a lamp harmonic associated with the excitation wavelength.

The emission lifetimes of **PS(Nd(TTA)$_3$(bpy)$_2$)@SiO$_2$** in both H_2O and D_2O were biexponential, with different contributions for each (**Table 6.3**). The solvation number was calculated to be zero in all cases. Despite the differences in contribution, the difference in the larger component in each solvent was not large, leading to the assumption of a more protected environment from external solvent, hence non-radiative quenching was not greatly reduced by the change in suspension solvent.

As with **PS(Nd(TTA)$_3$(bpy)$_2$)@SiO$_2$**, direct excitation of ligand in **PS(Er(TTA)$_3$bpy)@SiO$_2$** suspended in D_2O gave the expected emission for the erbium complex at 1531 nm corresponding to the weak $^4I_{13/2} \rightarrow {}^4I_{15/2}$ transition (**Figure 6.22**).

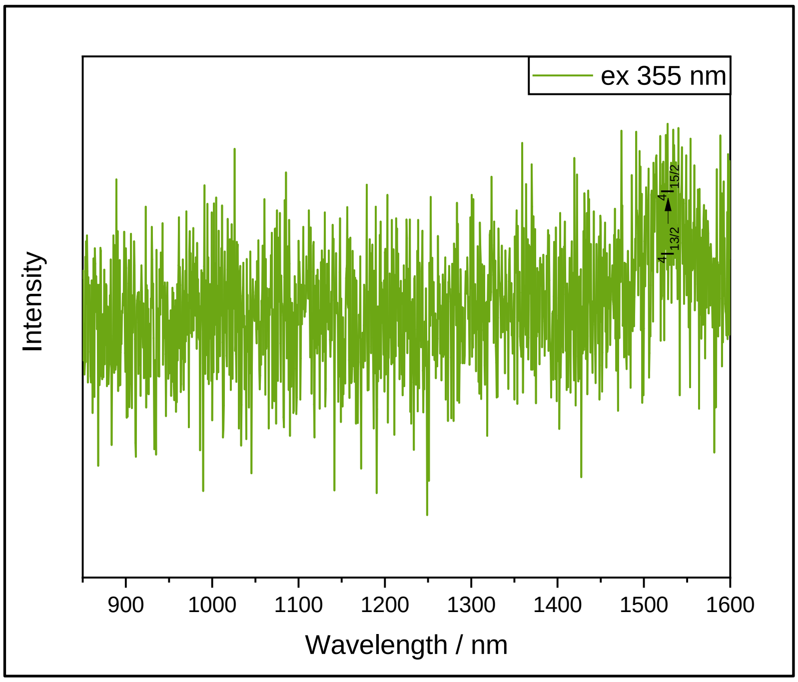

Figure 6.22 Emission spectrum of **PS(Er(TTA)$_3$bpy)@SiO$_2$**, recorded in D_2O. The slit widths were set to 10 and 3 nm for excitation and emission respectively.

Ligand emission was also investigated, and could be observed in H_2O, with excitation at 300 nm giving TTA singlet emission (**Figure 6.23**). However unlike previous examples, excitation at 262 nm only led to polystyrene emission and thus no energy transfer between the core and complex was observed. This may suggest a different configuration of the complex inside the particle, and account for the poor emission observed.

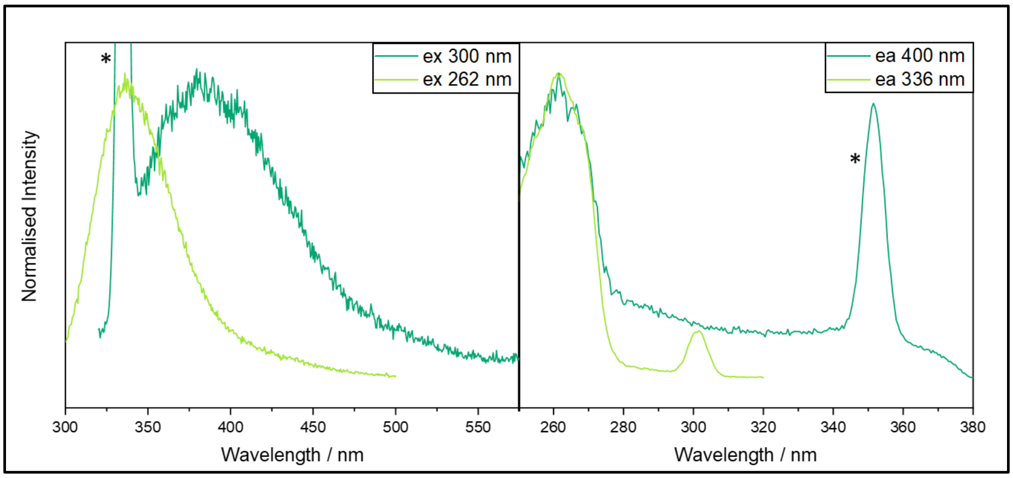

Figure 6.23 Emission (*left*) and excitation (*right*) spectra of **PS(Er(TTA)$_3$bpy)@SiO$_2$** between 250 – 600 nm, focusing on ligand photophysics. Recorded in water. *denotes a lamp harmonic associated with the excitation wavelength.

The solvation number of **PS(Er(TTA)$_3$bpy)@SiO$_2$** could not be obtained due to lack of emission in H_2O, however the lifetime could be recorded in D_2O (**Table 6.3**) which, unlike with **PS(Nd(TTA)$_3$(bpy)$_2$)@SiO$_2$**, was mono-exponential and thus suggests a single environment.

6.5 Conclusion

A series of known lanthanide complexes were encapsulated within core-shell particles, with their morphology and photophysical properties extensively examined, successfully providing the first examples of encapsulation of near-IR emitting species.

The examination of the particle morphology showed a broad range of particle sizes, unlike with organic dopants, with a maximum core diameter of 1012 nm observed for **PS(Yb(TTA)$_3$)@SiO$_2$**.

Intense emission of **PS(Eu(TTA)$_3$)@SiO$_2$** in a water suspension was observed, and the various experimental parameters obtained and compared to free complex. The changes observed in photophysical properties upon encapsulation were attributed to a change in symmetry of the complex, further confirming that the polymer core in these particles leads to restricted movement of the dopant, and hence follows from observations and discussion in **Chapter 3**. Time-resolved measurements (with the exception of those containing Gd^{3+} and Er^{3+} complexes) showed differences in emission lifetimes when suspended in D_2O and H_2O, implying diffusion of solvent between bulk and internal core environment.

The evidence of solvent exchange paves the way for the particles' use in sensing applications, as well biological applications in the case of **PS(Eu(TTA)$_3$)@SiO$_2$** and **PS(Gd(TTA)$_3$)@SiO$_2$.** Relaxivity measurements of the latter would be advantageous to carry out, due to the fairly mono-disperse nature of this set of particles and high gadolinium content making them potentially ideal as MRI agents. Perhaps a further investigation would be for the co-doping of these particles, both in terms of the photophysics and the morphology that may be obtained, and consequent biological applications. Functionalisation of the surface, already discussed in **Chapter 4**, could also be carried out for targeted applications.

6.6 Experimental

6.6.1 Preparation of Lanthanide Complexes

All **M(TTA)$_3$** complexes were synthesised *via* adaption of a method proposed by L-Y Zhang *et al*[37]. Both **Er(TTA)$_3$(bpy)** and **Nd(TTA)$_3$(bpy)$_2$** were synthesised by a method proposed by S. J. Lyle *et al*[38] for the synthesis of Eu(AA)$_3$.3H$_2$O (where AA = acetylacetone).

6.6.1.1 Eu(TTA)$_3$

HTTA (112 mg, 0.504 mmol) was dissolved in ethanol (5 mL), and the pH adjusted to 9 using NaOH. Eu(OTf)$_3$ (100 mg, 0.167 mmol) was dissolved in water (0.5 mL) and added to the reaction mixture, followed by more water (10 mL). The reaction was stirred at 80°C for 2 hours. Once cool, the mixture was filtered and the solid washed with water and chloroform before being dried in a desiccator to yield Eu(TTA)$_3$ as a white solid (20 mg, 14% yield); ASAP-MS (positive ion mode) found m/z = 816.90 $[Eu(TTA)_3+H]^+$

6.6.1.2 Yb(TTA)$_3$

HTTA (172 mg, 0.774 mmol) was dissolved in ethanol (5 mL), and the pH adjusted to 9 using NaOH. YbCl$_3$.6H$_2$O (100 mg, 0.258 mmol) was dissolved in water (0.5 mL) and added to the reaction mixture, followed by more water (10 mL). The reaction was stirred at 80°C for 2 hours. Once cool, the mixture was filtered and the solid washed with water and chloroform before being dried in a desiccator to yield Yb(TTA)$_3$ as a white solid (40 mg, 17% yield); ASAP-MS (positive ion mode) found m/z = $[Yb(TTA)_3+H]^+$ 837.95.

6.6.1.3 Nd(TTA)$_3$

HTTA (186 mg, 0.836 mmol) was dissolved in ethanol (5 mL), and the pH adjusted to 9 using NaOH. NdCl$_3$.6H$_2$O (100 mg, 0.278 mmol) was dissolved in water (0.5 mL) and added to the reaction mixture, followed by more water (10 mL). The reaction was stirred at 80°C for 2 hours. Once cool, the mixture was filtered and the solid washed with water and chloroform before being dried in a desiccator to yield Nd(TTA)$_3$ as a white solid (55 mg, 23% yield); ASAP-MS (positive ion mode) found m/z = $[Nd(TTA)_3(H_2O)_2+H]^+$ 841.88.

6.6.1.4 Gd(TTA)$_3$

HTTA (110 mg, 0.496 mmol) was dissolved in ethanol (5 mL), and the pH adjusted to 9 using NaOH. Gd(OTf)$_3$ (100 mg, 0.165 mmol) was dissolved in water (0.5 mL) and added to the reaction mixture, followed by more water (10 mL). The reaction was stirred at 80°C for 2 hours. Once cool, the mixture was filtered and the solid washed with water and chloroform before being dried in a desiccator to yield Gd(TTA)$_3$ as a white solid (40 mg, 25% yield); ASAP-MS (positive ion mode) found m/z = $[Gd(TTA)_3+H]^+$ 821.90.

6.6.1.5 Er(TTA)$_3$

HTTA (108 mg, 0.488 mmol) was dissolved in ethanol (5 mL), and the pH adjusted to 9 using NaOH. Er(OTf)$_3$ (100 mg, 0.162 mmol) was dissolved in water (0.5 mL) and added to the reaction mixture, followed by more water (10 mL). The reaction was stirred at 80°C for 2 hours. Once cool, the mixture was filtered and the solid washed with water and chloroform before being dried in a desiccator to yield Er(TTA)$_3$ as a white solid (23 mg, 16% yield); ASAP-MS (positive ion mode) found m/z = $[Er(TTA)_3+H]^+$ 829.90.

6.6.1.6 Er(TTA)$_3$(bpy)

Ammonia was bubbled into a stirring solution of Er(OTf)$_3$ (100 mg, 0.163 mmol), HTTA (108 mg, 0.488 mmol) and 2,2'-bipyridine (25 mg, 0.163 mmol) in methanol (5 mL) at room temperature *via* a heated ammonium hydroxide solution. After 2 hours the solvent was removed in vacuo and the resultant solid triturated in water to yield Er(TTA)$_3$(bpy) as a white solid (47 mg, 29% yield); ASAP-MS (positive ion mode) found m/z = $[M\text{-}bpy+H]^+$ 829.90 and $[M\text{-}TTA+H]^+$ 764.98.

6.6.1.7 Nd(TTA)$_3$(bpy)$_2$

Ammonia was bubbled into a stirring solution of $NdCl_3.6H_2O$ (100 mg, 0.279 mmol), HTTA (186 mg, 0.836 mmol) and 2,2'-bipyridine (43 mg, 0.279 mmol) in methanol (5 mL) at room temperature *via* a heated ammonium hydroxide solution. After 2 hours the solvent was removed in vacuo and the resultant solid triturated in water to yield Nd(TTA)$_3$(bpy)$_2$ as a white solid (61 mg, 20% yield); ASAP-MS (positive ion mode) found m/z = $[M\text{-}TTA]^+$ 896.02.

6.6.2 Preparation of particles - adapted from C. M. Janczak *et al*[28]

6.6.2.1 Synthesis of the polystyrene microsphere

Styrene (3.3 mL) was added to rapidly stirring degassed H2O (100 mL) heated to 75 °C under N_2. AIBA (10 mg) dissolved in H2O (200 µL) was added, and the reaction mixture was heated at 75 °C for 5.5 hours with vigorous stirring *via* stirrer bar. Once cool, excess styrene was removed in vacuo, and small aliquots of the aqueous polystyrene mixture was removed and lyophilized to determine mg/mL of nanoparticle solution. Polystyrene beads (14 mg/mL) were stored at room temperature in the dark until further use.

6.6.2.2 Encapsulation of Lanthanide complex

6.6.2.2.1 PS(Eu(TTA)$_3$)

Eu(TTA)$_3$ (0.065 mmol) was dissolved in iPrOH:$CHCl_3$ (0.1:0.9 mL) and added to the aqueous polystyrene solution (5 mL). The reaction mixture was stirred rapidly for 1 hour under N_2, and organic solvents were removed in vacuo to yield an aqueous solution of PS(Eu(TTA)$_3$). The polymer suspension was silica coated immediately.

6.6.2.2.2 PS(Gd(TTA)$_3$)

Gd(TTA)$_3$ (0.02 mmol) was dissolved in iPrOH:$CHCl_3$ (0.1:0.9 mL) and added to the aqueous polystyrene solution (5 mL). The reaction mixture was sonicated to disperse the organic droplets for 10 minutes, and then stirred rapidly for 3 hours under N_2, sonicating every hour for 10 minutes to re-disperse organic droplets. Organic solvents were removed *in vacuo* to yield an aqueous solution of PS(Gd(TTA)$_3$).

6.6.2.2.3 PS(Yb(TTA)$_3$)

Yb(TTA)$_3$ (0.048 mmol) was dissolved in iPrOH:$CHCl_3$ (0.1:0.9 mL) and added to the aqueous polystyrene solution (5 mL). The reaction mixture was stirred rapidly for 1 hour under N_2, and then sonicated. The opaque layer was separated from the solid, and organic solvent removed *in vacuo* to yield an aqueous solution of PS(Yb(TTA)$_3$).

6.6.2.2.4 PS(Nd(TTA)$_3$)

Nd(TTA)$_3$ (0.10 mmol) was dissolved in iPrOH:CHCl$_3$ (0.1:0.9 mL) with drops of ethanol, and added to the aqueous polystyrene solution (5 mL). The reaction mixture was sonicated to disperse the organic droplets for 10 minutes, and then stirred rapidly for 3 hours under N$_2$, sonicating every hour for 10 minutes to re-disperse organic droplets. Organic solvents were removed *in vacuo* to yield an aqueous solution of PS(Nd(TTA)$_3$).

6.6.2.2.5 PS(Er(TTA)$_3$)

Er(TTA)$_3$ (0.027 mmol) was dissolved in iPrOH:CHCl$_3$ (0.1:0.9 mL) with drops of ethanol to aid dissolution, and added to the aqueous polystyrene solution (5 mL). The reaction mixture was sonicated to disperse the organic droplets for 10 minutes, and then stirred rapidly for 3 hours under N$_2$, sonicating every hour for 10 minutes to re-disperse organic droplets. Organic solvents were removed *in vacuo* to yield an aqueous solution of PS(Er(TTA)$_3$).

6.6.2.2.6 PS(Nd(TTA)$_3$(bpy)$_2$)

Nd(TTA)$_3$(bpy)$_2$ (0.06 mmol) was dissolved in iPrOH:CHCl$_3$ (0.1:0.9 mL) with drops of ethanol to aid dissolution, and added to the aqueous polystyrene solution (5 mL). The reaction mixture was sonicated to disperse the organic droplets for 10 minutes, and then stirred rapidly for 3 hours under N$_2$, sonicating every hour for 10 minutes to re-disperse organic droplets. Organic solvents were removed *in vacuo* to yield an aqueous solution of PS(Nd(TTA)$_3$(bpy)$_2$).

6.6.2.2.7 PS(Er(TTA)$_3$(bpy))

Er(TTA)$_3$(bpy) (0.062 mmol) was dissolved in iPrOH:CHCl$_3$ (0.1:0.9 mL) with drops of ethanol, and added to the aqueous polystyrene solution (5 mL). The reaction mixture was sonicated to disperse the organic droplets for 10 minutes, and then stirred rapidly for 3 hours under N$_2$, sonicating after 1 and 3 hours for 10 minutes to re-disperse organic droplets. Organic solvents were removed *in vacuo* to yield an aqueous solution of PS(Er(TTA)$_3$(bpy)).

6.6.2.3 General procedure for silica coating

Polystyrene(Ln) (4 mL, approx) was dispersed in iPrOH (200 mL), H_2O (38 mL), and NH_4OH (5 mL) under N$_2$. The reaction mixture was stirred rapidly with dropwise addition of TEOS (2 mL, 8.96 mmol) over several minutes, and then stirred for a further hour. After this time the nanoparticles were collected *via* centrifugation (30 minutes, 4.4 rpm), washed several times with water and ethanol until washings no longer fluoresced under a UV lamp, before being dried under vacuum in a desiccator to yield **PS(Ln)@SiO_2** *(Where Ln = lanthanide complex).*

6.7 References

1. F. Cotton and G. Wilkinson, in *Advanced Inorganic Chemistry*, Wiley, US, 5th edn., 1988, pp. 955–962.
2. N. Greenwood, *Chemistry of the Elements*, Butterworth-Heinemann, Oxford, 2nd edn., 1997.
3. E. G. Moore, A. P. S. Samuel and K. N. Raymond, *Acc. Chem. Res.*, 2009, **42**, 542–552.
4. J.-C. G. Bünzli, *Chem. Rev.*, 2010, **110**, 2729–2755.
5. J.-C. G. Bünzli, *J. Lumin.*, 2016, **170**, 866–878.
6. J. A. Cotruvo, *ACS Cent. Sci.*, 2019, **5**, 1496–1506.
7. S. V. Eliseeva and J.-C. G. Bünzli, *Chem. Soc. Rev.*, 2010, **39**, 189–227.
8. P. Dorenbos, *J. Lumin.*, 2000, **91**, 91–106.
9. S. I. Weissman, *J. Chem. Phys.*, 1942, **10**, 214–217.
10. C. Piguet and J.-C. G. Bünzli, *Chem. Soc. Rev.*, 2005, **34**, 1048–1077.
11. J.-C. G. Bünzli and S. V. Eliseeva, in *Lanthanide Luminescence*, eds. P. Hänninen and H. Härmä, Springer Berlin Heidelberg, Berlin, Heidelberg, 2010, vol. 7, pp. 1–45.
12. M. H. V. Werts, R. T. F. Jukes and J. W. Verhoeven, *Phys. Chem. Chem. Phys.*, 2002, **4**, 1542–1548.
13. S. J. Strickler and R. A. Berg, *J. Chem. Phys.*, 1962, **37**, 814–822.
14. L. U. Khan, H. F. Brito, J. Hölsä, K. R. Pirota, D. Muraca, M. C. F. C. Felinto, E. E. S. Teotonio and O. L. Malta, *Inorg. Chem.*, 2014, **53**, 12902–12910.
15. M. F. Hazenkamp and G. Blasse, *Chem. Mater.*, 1990, **2**, 105–110.
16. A. Beeby, L. M. Bushby, D. Maffeo and J. A. G. Williams, *J. Chem. Soc. Dalton Trans.*, 2002, 48–54.
17. H. F. Brito, O. M. L. Malta, M. C. F. C. Felinto and E. E. de S. Teotonio, in *PATAI'S Chemistry of Functional Groups*, Wiley, USA, 2010.
18. J. E. Jones and S. J. A. Pope, *Dalton Trans.*, 2009, 8421–8425.
19. Z. Ye, M. Tan, G. Wang and J. Yuan, *J. Mater. Chem.*, 2004, **14**, 851–856.
20. H. Härmä, C. Graf and P. Hänninen, *J. Nanoparticle Res.*, 2008, **10**, 1221–1224.

21. J. Yang, S. Sandoval, J. G. Alfaro, S. Aschemeyer, A. Liberman, D. T. Martin, M. Makale, A. C. Kummel and W. C. Trogler, *J. Biomed. Opt.*, 2011, **16**, 066012.
22. A. V. S. Lourenço, C. A. Kodaira, E. M. Ramos-Sanchez, M. C. F. C. Felinto, H. Goto, M. Gidlund, O. L. Malta and H. F. Brito, *J. Inorg. Biochem.*, 2013, **123**, 11–17.
23. R. A. Sá Ferreira, S. S. Nobre, C. M. Granadeiro, H. I. S. Nogueira, L. D. Carlos and O. L. Malta, *J. Lumin.*, 2006, **121**, 561–567.
24. J. Desbiens, B. Bergeron, M. Patry and A. M. Ritcey, *J. Colloid Interface Sci.*, 2012, **376**, 12–19.
25. T. Aikawa, A. Mizuno, M. Kohri, T. Taniguchi, K. Kishikawa and T. Nakahira, *Colloids Surf. B Biointerfaces*, 2016, **145**, 152–159.
26. M. Cardoso Dos Santos, A. Runser, H. Bartenlian, A. M. Nonat, L. J. Charbonnière, A. S. Klymchenko, N. Hildebrandt and A. Reisch, *Chem. Mater.*, 2019, **31**, 4034–4041.
27. S. Qi and W. Yin, *J. Mater. Sci.*, 2011, **46**, 5288–5293.
28. C. M. Janczak, I. A. C. Calderon, Z. Mokhtari and C. A. Aspinwall, *ACS Appl. Mater. Interfaces*, 2018, **10**, 4953–4960.
29. H. Zhang, H. Song, H. Yu, X. Bai, S. Li, G. Pan, Q. Dai, T. Wang, W. Li, S. Lu, X. Ren and H. Zhao, *J. Phys. Chem. C*, 2007, **111**, 6524–6527.
30. L. G. Klapshina, W. E. Douglas, I. S. Grigoryev, E. Y. Ladilina, M. V. Shirmanova, S. A. Mysyagin, I. V. Balalaeva and E. V. Zagaynova, *Chem. Commun.*, 2010, **46**, 8398–8400.
31. J. S. Ananta, B. Godin, R. Sethi, L. Moriggi, X. Liu, R. E. Serda, R. Krishnamurthy, R. Muthupillai, R. D. Bolskar, L. Helm, M. Ferrari, L. J. Wilson and P. Decuzzi, *Nat. Nanotechnol.*, 2010, **5**, 815–821.
32. A. L. Doiron, K. Chu, A. Ali and L. Brannon-Peppas, *Proc. Natl. Acad. Sci.*, 2008, **105**, 17232–17237.
33. L. G. Klapshina, W. E. Douglas, I. S. Grigoryev, A. I. Korytin, S. A. Lavrentiev, M. A. Lopatin, A. Y. Lukyanov, V. V. Semenov, P. Gerbier and V. M. Treushnikov, *J. Mater. Chem.*, 2009, **19**, 3668–3676.
34. Y. Kobayashi, H. Morimoto, T. Nakagawa, Y. Kubota, K. Gonda and N. Ohuchi, *ISRN Nanotechnol.*, 2013, **2013**, e908614.
35. N. Gupta, A. Shrivastava and R. K. Sharma, *Int. J. Nanomedicine*, 2012, **2012:7**, 5491–5500.

36. G. Singh, B. H. McDonagh, S. Hak, D. Peddis, S. Bandopadhyay, I. Sandvig, A. Sandvig and W. R. Glomm, *J. Mater. Chem. B*, 2017, **5**, 418–422.
37. L.-Y. Zhang, Y.-J. Hou, M. Pan, L. Chen, Y.-X. Zhu, S.-Y. Yin, G. Shao and C.-Y. Su, *Dalton Trans.*, 2015, **44**, 15212–15219.
38. S. J. Lyle and A. D. Witts, *Inorganica Chim. Acta*, 1971, **5**, 481–484.
39. SPA Bead Technology PerkinElmer, https://www.perkinelmer.com/uk/lab-products-and-services/application-support-knowledgebase/radiometric/spa-beads.html, (accessed 14 November 2021).
40. V. de Zea Bermudez, L. D. Carlos, M. C. Duarte, M. M. Silva, C. J. R. Silva, M. J. Smith, M. Assunção and L. Alcácer, *J. Alloys Compd.*, 1998, **275–277**, 21–26.
41. K. Binnemans, *Coord. Chem. Rev.*, 2015, **295**, 1–45.
42. A. Ćirić, S. Stojadinović, M. Sekulić and M. D. Dramićanin, *J. Lumin.*, 2019, **205**, 351–356.
43. JOES – Judd-Ofelt from emission spectrum Software – OMAS Group, https://omasgroup.org/joes-software/, (accessed 11 January 2021).
44. K. Binnemans, in *Handbook on the Physics and Chemistry of Rare Earths*, eds. K. A. Gschneidner, J.-C. G. Bünzli and V. K. Pecharsky, Elsevier, Amsterdam, 2005, vol. 35, pp. 107–272.
45. A. Strasser and A. Vogler, *Inorganica Chim. Acta*, 2004, **357**, 2345–2348.
46. N. M. Shavaleev, S. J. A. Pope, Z. R. Bell, S. Faulkner and M. D. Ward, *Dalton Trans.*, 2003, 808–814.

7 Appendix

7.1 Emission Lifetime Decay Profiles

The emission lifetimes of **PS(Ox)@SiO$_2$** and the fluorophores in water frequently exhibited two components. The biexponential nature of the decay can clearly be seen for **PS(1)@SiO$_2$** from the decay curves (**Figure 7.1a**), when plotted *vs* the counts as a logarithmic scale. This curved logarithmic plot can be is compared to **1** in water (**Figure 7.1b**), which exhibited a mono-exponential decay, as shown by the straight line in the logarithmic plot.

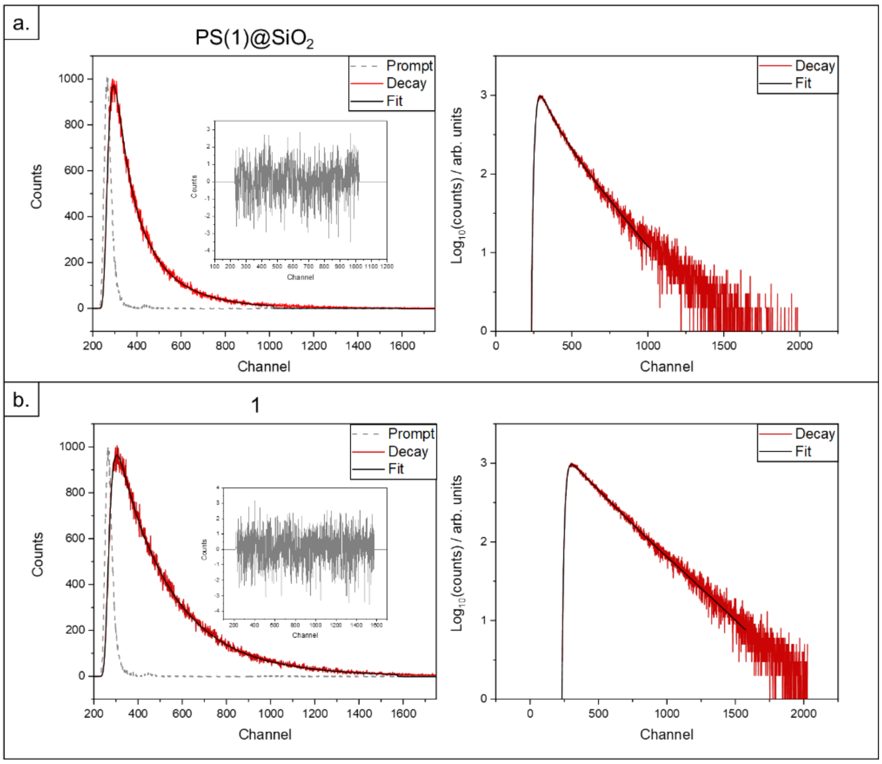

Figure 7.1 Emissive lifetime decay profile for **PS(1)@SiO$_2$** *(a)* and **1** in water *(b),* plotted as counts per channel *(left, inset shows residual counts)* and as a logarithmic scale *(right).*

Figure 7.2 shows a further example, where **PS(2)@SiO$_2$** and **2** in water both exhibited two component lifetimes, with the logarithmic plots both showing biexponential decay profiles.

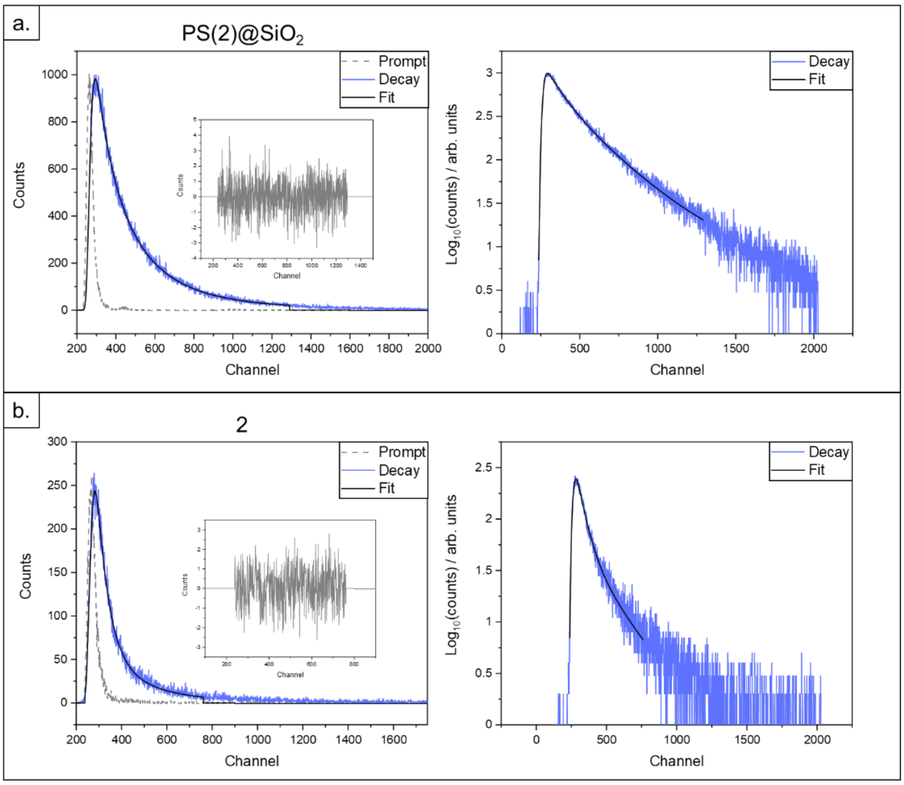

Figure 7.2 Emissive lifetime decay profile for **PS(2)@SiO₂** *(a)* and **2** in water *(b)*, plotted as counts per channel *(left, inset shows residual counts)* and as a logarithmic scale *(right)*.

7.2 X-ray Crystallography Data

7.2.1 5-(benzo[f]quinolin-3-yl)oxazole (1)

Table 7.1 Crystal data and structure refinement for **1**.

Compound	2018ncs0967
Formula	$C_{16}H_{10}N_2O$
***D*calc. / g cm⁻³**	1.447
***μ* /mm⁻¹**	0.093
Formula Weight	246.26
Colour	orange
Shape	cut blade
Size / mm³	0.180×0.160×0.090
T / K	100(2)
Crystal System	monoclinic
Space Group	$P2_{1/c}$
***a* / Å**	8.7924(2)
***b* / Å**	5.64640(10)
***c* / Å**	23.1073(5)
***α* / °**	90
***β* / °**	99.918(2)

γ / °	90
V / Å^3	1130.03(4)
Z	4
Z'	1
Wavelength / Å	0.71075
Radiation type	MoK$_\alpha$
Θ_{min} / °	2.352
Θ_{max} / °	28.699
Measured Refl.	14529
Independent Refl.	2912
Reflections with I > 2(I)	2404
R_{int}	0.0356
Parameters	172
Restraints	0
Largest Peak	0.387
Deepest Hole	-0.186
GooF	1.050
wR_2 (all data)	0.1186
wR_2	0.1114
R_1 (all data)	0.0541
R_1	0.0439

Table 7.2: Fractional Atomic Coordinates (×10^4) and Equivalent Isotropic Displacement Parameters (Å^2×10^3) for **1**. U_{eq} is defined as 1/3 of the trace of the orthogonalized U_{ij}.

Atom	X	y	z	U_{eq}
O(1)	-1774.7(10)	6097.2(16)	5660.8(4)	25.2(2)
N(1)	-3116.8(11)	3440(2)	5067.6(5)	25.3(2)
N(2)	1714.5(11)	2628.7(18)	5818.2(4)	21.6(2)
C(1)	-3130.0(14)	5468(2)	5322.7(5)	25.5(3)
C(2)	-1619.2(14)	2610(2)	5248.3(5)	24.1(3)
C(3)	-805.4(13)	4217(2)	5608.0(5)	21.8(3)
C(4)	782.0(14)	4372(2)	5919.8(5)	21.4(3)
C(5)	1263.9(14)	6283(2)	6299.2(5)	23.0(3)
C(6)	2770.4(14)	6374(2)	6577.2(5)	21.6(3)
C(7)	3807.1(13)	4587(2)	6476.5(5)	19.3(2)
C(8)	3216.1(13)	2733(2)	6088.6(5)	20.1(2)
C(9)	4223.9(14)	885(2)	5962.1(5)	22.8(3)
C(10)	5733.0(14)	890(2)	6207.8(5)	22.7(3)
C(11)	6382.2(13)	2716(2)	6605.9(5)	20.4(2)
C(12)	5426.5(13)	4574(2)	6745.5(5)	19.7(2)
C(13)	6086.7(14)	6321(2)	7147.0(5)	21.6(3)
C(14)	7625.9(14)	6240(2)	7394.7(5)	24.0(3)
C(15)	8575.2(14)	4430(2)	7247.2(5)	24.4(3)
C(16)	7959.9(14)	2692(2)	6860.4(5)	23.1(3)

Table 7.3 Anisotropic Displacement Parameters (×10^4) for **1**. The anisotropic displacement factor exponent takes the form: $-2\pi^2[h^2a^{*2} \times U_{11} + ... +2hka^* \times b^* \times U_{12}]$.

Atom	U_{11}	U_{22}	U_{33}	U_{23}	U_{13}	U_{12}
O(1)	20.1(4)	27.0(5)	27.0(5)	-2.6(4)	0.2(3)	0.8(3)
N(1)	19.2(5)	30.9(6)	25.3(5)	-1.0(4)	2.1(4)	-1.6(4)
N(2)	20.2(5)	22.1(5)	21.9(5)	0.7(4)	2.0(4)	-1.9(4)
C(1)	18.4(6)	32.0(7)	24.6(6)	-0.1(5)	-0.7(4)	-0.8(5)
C(2)	19.7(6)	26.7(6)	25.7(6)	-1.0(5)	3.1(4)	-1.4(5)
C(3)	19.2(6)	24.2(6)	22.4(6)	1.1(5)	4.8(4)	-0.4(5)
C(4)	20.2(6)	23.7(6)	20.4(6)	1.6(5)	3.9(4)	-3.0(5)
C(5)	19.9(6)	24.2(6)	25.2(6)	-1.3(5)	4.7(5)	1.0(5)

C(6)	21.2(6)	21.0(6)	22.7(6)	-2.7(5)	3.9(4)	-2.4(5)
C(7)	19.2(5)	19.7(6)	19.0(5)	1.8(4)	3.6(4)	-2.4(4)
C(8)	20.2(6)	20.4(6)	19.6(5)	1.8(4)	2.9(4)	-2.2(4)
C(9)	25.9(6)	19.7(6)	22.5(6)	-1.1(5)	2.9(5)	-2.3(5)
C(10)	24.4(6)	19.9(6)	24.1(6)	-0.9(5)	4.6(5)	1.8(5)
C(11)	20.6(6)	21.3(6)	19.2(5)	2.7(4)	3.2(4)	-0.6(4)
C(12)	19.6(6)	20.7(6)	18.8(5)	2.6(4)	3.7(4)	-1.5(4)
C(13)	20.5(6)	21.5(6)	23.0(6)	-1.2(5)	4.3(4)	-0.3(4)
C(14)	22.4(6)	26.0(6)	23.0(6)	-1.5(5)	2.3(4)	-5.1(5)
C(15)	17.3(6)	30.5(7)	24.5(6)	2.1(5)	1.1(4)	-1.4(5)
C(16)	21.1(6)	23.7(6)	24.5(6)	2.7(5)	3.9(4)	2.5(5)

Table 7.4 Bond Lengths in (Å) for **1**.

Atom	**Atom**	**Length/ Å**
O(1)	**C(1)**	1.3550(14)
O(1)	**C(3)**	1.3797(15)
N(1)	**C(1)**	1.2891(17)
N(1)	**C(2)**	1.3922(16)
N(2)	**C(4)**	1.3275(16)
N(2)	**C(8)**	1.3612(15)
C(2)	**C(3)**	1.3500(17)
C(3)	**C(4)**	1.4588(16)
C(4)	**C(5)**	1.4089(17)
C(5)	**C(6)**	1.3699(16)
C(6)	**C(7)**	1.4057(17)
C(7)	**C(8)**	1.4173(16)
C(7)	**C(12)**	1.4522(16)
C(8)	**C(9)**	1.4314(17)
C(9)	**C(10)**	1.3503(17)
C(10)	**C(11)**	1.4331(17)
C(11)	**C(12)**	1.4157(17)
C(11)	**C(16)**	1.4103(16)
C(12)	**C(13)**	1.4089(16)
C(13)	**C(14)**	1.3763(16)
C(14)	**C(15)**	1.3981(18)
C(15)	**C(16)**	1.3740(17)

Table 7.5 Bond Angles in (°) for **1**.

Atom	**Atom**	**Atom**	**Angle / °**
C(1)	**O(1)**	**C(3)**	104.04(10)
C(1)	**N(1)**	**C(2)**	104.15(10)
C(4)	**N(2)**	**C(8)**	117.81(10)
N(1)	**C(1)**	**O(1)**	114.86(11)
C(3)	**C(2)**	**N(1)**	109.38(11)
O(1)	**C(3)**	**C(4)**	117.61(10)
C(2)	**C(3)**	**O(1)**	107.57(10)
C(2)	**C(3)**	**C(4)**	134.81(12)
N(2)	**C(4)**	**C(3)**	115.84(11)
N(2)	**C(4)**	**C(5)**	123.32(11)
C(5)	**C(4)**	**C(3)**	120.84(11)
C(6)	**C(5)**	**C(4)**	118.91(11)
C(5)	**C(6)**	**C(7)**	119.84(11)
C(6)	**C(7)**	**C(8)**	117.21(11)
C(6)	**C(7)**	**C(12)**	123.28(10)
C(8)	**C(7)**	**C(12)**	119.51(10)
N(2)	**C(8)**	**C(7)**	122.90(11)
N(2)	**C(8)**	**C(9)**	117.41(11)

C(7)	**C(8)**	**C(9)**	119.68(11)
C(10)	**C(9)**	**C(8)**	120.69(11)
C(9)	**C(10)**	**C(11)**	121.70(11)
C(12)	**C(11)**	**C(10)**	119.53(11)
C(16)	**C(11)**	**C(10)**	121.02(11)
C(16)	**C(11)**	**C(12)**	119.45(11)
C(11)	**C(12)**	**C(7)**	118.87(10)
C(13)	**C(12)**	**C(7)**	122.73(11)
C(13)	**C(12)**	**C(11)**	118.39(11)
C(14)	**C(13)**	**C(12)**	120.97(11)
C(13)	**C(14)**	**C(15)**	120.56(11)
C(16)	**C(15)**	**C(14)**	119.72(11)
C(15)	**C(16)**	**C(11)**	120.89(11)

Table 7.6 Torsion Angles (°) for **1**.

Atom	**Atom**	**Atom**	**Atom**	**Angle / ˚**
O(1)	**C(3)**	**C(4)**	**N(2)**	-174.38(10)
O(1)	**C(3)**	**C(4)**	**C(5)**	5.19(17)
N(1)	**C(2)**	**C(3)**	**O(1)**	-0.06(14)
N(1)	**C(2)**	**C(3)**	**C(4)**	-178.79(12)
N(2)	**C(4)**	**C(5)**	**C(6)**	0.39(19)
N(2)	**C(8)**	**C(9)**	**C(10)**	179.06(11)
C(1)	**O(1)**	**C(3)**	**C(2)**	0.10(13)
C(1)	**O(1)**	**C(3)**	**C(4)**	179.08(10)
C(1)	**N(1)**	**C(2)**	**C(3)**	0.00(14)
C(2)	**N(1)**	**C(1)**	**O(1)**	0.08(14)
C(2)	**C(3)**	**C(4)**	**N(2)**	4.2(2)
C(2)	**C(3)**	**C(4)**	**C(5)**	-176.19(13)
C(3)	**O(1)**	**C(1)**	**N(1)**	-0.12(14)
C(3)	**C(4)**	**C(5)**	**C(6)**	-179.14(11)
C(4)	**N(2)**	**C(8)**	**C(7)**	1.03(17)
C(4)	**N(2)**	**C(8)**	**C(9)**	-178.10(10)
C(4)	**C(5)**	**C(6)**	**C(7)**	0.58(18)
C(5)	**C(6)**	**C(7)**	**C(8)**	-0.70(17)
C(5)	**C(6)**	**C(7)**	**C(12)**	178.91(11)
C(6)	**C(7)**	**C(8)**	**N(2)**	-0.11(17)
C(6)	**C(7)**	**C(8)**	**C(9)**	179.00(10)
C(6)	**C(7)**	**C(12)**	**C(11)**	-178.72(11)
C(6)	**C(7)**	**C(12)**	**C(13)**	2.12(18)
C(7)	**C(8)**	**C(9)**	**C(10)**	-0.09(18)
C(7)	**C(12)**	**C(13)**	**C(14)**	179.69(11)
C(8)	**N(2)**	**C(4)**	**C(3)**	178.38(10)
C(8)	**N(2)**	**C(4)**	**C(5)**	-1.17(17)
C(8)	**C(7)**	**C(12)**	**C(11)**	0.88(16)
C(8)	**C(7)**	**C(12)**	**C(13)**	-178.28(11)
C(8)	**C(9)**	**C(10)**	**C(11)**	0.57(18)
C(9)	**C(10)**	**C(11)**	**C(12)**	-0.30(18)
C(9)	**C(10)**	**C(11)**	**C(16)**	179.79(11)
C(10)	**C(11)**	**C(12)**	**C(7)**	-0.43(16)
C(10)	**C(11)**	**C(12)**	**C(13)**	178.77(11)
C(10)	**C(11)**	**C(16)**	**C(15)**	-179.25(11)
C(11)	**C(12)**	**C(13)**	**C(14)**	0.53(18)
C(12)	**C(7)**	**C(8)**	**N(2)**	-179.73(10)
C(12)	**C(7)**	**C(8)**	**C(9)**	-0.63(17)
C(12)	**C(11)**	**C(16)**	**C(15)**	0.84(18)
C(12)	**C(13)**	**C(14)**	**C(15)**	0.77(19)
C(13)	**C(14)**	**C(15)**	**C(16)**	-1.28(19)
C(14)	**C(15)**	**C(16)**	**C(11)**	0.46(19)

C(16)	**C(11)**	**C(12)**	**C(7)**	179.48(10)
C(16)	**C(11)**	**C(12)**	**C(13)**	-1.32(17)

Table 7.7 Hydrogen Fractional Atomic Coordinates (×10^4) and Equivalent Isotropic Displacement Parameters (Å^2×10^3) for **1**. U_{eq} is defined as 1/3 of the trace of the orthogonalised U_{ij}.

Atom	**x**	**y**	**z**	**U_{eq}**
H(1)	-4021.67	6446.41	5277.16	31
H(2)	-1230.72	1140.64	5135.94	29
H(5)	555.84	7488.82	6361.26	28
H(6)	3113.75	7641.64	6837.39	26
H(9)	3826.89	-358.72	5702.52	27
H(10)	6380.99	-347.89	6114.3	27
H(13)	5460.22	7573.05	7248.28	26
H(14)	8046.81	7423.32	7668.24	29
H(15)	9641.16	4402.58	7413.65	29
H(16)	8605.77	1458.46	6763.11	28

7.2.2 5-(10-chloroanthracen-9-yl)oxazole (2)

Table 7.8 Crystal data and structure refinement for **2**.

Compound	**2018ncs0694**
Formula	$C_{17}H_{10}ClNO$
$D_{calc.}$/ g cm^{-3}	1.534
μ/mm^{-1}	2.725
Formula Weight	279.71
Colour	yellow
Shape	needle
Size / mm^3	0.320×0.030×0.015
T / K	100(2)
Crystal System	monoclinic
Space Group	$P2_1/n$
a / Å	18.1934(8)
b / Å	3.8659(2)
c / Å	19.1544(8)
α / °	90
β / °	115.941(5)
γ / °	90
V / Å^3	1211.46(11)
Z	4
Z'	1
Wavelength / Å	1.54178
Radiation type	CuK$_\alpha$
Θ_{min} / °	2.795
Θ_{max} / °	68.246
Measured Refl.	9872
Independent Refl.	2223
Reflections with I > 2(I)	1929
R_{int}	0.0851
Parameters	181
Restraints	0
Largest Peak	0.868
Deepest Hole	-0.724
GooF	1.087

wR_2 (all data)	0.2121
wR_2	0.1996
R_1 (all data)	0.0809
R_1	0.0740

Table 7.9 Fractional Atomic Coordinates (×10^4) and Equivalent Isotropic Displacement Parameters (Å^2×10^3) for **2**. U_{eq} is defined as 1/3 of the trace of the orthogonalized U_{ij}.

Atom	**x**	**y**	**z**	**U_{eq}**
Cl(1)	3487.2(4)	4320(2)	3709.4(4)	33.0(3)
O(1)	1096.9(12)	4803(5)	5575.4(12)	26.8(5)
N(1)	1435.2(15)	6916(7)	6758.4(14)	30.7(6)
C(1)	3029.0(18)	4893(8)	4331.0(17)	24.0(6)
C(2)	2252.2(17)	6384(7)	4036.0(17)	23.6(6)
C(3)	1815.1(17)	7384(8)	3244.2(16)	25.5(7)
C(4)	1062.0(19)	8878(8)	2978.3(17)	26.8(7)
C(5)	708.1(18)	9500(8)	3487.8(17)	27.9(7)
C(6)	1110.1(17)	8590(8)	4255.0(16)	24.8(6)
C(7)	1884.9(16)	6890(8)	4556.5(16)	23.0(6)
C(8)	2295.1(18)	5780(7)	5336.0(16)	23.3(7)
C(9)	3080.7(17)	4264(7)	5619.4(16)	22.7(6)
C(10)	3517.0(17)	3057(8)	6400.8(16)	25.3(6)
C(11)	4268.7(18)	1547(8)	6653.1(17)	27.3(7)
C(12)	4645.9(18)	1230(8)	6151.6(18)	29.7(7)
C(13)	4258.8(17)	2336(8)	5405.1(17)	27.0(7)
C(14)	3462.5(17)	3852(7)	5110.1(16)	23.9(6)
C(15)	1890.0(17)	6105(7)	5852.3(17)	23.5(6)
C(16)	2087.5(18)	7347(8)	6565.5(16)	27.5(7)
C(17)	887.2(19)	5393(8)	6163.2(18)	30.1(7)

Table 7.10 Anisotropic Displacement Parameters (×10^4) for **2**. The anisotropic displacement factor exponent takes the form: $-2\pi^2[h^2a^{*2} \times U_{11} + ... + 2hka^* \times b^* \times U_{12}]$.

Atom	**U_{11}**	**U_{22}**	**U_{33}**	**U_{23}**	**U_{13}**	**U_{12}**
Cl(1)	30.3(5)	45.7(6)	29.2(5)	1.6(3)	18.7(4)	5.4(3)
O(1)	23.1(10)	32.3(12)	28.5(11)	-2.6(8)	14.5(8)	-1.5(8)
N(1)	34.3(14)	33.9(15)	28.6(13)	-1.4(11)	18.2(11)	-0.8(11)
C(1)	24.8(14)	24.8(15)	26.0(15)	-0.8(11)	14.5(12)	-2.5(11)
C(2)	25.1(14)	17.7(14)	28.5(15)	-2.4(11)	12.1(12)	-3.7(11)
C(3)	28.2(14)	25.6(16)	26.5(14)	-1.0(11)	15.3(12)	0.4(11)
C(4)	28.7(15)	25.3(16)	23.3(14)	2.2(11)	8.6(12)	-1.5(12)
C(5)	24.1(15)	30.0(17)	29.0(16)	0.8(12)	11.2(13)	0.1(11)
C(6)	24.3(14)	26.7(15)	25.3(14)	-1.5(11)	12.5(12)	-1.5(11)
C(7)	23.2(13)	20.5(14)	26.4(14)	-1.4(11)	12.0(11)	-2.5(11)
C(8)	26.3(14)	20.1(15)	24.7(14)	-1.8(10)	12.1(12)	-3.3(11)
C(9)	22.4(14)	20.2(15)	25.4(15)	-0.9(11)	10.4(12)	-2.9(10)
C(10)	26.0(14)	23.5(15)	26.5(14)	-1.7(11)	11.6(12)	-2.1(12)
C(11)	25.8(14)	23.6(15)	26.9(15)	-1.7(11)	6.4(12)	-3.9(12)
C(12)	24.9(14)	25.8(16)	35.0(17)	-0.8(12)	10.0(13)	1.6(12)
C(13)	26.3(14)	25.8(16)	31.6(15)	-3.0(12)	15.1(12)	-1.2(11)
C(14)	24.4(14)	20.2(15)	27.0(15)	-2.8(11)	10.9(12)	-3.1(11)
C(15)	21.6(13)	20.7(15)	28.4(15)	2.3(11)	11.1(12)	-0.7(11)
C(16)	27.3(14)	28.9(17)	27.7(14)	1.2(12)	13.5(12)	-0.8(12)
C(17)	29.2(16)	35.3(18)	33.1(17)	0.4(13)	20.2(14)	0.0(12)

Table 7.11 Bond Lengths in (Å) for **2**.

Atom	Atom	Length / Å
Cl(1)	C(1)	1.741(3)
O(1)	C(15)	1.395(3)
O(1)	C(17)	1.357(4)
N(1)	C(16)	1.399(4)
N(1)	C(17)	1.283(4)
C(1)	C(2)	1.397(4)
C(1)	C(14)	1.408(4)
C(2)	C(3)	1.424(4)
C(2)	C(7)	1.436(4)
C(3)	C(4)	1.364(4)
C(4)	C(5)	1.405(4)
C(5)	C(6)	1.370(4)
C(6)	C(7)	1.428(4)
C(7)	C(8)	1.413(4)
C(8)	C(9)	1.415(4)
C(8)	C(15)	1.475(4)
C(9)	C(10)	1.431(4)
C(9)	C(14)	1.433(4)
C(10)	C(11)	1.366(4)
C(11)	C(12)	1.409(4)
C(12)	C(13)	1.357(4)
C(13)	C(14)	1.430(4)
C(15)	C(16)	1.340(4)

Table 7.12 Bond Angles in (°) for **2**.

Atom	Atom	Atom	Angle /˚
C(17)	O(1)	C(15)	104.1(2)
C(17)	N(1)	C(16)	103.8(2)
C(2)	C(1)	Cl(1)	118.6(2)
C(2)	C(1)	C(14)	123.1(3)
C(14)	C(1)	Cl(1)	118.4(2)
C(1)	C(2)	C(3)	122.5(3)
C(1)	C(2)	C(7)	118.1(3)
C(3)	C(2)	C(7)	119.3(3)
C(4)	C(3)	C(2)	121.0(3)
C(3)	C(4)	C(5)	120.3(3)
C(6)	C(5)	C(4)	120.6(3)
C(5)	C(6)	C(7)	121.4(3)
C(6)	C(7)	C(2)	117.3(2)
C(8)	C(7)	C(2)	120.1(3)
C(8)	C(7)	C(6)	122.6(3)
C(7)	C(8)	C(9)	120.6(3)
C(7)	C(8)	C(15)	119.7(2)
C(9)	C(8)	C(15)	119.7(2)
C(8)	C(9)	C(10)	122.8(3)
C(8)	C(9)	C(14)	119.6(2)
C(10)	C(9)	C(14)	117.6(3)
C(11)	C(10)	C(9)	121.4(3)
C(10)	C(11)	C(12)	120.5(3)
C(13)	C(12)	C(11)	120.5(3)
C(12)	C(13)	C(14)	120.9(3)
C(1)	C(14)	C(9)	118.5(3)
C(1)	C(14)	C(13)	122.5(3)
C(13)	C(14)	C(9)	119.1(3)
O(1)	C(15)	C(8)	116.8(2)

C(16)	C(15)	O(1)	106.8(2)
C(16)	C(15)	C(8)	136.4(3)
C(15)	C(16)	N(1)	110.3(3)
N(1)	C(17)	O(1)	115.0(3)

Table 7.13 Torsion Angles (°) for **2**.

Atom	**Atom**	**Atom**	**Atom**	**Angle/˚**
Cl(1)	C(1)	C(2)	C(3)	1.4(4)
Cl(1)	C(1)	C(2)	C(7)	-179.1(2)
Cl(1)	C(1)	C(14)	C(9)	-178.9(2)
Cl(1)	C(1)	C(14)	C(13)	-0.3(4)
O(1)	C(15)	C(16)	N(1)	-0.6(3)
C(1)	C(2)	C(3)	C(4)	-179.1(3)
C(1)	C(2)	C(7)	C(6)	176.7(3)
C(1)	C(2)	C(7)	C(8)	-2.2(4)
C(2)	C(1)	C(14)	C(9)	1.6(4)
C(2)	C(1)	C(14)	C(13)	-179.8(3)
C(2)	C(3)	C(4)	C(5)	0.8(4)
C(2)	C(7)	C(8)	C(9)	2.0(4)
C(2)	C(7)	C(8)	C(15)	-176.0(2)
C(3)	C(2)	C(7)	C(6)	-3.8(4)
C(3)	C(2)	C(7)	C(8)	177.3(3)
C(3)	C(4)	C(5)	C(6)	-0.5(5)
C(4)	C(5)	C(6)	C(7)	-2.0(5)
C(5)	C(6)	C(7)	C(2)	4.2(4)
C(5)	C(6)	C(7)	C(8)	-177.0(3)
C(6)	C(7)	C(8)	C(9)	-176.8(3)
C(6)	C(7)	C(8)	C(15)	5.1(4)
C(7)	C(2)	C(3)	C(4)	1.4(4)
C(7)	C(8)	C(9)	C(10)	-179.2(3)
C(7)	C(8)	C(9)	C(14)	0.0(4)
C(7)	C(8)	C(15)	O(1)	50.2(4)
C(7)	C(8)	C(15)	C(16)	-130.9(4)
C(8)	C(9)	C(10)	C(11)	178.8(3)
C(8)	C(9)	C(14)	C(1)	-1.8(4)
C(8)	C(9)	C(14)	C(13)	179.6(3)
C(8)	C(15)	C(16)	N(1)	-179.6(3)
C(9)	C(8)	C(15)	O(1)	-127.9(3)
C(9)	C(8)	C(15)	C(16)	51.0(5)
C(9)	C(10)	C(11)	C(12)	1.9(5)
C(10)	C(9)	C(14)	C(1)	177.4(3)
C(10)	C(9)	C(14)	C(13)	-1.2(4)
C(10)	C(11)	C(12)	C(13)	-1.8(5)
C(11)	C(12)	C(13)	C(14)	0.1(5)
C(12)	C(13)	C(14)	C(1)	-177.3(3)
C(12)	C(13)	C(14)	C(9)	1.3(4)
C(14)	C(1)	C(2)	C(3)	-179.1(3)
C(14)	C(1)	C(2)	C(7)	0.4(4)
C(14)	C(9)	C(10)	C(11)	-0.4(4)
C(15)	O(1)	C(17)	N(1)	0.9(3)
C(15)	C(8)	C(9)	C(10)	-1.1(4)
C(15)	C(8)	C(9)	C(14)	178.0(2)
C(16)	N(1)	C(17)	O(1)	-1.2(4)
C(17)	O(1)	C(15)	C(8)	179.1(2)
C(17)	O(1)	C(15)	C(16)	-0.1(3)
C(17)	N(1)	C(16)	C(15)	1.1(4)

Table 7.14 Hydrogen Fractional Atomic Coordinates (×10^4) and Equivalent Isotropic Displacement Parameters (Å^2×10^3) for **2**. U_{eq} is defined as 1/3 of the trace of the orthogonalised U_{ij}.

Atom	**x**	**y**	**z**	U_{eq}
H(3)	2051.41	7003.8	2895.87	31
H(4)	775.59	9501.73	2446.58	32
H(5)	185.31	10560.63	3298.63	33
H(6)	868.33	9100.73	4593.55	30
H(10)	3278.89	3311.78	6751.34	30
H(11)	4538.86	704.62	7170.14	33
H(12)	5175.32	233.86	6337.49	36
H(13)	4520.63	2099.34	5073.7	32
H(16)	2597.5	8372.48	6893.01	33
H(17)	372.63	4727.76	6136.09	36

7.2.3 5-(4-(pyrrolidin-1-yl)phenyl)oxazole (7)

Table 7.15 Crystal data and structure refinement for **7**.

Compound	**2018ncs0695**
Formula	$C_{13}H_{14}N_2O$
$D_{calc.}$/ g cm^{-3}	1.303
μ / mm^{-1}	0.669
Formula Weight	214.26
Colour	orange
Shape	cut block
Size / mm^3	0.160×0.070×0.030
T / K	100(2)
Crystal System	orthorhombic
Flack Parameter	0.05(11)
Hooft Parameter	0.08(8)
Space Group	$P2_12_12_1$
a / Å	6.41320(10)
b / Å	7.34060(10)
c / Å	23.2065(3)
α / °	90
β / °	90
γ / °	90
V / Å^3	1092.49(3)
Z	4
Z'	1
Wavelength / Å	1.54178
Radiation type	CuK$_\alpha$
Θ_{min} / °	3.809
Θ_{max} / °	68.231
Measured Refl.	11764
Independent Refl.	1997
Reflections with I > 2(I)	1943
R_{int}	0.0315
Parameters	164
Restraints	95
Largest Peak	0.094
Deepest Hole	-0.187

GooF	1.047
wR_2 (all data)	0.0715
wR_2	0.0709
R_1 (all data)	0.0289
R_1	0.0281

Table 7.16 Fractional Atomic Coordinates (×10^4) and Equivalent Isotropic Displacement Parameters (Å^2×10^3) for **7**. U_{eq} is defined as 1/3 of the trace of the orthogonalized U_{ij}.

Atom	x	y	z	U_{eq}
O(1)	1163.9(18)	2211.8(17)	4103.3(5)	37.2(3)
N(2)	4489(2)	2600(2)	1491.5(6)	30.5(3)
N(1)	-1903(3)	3335(2)	4381.1(6)	38.6(4)
C(7)	3436(3)	2627(2)	2003.1(7)	27.5(3)
C(6)	1509(3)	3531(2)	2058.2(7)	29.3(4)
C(4)	1295(3)	2741(2)	3070.0(7)	28.0(4)
C(9)	3201(3)	1829(2)	3015.1(7)	29.7(4)
C(8)	4247(3)	1759(2)	2496.9(7)	29.9(4)
C(5)	483(3)	3586(2)	2579.5(7)	29.6(4)
C(3)	193(3)	2875(2)	3615.1(7)	30.0(4)
C(2)	-1663(3)	3551(3)	3784.9(7)	35.2(4)
C(13)	3684(3)	3342(3)	951.6(7)	34.7(4)
C(10)	6485(3)	1683(3)	1415.9(7)	35.7(4)
C(1)	-203(3)	2549(3)	4538.3(7)	38.6(4)
C(12B)	5195(4)	2610(4)	497.7(12)	39.2(7)
C(11B)	7221(4)	2337(4)	829.2(10)	38.8(7)
C(11)	6530(50)	1490(40)	761(8)	54(6)
C(12)	5580(50)	3290(40)	570(13)	59(8)

Table 7.17 Anisotropic Displacement Parameters (×10^4) for **7**. The anisotropic displacement factor exponent takes the form: $-2\pi^2[h^2a^{*2} \times U_{11} + ... + 2hka^* \times b^* \times U_{12}]$.

Atom	U_{11}	U_{22}	U_{33}	U_{23}	U_{13}	U_{12}
O(1)	39.2(7)	43.3(7)	29.0(6)	3.3(5)	-5.3(5)	5.0(6)
N(2)	28.1(7)	33.1(7)	30.4(7)	3.2(6)	-2.9(6)	3.5(6)
N(1)	43.3(9)	40.1(9)	32.4(8)	1.8(7)	1.2(7)	-0.3(8)
C(7)	26.7(8)	24.2(7)	31.7(8)	-0.3(7)	-5.4(6)	-1.4(7)
C(6)	29.6(9)	29.0(8)	29.3(8)	1.1(7)	-5.7(7)	2.2(7)
C(4)	28.6(8)	26.1(8)	29.4(8)	-1.6(6)	-5.0(6)	-1.6(7)
C(9)	29.1(8)	28.5(8)	31.4(8)	2.6(7)	-9.3(7)	0.0(7)
C(8)	25.2(8)	28.7(8)	35.7(9)	2.3(7)	-5.9(7)	1.8(7)
C(5)	27.4(9)	27.7(8)	33.6(8)	-1.8(7)	-5.8(7)	1.5(7)
C(3)	34.8(9)	26.5(8)	28.8(8)	0.4(6)	-7.6(7)	-1.7(7)
C(2)	35.9(10)	39.2(9)	30.3(9)	3.1(7)	-1.2(7)	2.5(8)
C(13)	34.1(9)	38.3(9)	31.6(9)	3.2(7)	-5.1(7)	1.8(8)
C(10)	27.5(9)	40.6(9)	38.9(10)	3.8(8)	-0.2(7)	3.2(8)
C(1)	46.0(11)	41.4(9)	28.4(8)	0.7(7)	-1.4(8)	0.2(9)
C(12B)	38.3(13)	46.0(15)	33.4(11)	1.7(11)	-0.3(9)	-1.5(12)
C(11B)	32.4(13)	45.4(15)	38.7(12)	5.3(11)	3.1(9)	1.7(11)
C(11)	36(13)	72(14)	53(8)	-6(11)	10(9)	4(11)
C(12)	55(13)	82(17)	40(12)	9(13)	6(10)	3(13)

Table 7.18 Bond Lengths in (Å) for **7**.

Atom	Atom	Length / Å
O(1)	C(3)	1.3815(19)
O(1)	C(1)	1.360(2)
N(2)	C(7)	1.366(2)

N(2)	C(13)	1.461(2)
N(2)	C(10)	1.457(2)
N(1)	C(2)	1.401(2)
N(1)	C(1)	1.287(2)
C(7)	C(6)	1.408(2)
C(7)	C(8)	1.410(2)
C(6)	C(5)	1.378(2)
C(4)	C(9)	1.399(2)
C(4)	C(5)	1.397(2)
C(4)	C(3)	1.453(2)
C(9)	C(8)	1.378(2)
C(3)	C(2)	1.348(3)
C(13)	C(12B)	1.528(3)
C(13)	C(12)	1.50(2)
C(10)	C(11B)	1.519(3)
C(10)	C(11)	1.527(19)
C(12B)	C(11B)	1.523(4)
C(11)	C(12)	1.52(2)

Table 7.19 Bond Angles in (°) for **7**.

Atom	Atom	Atom	Angle / ˚
C(1)	O(1)	C(3)	104.71(13)
C(7)	N(2)	C(13)	124.42(13)
C(7)	N(2)	C(10)	123.08(13)
C(10)	N(2)	C(13)	112.32(13)
C(1)	N(1)	C(2)	103.74(16)
N(2)	C(7)	C(6)	121.31(14)
N(2)	C(7)	C(8)	121.14(14)
C(6)	C(7)	C(8)	117.55(15)
C(5)	C(6)	C(7)	120.84(15)
C(9)	C(4)	C(3)	122.48(15)
C(5)	C(4)	C(9)	117.63(15)
C(5)	C(4)	C(3)	119.86(15)
C(8)	C(9)	C(4)	121.50(14)
C(9)	C(8)	C(7)	120.84(15)
C(6)	C(5)	C(4)	121.62(15)
O(1)	C(3)	C(4)	118.08(14)
C(2)	C(3)	O(1)	106.74(14)
C(2)	C(3)	C(4)	135.18(15)
C(3)	C(2)	N(1)	110.14(16)
N(2)	C(13)	C(12B)	103.64(16)
N(2)	C(13)	C(12)	102.1(12)
N(2)	C(10)	C(11B)	103.58(14)
N(2)	C(10)	C(11)	100.4(9)
N(1)	C(1)	O(1)	114.67(15)
C(11B)	C(12B)	C(13)	103.8(2)
C(10)	C(11B)	C(12B)	103.2(2)
C(12)	C(11)	C(10)	102(2)
C(13)	C(12)	C(11)	100.1(17)

Table 7.20 Torsion Angles (°) for **7**.

Atom	Atom	Atom	Atom	Angle / ˚
O(1)	C(3)	C(2)	N(1)	0.14(19)
N(2)	C(7)	C(6)	C(5)	-178.50(15)
N(2)	C(7)	C(8)	C(9)	178.41(15)
N(2)	C(13)	C(12B)	C(11B)	-27.1(3)

N(2)	C(13)	C(12)	C(11)	39(3)
N(2)	C(10)	C(11B)	C(12B)	-31.9(3)
N(2)	C(10)	C(11)	C(12)	38(3)
C(7)	N(2)	C(13)	C(12B)	-167.99(19)
C(7)	N(2)	C(13)	C(12)	169.5(15)
C(7)	N(2)	C(10)	C(11B)	-169.10(19)
C(7)	N(2)	C(10)	C(11)	160.8(14)
C(7)	C(6)	C(5)	C(4)	-0.6(2)
C(6)	C(7)	C(8)	C(9)	-1.2(2)
C(4)	C(9)	C(8)	C(7)	0.7(2)
C(4)	C(3)	C(2)	N(1)	-178.80(18)
C(9)	C(4)	C(5)	C(6)	0.0(2)
C(9)	C(4)	C(3)	O(1)	5.8(2)
C(9)	C(4)	C(3)	C(2)	-175.38(18)
C(8)	C(7)	C(6)	C(5)	1.1(2)
C(5)	C(4)	C(9)	C(8)	-0.1(2)
C(5)	C(4)	C(3)	O(1)	-172.38(14)
C(5)	C(4)	C(3)	C(2)	6.5(3)
C(3)	O(1)	C(1)	N(1)	0.1(2)
C(3)	C(4)	C(9)	C(8)	-178.31(15)
C(3)	C(4)	C(5)	C(6)	178.26(15)
C(2)	N(1)	C(1)	O(1)	0.0(2)
C(13)	N(2)	C(7)	C(6)	-5.3(2)
C(13)	N(2)	C(7)	C(8)	175.07(15)
C(13)	N(2)	C(10)	C(11B)	15.6(2)
C(13)	N(2)	C(10)	C(11)	-14.5(14)
C(13)	C(12B)	C(11B)	C(10)	36.7(3)
C(10)	N(2)	C(7)	C(6)	179.96(14)
C(10)	N(2)	C(7)	C(8)	0.3(3)
C(10)	N(2)	C(13)	C(12B)	7.2(2)
C(10)	N(2)	C(13)	C(12)	-15.3(15)
C(10)	C(11)	C(12)	C(13)	-48(3)
C(1)	O(1)	C(3)	C(4)	179.00(15)
C(1)	O(1)	C(3)	C(2)	-0.16(18)
C(1)	N(1)	C(2)	C(3)	-0.1(2)

Table 7.21 Hydrogen Fractional Atomic Coordinates (×10^4) and Equivalent Isotropic Displacement Parameters (Å^2×10^3) for **7**. U_{eq} is defined as 1/3 of the trace of the orthogonalised U_{ij}.

Atom	**x**	**y**	**z**	U_{eq}
H(6)	909.54	4110.03	1731.82	35
H(9)	3787.83	1245.86	3342.58	36
H(8)	5530.3	1117.57	2471.82	36
H(5)	-808.54	4213.72	2606	35
H(2)	-2662.34	4094.13	3536.44	42
H(13A)	3689.59	4690.05	957.88	42
H(13B)	2245.68	2910.35	877.65	42
H(13C)	3169.8	4603.04	1002.54	42
H(13D)	2546.03	2576.27	794.89	42
H(10A)	6310.99	342.52	1420.58	43
H(10B)	7480.59	2037.14	1721.94	43
H(10C)	6507.01	481.22	1609.7	43
H(10D)	7657.47	2434.1	1558.79	43
H(1)	75.02	2228.78	4927.46	46
H(12A)	4688.61	1444.3	335.27	47
H(12B)	5382.1	3497.43	180.62	47
H(11A)	8114.7	1413.93	640.24	47
H(11B)	8006.61	3493.72	862.11	47

H(11C)	7975.39	1353.31	616.36	64
H(11D)	5684.64	441.36	630.5	64
H(12C)	6525.18	4325.89	645.31	71
H(12D)	5196.77	3268.66	156.6	71

Table 7.22 Atomic Occupancies for all atoms that are not fully occupied in **7**.

Atom	Occupancy
H(13A)	0.904(8)
H(13B)	0.904(8)
H(13C)	0.096(8)
H(13D)	0.096(8)
H(10A)	0.904(8)
H(10B)	0.904(8)
H(10C)	0.096(8)
H(10D)	0.096(8)
C(12B)	0.904(8)
H(12A)	0.904(8)
H(12B)	0.904(8)
C(11B)	0.904(8)
H(11A)	0.904(8)
H(11B)	0.904(8)
C(11)	0.096(8)
H(11C)	0.096(8)
H(11D)	0.096(8)
C(12)	0.096(8)
H(12C)	0.096(8)
H(12D)	0.096(8)

7.3 TD-DFT

Table 7.23 TD-DFT data for **1**

#	State	Transition energy (nm)	Participating MO	Transition character
1	Singlet	346 (0.2608)[a]	HOMO→LUMO (0.61)[b] HOMO-1→LUMO (-0.23) HOMO-1→LUMO+1 (0.20) HOMO→LUMO+1 (0.17)	π→π*
2	Singlet	321 (0.3008)	HOMO-1→LUMO (0.57) HOMO→LUMO (0.29) HOMO→LUMO+1 (-0.28)	π→π*
3	Singlet	295 (0.0943)	HOMO-1→LUMO+1 (0.60) HOMO-1→LUMO (0.32) HOMO-2→LUMO (0.12)	π→π*
4	Singlet	286 (0.9360)	HOMO-1→LUMO+1 (0.63) HOMO→LUMO (-0.20) HOMO→LUMO+3 (-0.15) HOMO-2→LUMO (-0.13)	π→π*
5	Singlet	284 (0.0016)	HOMO-3 → LUMO (0.70)	π→π*
6	Singlet	263 (0.0387)	HOMO-1→LUMO (0.57) HOMO→LUMO+2 (0.22) HOMO-1→LUMO+2 (0.17) HOMO-2→LUMO+1 (0.16) HOMO-4→LUMO (-0.13) HOMO-1→LUMO+1 (0.12)	π→π*

			HOMO→LUMO+1 (-0.11)	
7	Singlet	253 (0.0001)	HOMO-1→LUMO+1 (0.69) HOMO-3→LUMO+2 (0.11)	n→π*
8	Singlet	252 (0.1650)	HOMO→LUMO+2 (0.58) HOMO-2→LUMO (-0.28) HOMO→LUMO+3 (0.16) HOMO-4→LUMO (-0.15) HOMO-4→LUMO+1 (0.12)	π→π*
9	Singlet	247 (0.0016)	HOMO-1→LUMO+1 (0.46) HOMO→LUMO+3 (0.35) HOMO-1→LUMO+2 (0.25) HOMO→LUMO+2 (-0.19) HOMO-2→LUMO (-0.18) HOMO-4→LUMO (-0.12)	π→π*
10	Singlet	241 (0.0161)	HOMO-2→LUMO+1 (0.41) HOMO-1→LUMO+2 (-0.38) HOMO-4→LUMO (0.32) HOMO→LUMO+2 (0.15) HOMO-1→LUMO+3 (-0.15) HOMO-4→LUMO+1 (0.11)	π→π*
11	Singlet	232 (0.0214)	HOMO-1→LUMO+2 (0.45) HOMO-4→LUMO (0.43); HOMO-4→LUMO+1 (-0.18) HOMO→LUMO+3 (-0.14) HOMO-1→LUMO+3 (-0.12) HOMO→LUMO+4 (-0.11) HOMO→LUMO+2 (0.10)	π→π*
12	Singlet	228 (0.2711)	HOMO→LUMO+3 (0.41) HOMO-4→LUMO+1 (0.27) HOMO-2→LUMO+1 (-0.27) HOMO-1→LUMO+3 (-0.26) HOMO-4→LUMO (0.24) HOMO-1→LUMO+1 (0.15) HOMO→LUMO+2 (-0.12)	π→π*
13	Singlet	223 (0.0000)	HOMO-5→LUMO (0.67) HOMO-5→LUMO+1 (-0.13) HOMO-5→LUMO+2 (-0.11) HOMO-5→LUMO+3 (0.11)	n→π*
14	Singlet	220 (0.0817)	HOMO-1→LUMO+3 (0.52) HOMO→LUMO+3 (0.26) HOMO-2→LUMO+2 (0.24) HOMO-4→LUMO (0.18) HOMO-6→LUMO (-0.12)	π→π*
15	Singlet	217 (0.0011)	HOMO→LUMO+5 (0.69)	π→π*
16	Singlet	214 (0.0724)	HOMO→LUMO+4 (0.62) HOMO-4→LUMO+1 (-0.22) HOMO-1→LUMO+4 (0.12) HOMO-6→LUMO+1 (-0.11)	π→π*
17	Singlet	212 (0.1299)	HOMO-4→LUMO+1 (0.50) HOMO→LUMO+4 (0.23) HOMO-1→LUMO+2 (0.20) HOMO→LUMO+3 (-0.18) HOMO-2→LUMO+2 (0.16) HOMO-6→LUMO (0.15) HOMO-1→LUMO+3 (0.13) HOMO-1→LUMO+4 (-0.14)	π→π*
18	Singlet	209 (0.0041)	HOMO-1→LUMO+5 (0.53); HOMO→LUMO+6 (-0.44)	π→π*, π→σ*
19	Singlet	206 (0.0006)	HOMO-3→LUMO+2 (0.66) HOMO-3→LUMO+3 (0.20)	n→π*

			HOMO-3→LUMO+1 (-0.12)	
20	Singlet	205 (0.0377)	HOMO-1→LUMO+4 (0.53) HOMO-6→LUMO (0.29) HOMO-1→LUMO+3 (0.19) HOMO-4→LUMO (0.13) HOMO-2→LUMO+3 (-0.13) HOMO-4→LUMO+1 (0.10) HOMO-2→LUMO+2 (-0.10)	π→π*

[a] Oscillator strength; [b] expansion coefficient

Table 7.24 TD-DFT data for **2**

#	**State**	**Transition energy (nm)**	**Participating MO**	**Transition character**
1	Singlet	415 (0.1557)[a]	HOMO→LUMO (0.70)[b]	π→π*
2	Singlet	329 (0.0016)	HOMO→LUMO+1 (0.49) HOMO-1→LUMO (0.37) HOMO-2→LUMO (0.35)	π→π*
3	Singlet	316 (0.0048)	HOMO-1→LUMO (0.52) HOMO-2→LUMO (-0.46)	π→π*
4	Singlet	286 (0.0004)	HOMO-3→LUMO (0.66) HOMO→LUMO+3 (0.24)	π→π*
5	Singlet	275 (0.0247)	HOMO→LUMO+2 (0.69)	π→π*
6	Singlet	262 (0.0031)	HOMO→LUMO+3 (0.65)	π→π*
7	Singlet	259 (1.8151)	HOMO→LUMO+1 (0.50) HOMO-2→LUMO (-0.39) HOMO-1→LUMO (-0.28)	π→π*
8	Singlet	252 (0.0278)	HOMO-4→LUMO (0.65) HOMO→LUMO+5 (0.22)	π→π*
9	Singlet	246 (0.0024)	HOMO→LUMO+4 (0.69)	π→σ*
10	Singlet	234 (0.0102)	HOMO-5→LUMO (0.51) HOMO→LUMO+5 (-0.28) HOMO-3→LUMO+1 (-0.22) HOMO-1→LUMO+1 (-0.20) HOMO-7→LUMO (-0.13) HOMO-2→LUMO+1 (0.12) HOMO-2→LUMO+3 (0.10)	π→π*
11	Singlet	231 (0.0313)	HOMO→LUMO+5 (0.51) HOMO→LUMO+6 (0.28) HOMO-5→LUMO (0.26) HOMO-4→LUMO (-0.18) HOMO-1→LUMO+1 (-0.12) HOMO→LUMO+8 (-0.12)	π→π*
12	Singlet	231 (0.0712)	HOMO-1→LUMO+1 (0.53) HOMO-2→LUMO+1 (-0.35) HOMO-5→LUMO (0.28)	π→π*
13	Singlet	229 (0.0107)	HOMO→LUMO+6 (0.57) HOMO→LUMO+5 (-0.24) HOMO→LUMO+8 (-0.21) HOMO-5→LUMO (-0.14) HOMO-4→LUMO (0.13) HOMO-7→LUMO (-0.11)	π→σ*
14	Singlet	226 (0.0001)	HOMO-6→LUMO (0.70)	n→π*
15	Singlet	223 (0.0028)	HOMO-3→LUMO+1 (0.45) HOMO-7→LUMO (0.25) HOMO-2→LUMO+3 (-0.24) HOMO-5→LUMO (0.23) HOMO-1→LUMO+3 (-0.21) HOMO→LUMO+5 (-0.17) HOMO→LUMO+7 (-0.12)	π→π*

16	Singlet	221 (0.0029)	HOMO→LUMO+7 (0.68)	π→σ*
17	Singlet	217 (0.2096)	HOMO-2→LUMO+1 (0.55) HOMO-1→LUMO+1 (0.37) HOMO-3→LUMO+3 (0.15) HOMO-1→LUMO+2 (0.10)	π→π*
18	Singlet	216 (0.0120)	HOMO→LUMO+8 (0.62) HOMO→LUMO+6 (0.25) HOMO→LUMO+10 (-0.14)	π→σ*
19	Singlet	213 (0.0118)	HOMO→LUMO+9 (0.66) HOMO-1→LUMO+2 (0.18)	n→π*
20	Singlet	212 (0.0317)	HOMO-7→LUMO (0.54) HOMO-1→LUMO+3 (0.21) HOMO-1→LUMO+2 (-0.20) HOMO-2→LUMO+3 (0.19) HOMO-3→LUMO+1 (-0.14) HOMO→LUMO+9 (0.13) HOMO→LUMO+12 (0.11) HOMO→LUMO+11 (-0.11)	π→π*, n→π*

[a] Oscillator strength; [b] expansion coefficient

Table 7.25 TD-DFT data for **3**

#	**State**	**Transition energy (nm)**	**Participating MO**	**Transition character**
1	Singlet	377 (0.6303)[a]	HOMO→LUMO (0.69)[b] HOMO-1→LUMO+1 (0.12)	π→π*
2	Singlet	345 (0.0002)	HOMO→LUMO+1 (0.62) HOMO→LUMO+1 (0.52) HOMO-1→LUMO (-0.46)	π→π*
3	Singlet	299 (0.0029)	HOMO→LUMO+2 (0.62) HOMO-2→LUMO (-0.25) HOMO→LUMO+3 (0.18) HOMO-3→LUMO (0.10)	π→π*
4	Singlet	291 (0.3502)	HOMO-1→LUMO (0.48) HOMO→LUMO+1 (0.38) HOMO-2→LUMO (-0.26) HOMO→LUMO+3 (-0.15)	π→π*
5	Singlet	285 (0.0534)	HOMO-2→LUMO (0.48) HOMO→LUMO+3 (0.30) HOMO-3→LUMO (-0.27) HOMO→LUMO+1 (0.21) HOMO→LUMO+2 (0.18) HOMO-1→LUMO (0.16)	π→π*
6	Singlet	278 (0.0540)	HOMO-3→LUMO (0.53) HOMO→LUMO+3 (0.40) HOMO→LUMO+2 (-0.17) HOMO→LUMO+1 (0.11)	π→π*
7	Singlet	269 (0.0696)	HOMO→LUMO+3 (0.41) HOMO-3→LUMO (-0.35) HOMO-2→LUMO (-0.31) HOMO-1→LUMO+1 (-0.21) HOMO→LUMO+2 (-0.20)	π→π*
8	Singlet	248 (0.0089)	HOMO→LUMO+4 (0.58) HOMO-4→LUMO (0.30) HOMO-1→LUMO+2 (-0.18) HOMO-3→LUMO+1 (-0.13)	π→π*
9	Singlet	246 (0.1452)	HOMO-1→LUMO+1 (0.47) HOMO-2→LUMO+1 (-0.41) HOMO-1→LUMO+2 (0.16) HOMO-4→LUMO (0.12)	π→π*

			HOMO-2→LUMO (-0.11)	
10	Singlet	245 (0.0773)	HOMO-1→LUMO+2 (0.47) HOMO-1→LUMO+1 (-0.30) HOMO-3→LUMO+1 (0.26) HOMO→LUMO+4 (0.20) HOMO-2→LUMO+1 (-0.16) HOMO-1→LUMO+3 (0.13)	π→π*
11	Singlet	239 (0.0326)	HOMO→LUMO+5 (0.63) HOMO-4→LUMO (0.17) HOMO-2→LUMO+1 (-0.13)	π→σ*
12	Singlet	236 (0.2214)	HOMO-1→LUMO+3 (0.37) HOMO-3→LUMO+1 (0.32) HOMO-2→LUMO+1 (0.28) HOMO-1→LUMO+1 (0.26) HOMO→LUMO+5 (0.23) HOMO→LUMO+4 (0.11)	π→π*
13	Singlet	230 (0.4940)	HOMO-1→LUMO+2 (0.36) HOMO-1→LUMO+3 (-0.33) HOMO-2→LUMO+1 (0.32) HOMO-4→LUMO (-0.23) HOMO-3→LUMO+1 (-0.14) HOMO-1→LUMO+1 (0.13) HOMO→LUMO+4 (0.12)	π→π*
14	Singlet	227 (0.0650)	HOMO-4→LUMO (0.44) HOMO→LUMO+7 (0.28) HOMO-2→LUMO+1 (0.24) HOMO→LUMO+4 (-0.24) HOMO-1→LUMO+2 (0.17) HOMO→LUMO+5 (-0.11)	π→π*
15	Singlet	226 (0.0018)	HOMO→LUMO+6 (0.69) HOMO→LUMO+7 (0.10)	π→σ*
16	Singlet	223 (0.0027)	HOMO→LUMO+7 (0.60) HOMO-4→LUMO (-0.21) HOMO-5→LUMO (0.18) HOMO-3→LUMO+1 (0.10)	π→σ*
17	Singlet	221 (0.0059)	HOMO-5→LUMO (0.59) HOMO→LUMO+8 (0.25) HOMO-1→LUMO+3 (0.18)	π→π*, n→π*
18	Singlet	220 (0.0451)	HOMO-3→LUMO+1 (0.42) HOMO-1→LUMO+3 (-0.34) HOMO→LUMO+8 (0.28) HOMO-2→LUMO+2 (0.25) HOMO-1→LUMO+2 (-0.16)	π→π*
19	Singlet	216 (0.0061)	HOMO-2→LUMO+2 (0.36) HOMO-3→LUMO+2 (0.27) HOMO-2→LUMO+3 (0.26) HOMO-6→LUMO (-0.25) HOMO-3→LUMO+1 (-0.17) HOMO-5→LUMO (0.16) HOMO-3→LUMO+3 (-0.14) HOMO-1→LUMO+4 (-0.12) HOMO→LUMO+8 (-0.12) HOMO-4→LUMO (0.11) HOMO-4→LUMO+1 (-0.11)	π→π*
20	Singlet	215 (0.0058)	HOMO→LUMO+8 (0.51) HOMO-5→LUMO (-0.18) HOMO→LUMO+11 (0.17) HOMO-3→LUMO+1 (-0.16) HOMO-4→LUMO (-0.15) HOMO→LUMO+10 (-0.15)	π→π*

			HOMO-2→LUMO+3 (0.14) HOMO-4→LUMO+1 (-0.14) HOMO-1→LUMO+3 (0.13)	

[a] Oscillator strength; [b] expansion coefficient

Table 7.26 TD-DFT data for **4**

#	State	Transition energy (nm)	Participating MO	Transition character
1	Singlet	329 (0.0031)[a]	HOMO-1→LUMO (-0.46)[b] HOMO→LUMO+1 (0.52)	π→π*
2	Singlet	329 (0.3938)	HOMO→LUMO (0.68) HOMO-1→LUMO+1 (0.16)	π→π*
3	Singlet	289 (0.1619)	HOMO-1→LUMO (0.51) HOMO→LUMO+1 (0.45)	π→π*
4	Singlet	270 (0.0232)	HOMO→LUMO+2 (0.54) HOMO-2→LUMO (0.43)	π→π*
5	Singlet	267 (0.5801)	HOMO-1→LUMO+1 (0.58) HOMO-2→LUMO+1 (-0.31) HOMO→LUMO+2 (0.18) HOMO→LUMO (-0.14)	π→π*
6	Singlet	256 (0.3892)	HOMO-2→LUMO (0.46) HOMO→LUMO+2 (-0.37) HOMO-1→LUMO+1 (0.32) HOMO-1→LUMO+2 (0.15)	π→π*
7	Singlet	251 (0.0523)	HOMO-1→LUMO+2 (0.46) HOMO-2→LUMO+1 (0.41) HOMO-3→LUMO+1 (-0.18) HOMO-1→LUMO+1 (-0.12) HOMO→LUMO+3 (-0.15) HOMO-4→LUMO (0.11)	π→π*
8	Singlet	245 (0.0584)	HOMO→LUMO+3 (0.53) HOMO-3→LUMO (0.40) HOMO-2→LUMO+1 (0.16)	π→π*
9	Singlet	234 (0.0129)	HOMO-2→LUMO+1 (0.48) HOMO-1→LUMO+2 (-0.30) HOMO-3→LUMO (-0.24) HOMO-3→LUMO+1 (0.22) HOMO-1→LUMO+3 (0.13) HOMO→LUMO+3 (0.11)	π→π*
10	Singlet	229 (0.0045)	HOMO→LUMO+4 (0.38) HOMO-4→LUMO (0.27) HOMO→LUMO+3 (0.23) HOMO→LUMO+5 (0.21) HOMO-3→LUMO (-0.21) HOMO-1→LUMO+3 (-0.21) HOMO-3→LUMO+1 (-0.20) HOMO-1→LUMO+2 (-0.19)	π→π*
11	Singlet	227 (0.0028)	HOMO→LUMO+4 (0.56) HOMO-3→LUMO+1 (0.23) HOMO-1→LUMO+3 (0.20) HOMO-3→LUMO (0.13) HOMO-4→LUMO (-0.11) HOMO→LUMO+3 (-0.11)	π→π*
12	Singlet	223 (0.1381)	HOMO-4→LUMO (0.37) HOMO→LUMO+5 (0.33) HOMO-3→LUMO (0.28) HOMO→LUMO+3 (-0.19) HOMO-1→LUMO+2 (-0.15) HOMO-1→LUMO+3 (0.13)	π→π*

			HOMO-3→LUMO+1 (0.13) HOMO-2→LUMO+1 (0.11) HOMO→LUMO+7 (-0.10)	
13	Singlet	221 (0.1612)	HOMO-1→LUMO+3 (0.31) HOMO→LUMO+5 (0.31) HOMO-1→LUMO+2 (0.26) HOMO-3→LUMO (-0.24) HOMO-3→LUMO+1 (0.24) HOMO→LUMO+3 (0.22) HOMO-2→LUMO+1 (-0.16) HOMO-2→LUMO+2 (-0.10)	π→π*
14	Singlet	216 (0.0977)	HOMO→LUMO+5 (0.42) HOMO-4→LUMO (-0.36) HOMO-1→LUMO+3 (-0.27) HOMO→LUMO+7 (0.17) HOMO-5→LUMO (0.16) HOMO→LUMO+6 (-0.12) HOMO-3→LUMO+1 (0.11)	π→π*
15	Singlet	214 (0.0254)	HOMO-5→LUMO (0.63) HOMO→LUMO+6 (-0.14) HOMO-5→LUMO+2 (-0.13) HOMO-1→LUMO+3 (0.12) HOMO-4→LUMO (0.11) HOMO-5→LUMO+3 (-0.11)	π→π*
16	Singlet	214 (0.0068)	HOMO→LUMO+6 (0.65) HOMO-5→LUMO (0.16) HOMO-1→LUMO+4 (-0.14)	π→σ*
17	Singlet	212 (0.1661)	HOMO→LUMO+7 (0.58) HOMO-3→LUMO+1 (-0.25) HOMO-1→LUMO+3 (0.22)	π→σ*
18	Singlet	209 (0.1158)	HOMO-1→LUMO+4 (0.44) HOMO→LUMO+8 (-0.36) HOMO-2→LUMO+2 (0.28) HOMO-3→LUMO+1 (-0.15) HOMO-1→LUMO+3 (0.13) HOMO→LUMO+7 (-0.13)	π→π*
19	Singlet	209 (0.0279)	HOMO-2→LUMO+2 (0.45) HOMO-3→LUMO+1 (0.29) HOMO-1→LUMO+3 (-0.23) HOMO-4→LUMO (0.18) HOMO→LUMO+7 (0.16) HOMO-4→LUMO+1 (-0.16) HOMO→LUMO+5 (-0.12) HOMO-3→LUMO (-0.10)	π→π*
20	Singlet	208 (0.0474)	HOMO-1→LUMO+4 (0.48) HOMO→LUMO+8 (0.30) HOMO→LUMO+7 (0.20) HOMO-2→LUMO+2 (-0.20) HOMO→LUMO+6 (0.17) HOMO-4→LUMO+1 (0.15) HOMO-3→LUMO+1 (0.10)	π→π*

[a] Oscillator strength; [b] expansion coefficient

Table 7.27 TD-DFT data for **5**

#	State	Transition energy (nm)	Participating MO	Transition character
1	Singlet	327 (1.1031)[a]	HOMO→LUMO (0.70)[b]	π→π*
2	Singlet	291 (0.0037)	HOMO→LUMO+1 (0.64) HOMO-3→LUMO (0.26)	π→π*

3	Singlet	273 (0.0176)	HOMO-1→LUMO (0.60) HOMO→LUMO+3 (-0.31) HOMO→LUMO+1 (-0.12)	π→π*
4	Singlet	254 (0.0085)	HOMO-2→LUMO (0.52) HOMO→LUMO+2 (-0.43) HOMO→LUMO+3 (-0.16)	π→π*
5	Singlet	247 (0.0109)	HOMO-3→LUMO (0.54) HOMO→LUMO+1 (-0.23) HOMO→LUMO+2 (0.21) HOMO→LUMO+3 (-0.20) HOMO-1→LUMO (-0.20) HOMO-2→LUMO (0.11)	π→π*
6	Singlet	241 (0.0141)	HOMO→LUMO+2 (0.46) HOMO-2→LUMO (0.43) HOMO-3→LUMO (-0.19) HOMO→LUMO+3 (0.16) HOMO-1→LUMO+1 (0.12)	π→π*
7	Singlet	237 (0.1210)	HOMO→LUMO+3 (0.52) HOMO-3→LUMO (0.29) HOMO-1→LUMO (0.27) HOMO→LUMO+2 (-0.15) HOMO-1→LUMO+2 (-0.11) HOMO→LUMO+1 (-0.11)	π→π*
8	Singlet	232 (0.0000)	HOMO→LUMO+4 (0.69)	π→π*
9	Singlet	226 (0.0027)	HOMO-1→LUMO+1 (0.60) HOMO→LUMO+5 (0.33)	π→π*
10	Singlet	222 (0.0335)	HOMO-2→LUMO+1 (0.60) HOMO→LUMO+5 (0.28) HOMO-1→LUMO+2 (-0.15)	π→π*
11	Singlet	220 (0.0035)	HOMO→LUMO+6 (0.68) HOMO-2→LUMO+4 (0.10)	π→σ*
12	Singlet	219 (0.0095)	HOMO→LUMO+5 (0.50) HOMO-2→LUMO+1 (-0.29) HOMO-1→LUMO+1 (-0.27) HOMO-3→LUMO+1 (0.16) HOMO-3→LUMO+3 (-0.11)	π→π*
13	Singlet	214 (0.0001)	HOMO-4→LUMO (0.66) HOMO-4→LUMO+2 (-0.18) HOMO→LUMO+7 (0.17)	n→π*
14	Singlet	213 (0.2179)	HOMO-3→LUMO+1 (0.62) HOMO-1→LUMO+3 (0.22) HOMO-3→LUMO+3 (0.11) HOMO-2→LUMO+1 (0.11) HOMO-5→LUMO (0.10)	π→π*
15	Singlet	213 (0.0006)	HOMO→LUMO+7 (0.68) HOMO-4→LUMO (-0.16)	π→σ*
16	Singlet	208 (0.0248)	HOMO-1→LUMO+2 (0.53) HOMO-2→LUMO+3 (-0.34) HOMO-2→LUMO+2 (0.12) HOMO→LUMO+3 (0.11) HOMO-5→LUMO (-0.11)	π→π*
17	Singlet	206 (0.0005)	HOMO→LUMO+8 (0.68)	π→σ*
18	Singlet	201 (0.1160)	HOMO-3→LUMO+2 (0.49) HOMO-5→LUMO (0.25) HOMO-1→LUMO+3 (-0.25) HOMO-2→LUMO+2 (0.16) HOMO→LUMO+11 (-0.16) HOMO-1→LUMO+2 (0.15) HOMO-2→LUMO+3 (0.14) HOMO-3→LUMO+3 (-0.14)	π→π*

19	Singlet	200 (0.0041)	HOMO→LUMO+9 (0.69)	π→σ*
20	Singlet	200 (0.0625)	HOMO-5→LUMO (0.41) HOMO-2→LUMO+2 (-0.27) HOMO-2→LUMO+3 (-0.27) HOMO-3→LUMO+2 (-0.24) HOMO-1→LUMO+3 (-0.21) HOMO→LUMO+11 (-0.20)	π→π*

[a] Oscillator strength; [b] expansion coefficient

Table 7.28 TD-DFT data for **6**

#	**State**	**Transition energy (nm)**	**Participating MO**	**Transition character**
1	Singlet	323 (1.0669)[a]	HOMO→LUMO (0.70)[b]	π→π*
2	Singlet	283 (0.0107)	HOMO→LUMO+1 (0.48) HOMO-1→LUMO (0.44) HOMO→LUMO+2 (-0.25)	π→π*
3	Singlet	277 (0.0135)	HOMO-3→LUMO (0.47) HOMO-1→LUMO (0.30) HOMO→LUMO+1 (-0.28) HOMO-2→LUMO (0.26)	π→π*
4	Singlet	267 (0.0097)	HOMO→LUMO+1 (0.40) HOMO→LUMO+2 (0.39) HOMO-3→LUMO (0.32) HOMO-1→LUMO (-0.22) HOMO-4→LUMO (0.10)	π→π*
5	Singlet	254 (0.0237)	HOMO-2→LUMO (0.54) HOMO→LUMO+3 (0.38) HOMO-3→LUMO (-0.19) HOMO-1→LUMO (-0.13)	π→π*
6	Singlet	246 (0.0019)	HOMO-3→LUMO+1 (0.45) HOMO-1→LUMO+1 (0.42) HOMO-2→LUMO+1 (0.25) HOMO-3→LUMO+3 (-0.12) HOMO-1→LUMO+3 (-0.11)	π→π*
7	Singlet	241 (0.0222)	HOMO→LUMO+3 (0.46) HOMO→LUMO+2 (0.35) HOMO-2→LUMO (-0.27) HOMO-1→LUMO (0.25)	π→π*
8	Singlet	238 (0.0585)	HOMO→LUMO+3 (0.36) HOMO→LUMO+2 (-0.36) HOMO-3→LUMO (0.32) HOMO-1→LUMO (-0.24) HOMO-2→LUMO (-0.19)	π→π*
9	Singlet	227 (0.0075)	HOMO-4→LUMO (0.49) HOMO-2→LUMO+1 (-0.40) HOMO-1→LUMO+1 (0.16) HOMO→LUMO+2 (-0.13) HOMO→LUMO+1 (-0.10)	π→π*
10	Singlet	222 (0.0000)	HOMO→LUMO+4 (0.67) HOMO→LUMO+6 (-0.20)	π→σ*
11	Singlet	219 (0.0553)	HOMO-1→LUMO+1 (0.51) HOMO-3→LUMO+1 (-0.44) HOMO-4→LUMO (-0.12) HOMO-1→LUMO+2 (0.10)	π→π*
12	Singlet	218 (0.0003)	HOMO-5→LUMO (0.67) HOMO-5→LUMO+3 (-0.18)	n→π*
13	Singlet	217 (0.0451)	HOMO→LUMO+5 (0.62) HOMO-2→LUMO+1 (0.16) HOMO-6→LUMO (0.14)	π→π*

			HOMO-7→LUMO (0.11) HOMO-4→LUMO (0.10)	
14	Singlet	212 (0.0489)	HOMO-2→LUMO+1 (0.39) HOMO-4→LUMO (0.33) HOMO-2→LUMO+2 (-0.31) HOMO→LUMO+5 (-0.19) HOMO-3→LUMO+1 (-0.17) HOMO-1→LUMO+2 (-0.14) HOMO-1→LUMO+3 (-0.14)	π→π*
15	Singlet	211 (0.0086)	HOMO-1→LUMO+3 (0.45) HOMO-3→LUMO+3 (0.33) HOMO-2→LUMO+3 (0.23) HOMO→LUMO+6 (0.17) HOMO-2→LUMO+1 (0.12) HOMO-3→LUMO (-0.11) HOMO-3→LUMO+5 (-0.11)	π→π*
16	Singlet	210 (0.0041)	HOMO→LUMO+6 (0.63) HOMO→LUMO+4 (0.19) HOMO-2→LUMO+4 (-0.11) HOMO-1→LUMO+3 (-0.10)	π→σ*
17	Singlet	208 (0.0543)	HOMO-3→LUMO+2 (0.45) HOMO-1→LUMO+2 (0.44) HOMO-2→LUMO+2 (0.15) HOMO-3→LUMO+1 (-0.14) HOMO-1→LUMO+3 (-0.13) HOMO-4→LUMO (0.12) HOMO-1→LUMO+1 (-0.10)	π→π*
18	Singlet	205 (0.0187)	HOMO-2→LUMO+2 (0.52) HOMO-6→LUMO (0.35) HOMO-4→LUMO (0.16) HOMO-1→LUMO+2 (-0.15)	π→π*
19	Singlet	203 (0.0281)	HOMO-3→LUMO+3 (0.46) HOMO-1→LUMO+3 (-0.40) HOMO-6→LUMO (0.16) HOMO-3→LUMO+2 (0.16) HOMO-1→LUMO+2 (-0.14) HOMO-2→LUMO+3 (0.11)	π→π*
20	Singlet	202 (0.0386)	HOMO-6→LUMO (0.40) HOMO→LUMO+7 (0.32) HOMO-3→LUMO+2 (0.25) HOMO-2→LUMO+2 (-0.22) HOMO-1→LUMO+3 (0.18) HOMO-2→LUMO+3 (-0.12) HOMO-4→LUMO (-0.12) HOMO-4→LUMO+1 (-0.12) HOMO-3→LUMO+3 (-0.12)	π→π*, π→σ*

[a] Oscillator strength; [b] expansion coefficient

Table 7.29 TD-DFT data for **7**

#	**State**	**Transition energy (nm)**	**Participating MO**	**Transition character**
1	Singlet	322 (0.8777)[a]	HOMO→LUMO (0.70)[b]	π→π*
2	Singlet	307 (0.0335)	HOMO→LUMO+1 (0.69) HOMO-2→LUMO (0.14)	π→π*
3	Singlet	274 (0.0156)	HOMO→LUMO+2 (0.70)	π→π*
4	Singlet	252 (0.0059)	HOMO→LUMO+4 (0.70)	π→σ*
5	Singlet	250 (0.0568)	HOMO→LUMO+3 (0.69)	π→π*
6	Singlet	243 (0.0007)	HOMO→LUMO+5 (0.70)	π→σ*
7	Singlet	233 (0.0253)	HOMO→LUMO+7 (0.67)	π→π*

			HOMO→LUMO+6 (-0.16)	
8	Singlet	232 (0.0038)	HOMO→LUMO+6 (0.66) HOMO→LUMO+7 (0.16) HOMO→LUMO+9 (0.14)	π→σ*
9	Singlet	227 (0.0654)	HOMO-1→LUMO (0.66) HOMO-2→LUMO (0.14)	π→π*
10	Singlet	225 (0.0386)	HOMO-2→LUMO (0.49) HOMO-1→LUMO+1 (-0.33) HOMO-1→LUMO (-0.13) HOMO→LUMO+8 (0.21) HOMO→LUMO+9 (-0.26)	π→π*
11	Singlet	225 (0.0138)	HOMO→LUMO+8 (-0.37) HOMO→LUMO+9 (0.47) HOMO-2→LUMO (0.26) HOMO-1→LUMO+1 (-0.18)	π→σ*
12	Singlet	224 (0.0028)	HOMO→LUMO+8 (0.55) HOMO→LUMO+9 (0.41)	π→σ*
13	Singlet	216 (0.0353)	HOMO-1→LUMO+1 (0.58) HOMO-2→LUMO (0.36)	π→π*
14	Singlet	214 (0.0020)	HOMO→LUMO+10 (0.69)	π→σ*
15	Singlet	208 (0.0185)	HOMO→LUMO+11 (0.60) HOMO→LUMO+12 (0.33)	π→σ*
16	Singlet	207 (0.0082)	HOMO→LUMO+12 (0.58) HOMO→LUMO+11 (-0.34)	π→π*
17	Singlet	204 (0.0503)	HOMO→LUMO+13 (0.68)	π→π*
18	Singlet	203 (0.0020)	HOMO→LUMO+14 (0.68)	π→σ*
19	Singlet	200 (0.0013)	HOMO-3→LUMO (0.68) HOMO-3→LUMO+3 (0.15)	n→π*
20	Singlet	198 (0.0285)	HOMO→LUMO+15 (0.68) HOMO→LUMO+16 (-0.14)	π→σ*

[a] Oscillator strength; [b] expansion coefficient

7.4 TDA based TD-DFT

Table 7.30 TDA-DFT data for **8**

#	State	Transition energy (nm)	Participating MO	Transition character
1	Singlet	369 (1.4810)[a]	HOMO→LUMO (0.69)[b]	π→π*
2	Singlet	333 (0.0543)	HOMO→LUMO+1 (0.46) HOMO-1→LUMO (-0.41) HOMO-2→LUMO (-0.15) HOMO-2→LUMO+2 (-0.15) HOMO→LUMO+2 (0.14) HOMO-1→LUMO+1 (0.12) HOMO→LUMO (0.10)	π→π*
3	Singlet	312 (0.0255)	HOMO-1→LUMO (0.46) HOMO→LUMO+1 (0.44) HOMO→LUMO+2 (-0.22) HOMO-2→LUMO (-0.18)	π→π*
4	Singlet	297 (0.0255)	HOMO-2→LUMO (0.58) HOMO→LUMO+1 (0.24) HOMO-1→LUMO+1 (-0.22) HOMO→LUMO+2 (0.15)	π→π*
5	Singlet	292 (0.0884)	HOMO→LUMO+2 (0.59) HOMO-1→LUMO (0.24) HOMO-1→LUMO+1 (0.16)	π→π*

			HOMO-2→LUMO+1 (0.15) HOMO-2→LUMO (-0.10)	
6	Singlet	289 (0.0116)	HOMO-3→LUMO (0.50) HOMO→LUMO+3 (0.40) HOMO-3→LUMO+1 (0.15) HOMO-3→LUMO+2 (-0.15) HOMO-2→LUMO+3 (0.13) HOMO-1→LUMO+3 (-0.11)	π→π*
7	Singlet	287 (0.0022)	HOMO-5→LUMO (0.63) HOMO-5→LUMO+1 (-0.28) HOMO-5→LUMO+2 (0.14)	n→π*
8	Singlet	275 (0.4900)	HOMO-1→LUMO+1 (0.56) HOMO-2→LUMO (0.24) HOMO-4→LUMO (-0.20) HOMO→LUMO+2 (-0.17) HOMO-2→LUMO+2 (-0.12)	π→π*
9	Singlet	273 (0.1024)	HOMO-1→LUMO+2 (0.42) HOMO-2→LUMO+1 (0.41) HOMO-4→LUMO (-0.23) HOMO-1→LUMO (-0.17) HOMO-1→LUMO+5 (0.11) HOMO-1→LUMO+1 (-0.11)	π→π*
10	Singlet	258 (0.0338)	HOMO-2→LUMO+1 (0.42) HOMO-4→LUMO (0.37) HOMO-2→LUMO+2 (-0.26) HOMO→LUMO+4 (0.18) HOMO-6→LUMO (-0.13) HOMO-1→LUMO+2 (-0.13) HOMO-4→LUMO+1 (-0.12) HOMO-2→LUMO+4 (-0.11)	π→π*
11	Singlet	255 (0.0004)	HOMO-5→LUMO+1 (0.58) HOMO-5→LUMO+2 (0.32) HOMO-5→LUMO (0.19) HOMO-5→LUMO+4 (-0.13)	n→π*
12	Singlet	253 (0.1611)	HOMO-1→LUMO+2 (0.42) HOMO-4→LUMO (0.35) HOMO→LUMO+4 (0.24) HOMO-2→LUMO+1 (-0.21) HOMO→LUMO+5 (0.19) HOMO-1→LUMO+1 (0.11)	π→π*
13	Singlet	251 (0.2931)	HOMO-2→LUMO+2 (0.46) HOMO-1→LUMO+2 (-0.26) HOMO→LUMO+5 (0.25) HOMO-4→LUMO (0.15) HOMO-2→LUMO+1 (0.15) HOMO-1→LUMO+5 (0.14) HOMO-1→LUMO+1 (0.13) HOMO-4→LUMO+1 (0.10)	π→π*
14	Singlet	250 (0.0438)	HOMO-3→LUMO (0.45) HOMO→LUMO+3 (-0.33) HOMO-3→LUMO+1 (-0.31) HOMO-3→LUMO+2 (0.26)	π→π*
15	Singlet	246 (0.1783)	HOMO→LUMO+4 (0.53) HOMO-4→LUMO (-0.25) HOMO-2→LUMO+2 (0.22) HOMO-6→LUMO (-0.18) HOMO-2→LUMO+4 (-0.11) HOMO→LUMO+5 (-0.10)	π→π*
16	Singlet	244 (0.0004)	HOMO-7→LUMO (0.67) HOMO-5→LUMO+2 (0.15)	n→π*

			HOMO-7→LUMO+1 (0.11)	
17	Singlet	237 (0.0112)	HOMO-4→LUMO+1 (0.38) HOMO→LUMO+5 (0.27) HOMO-6→LUMO (0.26) HOMO-2→LUMO+2 (-0.24) HOMO→LUMO+4 (0.21) HOMO→LUMO+6 (-0.12) HOMO-6→LUMO+1 (-0.12) HOMO-2→LUMO+4 (0.11) HOMO-1→LUMO+2 (-0.10)	π→π*
18	Singlet	234 (0.0854)	HOMO-3→LUMO+1 (0.42) HOMO→LUMO+3 (-0.40) HOMO-2→LUMO+3 (0.26) HOMO-1→LUMO+3 (-0.21) HOMO-4→LUMO+1 (0.12) HOMO-4→LUMO+3 (-0.11)	π→π*
19	Singlet	233 (0.0151)	HOMO-4→LUMO+1 (0.47) HOMO-6→LUMO (-0.33) HOMO→LUMO+5 (-0.24) HOMO-3→LUMO+1 (-0.11)	π→π*
20	Singlet	229 (0.0004)	HOMO-3→LUMO+2 (0.47) HOMO-3→LUMO+1 (0.40) HOMO-2→LUMO+3 (-0.21) HOMO-1→LUMO+3 (0.18) HOMO→LUMO+3 (0.12)	π→π*

[a] Oscillator strength; [b] expansion coefficient

Table 7.31 TDA-DFT data for **9**

#	**State**	**Transition energy (nm)**	**Participating MO**	**Transition character**
1	Singlet	411 (0.4970)[a]	HOMO→LUMO (0.67)[b] HOMO-1→LUMO (0.16)	π→π*
2	Singlet	362 (0.0622)	HOMO-1→LUMO (0.56) HOMO→LUMO+1 (-0.40)	π→π*
3	Singlet	346 (0.0534)	HOMO→LUMO+1 (0.56) HOMO-1→LUMO (0.37) HOMO→LUMO (-0.12)	π→π*
4	Singlet	321 (0.0005)	HOMO→LUMO+2 (0.50) HOMO-4→LUMO (0.46) HOMO-1→LUMO+2 (-0.13) HOMO-3→LUMO (0.12)	π→π*
5	Singlet	305 (0.3527)	HOMO-1→LUMO+1 (0.68)	π→π*
6	Singlet	288 (0.0049)	HOMO-2→LUMO (0.40) HOMO-2→LUMO+1 (0.37) HOMO-1→LUMO+3 (-0.31) HOMO→LUMO+3 (-0.28)	π→π*
7	Singlet	287 (0.0248)	HOMO-3→LUMO (0.65) HOMO-4→LUMO (-0.16)	π→π*
8	Singlet	274 (0.0011)	HOMO-5→LUMO (0.63) HOMO→LUMO+5 (-0.30)	π→π*
9	Singlet	273 (0.0025)	HOMO-2→LUMO (0.57) HOMO-2→LUMO+1 (-0.30) HOMO→LUMO+3 (0.19) HOMO-1→LUMO+3 (0.16) HOMO-3→LUMO (0.13)	π→π*
10	Singlet	261 (0.0202)	HOMO-3→LUMO+1 (0.47) HOMO→LUMO+4 (-0.40) HOMO-1→LUMO+2 (-0.17) HOMO-1→LUMO+4 (-0.11)	π→π*

			HOMO→LUMO+2 (-0.13) HOMO→LUMO+3 (0.13) HOMO-4→LUMO (0.10)	
11	Singlet	260 (0.1706)	HOMO-1→LUMO+2 (0.51) HOMO→LUMO+2 (0.34) HOMO-4→LUMO (-0.20) HOMO-3→LUMO+1 (0.16) HOMO→LUMO+4 (-0.14) HOMO-3→LUMO+2 (0.11)	π→π*
12	Singlet	255 (0.1451)	HOMO→LUMO+4 (0.44) HOMO-3→LUMO+1 (0.41) HOMO→LUMO+3 (-0.17) HOMO→LUMO+6 (0.15) HOMO-6→LUMO (0.14) HOMO-1→LUMO+3 (0.13) HOMO-1→LUMO+4 (-0.10)	π→π*
13	Singlet	251 (0.0446)	HOMO→LUMO+3 (0.54) HOMO-1→LUMO+3 (-0.25) HOMO→LUMO+5 (0.20) HOMO-2→LUMO+1 (0.19) HOMO→LUMO+4 (0.19)	π→π*
14	Singlet	250 (0.0143)	HOMO→LUMO+5 (0.57) HOMO-5→LUMO (0.27) HOMO→LUMO+4 (-0.17) HOMO→LUMO+3 (-0.16)	π→π*
15	Singlet	247 (0.1313)	HOMO-4→LUMO+1 (0.60) HOMO-4→LUMO (0.21) HOMO-1→LUMO+2 (0.17) HOMO-3→LUMO+1 (0.13) HOMO-6→LUMO (-0.13)	π→π*
16	Singlet	244 (0.0931)	HOMO-6→LUMO (0.60) HOMO-4→LUMO+1 (0.15) HOMO→LUMO+4 (-0.15) HOMO-6→LUMO+1 (0.14) HOMO-7→LUMO+1 (-0.13) HOMO→LUMO+6 (0.12)	n→π*
17	Singlet	238 (0.0437)	HOMO-7→LUMO (0.56) HOMO-6→LUMO+1 (-0.28) HOMO→LUMO+6 (0.15) HOMO-1→LUMO+4 (-0.15) HOMO-7→LUMO+1 (0.12)	n→π*
18	Singlet	233 (2.2118)	HOMO-1→LUMO+2 (0.38) HOMO-4→LUMO (0.37) HOMO→LUMO+2 (-0.30) HOMO-4→LUMO+1 (-0.27)	π→π*
19	Singlet	231 (0.0822)	HOMO-1→LUMO+4 (0.59) HOMO-5→LUMO+1 (-0.21) HOMO-3→LUMO+1 (0.13) HOMO-6→LUMO+1 (-0.13) HOMO-6→LUMO (0.12) HOMO-2→LUMO+3 (-0.10)	π→π* n→π*
20	Singlet	230 (0.1030)	HOMO-5→LUMO+1 (0.53) HOMO-7→LUMO (0.23) HOMO-6→LUMO+1 (0.21) HOMO-1→LUMO+4 (0.21) HOMO-7→LUMO+1 (-0.13) HOMO-6→LUMO (-0.10)	n→π* π→π*

[a] Oscillator strength; [b] expansion coefficient

Table 7.32 TDA-DFT data for **10**

#	State	Transition energy (nm)	Participating MO	Transition character
1	Singlet	402 (1.4645)[a]	HOMO→LUMO (0.68)[b]	π→π*
2	Singlet	352 (0.0014)	HOMO→LUMO+1 (0.50) HOMO-1→LUMO (0.40) HOMO→LUMO+2 (-0.21) HOMO-2→LUMO (-0.16)	π→π*
3	Singlet	332 (0.0027)	HOMO→LUMO+2 (0.46) HOMO-2→LUMO (0.39) HOMO→LUMO+1 (0.30) HOMO-2→LUMO+1 (-0.10)	π→π*
4	Singlet	320 (0.0375)	HOMO-1→LUMO (0.55) HOMO→LUMO+1 (-0.34) HOMO-2→LUMO+2 (-0.15) HOMO-2→LUMO (0.13) HOMO→LUMO (0.10)	π→π*
5	Singlet	292 (0.1768)	HOMO-1→LUMO+1 (0.64) HOMO-2→LUMO (-0.15) HOMO→LUMO+4 (-0.13) HOMO→LUMO+2 (0.12)	π→π*
6	Singlet	290 (0.0036)	HOMO-3→LUMO (0.41) HOMO→LUMO+3 (0.34) HOMO-3→LUMO+1 (0.30) HOMO-1→LUMO+3 (-0.26) HOMO→LUMO+4 (0.15) HOMO-1→LUMO+4 (-0.11)	π→π*
7	Singlet	288 (0.0104)	HOMO→LUMO+4 (0.52) HOMO-4→LUMO (0.26) HOMO→LUMO+3 (-0.24) HOMO-5→LUMO (0.15) HOMO-2→LUMO (-0.15) HOMO-1→LUMO+1 (0.13) HOMO→LUMO+5 (0.11)	π→π*
8	Singlet	280 (0.1986)	HOMO-2→LUMO (0.42) HOMO→LUMO+2 (-0.29) HOMO-4→LUMO (-0.26) HOMO→LUMO+5 (0.19) HOMO-2→LUMO+1 (0.17) HOMO-1→LUMO+1 (0.14) HOMO→LUMO+4 (0.14) HOMO-5→LUMO (0.12)	π→π*
9	Singlet	275 (0.0705)	HOMO-4→LUMO (0.43) HOMO-5→LUMO (0.30) HOMO→LUMO+2 (-0.24) HOMO→LUMO+4 (-0.22) HOMO→LUMO+5 (-0.19) HOMO-2→LUMO (0.14) HOMO-1→LUMO+2 (0.14) HOMO-1→LUMO+1 (0.11)	π→π*
10	Singlet	268 (0.0553)	HOMO-5→LUMO (0.54) HOMO-1→LUMO+2 (-0.23) HOMO→LUMO+2 (0.19) HOMO→LUMO+5 (0.18) HOMO-5→LUMO+1 (-0.14) HOMO-4→LUMO (-0.13)	π→π*
11	Singlet	264 (0.0066)	HOMO-2→LUMO+1 (0.53) HOMO-1→LUMO+2 (-0.32) HOMO-4→LUMO (0.22) HOMO→LUMO+5 (-0.11)	π→π*
12	Singlet	260 (0.0348)	HOMO-3→LUMO (0.52)	π→π*

			HOMO→LUMO+3 (-0.38) HOMO-3→LUMO+1 (-0.21) HOMO→LUMO+4 (-0.17)	
13	Singlet	258 (0.3397)	HOMO→LUMO+5 (0.47) HOMO-1→LUMO+2 (0.32) HOMO-2→LUMO+1 (0.23) HOMO-4→LUMO (0.17) HOMO-2→LUMO+2 (-0.15) HOMO→LUMO+4 (-0.13)	π→π*
14	Singlet	253 (0.0924)	HOMO-1→LUMO+2 (0.34) HOMO-4→LUMO+1 (-0.32) HOMO→LUMO+5 (-0.27) HOMO-2→LUMO+1 (0.22) HOMO-4→LUMO (-0.17) HOMO-2→LUMO (-0.13) HOMO→LUMO+6 (-0.12) HOMO-5→LUMO (0.11)	π→π*
15	Singlet	251 (0.0221)	HOMO-3→LUMO+1 (0.38) HOMO→LUMO+3 (-0.37) HOMO-1→LUMO+3 (-0.30) HOMO→LUMO+4 (-0.18) HOMO-3→LUMO (-0.17) HOMO-1→LUMO+4 (-0.14)	π→π*
16	Singlet	247 (0.0241)	HOMO-4→LUMO+1 (0.43) HOMO→LUMO+6 (0.25) HOMO-6→LUMO (0.20) HOMO-1→LUMO+4 (-0.20) HOMO-1→LUMO+2 (0.19) HOMO-2→LUMO+1 (0.15) HOMO-1→LUMO+3 (0.11) HOMO-5→LUMO (0.10) HOMO-1→LUMO+5 (0.10) HOMO→LUMO+5 (-0.10)	π→π* n→π*
17	Singlet	242 (0.0120)	HOMO-7→LUMO (0.44) HOMO-6→LUMO (-0.41) HOMO-4→LUMO+1 (0.21) HOMO-7→LUMO+1 (0.20) HOMO-6→LUMO+1 (-0.14)	π→π* n→π*
18	Singlet	238 (0.0661)	HOMO→LUMO+6 (0.41) HOMO-4→LUMO+1 (-0.31) HOMO-7→LUMO (0.29) HOMO-1→LUMO+4 (-0.18) HOMO-6→LUMO (0.16) HOMO-5→LUMO+2 (-0.11) HOMO-1→LUMO+2 (-0.10) HOMO-6→LUMO+1 (-0.10)	π→π* n→π*
19	Singlet	236 (0.0229)	HOMO-1→LUMO+4 (0.38) HOMO→LUMO+6 (0.25) HOMO-2→LUMO+4 (-0.24) HOMO-5→LUMO+2 (0.21) HOMO-5→LUMO+1 (-0.21) HOMO-1→LUMO+3 (-0.18) HOMO-7→LUMO (0.14) HOMO-4→LUMO+2 (0.12) HOMO-2→LUMO+3 (0.11) HOMO-1→LUMO+5 (0.11) HOMO→LUMO+5 (-0.10)	π→π*
20	Singlet	229 (0.0460)	HOMO-5→LUMO+1 (0.40) HOMO-1→LUMO+4 (0.33) HOMO-5→LUMO+2 (-0.24)	π→π*

			HOMO-1→LUMO+5 (-0.18) HOMO-2→LUMO+4 (0.16) HOMO-1→LUMO+3 (-0.16) HOMO-2→LUMO+5 (0.11) HOMO-5→LUMO (0.10)	

[a] Oscillator strength; [b] expansion coefficient

Table 7.33 TDA-DFT data for **11**

#	**State**	**Transition energy (nm)**	**Participating MO**	**Transition character**
1	Singlet	366 (0.9989)[a]	HOMO→LUMO (0.70)[b]	π→π*
2	Singlet	324 (0.0010)	HOMO→LUMO+2 (0.47) HOMO-2→LUMO (0.35) HOMO-2→LUMO+1 (0.21) HOMO-1→LUMO (0.21) HOMO→LUMO+1 (-0.18) HOMO-1→LUMO+2 (0.17)	π→π*
3	Singlet	316 (0.0181)	HOMO-1→LUMO (-0.40) HOMO→LUMO+1 (0.51) HOMO→LUMO+2 (0.21) HOMO-2→LUMO (0.16)	π→π*
4	Singlet	299 (0.1798)	HOMO-1→LUMO (0.49) HOMO→LUMO+1 (0.40) HOMO-2→LUMO (-0.17) HOMO-2→LUMO+2 (-0.15)	π→π*
5	Singlet	289 (0.1213)	HOMO-2→LUMO (0.51) HOMO→LUMO+2 (-0.42) HOMO-1→LUMO (0.14) HOMO→LUMO+1 (0.11)	π→π*
6	Singlet	288 (0.0058)	HOMO-3→LUMO (0.48) HOMO→LUMO+3 (0.41) HOMO-1→LUMO+3 (-0.22) HOMO-3→LUMO+1 (-0.19)	π→π*
7	Singlet	272 (0.0152)	HOMO-1→LUMO+1 (0.58) HOMO-4→LUMO (-0.28) HOMO-2→LUMO+2 (-0.20) HOMO→LUMO+4 (-0.12)	π→π*
8	Singlet	269 (0.0088)	HOMO-2→LUMO+1 (0.47) HOMO-1→LUMO+2 (0.38) HOMO-2→LUMO (-0.21) HOMO→LUMO+2 (-0.20) HOMO-4→LUMO+2 (-0.14)	π→π*
9	Singlet	265 (0.0291)	HOMO-4→LUMO (0.53) HOMO-1→LUMO+1 (0.31) HOMO→LUMO+4 (0.30)	π→π*
10	Singlet	255 (0.3647)	HOMO→LUMO+4 (0.56) HOMO-4→LUMO (-0.31) HOMO-5→LUMO (0.15) HOMO-2→LUMO+2 (-0.10)	π→π*
11	Singlet	249 (0.1978)	HOMO-1→LUMO+2 (0.49) HOMO-2→LUMO+1 (-0.41) HOMO→LUMO+5 (0.14) HOMO-2→LUMO+2 (0.12) HOMO-5→LUMO (-0.11)	π→π*
12	Singlet	247 (0.0807)	HOMO→LUMO+3 (0.46) HOMO-3→LUMO (-0.44) HOMO-3→LUMO+1 (-0.24) HOMO-1→LUMO+3 (0.13)	π→π*
13	Singlet	244 (0.1592)	HOMO→LUMO+5 (0.44)	π→π*

			HOMO-5→LUMO (0.32) HOMO-4→LUMO+1 (0.27) HOMO-2→LUMO+2 (0.21) HOMO-6→LUMO (0.13)	
14	Singlet	240 (0.7046)	HOMO-2→LUMO+2 (0.52) HOMO-5→LUMO (-0.21) HOMO-1→LUMO+1 (0.16) HOMO-6→LUMO (-0.15) HOMO→LUMO+4 (0.14) HOMO-1→LUMO+2 (-0.14) HOMO-4→LUMO (-0.10)	π→π*
15	Singlet	239 (0.0227)	HOMO-6→LUMO (0.63) HOMO→LUMO+5 (-0.14) HOMO-6→LUMO+1 (-0.10)	n→π* π→π*
16	Singlet	239 (0.0083)	HOMO-3→LUMO+1 (0.46) HOMO-1→LUMO+3 (0.37) HOMO→LUMO+3 (0.26) HOMO-3→LUMO (0.15) HOMO-4→LUMO+3 (0.12) HOMO-6→LUMO (0.11)	π→π*
17	Singlet	236 (0.0445)	HOMO-2→LUMO+4 (0.37) HOMO-4→LUMO+2 (-0.32) HOMO-5→LUMO+2 (-0.30) HOMO-2→LUMO+5 (0.17) HOMO-7→LUMO (0.15) HOMO-1→LUMO+4 (0.15) HOMO-4→LUMO+1 (0.14) HOMO→LUMO+6 (0.11) HOMO-7→LUMO+1 (0.11) HOMO-1→LUMO+2 (-0.11)	π→π*
18	Singlet	233 (0.0987)	HOMO-4→LUMO+1 (0.58) HOMO-5→LUMO (-0.19) HOMO-2→LUMO+2 (-0.16) HOMO-2→LUMO+4 (-0.14) HOMO→LUMO+5 (-0.13) HOMO-5→LUMO+1 (-0.10)	π→π*
19	Singlet	226 (0.0783)	HOMO→LUMO+5 (0.41) HOMO-5→LUMO (-0.37) HOMO-1→LUMO+4 (-0.22) HOMO-4→LUMO+2 (-0.17) HOMO-2→LUMO+2 (-0.11) HOMO-1→LUMO+3 (0.11) HOMO-7→LUMO (0.10)	π→π*
20	Singlet	221 (0.0583)	HOMO→LUMO+6 (0.38) HOMO-4→LUMO+2 (0.36) HOMO-7→LUMO (0.32) HOMO-4→LUMO+1 (-0.12) HOMO-1→LUMO+4 (0.11) HOMO-7→LUMO+1 (0.10)	π→π* n→π*

[a] Oscillator strength; [b] expansion coefficient

Table 7.34 TDA-DFT data for **12**

#	**State**	**Transition energy (nm)**	**Participating MO**	**Transition character**
1	Singlet	449 (0.2706)[a]	HOMO→LUMO (0.68)[b] HOMO-1→LUMO (0.15)	π→π* (ISC)
2	Singlet	376 (0.0000)	HOMO-4→LUMO (0.68) HOMO-4→LUMO+1 (-0.17)	n→π*
3	Singlet	359 (1.0737)	HOMO→LUMO+1 (0.62)	π→π*

			HOMO-1→LUMO (-0.27) HOMO→LUMO (0.12)	
4	Singlet	351 (0.1505)	HOMO-1→LUMO (0.59) HOMO→LUMO+1 (0.31) HOMO-3→LUMO (-0.17) HOMO→LUMO (-0.13)	π→π*
5	Singlet	310 (0.0219)	HOMO→LUMO+2 (0.57) HOMO-3→LUMO (0.25) HOMO-5→LUMO (-0.23) HOMO-6→LUMO (0.13) HOMO-1→LUMO+1 (0.12)	π→π*
6	Singlet	297 (0.0163)	HOMO-1→LUMO+1 (0.56) HOMO-5→LUMO (0.34) HOMO-3→LUMO+2 (0.11) HOMO→LUMO+2 (0.10)	π→π*
7	Singlet	294 (0.0042)	HOMO-2→LUMO (0.54) HOMO→LUMO+3 (0.30) HOMO-2→LUMO+1 (0.29) HOMO-1→LUMO+3 (-0.13) HOMO-2→LUMO+2 (0.10)	π→π*
8	Singlet	290 (0.1747)	HOMO-3→LUMO (0.60) HOMO→LUMO+2 (-0.26) HOMO-1→LUMO (0.19)	π→π*
9	Singlet	280 (0.2440)	HOMO-5→LUMO (0.45) HOMO-1→LUMO+1 (-0.33) HOMO→LUMO+2 (0.23) HOMO-1→LUMO+2 (-0.19) HOMO-3→LUMO+1 (-0.16)	π→π*
10	Singlet	279 (0.0251)	HOMO-2→LUMO (0.45) HOMO-2→LUMO+1 (-0.36) HOMO→LUMO+3 (-0.32) HOMO-2→LUMO+2 (-0.15) HOMO-1→LUMO+3 (0.13)	π→π*
11	Singlet	267 (0.0261)	HOMO-6→LUMO (0.51) HOMO→LUMO+4 (-0.29) HOMO-1→LUMO+2 (0.15) HOMO→LUMO+5 (-0.15) HOMO-3→LUMO (-0.12) HOMO-6→LUMO+2 (-0.11) HOMO-1→LUMO+5 (-0.11) HOMO→LUMO+2 (-0.10)	π→π*
12	Singlet	257 (0.0000)	HOMO-4→LUMO+1 (0.59) HOMO-4→LUMO+2 (-0.34) HOMO-4→LUMO (0.17)	n→π*
13	Singlet	255 (0.5342)	HOMO-1→LUMO+2 (0.51) HOMO→LUMO+4 (0.37) HOMO-5→LUMO (0.16) HOMO→LUMO+5 (-0.15) HOMO-3→LUMO+1 (0.13)	π→π*
14	Singlet	249 (0.0821)	HOMO-3→LUMO+1 (0.48) HOMO-1→LUMO+2 (-0.36) HOMO→LUMO+4 (0.20) HOMO→LUMO+5 (-0.20) HOMO-6→LUMO (0.16)	π→π*
15	Singlet	248 (0.0003)	HOMO-7→LUMO (0.60) HOMO-7→LUMO+1 (0.35)	n→π*
16	Singlet	242 (0.1267)	HOMO-2→LUMO+1 (0.43) HOMO→LUMO+3 (-0.43) HOMO-2→LUMO+2 (-0.21) HOMO→LUMO+4 (-0.16)	π→π*

			HOMO-1→LUMO+3 (-0.14)	
17	Singlet	241 (0.0969)	HOMO→LUMO+4 (0.33) HOMO→LUMO+5 (0.32) HOMO-6→LUMO (0.30) HOMO-3→LUMO+1 (-0.24) HOMO-8→LUMO (0.13) HOMO-2→LUMO+1 (0.13) HOMO-6→LUMO+1 (-0.13) HOMO-5→LUMO+1 (0.10) HOMO→LUMO+3 (-0.10)	π→π*
18	Singlet	236 (0.0305)	HOMO→LUMO+5 (0.35) HOMO-5→LUMO+1 (0.34) HOMO-3→LUMO+1 (0.25) HOMO→LUMO+4 (-0.20) HOMO-6→LUMO+1 (-0.20) HOMO-5→LUMO (0.18) HOMO-2→LUMO+2 (0.15)	π→π*
19	Singlet	234 (0.0084)	HOMO-2→LUMO+2 (0.45) HOMO-1→LUMO+3 (-0.39) HOMO→LUMO+3 (-0.24) HOMO-5→LUMO+1 (-0.15) HOMO-3→LUMO+3 (-0.12) HOMO-2→LUMO+1 (-0.12)	π→π*
20	Singlet	233 (0.0352)	HOMO-5→LUMO+1 (0.47) HOMO→LUMO+5 (-0.31) HOMO-3→LUMO+1 (-0.24) HOMO-8→LUMO (-0.18) HOMO-6→LUMO+1 (-0.10)	π→π*

[a] Oscillator strength; [b] expansion coefficient

Table 7.35 TDA-DFT data for **13**

#	State	Transition energy (nm)	Participating MO	Transition character
1	Singlet	408 (0.8821)[a]	HOMO→LUMO (0.70)[b]	π→π*
2	Singlet	309 (0.5689)	HOMO-1→LUMO (0.56) HOMO→LUMO+1 (-0.40)	π→π*
3	Singlet	298 (0.0003)	HOMO→LUMO+2 (0.57) HOMO-3→LUMO (0.32) HOMO-1→LUMO+2 (0.19) HOMO→LUMO+1 (-0.16)	π→π*
4	Singlet	290 (0.1327)	HOMO→LUMO+3 (0.47) HOMO→LUMO+1 (0.36) HOMO-1→LUMO (0.27) HOMO-4→LUMO+1 (-0.12) HOMO-4→LUMO (0.11) HOMO→LUMO+2 (0.10)	π→π*
5	Singlet	287 (0.2384)	HOMO→LUMO+3 (0.46) HOMO→LUMO+1 (-0.40) HOMO-1→LUMO (-0.26) HOMO-4→LUMO+1 (-0.11)	π→π*
6	Singlet	268 (0.0502)	HOMO-3→LUMO (0.44) HOMO→LUMO+2 (-0.38) HOMO-1→LUMO+2 (0.36) HOMO-2→LUMO+2 (-0.12)	π→π*
7	Singlet	262 (0.0856)	HOMO-2→LUMO (0.64) HOMO→LUMO+4 (-0.19) HOMO-1→LUMO+1 (0.15)	π→π*
8	Singlet	244 (0.0293)	HOMO→LUMO+4 (0.54) HOMO-1→LUMO+1 (0.38)	π→π*

			HOMO-4→LUMO (-0.15)	
9	Singlet	242 (0.0288)	HOMO-4→LUMO (0.67) HOMO→LUMO+3 (-0.13) HOMO-1→LUMO+1 (0.11) HOMO→LUMO+4 (0.11)	π→π*
10	Singlet	240 (0.0396)	HOMO-1→LUMO+1 (0.53) HOMO→LUMO+4 (-0.33) HOMO-2→LUMO (-0.20) HOMO-1→LUMO+2 (0.15)	π→π*
11	Singlet	238 (0.0010)	HOMO-5→LUMO (0.70)	n→π*
12	Singlet	228 (0.0169)	HOMO-1→LUMO+3 (0.67) HOMO-2→LUMO+3 (0.17)	π→π*
13	Singlet	223 (0.3949)	HOMO-1→LUMO+2 (0.39) HOMO-3→LUMO+1 (0.38) HOMO-3→LUMO (-0.36) HOMO-3→LUMO+4 (-0.13)	π→π*
14	Singlet	214 (0.0190)	HOMO-1→LUMO+4 (0.49) HOMO-6→LUMO (0.44) HOMO-3→LUMO+2 (0.13) HOMO-7→LUMO (-0.12)	π→π*
15	Singlet	212 (0.0815)	HOMO-2→LUMO+2 (0.49) HOMO-1→LUMO+2 (0.31) HOMO-3→LUMO+1 (-0.28) HOMO-2→LUMO+1 (-0.15) HOMO-3→LUMO+4 (0.14)	π→π*
16	Singlet	208 (0.1027)	HOMO-2→LUMO+1 (0.63) HOMO-1→LUMO+4 (-0.17) HOMO-2→LUMO+2 (0.12) HOMO-6→LUMO (0.12) HOMO-3→LUMO+2 (0.11) HOMO→LUMO+6 (-0.11)	π→π*
17	Singlet	205 (0.0204)	HOMO→LUMO+5 (0.64) HOMO-4→LUMO+1 (-0.20) HOMO-1→LUMO+5 (-0.12) HOMO-2→LUMO+3 (0.11)	π→σ*
18	Singlet	204 (0.0319)	HOMO-4→LUMO+1 (0.46) HOMO-2→LUMO+3 (-0.30) HOMO→LUMO+5 (0.25) HOMO-6→LUMO (-0.16) HOMO-1→LUMO+4 (0.15) HOMO→LUMO+6 (-0.12) HOMO-6→LUMO+3 (-0.12)	π→π* π→σ*
19	Singlet	202 (0.0396)	HOMO-1→LUMO+4 (0.37) HOMO-6→LUMO (-0.33) HOMO→LUMO+6 (-0.28) HOMO-4→LUMO+1 (-0.21) HOMO-3→LUMO+1 (0.16) HOMO-2→LUMO+2 (0.15) HOMO-2→LUMO+3 (0.15)	π→π*
20	Singlet	196 (0.0001)	HOMO-5→LUMO+1 (0.63) HOMO-11→LUMO (0.21) HOMO-10→LUMO (-0.14) HOMO-13→LUMO (-0.14)	n→π*

[a] Oscillator strength; [b] expansion coefficient

Table 7.36 TDA-DFT data for **14**

#	**State**	**Transition energy (nm)**	**Participating MO**	**Transition character**
1	Singlet	344 (1.1421)[a]	HOMO→LUMO (0.64)[b]	π→π*

			HOMO→LUMO+1 (-0.19) HOMO-1→LUMO (-0.18)	
2	Singlet	322 (0.5337)	HOMO-1→LUMO (0.50) HOMO→LUMO+1 (0.38) HOMO→LUMO (0.27) HOMO-1→LUMO+2 (0.11)	π→π*
3	Singlet	291 (0.0306)	HOMO→LUMO+1 (0.52) HOMO-1→LUMO (-0.41) HOMO→LUMO+2 (-0.14) HOMO-2→LUMO (0.10)	π→π*
4	Singlet	289 (0.0004)	HOMO-3→LUMO (0.53) HOMO-4→LUMO (-0.38) HOMO-4→LUMO+1 (0.16) HOMO-4→LUMO+2 (-0.15) HOMO-3→LUMO+2 (-0.11)	n→π*
5	Singlet	284 (0.0031)	HOMO-4→LUMO (0.52) HOMO-3→LUMO (0.33) HOMO-3→LUMO+2 (-0.27) HOMO-3→LUMO+1 (0.18)	n→π*
6	Singlet	280 (0.4955)	HOMO-1→LUMO+1 (0.56) HOMO-2→LUMO (-0.29) HOMO→LUMO+2 (-0.25)	π→π*
7	Singlet	269 (0.1025)	HOMO→LUMO+2 (0.57) HOMO-2→LUMO (-0.33) HOMO-1→LUMO (-0.10) HOMO-1→LUMO+2 (0.11)	π→π*
8	Singlet	260 (0.0606)	HOMO-1→LUMO+2 (0.33) HOMO-2→LUMO (-0.30) HOMO→LUMO+3 (-0.28) HOMO-1→LUMO+1 (-0.28) HOMO-2→LUMO+1 (0.24) HOMO→LUMO+2 (-0.17)	π→π*
9	Singlet	258 (0.0065)	HOMO→LUMO+3 (0.52) HOMO-1→LUMO+2 (0.30) HOMO-2→LUMO+1 (0.23) HOMO-5→LUMO (-0.10)	π→π*
10	Singlet	255 (0.0003)	HOMO-4→LUMO+1 (0.60) HOMO-3→LUMO+1 (-0.27) HOMO-4→LUMO (0.15) HOMO-4→LUMO+4 (0.13) HOMO-4→LUMO+2 (0.12)	n→π*
11	Singlet	247 (0.1112)	HOMO-2→LUMO (0.39) HOMO→LUMO+4 (-0.35) HOMO→LUMO+3 (-0.25) HOMO-1→LUMO+1 (0.17) HOMO-1→LUMO+2 (0.17) HOMO→LUMO+2 (0.14) HOMO→LUMO+5 (0.14)	π→π*
12	Singlet	242 (0.0039)	HOMO-3→LUMO+3 (0.58) HOMO-4→LUMO+3 (0.22) HOMO-3→LUMO+2 (0.22) HOMO-3→LUMO (0.13) HOMO-7→LUMO (0.13)	n→π*
13	Singlet	241 (0.0791)	HOMO-1→LUMO+2 (0.40) HOMO-5→LUMO (0.35) HOMO→LUMO+4 (0.33) HOMO-2→LUMO+1 (-0.15) HOMO-2→LUMO (0.11) HOMO-1→LUMO+5 (0.11) HOMO→LUMO+1 (-0.10)	π→π*

14	Singlet	240 (0.0480)	HOMO-2→LUMO+1 (0.51) HOMO-5→LUMO (0.32) HOMO-1→LUMO+2 (-0.23) HOMO-1→LUMO+4 (0.14) HOMO→LUMO+4 (0.13) HOMO-2→LUMO+4 (0.12)	π→π*
15	Singlet	237 (0.0003)	HOMO-7→LUMO (0.64) HOMO-3→LUMO+3 (-0.15) HOMO-7→LUMO+2 (-0.12) HOMO-4→LUMO+2 (0.12) HOMO-7→LUMO+1 (0.11)	n→π*
16	Singlet	228 (0.0005)	HOMO-3→LUMO+1 (0.42) HOMO-3→LUMO+2 (-0.35) HOMO-3→LUMO (-0.26) HOMO-3→LUMO+3 (0.22) HOMO-4→LUMO+1 (0.17) HOMO-4→LUMO (-0.15) HOMO-7→LUMO (0.10)	n→π*
17	Singlet	228 (0.0168)	HOMO-1→LUMO+3 (0.44) HOMO-6→LUMO (-0.28) HOMO→LUMO+3 (-0.22) HOMO→LUMO+5 (-0.19) HOMO-2→LUMO+2 (-0.19) HOMO-5→LUMO (-0.14) HOMO-5→LUMO+1 (-0.12) HOMO-2→LUMO+3 (-0.11) HOMO-8→LUMO+3 (-0.11) HOMO-1→LUMO+4 (0.10)	π→π*
18	Singlet	224 (0.4241)	HOMO-1→LUMO+4 (0.30) HOMO→LUMO+4 (-0.29) HOMO-5→LUMO+1 (-0.27) HOMO-5→LUMO (0.26) HOMO-1→LUMO+3 (0.15) HOMO-1→LUMO+1 (-0.14) HOMO→LUMO+3 (0.13) HOMO-2→LUMO+1 (-0.13) HOMO-6→LUMO (0.12)	π→π*
19	Singlet	222 (0.0557)	HOMO-1→LUMO+3 (0.49) HOMO-2→LUMO+2 (0.29) HOMO→LUMO+5 (0.24) HOMO-6→LUMO (0.23) HOMO-5→LUMO+1 (0.15) HOMO→LUMO+4 (0.11)	π→π*
20	Singlet	221 (0.1483)	HOMO-2→LUMO+2 (0.46) HOMO-1→LUMO+4 (0.26) HOMO-6→LUMO (-0.24) HOMO-5→LUMO (-0.22) HOMO→LUMO+4 (0.21) HOMO-5→LUMO+1 (-0.13) HOMO-1→LUMO+3 (-0.11)	π→π*

[a] Oscillator strength; [b] expansion coefficient

Table 7.37 TDA-DFT data for **15**

#	**State**	**Transition energy (nm)**	**Participating MO**	**Transition character**
1	Singlet	396 (0.4438)[a]	HOMO→LUMO (0.68)[b] HOMO-1→LUMO (-0.10)	π→π*
2	Singlet	335 (0.0312)	HOMO→LUMO+1 (0.61) HOMO-1→LUMO (-0.34)	π→π*

3	Singlet	323 (0.0429)	HOMO-1→LUMO (0.56) HOMO→LUMO+1 (0.29) HOMO→LUMO+2 (-0.20) HOMO-2→LUMO (-0.20)	π→π*
4	Singlet	320 (0.0122)	HOMO→LUMO+2 (0.47) HOMO-2→LUMO (0.44) HOMO-1→LUMO (0.23) HOMO→LUMO+1 (0.15)	π→π*
5	Singlet	281 (0.0011)	HOMO-3→LUMO+1 (0.56) HOMO-3→LUMO (-0.42)	n→π*
6	Singlet	274 (0.0006)	HOMO-4→LUMO (0.64) HOMO→LUMO+4 (0.29)	π→π*
7	Singlet	272 (0.0113)	HOMO→LUMO+3 (0.68) HOMO-1→LUMO+1 (-0.12) HOMO-1→LUMO+6 (-0.10)	π→π*
8	Singlet	259 (0.6935)	HOMO-1→LUMO+1 (0.66) HOMO→LUMO+3 (0.14)	π→π*
9	Singlet	256 (0.0057)	HOMO-3→LUMO (0.56) HOMO-3→LUMO+1 (0.41)	n→π*
10	Singlet	249 (0.0293)	HOMO→LUMO+4 (0.58) HOMO-4→LUMO (-0.26) HOMO-5→LUMO (0.14) HOMO→LUMO+5 (0.13) HOMO-1→LUMO+2 (0.11)	π→π*
11	Singlet	246 (0.4492)	HOMO-5→LUMO (0.37) HOMO→LUMO+5 (0.28) HOMO-2→LUMO (-0.27) HOMO→LUMO+2 (0.26) HOMO-6→LUMO (0.22) HOMO-1→LUMO+2 (-0.22) HOMO-2→LUMO+1 (0.15)	π→π*
12	Singlet	245 (0.6318)	HOMO-5→LUMO (0.30) HOMO-2→LUMO (0.30) HOMO→LUMO+2 (-0.29) HOMO-1→LUMO+2 (0.25) HOMO→LUMO+4 (-0.22) HOMO→LUMO+5 (0.20) HOMO-6→LUMO (0.18) HOMO-2→LUMO+1 (-0.12)	π→π*
13	Singlet	241 (0.0058)	HOMO-3→LUMO+3 (0.69)	n→π*
14	Singlet	238 (0.0030)	HOMO-2→LUMO+1 (0.60) HOMO-1→LUMO+2 (0.34)	π→π*
15	Singlet	237 (0.0357)	HOMO-1→LUMO+3 (0.51) HOMO-6→LUMO (-0.30) HOMO-6→LUMO+1 (0.18) HOMO-5→LUMO+1 (-0.15) HOMO-5→LUMO (0.12) HOMO-8→LUMO+1 (0.12) HOMO-1→LUMO+1 (-0.12) HOMO→LUMO+3 (0.11) HOMO-2→LUMO+1 (-0.11)	π→π*
16	Singlet	234 (0.0145)	HOMO-7→LUMO (0.53) HOMO-7→LUMO+1 (-0.23) HOMO→LUMO+5 (0.22) HOMO-6→LUMO (-0.20) HOMO-6→LUMO+1 (0.12) HOMO-5→LUMO+1 (0.12) HOMO-1→LUMO+3 (-0.11)	n→π*
17	Singlet	231 (0.0339)	HOMO→LUMO+5 (0.37) HOMO-6→LUMO (-0.37)	π→π* n→π*

			HOMO-7→LUMO (-0.31) HOMO-8→LUMO (0.18) HOMO-4→LUMO+2 (0.16) HOMO-1→LUMO+3 (-0.15)	
18	Singlet	229 (0.0392)	HOMO-5→LUMO (0.45) HOMO→LUMO+5 (-0.35) HOMO-6→LUMO (-0.26) HOMO-1→LUMO+3 (-0.20)	π→π*
19	Singlet	227 (1.7457)	HOMO-1→LUMO+2 (0.49) HOMO-2→LUMO (-0.29) HOMO-2→LUMO+1 (-0.27) HOMO→LUMO+2 (0.25)	π→π*
20	Singlet	223 (0.0307)	HOMO-4→LUMO+1 (0.62) HOMO-7→LUMO+1 (0.17) HOMO-9→LUMO (-0.14) HOMO-7→LUMO (0.11) HOMO-6→LUMO+1 (-0.11)	π→π* n→π*

[a] Oscillator strength; [b] expansion coefficient

Table 7.38 TDA-DFT data for **16**

#	State	Transition energy (nm)	Participating MO	Transition character
1	Singlet	384 (1.0754)[a]	HOMO→LUMO (0.68)[b] HOMO→LUMO+1 (0.13)	π→π*
2	Singlet	340 (0.0069)	HOMO-1→LUMO (0.44) HOMO→LUMO+2 (0.41) HOMO→LUMO+1 (-0.30) HOMO-2→LUMO (-0.18)	π→π*
3	Singlet	318 (0.0795)	HOMO→LUMO+1 (0.54) HOMO→LUMO+2 (0.32) HOMO-2→LUMO (-0.28)	π→π*
4	Singlet	294 (0.4840)	HOMO-1→LUMO (0.44) HOMO-2→LUMO (0.34) HOMO→LUMO+1 (0.27) HOMO-1→LUMO+2 (0.16) HOMO→LUMO+3 (0.15) HOMO-2→LUMO+2 (-0.13) HOMO→LUMO+2 (-0.10)	π→π*
5	Singlet	283 (0.0300)	HOMO-3→LUMO (0.46) HOMO-3→LUMO+1 (0.37) HOMO→LUMO+4 (0.30) HOMO→LUMO+3 (-0.13) HOMO-4→LUMO (0.11) HOMO→LUMO+2 (-0.10)	n→π* π→π*
6	Singlet	283 (0.0544)	HOMO→LUMO+4 (0.46) HOMO-3→LUMO (-0.28) HOMO-3→LUMO+1 (-0.25) HOMO-4→LUMO (0.22) HOMO→LUMO+3 (-0.20) HOMO-1→LUMO (0.15) HOMO→LUMO+2 (-0.15)	π→π* n→π*
7	Singlet	278 (0.0179)	HOMO→LUMO+3 (0.62) HOMO→LUMO+4 (0.24) HOMO-4→LUMO (0.15)	π→π*
8	Singlet	274 (0.1317)	HOMO-4→LUMO (0.36) HOMO-2→LUMO (-0.35) HOMO→LUMO+4 (-0.32) HOMO→LUMO+2 (-0.28) HOMO-1→LUMO (0.16)	π→π*

			HOMO-1→LUMO+1 (0.12)	
9	Singlet	268 (0.1062)	HOMO-4→LUMO (0.48) HOMO-1→LUMO+1 (-0.32) HOMO-2→LUMO (0.27) HOMO→LUMO+2 (0.19) HOMO→LUMO+4 (-0.12)	π→π*
10	Singlet	257 (0.0461)	HOMO-1→LUMO+1 (0.57) HOMO→LUMO+2 (0.20) HOMO-1→LUMO+2 (0.18) HOMO-4→LUMO (0.15) HOMO-2→LUMO (0.15) HOMO→LUMO+3 (-0.10)	π→π*
11	Singlet	249 (0.0772)	HOMO→LUMO+5 (0.47) HOMO-2→LUMO+1 (-0.35) HOMO-5→LUMO (-0.28) HOMO-2→LUMO+2 (0.12)	π→π*
12	Singlet	247 (0.0324)	HOMO-1→LUMO+2 (0.41) HOMO-2→LUMO+1 (-0.33) HOMO-5→LUMO (0.25) HOMO→LUMO+5 (-0.23) HOMO-2→LUMO+2 (0.17) HOMO-6→LUMO (0.12) HOMO-1→LUMO+1 (-0.12)	π→π*
13	Singlet	243 (0.0051)	HOMO-3→LUMO+3 (0.55) HOMO-3→LUMO+1 (0.29) HOMO-3→LUMO (-0.28) HOMO-3→LUMO+2 (0.12)	n→π*
14	Singlet	238 (0.1255)	HOMO-1→LUMO+2 (0.34) HOMO-2→LUMO+1 (0.33) HOMO-1→LUMO+3 (0.26) HOMO-2→LUMO+2 (0.19) HOMO-6→LUMO (-0.15) HOMO-3→LUMO+3 (-0.13) HOMO→LUMO+5 (0.12) HOMO-5→LUMO (-0.11)	π→π*
15	Singlet	237 (0.0050)	HOMO-3→LUMO+3 (0.36) HOMO-3→LUMO+1 (-0.33) HOMO-7→LUMO (0.27) HOMO-3→LUMO (0.27) HOMO-1→LUMO+3 (0.18) HOMO→LUMO+5 (0.12) HOMO-7→LUMO+1 (0.11)	n→π*
16	Singlet	235 (0.1390)	HOMO-1→LUMO+3 (0.38) HOMO-5→LUMO (0.26) HOMO-2→LUMO+1 (-0.25) HOMO-3→LUMO+1 (0.18) HOMO-1→LUMO+2 (-0.16) HOMO-7→LUMO (0.15) HOMO-3→LUMO (-0.15) HOMO-2→LUMO+3 (0.14) HOMO-3→LUMO+3 (-0.13) HOMO-6→LUMO (-0.12) HOMO→LUMO+3 (-0.10)	π→π* n→π*
17	Singlet	234 (0.0327)	HOMO-7→LUMO (0.42) HOMO-6→LUMO (0.28) HOMO-3→LUMO+1 (0.21) HOMO-7→LUMO+1 (0.20) HOMO-2→LUMO+1 (0.18) HOMO-3→LUMO (-0.17) HOMO-1→LUMO+3 (-0.15)	π→π* n→π*

			HOMO-6→LUMO+1 (0.14)	
18	Singlet	233 (0.0099)	HOMO-1→LUMO+4 (0.46) HOMO-4→LUMO+2 (-0.38) HOMO-4→LUMO+1 (0.22) HOMO-2→LUMO+4 (-0.20)	π→π*
19	Singlet	224 (0.4080)	HOMO-5→LUMO (0.32) HOMO-2→LUMO+2 (0.31) HOMO-4→LUMO+1 (-0.25) HOMO-1→LUMO+3 (-0.21) HOMO→LUMO+5 (0.19) HOMO→LUMO+6 (-0.19) HOMO-2→LUMO+1 (0.14) HOMO-1→LUMO+2 (-0.14) HOMO-8→LUMO (-0.10)	π→π*
20	Singlet	222 (0.0348)	HOMO-6→LUMO (0.36) HOMO→LUMO+6 (-0.30) HOMO-4→LUMO+1 (0.26) HOMO-8→LUMO (-0.23) HOMO-7→LUMO (-0.19) HOMO-1→LUMO+3 (0.18) HOMO-5→LUMO (-0.12) HOMO-1→LUMO+2 (-0.10)	π→π* n→π*

[a] Oscillator strength; [b] expansion coefficient

Table 7.39 TDA-DFT data for **17**

#	**State**	**Transition energy (nm)**	**Participating MO**	**Transition character**
1	Singlet	342 (0.9157)[a]	HOMO→LUMO (0.69)[b]	π→π*
2	Singlet	322 (0.0000)	HOMO-1→LUMO (0.46) HOMO→LUMO+2 (0.46) HOMO→LUMO+1 (0.18) HOMO-1→LUMO+1 (0.16)	π→π*
3	Singlet	292 (0.0491)	HOMO→LUMO+1 (0.56) HOMO→LUMO+2 (-0.32) HOMO-2→LUMO (-0.22)	π→π*
4	Singlet	281 (0.0373)	HOMO-3→LUMO (0.53) HOMO-3→LUMO+1 (-0.30) HOMO-1→LUMO (-0.25) HOMO→LUMO+2 (0.19) HOMO→LUMO+1 (0.10)	n→π* π→π*
5	Singlet	281 (0.1828)	HOMO-1→LUMO (0.43) HOMO→LUMO+2 (-0.31) HOMO-3→LUMO (0.30) HOMO→LUMO+1 (-0.25) HOMO-3→LUMO+1 (-0.17) HOMO-1→LUMO+2 (0.10)	π→π* n→π*
6	Singlet	275 (0.2881)	HOMO-2→LUMO (0.60) HOMO→LUMO+3 (0.20) HOMO-1→LUMO+2 (-0.19) HOMO→LUMO+1 (0.15)	π→π*
7	Singlet	266 (0.0720)	HOMO→LUMO+3 (0.64) HOMO-2→LUMO (-0.15) HOMO-1→LUMO+2 (0.13)	π→π*
8	Singlet	256 (0.0175)	HOMO-1→LUMO+1 (0.52) HOMO-2→LUMO+2 (0.31) HOMO-1→LUMO+2 (-0.18) HOMO→LUMO+2 (-0.17) HOMO→LUMO+4 (-0.15) HOMO-1→LUMO+4 (-0.11)	π→π*

9	Singlet	249 (0.0617)	HOMO→LUMO+4 (0.54) HOMO-4→LUMO (0.38) HOMO-1→LUMO+1 (0.14) HOMO-2→LUMO+1 (0.12)	π→π*
10	Singlet	244 (0.4436)	HOMO-1→LUMO+2 (0.42) HOMO-2→LUMO+1 (-0.32) HOMO-1→LUMO+1 (0.23) HOMO-4→LUMO (0.20) HOMO-2→LUMO (0.19) HOMO→LUMO+4 (-0.14) HOMO-1→LUMO+4 (0.13) HOMO→LUMO+1 (0.12) HOMO→LUMO+3 (-0.10)	π→π*
11	Singlet	241 (0.0031)	HOMO-3→LUMO+3 (0.66) HOMO-3→LUMO+1 (0.16) HOMO-3→LUMO (0.13)	n→π*
12	Singlet	236 (0.4210)	HOMO-2→LUMO+2 (0.33) HOMO-1→LUMO+2 (0.33) HOMO-4→LUMO+2 (0.26) HOMO-1→LUMO+4 (-0.26) HOMO-1→LUMO+1 (-0.19) HOMO-2→LUMO+1 (0.12) HOMO-1→LUMO+3 (-0.11) HOMO-5→LUMO (0.10)	π→π*
13	Singlet	235 (0.2675)	HOMO-2→LUMO+1 (0.52) HOMO-2→LUMO+2 (-0.23) HOMO-1→LUMO+2 (0.22) HOMO-1→LUMO+4 (0.15) HOMO-1→LUMO+1 (0.14) HOMO→LUMO+4 (-0.10)	π→π*
14	Singlet	232 (0.0137)	HOMO-7→LUMO (0.54) HOMO-6→LUMO (-0.31) HOMO-7→LUMO+1 (-0.15) HOMO-3→LUMO+1 (0.10)	n→π* π→π*
15	Singlet	229 (0.1718)	HOMO-2→LUMO+2 (0.32) HOMO-1→LUMO+4 (0.28) HOMO-4→LUMO (-0.26) HOMO-4→LUMO+2 (-0.21) HOMO-2→LUMO+3 (-0.17) HOMO-1→LUMO+3 (0.16) HOMO→LUMO+4 (0.15) HOMO-5→LUMO (-0.14) HOMO-7→LUMO (0.13) HOMO-1→LUMO+2 (0.11) HOMO→LUMO+5 (-0.11)	π→π*
16	Singlet	227 (0.1043)	HOMO-1→LUMO+3 (0.29) HOMO-2→LUMO+3 (-0.26) HOMO-2→LUMO+2 (-0.24) HOMO-6→LUMO (-0.23) HOMO-4→LUMO (-0.19) HOMO→LUMO+5 (0.17) HOMO→LUMO+4 (0.16) HOMO-4→LUMO+2 (0.16) HOMO-1→LUMO+4 (-0.15) HOMO-1→LUMO+1 (0.14) HOMO-4→LUMO+1 (0.11) HOMO→LUMO+3 (-0.11)	π→π* n→π*
17	Singlet	225 (0.0185)	HOMO-5→LUMO (0.41) HOMO→LUMO+5 (0.28) HOMO-4→LUMO (-0.23)	π→π*

			HOMO-2→LUMO+3 (0.21) HOMO→LUMO+4 (0.18) HOMO-2→LUMO+1 (-0.18) HOMO-1→LUMO+4 (0.13)	
18	Singlet	224 (0.0005)	HOMO-3→LUMO+1 (0.54) HOMO-3→LUMO (0.33) HOMO-3→LUMO+3 (-0.18) HOMO-3→LUMO+2 (-0.14) HOMO-7→LUMO (-0.12)	n→π*
19	Singlet	222 (0.0640)	HOMO-1→LUMO+3 (0.61) HOMO-4→LUMO (0.16) HOMO-2→LUMO+3 (0.15) HOMO-2→LUMO+2 (0.13) HOMO→LUMO+4 (-0.11)	π→π*
20	Singlet	216 (0.1281)	HOMO-2→LUMO+3 (0.28) HOMO-4→LUMO (-0.28) HOMO→LUMO+5 (-0.23) HOMO-5→LUMO (-0.22) HOMO-6→LUMO (0.19) HOMO-7→LUMO (0.17) HOMO-1→LUMO+4 (-0.15) HOMO-5→LUMO+1 (-0.14) HOMO-4→LUMO+1 (0.14) HOMO-4→LUMO+2 (0.14) HOMO→LUMO+4 (0.13) HOMO-8→LUMO (-0.11)	π→π* n→π*

[a] Oscillator strength; [b] expansion coefficient

Table 7.40 TDA-DFT data for **18**

#	State	Transition energy (nm)	Participating MO	Transition character
1	Singlet	430 (0.1943)[a]	HOMO→LUMO (0.68)[b] HOMO-1→LUMO (0.11)	π→π* ISC
2	Singlet	376 (0.0000)	HOMO-2→LUMO (0.64) HOMO-3→LUMO (-0.22) HOMO-2→LUMO+1 (0.16)	n→π*
3	Singlet	333 (1.2776)	HOMO→LUMO+1 (0.68) HOMO-4→LUMO (-0.11)	π→π*
4	Singlet	314 (0.1805)	HOMO-1→LUMO (0.67) HOMO→LUMO (-0.12) HOMO-4→LUMO (0.10)	π→π*
5	Singlet	295 (0.2130)	HOMO-4→LUMO (0.50) HOMO→LUMO+2 (-0.41) HOMO-5→LUMO (-0.15) HOMO→LUMO+1 (0.13) HOMO-1→LUMO (-0.12)	π→π*
6	Singlet	288 (0.0009)	HOMO-3→LUMO (0.46) HOMO-3→LUMO+1 (-0.41) HOMO-3→LUMO+2 (0.24) HOMO-2→LUMO (0.16) HOMO-2→LUMO+1 (-0.15)	n→π*
7	Singlet	276 (0.1783)	HOMO→LUMO+2 (0.44) HOMO-4→LUMO (0.37) HOMO-1→LUMO+1 (-0.24) HOMO-5→LUMO (0.20) HOMO→LUMO+4 (-0.14)	π→π*
8	Singlet	265 (0.0581)	HOMO-5→LUMO (0.42) HOMO→LUMO+3 (-0.41) HOMO→LUMO+2 (-0.21)	π→π*

			HOMO→LUMO+4 (-0.20)	
9	Singlet	262 (0.0255)	HOMO→LUMO+3 (0.49) HOMO-5→LUMO (0.29) HOMO-1→LUMO+1 (0.29) HOMO→LUMO+4 (-0.15) HOMO→LUMO+2 (-0.14)	π→π*
10	Singlet	261 (0.0005)	HOMO-3→LUMO (0.48) HOMO-3→LUMO+1 (0.39) HOMO-2→LUMO (0.16) HOMO-3→LUMO+2 (-0.23) HOMO-2→LUMO+1 (0.15)	n→π*
11	Singlet	257 (0.0000)	HOMO-2→LUMO+1 (0.60) HOMO-2→LUMO+2 (0.23) HOMO-3→LUMO+1 (-0.22) HOMO-2→LUMO (-0.16)	n→π*
12	Singlet	244 (0.0057)	HOMO-6→LUMO (0.60) HOMO→LUMO+4 (0.26) HOMO-1→LUMO+1 (0.14) HOMO→LUMO+5 (0.14)	π→π*
13	Singlet	242 (0.0030)	HOMO-7→LUMO (0.49) HOMO-3→LUMO+3 (0.35) HOMO-7→LUMO+1 (-0.29) HOMO-2→LUMO+3 (0.12) HOMO-3→LUMO+1 (0.11) HOMO-3→LUMO+2 (0.10)	n→π*
14	Singlet	241 (0.0011)	HOMO-3→LUMO+3 (0.52) HOMO-7→LUMO (-0.35) HOMO-7→LUMO+1 (0.19) HOMO-2→LUMO+3 (0.18) HOMO-3→LUMO+2 (0.10)	n→π*
15	Singlet	241 (0.3140)	HOMO-1→LUMO+1 (0.54) HOMO-4→LUMO (0.22) HOMO→LUMO+3 (-0.21) HOMO→LUMO+2 (0.20) HOMO-6→LUMO (-0.14) HOMO-5→LUMO (-0.12)	π→π*
16	Singlet	235 (0.0886)	HOMO→LUMO+4 (0.37) HOMO-5→LUMO+1 (0.34) HOMO-4→LUMO+1 (-0.30) HOMO-5→LUMO (0.27) HOMO-6→LUMO (-0.17)	π→π*
17	Singlet	231 (0.0498)	HOMO-4→LUMO+1 (0.61) HOMO→LUMO+4 (0.20) HOMO-5→LUMO+1 (0.14) HOMO-5→LUMO (0.13)	π→π*
18	Singlet	227 (0.0544)	HOMO-8→LUMO (0.45) HOMO-1→LUMO+2 (-0.32) HOMO-6→LUMO+1 (0.20) HOMO-5→LUMO+1 (-0.17) HOMO-1→LUMO+3 (-0.14) HOMO→LUMO+5 (-0.14) HOMO→LUMO+3 (-0.13) HOMO→LUMO+4 (0.11) HOMO-8→LUMO+3 (-0.10)	π→π*
19	Singlet	226 (0.1683)	HOMO-1→LUMO+2 (0.44) HOMO-5→LUMO+1 (-0.29) HOMO-8→LUMO (0.26) HOMO→LUMO+5 (0.24) HOMO-6→LUMO (-0.17) HOMO-9→LUMO (0.15)	π→π*

			HOMO→LUMO+4 (0.14)	
20	Singlet	223 (0.0332)	HOMO→LUMO+5 (0.36) HOMO-5→LUMO+1 (0.35) HOMO-8→LUMO (0.30) HOMO→LUMO+4 (-0.23) HOMO-6→LUMO+1 (-0.19) HOMO-9→LUMO (-0.12)	π→π*

[a] Oscillator strength; [b] expansion coefficient

Table 7.41 TDA-DFT data for **19**

#	State	Transition energy (nm)	Participating MO	Transition character
1	Singlet	389 (0.9650)[a]	HOMO→LUMO (0.70)[b]	π→π*
2	Singlet	317 (0.0623)	HOMO→LUMO+1 (0.70)	π→π*
3	Singlet	297 (0.1311)	HOMO→LUMO+2 (0.53) HOMO→LUMO+3 (0.42) HOMO-2→LUMO (-0.13)	π→π*
4	Singlet	279 (0.5316)	HOMO→LUMO+3 (0.46) HOMO-1→LUMO (-0.38) HOMO→LUMO+2 (-0.35)	π→π*
5	Singlet	271 (0.0017)	HOMO-3→LUMO (0.69) HOMO-3→LUMO+1 (0.12)	n→π*
6	Singlet	265 (0.0183)	HOMO→LUMO+4 (0.68)	π→π*
7	Singlet	260 (0.2503)	HOMO-1→LUMO (0.57) HOMO→LUMO+2 (-0.27) HOMO→LUMO+3 (0.25)	π→π*
8	Singlet	247 (0.0057)	HOMO→LUMO+5 (0.65) HOMO→LUMO+6 (0.17) HOMO→LUMO+7 (-0.12)	π→σ*
9	Singlet	239 (0.0382)	HOMO-2→LUMO (0.68) HOMO→LUMO+3 (0.11)	π→π*
10	Singlet	239 (0.0037)	HOMO-3→LUMO+1 (0.66) HOMO-3→LUMO+2 (-0.17)	n→π*
11	Singlet	238 (0.0036)	HOMO-1→LUMO+1 (0.61) HOMO-4→LUMO (-0.20) HOMO-5→LUMO (0.19)	π→π* n→π*
12	Singlet	238 (0.0005)	HOMO→LUMO+6 (0.59) HOMO→LUMO+7 (0.36)	π→σ*
13	Singlet	229 (0.0012)	HOMO→LUMO+7 (0.56) HOMO→LUMO+6 (-0.31) HOMO→LUMO+10 (-0.17) HOMO→LUMO+5 (0.16)	π→σ*
14	Singlet	226 (0.0121)	HOMO→LUMO+8 (0.67) HOMO→LUMO+9 (-0.13)	
15	Singlet	225 (0.0035)	HOMO-6→LUMO (0.62) HOMO-5→LUMO (0.32)	n→π*
16	Singlet	223 (0.0000)	HOMO→LUMO+9 (0.59) HOMO→LUMO+13 (-0.26) HOMO→LUMO+10 (-0.11) HOMO→LUMO+11 (-0.11) HOMO-1→LUMO+2 (0.10)	π→σ*
17	Singlet	223 (0.0051)	HOMO-1→LUMO+2 (0.59) HOMO-1→LUMO+3 (0.25) HOMO-4→LUMO (0.19) HOMO-1→LUMO+1 (0.10)	π→π*
18	Singlet	218 (0.0182)	HOMO-1→LUMO+3 (0.47) HOMO-4→LUMO (-0.44) HOMO-1→LUMO+1 (-0.20)	π→π*
19	Singlet	218 (0.0008)	HOMO→LUMO+11 (0.50)	π→σ*

			HOMO→LUMO+13 (0.29) HOMO→LUMO+9 (0.26) HOMO→LUMO+10 (0.21)	
20	Singlet	215 (0.0017)	HOMO→LUMO+10 (0.61) HOMO→LUMO+13 (-0.26) HOMO→LUMO+5 (0.13) HOMO→LUMO+11 (-0.12) HOMO→LUMO+7 (0.11)	$\pi \rightarrow \sigma^*$

[a] Oscillator strength; [b] expansion coefficient

Table 7.42 TDA-DFT data for ***fac*-[Re(14)(CO)$_3$Br]**

#	**State**	**Transition energy (nm)**	**Participating MO**	**Transition character**
1	Singlet	493 (0.0038)[a]	HOMO→LUMO (0.70)[b] HOMO→LUMO+1 (0.11)	^{1}MLCT ^{1}XLCT
2	Singlet	463 (0.0554)	HOMO-1→LUMO (0.70)	^{1}MLCT ^{1}XLCT
3	Singlet	385 (0.0025)	HOMO-4→LUMO (0.69) HOMO-4→LUMO+1 (0.13)	^{1}MLCT
4	Singlet	369 (0.6780)	HOMO-2→LUMO (0.68)	$\pi \rightarrow \pi^*$
5	Singlet	353 (0.0015)	HOMO→LUMO+1 (0.58) HOMO-3→LUMO (-0.27) HOMO→LUMO+2 (0.22) HOMO→LUMO+3 (0.12)	^{1}MLCT $\pi \rightarrow \pi^*$
6	Singlet	347 (0.3808)	HOMO-3→LUMO (0.58) HOMO→LUMO+1 (0.24) HOMO-1→LUMO+1 (-0.14) HOMO-2→LUMO+1 (0.13) HOMO→LUMO+2 (0.11)	$\pi \rightarrow \pi^*$ ^{1}MLCT ^{1}XLCT
7	Singlet	341 (0.0475)	HOMO-1→LUMO+1 (0.62) HOMO-3→LUMO (0.13) HOMO-1→LUMO+2 (0.24) HOMO-1→LUMO+3 (0.12)	^{1}MLCT $\pi \rightarrow \pi^*$ ^{1}XLCT
8	Singlet	327 (0.0118)	HOMO-6→LUMO (0.44) HOMO→LUMO+3 (-0.36) HOMO→LUMO+2 (-0.33) HOMO→LUMO+1 (0.22)	^{1}MLCT
9	Singlet	325 (0.0621)	HOMO-5→LUMO (0.59) HOMO-6→LUMO (0.23) HOMO→LUMO+2 (0.15) HOMO→LUMO+3 (0.14) HOMO-7→LUMO (0.11) HOMO→LUMO+1 (-0.10)	^{1}MLCT $\pi \rightarrow \pi^*$
10	Singlet	321 (0.1096)	HOMO-6→LUMO (0.47) HOMO-5→LUMO (-0.32) HOMO→LUMO+2 (0.27) HOMO→LUMO+3 (0.26) HOMO→LUMO+1 (-0.11)	^{1}MLCT $\pi \rightarrow \pi^*$
11	Singlet	318 (0.0334)	HOMO-1→LUMO+3 (0.47) HOMO-1→LUMO+2 (0.44) HOMO-1→LUMO+1 (-0.27)	^{1}MLCT
12	Singlet	308 (0.2406)	HOMO-2→LUMO+1 (0.56) HOMO-3→LUMO (-0.21) HOMO-3→LUMO+3 (0.15) HOMO-3→LUMO+2 (-0.15) HOMO-2→LUMO+2 (-0.14) HOMO→LUMO+3 (-0.12) HOMO-2→LUMO (0.11) HOMO-3→LUMO+1 (-0.11)	$\pi \rightarrow \pi^*$

			HOMO-7→LUMO (-0.10)	
13	Singlet	301 (0.0281)	HOMO→LUMO+3 (0.49) HOMO→LUMO+2 (-0.47) HOMO-2→LUMO+1 (0.13) HOMO→LUMO+1 (0.11)	^{1}MLCT π→π* ^{1}XLCT
14	Singlet	298 (0.0015)	HOMO-8→LUMO (0.61) HOMO-8→LUMO+1 (-0.30) HOMO-9→LUMO (-0.13)	π→π* ^{1}XLCT
15	Singlet	295 (0.0035)	HOMO-1→LUMO+2 (0.45) HOMO-1→LUMO+3 (-0.45) HOMO→LUMO+4 (0.17) HOMO-1→LUMO+4 (-0.12) HOMO-3→LUMO+1 (0.11)	^{1}MLCT π→π* ^{1}XLCT d-d
16	Singlet	293 (0.0014)	HOMO-4→LUMO+1 (0.55) HOMO-4→LUMO+2 (0.25) HOMO→LUMO+4 (-0.20) HOMO-1→LUMO+3 (-0.14) HOMO-4→LUMO+3 (0.13) HOMO-1→LUMO+2 (0.12) HOMO-4→LUMO (-0.12)	^{1}MLCT d-d ^{1}XLCT
17	Singlet	292 (0.0050)	HOMO-1→LUMO+4 (0.44) HOMO→LUMO+4 (-0.43) HOMO-4→LUMO+1 (-0.17) HOMO-1→LUMO+3 (-0.12) HOMO-3→LUMO+1 (0.11) HOMO-1→LUMO+2 (0.10)	d-d ^{1}MLCT π→π*
18	Singlet	291 (0.0040)	HOMO-1→LUMO+4 (0.44) HOMO→LUMO+4 (0.37) HOMO-3→LUMO+1 (0.18) HOMO-4→LUMO+1 (0.16) HOMO-2→LUMO+2 (0.14) HOMO-1→LUMO+6 (-0.13)	d-d π→π* ^{1}MLCT
19	Singlet	290 (0.0030)	HOMO-3→LUMO+1 (0.48) HOMO-2→LUMO+2 (0.31) HOMO-1→LUMO+4 (-0.24) HOMO-2→LUMO+1 (0.16) HOMO→LUMO+4 (-0.13) HOMO-1→LUMO+3 (0.12)	π→π* d-d ^{1}MLCT
20	Singlet	282 (0.0005)	HOMO→LUMO+6 (0.57) HOMO→LUMO+5 (-0.25) HOMO-4→LUMO+4 (0.20) HOMO→LUMO+7 (0.11) HOMO-9→LUMO (0.11)	d-d ^{1}MLCT ^{1}XLCT

[a] Oscillator strength; [b] expansion coefficient

Table 7.43 TDA-DFT data for ***fac*-[Re(15)(CO)$_3$Br]**

#	**State**	**Transition energy (nm)**	**Participating MO**	**Transition character**
1	Singlet	472 (0.0023)[a]	HOMO-1→LUMO (0.61)[b] HOMO-1→LUMO+1 (-0.26) HOMO→LUMO (-0.21)	^{1}MLCT ^{1}XLCT π→π*
2	Singlet	445 (0.0781)	HOMO-2→LUMO (0.64) HOMO-2→LUMO+1 (-0.25) HOMO→LUMO (0.16)	^{1}MLCT ^{1}XLCT π→π*
3	Singlet	427 (0.1427)	HOMO→LUMO (0.62) HOMO-1→LUMO (0.22) HOMO→LUMO+1 (-0.17) HOMO-2→LUMO (-0.15)	^{1}MLCT ^{1}XLCT π→π*
4	Singlet	384 (0.0247)	HOMO-1→LUMO+1 (0.56)	^{1}MLCT

			HOMO→LUMO+1 (-0.33) HOMO-1→LUMO (0.24) HOMO→LUMO (-0.11)	^{1}XLCT π→π*
5	Singlet	375 (0.1649)	HOMO→LUMO+1 (0.48) HOMO-3→LUMO (0.31) HOMO-1→LUMO+1 (0.29) HOMO-3→LUMO+1 (-0.14) HOMO→LUMO (0.13) HOMO-2→LUMO+1 (-0.13) HOMO-1→LUMO (0.10)	π→π* ^{1}MLCT ^{1}XLCT
6	Singlet	375 (0.0439)	HOMO-3→LUMO (0.56) HOMO→LUMO+1 (-0.26) HOMO-3→LUMO+1 (-0.25) HOMO-1→LUMO+1 (-0.15) HOMO-2→LUMO+1 (0.13)	^{1}MLCT π→π* ^{1}XLCT
7	Singlet	373 (0.0152)	HOMO-2→LUMO+1 (0.63) HOMO-2→LUMO (0.24) HOMO→LUMO+1 (0.17)	^{1}MLCT ^{1}XLCT π→π*
8	Singlet	334 (0.0028)	HOMO-1→LUMO+2 (0.63) HOMO→LUMO+2 (-0.23) HOMO-4→LUMO (-0.18)	^{1}MLCT π→π* ^{1}XLCT
9	Singlet	325 (0.0004)	HOMO-2→LUMO+2 (0.67) HOMO-4→LUMO (0.19)	^{1}MLCT ^{1}XLCT
10	Singlet	322 (0.0355)	HOMO-4→LUMO (0.54) HOMO-5→LUMO (-0.24) HOMO-2→LUMO+2 (-0.20) HOMO-4→LUMO+1 (-0.17) HOMO-1→LUMO+2 (0.16) HOMO-7→LUMO (0.15) HOMO-5→LUMO+1 (0.10) HOMO-7→LUMO+1 (-0.10)	^{1}MLCT ^{1}XLCT π→π*
11	Singlet	319 (0.0035)	HOMO→LUMO+3 (0.47) HOMO-6→LUMO (0.37) HOMO-6→LUMO+1 (0.35) HOMO-1→LUMO+3 (0.11)	π→π* ^{1}MLCT ^{1}XLCT
12	Singlet	315 (0.0827)	HOMO-5→LUMO (0.58) HOMO-5→LUMO+1 (-0.22) HOMO-4→LUMO (0.19) HOMO-1→UMO+2 (0.19) HOMO→LUMO+2 (0.15)	^{1}MLCT ^{1}XLCT π→π*
13	Singlet	312 (0.0016)	HOMO-3→LUMO+1 (0.64) HOMO-3→LUMO (0.29)	^{1}MLCT
14	Singlet	308 (0.0148)	HOMO→LUMO+2 (0.64) HOMO-1→LUMO+2 (0.19) HOMO-5→LUMO (-0.17)	π→π* ^{1}MLCT ^{1}XLCT
15	Singlet	296 (0.0424)	HOMO-4→LUMO+1 (0.58) HOMO-7→LUMO (-0.27) HOMO-4→LUMO (0.23) HOMO-7→LUMO+1 (-0.13)	^{1}MLCT ^{1}XLCT π→π*
16	Singlet	291 (0.0067)	HOMO-1→LUMO+4 (0.50) HOMO-2→LUMO+4 (0.42) HOMO→LUMO+4 (-0.16) HOMO-2→LUMO+5 (-0.14)	d-d
17	Singlet	291 (0.0036)	HOMO-2→LUMO+4 (0.53) HOMO-1→LUMO+4 (-0.35) HOMO-2→LUMO+5 (0.15) HOMO-1→LUMO+5 (0.12) HOMO→LUMO+4 (0.11) HOMO-5→LUMO+4 (-0.11)	d-d
18	Singlet	285 (0.0290)	HOMO-6→LUMO (0.54)	π→π*

			HOMO-6→LUMO+1 (-0.41) HOMO→LUMO+3 (-0.12)	
19	Singlet	284 (0.0013)	HOMO-1→LUMO+5 (0.59) HOMO-3→LUMO+4 (-0.19) HOMO→LUMO+5 (-0.17) HOMO-2→LUMO+4 (-0.12) HOMO-1→LUMO+7 (0.10)	d-d ^{1}LMCT ^{1}MLCT
20	Singlet	281 (0.1026)	HOMO-7→LUMO (0.43) HOMO-3→LUMO+2 (0.41) HOMO-8→LUMO (-0.21) HOMO-4→LUMO+1 (0.20) HOMO-8→LUMO+1 (-0.15)	^{1}MLCT π→π* ^{1}XLCT

[a] Oscillator strength; [b] expansion coefficient

Table 7.44 TDA-DFT data for ***fac*-[Re(16)(CO)$_3$Br]**

#	**State**	**Transition energy (nm)**	**Participating MO**	**Transition character**
1	Singlet	480 (0.0188)[a]	HOMO-1→LUMO (0.60)[b] HOMO→LUMO (-0.33) HOMO-1→LUMO+1 (-0.15)	^{1}MLCT ^{1}XLCT π→π*
2	Singlet	452 (0.1012)	HOMO-2→LUMO (0.69) HOMO-2→LUMO+1 (-0.14)	^{1}MLCT ^{1}XLCT
3	Singlet	432 (0.5085)	HOMO→LUMO (0.61) HOMO-1→LUMO (0.33)	π→π* ^{1}MLCT ^{1}XLCT
4	Singlet	377 (0.0011)	HOMO-3→LUMO (0.68) HOMO-3→LUMO+1 (-0.19)	^{1}MLCT
5	Singlet	358 (0.0930)	HOMO-1→LUMO+1 (0.51) HOMO→LUMO+1 (-0.41) HOMO-1→LUMO+2 (-0.16) HOMO-1→LUMO (0.13)	^{1}MLCT ^{1}XLCT π→π*
6	Singlet	348 (0.1261)	HOMO-2→LUMO+1 (0.54) HOMO-1→LUMO+1 (0.26) HOMO-4→LUMO (0.21) HOMO→LUMO+1 (0.20) HOMO-2→LUMO+2 (-0.15) HOMO-2→LUMO (0.12)	^{1}MLCT ^{1}XLCT π→π*
7	Singlet	344 (0.1655)	HOMO-4→LUMO (0.47) HOMO-2→LUMO+1 (-0.33) HOMO→LUMO+3 (0.24) HOMO→LUMO+1 (0.20) HOMO-4→LUMO+1 (0.14) HOMO→LUMO+2 (0.11)	π→π* ^{1}MLCT ^{1}XLCT
8	Singlet	338 (0.2662)	HOMO→LUMO+1 (0.43) HOMO-1→LUMO+1 (0.30) HOMO→LUMO+3 (-0.25) HOMO-4→LUMO (-0.20) HOMO-2→LUMO+1 (-0.17) HOMO-4→LUMO+1 (-0.13) HOMO-5→LUMO (-0.12) HOMO→LUMO+2 (-0.11) HOMO-4→LUMO+3 (-0.10)	π→π* ^{1}MLCT ^{1}XLCT
9	Singlet	330 (0.0012)	HOMO-1→LUMO+2 (0.50) HOMO→LUMO+2 (-0.35) HOMO-5→LUMO (0.20) HOMO-1→LUMO+1 (0.18) HOMO-6→LUMO (0.15) HOMO→LUMO+3 (0.12)	^{1}MLCT ^{1}XLCT π→π*
10	Singlet	324 (0.0362)	HOMO-5→LUMO (0.51)	^{1}MLCT

			HOMO-6→LUMO (-0.26) HOMO-2→LUMO+2 (0.19) HOMO-7→LUMO (-0.16) HOMO-4→LUMO (-0.13) HOMO-1→LUMO+2 (-0.13) HOMO-4→LUMO+1 (0.12) HOMO→LUMO+3 (0.10)	^{1}XLCT π→π*
11	Singlet	321 (0.0037)	HOMO-2→LUMO+2 (0.63) HOMO-2→LUMO+1 (0.17) HOMO-1→LUMO+2 (0.14) HOMO-5→LUMO (-0.12) HOMO-6→LUMO (0.11)	^{1}MLCT ^{1}XLCT π→π*
12	Singlet	318 (0.0646)	HOMO-6→LUMO (0.58) HOMO-1→LUMO+2 (-0.30) HOMO-5→LUMO (0.18) HOMO-6→LUMO+1 (-0.11)	^{1}MLCT ^{1}XLCT π→π*
13	Singlet	308 (0.0819)	HOMO→LUMO+2 (0.51) HOMO-1→LUMO+2 (0.27) HOMO-7→LUMO (-0.21) HOMO-6→LUMO (0.17) HOMO→LUMO+3 (-0.16) HOMO-5→LUMO (0.13) HOMO-2→LUMO+2 (-0.12) HOMO-4→LUMO+1 (-0.11)	π→π* ^{1}MLCT ^{1}XLCT
14	Singlet	306 (0.1360)	HOMO-4→LUMO (0.39) HOMO-4→LUMO+1 (-0.36) HOMO→LUMO+3 (-0.29) HOMO→LUMO+2 (-0.20) HOMO-5→LUMO (0.19)	π→π*
15	Singlet	295 (0.0010)	HOMO-3→LUMO+1 (0.62) HOMO-3→LUMO+2 (-0.22) HOMO-3→LUMO (0.18) HOMO-1→LUMO+4 (0.11)	^{1}MLCT d-d
16	Singlet	293 (0.0075)	HOMO-2→LUMO+4 (0.45) HOMO-1→LUMO+4 (-0.41) HOMO→LUMO+4 (0.25) HOMO-3→LUMO+1 (0.12)	d-d ^{1}LMCT
17	Singlet	292 (0.1013)	HOMO-7→LUMO (0.52) HOMO-8→LUMO (0.24) HOMO-2→LUMO+4 (0.18) HOMO-5→LUMO (0.15) HOMO→LUMO+5 (0.14) HOMO-8→LUMO+1 (0.13) HOMO-7→LUMO+1 (0.11) HOMO→LUMO+2 (0.11)	π→π* ^{1}MLCT ^{1}XLCT d-d
18	Singlet	291 (0.0159)	HOMO-2→LUMO+4 (0.46) HOMO-1→LUMO+4 (0.39) HOMO-2→LIMO+6 (0.14) HOMO-7→LUMO (-0.14) HOMO-6→LUMO+4 (-0.11) HOMO→LUMO+4 (-0.10) HOMO-8→LUMO (-0.10)	d-d ^{1}LMCT π→π*
19	Singlet	283 (0.0019)	HOMO-1→LUMO+6 (0.48) HOMO-1→LUMO+7 (0.24) HOMO→LUMO+6 (-0.21) HOMO-3→LUMO+4 (0.18) HOMO-1→LUMO+5 (0.17) HOMO-1→LUMO+3 (-0.15) HOMO-8→LUMO (0.13) HOMO-2→LUMO+4 (0.11)	d-d ^{1}MLCT ^{1}LMCT ^{1}XLCT π→π*

20	Singlet	282 (0.2896)	HOMO-8→LUMO (0.50) HOMO-7→LUMO (-0.23) HOMO-4→LUMO+1 (0.22) HOMO-5→LUMO (-0.16) HOMO-8→LUMO+1 (0.11) HOMO-4→LUMO+3 (0.11) HOMO→LUMO+5 (0.11) HOMO-1→LUMO+6 (-0.11) HOMO→LUMO+3 (-0.11)	π→π* ^{1}MLCT ^{1}XLCT ^{1}LMCT

[a] Oscillator strength; [b] expansion coefficient

Table 7.45 TDA-DFT data for ***fac*-[Re(17)(CO)$_3$Br]**

#	**State**	**Transition energy (nm)**	**Participating MO**	**Transition character**
1	Singlet	480 (0.0029)[a]	HOMO→LUMO (0.70)[b]	^{1}MLCT ^{1}XLCT
2	Singlet	452 (0.0631)	HOMO-1→LUMO (0.69)	^{1}MLCT ^{1}XLCT
3	Singlet	386 (0.4898)	HOMO-2→LUMO (0.68) HOMO-4→LUMO (0.10)	π→π* ^{1}MLCT
4	Singlet	377 (0.0131)	HOMO-4→LUMO (0.69) HOMO-4→LUMO+1 (0.11) HOMO-2→LUMO (-0.10)	^{1}MLCT π→π*
5	Singlet	344 (0.0254)	HOMO-3→LUMO (0.67) HOMO-2→LUMO+3 (-0.16) HOMO-3→LUMO+1 (-0.13)	π→π*
6	Singlet	342 (0.0175)	HOMO→LUMO+1 (0.60) HOMO→LUMO+2 (0.33)	^{1}MLCT ^{1}XLCT
7	Singlet	333 (0.0098)	HOMO-1→LUMO+1 (0.61) HOMO-1→LUMO+2 (0.33)	^{1}MLCT ^{1}XLCT
8	Singlet	322 (0.0038)	HOMO-5→LUMO (0.60) HOMO-6→LUMO (0.30) HOMO-7→LUMO (0.16)	^{1}MLCT ^{1}XLCT π→π*
9	Singlet	320 (0.0247)	HOMO-6→LUMO (0.47) HOMO→LUMO+2 (-0.38) HOMO→LUMO+1 (0.26) HOMO-5→LUMO (-0.20)	^{1}MLCT ^{1}XLCT π→π*
10	Singlet	315 (0.1083)	HOMO→LUMO+2 (0.49) HOMO-6→LUMO (0.38) HOMO-5→LUMO (-0.19) HOMO→LUMO+1 (-0.19)	^{1}MLCT ^{1}XLCT π→π*
11	Singlet	311 (0.0189)	HOMO-1→LUMO+2 (0.61) HOMO-1→LUMO+1 (-0.33)	^{1}MLCT ^{1}XLCT
12	Singlet	304 (0.0194)	HOMO-2→LUMO+3 (0.44) HOMO-3→LUMO+1 (0.41) HOMO-3→LUMO (0.20) HOMO-3→LUMO+2 (-0.18) HOMO-2→LUMO+1 (-0.16) HOMO→LUMO+3 (-0.14)	π→π* ^{1}MLCT ^{1}XLCT
13	Singlet	301 (0.2234)	HOMO-2→LUMO+1 (0.64) HOMO-3→LUMO+3 (-0.15) HOMO-3→LUMO+1 (0.13)	π→π*
14	Singlet	293 (0.0074)	HOMO→LUMO+4 (0.53) HOMO-1→LUMO+4 (0.40) HOMO-1→LUMO+6 (0.12) HOMO-5→LUMO+4 (0.10)	d-d
15	Singlet	291 (0.0110)	HOMO-1→LUMO+4 (0.53) HOMO→LUMO+4 (-0.34) HOMO-1→LUMO+6 (-0.13)	d-d

			HOMO→LUMO+6 (-0.12) HOMO-6→LUMO+4 (-0.11)	
16	Singlet	288 (0.2141)	HOMO-2→LUMO+2 (0.47) HOMO-7→LUMO (0.46)	π→π* ^{1}MLCT ^{1}XLCT
17	Singlet	286 (0.0091)	HOMO-4→LUMO+1 (0.58) HOMO-4→LUMO+2 (0.35) HOMO-7→LUMO (-0.10)	^{1}MLCT ^{1}XLCT π→π*
18	Singlet	283 (0.0032)	HOMO→LUMO+6 (0.54) HOMO→LUMO+5 (-0.30) HOMO-4→LUMO+4 (-0.19) HOMO→LUMO+3 (0.15) HOMO-1→LUMO+4 (0.10)	d-d ^{1}MLCT ^{1}XLCT
19	Singlet	281 (0.0048)	HOMO→LUMO+3 (0.66) HOMO→LUMO+6 (-0.14) HOMO-2→LUMO+3 (0.10)	^{1}MLCT ^{1}XLCT d-d π→π*
20	Singlet	280 (0.2877)	HOMO-2→LUMO+2 (0.45) HOMO-7→LUMO (-0.44) HOMO-5→LUMO (0.15) HOMO-3→LUMO+3 (0.15) HOMO→LUMO+3 (0.11)	π→π* ^{1}MLCT ^{1}XLCT

[a] Oscillator strength; [b] expansion coefficient

Table 7.46 TDA-DFT data for ***fac*-[Re(18)(CO)$_3$Br]**

#	**State**	**Transition energy (nm)**	**Participating MO**	**Transition character**
1	Singlet	488 (0.0064)[a]	HOMO→LUMO (0.58)[b] HOMO→LUMO+1 (-0.39)	^{1}MLCT ^{1}XLCT
2	Singlet	461 (0.0535)	HOMO-1→LUMO (0.60) HOMO-1→LUMO+1 (-0.36)	^{1}MLCT ^{1}XLCT
3	Singlet	413 (0.1484)	HOMO→LUMO+1 (0.42) HOMO-2→LUMO (0.41) HOMO→LUMO (0.29) HOMO-2→LUMO+1 (0.22)	^{1}MLCT ^{1}XLCT π→π*
4	Singlet	402 (0.1282)	HOMO-2→LUMO (0.44) HOMO→LUMO+1 (-0.39) HOMO→LUMO (-0.27) HOMO-2→LUMO+1 (0.18) HOMO-1→LUMO+1 (0.13) HOMO-1→LUMO (0.12)	π→π* ^{1}MLCT ^{1}XLCT
5	Singlet	394 (0.0096)	HOMO-1→LUMO+1 (0.58) HOMO-1→LUMO (0.35) HOMO-2→LUMO (-0.15)	^{1}MLCT ^{1}XLCT π→π*
6	Singlet	382 (0.0007)	HOMO-3→LUMO (0.56) HOMO-3→LUMO+1 (-0.41)	^{1}MLCT
7	Singlet	379 (0.0000)	HOMO-6→LUMO (0.53) HOMO-6→LUMO+1 (0.44)	n→π*
8	Singlet	364 (0.6882)	HOMO-2→LUMO+1 (0.62) HOMO-2→LUMO (-0.29)	π→π*
9	Singlet	339 (0.0349)	HOMO→LUMO+2 (0.62) HOMO→LUMO+3 (-0.27)	^{1}MLCT ^{1}XLCT
10	Singlet	330 (0.0147)	HOMO-1→LUMO+2 (0.63) HOMO-1→LUMO+3 (-0.28)	^{1}MLCT ^{1}XLCT
11	Singlet	326 (0.0001)	HOMO-3→LUMO+1 (0.55) HOMO-3→LUMO (0.43) HOMO-3→LUMO+2 (0.10)	^{1}MLCT
12	Singlet	325 (0.0180)	HOMO-4→LUMO (0.51) HOMO-5→LUMO (0.29)	^{1}XLCT ^{1}MLCT

			HOMO-4→LUMO+1 (-0.28) HOMO-5→LUMO+1 (-0.20)	π→π*
13	Singlet	321 (0.0861)	HOMO-5→LUMO (0.49) HOMO-4→LUMO (-0.31) HOMO-5→LUMO+1 (-0.30) HOMO-4→LUMO+1 (0.15) HOMO→LUMO+2 (-0.14)	^{1}XLCT ^{1}MLCT π→π*
14	Singlet	307 (0.0222)	HOMO→LUMO+3 (0.61) HOMO→LUMO+2 (0.24) HOMO-7→LUMO (0.11)	^{1}MLCT ^{1}XLCT π→π*
15	Singlet	302 (0.0474)	HOMO-7→LUMO (0.41) HOMO-2→LUMO+2 (0.28) HOMO-1→LUMO+3 (0.27) HOMO-10→LUMO (0.18) HOMO→LUMO+3 (-0.15) HOMO-4→LUMO+1 (-0.14) HOMO-1→LUMO+2 (0.13) HOMO-1→LUMO+3 (0.12) HOMO-8→LUMO+1 (0.12) HOMO-8→LUMO (0.11) HOMO-7→LUMO+1 (0.11)	π→π* ^{1}MLCT ^{1}XLCT
16	Singlet	300 (0.1166)	HOMO-1→LUMO+3 (0.55) HOMO-1→LUMO+2 (0.23) HOMO-7→LUMO (-0.23) HOMO-4→LUMO+1 (0.17)	^{1}MLCT ^{1}XLCT π→π*
17	Singlet	298 (0.1322)	HOMO-4→LUMO+1 (0.43) HOMO-8→LUMO (0.33) HOMO-4→LUMO (0.27) HOMO-2→LUMO+2 (0.24) HOMO-1→LUMO+3 (-0.13)	^{1}MLCT ^{1}XLCT π→π*
18	Singlet	293 (0.0070)	HOMO→LUMO+4 (0.50) HOMO-1→LUMO+4 (0.42) HOMO-4→LUMO+4 (0.11) HOMO-1→LUMO+3 (-0.11) HOMO-1→LUMO+6 (0.10)	d-d ^{1}MLCT ^{1}XLCT
19	Singlet	291 (0.0053)	HOMO-1→LUMO+4 (0.51) HOMO→LUMO+4 (-0.38) HOMO-1→LUMO+6 (-0.14) HOMO-1→LUMO+5 (0.13) HOMO-5→LUMO+4 (-0.11)	d-d ^{1}MLCT ^{1}XLCT
20	Singlet	286 (0.0460)	HOMO-5→LUMO+1 (0.54) HOMO-5→LUMO (0.38) HOMO-2→LUMO+2 (-0.15)	^{1}MLCT ^{1}XLCT π→π*

[a] Oscillator strength; [b] expansion coefficient

Table 7.47 TDA-DFT data for ***fac*-[Re(19)(CO)$_3$Br]**

#	**State**	**Transition energy (nm)**	**Participating MO**	**Transition character**
1	Singlet	467 (0.2701)[a]	HOMO→LUMO (0.50)[b] HOMO-1→LUMO (-0.49)	π→π* ^{1}MLCT ^{1}XLCT
2	Singlet	447 (0.4222)	HOMO-1→LUMO (0.50) HOMO→LUMO (0.45) HOMO-2→LUMO (-0.22)	^{1}MLCT ^{1}XLCT π→π*
3	Singlet	433 (0.0861)	HOMO-2→LUMO (0.66) HOMO→LUMO (0.21) HOMO-1→LUMO (0.11)	^{1}MLCT ^{1}XLCT π→π*
4	Singlet	366 (0.0000)	HOMO-3→LUMO (0.70)	^{1}MLCT
5	Singlet	346 (0.1246)	HOMO→LUMO+1 (0.66)	π→π*

			HOMO-1→LUMO+1 (-0.18) HOMO-5→LUMO (0.10)	^{1}MLCT ^{1}XLCT
6	Singlet	329 (0.0192)	HOMO-1→LUMO+1 (0.67) HOMO→LUMO+1 (0.20)	^{1}MLCT ^{1}XLCT π→π*
7	Singlet	323 (0.0052)	HOMO-2→LUMO+1 (0.69) HOMO-4→LUMO (0.10)	^{1}MLCT ^{1}XLCT π→π*
8	Singlet	315 (0.0271)	HOMO-4→LUMO (0.58) HOMO-6→LUMO (0.28) HOMO-5→LUMO (0.24)	^{1}XLCT π→π*
9	Singlet	308 (0.1118)	HOMO-5→LUMO (0.65) HOMO-4→LUMO (-0.20) HOMO→LUMO+1 (-0.10)	^{1}XLCT π→π* ^{1}MLCT
10	Singlet	294 (0.1602)	HOMO-1→LUMO+3 (0.47) HOMO-2→LUMO+3 (-0.31) HOMO→LUMO+2 (0.24) HOMO→LUMO+3 (-0.20) HOMO-2→LUMO+5 (-0.13) HOMO-6→LUMO (-0.12)	d-d π→π* ^{1}LMCT
11	Singlet	293 (0.6658)	HOMO→LUMO+2 (0.47) HOMO-6→LUMO (-0.30) HOMO-2→LUMO+3 (0.29) HOMO-7→LUMO (0.15) HOMO-1→LUMO+3 (-0.14) HOMO→LUMO+4 (-0.10)	π→π* ^{1}XLCT d-d
12	Singlet	291 (0.0756)	HOMO-2→LUMO+3 (0.51) HOMO-1→LUMO+3 (0.32) HOMO-6→LUMO (0.15) HOMO-1→LUMO+5 (0.14) HOMO-2→LUMO+5 (-0.13) HOMO→LUMO+2 (-0.13) HOMO-5→LUMO+3 (0.11) HOMO-1→LUMO+2 (-0.11)	d-d π→π* ^{1}XLCT ^{1}MLCT
13	Singlet	285 (0.0149)	HOMO-1→LUMO+5 (0.48) HOMO-1→LUMO+2 (-0.31) HOMO-3→LUMO+3 (0.16) HOMO-2→LUMO+3 (-0.16) HOMO-1→LUMO+3 (-0.16) HOMO-1→LUMO+4 (-0.15) HOMO-6→LUMO (0.13) HOMO→LUMO+5 (-0.13)	d-d ^{1}MLCT ^{1}XLCT
14	Singlet	284 (0.0595)	HOMO→LUMO+4 (0.49) HOMO-7→LUMO (-0.31) HOMO-6→LUMO (-0.31) HOMO-7→LUMO+2 (0.13) HOMO→LUMO+5 (0.13) HOMO-4→LUMO (0.12)	π→π* ^{1}XLCT ^{1}LMCT
15	Singlet	279 (0.0001)	HOMO-3→LUMO+1 (0.70)	^{1}MLCT
16	Singlet	273 (0.0835)	HOMO-2→LUMO+2 (0.44) HOMO-6→LUMO (0.25) HOMO→LUMO+2 (0.24) HOMO-2→LUMO+5 (-0.16) HOMO-1→LUMO+5 (-0.16) HOMO-7→LUMO (-0.15) HOMO-4→LUMO (-0.15) HOMO-1→LUMO+2 (-0.13) HOMO→LUMO+4 (0.11)	^{1}MLCT ^{1}XLCT π→π* d-d
17	Singlet	272 (0.0025)	HOMO→LUMO+3 (0.64) HOMO-1→LUMO+3 (0.20)	^{1}LMCT d-d

18	Singlet	270 (0.0203)	HOMO-8→LUMO (0.48) HOMO-2→LUMO+2 (0.24) HOMO-1→LUMO+2 (0.21) HOMO-2→LUMO+5 (-0.17) HOMO→LUMO+2 (-0.17) HOMO-7→LUMO (0.16) HOMO-1→LUMO+5 (0.15) HOMO-6→LUMO (-0.13)	^{1}XLCT ^{1}MLCT d-d π→π*
19	Singlet	269 (0.0183)	HOMO-1→LUMO+2 (0.50) HOMO-8→LUMO (-0.31) HOMO-1→LUMO+5 (0.22) HOMO→LUMO+5 (-0.17) HOMO-2→LUMO+2 (0.16) HOMO-7→LUMO (-0.14)	^{1}MLCT ^{1}XLCT d-d ^{1}LMCT π→π*
20	Singlet	267 (0.0494)	HOMO-7→LUMO (0.54) HOMO→LUMO+4 (0.38) HOMO-8→LUMO (-0.15) HOMO-6→LUMO (0.13)	π→π* ^{1}MLCT ^{1}XLCT

[a] Oscillator strength; [b] expansion coefficient

7.5 Cartesian coordinates of DFT calculated species

7.5.1 5-(benzo[f]quinolin-3-yl)oxazole (1)

O	-4.0957537556	-1.1062986919	0.0002126231
N	-5.4492719951	0.6555278661	0.0001230215
N	-1.1299834308	0.9652523333	-0.0000590557
C	-5.3632237064	-0.6365063638	0.0002653231
H	-6.1565623141	-1.3666646630	0.0004107179
C	-4.1328512157	1.0945541224	-0.0000061643
H	-3.8741766908	2.1397932734	-0.0001291470
C	-3.2991434992	0.0170413594	0.0000350070
C	-1.8509088842	-0.1518782816	-0.0000964850
C	-1.2641088500	-1.4364549081	-0.0003167830
H	-1.8860956654	-2.3213829725	-0.0004618327
C	0.1088907092	-1.5368820634	-0.0003610660
H	0.5617070278	-2.5197216330	-0.0006273418
C	0.9091004983	-0.3759605634	-0.0001698727
C	0.2195257871	0.8711579421	-0.0000977539
C	0.9677151557	2.0957991261	-0.0001256934
H	0.4115684749	3.0255576813	-0.0002060058
C	2.3255749080	2.0799807652	-0.0000588402

H	2.8826875557	3.0107296702	-0.0000507169
C	3.0623762333	0.8477477192	0.0000274704
C	2.3617906266	-0.3928393356	-0.0000310108
C	3.1174596489	-1.5876017938	0.0000607900
H	2.6179571374	-2.5478468671	0.0001277189
C	4.4990063626	-1.5589717352	0.0001658735
H	5.0550855378	-2.4893659433	0.0001901561
C	5.1868837997	-0.3317903853	0.0002157054
H	6.2705931761	-0.3176493256	0.0003288722
C	4.4756891267	0.8507141808	0.0001653243
H	4.9953936925	1.8028202335	0.0002378877

7.5.2 5-(10-chloroanthracen-9-yl)oxazole (2)

Cl	-3.7772644204	0.1545658917	0.0571997471
O	2.9708752074	0.2526225538	1.0281593481
N	4.4659921131	-0.3122256413	-0.5146691420
C	-2.0145761397	0.0731393108	0.0114624835
C	-1.2903314434	1.2757328571	-0.0125154679
C	-1.9088284991	2.5649195420	-0.0020871484
H	-2.9871164920	2.6271415688	0.0390499053
C	-1.1604786644	3.7083704957	-0.0470860491
H	-1.6501502011	4.6750903273	-0.0389847746
C	0.2571411858	3.6382929021	-0.1113871403
H	0.8381536624	4.5518724727	-0.1585753881
C	0.8881482347	2.4254621967	-0.1168225448
H	1.9681551645	2.3836452061	-0.1698053894
C	0.1514990950	1.2003209721	-0.0586956184
C	0.7946264663	-0.0559751887	-0.0629304341
C	0.0419627146	-1.2493991842	-0.0274841845
C	0.6611530674	-2.5395964018	-0.0028306553
H	1.7414253690	-2.5962216016	-0.0060850969
C	-0.0803733082	-3.6875066153	0.0267717616
H	0.4143312144	-4.6515413013	0.0473020808
C	-1.4999024140	-3.6247574911	0.0336700458
H	-2.0778818208	-4.5412781069	0.0521917929

C	-2.1387641296	-2.4162966358	0.0233520712
H	-3.2188177328	-2.3770209923	0.0350979842
C	-1.4028323165	-1.1901011420	0.0000374913
C	2.2655729278	-0.1159432095	-0.1052298957
C	3.1856832014	-0.4582610218	-1.0413325850
H	3.0166569259	-0.7935695353	-2.0517806842
C	4.2729749698	0.1043379236	0.6940893638
H	5.0037429341	0.3424250151	1.4507141013

7.5.3 5-(pyrene-1-yl)oxazole (3)

C	4.3346017939	-1.6925495460	0.0405402325
C	3.1119043942	-2.3553208743	0.1008822313
C	1.9064936000	-1.6358934475	0.0894116184
C	1.9420049679	-0.2128688135	0.0138651507
C	3.2017911492	0.4574372527	-0.0401433951
C	4.3818809939	-0.3022779898	-0.0279415561
C	0.6284182182	-2.2808111941	0.1637430025
C	0.7260655422	0.5371872314	-0.0022610579
C	-0.5365131231	-0.1355206728	0.0410454374
C	-0.5317356002	-1.5707898921	0.1413425666
C	-1.7254245954	0.6399585677	0.0149766251
C	-1.6356298537	2.0407171128	-0.0228901130
C	-0.4125051874	2.6909370616	-0.0490271737
C	0.7856200342	1.9624046699	-0.0509858325
C	2.0659209395	2.6096519604	-0.1033610874
C	3.2205401199	1.8919821903	-0.1016054298
H	4.1805383533	2.3952984873	-0.1430576368
H	2.0923827898	3.6931594874	-0.1450976748
H	0.5994597522	-3.3622898398	0.2436391458
H	5.2568257546	-2.2622198705	0.0495603260
H	3.0809680120	-3.4379527824	0.1588273563
H	5.3381271598	0.2077459463	-0.0710214335
H	-1.4734449030	-2.0970879795	0.2018440694
H	-2.5483745467	2.6234066519	-0.0564449647
H	-0.3778166149	3.7739906021	-0.0881170160

C	-3.0676244171	0.0615599403	0.0528459768
C	-4.2258144906	0.4339890290	0.6662053921
N	-5.2428407335	-0.4470867227	0.3195942699
H	-4.3908756941	1.2590797933	1.3397266326
C	-4.6779796719	-1.3003861226	-0.4710475740
H	-5.1118779524	-2.1543712430	-0.9661991636
O	-3.3622644869	-1.0681988748	-0.6867987042

7.5.4 5-(phenanthren-9-yl)oxazole (4)

C	-3.5309087757	-2.4294380956	-0.0545432447
C	-2.1549954075	-2.5044106366	-0.0146490865
C	-1.3642334800	-1.3303221958	-0.0035614441
C	-1.9907388655	-0.0541476774	-0.0316224516
C	-3.4032027629	-0.0108632690	-0.0765448413
C	-4.1567646385	-1.1694756348	-0.0871775783
C	0.0599483809	-1.4195539141	0.0068134317
C	-1.1534151700	1.1375344191	-0.0005541035
C	0.2693311972	1.0115455810	0.0385080461
C	0.8661015745	-0.3132252327	0.0051440261
C	1.0520124077	2.1856478385	0.1438173707
H	2.1259457748	2.1025107177	0.2295930676
C	0.4744245359	3.4388026092	0.1675743259
C	-0.9211912291	3.5660238534	0.0898393571
C	-1.7114913330	2.4367368040	0.0160508060
H	0.5063430615	-2.4067359700	-0.0132542550
H	-4.1287024135	-3.3334672453	-0.0628150164
H	-1.6576599401	-3.4681686104	0.0060334661
H	-3.9196211435	0.9393398854	-0.1023573086
H	-5.2383125641	-1.1049140045	-0.1209476860
H	1.0988431936	4.3205264474	0.2537217247
H	-1.3809757050	4.5474805136	0.1024392935
H	-2.7853381321	2.5603558225	-0.0208876604
C	2.3150079694	-0.5122590515	-0.0513574368
C	3.3764836531	0.0980070766	-0.6516782924
N	4.5328996547	-0.6372048883	-0.4201062052

H	3.3891592464	0.9904025596	-1.2541898043
C	4.1409631478	-1.6416751424	0.2936442128
H	4.7249768153	-2.4539337615	0.6959983282
O	2.8163821225	-1.6458157688	0.5611488358

7.5.5 5-(fluorene-2-yl)oxazole (5)

H	1.4654887554	-2.4112045064	0.8780173911
C	4.8302726602	0.9714724515	-0.0000144143
C	5.1411163531	-0.3926938389	-0.0000306996
C	4.1259463739	-1.3546769101	-0.0000569220
C	2.8010208596	-0.9357665845	-0.0000648048
C	2.4870509624	0.4389408238	-0.0000334285
C	3.5022161366	1.3985488757	-0.0000133732
H	5.6301203169	1.7034838500	0.0000069194
H	6.1789477800	-0.7064363434	-0.0000259458
H	4.3746531424	-2.4107166209	-0.0000668012
H	3.2691605567	2.4576912266	0.0000062232
C	1.5312154963	-1.7593756367	-0.0000678969
H	1.4653713045	-2.4109274186	-0.8783626686
C	0.4482401464	-0.7022596747	0.0000687852
C	-0.9286575015	-0.8607898948	0.0001277667
C	-1.7553112700	0.2779753318	0.0001488771
C	-1.1688792944	1.5588771977	0.0001797176
C	0.2115698480	1.7167841317	0.0000524409
C	1.0272438345	0.5819198456	0.0000279121
H	-1.3712448505	-1.8496212214	0.0001029069
H	0.6393377952	2.7129237237	0.0000597178
C	-3.2048213555	0.1469075862	-0.0000148127
C	-4.2552726639	1.0180815651	-0.0002477065
N	-5.4490247635	0.3073127045	-0.0001894785
H	-4.2392835005	2.0954148111	-0.0004097571
C	-5.0888299513	-0.9348880445	0.0000107652
H	-5.7062548411	-1.8186876121	0.0003701601
H	-1.8012586633	2.4387272617	0.0003229412
O	-3.7483235125	-1.1207724241	0.0001090031

7.5.6 5-(4-(pyridin-2-yl)phenyl)oxazole (6)

C	-1.1122989899	0.0537758817	-0.0169562344
C	-0.3750712737	-1.1232973138	0.1769620439
C	1.0134606098	-1.1098381624	0.1816071503
C	1.7179471256	0.0879645659	-0.0191236028
C	0.9841891566	1.2675804483	-0.2257735919
C	-0.4032090774	1.2484874224	-0.2219894896
C	-2.5979403163	0.0186508826	-0.0050498728
C	-4.5150990807	-1.2253021686	-0.3158703742
C	-5.3456883612	-0.1509430948	-0.0052821567
C	-4.7463875844	1.0602541839	0.3299365018
C	-3.3592317617	1.1476982252	0.3345475922
H	-0.9047958322	-2.0542484968	0.3322269348
H	1.5568208627	-2.0319947272	0.3449341142
H	1.4984580671	2.2053429252	-0.3994365371
H	-0.9347125323	2.1744817655	-0.4043348776
H	-4.9421691759	-2.1893533596	-0.5775269550
H	-6.4222793886	-0.2662943005	-0.0217050657
H	-5.3483865829	1.9224400800	0.5927790170
H	-2.8757961021	2.0736647283	0.6171144533
N	-3.1813040271	-1.1537396562	-0.3188940800
C	3.1720634818	0.1184021097	-0.0164074450
C	4.1182110520	1.0924203105	-0.1482102840
N	5.3831476516	0.5259227187	-0.0608227393
H	3.9814724763	2.1508003287	-0.2968006802
C	5.1629914276	-0.7366099378	0.1165442008
H	5.8752462596	-1.5374220041	0.2341484086
O	3.8524522889	-1.0685198049	0.1558765372

7.5.7 5-(4-(pyrrolidin-1-yl)phenyl)oxazole (7)

O	-3.6898993112	-1.0589524292	0.0268500292
N	2.6450965461	-0.0055412235	-0.0001896052

N	-5.2069002293	0.5444124741	-0.0109161901
C	1.2838154145	0.0228852429	-0.0015160267
C	0.5761145123	1.2415820197	-0.0799814985
H	1.1146448378	2.1764523209	-0.1510094833
C	-1.5529924614	0.0850576092	-0.0043728291
C	-0.8571822080	-1.1231867528	0.0716703111
H	-1.4072296362	-2.0539520782	0.1346630755
C	0.5242388679	-1.1619536718	0.0743606608
H	1.0210217001	-2.1197149884	0.1449642242
C	-0.8034243919	1.2625745007	-0.0804608680
H	-1.3065596362	2.2203986835	-0.1471376868
C	-3.0060946917	0.1286558680	-0.0034355288
C	-3.9396532155	1.1122858187	-0.0259230970
H	-3.7966300678	2.1794366210	-0.0497132364
C	3.4819657420	1.1906425643	0.0224827691
C	3.4296463512	-1.2365429932	-0.0203439567
C	-4.9952280706	-0.7228345872	0.0201867314
H	-5.7102362116	-1.5292866242	0.0412348520
C	4.8487221061	-0.7510278207	-0.3095459853
C	4.8780042698	0.6442287579	0.3155483302
H	3.1443290027	1.8915119370	0.7899935198
H	3.4496233994	1.7110289539	-0.9432196698
H	5.0259882845	0.5682705132	1.3956708767
H	5.6646166912	1.2809426067	-0.0888361509
H	5.6060358746	-1.4210786324	0.0969022361
H	5.0027695444	-0.6815191402	-1.3892542591
H	3.3719086039	-1.7548428158	0.9453326267
H	3.0639445717	-1.9223259788	-0.7886646659

7.5.8 5-(benzo[f]quinolin-3-yl)-2-(naphthalen-1-yl)oxazole (8)

C	-6.0616742788	-0.6400534862	-0.0001695176
C	-5.4989872413	-1.9600142494	-0.0044848148
C	-4.1543103517	-2.1583936883	-0.0057106598
C	-3.2471603582	-1.0461497857	-0.0025489413
C	-3.7650146136	0.2813565069	0.0018172327

C	-2.8166547228	1.3253872268	0.0047826687
C	-1.4690483241	1.0409570068	0.0031099016
C	-1.0648315403	-0.3140276781	-0.0014582900
C	0.3423118522	-0.6801267162	-0.0040064510
C	1.0035808660	-1.8778607790	-0.0076212418
N	2.3493121994	-1.6441191791	-0.0084722349
C	2.4824519997	-0.3447434707	-0.0056935241
C	3.6822718674	0.4892794805	-0.0053355729
C	3.5090587525	1.8675063051	-0.0104873338
C	4.6033011947	2.7508639991	-0.0103834323
C	5.8857408491	2.2561351264	-0.0047325973
C	6.1198620225	0.8574321067	0.0009822484
C	5.0149607977	-0.0564957419	0.0007556294
C	5.3016879643	-1.4480206369	0.0070473079
C	6.6015183767	-1.9048630039	0.0129095865
C	7.6874235050	-1.0026673527	0.0129431945
C	7.4462635868	0.3505246480	0.0070941671
O	1.2886635298	0.2919074479	-0.0022306233
N	-1.9300456265	-1.3168447032	-0.0041425998
C	-5.1995431791	0.4932625629	0.0030168390
C	-5.7844900400	1.7792959941	0.0071164548
C	-7.1573408745	1.9407020595	0.0081091110
C	-8.0055007064	0.8189962091	0.0050172269
C	-7.4614445167	-0.4500292972	0.0009192607
H	-6.1825792057	-2.8132264801	-0.0068024260
H	-3.7181123994	-3.1590642490	-0.0090286127
H	-3.1396614110	2.3676140419	0.0082982104
H	-0.7244456461	1.8377069712	0.0053248369
H	0.5742552640	-2.8770066585	-0.0095210234
H	2.4974358270	2.2750427339	-0.0151665531
H	4.4239599643	3.8281944564	-0.0147847670
H	6.7442561497	2.9328133905	-0.0044295466
H	4.4679686852	-2.1489678674	0.0067661849
H	6.7928245102	-2.9809183082	0.0176293633
H	8.7127224440	-1.3803452803	0.0176708565
H	8.2752786339	1.0632187564	0.0071421965

H	-5.1505349348	2.6673689375	0.0095493947
H	-7.5840598501	2.9464792861	0.0113209440
H	-9.0897559131	0.9528803977	0.0058125539
H	-8.1103231970	-1.3298225838	-0.0015634992

7.5.9 5-(10-chloroanthracen-9-yl)-2-(naphthalen-1-yl)oxazole (9)

Cl	-6.0050026278	0.6208821103	-0.3741822375
C	-4.3205871229	0.2802382919	-0.1189490434
C	-3.8686190812	-1.0421372677	-0.2649959616
C	-4.7425606701	-2.1164086786	-0.6146194410
C	-4.2682810462	-3.3887616491	-0.7813658940
C	-2.8841159902	-3.6606982228	-0.6210195959
C	-2.0168255292	-2.6591817141	-0.2767842417
C	-2.4664221584	-1.3180779137	-0.0654910359
C	-1.5857856153	-0.2735163872	0.3025718488
C	-0.1691214405	-0.5636423241	0.5436248997
C	0.5096702833	-1.3906775658	1.3935353820
N	1.8565533264	-1.2377209046	1.1999326724
C	1.9751666091	-0.3430876704	0.2592936226
C	3.1648205751	0.2274366355	-0.3730668774
C	2.9715009859	1.1661326477	-1.3783427996
C	4.0536631539	1.7696383830	-2.0442618434
C	5.3427628579	1.4343430571	-1.7054730324
C	5.5965847697	0.4813320024	-0.6861957808
C	4.5044664924	-0.1431289123	0.0019363810
C	4.8100136612	-1.0910527049	1.0155498649
C	6.1157984178	-1.4002448940	1.3275534878
C	7.1891766517	-0.7838604777	0.6481933641
C	6.9297135521	0.1376309039	-0.3381277512
O	0.7752903893	0.1038676750	-0.1762778066
C	-2.0697375402	1.0473016087	0.4568743304
C	-3.4626499325	1.3384581472	0.2280963772
C	-3.9229143721	2.6816786354	0.3795829978
C	-3.0694848666	3.6829899556	0.7555736540
C	-1.7030051033	3.3971215272	1.0123357537

C	-1.2223679022	2.1233920556	0.8673600638
H	-5.8025750944	-1.9002782708	-0.7505364214
H	-4.9537906430	-4.1959646521	-1.0493406872
H	-2.5082103618	-4.6739909405	-0.7804059136
H	-0.9541327114	-2.8776873391	-0.1686102776
H	0.0999823152	-2.0724071916	2.1366959834
H	1.9536355844	1.4407164409	-1.6584421857
H	3.8590215000	2.5031291652	-2.8297478582
H	6.1915105528	1.8965432957	-2.2163045136
H	3.9858101525	-1.5705699026	1.5423109559
H	6.3220973058	-2.1330034801	2.1118138329
H	8.2195140985	-1.0396759587	0.9069017300
H	7.7491033950	0.6241702641	-0.8739323388
H	-4.9759456417	2.8945210218	0.1933120860
H	-3.4416384328	4.7039564096	0.8670649575
H	-1.0318461310	4.1981656059	1.3306100947
H	-0.1708449755	1.9211797598	1.0700700454

7.5.10 5-(3a1,5a1-dihydropyren-1-yl)-2-(naphthalen-1-yl)oxazole (10)

C	-3.4400644270	0.4463841082	0.1120765063
C	-4.6702865572	-0.2498551063	-0.0906098201
C	-4.6657198267	-1.6399915439	-0.4030954789
C	-5.8854419169	-2.3084049703	-0.5921936411
C	-7.0935382960	-1.6262153573	-0.4783321809
C	-7.1098830454	-0.2661062950	-0.1797098050
C	-5.9138766721	0.4421574598	0.0149400329
C	-5.9023942675	1.8450160303	0.3143303711
C	-4.7311604150	2.5148776559	0.4932324342
C	-3.4682810183	1.8430804536	0.3984628690
C	-2.2531564567	2.5209401905	0.5787589960
C	-1.0472759542	1.8436425456	0.5149810454
C	-0.9905128454	0.4616148231	0.2637979959
C	0.3181800935	-0.1778813808	0.2842618004
C	0.8253696565	-1.4009740314	0.6454588303
N	2.1881619277	-1.3794297191	0.5400904034

C	2.4899806250	-0.1788828095	0.1303029532
C	3.7842180418	0.4289410642	-0.1732553343
C	3.7871562453	1.7320819728	-0.6545838721
C	4.9832195211	2.4006204701	-0.9721395323
C	6.1907273176	1.7645904188	-0.8090743693
C	6.2452076987	0.4337409084	-0.3217734242
C	5.0349524935	-0.2618684312	0.0059332204
C	5.1419363926	-1.5931336271	0.4909236383
C	6.3710921831	-2.1969251393	0.6418282407
C	7.5612041044	-1.5095859812	0.3182054755
C	7.4943519835	-0.2204042229	-0.1538898726
O	1.3932155262	0.5936572395	-0.0356259036
C	-2.1951444686	-0.2509961653	0.0239487965
C	-2.2286004646	-1.6403111987	-0.3370121271
C	-3.4023597306	-2.3013028724	-0.5367716209
H	-5.8755237072	-3.3745267029	-0.8331235790
H	-8.0349705322	-2.1603576871	-0.6273116240
H	-8.0608015239	0.2662952520	-0.0954242759
H	-6.8584139084	2.3691380458	0.3925922617
H	-4.7331751249	3.5850201722	0.7156797462
H	-2.2648855531	3.5931064815	0.7897647830
H	-0.1153741985	2.3851423596	0.6863525707
H	0.2927151052	-2.2770994869	1.0080424173
H	2.8361943743	2.2481201449	-0.7926988324
H	4.9420613137	3.4249271859	-1.3489691200
H	7.1266931532	2.2739722401	-1.0529206927
H	4.2266579938	-2.1291160279	0.7393274639
H	6.4239760366	-3.2221156287	1.0169873960
H	8.5286808552	-2.0018673670	0.4431083176
H	8.4060157791	0.3262838746	-0.4092206940
H	-1.2888498848	-2.1722975231	-0.4816475042
H	-3.3932579515	-3.3569690211	-0.8201769728

7.5.11 2-(naphthalen-1-yl)-5-(phenanthren-9-yl)oxazole (11)

C	-4.1054778260	0.7716525024	0.1183893576

C	-4.3846467492	-0.6360523879	-0.1179460447
C	-3.2929157979	-1.5300175396	-0.2886742318
C	-3.5372564257	-2.9074315380	-0.5001730029
C	-4.8255701534	-3.3983143878	-0.5457415503
C	-5.9099633008	-2.5174853407	-0.3826368245
C	-5.6919658923	-1.1680571118	-0.1742944198
C	-1.9590099769	-1.0266693597	-0.2737796386
C	-1.6743678532	0.3018583734	-0.0862286863
C	-0.2790873596	0.7229282886	-0.1611738513
C	0.4061865739	1.8312254765	-0.5895032566
N	1.7509432402	1.5895185848	-0.5260788382
C	1.8675213549	0.3725435916	-0.0736350265
C	3.0554661844	-0.4277174991	0.2192968286
C	2.8640677624	-1.6834139100	0.7815859841
C	3.9457456539	-2.5261467597	1.0951751330
C	5.2331229391	-2.1141698251	0.8460460229
C	5.4852687984	-0.8413067806	0.2734583862
C	4.3936878900	0.0299668605	-0.0510361814
C	4.6976587880	1.2941025613	-0.6242170010
C	6.0015236581	1.6710605274	-0.8607892704
C	7.0744624631	0.8112778579	-0.5397399611
C	6.8163805161	-0.4190762782	0.0160601977
O	0.6662610721	-0.2015528754	0.1605408300
C	-2.7572042829	1.2374961578	0.1582939192
C	-2.5181561786	2.5955444559	0.4710030941
C	-3.5552355071	3.4806170703	0.6903255962
C	-4.8826128529	3.0333972511	0.6083136225
C	-5.1439265381	1.7047343486	0.3372294094
H	-2.6836805815	-3.5779103324	-0.6300300550
H	-5.0043741208	-4.4635528125	-0.7095235632
H	-6.9328131547	-2.8997834774	-0.4201165765
H	-6.5554132303	-0.5134805222	-0.0512208953
H	-1.1424492000	-1.7297967792	-0.4507120268
H	0.0109886922	2.7701028292	-0.9701434494
H	1.8481063405	-2.0220664367	0.9886268526
H	3.7524750083	-3.5057497650	1.5378187441

H	6.0816722559	-2.7603100822	1.0859069487
H	3.8739248553	1.9631729082	-0.8701102453
H	6.2065033073	2.6494502934	-1.3026999922
H	8.1033147212	1.1244544338	-0.7329733738
H	7.6352974333	-1.0971397245	0.2704191638
H	-1.4920300140	2.9481011666	0.5676221600
H	-3.3389872727	4.5230216573	0.9355070707
H	-5.7091499696	3.7282427192	0.7742495030
H	-6.1822520683	1.3737572463	0.3019533158

7.5.12 2-(2-(naphthalen-1-yl)oxazol-5-yl)-9H-fluoren-9-one (12)

O	4.7575706705	-2.7495987840	-0.0008596413
C	4.6670592324	-1.5430183494	-0.0004468867
C	5.7757092438	-0.5423676699	-0.0000848312
C	5.2251535092	0.7540066703	0.0003466584
C	6.0620984673	1.8636465024	0.0007365262
C	7.4473126277	1.6526437371	0.0006871162
C	7.9873266973	0.3641684992	0.0002571462
C	7.1460420415	-0.7540828718	-0.0001366754
C	3.7530137212	0.6387349036	0.0002809632
C	3.4115813367	-0.7273812355	-0.0001893046
C	2.1009224822	-1.1587861811	-0.0003672429
C	1.0715396393	-0.1940745050	-0.0000596798
C	-0.3175718546	-0.6127872178	-0.0002247981
C	-0.9571987906	-1.8249169751	-0.0003805859
N	-2.3082000146	-1.6217488159	-0.0004503096
C	-2.4704008196	-0.3270858136	-0.0003379212
C	-3.6878760498	0.4808955688	-0.0003951492
C	-3.5448459752	1.8627752545	-0.0009124293
C	-4.6581385958	2.7220684985	-0.0009945716
C	-5.9295424341	2.1997740495	-0.0005575401
C	-6.1331973940	0.7962375886	-0.0000175194
C	-5.0086964191	-0.0935256558	0.0000721134
C	-5.2652488111	-1.4910190368	0.0006488436
C	-6.5548602401	-1.9759497437	0.0010931514

C	-7.6600823475	-1.0974809009	0.0009873591
C	-7.4483486508	0.2606109045	0.0004474050
O	-1.2896634260	0.3348531656	-0.0001929310
C	1.4138666191	1.1698785662	0.0004135442
C	2.7452694583	1.5950935143	0.0005847320
H	5.6594532975	2.8791305218	0.0010740688
H	8.1188052727	2.5148474875	0.0009909158
H	9.0716586347	0.2321745554	0.0002287035
H	7.5476650526	-1.7703438027	-0.0004781579
H	1.8814272588	-2.2290032743	-0.0007512794
H	-0.5223856898	-2.8224673429	-0.0004305452
H	-2.5423374921	2.2922076232	-0.0012879082
H	-4.5023354693	3.8030719431	-0.0014161698
H	-6.8024051048	2.8578021667	-0.0006189955
H	-4.4167990907	-2.1740941220	0.0007020357
H	-6.7228092854	-3.0559076717	0.0015292577
H	-8.6769603837	-1.4973236011	0.0013394039
H	-8.2927658239	0.9549792309	0.0003649264
H	0.6149119384	1.9135564805	0.0006682846
H	2.9736987805	2.6632278083	0.0009556620

7.5.13 2-(naphthalen-1-yl)-5-(4-(pyrrolidin-1-yl)phenyl)oxazole (13)

C	-4.2740953967	-0.0911872704	0.0039197427
N	-5.6085875142	0.1781080448	-0.0016499549
C	-6.1600545661	1.5200863016	0.0617593475
C	-7.6436478497	1.2854657542	0.3271930884
C	-7.9098203870	-0.0508988396	-0.3585331096
C	-6.6380192213	-0.8437744027	-0.0750153398
C	-3.7909143031	-1.4232520161	0.0385490783
C	-2.4326355695	-1.6904115642	0.0427301579
C	-1.4780805059	-0.6582061325	0.0150217012
C	-0.0600963526	-0.9548822751	0.0200316702
C	0.6894779072	-2.1044791087	0.0391358613
N	2.0183181528	-1.7790772481	0.0332740063
C	2.0634539577	-0.4768112182	0.0111602566

C	3.2003478131	0.4404594978	-0.0042454938
C	2.9325155273	1.8038484460	-0.0212761091
C	3.9628614462	2.7614183274	-0.0367517961
C	5.2774073983	2.3599983828	-0.0352261217
C	5.6080553207	0.9807023604	-0.0182366229
C	4.5694721182	-0.0078049470	-0.0024522520
C	4.9522043390	-1.3761981556	0.0137783067
C	6.2803262266	-1.7427898630	0.0143978252
C	7.3008752180	-0.7672195425	-0.0009333000
C	6.9662666794	0.5659737572	-0.0168252104
O	0.8245268518	0.0753513964	0.0022658174
C	-1.9542384760	0.6632503501	-0.0178212744
C	-3.3109576926	0.9462778431	-0.0244180029
H	-5.9985421678	2.0652837996	-0.8889677662
H	-5.6813438240	2.1113219098	0.8602467949
H	-8.2736242143	2.1046139272	-0.0470864566
H	-7.8197625755	1.1966676014	1.4114973128
H	-8.0235091360	0.0967510867	-1.4447604343
H	-8.8136320925	-0.5594144363	0.0054576830
H	-6.4176576607	-1.5767543437	-0.8689733981
H	-6.7134563428	-1.4062738628	0.8763169807
H	-4.4923354435	-2.2575048328	0.0719814673
H	-2.1056664395	-2.7328188658	0.0731247785
H	0.3473280219	-3.1371399821	0.0559392333
H	1.8946779619	2.1391030411	-0.0224381284
H	3.7077474583	3.8234822762	-0.0498319091
H	6.0861299389	3.0954317321	-0.0471524546
H	4.1672772359	-2.1317250779	0.0260476386
H	6.5457737383	-2.8029926691	0.0270111711
H	8.3500956127	-1.0725924321	-0.0001079131
H	7.7442184544	1.3340378454	-0.0287597921
H	-1.2403515028	1.4892796048	-0.0434076105
H	-3.6319177032	1.9878228345	-0.0612865144

7.5.14 5-(benzo[f]quinolin-3-yl)-2-(pyridin-2-yl)oxazole (14)

C	-5.0428053457	-0.4800289702	-0.0002584742
C	-4.5585748778	-1.8308269584	-0.0005014538
C	-3.2279440341	-2.1079625923	-0.0004593688
C	-2.2574393577	-1.0506669482	-0.0001555700
C	-2.6961521400	0.3050666436	0.0001151810
C	-1.6882379953	1.2916705316	0.0004462739
C	-0.3597640869	0.9283959874	0.0004820195
C	-0.0361249028	-0.4479813925	0.0002040517
C	1.3479623234	-0.8953030704	0.0002155057
C	1.9433043096	-2.1298133353	0.0005905272
N	3.3009737432	-1.9762867026	0.0003888552
C	3.4940151811	-0.6891544423	0.0002914996
C	4.7570334710	0.0536892019	0.0000668876
N	5.8775762798	-0.6748185132	0.0000943447
C	7.0389974829	-0.0335800087	-0.0001675551
C	7.1539120179	1.3586628422	-0.0004638234
C	5.9845688732	2.1143755110	-0.0005126715
C	4.7593687776	1.4559882359	-0.0002605283
O	2.3475409004	0.0220487162	0.0000239463
N	-0.9582301094	-1.3982891185	-0.0001193883
C	-4.1158713267	0.6009543233	0.0000453975
C	-4.6245172478	1.9190315649	0.0002600593
C	-5.9855294886	2.1603941845	0.0001858414
C	-6.8979000534	1.0902559228	-0.0001066430
C	-6.4291534005	-0.2084454704	-0.0003258408
H	-5.2911054785	-2.6422581243	-0.0007257313
H	-2.8508826402	-3.1323557122	-0.0006466035
H	-1.9493183186	2.3511093329	0.0006757698
H	0.4305158041	1.6798335394	0.0007268507
H	1.4553441002	-3.1019371192	0.0007975002
H	7.9398678627	-0.6580521101	-0.0001089579
H	8.1377716718	1.8318526203	-0.0006536301
H	6.0239373292	3.2061538660	-0.0007551464
H	3.8198105961	2.0098947788	-0.0003134631
H	-3.9398355541	2.7685850696	0.0004833559
H	-6.3526121508	3.1894264686	0.0003525680

H	-7.9724320522	1.2874532274	-0.0001617608
H	-7.1285172799	-1.0486657852	-0.0005568967

7.5.15 5-(10-chloroanthracen-9-yl)-2-(pyridin-2-yl)oxazole (15)

Cl	-5.0406348830	0.8494940887	0.6165335278
C	-3.3999882653	0.4196526913	0.2407517417
C	-2.4850649021	1.4443214977	-0.0581313414
C	-1.1296655963	1.0810047675	-0.3867654979
C	-0.2264801017	2.1295566420	-0.7460204654
C	-0.6193831471	3.4410155013	-0.7525806065
C	-1.9477593202	3.7948331990	-0.3986005371
C	-2.8529657146	2.8240322892	-0.0662142422
C	-3.0390621937	-0.9383840061	0.2446764664
C	-1.6720874699	-1.2898471457	-0.0550361098
C	-1.3118230126	-2.6723084363	0.0103540650
C	-2.2322204230	-3.6397126158	0.3114994726
C	-3.5832412054	-3.2898152057	0.5720487221
C	-3.9710035467	-1.9781021879	0.5453718142
C	-0.7365964226	-0.2781337865	-0.3759613921
C	0.6420955228	-0.6408304771	-0.7182508331
C	1.2189701612	-1.4287528926	-1.6774821934
N	2.5813418053	-1.3949314574	-1.5447175745
C	2.7978047216	-0.6076515107	-0.5343587210
C	4.0736443614	-0.2043450927	0.0654021801
N	5.1803265639	-0.7051960790	-0.4918099651
C	6.3512325329	-0.3599091354	0.0286327091
C	6.4888249042	0.4958568547	1.1240710344
C	5.3332524852	1.0149798828	1.7017798306
C	4.0984585284	0.6622514911	1.1674303225
O	1.6664115575	-0.1155060964	0.0106565268
H	0.7964256211	1.8747969965	-1.0226514230
H	0.0922066144	4.2201495480	-1.0354176538
H	-2.2495513523	4.8446817534	-0.4003672720
H	-3.8777030642	3.0903699087	0.1942639197
H	-0.2747720845	-2.9524465423	-0.1764241336

H	-1.9242028857	-4.6867912345	0.3581433896
H	-4.3119317417	-4.0696732357	0.8046357209
H	-5.0045672281	-1.7036490009	0.7580755826
H	0.7213077364	-2.0032282520	-2.4571089676
H	7.2410969793	-0.7859837959	-0.4491033567
H	7.4794650644	0.7445095957	1.5098480879
H	5.3904485508	1.6878230092	2.5606441765
H	3.1679482664	1.0447093600	1.5891340105

7.5.16 5-(pyren-1-yl)-2-(pyridin-2-yl)oxazole (16)

C	-2.9733128357	-1.8077797723	0.3470907060
C	-4.3840518747	-1.9121421857	0.5794675855
C	-5.1934052791	-0.8202531426	0.5108018372
C	-4.6624353613	0.4744821283	0.1963685517
C	-5.4810273373	1.6115504069	0.1127329173
C	-4.9429552105	2.8567222166	-0.2020916286
C	-3.5786906889	2.9941637513	-0.4423188038
C	-2.1297189565	-2.9265553356	0.4135072342
C	-0.7669743800	-2.7967458380	0.2089653447
C	-0.1765882781	-1.5545415535	-0.0823759376
C	1.2665418269	-1.5522469036	-0.2838933575
C	2.1396901209	-2.5045702893	-0.7507405462
N	3.4174072074	-2.0227600557	-0.7011171334
C	3.3037126586	-0.8217124070	-0.2184308909
C	4.3500863127	0.1649892899	0.0585985212
N	5.6005609014	-0.1878170914	-0.2561677167
C	6.5731888219	0.6822526592	-0.0163185048
C	6.3623366287	1.9436874074	0.5456059751
C	5.0587641925	2.3069402554	0.8735037582
C	4.0283408761	1.4054103832	0.6288071529
O	2.0267393361	-0.4767013160	0.0538472354
C	-0.9999596270	-0.4010868858	-0.1850326001
C	-0.4979696365	0.8991406583	-0.5364547179
C	-1.3176705742	1.9830964142	-0.6220704413
C	-2.7233130545	1.8838407672	-0.3675120995

C	-3.2613215531	0.6058085029	-0.0411290113
C	-2.4060721490	-0.5351010296	0.0426556044
H	-4.7984207062	-2.8957166130	0.8151154775
H	-6.2673758316	-0.9136399286	0.6913383302
H	-6.5533926730	1.5071365098	0.2970959357
H	-5.5961911677	3.7304080435	-0.2634269596
H	-3.1593788131	3.9717072571	-0.6940543058
H	-2.5549132085	-3.9051485173	0.6490477313
H	-0.1263799779	-3.6759747221	0.3034673986
H	1.9067285388	-3.4965369856	-1.1339542178
H	7.5874816158	0.3646968720	-0.2848389745
H	7.2026903029	2.6184653486	0.7200621167
H	4.8443173726	3.2819802715	1.3172986103
H	2.9937050922	1.6481724172	0.8750838549
H	0.5639096062	1.0182520871	-0.7439524409
H	-0.9056395365	2.9577515703	-0.8964863530

7.5.17 5-(phenanthren-9-yl)-2-(pyridin-2-yl)oxazole (17)

C	-0.7496993054	-0.3416981707	-0.1503279681
C	0.6064374935	-0.8564686813	-0.3114424865
C	1.1913956417	-1.9818640875	-0.8403076623
N	2.5525137762	-1.8491722199	-0.8181488059
C	2.7655491165	-0.6804775184	-0.2924010808
C	4.0397778138	-0.0137106097	-0.0126027888
N	5.1477008628	-0.6703950680	-0.3704271595
C	6.3188231277	-0.0944190900	-0.1310889645
C	6.4564052859	1.1577429558	0.4727805733
C	5.3000234903	1.8382368575	0.8447167033
C	4.0648708784	1.2471849533	0.6006543751
O	1.6307337263	-0.0288954336	0.0323162588
C	-0.9411326584	1.0134326639	-0.2397758061
C	-2.2335463400	1.6111969112	-0.1673936902
C	-2.3823902730	3.0136505273	-0.2798864753
C	-3.6315365845	3.5975225023	-0.2415173854
C	-4.7717094600	2.7875834627	-0.0919695769

C	-4.6472004447	1.4150875526	0.0202062135
C	-3.3817034729	0.7882453194	-0.0100720157
C	-3.1995219844	-0.6484171796	0.1246107760
C	-1.8891393287	-1.2115625005	0.0785968524
C	-1.7403419792	-2.6010696586	0.2938376710
C	-2.8316597860	-3.4218591064	0.4995145471
C	-4.1241732969	-2.8758886393	0.5019859592
C	-4.2957103806	-1.5168007462	0.3271830684
H	0.7082010700	-2.8594170092	-1.2640801316
H	7.2092249006	-0.6567744806	-0.4354362911
H	7.4473817382	1.5823706760	0.6449214985
H	5.3571009673	2.8195851634	1.3215178724
H	3.1344960699	1.7439417759	0.8789575009
H	-0.0815407546	1.6664838378	-0.4044745232
H	-1.4867460314	3.6285325196	-0.4012587271
H	-3.7366256746	4.6813937804	-0.3291819681
H	-5.7640996251	3.2437971619	-0.0639036979
H	-5.5520138139	0.8172791826	0.1348378929
H	-0.7406632924	-3.0326235464	0.3244780892
H	-2.6846305022	-4.4911267499	0.6682507414
H	-4.9934109026	-3.5189856671	0.6579539160
H	-5.3069518487	-1.1102084224	0.3571145056

7.5.18 2-(2-(pyridin-2-yl)oxazol-5-yl)-9H-fluoren-9-one (18)

O	3.8818609630	2.6553284679	-0.0000121734
C	3.7151226805	1.4570146915	0.0000059965
C	4.7583493495	0.3882793775	0.0000258164
C	4.1272340579	-0.8707075859	0.0000231309
C	4.8922303418	-2.0310713765	0.0000250698
C	6.2880177115	-1.9079466941	0.0000328939
C	6.9082313387	-0.6561176393	0.0000379658
C	6.1392819794	0.5130444680	0.0000335958
C	2.6653106710	-0.6626896710	0.0000072696
C	2.4104697174	0.7221306228	-0.0000108612
C	1.1292266227	1.2347506277	-0.0000339024

C	1.5998181619	-1.5542721283	0.0000058847
C	0.2978146605	-1.0465094674	-0.0000086672
C	0.0419479903	0.3361637301	-0.0000248996
C	-1.3185257352	0.8408609224	-0.0000611750
C	-1.8839339818	2.0920816562	-0.0000921410
N	-3.2456137214	1.9774561154	-0.0000731198
C	-3.4750313403	0.6975880295	-0.0000216718
C	-4.7578954742	-0.0094566904	-0.0000180771
N	-5.8576438677	0.7503949406	0.0001647252
C	-7.0365737983	0.1419436146	0.0002212614
C	-7.1907362956	-1.2465478609	0.0000577936
C	-6.0430653389	-2.0347757545	-0.0001070371
C	-4.7998147812	-1.4112120493	-0.0001462463
O	-2.3475504521	-0.0446767356	-0.0000166257
H	4.4262905137	-3.0191510545	0.0000213078
H	6.9038111744	-2.8107706798	0.0000349785
H	7.9987335883	-0.5928289925	0.0000447207
H	6.6042273407	1.5018977137	0.0000390530
H	0.9760515013	2.3163985201	-0.0000632520
H	1.7612103734	-2.6345360053	0.0000220634
H	-0.5462255252	-1.7386005893	-0.0000053193
H	-1.3841020839	3.0591314563	-0.0001032232
H	-7.9196922937	0.7913833402	0.0003252410
H	-8.1875443866	-1.6918719504	0.0000684653
H	-6.1130603491	-3.1250577869	-0.0002276507
H	-3.8762518751	-1.9914702202	-0.0002792263

7.5.19 2-(pyridin-2-yl)-5-(4-(pyrrolidin-1-yl)phenyl)oxazole (19)

C	-0.9678994840	1.1110355741	-0.0329770677
C	0.4333156981	0.7445686466	-0.0234506873
C	0.8444315033	-0.5988030539	0.0008799531
C	2.1856338841	-0.9474143570	0.0115675971
C	3.1981340055	0.0425101388	-0.0034116894
N	4.5177560953	-0.2908209085	0.0064392338
C	5.0049512044	-1.6570251338	-0.0678858871

C	6.4986976576	-1.4907293229	-0.3275645502
C	6.8263029592	-0.1754452341	0.3721387858
C	5.5947097361	0.6800145624	0.0930747386
C	2.7804216419	1.3967845354	-0.0289782500
C	1.4369111805	1.7295595014	-0.0376400035
C	-1.6598987248	2.2991406173	-0.0633751779
N	-3.0039482749	2.0475825044	-0.0549193066
C	-3.1047678522	0.7527991091	-0.0205253727
C	-4.3084171372	-0.0777103975	0.0043823210
N	-5.4814869277	0.5657014267	0.0066363975
C	-6.5920248317	-0.1602280852	0.0283250463
C	-6.6059059966	-1.5566931510	0.0494190329
C	-5.3831687658	-2.2237712622	0.0476535646
C	-4.2101916871	-1.4777490293	0.0248288628
O	-1.9044473881	0.1278131834	-0.0064139072
H	0.0910205240	-1.3892484699	0.0158904176
H	2.4556787551	-2.0035359156	0.0413144937
H	4.5008416179	-2.2173450135	-0.8729415074
H	4.8150162802	-2.2023615831	0.8774685338
H	6.6816793044	-1.3995337750	-1.4105263732
H	7.0879569582	-2.3426600556	0.0397659547
H	7.7544008822	0.2928975316	0.0154633443
H	6.9295725793	-0.3389204899	1.4571377887
H	5.6999625007	1.2474980251	-0.8523830893
H	5.4067821345	1.4147967803	0.8936478888
H	3.5216551439	2.1962159889	-0.0510322873
H	1.1610500118	2.7867979362	-0.0595574925
H	-1.2606941489	3.3111950074	-0.0907249807
H	-7.5366960028	0.3963314200	0.0293582270
H	-7.5523715018	-2.1006210576	0.0667810958
H	-5.3416752929	-3.3155435740	0.0635885168
H	-3.2322567701	-1.9607713644	0.0221991592

7.5.20 *fac*-[Re(14)(CO)$_3$Br]

Br	2.6909647217	-0.3432994027	2.3458391089

Re	2.9366559579	-0.6752564285	-0.2644694366
C	3.0641571898	-0.8263278747	-2.1670938114
O	3.1494595027	-0.9220514437	-3.3171856268
C	4.8306431372	-0.9631839859	-0.1076187726
O	5.9701444551	-1.1092714242	-0.0049486173
N	0.8322436843	-0.0453543573	-0.2957310046
C	0.6574865679	1.2519014039	-0.2346954530
C	1.7630469888	2.1826109805	-0.2390616835
N	2.9657704412	1.5663331669	-0.2994979668
C	4.0655607668	2.3237414307	-0.3162425546
C	4.0150971793	3.7142729965	-0.2745245317
C	2.7757113403	4.3463959209	-0.2111311929
C	1.6234441144	3.5678768574	-0.1938262452
O	-0.6220043364	1.5940686991	-0.1762482272
C	-1.3247937440	0.4262508411	-0.1968452044
C	-2.7790631646	0.4607442308	-0.1394773175
C	-3.4825291146	1.6801992643	-0.0433252603
C	-4.8592157219	1.6349652177	0.0093774044
C	-5.5334915003	0.3978586751	-0.0323380853
C	-6.9766961272	0.2636432053	0.0183091830
C	-7.8464575019	1.3725207761	0.1134668819
C	-9.2174900835	1.2028958214	0.1597582584
C	-9.7765673387	-0.0864238490	0.1124747064
C	-8.9500989569	-1.1885959768	0.0191300121
C	-7.5463660813	-1.0404127163	-0.0294941434
C	-6.6902604949	-2.1882469876	-0.1262328687
C	-5.3379210452	-2.0638551375	-0.1747253219
C	-4.7202597931	-0.7697587200	-0.1294674824
N	-3.3781638066	-0.7177629793	-0.1813901093
C	-0.4200287855	-0.5983635352	-0.2711422226
C	2.6598779155	-2.5723424589	-0.1254200287
O	2.4665060965	-3.7049058349	-0.0346346174
H	5.0201558203	1.7966779890	-0.3616485139
H	4.9442646171	4.2853739834	-0.2894687892
H	2.7063697846	5.4352992297	-0.1750046428
H	0.6289616303	4.0128838956	-0.1443270758

H	-2.9476325379	2.6299644857	-0.0098640163
H	-5.4179668769	2.5688360355	0.0850761680
H	-7.4405068267	2.3845178670	0.1518458256
H	-9.8687473625	2.0768973025	0.2337260622
H	-10.8609129289	-0.2138769268	0.1496502921
H	-9.3734661769	-2.1956531560	-0.0183929101
H	-7.1542755626	-3.1774093834	-0.1601260948
H	-4.6794354808	-2.9311939336	-0.2478821622
H	-0.6042826468	-1.6680352213	-0.3014005859

7.5.21 *fac*-[Re(15)(CO)$_3$Br]

Br	-2.4542855056	-1.9023630967	-1.3563471151
Re	-2.7961262403	-0.1981930012	0.6378324765
C	-2.9761587031	1.0994208487	2.0310125426
O	-3.0921743554	1.8813759021	2.8761597897
N	-0.6433862072	0.1362709815	0.3623583443
C	-0.3451555955	0.9549850254	-0.6137558873
O	0.9574922776	1.0450390268	-0.8300461913
C	1.5544904985	0.2058636127	0.0767411189
C	3.0134733747	0.0722643475	0.0660645803
C	3.8174779141	1.1802038454	0.4134099132
C	3.2545509159	2.4366517970	0.7958784890
C	4.0486021930	3.5005995796	1.1298867025
C	5.4628542807	3.3778639166	1.1041525026
C	6.0454421913	2.1887303487	0.7587246344
C	5.2522500757	1.0538797947	0.4107390701
C	5.8133771359	-0.1921964762	0.0778417467
Cl	7.5402807022	-0.3556872099	0.0899828409
C	5.0314404396	-1.3098581988	-0.2637282821
C	3.5962747078	-1.1670409539	-0.2823693843
C	2.8154816164	-2.2973082618	-0.6792732910
C	3.4034743525	-3.4899703251	-1.0040376147
C	4.8152430962	-3.6335689478	-0.9565419917
C	5.6040797182	-2.5733355658	-0.6022440181
C	0.5541999029	-0.3530564445	0.8199434998

N	-2.6143963304	1.3536253926	-0.9701831430
C	-3.6374505367	1.9448612601	-1.5929916436
C	-3.4541290576	2.8571191153	-2.6283300690
C	-2.1597338454	3.1685640488	-3.0371295591
C	-1.0865782153	2.5595275226	-2.3952012087
C	-1.3586727166	1.6597290071	-1.3679140186
C	-4.7055786235	-0.4118771303	0.5806861165
O	-5.8514052918	-0.5281184380	0.5193718663
C	-2.6999418955	-1.6020275561	1.9474164822
O	-2.6143126781	-2.4474323909	2.7261822586
H	2.1696446678	2.5457887805	0.8262529220
H	3.5924732045	4.4492666207	1.4219428158
H	6.0867163731	4.2345860791	1.3682997518
H	7.1310754284	2.0883310281	0.7478054437
H	1.7300512076	-2.2003819524	-0.7327946707
H	2.7820383365	-4.3356185549	-1.3070792406
H	5.2722743159	-4.5920320856	-1.2124489834
H	6.6891230285	-2.6767424968	-0.5759070431
H	0.6262166399	-1.0651302715	1.6377865207
H	-4.6385218644	1.6752304650	-1.2518722515
H	-4.3248539105	3.3100184877	-3.1043008956
H	-1.9866347047	3.8781234479	-3.8485816592
H	-0.0531151701	2.7660938197	-2.6765484317

7.5.22 ***fac*-[Re(16)(CO)$_3$Br]**

Br	2.5881168029	-0.5542662618	-2.3213223394
Re	3.1639397438	0.5186532569	0.0249739581
C	3.5119452342	1.2295175308	1.7661157774
O	3.7309198267	1.6613048969	2.8173211898
N	0.9830388788	0.5305291291	0.2887997087
C	0.4817982699	-0.6167885330	0.6695204068
O	-0.8418869229	-0.5965870079	0.7445521469
C	-1.2313704236	0.6628048411	0.3783458127
C	-2.6348934751	1.0467892699	0.4033431762
C	-2.9150120862	2.3766051966	0.7614162678

C	-4.2132923587	2.8518340268	0.8225611437
C	-5.2973727887	2.0086028985	0.5358853708
C	-6.6518070922	2.4709442211	0.6180698774
C	-7.6966721468	1.6460492048	0.3354263973
C	-5.0412321706	0.6578153668	0.1551843512
C	-6.1402483099	-0.1993330416	-0.1542367334
C	-7.4787419438	0.2855552285	-0.0622875214
C	-8.5423555881	-0.5780652553	-0.3661494137
C	-8.3044110563	-1.8928047381	-0.7588675545
C	-7.0017591240	-2.3729071316	-0.8590983693
C	-5.9087677836	-1.5438548039	-0.5623858087
C	-4.5551457989	-1.9971695751	-0.6695813681
C	-3.5038387262	-1.1858463773	-0.3680112163
C	-3.7004316258	0.1669301056	0.0745026274
C	-0.0859783553	1.3630858746	0.0923924382
N	2.6286111150	-1.5130240984	0.8076053893
C	3.4957635032	-2.4958318908	1.0644371128
C	3.0900619064	-3.7567416265	1.4921456233
C	1.7308230178	-4.0106628913	1.6602623119
C	0.8184728264	-2.9947139791	1.3970980782
C	1.3089338691	-1.7620424993	0.9713974301
C	5.0440029319	0.2145538005	-0.2347081194
O	6.1674518285	0.0043186310	-0.3896506985
C	3.3632107616	2.2713450976	-0.7379398713
O	3.4536001820	3.3234822005	-1.2002784685
H	-2.0895266405	3.0408492092	1.0257389498
H	-4.4016258021	3.8872051077	1.1155885036
H	-6.8278426003	3.5077450013	0.9151500151
H	-8.7246464469	2.0111769223	0.4032478216
H	-9.5666525829	-0.2037752059	-0.2927168313
H	-9.1452227335	-2.5499969406	-0.9926661416
H	-6.8170955932	-3.4033805558	-1.1731242799
H	-4.3735356048	-3.0197578885	-1.0102647604
H	-2.4914653957	-1.5717644831	-0.4746376096
H	0.0253462597	2.3858668190	-0.2567517077
H	4.5524947110	-2.2646376441	0.9192730887

H	3.8402332908	-4.5243206973	1.6865671606
H	1.3837064287	-4.9906252661	1.9936580081
H	-0.2560547067	-3.1409664361	1.5147543703

7.5.23 *fac*-[Re(17)(CO)$_3$Br]

Br	-2.4770975995	0.9508987349	2.0907020224
Re	-2.6305968366	0.4102373900	-0.4919328946
C	-2.6840061948	-0.0654372646	-2.3437973950
O	-2.7247705409	-0.3499883068	-3.4648072556
N	-0.4767229774	0.0279479804	-0.2925814604
C	-0.1802264121	-1.1579148432	0.1731093745
O	1.1216250238	-1.3264869734	0.3501125370
C	1.7203612056	-0.1534163299	-0.0229890519
C	3.1772016919	-0.1113385354	-0.0012081341
C	3.8551090284	-1.2781299240	-0.2441392119
C	5.2772084277	-1.3299586723	-0.3212390495
C	5.9349543824	-2.5534238975	-0.5886849475
C	7.3088724615	-2.6066884146	-0.6962765696
C	8.0621580167	-1.4289819998	-0.5418204213
C	7.4375933357	-0.2236319694	-0.2793910734
C	6.0331790916	-0.1373183396	-0.1573067677
C	5.3339195659	1.1031819069	0.1394802328
C	3.9109953751	1.1163382789	0.2419390047
C	3.2658569722	2.3180199402	0.6137008952
C	3.9783790016	3.4807559688	0.8309900159
C	5.3740500370	3.4807194608	0.6877895197
C	6.0317944465	2.3118137393	0.3589652589
C	0.7154997043	0.6897642662	-0.4267597746
N	-2.4428332641	-1.7169139124	0.1931536806
C	-3.4625055676	-2.5509310759	0.4128924679
C	-3.2792710958	-3.8423042470	0.8992279619
C	-1.9879253944	-4.2876234892	1.1713674803
C	-0.9181188950	-3.4280300906	0.9462967823
C	-1.1895212802	-2.1522478877	0.4571930369
C	-4.5487170843	0.5310379912	-0.4595370638

O	-5.7004429407	0.5810718550	-0.4228817000
C	-2.5430343761	2.2708210110	-0.9649362187
O	-2.4619850922	3.3875268882	-1.2394337931
H	3.2975798546	-2.2006673747	-0.4193198114
H	5.3333084192	-3.4577292671	-0.7114502498
H	7.8100489458	-3.5550676521	-0.9026319525
H	9.1506030898	-1.4642253025	-0.6293797861
H	8.0535594163	0.6688349954	-0.1659026170
H	2.1865290244	2.3272148599	0.7631530062
H	3.4539057818	4.3932459529	1.1230944854
H	5.9437885196	4.3980069074	0.8527051942
H	7.1189263664	2.3293490210	0.2788631033
H	0.7750665473	1.6983757288	-0.8244803266
H	-4.4612016676	-2.1689002371	0.1942838777
H	-4.1474201787	-4.4822297623	1.0622756779
H	-1.8149848427	-5.2943714014	1.5566353014
H	0.1121134228	-3.7257760601	1.1454285048

7.5.24 *fac*-[Re(18)(CO)$_3$Br]

Br	2.8030874077	-0.3309462074	2.3388728772
Re	3.0577014501	-0.5524661279	-0.2818640074
C	3.1771503141	-0.6348595696	-2.1892707074
O	3.2578892145	-0.6883130876	-3.3424302001
N	0.8718530111	-0.3195362048	-0.2788484048
C	0.4633166543	0.9216829617	-0.2018190161
O	-0.8573354048	1.0213894677	-0.1416389858
C	-1.3415169979	-0.2543912461	-0.1770032504
C	-2.7783852410	-0.4478128422	-0.1288290571
C	-3.3148001383	-1.7480929012	-0.1259237033
C	-4.6914591542	-1.9712717907	-0.0865022386
C	-5.5451647262	-0.8735517969	-0.0494070243
C	-7.0178678074	-0.7732492205	-0.0062839853
C	-8.0056732182	-1.7503217798	0.0095940021
C	-9.3449000800	-1.3401901548	0.0514128583
C	-9.6907322026	0.0130309292	0.0766676353

C	-8.6966036533	0.9978676466	0.0605736085
C	-7.3723587508	0.5892794570	0.0192775814
C	-6.1302977146	1.4174975844	-0.0068458122
O	-6.0411209302	2.6235031738	0.0029209900
C	-5.0076685664	0.4262741254	-0.0500675665
C	-3.6472480463	0.6602817189	-0.0879587343
C	-0.2583734776	-1.0922030198	-0.2620853340
N	2.6740116408	1.6563925660	-0.2650376872
C	3.6153919753	2.6037215455	-0.2681202466
C	3.3097267735	3.9601438408	-0.2007130558
C	1.9752932094	4.3518179129	-0.1253630321
C	0.9860461294	3.3743421258	-0.1213464252
C	1.3784542073	2.0395348939	-0.1918934530
C	4.9748772487	-0.4905359525	-0.1573382262
O	6.1234526487	-0.4282228628	-0.0738042098
C	3.1355948535	-2.4701973033	-0.1872117539
O	3.1531677702	-3.6210886896	-0.1228656507
H	-2.6428673660	-2.6085896424	-0.1526448795
H	-5.0757281798	-2.9932724210	-0.0844875832
H	-7.7553952062	-2.8134240378	-0.0097303247
H	-10.1345994302	-2.0953199297	0.0644882392
H	-10.7438268623	0.3011821352	0.1091806703
H	-8.9465901945	2.0613410536	0.0797742299
H	-3.2624973954	1.6819581753	-0.0874382875
H	-0.2222812123	-2.1768739904	-0.3089136402
H	4.6507161394	2.2631012628	-0.3243406640
H	4.1176964325	4.6929023105	-0.2055658257
H	1.7066425352	5.4085005846	-0.0698153905
H	-0.0732258514	3.6276497991	-0.0627680249

7.5.25 *fac*-[Re(19)(CO)$_3$Br]

Br	2.4695164639	-0.3408165821	2.3459723028
Re	2.6855041632	-0.6252640945	-0.2741699047
C	2.7884741526	-0.7487168615	-2.1793476928
O	2.8595086468	-0.8280398900	-3.3321034815

N	0.5366977107	-0.1758385155	-0.2731736852
C	0.2548641977	1.1012621155	-0.2178606495
O	-1.0532881216	1.3307656834	-0.1627445694
C	-1.6636407433	0.1085003649	-0.1797607393
C	-3.1042770350	0.0506822360	-0.1308995402
C	-3.8857256129	1.2189214504	-0.0833782759
C	-5.2671235325	1.1609822665	-0.0400382472
C	-5.9472460047	-0.0834791302	-0.0398309920
N	-7.3015745257	-0.1486838865	0.0026467882
C	-8.1630600451	1.0138829673	0.1475893221
C	-9.5319340071	0.4107314918	0.4445645218
C	-9.4915452446	-0.9205700597	-0.2986625506
C	-8.0553607355	-1.3890198971	-0.0903791179
C	-5.1538368683	-1.2594128997	-0.0856547296
C	-3.7746430776	-1.1868129777	-0.1302040733
C	-0.6622125490	-0.8338788736	-0.2488059966
N	2.5282148425	1.6099989757	-0.2890358958
C	3.5595795916	2.4589857898	-0.3041317595
C	3.3926031158	3.8393982703	-0.2568437385
C	2.1025125063	4.3625322432	-0.1888941866
C	1.0211236779	3.4898776450	-0.1721907805
C	1.2754559599	2.1194539717	-0.2232595197
C	4.5997971843	-0.7531757404	-0.1546372148
O	5.7497504030	-0.8032106572	-0.0749060112
C	2.5689258845	-2.5392127694	-0.1484432262
O	2.4700904624	-3.6851006371	-0.0650709311
H	-3.3961023848	2.1949732321	-0.0849066566
H	-5.8334554421	2.0921801149	-0.0150097643
H	-8.1767176326	1.6161427549	-0.7813478755
H	-7.8102399787	1.6716975880	0.9587394954
H	-10.3569322288	1.0648702020	0.1297512828
H	-9.6367607311	0.2374119757	1.5277726747
H	-9.6808020864	-0.7614014984	-1.3725576915
H	-10.2285121918	-1.6497473650	0.0656993544
H	-7.6933783891	-2.0129770138	-0.9238974308
H	-7.9527908993	-1.9865515815	0.8359115967

H	-5.6299515094	-2.2399631746	-0.0748549361
H	-3.2037390188	-2.1179871983	-0.1589367097
H	-0.7329302088	-1.9171146998	-0.2785710694
H	4.5553837170	2.0147971929	-0.3537953119
H	4.2697438296	4.4875107180	-0.2711878694
H	1.9404394976	5.4415320905	-0.1485525632
H	-0.0073850282	3.8487723430	-0.1185897453

7.6 Predicted % contribution from Br p-orbitals in the HOMO-X states

Table 7.48 Predicted % contribution from Br p-orbitals for ***fac*-[Re(14)(CO)$_3$Br]**

	p_x / %	**p_y / %**	**p_z / %**	**Total / %**
HOMO-4	0.47167	0.46747	0.00603	0.94517
HOMO-3	2.35050	0.04281	0.26960	2.66291
HOMO-2	3.46933	0.01710	0.27706	3.76350
HOMO-1	16.12155	29.44549	0.82462	46.39167
HOMO	26.87443	15.99974	0.02034	42.89450

Table 7.49 Predicted % contribution from Br p-orbitals for ***fac*-[Re(15)(CO)$_3$Br]**

	p_x / %	**p_y / %**	**p_z / %**	**Total / %**
HOMO-4	33.51691	1.88294	3.70291	39.10276
HOMO-3	0.27219	0.18092	0.32582	0.77893
HOMO-2	23.29880	14.99091	7.17926	45.46897
HOMO-1	19.23682	10.21588	12.16740	41.62011
HOMO	0.69940	1.06087	0.71647	2.47674

Table 7.50 Predicted % contribution from Br p-orbitals for ***fac*-[Re(16)(CO)$_3$Br]**

	p_x / %	**p_y / %**	**p_z / %**	**Total / %**
HOMO-4	2.80090	0.63921	0.32825	3.76836
HOMO-3	0.46806	0.26234	0.02766	0.75805
HOMO-2	28.89903	10.77769	6.98893	46.66566
HOMO-1	13.21546	26.26624	2.28257	41.76426
HOMO	2.25972	1.88038	0.22564	4.36574

Table 7.51 Predicted % contribution from Br p-orbitals for ***fac*-[Re(17)(CO)$_3$Br]**

	p_x / %	**p_y / %**	**p_z / %**	**Total / %**
HOMO-4	0.39292	0.31738	0.09360	0.80390
HOMO-3	0.05598	0.00211	0.00902	0.06710
HOMO-2	5.25115	0.15030	0.25693	5.65838
HOMO-1	19.15103	25.85944	0.99844	46.00891
HOMO	22.68895	17.88844	1.03940	41.61679

Table 7.52 Predicted % contribution from Br p-orbitals for ***fac*-[Re(18)(CO)$_3$Br]**

	p_x / %	**p_y / %**	**p_z / %**	**Total / %**
HOMO-4	38.49922	3.43116	3.22022	45.15060
HOMO-3	0.43211	0.30667	0.01831	0.75708
HOMO-2	5.49063	0.38289	0.35663	6.23015
HOMO-1	23.31584	22.73245	0.48452	46.53280
HOMO	19.76627	22.68636	0.01003	42.46265

Table 7.53 Predicted % contribution from Br p-orbitals for ***fac*-[Re(19)(CO)$_3$Br]**

	p_x / %	**p_y / %**	**p_z / %**	**Total / %**
HOMO-4	26.60078	0.34400	2.94253	29.88730
HOMO-3	0.32043	0.37147	0.02137	0.71327
HOMO-2	19.65393	26.60973	0.51182	46.77548
HOMO-1	25.11160	18.75460	0.02331	43.88951
HOMO	0.04883	0.17105	0.02902	0.24890